

DIAMOND
AND
RELATED
MATERIALS

**INTERNATIONAL JOURNAL
ON THE SCIENCE AND TECHNOLOGY
OF DIAMOND AND RELATED MATERIALS**

Editor-in-Chief
R. Messier

Associate Editors

J. C. Angus
T. R. Anthony
P. K. Bachmann
A. M. Bonnot
I. Buckley-Golder
A. T. Collins
R. F. Davis
K. Y. Eun
O. Fukunaga
J. T. Glass
A. Grill
S.-T. Lee
H. Matsunami
Y. Sato
M. N. Yoder

Guest Editor

K. Zekentes

**Proceedings of
ECSCRM 1996,
the 1st European
Conference on
Silicon Carbide and
Related Materials,
6-9 October 1996,
Heraklion, Greece**

DISTRIBUTION STATEMENT A

Approved for public release;
Distribution Unlimited

DTIC QUALITY IMPROVED 3



ELSEVIER

19971121 100

DIAMOND AND RELATED MATERIALS

Editor-in-Chief

R. Messier, 265 Materials Research Laboratory, Pennsylvania State University, University Park, PA 16802-4801, USA.
Tel: (1-814) 865-3704 or 865-3423. Fax: (1-814) 863-7039. e-mail: rfm2@psuvm.psu.edu

Associate Editors

J. C. Angus, Chemical Engineering Department, Case Western Reserve University, Cleveland, OH 44106, USA.
Tel: (1-216) 368-4133. Fax: (1-216) 368-3016. e-mail: jca3@po.cwru.edu.

T. R. Anthony, GE Corporate R&D, One Research Circle, Bldg. K-1, Room 1C30, Schenectady, NY 12309, USA.
Tel: (1-518) 387-6160. Fax: (1-518) 387-7563. e-mail: anthony@crdgw2.crd.ge.com

P. K. Bachmann, Philips GmbH, Research Laboratories Aachen, Postfach 1980, Weissausstrasse, 52066 Aachen, Germany.
Tel and fax: (49) 241 6003314. e-mail: bachmann@pfa.philips.de

A. M. Bonnot, Centre National de la Recherche Scientifique/LEPES, BP 166X, 38042 Grenoble Cedex 9, France.
Tel: (33) 76 88 79 93. Fax: (33) 76 88 79 88. e-mail: bonnot@lepes.polycnrs.gre.fr

I. Buckley-Golder, AEA Technology, Surface Science & Technology, Harwell Laboratory, Bldg. 552, Didcot, Oxon, OX11 0RA, UK.
Tel: (44) 1235 434 574. Fax: (44) 1235 432 697. e-mail: ian.buckley-golder@aea.org.uk

A. T. Collins, Wheatstone Physics Laboratory, King's College London, Strand, London WC2R 2LS, UK.
Tel: (44) 171 873 2584. Fax: (44) 171 873 2160. e-mail: act@maxwell.ph.kcl.ac.uk

R. F. Davis, North Carolina State University, Materials Research Center, Campus Box 7919, Raleigh, NC 27695-7919, USA.
Tel: (1-919) 515-2377. Fax: (1-919) 515-7724. e-mail: davis@mat.mte.ncsu.edu

K. Y. Eun, Division of Ceramics, Korea Institute of Science and Technology (KIST), PO Box 131, Cheongryang, Seoul 130-650, South Korea.
Tel: (82) 2-958-5491. Fax: (82) 2-958-5509. e-mail: kyeun@kistmail.kist.re.kr

O. Fukunaga, Ace-Tech Co. Ltd., 1-167-1, Higashi Ome, Ome 198, Japan.
Tel: (81) 428 21 1225. Fax: (81) 428 20 7341. e-mail: ofukunag@o.cc.titech.ac.jp

J. T. Glass, Materials Science and Engineering (NCSU), Kobe Steel USA, Inc., 79 Alexander Drive, P.O. 13608, 4401 Bldg.-Suite 101, Research Triangle Park, NC 27709, USA.
Tel: (1-919) 549-9823. Fax: (1-919) 549-8460. e-mail: 76376.2310@compuserve.com

A. Grill, IBM, Thomas J. Watson Research Center, P.O. Box 218, Yorktown Heights, NY 10598
Tel: 914 945 1492. Fax: 914 945 2141. e-mail: agrill@watson.ibm.com

S.-T. Lee, Department of Physics, City University of Hong Kong, 83 Tat Chee Avenue, Kowloon, Hong Kong.
Tel: (852) 2788 9606. Fax: (852) 2788 7830. e-mail: apannale@cityu.edu.hk

H. Matsunami, Kyoto University, Department of Electrical Engineering, Yoshida Honmachi, Sakyo-ku, Kyoto 606-01, Japan.
Tel: (81) 75-753 5340. Fax: (81) 75-75 1576. e-mail: matsunam@kuee.kyoto-u.ac.jp

Y. Sato, National Institute for Research in Inorganic Materials, 1-1 Namiki, Tsukuba, Ibaraki 305, Japan.
Tel: (81) 298-51-3351. Fax: (81) 298-52-7449

M. N. Yoder, Electronics Division, Office of Naval Research, 800 N Quincy Street, Arlington, VA 22217-5660, USA.
Tel: (1-703) 696-4216. Fax: (1-703) 696-2611. e-mail: yoderm@onrhq.onr.navy.mil

Types of Contributions

- original papers
- invited or contributed reviews on specific topics
- Letters on topics requiring rapid publication. These should be no longer than 2000 words (allowing approximately 350 words per figure or table).
- notices of meetings, symposia and short courses

Scope

Diamond and Related Materials is an international, interdisciplinary journal which publishes articles covering both basic and applied research on diamond materials and related materials. These include cubic boron nitride and materials with characteristics and properties approaching or possibly exceeding those of diamond. The primary emphasis is on vapour-deposited materials; also important are high-temperature/high-pressure synthetic materials, as well as relevant natural diamond research and characterization. Papers published cover all fundamental and technological aspects of synthesis, characterization, properties, devices and generic applications of these materials.

Frequency

One volume per year, in 12 issues.

Abstracting/Indexing Services

This journal is cited by the following services:

ASM International (Non-Ferrous Metals Alerts), Cambridge Scientific Abstracts, Chemical Abstracts, Engineering Information Inc., FIZ Karlsruhe, Geo Abstracts, GEOBASE, INSPEC, Institute for Scientific Information (Current Contents/Engineering, Technology and Applied Science, Research Alert, Materials Science Citation Index, Science Citation Index, SciSearch), Materials Information (Metals Abstracts, Engineered Materials Abstracts), PASCAL/Centre National de Recherche Scientifique, Surface Treatment Technology Abstracts, Tribology and Corrosion Abstracts. Pre-publication abstracts of articles in *Diamond and Related Materials* and other related journals are now available weekly in electronic form via CoDAS, a new direct alerting service in condensed matter and materials science run jointly by Elsevier Science and Institute of Physics Publishing. For details on a free one-month subscription contact Paul Bancroft on fax +44 1179 294318 or e-mail bancroft@ioppublishing.co.uk.

Advertising Information

Advertising orders and enquiries may be sent to:

International: Elsevier Science, Advertising Department, The Boulevard, Langford Lane, Kidlington, Oxford OX5 1GB, UK. Tel.: +44 (1865) 843 565. Fax: +44 (1865) 843 952. **USA and Canada:** Weston Media Associates; Dan Lipner, P.O. Box 1110, Greens Farms, CT 06436-1110, USA. Tel.: +1 (203) 261 2500. Fax: +1 (203) 261 0101. **Japan:** Elsevier Science Japan, 9-15 Higashi-Azabu 1-chome, Minato-ku, Tokyo 106; Tel: +81-3-5561-5032; Fax: +81-5561-5045.

Subscription Information 1997

Volume 6, containing 12 issues, is scheduled for publication. Prices are available from the publishers upon request. Subscriptions are accepted on a prepaid basis only. Issues are sent by SAL (Surface Air Lifted) mail wherever this service is available. Airmail rates are available upon request. Please address all requests regarding orders and subscription queries to:

ELSEVIER SCIENCE S.A., P.O. Box 564, 1001 Lausanne, Switzerland.

Telephone: +41 21 320 73 81; Telex: 450 620 ELSA CH;
Telefax: +41 21 323 54 44.

Customers in Japan may obtain information from:

Elsevier Science Japan
Customer Support DTP, 9-15, Higashi-Azabu 1-chome, Minato-ku, Tokyo 106, Japan.
Telephone: 81 35561 5033; Fax: 81 35561 5047;
E-mail: kyfo4035@niftyserve.or.jp

US and Canadian customers may obtain information from:
ELSEVIER SCIENCE INC.,

Attn: Journal Information Center, 655 Avenue of the Americas, New York, NY 10010, USA.
Telephone: (212) 633-3750; Telex: 420-643 AEP UI;
Telefax: (212) 633-3764.

US mailing notice — *Diamond and Related Materials* (ISSN 0925-9635) is published monthly by Elsevier Science S.A. (PO Box 564, 1001 Lausanne). Annual subscription price in the USA is US\$1303 (valid in North, Central and South America), including air speed delivery. Second class postage rate is paid at Jamaica, NY 11431.

USA POSTMASTER: Send address changes to *Diamond and Related Materials* Publications Expediting, Inc., 200 Meacham Avenue, Elmont, NY 11003.

AIRFREIGHT AND MAILING in the USA by Publications Expediting Inc., 200 Meacham Avenue, Elmont, NY 11003.



ELSEVIER

Volume 6, Number 10, August 1997

**DIAMOND
AND
RELATED
MATERIALS**

Contents

Proceedings of the 1st European Conference on Silicon Carbide and Related Materials (ECSCRM 1996)

Guest Editor: K. Zekentes

Preface	xxxix
Organizers and Sponsors	xxxxi
Progress in the study of optical and related properties of SiC since 1992	1243
W.J. Choyke and R.P. Devaty	
<i>SiC bulk growth</i>	
Defects formation in sublimation grown 6H-SiC single crystal boules*	1249
R. Madar, M. Anikin, K. Chourou, M. Labeau, M. Pons, E. Blanquet, J.M. Dedulle, C. Bernard, S. Milita and J. Baruchel	
Sublimation growth of 4H- and 6H-SiC boule crystals	1262
V.D. Heydemann, N. Schulze, D.L. Barrett and G. Pensl	
Growth of SiC from the liquid phase: wetting and dissolution of SiC	1266
M. Syväjärvi, R. Yakimova and E. Janzén	
The kinetic growth model applied to micropipes in 6H-SiC	1269
J. Heindl, W. Dorsch, R. Eckstein, D. Hofmann, T. Marek, S. Müller, H.P. Strunk and A. Winnacker	
Growth-related structural defects in seeded sublimation-grown SiC	1272
M. Tuominen, R. Yakimova, E. Prieur, A. Ellison, T. Tuomi, A. Vehanen and E. Janzén	
<i>SiC epitaxial growth</i>	
Surface polarity dependence in step-controlled epitaxy: progress in SiC epitaxy*	1276
H. Matsunami and T. Kimoto	
Growth and doping via gas-source molecular beam epitaxy of SiC and SiC/AlN heterostructures and their microstructural and electrical characterization*	1282
R.S. Kern, K. Järrendahl, S. Tanaka and R.F. Davis	
High quality 4H-SiC grown on various substrate orientations	1289
A. Henry, I.G. Ivanov, T. Egilsson, C. Hallin, A. Ellison, O. Kordina, U. Lindefelt and E. Janzén	
Hydrogen incorporation in epitaxial layers of 4H- and 6H-silicon carbide grown by vapor phase epitaxy	1293
A. Schöner, K. Rottner, N. Nordell, M. Linnarsson, C. Peppermüller and R. Helbig	
The origin of 3C polytype inclusions in epitaxial layers of silicon carbide grown by chemical vapour deposition	1297
C. Hallin, A.O. Konstantinov, B. Pécz, O. Kordina and E. Janzén	
SiC and group III nitride growth in MOVPE production reactors	1301
R. Beccard, D. Schmitz, E.G. Woelk, G. Strauch and H. Jürgensen	
Growth of SiC films obtained by LPCVD	1306
M.T. Clavaguera-Mora, J. Rodríguez-Viejo, Z. El Felk, E. Hurtós, S. Berberich, J. Stoemenos and N. Clavaguera	
Chemical conversion of Si to SiC by solid source MBE and RTCVD	1311
J. Pezoldt, V. Cimalla, T. Stauden, G. Ecke, G. Eichhorn, F. Scharmann and D. Schipanski	

* Invited papers.

Hexagonal and cubic SiC thin films on SiC deposited by solid source MBE	1316
A. Fissel, K. Pfennighaus, U. Kaiser, B. Schröter and W. Richter	
Hydrogen-, boron-, and hydrogen-boron-related low temperature photoluminescence of 6H-SiC	1321
C. Peppermüller, A. Schöner, K. Rottner and R. Helbig	
<i>SiC characterization: Crystal structure and defects: Optical and electrical properties</i>	
Carrier lifetimes in SiC, studied by time resolved photoluminescence spectroscopy*	1324
J.P. Bergman	
Analysis of transport properties of β -SiC films: determination of donor density and compensation ratio	1329
S. Contreras, C. Dezauzier, P. Thomas and J.L. Robert	
Radiation-induced defect centers in 4H silicon carbide	1333
T. Dalibor, G. Pensl, T. Kimoto, H. Matsunami, S. Sridhara, R.P. Devaty and W.J. Choyke	
Thermal properties of β -SiC epitaxial layers between 150 °C and 500 °C measured by using microstructures	1338
C. Wagner and G. Krötz	
Valence band dispersion of hexagonal SiC	1342
G. Wellenhofer and U. Rössler	
Polytypism and surface structure of SiC	1346
P. Käckell, J. Furthmüller and F. Bechstedt	
Structure and morphology of SiC surfaces studied by LEED, AES, HREELS and STM	1349
U. Starke, J. Bernhardt, M. Franke, J. Schardt and K. Heinz	
Investigation of modified 3C SiC(100) surfaces by surface-sensitive techniques	1353
T. Balster, F.S. Tautz, H. Ibach and J.A. Schaefer	
Angle resolved photoemission and the band structure of 6H-SiC	1358
M. Hollering, A. Ziegler, R. Graupner, B. Mattern, L. Ley, A.P.J. Stampfl, J.D. Riley and R.C.G. Leckey	
Topology of twin junctions in epitaxial β -SiC	1362
V. Papaioannou, P. Komninou, G.P. Dimitrakopoulos, K. Zekentes, B. Pecz, T. Karakostas and J. Stoemenos	
Micropipe defects and voids at β -SiC/Si(100) interfaces	1365
R. Scholz, U. Gösele, E. Niemann, D. Leidich and F. Wischmeyer	
Wafer warpage, crystal bending and interface properties of 4H-SiC epi-wafers	1369
A. Ellison, H. Radamson, M. Tuominen, S. Milita, C. Hallin, A. Henry, O. Kordina, T. Tuomi, R. Yakimova, R. Madar and E. Janzén	
Nonlinear optical mapping of 3C-inclusions in 6H-SiC-epilayers	1374
C. Meyer, G. Lüpke, E. Stein von Kamienski, A. Götz and H. Kurz	
Deep luminescent centres in electron-irradiated 6H SiC	1378
N.T. Son, E. Sörman, M. Singh, W.M. Chen, C. Hallin, O. Kordina, B. Monemar, J.L. Lindström and E. Janzén	
Optically detected magnetic resonance studies of defects in 3C SiC epitaxial layers	1381
N.T. Son, E. Sörman, W.M. Chen, C. Hallin, O. Kordina, B. Monemar and E. Janzén	
Optical investigation of thick 3C-SiC layers deposited on bulk silicon by CVD	1385
J.M. Bluet, J. Camassel, L.A. Falkovsky and A. Leycuras	
Characterization of electrically active deep level defects in 4H and 6H SiC	1388
J.P. Doyle, M.O. Aboelfotoh, B.G. Svensson, A. Schöner and N. Nordell	
High field/high temperature performance of semi-insulating silicon carbide	1392
T.S. Sudarshan, G. Gradinaru, G. Korony, S.A. Gradinaru and W. Mitchel	
OBIC studies on 6H-SiC Schottky rectifiers with different surface pretreatments	1396
M. Frischholz, K. Rottner, A. Schöner, T. Dalibor and G. Pensl	
<i>SiC processing: Oxidation, metallization, ion implantation and etching</i>	
SiC device technology: remaining issues*	1400
J.W. Palmour, L.A. Lipkin, R. Singh, D.B. Slater, Jr, A.V. Suvorov and C.H. Carter, Jr	

* Invited papers.

Silicon carbide for microwave power applications*	1405
C. Brylinski	
Aluminium implantation of <i>p</i> -SiC for ohmic contacts	1414
L. Spie, O. Nennowitz, H. Weishart, J. Lindner, W. Skorupa, H. Romanus, F. Erler and J. Pezoldt	
Fabrication of high-quality oxides on SiC by remote PECVD	1420
A. Gölz, S. Groß, R. Janssen, E. Stein von Kamienski and H. Kurz	
An interface study of vapor-deposited rhenium with the two (0001) polar faces of single crystal 6H-SiC	1424
S. Kennou, A. Siokou, I. Dontas and S. Ladas	
TEM study of Ni and Ni ₂ Si ohmic contacts to SiC	1428
B. Pécz, G. Radnócz, S. Cassette, C. Brylinski, C. Arnodo and O. Noblanc	
Ion beam assisted deposition of a tungsten compound layer on 6H-silicon carbide	1432
H. Weishart, V. Heera, W. Matz and W. Skorupa	
Hafnium, cadmium and indium impurities in 4H-SiC observed by perturbed angular correlation spectroscopy	1436
T. Licht, N. Achtinger, D. Forkel-Wirth, K. Freitag, J. Grillenberger, M. Kaltenhäuser, U. Reislöhner, M. Rüb, M. Uhrmacher, W. Witthuhn and ISOLDE Collaboration	
Nuclear transmutation doping of 6H-silicon carbide with phosphorous	1440
H. Heissenstein, C. Peppermüller and R. Helbig	
Investigation of the effects of high temperature implantation and post implantation annealing on the electrical behavior of nitrogen implanted β -SiC films	1445
W. Reichert, R. Lossy, M. González Sirgo, E. Obermeier and W. Skorupa	
β -SiC films on SOI substrates for high temperature applications	1448
W. Reichert, E. Obermeier and J. Stoemenos	
Surface chemistry of 6H-SiC(0001̄) after reactive ion etching	1451
N. Sieber, M. Hollering and L. Ley	
Preferential etching of SiC crystals	1456
R. Yakimova, A.-L. Hylén, M. Tuominen, M. Syväjärvi and E. Janzén	
Schottky contact investigation on reactive ion etched 6H α -SiC	1459
G. Constantinidis, J. Kuzmik and K. Michelakis	
Comparative investigation of ECR-RIE patterns on Si and C faces of 6H-SiC using a CF ₄ /O ₂ gas mixture	1463
R. Bonnot, A.L. Syrkin, G. Lévéque, J.M. Bluet and J. Camassel	
Anisotropic oxidation of silicon carbide	1467
K. Christiansen, S. Christiansen, M. Albrecht, H.P. Strunk and R. Helbig	
“Carbon cluster model” for electronic states at SiC/SiO ₂ interfaces	1472
M. Bassler, G. Pensl and V. Afanas'ev	
<i>SiC-based devices and applications</i>	
Investigation of walk-out phenomena in SiC mesa diodes with SiO ₂ /Si ₃ N ₄ passivation	1476
Z. Ovuka and M. Bakowski	
Overview of SiC power electronics*	1480
V.E. Chelnokov, A.L. Syrkin and V.A. Dmitriev	
2.5 kV ion-implanted <i>p</i> ⁺ <i>n</i> diodes in 6H-SiC	1485
K.H. Rottner, A. Schöner, S.M. Savage, M. Frischholz, C. Hallin, O. Kordina and E. Janzén	
High field and high temperature stress of n-SiC MOS capacitors	1489
E. Bano, T. Ouisse, C. Leonhard, A. Gölz and E.G. Stein Von Kamienski	
Low frequency noise in silicon carbide Schottky diodes	1494
L. Anghel, T. Ouisse, T. Billon, P. Lassagne and C. Jaussaud	
Passivation of interface traps in MOS-Devices on <i>n</i> - and <i>p</i> -type 6H-SiC	1497
E.G. Stein von Kamienski, C. Leonhard, S. Scharnholz, A. Gölz and H. Kurz	

Numerical study of avalanche breakdown of 6H-SiC planar <i>p–n</i> junctions	1500
E. Stefanov, L. Bailon and J. Barbolla	
Temperature dependence of electrical properties of 6H-SiC buried gate JFET	1504
C. Raynaud, C. Richier and G. Guillot	
Microwave Power MESFET on 4H-SiC	1508
O. Noblanc, E. Chartier, C. Arnodo and C. Brylinski	
The potential of SiC and GaN for application in high speed devices	1512
F. Schwierz, M. Kittler, H. Förster and D. Schipanski	
<i>Nitrides growth and characterization</i>	
Thermodynamics and high-Pressure growth of (Al, Ga, In)N single crystals*	1515
S. Krukowski	
Residual strains in GaN grown on 6H-SiC	1524
I.P. Nikitina, M.P. Sheglov, Y. Melnik, K.G. Irvine and V.A. Dmitriev	
Structural and electrical properties of Schottky barriers on n-GaN	1528
E.V. Kalinina, N.I. Kuznetsov, A.I. Babanin, V.A. Dmitriev and A.V. Shchukarev	
Structural properties of GaN grown on SiC substrates by hydride vapor phase epitaxy	1532
Y. Melnik, I.P. Nikitina, A.E. Nikolaev and V.A. Dmitriev	
Contactless characterisation of 2D-electrons in GaN/AlGaN HFETs	1536
H. Alause, C. Skierbiszewski, M. Dyakonov, W. Knap, M.L. Sadowski, S. Huant, J. Young, M. Asif Khan and Q. Chen	
Identification of the cubic and hexagonal polytypes of GaN with X-ray absorption measurements	1539
M. Katsikini, E.C. Paloura, T.S. Cheng and C.T. Foxon	
<i>Amorphous SiC and other SiC-related materials</i>	
Colour sensing applications of hydrogenated amorphous silicon carbide*	1542
G. Müller	
Surface and bulk effects in ex-situ hydrogenated α -SiC thin films	1547
J. Kalomiros, E.C. Paloura, C. Janowitz, B. Theys and A. Anagnostopoulos	
Optical study of boron nitride thin films prepared by plasma-enhanced chemical vapor deposition	1550
M.C. Polo, M. Ben el Mekki, J.L. Andújar, N. Mestres and J. Pascual	
Electrical properties of PECVD amorphous silicon–carbon alloys from amorphous–crystalline heterojunctions	1555
L.F. Marsal, J. Pallarès, X. Correig, M. Domínguez, D. Bardés, J. Calderer and R. Alcubilla	
Effects of thermal and laser annealing on silicon carbide nanopowder produced in radio frequency glow discharge	1559
G. Viera, S.N. Sharma, J. Costa, R.Q. Zhang, J.L. Andújar and E. Bertran	
Emission and excitation spectra of silicon-related luminescent centers in CVD-grown diamond films	1564
M.C. Rossi, S. Salvatori, F. Galluzzi, R.M. Montereali and F. Somma	
Amorphous $\text{GaAs}_{1-x}\text{N}_x$ thin films on crystalline Si substrates: growth and characterizations	1568
D. Lollman, K. Aguir, B. Roumiguières and H. Carchano	
Conference Calendar	1573
Author Index	1575
Subject Index	1581

* Invited papers.

Preface

The first European Conference on Silicon Carbide and Related Materials (ECSCRM 96) was held in Heraklion, Crete, Greece from October 6 to October 9, 1996. This was the first event of a series of biannual conferences addressing wide band gap semiconductors research field and supported by the European Union through the "Euroconferences" action. The next conference will be held in Montpellier, France in 1998.

The conference was attended by 140 scientists from 13 countries representing most of the European research groups active in the subject. Thirteen invited talks, 18 oral and 61 poster contributions were presented in 8 oral and 2 poster sessions. These 92 contributions demonstrated the rapid development of wide band gap semiconductor research. Moreover, two panel discussions on *European effort on SiC wafer production & SiC bulk and epitaxial growth apparatus* and on *SiC-based devices and applications* were organized.

Two main research areas were covered by the majority of presentations namely the SiC material aspect and the device-oriented aspect as well as balancing academic and industrial participation. The topics covered by the oral sessions were:

1. SiC bulk growth.
2. SiC epitaxial growth.
3. SiC characterization: Crystal structure & defects; Optical and electrical properties.
4. SiC processing: Oxidation, metallization, ion implantation and etching.
5. SiC-based devices and applications.
6. Nitrides growth and characterization.
7. Amorphous SiC and other SiC-related materials.

The above topical structure is followed in this volume. The contributions were reviewed according to the "Diamond & Related Materials" Journal refereeing procedure and 75 manuscripts were accepted and published in this volume. The Editor wishes to thank the referees who conscientiously reported on manuscripts.

Konstantinos Zekentes



Organizers and Sponsors of ECSCRM 1996

Conference Chairman

J. Stoemenos (Arist. Univ. Thessaloniki)

Scientific Program Committee

A. Christou (University of Maryland, USA)
E. Janzen (Linköping University, SWEDEN)
C. Jaussaud (CENG/LETI/DMEL, FRANCE)
M. T. Mora (Univ. Autonoma Barcelona, SPAIN)
E. Obermeier (Techn. Univ. Berlin, GERMANY)
G. Pensi (Erlangen Univ., GERMANY)
J. L. Robert (Universite de Montpellier II, FRANCE)
Y. M. Tairov (St. Peterbourg University, RUSSIA)

Local Committee

G. Constantinidis (FORTH/IESL)
P. Panayotatos (FORTH/IESL, Univ. of Crete, Rutgers Univ.)
K. Zekentes (FORTH/IESL)

Sponsored By:

- Training and Mobility of Researchers Programme
(EuroConferences). Commission of the European Union
- Foundation for Research and Technology-Hellas
- Greek Ministry of Culture
- General Secretariat of Research and Technology (Greece)
- Aristotle University of Thessaloniki (Greece)
- US Army/European Research Office



Progress in the study of optical and related properties of SiC since 1992

W.J. Choyke *, R.P. Devaty

Department of Physics and Astronomy, University of Pittsburgh, Pittsburgh, PA 15260, USA

Abstract

A selected review is given of some of the advances made in the understanding of the optical and related properties of SiC during the years 1992–1996. Areas which are briefly covered are ultraviolet reflectivity and band structure, phonon replicas and the positions in k -space of the conduction band minima, cyclotron resonance and effective masses, pressure dependence of the electronic energy gap, electronic Raman scattering in heavily doped SiC, acceptors and donors, transition metals, thermoluminescence, porous SiC, and erbium-implanted 3C, 4H, 6H and 15R SiC. © 1997 Elsevier Science S.A.

Keywords: Band structure; Effective masses; Experiments; Review; Silicon carbide

1. Introduction

As the field of SiC grows, the task of reviewing in a very limited space becomes harder and harder. We have chosen to start where our last review stopped [1]. Only a few selected topics have been chosen with the full knowledge that other equally interesting contributions have been left unmentioned. We apologize for having had to pick and choose, and fully recognize that our selection was biased by our own interests.

2. VUV reflectivity and band structure of SiC

It has been recognized for a long time that the occurrence of as many as 170 polytypes of SiC leads to strong differences in many of the properties of these polytypes. A striking example is the variation of the minimum indirect band gap from 2.42 eV in 3C SiC to 3.33 eV in 2H SiC, as well as the notable changes in the locations of the conduction-band minima. In recent years there has been substantial progress in SiC boule growth for substrates which are subsequently used for epitaxial growth of relatively thick and perfect layers of single-crystal material. This development enables one to obtain sufficiently large samples for absolute reflectivity

measurements in the vacuum ultraviolet. More importantly, the epitaxial layers have flat specular surfaces in “as-grown” form. This is critical, since polishing introduces surface damage which can seriously perturb the reflectivity results in the ultraviolet due to the very small penetration depth of the light into the surface. With good “as-grown” surfaces in hand, a systematic VUV-reflectivity (4–10 eV) investigation of the polytypes 3C, 4H, 6H and 15R SiC was conducted [2–4]. In parallel with the experimental study, a series of band-structure and optical response function calculations was carried out and used to interpret the data. The reflectivities of 3C, 4H, 6H and 15R SiC were found to have significant differences. The positions of all major features are in good agreement with those obtained from density functional theory (DFT) calculations in the local density approximation (LDA) using the scalar-relativistic linear muffin-tin orbital (LMTO) method in the atomic sphere approximation (ASA) modified by a polytype- and energy-independent upward shift of the conduction bands, which at the same time provides good agreement for the minimum band gaps. The major peaks in the reflectivity are associated with relatively extended areas of nearly parallel bands at general k points, and not with critical point transitions at symmetry points. The trend of minimum and specific k -point band gaps of five polytypes of SiC with hexagonality has been discussed.

* Corresponding author. Fax: +1 412 6241479.

3. Phonon replicas and conduction band minima

For more than 30 years band-structure calculations have been carried out on the polytypes of SiC, with most emphasis being placed on the 3C SiC or zincblende structure. In the last few years, it has become possible to perform first-principles calculations, making much higher precision available [5–7]. An important question which these modern calculations are being used to answer is where in the Brillouin zone are the conduction-band minima of the various polytypes located? For the zincblende structure (3C SiC) there is universal agreement that the minima are at the X point, but for some of the other common polytypes there is still a certain measure of uncertainty. There appears to be agreement amongst all the current band-structure calculations of 4H SiC that the minima are at the M points, and that the minima for 6H SiC are at a point U which is located somewhere on the line between L and M. Fortunately, the recent theoretical progress has made it possible to calculate phonon energies associated with the M, U and L points in the hexagonal zone [8], making it possible to undertake a comparison between theory and experiment [9,10]. New higher-resolution measurements of phonon energies have been obtained from the phonon replicas in the recombination radiation of an exciton in a nitrogen four-particle complex in the spectra of 4H and 6H SiC epitaxial films oriented in the (11̄20) planes. In the case of 4H SiC, the experimental phonon replica energies and the calculated phonon energies at the M point are in fair alignment, whereas the calculated L-point energies are definitely not in contention. If the minimum in 4H SiC is at the M point, we have three conduction band minima. However, if it were at the U point we would have six minima and at some interior point, as previously conjectured, we would have 12 minima. In the case of 4H SiC it was possible to make careful new Hall measurements on lightly doped n-type 4H SiC samples, and a careful fit was able to deduce that for the deeper nitrogen donor, consistency with the optical data could only be obtained if one assumed three minima. One concludes that the conduction band minimum in 4H SiC is at the M point. The latest high-resolution phonon replica spectrum of 6H SiC is somewhat more complicated than that of 4H SiC, but there are many sharp lines which can be compared with the theoretically calculated phonon energies. The fit to either the M or the U point is not absolutely satisfactory, but the L point is again out of contention. We think the fit to the U point (calculated location of the conduction band minimum) is somewhat better, and this is also in line with band structure calculations. Unfortunately, the deep nitrogen-donor levels in 6H SiC are considerably deeper than the deep nitrogen-donor level in 4H SiC, and Hall measurements are unable to break the tie between M and U. Nevertheless, the

consensus of present opinion is that the minimum in 6H SiC is located at a U point.

4. Cyclotron resonance and effective masses of 4H and 6H SiC

In 3C SiC, effective masses obtained from two electron transition luminescence [11], far infrared cyclotron resonance [12] and infrared optical absorption [13] gave very good agreement. These results were based on an analysis using a simplified effective mass model by Faulkner [14]. This success prompted the same use of the Faulkner model for infrared optical absorption in 6H, 4H and 15R SiC [15–17] to obtain effective masses in these polytypes. Shortly thereafter, new first-principles band calculations [7] and the finding that 4H SiC has a much smaller and opposite anisotropy of the electron mobility with respect to the c axis than does 6H or 15R SiC [18] cast doubts on these results. The situation has been clarified considerably recently in a number of papers on optically detected cyclotron resonance (ODCR) [19–21] and the theoretical analysis given by Lambrecht and Segall [7].

The data on the electron effective mass tensor in 4H SiC and the theory are now in good agreement. However, the agreement in 6H SiC is still somewhat unsatisfactory. One obtains the correct sign of the anisotropy, but the magnitude of the heavy mass still varies by almost a factor of two between theory and experiment.

5. Pressure dependence of the bandgap of 6H SiC

A number of theoretical studies have appeared in the last two years addressing the pressure-dependent properties of SiC [22–26]. An interesting experimental and theoretical study of the pressure dependence of the electronic energy band gap of 6H SiC was reported this summer [27]. In this contribution, low-temperature photoluminescence experiments were carried out with nitrogen-doped 6H SiC under hydrostatic pressures up to 5 GPa. By measuring the energy shifts of the sharp exciton no-phonon emission lines as a function of hydrostatic pressure, the authors determined the pressure coefficient of the indirect gap of 6H SiC (2.0 meV GPa^{-1}). Theoretical ab-initio calculations of the band structure of polytypes 6H, 4H and 3C SiC under hydrostatic pressure were carried out and compared with the available experimental data.

6. Electronic Raman scattering

In a recent series of papers [28–32] there is a wealth of new information on electronic Raman scattering from heavily doped n-type 4H and 6H SiC. In Ref. [28], Raman scattering measurements at room temperature have been made of the LO-phonon plasmon-coupled (LOPC) modes in n-type 4H and 6H SiC with doping concentrations ranging from 5×10^{16} to $1.3 \times 10^{18} \text{ cm}^{-3}$. The axial type mode and the planar type mode have been observed separately. A line-shape analysis of these spectra yields values for the plasmon frequency, carrier damping and phonon damping. For 6H SiC, it is found that there is a large difference between the axial and planar type modes, which is consistent with the Hall mobility anisotropy in 6H SiC. For 4H SiC a small anisotropy is found, again in agreement with Hall mobility measurements. “Fano interference” was first observed by Colwell and Klein [33] in Raman spectra taken on n-type 6H SiC. Now, Harima and Nakashima [30,32] compare the Fano interference in n-type 4H and 6H SiC. Data is presented on the spectral line-shape variation when the carrier density is varied from $n = 1 \times 10^{18}$ to $2 \times 10^{19} \text{ cm}^{-3}$. In 4H SiC, single-particle excitations of free carriers give a relatively large contribution to the Fano interference. In 6H SiC, excitations of bound electrons principally take part in the interference. Finally, in Ref. [32] a systematic Raman study is made of heavily doped n-type 4H and 6H SiC in order to determine at which carrier concentration 4H and 6H undergo the semiconductor-to-metal transition. It is found that down to 35 K at a doping value of $1.8 \times 10^{19} \text{ cm}^{-3}$ there is only a very slight freeze out as well as no sharpening of the LOPC peak at $960\text{--}980 \text{ cm}^{-1}$. One concludes that for 6H SiC a metallic transition takes place in the neighborhood of this level of doping. In 4H SiC, delocalization is observed earlier, at about $6 \times 10^{18} \text{ cm}^{-3}$ carriers. This is consistent with the fact that the ionization energy of the shallow donor in 4H is about 50 meV, whereas it is about 80 meV for 6H SiC.

7. Dopants in SiC

For over 40 years, shallow impurity levels have been studied in SiC. Nevertheless, we still have many questions regarding the nature of even the best known n- and p-type dopants, nitrogen and aluminum. CVD technology is currently producing SiC single-crystal films with net carrier concentrations as low as 10^{13} cm^{-3} . This poses a difficult problem for $C\text{--}V$ and Hall measurements. Clemen et al. [34] showed how to determine the nitrogen impurity concentration of 6H SiC for concentrations from 10^{16} to 10^{13} cm^{-3} by means of low-temperature photoluminescence. Henry et al. [35] improved on these measurements by showing the addi-

tional correction one has to make for donor compensation and making a special point of the fact that these calibrations are valid for a specific excitation intensity. Ivanov et al. [36] have extended this work to 4H SiC. Phosphorus is also a shallow donor in SiC, and it has been introduced into the SiC lattice by means of neutron transmutation of ^{30}Si [37,38], ion implantation [39–42], chemical vapor deposition [43–45] and by diffusion into a bulk sample [46]. In 6H SiC, from EPR and ENDOR [46] experiments one deduces that the phosphorus is on a Si lattice site, as well as forming a phosphorus-related complex. From transport measurements in 6H SiC one obtains two ionization energies [42], one of about 80 meV and the other of approximately 110 meV. Substantial progress has been made since 1992 on the study of the acceptors boron, aluminum and gallium. Reinke et al. [47], using EPR and ODEPR, suggested that the shallow acceptor site of boron is associated with the Si lattice site. Fukomoto [48], from a first-principles calculation of p-type impurities in 3C SiC, concluded that both Al and B form shallow acceptor levels on a Si site and a deep level on a C site. For Al, a Si site has a lower formation energy than a C site, regardless of the composition, while for B the lower formation energy site depends on the composition. A C site is favorable for B under Si-rich conditions, and a Si site under C-rich conditions. These predictions are in good accord with results from low-temperature photoluminescence and Hall measurements on boron-doped CVD samples [49]. In these experiments, a very clear photoluminescence neutral four-particle complex signature has been established for the shallow boron level in 4H SiC. For the deep boron center, at low temperature, N–B donor–acceptor pairs are observed, and as the temperature is raised sufficiently one observes free-to-bound transitions. Finally, in a splendid combination of crystal growth and spectroscopy, the Linköping group has investigated bound excitons in gallium-doped 3C, 4H and 6H SiC [50]. Several no-phonon lines are observed, which are unfortunately superimposed on the nitrogen no-phonon lines in 4H and 6H SiC. A comparison is made with the no-phonon lines observed in p-type Al-doped SiC. It is shown that Haynes’ rule applies for the acceptors Al and Ga in SiC.

8. Transition metals in SiC

In the words of the authors of Ref. [51], transition metals in semiconductors are known and feared as omnipresent and practically unavoidable contaminations. In SiC, Ti and V have been thoroughly studied by resonance techniques [52–56], and for 6H SiC there have also been publications on Mn [57], Cr [58] and Sc [59]. In two very recent publications [51,60], Mo impurities have been identified by electron spin resonance,

optically detected magnetic resonance (ESR, ODMR) and magnetic circular dichroism (MCD) in 6H and 15R SiC. In both polytypes, two charge states are found: Mo⁴⁺(4d²) and Mo³⁺(4d³). Crystal field absorption lines of Mo⁴⁺(4d²) in the range 1.0–1.25 eV are attributed to ³A₂-to-³T₂ transitions. Mo impurities on different inequivalent lattice sites are resolved.

9. Thermoluminescence

Thermoluminescence has been observed in SiC for over 40 years, and very crude empirical correlations with polytypism and doping have been used to great advantage. However, there are few early reports [61,62] where thermoluminescence was used to try to obtain ionization energies or other quantitative results associated with deep levels in 6H SiC. This interesting phenomenon has recently been revisited by Stiasny and Helbig in an extensive set of investigations, primarily on n- and p-type 6H SiC [63–65]. They measured thermal luminescence (TL) and thermally stimulated conductivity (TSC) in the temperature range 12–300 K. A model consisting of one species of trap and recombination center was used to describe the processes. This analysis applied to the main glow-curve peaks leads to the thermal activation energy of the emptied traps. TL as a function of excitation wavelength was used to deduce the energy required for the charge transfer of an impurity. Such experiments yield a range of energies between 1.65 and 1.9 eV to recharge a given recombination center. In Ref. [66] Stiasny has further enlarged these investigations to encompass single-crystal CVD films of 6H SiC, 2 MeV electron irradiations with a fluence of $1 \times 10^{18} \text{ cm}^{-2}$ and fast neutron bombardments to fluences of $5 \times 10^{17} \text{ cm}^{-2}$.

10. Porous SiC

In the early 1990s it was shown that porous Si exhibited bright room-temperature photoluminescence above the normal band-edge of Si. This created a great deal of interest, since many researchers felt that this phenomenon had to be due to quantum confinement of the carriers within the microcrystallites in the porous network. In addition, there was the great lure that this enhanced quantum efficiency would make Si an inexpensive optoelectronic material. Naturally, one hoped that if this worked in Si, for whatever reason, it would also work for such a large indirect band-gap semiconductor as SiC, promising efficient LEDs in the ultraviolet. In Ref. [67] it was shown that porous SiC can be fabricated by anodization in HF. Nanocrystals of 1.5 nm were studied by TEM. Cathodoluminescence spectra at 300 K of 6H SiC porous material did show a small peak at

3.7 eV, but it was not certain whether this peak came from the SiC crystallites or from an oxide coating the crystallites. Matsumoto et al. [68] observed a luminescence peak at 460 nm from porous 6H SiC excited at 300 K with a 3250 nm He–Cd laser and did not report any luminescence in the UV. The intensity of the visible luminescence from porous SiC is estimated to be about 100 times stronger than that from the substrate. Konstantinov et al. [69] gave a detailed description of their material preparation and discussed a number of electrical characteristics of porous SiC. They obtained room-temperature photoluminescence spectra of 6H, 4H and 3C porous SiC under UV laser excitation, but also did not observe any peak in the UV. Strangely, the luminescence peak response of porous 6H, 4H and 3C SiC is almost the same and does not follow the normal polytype dependence. A detailed study of the infrared reflectance at near-normal incidence of thick p-type porous SiC layers was performed by MacMillan et al. [70]. Striking differences are observed in the restrahl region room-temperature reflectance of thick porous 6H SiC layers compared to that of bulk single-crystal 6H SiC. Several effective medium models, based on different morphologies of the component materials, 6H SiC and air, are used to obtain the frequency-dependent dielectric function of porous 6H SiC, from which calculated reflectance spectra are generated. The best match between measured and calculated spectra is obtained for the Maxwell–Garnett model with SiC acting as the host material and air cavities acting as the inclusion material. These experiments also indicate that the crystallites in the porous medium are at most lightly oxidized. This infrared technique may provide a simple non-destructive method by which the porosity of a layer may be determined by the location of a specific feature in the reflectivity.

11. Erbium-implanted crystals of 3C, 6H, 4H and 15R SiC

For the past 14 years there has been an intense interest in the intra-4f shell, 1.54 μm luminescence of Er³⁺(4f¹¹) in numerous semiconductors. One is looking for an ideal semiconductor system in which stable, room-temperature 1.54 μm light-emitting diodes or diode lasers may be fabricated, since 1.54 μm lies in the region of minimum light attenuation for silica-based optical fibers. In 1994, Choyke et al. [71] started to investigate the optical properties of implanted erbium in various polytypes of SiC. An intense line spectrum in the neighborhood of 1.54 μm was observed in annealed (1700 °C) 3C, 6H, 4H and 15R SiC. No major differences were found for the spectra of the hexagonal and rhombohedral polytypes, but a considerable difference was found for cubic (3C) SiC. Luminescence data were

obtained from 2 to 525 K, and in all polytypes the luminescence drop-off occurred well above room temperature, in stark contrast to most other semiconductors. A more detailed study of the post-implantation annealing temperature on the 1.54 μm emission in Er-implanted 6H SiC was reported by Steckl et al. [72]. The 4f¹¹ Er³⁺ free ion spectrum is split by the spin-orbit and Coulomb interactions into many multiplets. One might therefore expect that when the erbium is embedded in the SiC matrix a whole series of spectra should be observed. Indeed this is so, and has been reported together with details of the fine structure in several very recent publications [73–75]. Finally, the issue whether 1.54 μm Er-doped LEDs can be made in SiC has also been resolved [76]. Saturation effects in the diodes have been studied and the integrated electroluminescence intensity was found to increase with donor concentration of the samples up to mid-10¹⁷ cm⁻³.

12. Conclusions

Very considerable progress has been made in the last few years in our understanding of the band structure of the SiC polytypes. More modest progress has been made in the understanding of shallow and deep centers. New phenomena have been unearthed, and better diagnostic techniques are coming along every day. However, the large knowledge base so necessary for the full industrial exploitation of SiC is still mostly empty. We have much to do in the coming years!

References

- [1] G. Pensl, W.J. Choyke, Physica B 185 (1993) 264–283.
- [2] W.R.L. Lambrecht, B. Segall, W. Sutrop, M. Yoganathan, R.P. Devaty, W.J. Choyke, J.A. Edmond, J.A. Powell, M. Alouani, Appl. Phys. Lett. 63 (1993) 2747–2749.
- [3] W. Sutrop, M. Yoganathan, R.P. Devaty, W.J. Choyke, J.A. Edmond, J.A. Powell, W.R.L. Lambrecht, B. Segall, M. Alouani, Inst. Phys. Conf. Ser. 137 (1993) 169–172.
- [4] W.R.L. Lambrecht, B. Segall, M. Yoganathan, W. Sutrop, R.P. Devaty, W.J. Choyke, J.A. Edmond, J.A. Powell, M. Alouani, Phys. Rev. B 50 (1994) 10722–10726.
- [5] P. Käckell, B. Wenzian, F. Bechstedt, Phys. Rev. B 50 (1994) 10761.
- [6] W.R.L. Lambrecht, Mater. Res. Soc. Symp. Proc. 339 (1994) 565.
- [7] W.R.L. Lambrecht, B. Segall, Phys. Rev. B 52 (1995) R2249.
- [8] M. Hoffman, A. Zywietsz, K. Karch, F. Bechstedt, Phys. Rev. B 50 (1994) 13401.
- [9] W.R.L. Lambrecht, S. Limpijumnong, B. Segall, Inst. Phys. Conf. Ser. 142 (1996) 263–268.
- [10] W.J. Choyke, R.P. Devaty, L.L. Clemen, M.F. MacMillan, M. Yoganathan, G. Pensl, Inst. Phys. Conf. Ser. 142 (1996) 257–262.
- [11] P.J. Dean, W.J. Choyke, L. Patrick, J. Luminescence 15 (1977) 299–314.
- [12] R. Kaplan, R.J. Wagner, H.J. Kim, R.F. Davis, Solid State Commun. 55 (1985) 67.
- [13] W.J. Moore, P.J. Lin-Chung, Freitas J.A., Jr., Y.M. Altaisky, V.L. Zuev, L.M. Ivanova, Phys. Rev. B 48 (1993) 12289–12291.
- [14] R.A. Faulkner, Phys. Rev. 184 (1969) 713.
- [15] W. Sutrop, G. Pensl, W.J. Choyke, R. Stein, S. Leibenzeder, J. Appl. Phys. 73 (1992) 3708.
- [16] W. Götz, A. Schöner, G. Pensl, W. Sutrop, W.J. Choyke, R. Stein, S. Leibenzeder, J. Appl. Phys. 73 (1993) 3332.
- [17] Th. Troffer, W. Götz, A. Schöner, W. Sutrop, G. Pensl, R.P. Devaty, W.J. Choyke, Inst. Phys. Conf. Ser. 137 (1994) 173–176.
- [18] M. Schadt, G. Pensl, R.P. Devaty, W.J. Choyke, R. Stein, D. Stephan, Appl. Phys. Lett. 63 (1994) 3120.
- [19] N.T. Son, O. Kordina, A.O. Konstantinov, W.M. Chen, E. Sörman, B. Monemar, E. Janzen, Appl. Phys. Lett. 65 (1994) 3209.
- [20] N.T. Son, W.M. Chen, O. Kordina, A.O. Konstantinov, B. Monemar, E. Janzen, D.M. Hofmann, D. Volm, M. Drechsler, B.K. Meyer, Appl. Phys. Lett. 66 (1995) 1074.
- [21] D. Volm, B.K. Meyer, D.M. Hofmann, W.M. Chen, N.T. Son, C. Persson, U. Lindfelt, O. Kordina, E. Sörman, A.O. Konstantinov, B. Monemar, E. Janzen, Phys. Rev. B 53 (1996) 15409–15412.
- [22] P. Käckell, B. Wenzien, F. Bechstedt, Phys. Rev. B 50 (1994) 17037–17046.
- [23] K. Karch, A. Zywietsz, F. Bechstedt, P. Pavone, D. Strauch, Inst. Phys. Conf. Ser. 142 (1996) 337–340.
- [24] K. Karch, F. Bechstedt, P. Pavone, D. Strauch, Phys. Rev. B 53 (1996) 13400.
- [25] K. Karch, F. Bechstedt, Phys. Rev. Lett. 77 (1996) 1660–1661.
- [26] K. Karch, F. Bechstedt, Europhys. Lett. 35 (1996) 195–200.
- [27] F. Engelbrecht, J. Zeman, G. Wellenhofer, C. Peppermüller, R. Helbig, G. Martinez, U. Rössler, Phys. Status Solidi, (b) 198, 81 (1996).
- [28] H. Harima, S. Nakashima, T. Uemura, J. Appl. Phys. 78 (1995) 1996–2005.
- [29] S. Nakashima, H. Harima, Inst. Phys. Conf. Ser. 142 (1996) 269–274.
- [30] H. Harima, S. Nakashima, Inst. Phys. Conf. Ser. 142 (1996) 365–368.
- [31] S. Nakashima, H. Harima, ICORS XV, 1996, pp. 932–933.
- [32] H. Harima, S. Nakashima, T. Hamamoto, ICORS XV, 1996, pp. 952–953.
- [33] P.J. Colwell, M.V. Klein, Phys. Rev. B 6 (1972) 498.
- [34] L.L. Clemen, M. Yoganathan, W.J. Choyke, R.P. Devaty, H.S. Kong, J.A. Edmond, D.J. Larkin, J.A. Powell, Burk A.A., Jr., Inst. Phys. Conf. Ser. 137 (1994) 251.
- [35] A. Henry, O. Kordina, C. Hallin, C. Hemmingsson, E. Janzen, Appl. Phys. Lett. 65 (1994) 2457–2459.
- [36] I.G. Ivanov, C. Hallin, A. Henry, O. Kordina, E. Janzen, J. Appl. Phys. 80 (1996) 3504.
- [37] A.I. Veinger, A.G. Zabrodskii, G.A. Lomakina, E.N. Mokhov, Sov. Phys. Solid State 28 (1986) 917.
- [38] E.N. Kalabukhova, S.N. Lukin, E.N. Mokhov, Phys. Solid State 35 (1993) 361.
- [39] T. Sugii, T. Ito, J. Electrochem. Soc. 134 (1987) 2545.
- [40] K. Shibahara, T. Takeuchi, S. Nishino, H. Matsunami, Jpn. J. Appl. Phys. 28 (1989) 1341.
- [41] H. Sonntag, S. Kalbitzer, Appl. Phys. A 61 (1995) 363.
- [42] T. Troffer, C. Peppermüller, G. Pensl, K. Rottner, A. Schöner, J. Appl. Phys. 80 (1996) 3739.
- [43] H.J. Kim, R.F. Davis, J. Electrochem. Soc. 133 (1986) 2350.
- [44] S. Hasegawa, N. Furuta, T. Takeshita, T. Inikuma, Y. Kurata, J. Appl. Phys. 72 (1992) 1374.
- [45] D.J. Larkin, private communication.
- [46] S. Greulich-Weber, M. Feege, J.-M. Spaeth, E.N. Kalabukhova, S.N. Lukin, E.N. Mokhov, Solid State Commun. 93 (1995) 393.

- [47] J. Reinke, S. Greulich-Weber, J.-M. Spaeth, E.N. Kalabukhova, S.N. Lukin, E.N. Mokhov, Inst. Phys. Conf. Ser. 137 (1994) 211–214.
- [48] A. Fukimoto, Phys. Rev. B 53 (1996) 4458–4461.
- [49] S.G. Sridhara, L.L. Clemen, R.P. Devaty, W.J. Choyke, D.J. Larkin, T. Troffer, G. Pensl, to be published.
- [50] A. Henry, C. Hallin, I.G. Ivanov, J.P. Bergman, O. Kordina, U. Lindefelt, E. Janzén, Phys. Rev. B 53 (1996) 13503–13506.
- [51] K.F. Dombrowski, M. Kunzer, U. Kaufmann, J. Schneider, P.G. Baranov, E.N. Mokhov, Phys. Rev. B 54 (1996) 7323–7327.
- [52] K. Maier, H.D. Müller, J. Schneider, Mater. Sci. Forum 83–87 (1992) 1183.
- [53] M. Kunzer, H.D. Müller, U. Kaufmann, Phys. Rev. B 48 (1993) 10846.
- [54] M. Kunzer, U. Kaufmann, K. Maier, J. Schneider, Mater. Sci. Eng. B 29 (1995) 118.
- [55] K.F. Dombrowski, U. Kaufmann, M. Kunzer, K. Maier, J. Schneider, V.B. Shields, M.G. Spencer, Appl. Phys. Lett. 65 (1994) 1811.
- [56] K.F. Dombrowski, U. Kaufmann, M. Kunzer, K. Maier, J. Schneider, V.B. Shields, M.G. Spencer, Phys. Rev. B 50 (1994) 18034.
- [57] M. Feege, S. Greulich-Weber, J.M. Spaeth, Semicond. Sci. Technol. 8 (1993) 1620.
- [58] P.G. Baranov, V.A. Khramstov, E.N. Mokhov, Semicond. Sci. Technol. 9 (1994) 1340.
- [59] P.G. Baranov, N.G. Romanov, Mater. Sci. Forum 83–87 (1992) 1207.
- [60] J. Baur, M. Kunzer, K.F. Domrowski, U. Kaufmann, J. Schneider, P.G. Baranov, E.N. Mokhov, Mater. Sci. Engng. B, 46 (1997) 313–316.
- [61] A. Halparin, E. Zacks, E. Silberg, J. Luminescence 6 (1973) 304.
- [62] M.P. Lisita, O.V. Vakulenk, Y.S. Krasnov, V.N. Solodov, Sov. Phys. Semicond. 5 (1972) 1785.
- [63] Th. Stiasny, R. Helbig, Inst. Phys. Conf. Ser. 137 (1994) 151–154.
- [64] Th. Stiasny, R. Helbig, Inst. Phys. Conf. Ser. 142 (1996) 389–392.
- [65] Th. Stiasny, R. Helbig, J. Appl. Phys. 79 (1996) 4152–4156.
- [66] Th. Stiasny, PhD dissertation, University of Erlangen-Nürnberg, 1996.
- [67] J.S. Shor, L. Bemis, A.D. Kurtz, M. MacMillan, W.J. Choyke, I. Grimberg, B.Z. Weiss, Inst. Phys. Conf. Ser. 137 (1994) 193–196.
- [68] T. Matsumoto, J. Takahashi, T. Tamaki, T. Futagi, H. Mimura, Y. Kanemitsu, Appl. Phys. Lett. 64 (1994) 226–228.
- [69] A.O. Konstantinov, C.I. Harris, A. Henry, E. Janzén, Inst. Phys. Conf. Ser. 142 (1996) 1079–1082.
- [70] M.F. MacMillan, R.P. Devaty, W.J. Choyke, D.R. Goldstein, J.E. Spanier, A.D. Kurtz, J. Appl. Phys. 80 (1996) 2412–2419.
- [71] W.J. Choyke, R.P. Devaty, L.L. Clemen, M. Yoganathan, G. Pensl, Ch. Hässler, Appl. Phys. Lett. 65 (1994) 1668–1670.
- [72] A.J. Steckl, J. Devrajan, W.J. Choyke, R.P. Devaty, M. Yoganathan, S.W. Novak, J. Electron. Mater. 25 (1996) 869–873.
- [73] W.J. Choyke, R.P. Devaty, L.L. Clemen, M.F. MacMillan, M. Yoganathan, G. Pensl, Inst. Phys. Conf. Ser. 142 (1996) 257–262.
- [74] M. Yoganathan, W.J. Choyke, R.P. Devaty, G. Pensl, J.A. Edmond, Mat. Res. Soc. Symp. Proc. Vol 422 (1996) 339.
- [75] W.J. Choyke, R.P. Devaty, M. Yoganathan, G. Pensl, J.A. Edmond, Shallow-Level Centres in Semiconductors (Amsterdam, 17–19 July 1996). Eds: C.A.J. Ammerlaan and B. Pajot, World Scientific Publishing Company 1997, pp. 297–302.
- [76] M. Yoganathan, W.J. Choyke, R.P. Devaty, G. Pensl, J.A. Edmond, Inst. Phys. Conf. Ser. 142 (1996) 377–380.

Defects formation in sublimation grown 6H-SiC single crystal boules

R. Madar ^{a,*}, M. Anikin ^a, K. Chourou ^a, M. Labeau ^a, M. Pons ^b, E. Blanquet ^b, J.M. Dedulle ^a, C. Bernard ^b, S. Milita ^c, J. Baruchel ^c

^a LMGP-UMR 5628 CNRS, ENSPG, BP 46-38402 St Martin d'Hères, France

^b LTPCM, UMR 5614 CNRS, ENSEEG, BP 75, 38402 St Martin d'Hères, France

^c ESRF, BP 220-38043 Grenoble, France

Abstract

A perfect understanding of the origin of defects in connection with crystal growth conditions is of prime importance for the future of SiC based electronic. In the generally used modified Lely method (M-Lely), the growth takes place by incongruent sublimation from SiC powder on a monocrystalline SiC seed at low pressure and high temperature. We have recently proposed beginning the growth process at the inverted sign of temperature gradient and low argon pressure. In these conditions, nucleation at low temperature is suppressed and sublimation polishing etching takes place. Then the sign of the temperature gradient is slowly inverted to start the growth.

The influence of this nucleation step on the nature and density of defects has been studied by structural analysis using X-ray diffraction, optical and electronic microscopy, atomic force microscopy and synchrotron white beam X-ray topography. The results are discussed in the light of our present understanding of the sublimation process. © 1997 Elsevier Science S.A.

Keywords: Silicon carbide; Defects; Synchrotron radiation

1. Introduction

In view of the increasing importance of silicon carbide as a material for high temperature, high power and high frequency electronic device applications [1–3], it may seem quite surprising that a good understanding of the nature of the defects and formation during the crystal growth of this material has not yet been achieved. This situation results in part from the fact that the material itself is quite complex, crystallizing into several modifications known as polytypes whose c parameters vary with the stacking sequence [4]. More than 250 different polytypes have already been reported, the 3C, 4H, 6H and 15R being the more familiar. Moreover, the fact that SiC decomposes before melting makes its crystal growth process much more difficult than for other industrial semiconductors, that is, silicon or gallium arsenide which both melt congruently.

All silicon carbide single crystals are presently produced from the vapour phase by the sublimation of silicon carbide powder according to the technique first

proposed by Lely in 1955 [5]. Since this date, several modifications of this original process have been proposed and used for the growth of large silicon carbide boules [6–20]. The most important one is the introduction of the so-called modified Lely method (M-Lely) by Tairov and Tsvetkov [6] who proposed to grow on SiC single crystalline seed which are placed in the holes of a graphite crystallization cylinder. In this original process, the temperature of the source was always maintained higher than that of the seed. In these conditions, the only way to avoid nucleation during the heating step is to maintain a high pressure of argon (ca 1 atm) in the crucible and to start the growth by a controlled decrease of this pressure. As a result, a lot of defects due mainly to damages and contaminations on the seed surface are usually generated in the initial stage of growth and penetrate the growing ingot.

With some modifications of the geometrical arrangement of the experimental set-up, this procedure has been used by most of the research teams working on this subject. The best results obtained so far have been reported by Cree Research [17].

We have recently proposed a modification of this original process by starting the growth process at the

* Corresponding author. Fax: 33 768 26394;
e-mail: roland.madar@inpg.fr

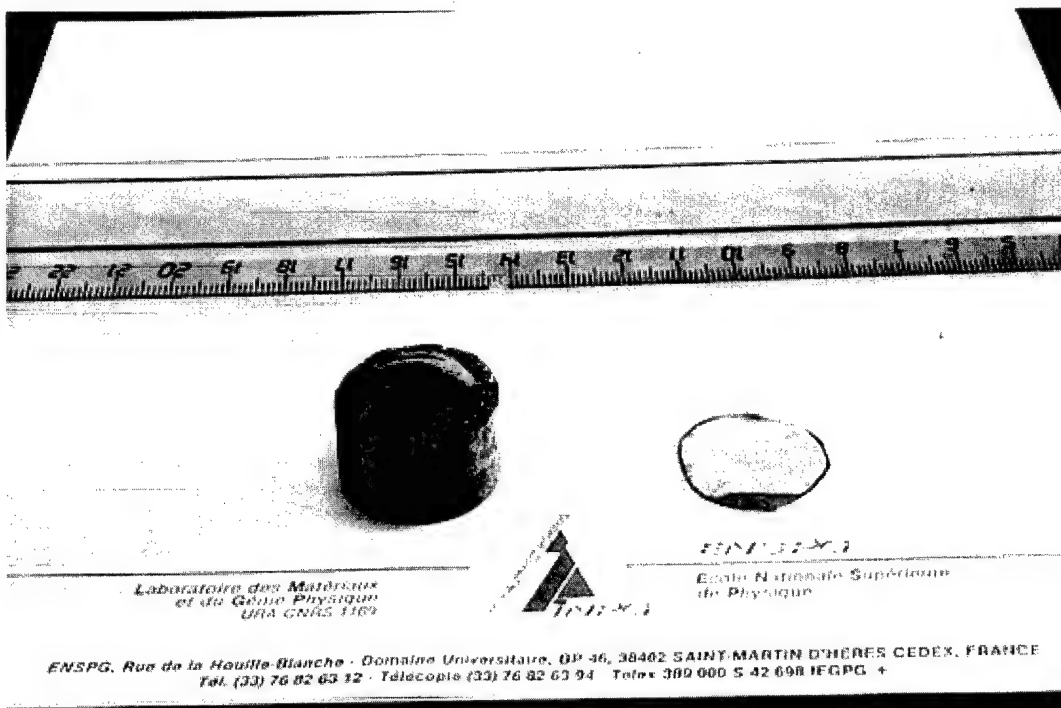


Fig. 1. The 1", 10 mm length 6H-SiC ingot and wafer.

inversed sign of the temperature gradient and fixed low Ar pressure [15,16]. In these conditions nucleation at low temperature is suppressed and a sublimation polishing etching of the seed takes place at high temperature. The nucleation is controlled by the temperature gradient and the crystal growth starts as the sign of the temperature gradient is slowly inverted.

It is the aim of the present paper to give through an analysis of the results obtained so far on the crystal growth of 6H-SiC some indications about the relations between growth conditions and defects formation.

2. Experimental

The sublimation system used to grow the 6H single crystal SiC has been previously described [16]. The design is similar to the construction previously described by Yu.M. Tairov [7] with some modifications to maintain equilibrium pressure over the seed during the sublimation etching. High purity silicon carbide powder is used after chemical treatments as a source in a graphite crucible which is heated by a Radio Frequency (RF) inductive heating system. A monocrystalline seed, Lely 6H-SiC plate, (0001) Si orientation, etched in molten alkali, was set on the graphite lid. The temperature gradient between the source and the seed was accurately controlled by displacement of the induction heating coil.

The crucible covered with graphite felt is placed into the growth system consisting of concentric water cooled quartz tubes within stainless steel end flanges. This

system, which can be pumped down to 10^{-6} Torr before growth, provides a very clean environment for the crystal growth process. In some aspects, it is quite similar to the systems used by other research teams working on this process.

Fig. 1 shows a typical 25 mm diameter and 10 mm height single crystal 6H-SiC boule grown by this process together with a nitrogen doped polished wafer cut from the boule.

2.1. Growth process

The growth of SiC results from sublimation of the SiC powder, mass transport in the vapour phase through the thermal gradient and condensation on the seed. The growth rate is determined by the growth temperature, temperature gradient, distance between the source and seed, pressure inside the crucible and purity and grain size of the SiC powder while the shape of the boule is mainly a function of the radial thermal gradient.

The growth process consists of four main steps:

- (1) Initial stage of heating and pumping. The crucible is open at low temperatures. The temperature of the source is lower than that of the seed.
- (2) Sublimation etching with 'in situ' polishing at high temperature; during this step, 40–100 μm of SiC are removed.
- (3) Inversion of the temperature gradient by coil displacement at high temperature. Argon pressure is slowly increased to decrease the growth rate. The

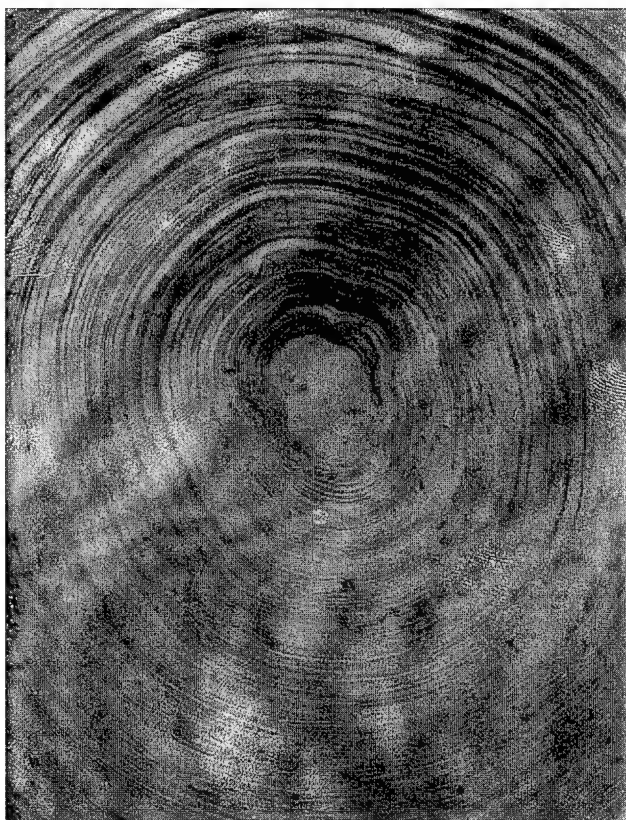


Fig. 2. Surface of a Lely SiC seed surface, Si orientation, after sublimation etching.

temperature gradient is slowly modified to begin the growth at a slow growth rate.

- (4) Growth at a growth rate of 1–2 mm h⁻¹ at low argon pressure at 2200–2400°C. The temperature gradient is slowly increased during growth.

In the initial stage the crucible was open to be pumped down and automatically closed at higher temperature. In fact, the crucible became vacuum-tight only during the process following the growth of polycrystalline SiC on the graphite lid.

The polishing etching takes place at high temperature with a seed temperature higher than the source temperature. During this step, the Si overpressure above the seed must be maintained close to equilibrium vapour pressure over SiC since if the silicon pressure is too low, carbonization of the seed takes place due to non-congruent evaporation of SiC in this temperature range. The effects of this polishing step can be seen on Fig. 2. The surface consists of large terraces with a mean step height of 60 Å depending on the Si/C ratio over the seed and increasing with decreasing Si pressure. Since the Si pressure decreases with an increasing temperature gradient, the displacement of the inductive coil must be accurately controlled to avoid a too large temperature gradient at the beginning of the growth process which

may lead to three-dimension nucleation on large terraces resulting from high step height.

2.2. Crystal evaluation

The polytype identification was made by X-ray diffraction, Raman spectroscopy and photoluminescence at low temperature. The crystal defect densities and distribution were assessed by optical and scanning electron microscopy on samples chemical etched in molten KOH at 500°C for 15 min in order to distinguish between dislocation pits, micropipes, low angle boundaries between grains and inclusions. The existence of domains with small disorientations was studied by high resolution X-ray diffraction and X-ray topography in transmission geometry using polychromatic (white beam) synchrotron radiation [21]. These measurements were carried out at ESRF-D5 optics beamline.

In the transmission topography, the sample is just placed into the white beam without the need of exact adjustments. Many lattice planes will find the reflection condition and form a Laue pattern, so that several topographies can simultaneously be recorded within one exposure on one film. The diffracted beam penetrates the crystal, so that all the defects within the crystal volume are recorded. An example of such investigation is given in Fig. 3 for a 6H Lely crystal. In the samples investigated it is easy to identify a contrast coming from dislocations, inclusions and disorientations. A fundamental advantage of the Laue technique in white beam compared to the monochromatic one is that the very strongly deformed regions of the crystal are fully imaged with the white beam, generating more or less strongly distorted topographies.

Section topography is easily realized by inserting a narrow collimating slit, typically 10 µm in width, in front of the crystal. A series of horizontal and vertical sections patterns after 2 mm shifts of the crystal have to be recorded in order to gain information from a large part of the specimen (Fig. 4). The main advantages of section topography are to reveal the location of defects in the depth of the crystal, to allow the identification of the character of planar defects (for example, to distinguish between the stacking faults and tilt boundaries) and easily determinate local and general disorientation (the lattice tilts are easily derived from the linear displacements from the Bragg diffracted beams).

Finally, for some selected samples, the growth surface morphology in the central region of the convex surface was studied by atomic force microscopy. The observations were performed in atmospheric air, using a Nanoscope II system (Digital Instruments, USA). Conventional pyramidal-shape Si₃N₄ cantilever tips were used and their spring constant was 0.12 N m⁻¹. Measurements were made using the constant-force mode

TRANSMISSION GEOMETRY

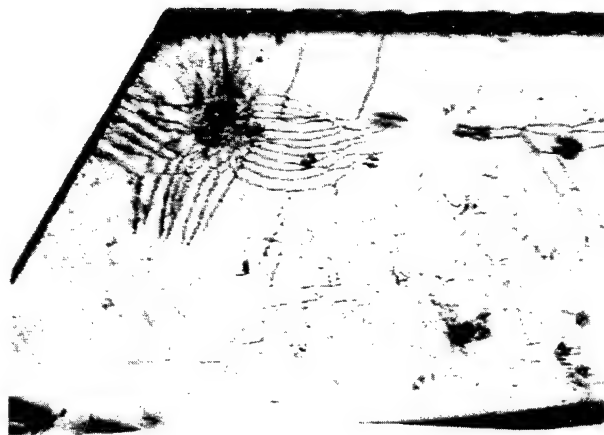
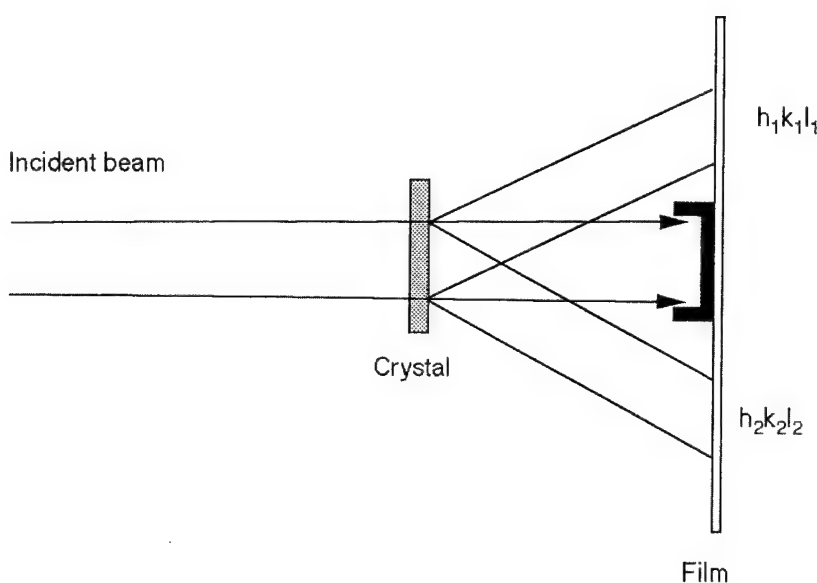


Fig. 3. Schematic representation of the experimental set-up for white beam synchrotron topography in transmission mode; topograph of a Lely 6H-SiC crystal.

of the atomic force microscope, where the force was of 10^{-8} N.

3. Results and discussion

3.1. Control of the polytype structure

Crystals having the same polytype structure as the seed can be grown if the growth occurs in step flow mode at low supersaturation or if the growth conditions correspond ‘thermodynamically’ to those required for the formation of this polytype, that is, 6H at high temperature and 3C at low temperature. It is well known that the polytype structure of the grown ingots

depends also on the composition of the vapour phase at a given temperature. It was shown, for example, that an excess of silicon, obtained using an additional Si source, may lead to the formation of ingots with 3C-SiC inclusions and in the case of high supersaturation, if the growth rate is too high at a given temperature the polytype may be modified. SiC-6H crystals grown at 2200°C at a growth rate >2 mm h $^{-1}$ had inclusions of 3C-SiC while the crystals grown at 2400°C at a growth rate of 2.5 mm h $^{-1}$ did not have inclusions of other polytypes.

So, by a careful control of the gas phase composition, we have achieved the reproducible growth of pure 6H-SiC boules of 1" diameter starting from 1 cm 2 6H-SiC Lely substrates used as seed. The knowledge

SECTION TOPOGRAPHY

HORIZONTAL SECTIONS

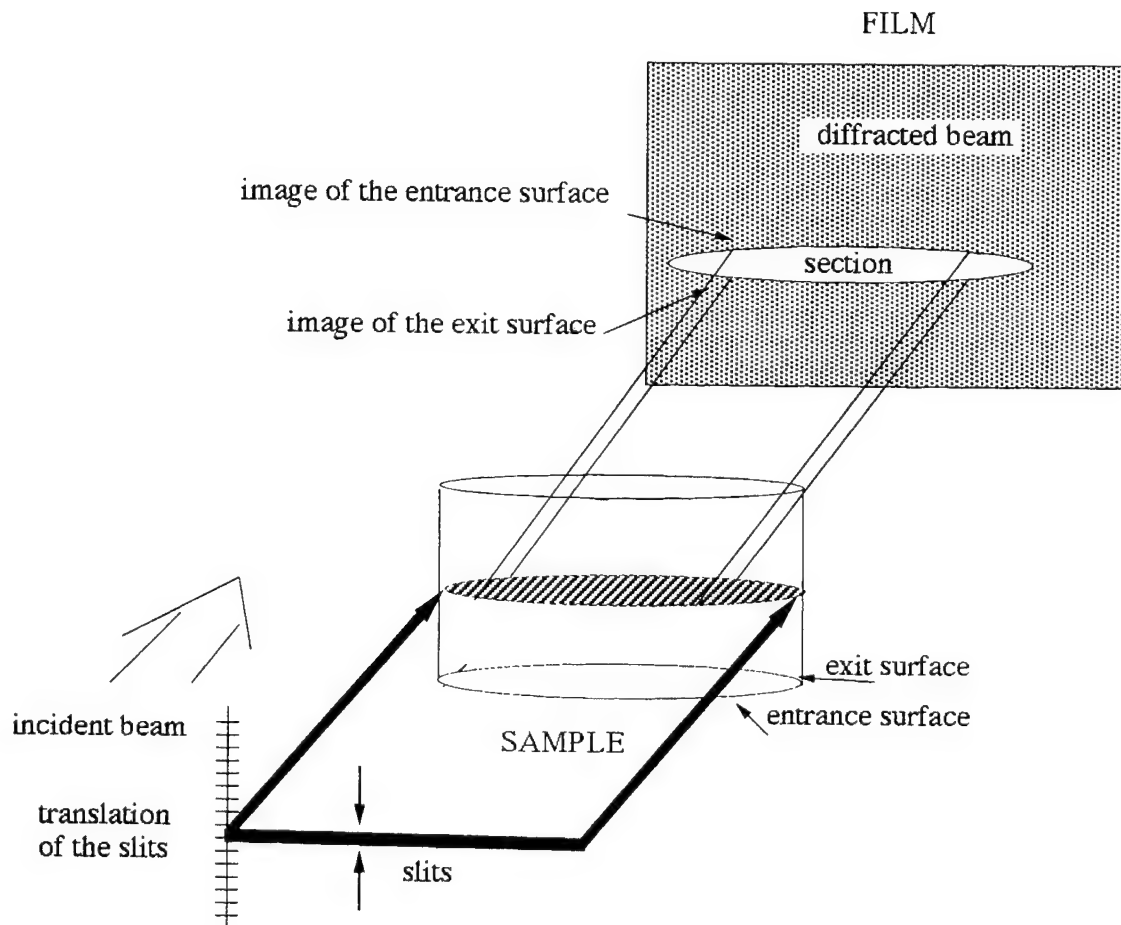


Fig. 4. Schematic representation of the experimental set-up for white beam synchrotron topography in horizontal section mode.

of the gas phase composition was made possible by a modelling of the sublimation process [22]. Thermodynamic modelling based on recently determined reliable thermodynamic data [23,24] was used to determine the most important reactive gaseous and solid species present in equilibrium conditions (Fig. 5). In addition heat transfer modelling (including induction heating, radiation, convection, conduction and multi-reflection) was performed to calculate the actual temperatures inside the reactor. Finally, mass transport modelling provided the chemical fields of the process and calculated deposition rates which were found to be closed to the experimental ones.

3.2. Nature and formation of lattice defects

The nature of lattice defects in both Lely and M-Lely crystals has been already extensively studied [13,25–31] and have been categorized as surface strain, internal strain centres, long range elastic deformation and dislocations [30]. Even if the formation of 'macrodefects and micropipes' are, in our opinion, strongly related to the stress in the crystal, they will be discussed separately below in a specific paragraph devoted to hollow defects.

In the simplest experimental configuration the growth starts simultaneously on the SiC seed, the pedestal part not covered by the seed and the remaining surface of the lid. At first, on these last two graphite surfaces, the

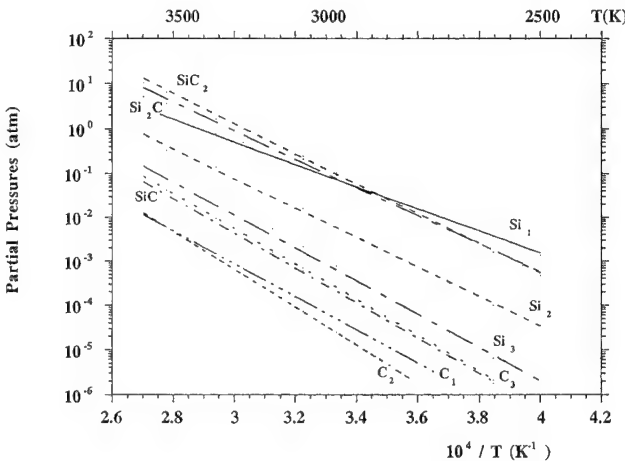


Fig. 5. Partial pressures of gaseous species over SiC as a function of temperature at equilibrium.

SiC deposit is essentially polycrystalline. Hence, the achievement of a cylindrical single crystal boule needs the enlargement or the original single crystal surface of growth at the expense of adjacent polycrystalline ilots.

This enlargement process has been studied by white beam synchrotron topography. We will just give in this paper some indications on the main information obtained to date. Fig. 6 shows the results of the analysis of a 6H wafer by both transmission and section topography. In the transmission mode, two different positions of the sample were investigated, one at the bottom of the sample [Fig. 6(a)] and the second one at the centre [Fig. 6(b)]. In both cases, the main contrast comes from disoriented regions. All the borders of the sample show highly deformed regions but the centre of the sample also presents localized regions with slight lattice planes disorientation (up to 0.42°). Despite the presence of these disoriented domains, which can be seen also on the section topographs [Fig. 6(c)], the sample is not bent, in fact from one to the other side of the crystal there is no disorientation.

The investigation of a SiC boule by horizontal and vertical topography sections (Fig. 7) reveals that the enlargement process results from a progressive alignment of adjacent to the seed and initially disoriented domains by a continuous deformation of the boundary zones during the growth. A complete description and analysis of the results obtained so far by this technique will be published elsewhere together with a comparison with the work already published on this subject [32–34].

The modelling provides a good understanding of this enlargement phenomenon based on the radial gradient along the growth surface. Due to this radial gradient, ingot diameter increases with an increase in length if the growth of polycrystalline SiC on the graphite lid follows the ingot growth. An increase in radial gradient increased the lateral growth rate. If the distance between the ingot and polycrystal increased, resublimation of the

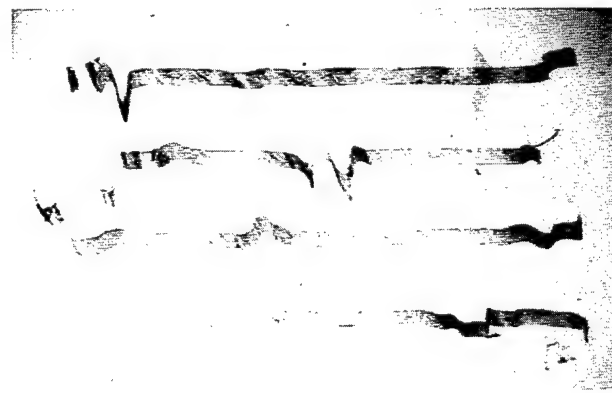
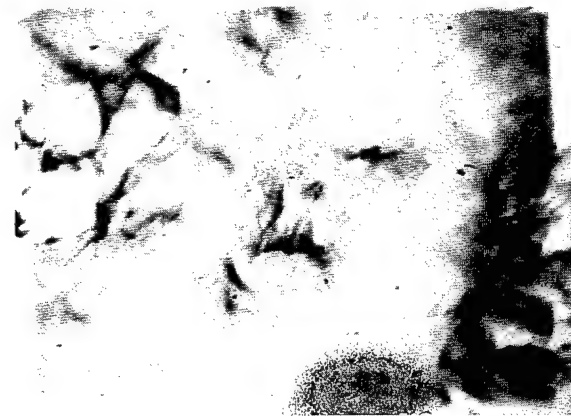
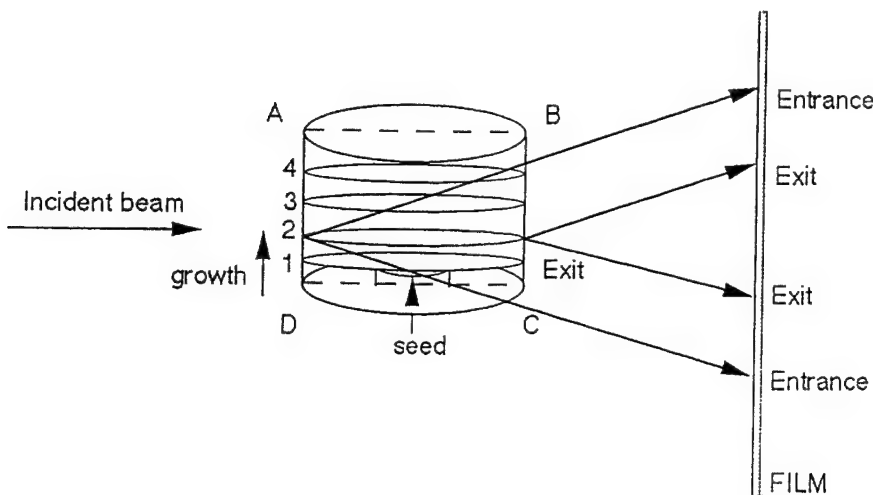


Fig. 6. White beam synchrotron topography analyses of a 6H-SiC substrate: (a) transmission topograph of the bottom; (b) transmission topograph at the centre; (c) corresponding sections (displacement between two sections: 2 mm).

ingot on polycrystal leads to a decrease in diameter with increasing crystal length.

X-ray topographies and chemical etching reveal the presence of domains with a high density of dislocation at the boundaries. Defect revelation is mainly done by



SECTION 1

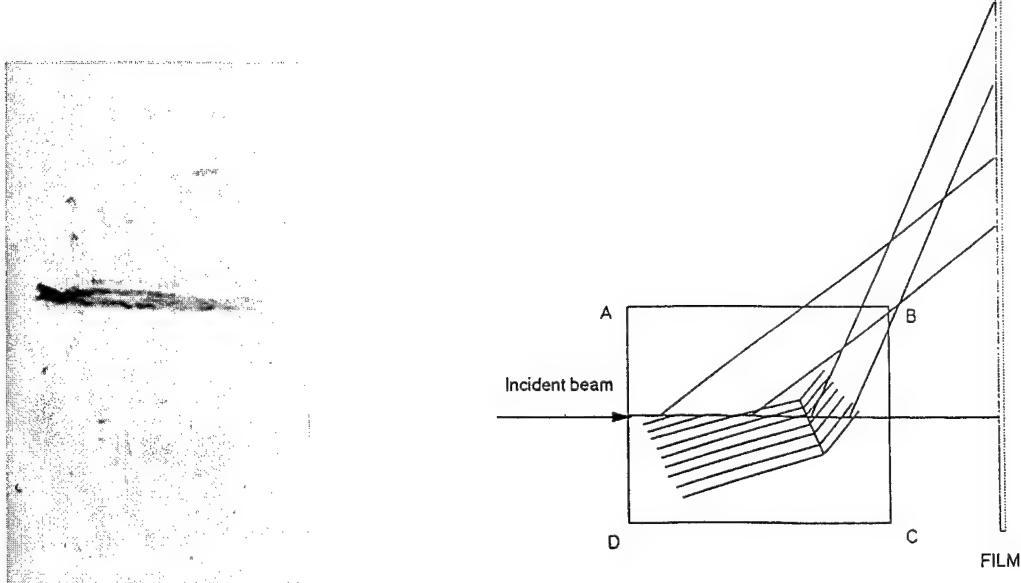


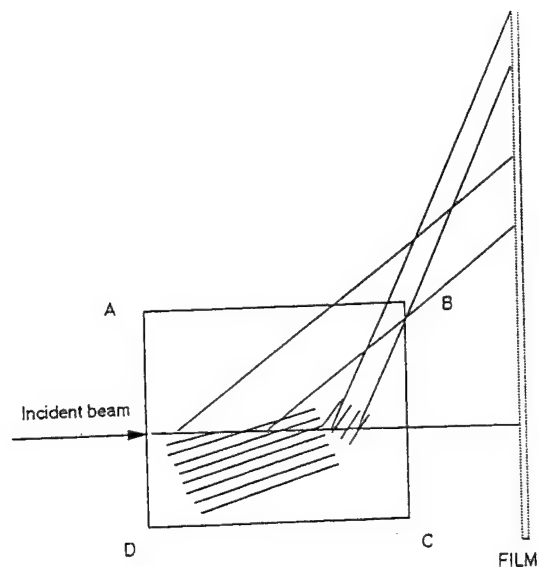
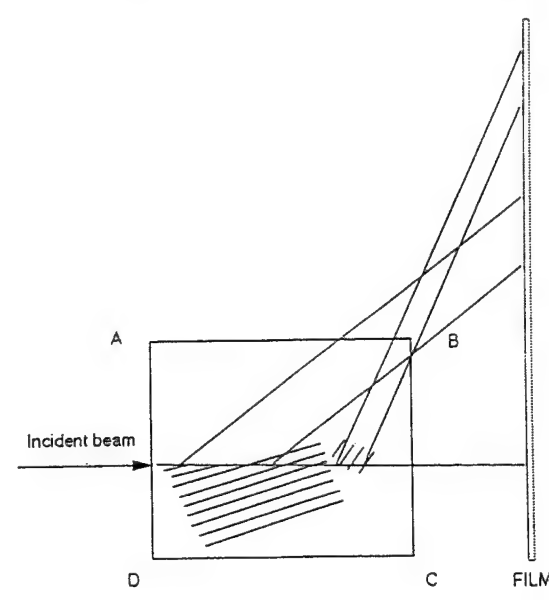
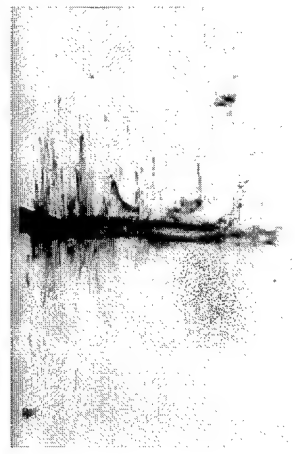
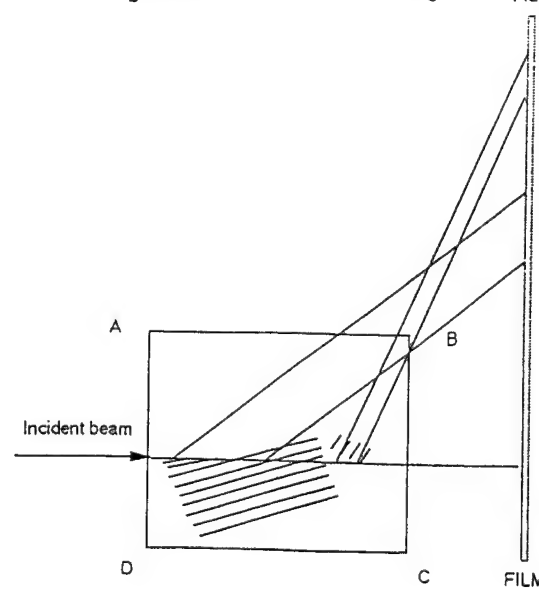
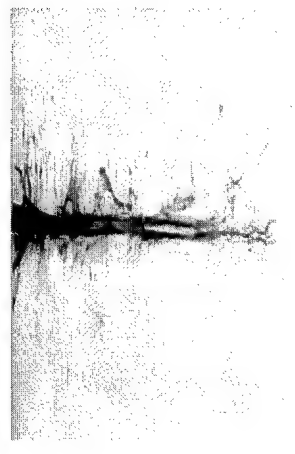
Fig. 7. Horizontal and vertical sections topography analysis of a SiC ingot.

etching in molten alkali, which reveals in addition to pinholes, dislocations and low-angle boundaries between the different domains. The dislocations seen in topographies or revealed as pits on the etched surface are screw dislocations along the growth axis, mixed dislocations with a screw component and pure edge dislocations lying in the basal plane.

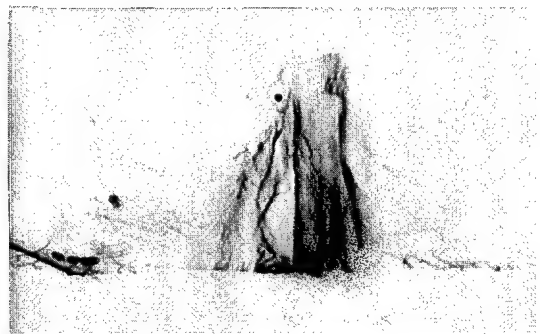
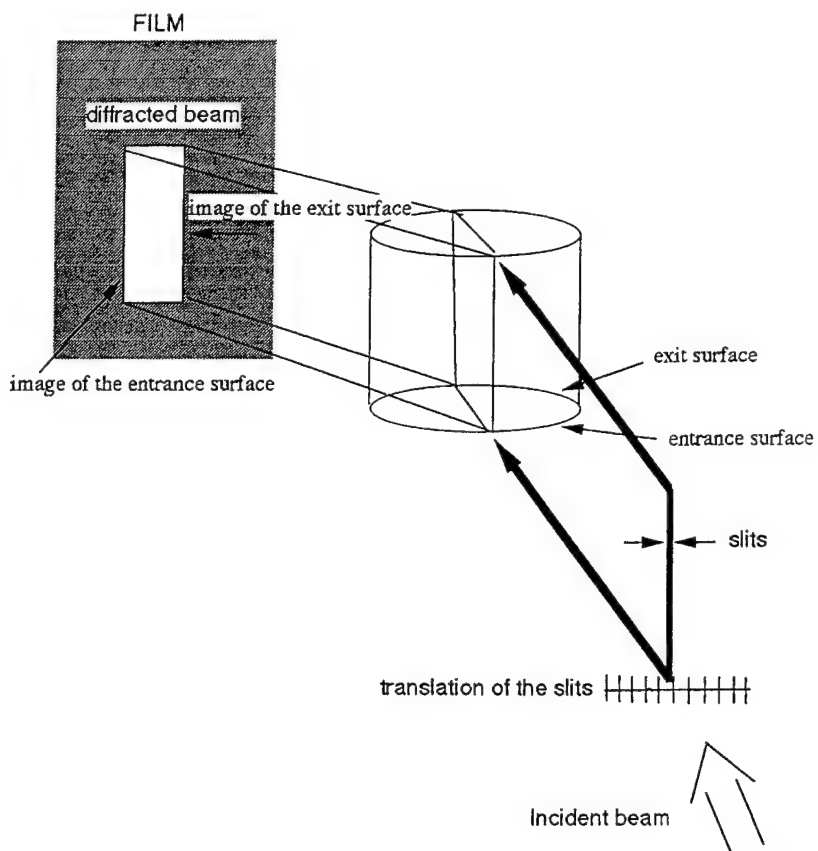
It must be kept in mind that chemical etching only allows the determination of the density of dislocations intersecting the surface. According to the classification of Koga et al. [10] they correspond to the medium size and small hexagonal pits appearing on the (0001) Si-side

face after etching. Each of these pits has six sidewalls corresponding to the traces of the six [1100] planes intersecting the surface and a pointed bottom (Fig. 8). The total dislocations density is in general higher than the mean value determined by this technique (ca 10^4 cm^{-2}) since the diffraction micrograph show a high density of dislocations lines lying parallel with (0001) planes.

Since the Lely 6H-SiC seed is characterized by a low density of dislocations lying mainly in the basal plane, we may consider that the high density generally reported for the SiC boules grown by the sublimation technique

SECTION 2**SECTION 3****SECTION 4**

VERTICAL SECTION



results from the growth process and can be related to four main parameters:

- (1) The nucleation step at the beginning of the growth.
- (2) The enlargement mechanism evoked before.
- (3) The instabilities resulting from poor process control.
- (4) The stresses leading to plastic deformation at high temperature.

These four problems have to be taken into account in the design of the growth system and definition of the

growth conditions. We have indeed found that the use of the sublimation etching step leads to a reduction by one order of magnitude of the dislocations density in the grown crystal. It must be possible to solve the two following problems by a specific design of the growth crucible and sophisticated electronic regulation systems.

The last point is much more difficult to put under control since it simultaneously involves the intrinsic physical characteristics of SiC: thermal conductivity;

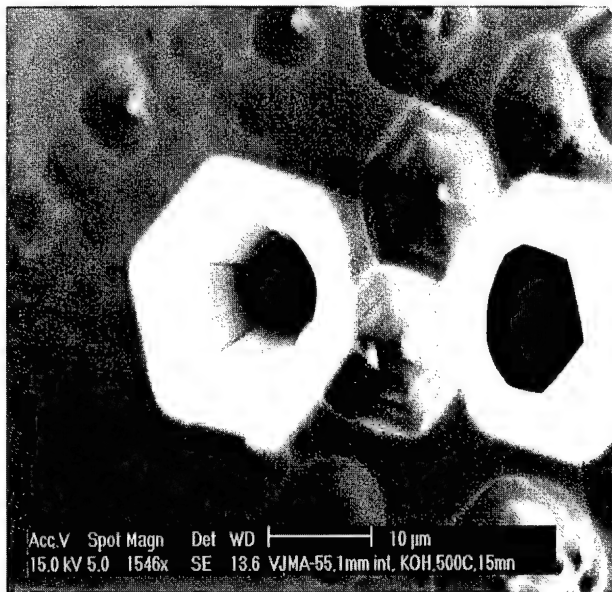
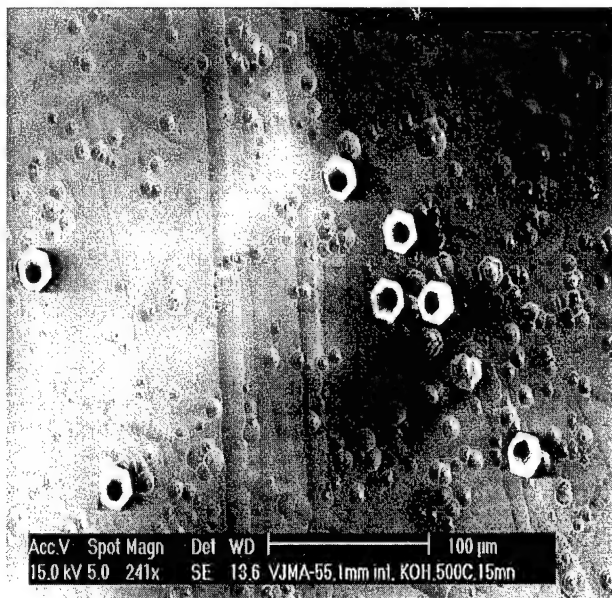


Fig. 8. SiC wafer surface, (0001) Si-side, after chemical etching which reveals etch pits and micropipes.

thermal expansion coefficient; emissivity at high temperature; and the specific characteristics of the growth system: source and seed temperatures; vertical and radial thermal gradient; shape of the crucible...; all parameters which determine the thermoelastic field in the growing crystal.

3.3. Hollow defects

We will classify in this common denomination the already reported formation of ‘macrodefects’ and micropipes in addition to pyramidal holes (Fig. 9), which have been observed in some of our crystals. They were found at the interface in non-optimal conditions of

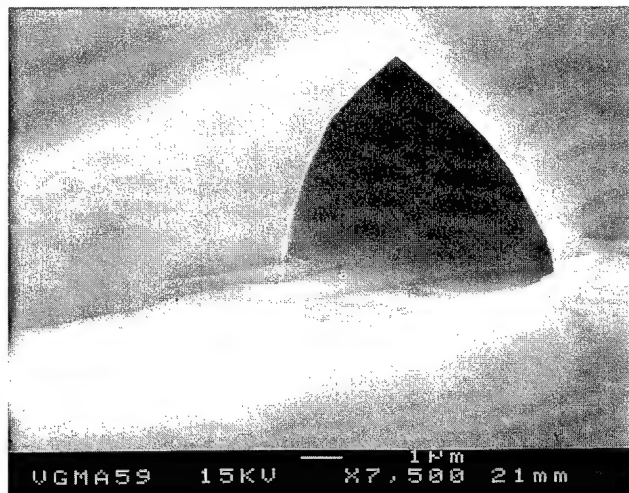


Fig. 9. SEM micrograph of a ‘pyramidal’ hole at the surface seed-ingot.

sublimation etching. As a result, the crystals starts to growth in the islands growth mode in place of the desired steps flow mechanism. The resulting nuclei formed on the surface may coalesce leading to the formation of pyramidal holes if, like for the growing ingot, their diameters increase with the increase of ingot height. The contamination of the seed surface may come from local carbonization if the Si overpressure is too low or deposition of impurities evaporated from the SiC powder.

Macrodefects are large vertical holes with horizontal enlargement at the end (Fig. 10). They start at the interface holder–seed and may penetrate deep into the growing crystal. The formation of these defects has been explained [12] by local sublimation of the seed and then the growing ingot. High temperature and large temperature gradient between the seed and graphite holder lead to local sublimation of the seed at the beginning of the growth and then to the macrodefect formation. These macrodefects can be eliminated by a specific design of the seed–holder attachment technique, which determines the local gradient at the interface between the seed and the holder. Another practical solution may consist in a modification of the thermoelastic field into the growing ingot in order to stop the progression of these macrodefects into the single crystal boule. Both solutions are presently under investigation.

A major problem in the growth of SiC single crystals is the appearance of hollow pipes, so-called pinholes or micropipes, growing along the c axis through the whole crystal. Their diameter may vary from a few nanometers to several ten micrometers from pipe to pipe and also along the same pipe. Facets have been recently observed by transmission electron microscopy in the walls of pipes having a typical diameter of 15 µm [35]. Typical density of these pipes ranges between 50 cm⁻² to several 1000 cm⁻² measured on basal plane while better results

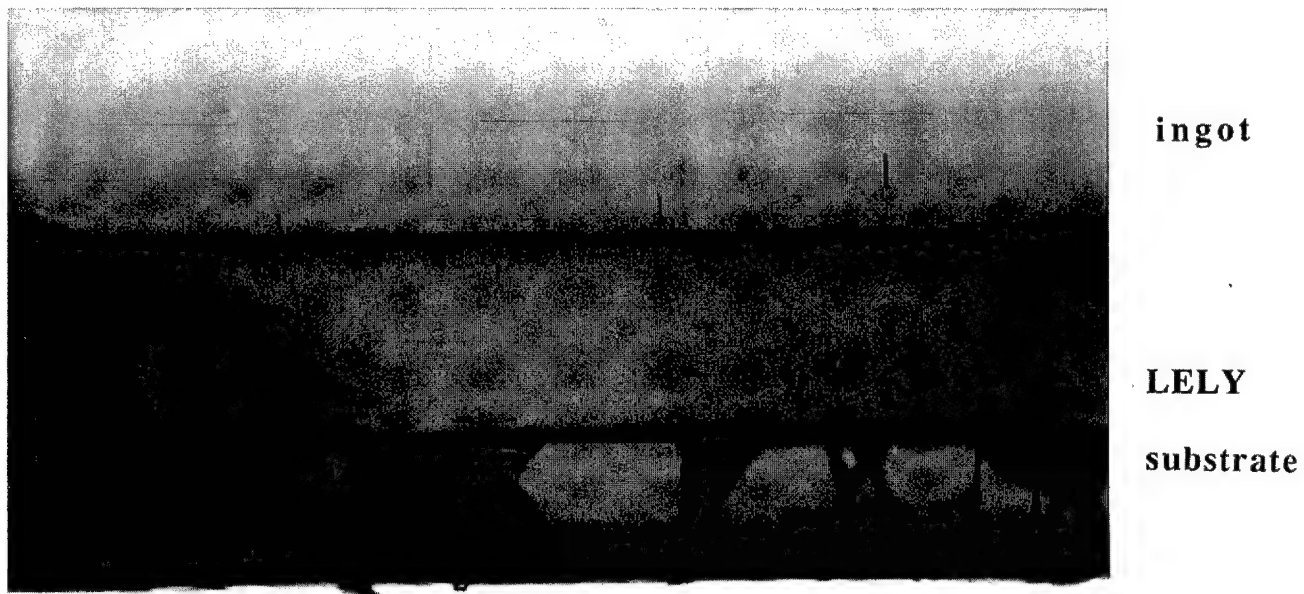


Fig. 10. Observation in transmitted height of macrodefects originating at the surface seed-graphite holder.

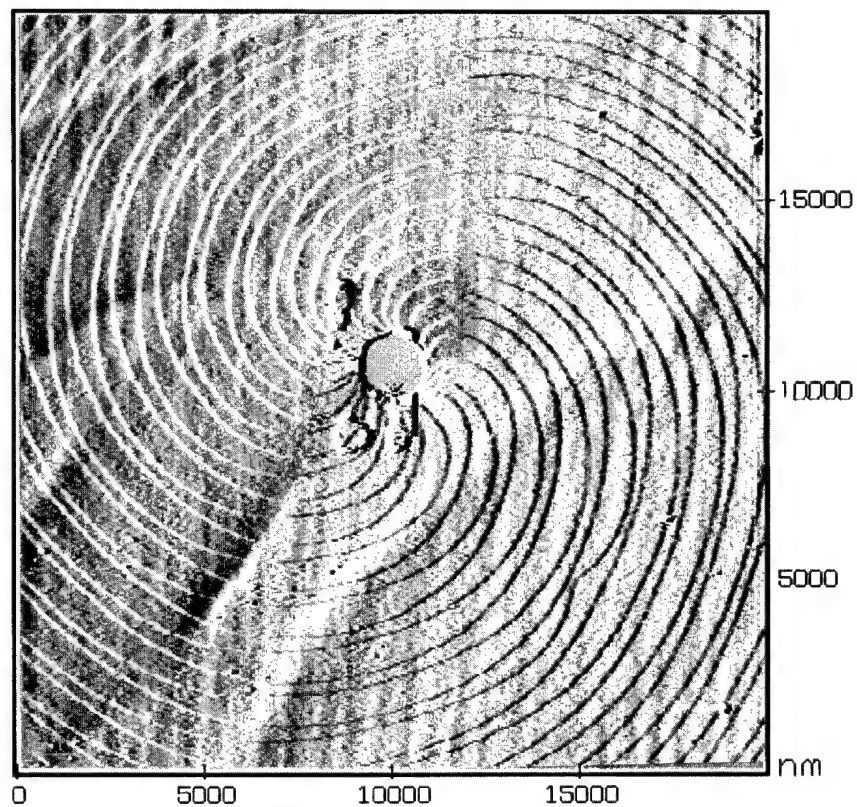


Fig. 11. Atomic force microscope observation of a micropipe at the centre of 24 left handed spirals.

have been reported recently by Cree Research without indications on the technical solutions used to achieve this goal [17]. The sublimation etch technique described above has permitted the reproducible growth of 6H-SiC crystals with $<100 \text{ cm}^{-2}$ pinholes density.

It has been reported that the concentration of pinholes varied over the surface of the wafers, (0001) orientation, in a similar manner to the concentration of misoriented domains [30]. Since in M-Lely crystals these domains are bordered by boundaries of high dislocations density, it is quite natural that the more often proposed explanations for the formation of micropipes are based on the original mechanisms proposed first by Franck [36] and then developed theoretically by different groups [37–44]. In its original work, Franck points out that a dislocation whose Burgers vector exceeds a critical value is only in equilibrium with an empty tube at its core of radius r such as:

$$r = \mu b^2 / 8\pi^2 \gamma$$

where γ is the specific surface energy of the material, μ its rigidity modulus and b is the modulus of the Burgers vector. The values generally accepted for γ and μ are 400 erg cm^{-2} and $16.6 \times 10^{11} \text{ erg cm}^{-3}$, respectively, leading to a value of 42 \AA^{-1} for μ/γ [30]. Quite different values have also been reported for this ratio [45–47] but the ones given above seem to be the more reliable. According to this model, a perfect screw dislocation in 6H-SiC whose Burgers vector is equal to the unit cell dimension along the c-axis should lead to a hole of 12.0 nm radius. To find values closer to what it is generally observed, one must consider the general case of a perfect screw dislocation in the 6H structure whose the Burgers vectors $b = 6mh$ [30], m being an integer and h the length of an unit monomolecular layer parallel to the basal plane: 0.2518 nm . The $6m$ unit step could be distributed in any manner between the limits of complete bunching into a single macrostep of height h . Fig. 11 obtained by atomic force microscopy on the flat top surface of an as grown ingot illustrates this point by showing a micropipe surrounded by 24 left handed spirals with step height of $3h$ originated from a screw dislocation of Burgers vector $6 \times 12h:18.129 \text{ nm}$ with a calculated $r = 1.72 \mu\text{m}$ quite close to the value deduced from Fig. 11.

A detailed analysis of step flow, step bunching and periodic delineation on the surface of 6H-SiC crystal is out of the scope of this paper and will be published elsewhere. However, based on these results, we may confirm that SiC can grow in a step flow mode from a spiral originated at an emerging screw dislocation: due to the stress a hollow core could develop and from this hollow core, a spiral step emerges. The bases of terrace risers are source of atomic steps and the lateral movement of these atomic steps on the treads causes the vertical growth of the crystal [48,49]. The growth will

depend on supersaturation and deposition temperature which will define the surface mobility of reactive chemical species on the terrace. However, in some conditions [48] macrosteps should be able to develop from the natural nucleation of monoatomic step rather than from dislocations. It must be pointed out that in the case of pure edge dislocation with Burgers vector parallel to the free surface, no spiral can be formed but under stress a hollow core will still develop.

In summary, the occurrence and characteristics of the micropipes depend on the dislocation network in the crystal, the supersaturation in reactive gaseous species and the stress field in the crystal during the growth. Hence, the production of SiC 6H single crystals with a low density of micropipes need at least two conditions: (1) The growth must occur in the step flow mode on well prepared surface and at low supersaturation. (2) The enlargement step must be strictly controlled to avoid the formation of a high density of screw dislocations along the c-axis.

References

- [1] R.F. Davis, Physica B 185 (1993) 1.
- [2] B.J. Baliga, IEEE Electron Device Letters EDL- 10 (1989) 455.
- [3] B.J. Baliga, Inst. Phys. Conf. Sci. 142 (1) (1996) 1.
- [4] G.R. Fisher, P. Barnes, Phil. Mag. B 61 (2) (1990) 217.
- [5] J.A. Lely, Ber. Dent. Keram-Ges, 32 (1955).
- [6] Yu.M. Tairov, V.F. Tsvetkov, J. Cryst. Growth 43 (1978) 209.
- [7] Yu.M. Tairov, Mater. Sci. Engng B29 (1995) 83.
- [8] D.L. Barrett, R.G. Seidensticker, W. Gaida, R.H. Hopkins, W.S. Choyke, J. Cryst. Growth 109 (1991) 17.
- [9] G. Ziegler, P. Lanig, D. Theis, C. Weyrich, IEEE. Trans. Electron Devices ED- 30 (1983) 277.
- [10] K. Koga, Y. Ueda, T. Nakata, T. Yamaguchi, T. Niina, Vacuum 30 (1987) 886.
- [11] D.L. Barrett, J.P. McHugh, H.M. Hobgood, R.H. Hopkins, P.G. McMullin, R.C. Clarke, W.J. Choyke, J. Cryst. Growth 128 (1993) 358.
- [12] R.A. Stein, Physica B 185 (1993) 211.
- [13] J. Takahashi, M. Kanaya, Y. Fujiwara, J. Cryst. Growth 135 (1994) 61.
- [14] S. Nishino, T. Higashino, T. Tanaka, J. Saraie, J. Cryst. Growth 147 (1995) 339.
- [15] M.M. Anikin, R. Madar, A. Rouault, I. Garcon, L. Di Coccio, J.L. Robert, J. Camassel, J.M. Bluet, Inst. Phys. Conf. Sci. 142 (1) (1996) 33.
- [16] M. Anikin, R. Madar, Proc. E-MRS Spring Meeting (1996).
- [17] V.F. Tsvetkov, S.T. Allen, H.S. Kong, C.H. Carter Jr, Inst. Phys. Conf. Sci. 142 (1) (1996) 17.
- [18] Yu.M. Tairov, Inst. Phys. Conf. Sci. 142 (1) (1996) 11.
- [19] K. Onoue, T. Nishikawa, M. Katsumo, N. Ohtani, H. Yashiro, M. Kanaya, Inst. Phys. Conf. Serv. 142 (1) (1996) 65.
- [20] N. Takanaka, S. Nishino, J. Saraie, Inst. Phys. Conf. Serv. 142 (1) (1996) 49.
- [21] J. Baruchel, Phys. Stat. Sol. (a) 141 (1994) 59.
- [22] M. Pons, E. Blanquet, J.M. Dedulle, R. Madar, C. Bernard, J. Electrochem. Soc., 143, 11 (1996) 3727.
- [23] P. Rocabois, C. Chatillon, C. Bernard, High Temp.-High Press. 27/28 (1995–1996) 3.

[24] P. Rocabois, C. Chatillon, C. Bernard, F. Genet, High Temp.–High Press. 27/28 (1995–1996) 25.

[25] S. Amelinckx, G. Strumane, J. Appl. Phys. 31 (8) (1960) 1359.

[26] I. Sunagawa, K. Narita, P. Bennema, B. van der Hoek, J. Cryst. Growth 42 (1977) 121.

[27] R.S. Rai, G. Siwgh, S.P. Sen Gupta, J. Cryst. Growth 61 (1983) 170.

[28] P. Bennema, J. Cryst. Growth 69 (1984) 182.

[29] A.N. Pilyankevich, V.F. Britun, Phys. Stat. Sol. (a) 82 (1984) 449.

[30] P. Krishna, S.S. Jiang, A.R. Lang, J. Cryst. Growth 71 (1985) 41.

[31] R.C. Glass, L.O. Kjellberg, V.F. Tsvetkov, J.E. Sundgren, E. Janzen, J. Cryst. Growth 132 (1993) 504.

[32] M. Tuominen, R. Yakimova, R.C. Glass, T. Tuomi, E. Janzen, J. Cryst. Growth 144 (1994) 267.

[33] M. Dudley, S. Wang, W. Huang, C.H. Carter Jr, V. Tsvetkov, C. Fazi, J. Phys. D: Appl. Phys. 28 (1995) A63.

[34] M. Tuominen, E. Prieur, R. Yakimova, R.C. Glass, T. Tuomi, E. Janzen, J. Cryst. Growth 165 (1996) 233.

[35] J. Heindl, M.P. Strunk, Phys. Stat. Sol. (b) (1996) K1.

[36] F.C. Franck, Acta. Cryst. 4 (1951) 497.

[37] N. Cabrera, M.M. Levine, Phil. Mag. 1 (1956) 450.

[38] F.C. Franck, Dis. Faraday Soc. 5 (1949) 5.

[39] W.K. Burton, N. Cabrera, F.C. Franck, Phil. Trans. Roy. Soc. 243 (1951) 299.

[40] I. Sunagawa, B. Bennema, J. Cryst. Growth 46 (1979) 451.

[41] I. Sunagawa, B. Bennema, J. Cryst. Growth 53 (1981) 490.

[42] B. van der Hoek, J.P. Van der Eerden, P. Bennema, J. Cryst. Growth 56 (1982) 108.

[43] B. van der Hoek, J.P. van der Eerden, P. Bennema, I. Sunagawa, J. Cryst. Growth 58 (1982) 365.

[44] B. van der Hoek, J.P. van der Eerden, P. Bennema, J. Cryst. Growth 56 (1982) 621.

[45] H. Tanaka, Y. Uemura, Y. Inomata, J. Cryst. Growth 53 (1981) 630.

[46] J.P. Golightly, Z. Krist. 130 (1969) 310.

[47] E. Pearson, T. Takai, T. Halicioglu, W.A. Tiller, J. Cryst. Growth 70 (1984) 33.

[48] P. Heuell, M.A. Kulakov, B. Bullemer, Silicon Carbide and Related Materials, Institute of Physics, London, 1994, p. 353.

[49] Z. Zhang, M.A. Kulakov, B. Bullemer, Silicon Carbide and Related Materials, Institute of Physics, London, 1994, p. 349.

Sublimation growth of 4H- and 6H-SiC boule crystals

V.D. Heydemann *, N. Schulze, D.L. Barrett ¹, G. Pensl

Institut für Angewandte Physik, Universität Erlangen-Nürnberg, Staudtstrasse 7, D-91058 Erlangen, Germany

Abstract

The dual-seed-crystal method is developed and used to study the growth of 4H- and 6H-SiC boule crystals by varying particular growth parameters, e.g. the distance between the growth front and the source material and the face polarity of the seeds. A range of values is elaborated for a series of growth parameters, which leads to the growth of single crystals. The grown SiC crystals are electrically and optically characterized. © 1997 Elsevier Science S.A.

Keywords: Sublimation growth; SiC polytypes; Nitrogen donors; Extended crystalline defects

1. Introduction

High quality silicon carbide (SiC) substrates of large diameter ($\varnothing \geq 5$ cm) are the basis for a commercial production of SiC-based electronic devices. During the last 3 years, a continuous progress has been achieved in extending the size and improving the quality of 4H- and 6H-SiC boule crystals. However, a series of physical problems, e.g. the control of growing a particular polytype (4H, 6H) or the avoidance of micropipes, are still not understood. We have started a SiC growth project in order to study the growth mechanism of the sublimation physical vapor transport and to provide SiC wafers for our optical and electrical characterization methods.

2. Experimental details

2.1. Dual-seed-crystal method

The modified Lely growth technique was first introduced by Tairov et al. [1] and Ziegler et al. [2]; variations of the growth arrangements are given by several authors [3–6]. The growth system we have used is described in Ref. [7].

In this system, two seed crystals with different properties can be fixed on the lid of the crucible (see Fig. 1). This dual-seed-crystal technique enables the simultaneous study of SiC growth on two seed crystals with

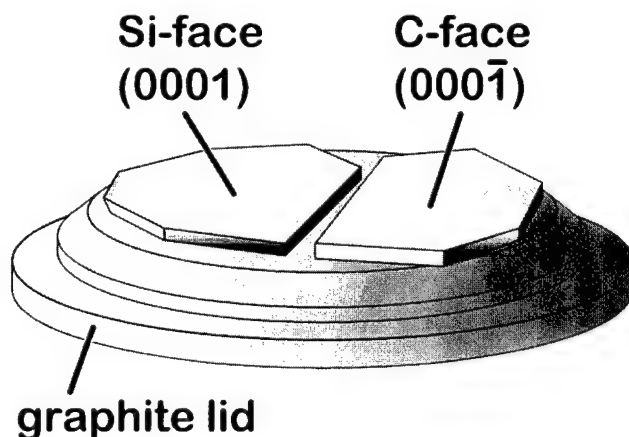


Fig. 1. Schematic demonstrating the dual seed crystal method for an example of two seeds with opposite face polarity.

different surface properties under identical growth conditions. The seeds may differ in face polarity (Si-face or C-face), orientation (on-axis or off-axis), surface treatment or polytype (4H or 6H).

2.2. Growth parameters

The growth of a particular SiC polytype depends not only on the properties of the seed crystal, but also on a variety of process parameters, which can be adjusted during the growth procedure. The diagrams in Fig. 2 show the dependence of the source temperature T_{source} , the seed temperature T_{seed} , their difference $\Delta T = T_{\text{source}} - T_{\text{seed}}$ and the argon pressure p_{Ar} in the crucible during a growth run.

* Corresponding author.

¹ Present address: 6141 Sanctuary Gardens Blvd., Port Orange, FL 32124, USA.

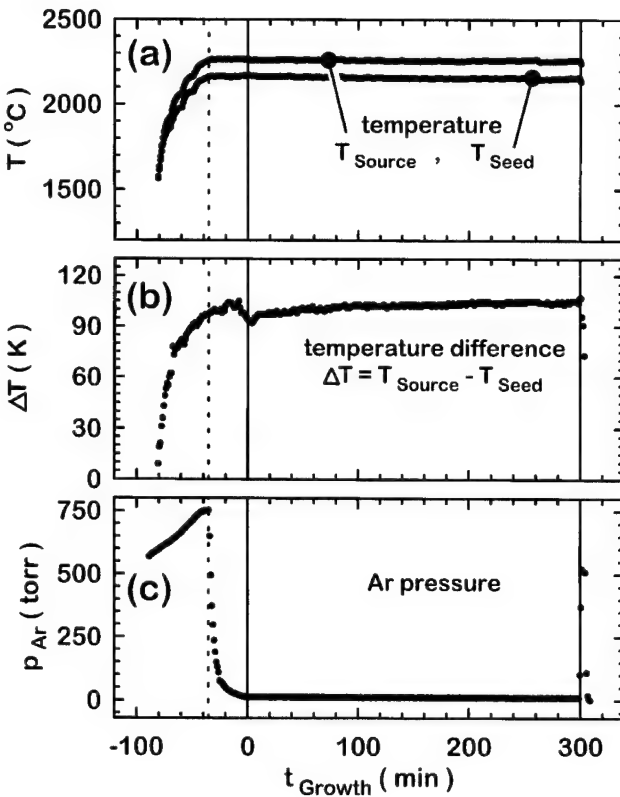


Fig. 2. Diagrams of (a) the source temperature T_{source} /seed temperature T_{seed} , (b) the temperature difference $\Delta T = T_{\text{source}} - T_{\text{seed}}$, and (c) the argon pressure p_{Ar} as a function of the growth time t_{Growth} during a typical growth run.

The most essential growth parameters and ranges in which these parameters have been varied in our experiments are listed in Table 1.

3. Results and discussion

3.1. SiC boule crystal grown by sequential runs

We succeeded in growing 6H- and 4H-SiC boule crystals of about 2.5 cm in diameter and typically 1–2 cm

Table 1
Ranges of values of essential growth parameters typically employed during growth experiments

Growth parameter	Range of used values/orientations
Source temperature	2200–2400°C
Temperature gradient	10–40 K/cm
Argon pressure	1–38 torr
Growth duration	1–15 h
Distance between growth front and source material	6–30 mm
Seed face	(0001)/(0001̄)
Seed orientation	On-axis/8° off-axis
Additional Si powder (related to the SiC source material)	0–100%

in length. Fig. 3 shows a central cross-sectional cut parallel to the c -axis of a 6H-SiC boule crystal, which is grown sequentially during four growth runs. In this case, we have used only one seed crystal (diameter $\varnothing \approx 10$ mm). The interfaces between successive growth runs visualize the growth front, demonstrating that the growth rate has been slightly higher in the right half of the figure. The edge regions show a high density of agglomerated micropipes, which arise from the graphite bottom. It seems that the micropipes grow from the interface lid-seed crystal through the seed crystal and continue into the SiC boule. Great care has, therefore, to be exercised in the selection of a suitable lid material and the method of fixing the seed crystal to the lid. The SiC part grown centrally above the seed crystal provides a low density of micropipes. We counted 12 micropipes cm^{-2} in an area of $4 \times 4 \text{ mm}^2$ in the bulk of the second run, and we could find no micropipe in an equivalent area of the third run. During the fourth growth run, the growth rate increased considerably owing to the shrinking distance between the growth front and the source material such that the growth resulted in polycrystalline SiC material.

3.2. Effect of the seed face polarity on the grown SiC crystal

The dual seed crystal method is a useful tool to study the effect of the seed face polarity on the polytype, morphology and impurity incorporation of SiC boules.

The growth of the 4H and 6H polytype strongly depends on the face polarity [Si-face (0001), C-face (0001)], which is offered for the sublimation growth. 4H-SiC growth is observed exclusively on C-faces, which is in agreement with findings reported [8]. We have observed in more detail 4H growth on on-axis aligned C-faces of 6H- or 4H-SiC seeds when the adjusted growth rates were greater than 1.1 g h^{-1} , and seed temperatures of 2150–2190°C were used. For 8° off-axis aligned C-faces of 6H seed crystals, the parameter range for 4H growth is slightly extended: $\Delta m_{\text{lid}}/\Delta t_{\text{growth}} \geq 0.5 \text{ g h}^{-1}$ and $2060^\circ\text{C} \leq T_{\text{Seed}} \leq 2190^\circ\text{C}$.

The incorporation of nitrogen (N) atoms as the dominating donor species in SiC also depends on the face polarity of the seed crystal, which is presented for the sublimation growth. As is demonstrated by the Hall effect results displayed in Fig. 4a (for an evaluation of the Hall effect data, see Ref. [9]), the incorporation of nitrogen donors in SiC crystals grown on the C-face of seed crystals is higher than in those grown on Si-faces. The ratio of the total concentration of nitrogen donors incorporated in crystals grown on C-faces to those grown on Si-faces increases with the nitrogen concentration ($[N]_N = 10^{17} \text{ cm}^{-3}–10^{19} \text{ cm}^{-3}$) itself:

$$\frac{[N_N](\text{C-face})}{[N_N](\text{Si-face})} = 2.2 \text{ to } 5$$

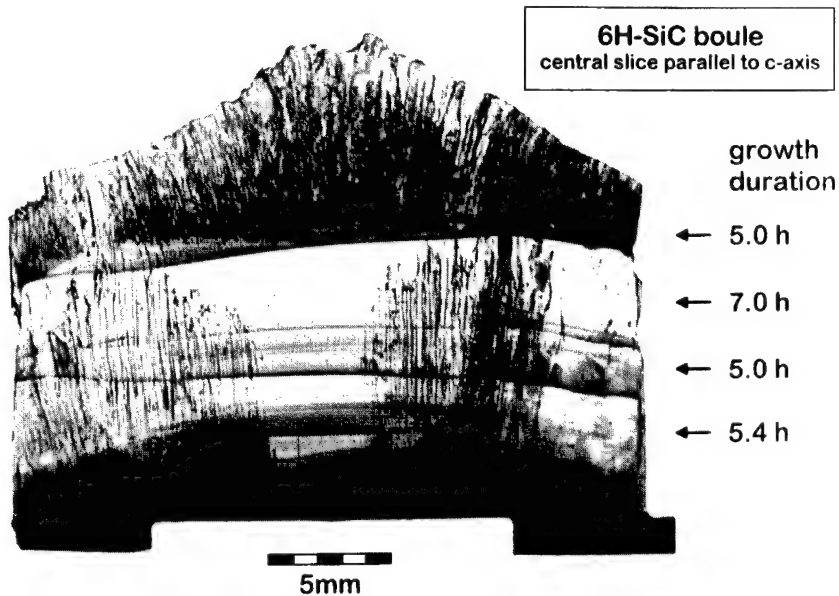


Fig. 3. Cross-sectional view parallel to the *c*-axis of a 6H-SiC crystal grown sequentially with four growth runs.

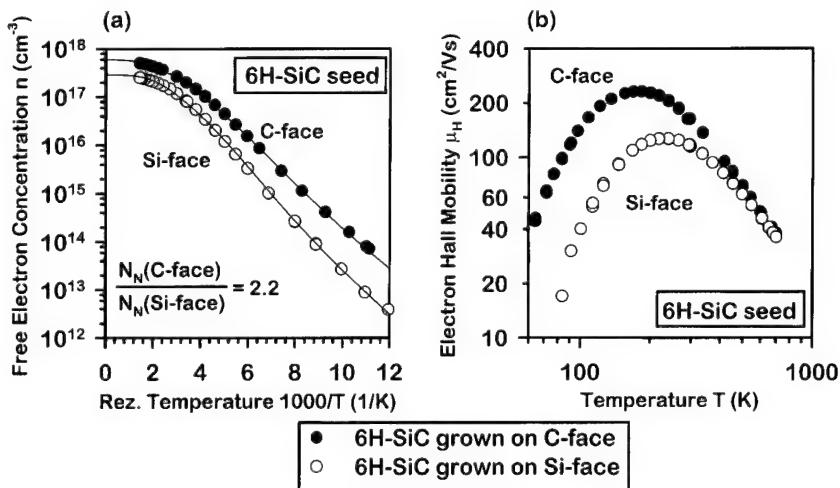


Fig. 4. Hall effect results taken on a pair of 6H-SiC crystals grown by the dual-seed-crystal method with opposite face orientation. (a) Free electron concentration, n , as a function of the reciprocal temperature, T^{-1} . (b) Electron Hall mobility, μ_{H} , as a function of the temperature, T .

This observation is independent of the SiC polytype (4H or 6H). Similar trends have also been reported in publications, where the corresponding SiC crystals were grown sequentially and not by the dual-seed method [10,11].

Fig. 4b reveals the electron Hall mobility of the samples investigated in Fig. 4a. Although the nitrogen concentration and the compensation (not shown here) in the 'C-face sample' are higher by approximately a factor of two, which results in a stronger electron scattering by impurities, the overall electron mobility in this sample is higher compared to that grown on the Si-face. This behavior is observed in all corresponding

pairs of SiC samples investigated. We believe that the lower electron mobility in 'Si-face samples' is caused by a degradation of the crystalline quality, as demonstrated in the micrographs of Fig. 5. Whereas the 'C-face sample' shows just eight micropipes, the 'Si-face sample' provides a high density of different extended defects.

4. Summary

We have demonstrated that the dual-seed-crystal method is a powerful tool to study the sublimation

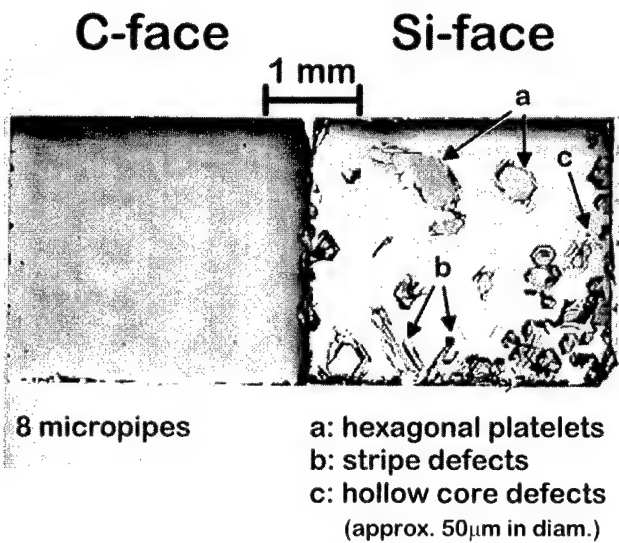


Fig. 5. Optical micrographs of the surface of the C-/Si-face sample characterized in Fig. 4 demonstrating the difference in crystalline defects.

growth of SiC. We succeeded in the growth of high-quality 4H- and 6H-SiC boules and determined ranges of suitable values for the different growth parameters.

Acknowledgement

The support of this work by the German Science Foundation (Sonderforschungsbereich 292) is gratefully acknowledged.

References

- [1] Yu.M. Tairov, V.F. Tsvetkov, J. Crystal Growth 43 (1978) 209.
- [2] G. Ziegler, P. Lanig, D. Theis, D. Weyrich, IEEE Trans. Electron Devices ED30 (1983) 277.
- [3] D.L. Barrett, R.G. Seidensticker, W. Gaida, R.H. Hopkins, W.J. Choyke, J. Crystal Growth 109 (1991) 17.
- [4] D.L. Barrett, J.P. McHugh, H.M. Hobgood, R.H. Hopkins, P.G. McMullin, R.C. Clarke, J. Crystal Growth 128 (1993) 358.
- [5] K. Furukawa, Y. Tajima, H. Saito, Y. Fujii, A. Suzuki, S. Nakajima, Jpn. J. Appl. Phys. 32 (1993) L645.
- [6] M. Kanaya, J. Takahashi, Y. Fujiwara, A. Moritani, Appl. Phys. Lett. 58 (1991) 56.
- [7] Heydemann, V.D., Schulze, N., Barrett D.L. and Pensl, G. Appl. Phys. Lett. 69 (1996) 3728.
- [8] R.A. Stein, P. Lanig, S. Leibenzeder, Mat. Sci. Eng. B11 (1992) 69.
- [9] G. Pensl, W.J. Choyke, Physica B185 (1993) 264.
- [10] J. Takahashi, N. Ohtani, M. Kanaya, Jpn. J. Appl. Phys. 34 (1995) 4694.
- [11] K. Onoue, T. Nishikawa, M. Katsuno, N. Ohtani, H. Yashiro, M. Kanaya in, Silicon carbide and related materials, Inst. Phys. Conf. Ser. 142 (1995) 65.

Growth of SiC from the liquid phase: wetting and dissolution of SiC

M. Syväjärvi ^{*a}, R. Yakimova ^{a,b}, E. Janzén ^a

^a Department of Physics and Measurement Technology, Linköping University, S-581 83 Linköping, Sweden

^b Outokumpu Semitronic AB, S-161 11 Bromma, Sweden

Abstract

The wetting properties of various Si–Sc melts on different faces of α -SiC wafers are studied and the dissolution morphologies investigated. The properties for on-axis wafers are found to be dependent on alloy composition and on polytype. The wetting properties of misoriented wafers are also investigated. From the results obtained, the interfacial energies on different faces are found to be dissimilar, and the surface free energy of 4H-SiC is compared with 6H-SiC. Owing to this, the growth mechanism is discussed. © 1997 Elsevier Science S.A.

Keywords: Dissolution; Growth; Liquid phase; Morphology; Silicon carbide; Surface energy; Wetting

1. Introduction

Silicon carbide (SiC) is a semiconductor which is suitable for electronic applications. However, the quality of the material still needs to be improved. In liquid-phase semiconductor growth, it is usual to dissolve the substrate surface prior to growth. This improves the structural quality of the grown material, since damage during wafer preparation is eliminated. Since the growth mechanism depends on the substrate surface morphology and the quality of the grown material depends critically on the quality of the growth interface, the dissolution process is a crucial step. Due to this, the wetting property is also important. In this study, the wetting properties and dissolution morphology of 6H- and 4H-SiC are investigated. The results are discussed in relation to the interfacial energies and the growth mechanism.

2. Experimental

Wetting and dissolution were carried out on both faces of commercial 6H- and 4H-SiC wafers (Cree Research Inc., USA). Both on-axis ($\langle 0001 \rangle$) and off-oriented wafers were used. The misorientation was 3.5° or 8° towards the $(11\bar{2}0)$ plane. Different solution compositions in the Si–Sc system were investigated. This

system was chosen since it is suitable for SiC liquid-phase growth [1,2]. The wetting properties have been studied for alloy compositions from Si:Sc = 60:40 to Si:Sc = 100:0 (wt.%). The Si:Sc = 60:40 (wt.%) composition corresponds to an eutectic point in the Si–Sc phase diagram with a melting point at ~ 1265 °C [3]. This composition is favorable concerning the growth rate and surface morphology of epitaxial layers grown in the Si–Sc–C system [4]. The Si used was cut from a high-resistivity wafer, while Sc was taken from a foil with 99.9% purity. The materials were cleaned by a degreasing procedure and dipped in HF to remove oxide prior to melting. Melting was carried out in vacuum or in an inert ambient (ultrapure Ar N60). The pure Si melt and the alloys were heated to about 1425 °C to minimize effects owing to insufficient mixing. To investigate the dissolution morphologies, after solidification the alloys were etched from the SiC wafers in a mixture of NHO_3 and HF. An optical microscope with Nomarski interference contrast was used for the study. The wetting angles were determined from photographs taken in the microscope in the transmission mode [5].

3. Results and discussion

The change of dissolution morphology with alloy composition is shown in Fig. 1 for 6H-SiC on-axis wafers (Si face). The morphology obtained with the pure Si melt exhibits small circular and hexagonal pits

* Corresponding author. Fax: +46 13 142337; e-mail: msy@ifm.liu.se

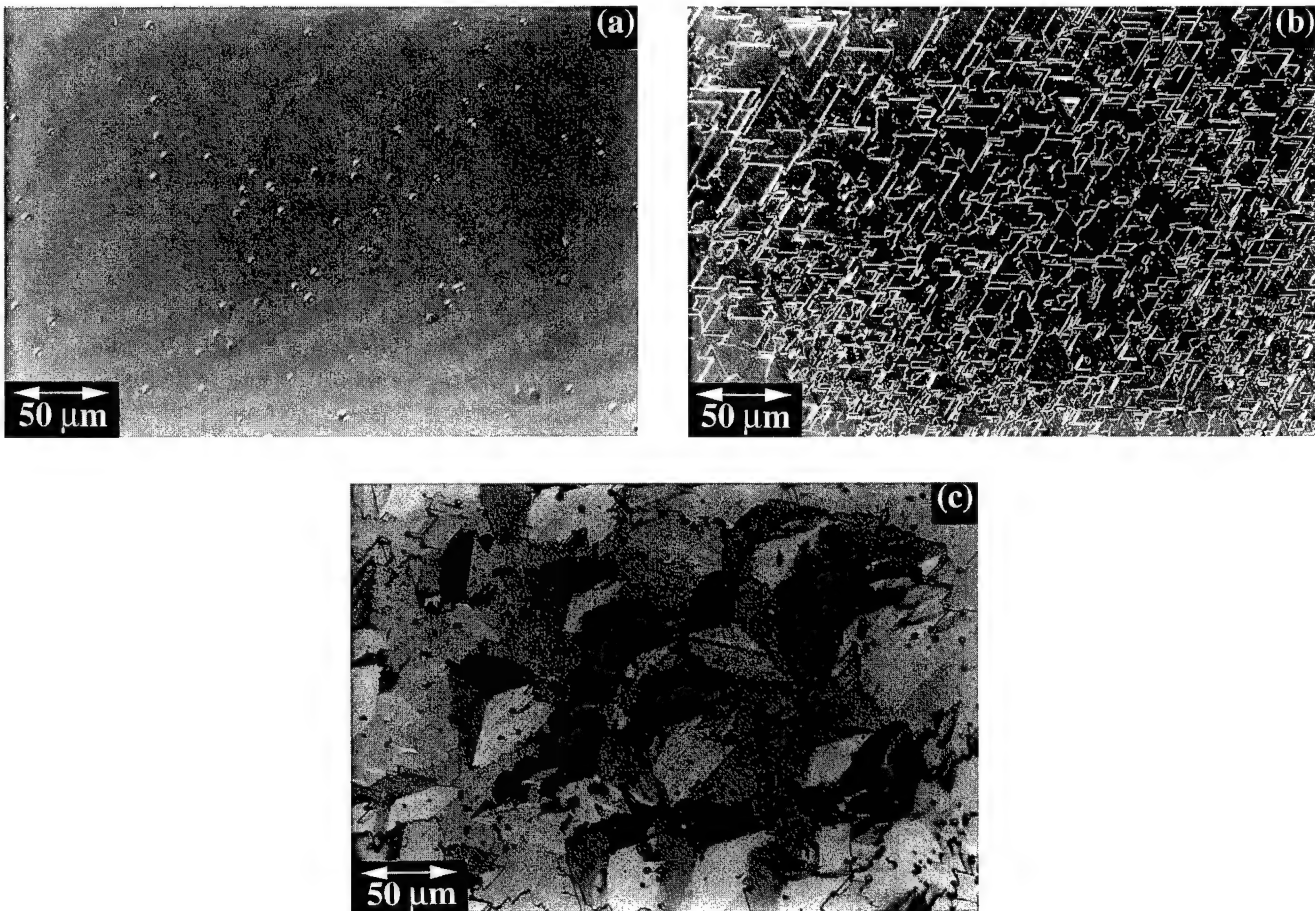


Fig. 1. Dissolution morphology of the 6H-SiC Si-face with different solvent compositions (wt. %): (a) Si:Sc = 100:0, (b) Si:Sc = 85:15, (c) Si:Sc = 60:40 (wafer orientation on-axis).

(Fig. 1(a)). For small amounts of Sc, the dissolved surface has triangular-shaped features (Fig. 1(b)). When the solvent is more Sc-rich, larger triangular pits are developed (Fig. 1(c)). When the Sc content is above 40 wt.%, the morphology roughens severely, and no clear dissolution patterns are observed. For pure Sc, the dissolution morphology is rough. These observations are explained by an increasing dissolution rate with increasing Sc content in the melt, and by the dissolution mechanism, which obviously has a reactive character. The dissolution morphology of the C face of 6H-SiC was smoother, most probably due to a lower surface energy.

The dissolution morphology of 4H-SiC on-axis wafers (Si face) shows a difference as compared to 6H-SiC under similar conditions. The surface has a rather smooth appearance, with a spiral dissolution being observed occasionally. Most commonly, the dissolution spiral appears where a micropipe is located.

The wetting angles measured for different alloy compositions are shown in Fig. 2(a). All angles are average values from 4–10 measurements. The wafer orientation was on-axis in order to reduce effects due to misorienta-

tion. The angle on the Si face decreases with increasing Sc content in the melt, due to the increasing solubility of SiC in the melt. A similar dependence is also seen at higher temperature [6] which is used when growing SiC from the liquid phase in the Si–Sc–C system. Measurement of the wetting angle on the C face was difficult when Sc was introduced into the Si melt. For a pure Si melt on on-axis wafers, the wetting angle is lower on the C face than on the Si face of 6H-SiC (Fig. 2(b)). With increasing misorientation the wetting angles approach similar values for different faces and polytypes. The wetting properties were not observed to depend on the wetting ambient, but the mixing of the alloy seems to improve in vacuum.

From the experimental values of the wetting angles, the interfacial energy of the melt/SiC system can be estimated using Young's equation, i.e. $\sigma_{6H} = \sigma_{int} + \sigma_{melt} \cos \theta$, where σ_{6H} is the surface free energy of 6H-SiC, σ_{melt} is the surface tension of the melt, σ_{int} is the interfacial energy of the melt/SiC system, and θ is the wetting angle. There is no reliable data on the surface free energy of α -SiC. However, since the surface atomic configuration of the 6H(0001) face is

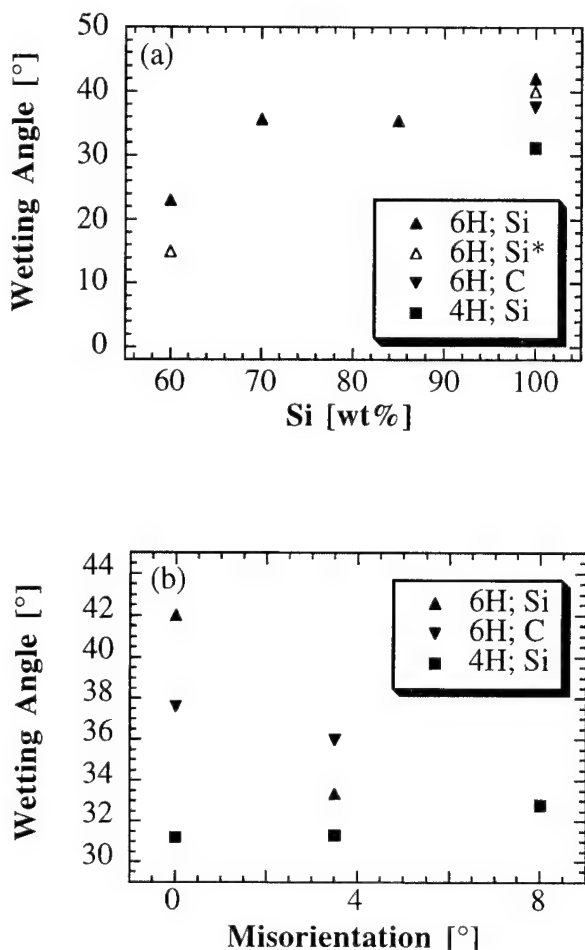


Fig. 2. (a) Dependence of the wetting angle of the faces of 4H- and 6H-SiC on alloy composition. Asterisked data are from Ref. [6] and were obtained at a higher temperature (1750 °C). Wafer orientation on-axis. (b) Dependence of the wetting angle on wafer misorientation for 6H- and 4H-SiC on different faces. Alloy composition: Si:Sc = 100:0 (wt.%).

similar to the 3C-SiC(111) face, the calculated data for the cubic polytype [7] are used. Consequently, the surface free energy for 6H-SiC is assumed to be $\sigma_{6H} = 1767 \text{ erg cm}^{-2}$ for the Si face and $\sigma_{6H} = 718 \text{ erg cm}^{-2}$ for the C face. Knowing the surface tension of molten Si ($\sigma_{Si} = 819 \text{ erg cm}^{-2}$) [8] and molten Sc ($\sigma_{Sc} = 1153 \text{ erg cm}^{-2}$) [9], and estimating the surface tension of the alloy [10], the interfacial energies of the pure Si melt and Si:Sc = 60:40 (wt.%) on the Si and C faces of SiC can be obtained. From Young's equation, the surface free energy for 4H-SiC (Si face) is thus deduced to be about $\sigma_{4H} = 1860 \text{ erg cm}^{-2}$, which is higher than that for 6H SiC (Si face). It is worth noting that the interfacial energy of the C face is much lower than that of the Si face of 6H-SiC, and that the interfacial energy is lower when using an alloy as compared to a pure Si melt. This result shows that growth in the Si-Sc-C system is energetically more favorable than growth in the Si-C system. Quantitative character-

istics have been used to obtain some indications of the possible growth mechanism. Basically, two-dimensional nucleation is considered as a possible growth mechanism when growing from the liquid phase on on-axis oriented substrates [11]. Using the relation between the interfacial energy and the supercooling [11], two-dimensional nucleation on 6H-SiC on-axis wafers may be excluded as a possible growth mechanism on the Si face, but it is likely to occur on the C face. This result is an interesting subject for further experimental study.

4. Conclusion

The wetting properties of Si-Sc melts on SiC improve with increasing Sc content in the melt. However, the dissolution morphology roughens and the reactive dissolution process is uncontrolled when using Sc-rich solvent compositions. The wetting and dissolution properties are different for the different faces of 6H-SiC and different α -SiC polytypes. From the experimental results, the surface free energy for 4H-SiC is estimated to be $\sim 1860 \text{ erg cm}^{-2}$ on the Si face, and this is higher as compared to 6H-SiC. The interfacial energy is lower on the C face than on the Si face for 6H-SiC. The results suggest different growth mechanisms on the different faces.

Acknowledgement

The Swedish National Space Board and the Swedish Board for Industrial and Technological Development (NUTEK) are acknowledged for financial support. We also thank Dr. T. Kimoto for providing information about the surface free energy of SiC.

References

- [1] R. Yakimova, T. Tuominen, A.S. Bakin, J.-O. Fornell, A. Vehanen, E. Janzén, Inst. Phys. Conf. Ser. 142 (1996) 101.
- [2] M. Syväjärvi, R. Yakimova, I.G. Ivanov, E. Janzén, Mat. Sci. Eng. B 46 (1997) 329–332.
- [3] V. Kotroczo, I.J. McColm, J. Alloys Comp. 203 (1994) 259.
- [4] R.T. Yakimova, A.A. Kalnin, Phys. Status Solidi (a) 32 (1975) 297.
- [5] A.W. Adamson, Physical Chemistry of Surfaces, Wiley, New York, 1990, p. 389.
- [6] R. Yakimova, PhD thesis, Leningrad, 1974 (in Russian).
- [7] T. Takai, T. Halicioglu, W.A. Tiller, Surf. Sci. 164 (1985) 341.
- [8] S-I. Chung, K. Izunome, A. Yokotani, S. Kimura, Jpn. J. Appl. Phys. 34 (1995) L631.
- [9] C.T. Horowitz (Ed.), Scandium, Academic Press, London, 1975, p. 105.
- [10] V.K. Semenchenko, Surface phenomena in metals and alloys, Pergamon Press, Oxford (1961).
- [11] L.N. Alexandrov, Kinetika obrazovanya i struktury tverdyh sloev, Nauka, Moscow, 1972, p. 145 (in Russian).

The kinetic growth model applied to micropipes in 6H-SiC

J. Heindl ^{a,*}, W. Dorsch ^a, R. Eckstein ^b, D. Hofmann ^b, T. Marek ^a, St.G. Müller ^b,
H.P. Strunk ^a, A. Winnacker ^b

^a Institut für Werkstoffwissenschaften, Mikrocharakterisierung Universität Erlangen-Nürnberg, Cauerstraße 6,
91058 Erlangen, Germany

^b Institut für Werkstoffwissenschaften, Werkstoffe der Elektrotechnik Universität Erlangen-Nürnberg,
Martensstraße 7, 91058 Erlangen, Germany

Abstract

In this study we investigated the as-grown {0001} Si surface of modified Lely-grown 6H-SiC using atomic force microscopy. We found micropipes that lie in the center of growth spirals whose radii ranged between 25 and 6000 nm. The screw component of the Burgers vector of the micropipe, which is synonymous with the total step height of the growth spiral, ranged from 1 to 25 unit-cells (1.5–37.5 nm). We fitted Frank's theory of hollow core dislocations, as modified by Cabrera and Levine concerning kinetic effects, to these experimental results and obtained values for surface energy and supersaturation at the inner side of the micropipe. © 1997 Elsevier Science S.A.

Keywords: Micropipes; Growth model; Scanning force microscopy

1. Introduction

Micropipes in silicon carbide (SiC) are known to be hollow defects aligned along the direction of growth of the crystal. As they can penetrate the whole crystal they are a significant problem in growing high grade SiC single crystals. Their radii range from a few nanometers to several tens of micrometers [1]. One proposal for the growth mechanism was given by Frank [2] who considered the hollow core dislocation model. If the Burgers vector of a screw dislocation exceeds a critical value (approximately 1 nm) then it is, due to the very high strain energy, energetically more favorable to remove the crystal material near the dislocation line and to create an additional surface in the form of a micropipe. In this paper we measure total step heights and radii of micropipes and compare this data with the model proposed by Cabrera and Levine [3] who extended Frank's model with respect to kinetic aspects.

2. Experimental

We investigated the as-grown 6H-SiC {0001} Si-terminated surfaces of two single crystals grown by

physical vapor transport according to the m-Lely technique. The crystals were grown at a pressure of 30 mbar and at temperatures of $2350 < T < 2450$ K as described in Ref. [4]. The radii and total step heights of the micropipes were measured with an atomic force microscope (AFM) in contact mode with pyramidal and high aspect ratio cantilevers. The total step height of a spiral was measured during one revolution around the accompanying micropipe (Fig. 1). Therefore upward and downward steps were considered to be of opposite sign and the absolute value of the sum represented the total step height.

3. Results and discussion

We found 14 micropipes all surrounded by spirals with step heights ranging from 1.5 (elementary Burgers vector) to 37.5 nm. Their radii ranged from 25 to 6000 nm, respectively. No difference between the two crystals could be observed. Fig. 2 shows the values as a plot suitable for discussion.

According to Frank [2] screw dislocations can minimize their total energy by removing material around the dislocation line and forming a hollow core. The relationship between the equilibrium radius of the hollow core

* Corresponding author.

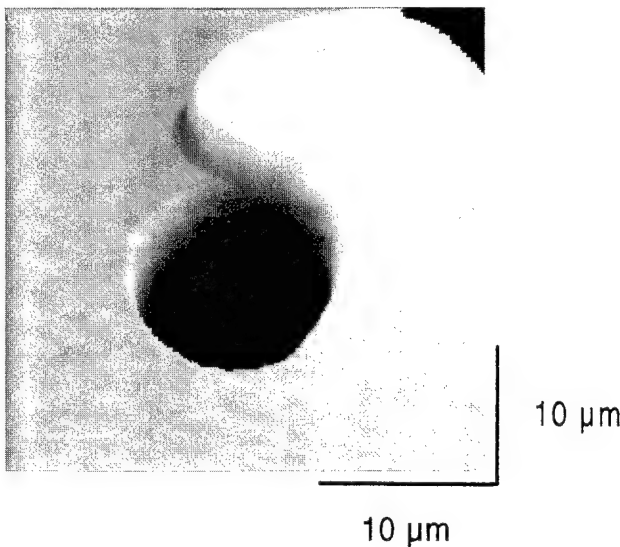


Fig. 1. Micropipe in 6H-SiC surrounded by spirals: the growth step and the edge of the micropipe are clearly visible. Atomic force microscopy.

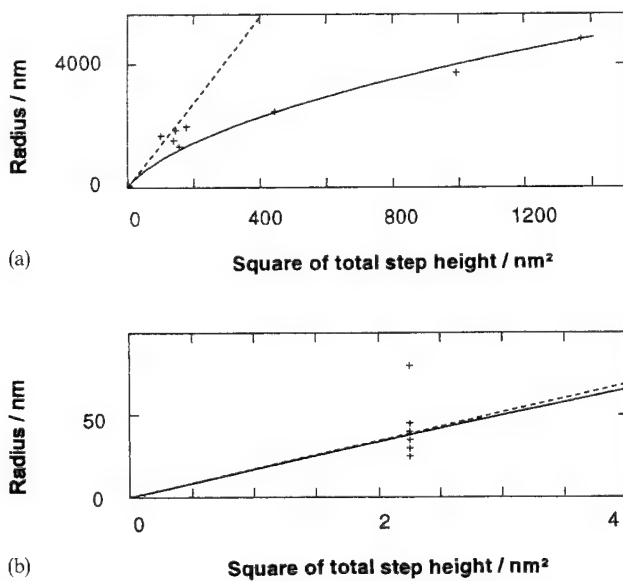


Fig. 2. (a) Total step heights versus radii of micropipes in 6H-SiC. The dashed line corresponds to the energetic approach of Frank [2], the solid line corresponds to the best fit obtained by including Cabrera and Levine's kinetic extension [4]. (b) Magnified view of the dependencies at small pipe radii. The six micropipes have unit cell Burgers vectors. At these small micropipes there is no significant difference between energetic and kinetic theory.

r_0 and the Burgers vector \mathbf{b} is given by:

$$r_0 = \frac{\mu \mathbf{b}^2}{8\pi^2 \gamma} \quad (1)$$

In our case we identify the Burgers vector \mathbf{b} with the total step height of the growth spiral. μ and γ denote the shear modulus and the surface energy, respectively. This linear dependence of radius r_0 on the square of the

Burgers vector, \mathbf{b}^2 , is represented in Fig. 2 with a dashed line. Our measured data do not fit this relationship (Fig. 2a) except for those concerning the micropipes with elementary Burgers vector (Fig. 2b). From these micropipes we obtain a value of μ/γ between 93 and 155 Å^{-1} . This is in sufficiently good agreement with the value of μ/γ between 63 and 91 Å^{-1} found by Dudley [5]. Using the room temperature value of $\mu = 1.9 \times 10^{11} \text{ J/m}^3$ we can derive an average surface energy for the inner surface of the micropipe of $\gamma = 0.14 \text{ J/m}^2$. This is a rather low value, but not too low to appear unphysical.

An overall fit can be obtained using Cabrera and Levine's [4] kinetic extension (solid line in Fig. 2). This approach considers the fact that the transition from the solid to the gaseous state involves a Gibbs free energy. This energy has to be spent on evaporating the material which would exist inside the volume of the micropipe with radius r_0 . Again, the equilibrium radius is obtained by minimizing the total energy, which leads to the Cabrera-Levine radius, r_{cl} , of the micropipe:

$$r_{cl} = -\frac{1}{2} r_c + \sqrt{\frac{1}{4} r_c^2 + r_0 r_c} \quad (2)$$

Here $r_c = \gamma \Omega / \Delta \sigma$ is the critical radius of a nucleus on an unstrained surface where $\Delta \sigma$ denotes the difference of the chemical potential between the solid and the gaseous state and Ω denotes the atomic volume. Using the surface energy value obtained above we can fit Eq. (2) to all our data in Fig. 2a and obtain $r_c = \gamma \Omega / \Delta \sigma = 1.4 \mu\text{m}$, yielding $\Delta \sigma = 1.1 \times 10^{-24} \text{ J}$. This rather low supersaturation is reasonable if we assume that the growth process is stopped by scarcity of SiC-powder in the growth chamber.

4. Summary and conclusion

In this study we measured radii and total step heights of micropipes in m-Lely 6H-SiC. The micropipes can be interpreted as hollow core dislocations. The relationship between micropipe radius and the total step height of the accompanying growth spirals can be understood by using the kinetic theory of Cabrera and Levine. Good agreement between the measured data and the theory yields a micropipe surface energy of 0.14 J/m^2 and a supersaturation of $1.1 \times 10^{-24} \text{ J}$.

Acknowledgement

This work was supported by the Deutsche Forschungsgemeinschaft (SFB 292 B3), the Bundesministerium

für Bildung und Forschung (BMBF), and Siemens AG, Erlangen (contract # 03 M 2746 BO).

References

- [1] J. Heindl, H.P. Strunk, Phys. State Sol. 193 (1996) K1.
- [2] F.C. Frank, Acta Crystal. 4 (1951) 497.
- [3] N. Cabrera, M.M. Levine, Phil. Mag. 1 (1956) 450.
- [4] D. Hofmann, M. Heinze, A. Winnacker, F. Durst, L. Kadinski, P. Kaufmann, Y. Makarov, M. Schäfer, J. Cryst. Growth 146 (1995) 214.
- [5] M. Dudley, W. Si, S. Wang, C. Carter, Jr., R. Glass, V. Tsvetkov, Proceedings of the Third European Symposium on X-ray Topography and High Resolution Diffraction, 1996, to be published in Il Nuovo Cimento D.

Growth-related structural defects in seeded sublimation-grown SiC

M. Tuominen ^{a,b,*}, R. Yakimova ^{a,b}, E. Prieur ^{c,e}, A. Ellison ^a, T. Tuomi ^d,
A. Vehanen ^{b,e}, E. Janzén ^{a,e}

^a Department for Physics and Measurement Technology, IFM, Linköping University, S-581 83 Linköping, Sweden

^b Outokumpu Semitronic AB, P.O. Box 111 92, S-161 11 Bromma, Sweden

^c European Synchrotron Radiation Facility, BP 220, F-38043 Grenoble, Cedex, France

^d Optoelectronics Laboratory, Helsinki University of Technology, FIN-02150 Espoo, Finland

^e Okmetic Ltd., P.O. Box 44, FIN-02631 Espoo, Finland

Abstract

Structural defects in 4H and 6H SiC wafers have been studied by means of synchrotron X-ray topography and optical microscopy. The effect of seed crystal attachment, orientation, growth face shape, reloading and continued growth are discussed. A comparison between 4H and 6H material is made also. The results relate the origin of different defects to the mentioned growth conditions. © 1997 Elsevier Science S.A.

Keywords: 4H SiC; 6H SiC; Sublimation; Synchrotron X-ray photography

1. Introduction

The main problem faced by the commercial applications of SiC is the quality of the substrates. The substrates are usually grown by sublimation methods, which causes inherent structural defects. In the seeded sublimation method the seed crystal attachment, reloading and continued growth, the growth front shape, the seed type and also the spiral growth mechanism have a crucial effect on the defect formation and appearance. Understanding of defect formation process is important to be able to eliminate defects. As long as the growth mechanism remains unchanged, defects due to the spiral growth mechanism are difficult to totally avoid, but the influence of the other factors can be studied and thus, minimized.

SiC material can normally be studied by optical microscopy obtaining a general picture of the wafer and its imperfections, like macro-defects and doping inhomogeneities. In order to gain more information about the misorientation, the types of defect and strain fields, synchrotron X-ray topography is needed [1]. In this work different kinds of sublimation-grown samples are studied to clarify the origin of defects and the ways of eliminating them.

* Corresponding author.

2. Growth technique and characterization methods

The material studied was grown using the seeded sublimation technique at Linköping University. The experimental setup is described in [2]. The growth temperature was about 2300 °C and the growth took place at a reduced argon pressure of 5 mbar. Growing either on the C- or the Si-face of the SiC seed resulted normally in 4H or 6H polytypes, respectively, independent of the seed polytype.

Optical microscopy studies were performed under reflected and transmitted light utilizing Nomarski interference contrast and polarized light. Synchrotron white beam projection and section topographs as well as grazing incidence reflection topographs [3,4] were made at D5 Optics beamline at ESRF in Grenoble, France. Reflected intensities (Laue patterns) were recorded on a Kodak Industrex SR film.

3. Results and discussion

3.1. Seed attachment and start of the growth

The rigid seed crystal attachment to the graphite lid can bend the seed crystal during the heating due to different thermal expansion coefficients of graphite and

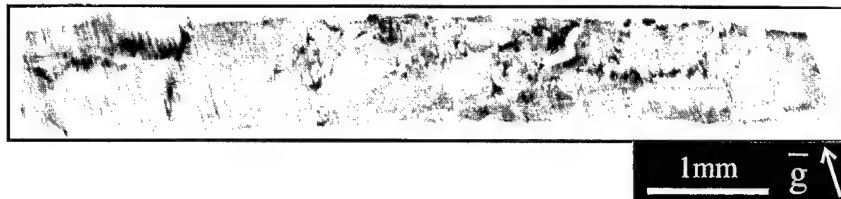


Fig. 1. A section topograph of an a-cut 4H SiC sample showing uniform bending.

SiC. This also causes bending of the lattice planes. Such a uniform bending is seen in the section topograph (Fig. 1) taken from a sample cut perpendicularly to the *c*-axis. The Laue pattern also shows bending effects. The bending may lead to formation of domains with low angle boundaries and polygonization in the growing crystal. Micropipes can be formed at these boundaries [5].

In addition, non-uniformities in the seed attachment may lead to variations in the temperature distribution. Voids can be formed between the substrate and the graphite lid. These voids may hinder the heat dissipation from the crystal. The disturbances cause an uneven surface with depressions corresponding to these voids. This leads to an inhomogeneous defect distribution and doping. Fig. 2 shows a projection topograph of a 4H wafer with one vertical line (L) corresponding probably to a series of dislocations. The line position corresponds to the bottom of the depression on the crystal surface. The dislocations are gathered there owing to the energy minimization. The measurement geometry and the dislocation visibility in different reflections suggest that their Burgers vectors are perpendicular to the surface. They might be the same kind of screw dislocations as reported in [6]. Along the line white spots are observed showing

the deformed core. There are also white curved boundaries (WB) in the picture. Because these boundaries can also be seen as color changes in the optical micrographs, they can be due to changes in defect and doping densities.

In the optical microscopy studies of the initially grown material, micropipes are found corresponding to some black inclusions at the seed-crystal interface. Often there is a defect in the substrate under the inclusion. Sometimes micropipes can change direction at the interface. At later stages of the growth these kind of micropipes are seen to unite or close up. The micropipes are observed in the vicinity of the voids on the reverse side of the seed.

At the initial stages of the growth the effect of the seed-crystal edges is enhanced. This can lead to a higher growth rate at the edges which results in an uneven surface. On the edges there are flat areas. Between these areas and the center of the crystal there are domain boundaries (DB) with defects (Fig. 3).

3.2. Defects due to interfaces and reloading

The cooling and heating procedures which are inevitable for the reloading can cause reformation in the structure. After reloading and the subsequent growth run the heavily bent sample shown in Fig. 1 started to create grain boundaries (GB) with polycrystalline

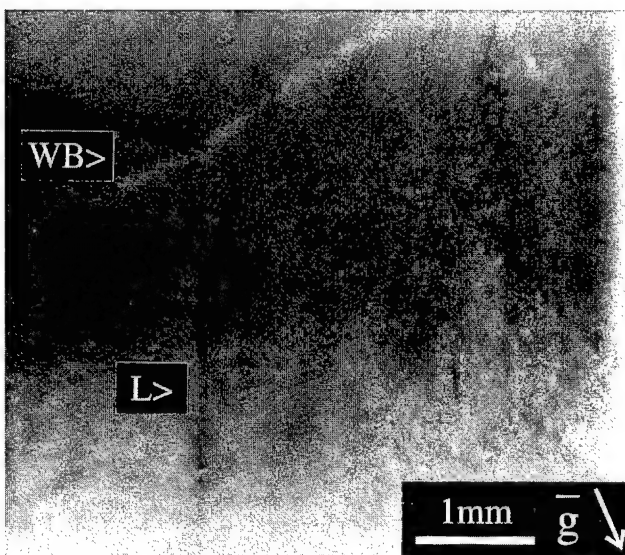


Fig. 2. A projection topograph ($g=0\bar{2}\bar{1}$, $\lambda=0.2363 \text{ \AA}$) of a 4H SiC crystal showing a dark line (L) of dislocations and white domain boundaries (WB).

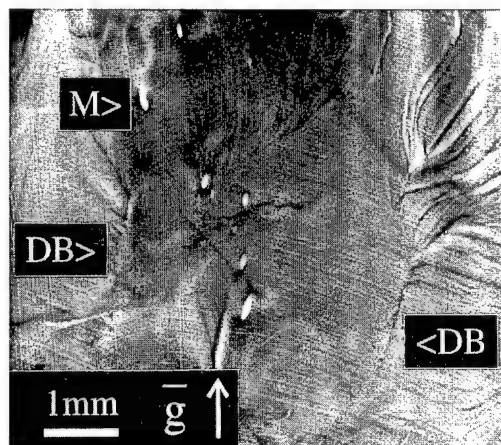


Fig. 3. A reflection topograph of a 6H SiC wafer with domain boundaries (DB) between the center and the edges. Also micropipes (M) are observed in the center.

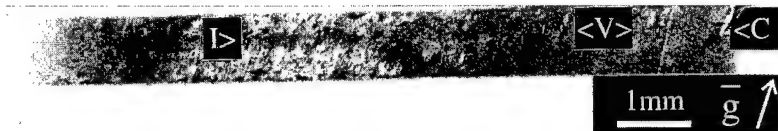


Fig. 4. A section topograph ($\mathbf{g} = 4\bar{3}10$, $\lambda = 0.3357 \text{ \AA}$) of a 4H SiC wafer showing an interface (I) between two different growth runs. Also images of voids (V) in the interface and cracks (C) are seen.

growth. It is believed that due to a recrystallization large angle grain boundaries are produced and the grain growth can cause the polycrystal boundaries.

The interfaces between different growth runs are also sources of macro-defects, especially micropipes. Fig. 4 shows a section topograph of a sample cut from an interface between two growth runs. The interface (I) is seen as a black line slightly above the center of the image. One can see several images of voids (V) at the interface as well as a large crack (C). The voids can act as a starting point for dislocations and micropipes. After reloading the new growth starts on a non-flat as-grown surface and voids can be formed. Sometimes there are pits on the surface, which can be formed under C rich conditions. In this case the voids are more frequent. Thus, the quality of the grown material degrades with increasing number of reloadings.

3.3. Defects due to different orientations of the growth face

Off-axis growth seems to generally improve the quality of the material. Domain formation and micropipe sizes are diminished. It is observed that instead of a large micropipe, many smaller ones or even several screw dislocation replace them. Basically the material looks the same as on-axis grown one, but in addition line defects lying parallel to the steps appear. They are usually near the central facet and are due to a terraced growth [7].

The misorientation between different domains seems to be small in off-axis grown wafers. The section topographs from such samples are not as bent as the ones taken from the highly misoriented samples [5].

The growth face orientation affects the doping homogeneity. In the topographs one can see darker and lighter areas due to different amounts of defects related to the growth face orientation. The best quality material is grown in the middle of the crystal where the growth front is perpendicular to the growth direction. Depending on the angle between the flat and the adjacent surface the doping difference changes as well as the amount of defects at the interface. The steeper the adjacent surface the more defects are generated. In the case of very steep adjacent surfaces formation of grooves is observed. In these grooves the nucleation is disturbed and other polytypes are found.

3.4. Comparison between 4H and 6H material

The comparison between 4H and 6H crystals reveals a difference in the micropipe and domain appearance. The micropipes seem to be larger and the domain misorientation greater in the 6H wafers. Their section topographs are distorted whereas those of the 4H wafers are almost straight. Though, some bending-like effect is observed owing to polygonization. This may be expected when applying the same growth conditions, since the Burgers vector for 6H polytype is longer than for 4H SiC. According to the topographs the regions between micropipes in 6H have less defects. The reason for this can be that the defects are gathered into the micropipes which are bigger.

Sometimes there is a tendency of formation of 6H instead of 4H on the C-face. If this happens it usually results in a very poor quality 6H material with a high density of micropipes. There are also inclusions of 15R polytype which create a lot of strain and twist in the material and even higher micropipe density.

4. Conclusion

The crystal quality depends on several factors. Among them the most important appears to be the seed quality and the seed attachment. The formation of macro-defects happens very easily and factors such as well-polished substrate surface and stress-free attachment should be taken good care of to avoid defect formation and polygonization. It is also essential to keep the growth face as flat as possible.

Acknowledgement

The synchrotron topographic measurements were carried out under experiment HC 544 at ESRF. The authors would like to thank Dr. José Baruchel and Dr. Jürgen Härtwig for the beam time and for the assistance. Special thanks to M. Syväjärvi for technical assistance during the growth experiments. This work was financially supported by the Swedish Board for Industrial and Technical Development (NUTEK).

References

- [1] M. Tuominen, E. Prieur, R. Yakimova, R.C. Glass, T. Tuomi, E. Janzén, *J. Crystal Growth* 165 (1996) 233–244.
- [2] R. Yakimova, M. Tuominen, E. Janzén, Epigress Application Bulletin, 1995 Epigress AB, S-223 70 Lund, Sweden.
- [3] T. Tuomi, K. Naukkarinen, P. Rabe, *Phys. Status Solidi (a)* 25 (1974) 93.
- [4] J. Baruchel, Y. Epelboin, J. Gastaldi, J. Härtwig, J. Kulda, P. Rejmankova, M. Schlenkev, F. Zontone, *Phys. Status Solidi (a)* 141 (1994) 59.
- [5] M. Tuominen, R. Yakimova, R.C. Glass, T. Tuomi, E. Janzén, *J. Crystal Growth* 144 (1994) 267–276.
- [6] M. Dudley, S. Wang, W. Huang, C.H. Carter Jr., V. Tsvetkov, C. Fazi, *J. Phys. D: Appl. Phys.* 28 (1995) A63–A68.
- [7] E. Bauser, H.P. Strunk, *J. Crystal Growth* 69 (1984) 561–580.

Surface polarity dependence in step-controlled epitaxy: progress in SiC epitaxy

Hiroyuki Matsunami *, Tsunenobu Kimoto

Department of Electronic Science and Engineering, Kyoto University, Yoshidahonmachi, Sakyo, Kyoto 606-01, Japan

Abstract

The dependence of surface polarity in step-controlled epitaxy of 6H- and 4H-SiC polytypes on off-oriented {0001} substrates was examined. Dominant step heights correspond to half (6H-) or a full (4H-) unit cells of the SiC polytypes. The background doping level can be reduced to less than 1×10^{14} per cm^3 by growth under C-rich conditions. High electron mobilities of $431 \text{ cm}^2 \text{ Vs}^{-1}$ for 6H-SiC and $851 \text{ cm}^2 \text{ Vs}^{-1}$ for 4H-SiC were obtained. The high quality of the epilayers was also elucidated, since the deep trap concentration detected by deep level analysis was in the order of 10^{12} per cm^3 . The surface polarity dependence and polytype dependence of impurity doping were demonstrated. © 1997 Elsevier Science S.A.

Keywords: Step-controlled epitaxy; Surface polarity dependance; Step bunching; C/Si ratio dependance

1. Introduction

Wide bandgap semiconductor silicon carbide (SiC) has been strongly anticipated as a candidate for high-temperature, high-power, and high-frequency/high-power electronic devices. Owing to the remarkable progress in homoepitaxy, various active semiconductor devices for the above purposes have been demonstrated [1].

In SiC epitaxial growth by chemical vapor deposition (CVD), step-flow growth on off-oriented SiC {0001} substrates ensures the polytype replication even at relatively low temperatures below 1600°C (step-controlled epitaxy) [2]. Several reports on epitaxial growth on SiC vicinal substrates have been published to clarify the step-flow growth [3–8]. There exist two competitive processes on a growing surface, step-flow growth from atomic steps and two-dimensional nucleation on a terrace. The supersaturation of chemical species contributing to crystal growth on substrate terraces, which determines the growth mode, strongly depends on growth temperature, C/Si ratio, and step structures. In addition, the nucleation rate and surface migration rate are different for substrate surface polarity (Si or C faces). It is, therefore, more important to control the supersaturation on a surface to get high-quality epilayers

without other polytype inclusions. In this paper, surface morphology, step bunching, and impurity doping in 6H-SiC and 4H-SiC epitaxial growth, especially surface polarity dependence, are discussed in detail.

2. Step-controlled epitaxy

Crystal growth was carried out by atmospheric-pressure CVD in a horizontal reaction tube. SiH_4 (1% in H_2) and C_3H_8 (1% in H_2) were used as source gases with H_2 carrier gas. The flow rates of SiH_4 and C_3H_8 were 0.05–0.60 sccm (typically 0.30 sccm) and 0.03–0.80 sccm (typically 0.20 sccm), respectively. The H_2 flow rate was fixed at 3.0 slm, which provides a linear gas velocity of $6\text{--}10 \text{ cm s}^{-1}$. N_2 was used for n-type doping, and trimethyl-aluminium (TMA), triethyl-aluminium (TEA) and B_2H_6 for p-type doping. Hydrogen chloride (HCl) gas was used for etching of a substrate surface before CVD growth.

Both (0001) Si and (0001)C faces were used to investigate the surface polarity dependence. Substrates were heated by radio-frequency induction. Before CVD growth, in-situ HCl etching was carried out to remove surface damage. The growth temperature was varied in the range of $1100\text{--}1600^\circ\text{C}$ (typically 1500°C).

Through various fundamental studies [9–11],

* Corresponding author.

the following features have been made clear in step-controlled epitaxy.

- (1) The rate-determining step is given by the supply of SiH₄.
- (2) Surface morphology depends on the C/Si ratio.
- (3) Step-flow growth is obtained for off-angles of more than 1°.
- (4) A small activation energy of 2.8 kcal mol⁻¹ in the temperature dependence of growth rate can be explained by a stagnant layer model [12].
- (5) From a surface diffusion model [13], the critical growth conditions for step-flow are predicted.

The nucleation and lateral growth of steps in SiC growth were studied through short-time growth [14,15]. The nucleus density increases significantly at low temperatures, which is attributed to the higher supersaturation caused by the reduced equilibrium vapor pressure and the suppressed surface diffusion of adsorbed species. The nucleus density is higher on (0001) \bar{C} faces than on (0001)Si faces by more than one order of magnitude probably owing to its lower surface free energy [16]. There exists anisotropy in lateral growth: the faster growth is obtained for the <1120> direction, and the lower for <1100> [14].

3. Surface morphology and step bunching

The step structure of 6H- and 4H-SiC epilayers was investigated [17]. As-grown samples without any surface treatments were examined using atomic force microscopy (AFM) and transmission electron microscopy (TEM) observations. Cross-sectional TEM observation was done using 400 keV, and each sample was examined along the <1100> or <1120> zone axis.

In AFM images of 6H-SiC epilayers grown on (0001) Si and (0001) \bar{C} faces, a distinctive difference in surface structure exists. An epitaxial layer on a (0001) Si face yields “apparent macrosteps” with a terrace width of 220–280 nm and a step height of 3–6 nm. High-resolution observation revealed that each macrostep on a (0001) Si face is not a single multiple-height step but composed of a number of “microsteps” [17]. On a (0001) \bar{C} face, the surface becomes rather flat and no macrosteps are observed. Although 4H-SiC epilayers had similar step structures, the 4H-SiC (0001) Si faces exhibited real macrosteps with 110–160 nm width and 10–15 nm height.

The mechanism for the formation of “apparent macrostep” on 6H- and 4H-SiC (0001) Si faces is not clear at present. However, the surface seems quite similar to “hill-and-valley (or faceted)” structure, which often appears on a surface grown with off-orientation from a low-index plane [18,19]. The off-oriented surfaces may spontaneously rearrange to minimize their total surface

energy, even if this involves an increase in the surface area. The surface free energy of SiC was calculated as 2220 erg cm⁻² for a (0001) Si face and 300 erg cm⁻² for a (0001) \bar{C} face [20]. The surface energy may be reduced by the formation of “hill-and-valley” structure on an off-oriented (0001) Si face, which has much higher surface energy.

Fig. 1 shows typical cross-sectional TEM images for 4H-SiC surfaces grown on (a) (0001) Si and (b) (0001) \bar{C} faces. The samples were examined along the <1120> zone axis to obtain clear lattice images. No island growth on the (0001) terraces are observed. On a (0001) Si face (Fig. 1(a)), the number of Si-C bilayers at bunched steps is four: the bunched steps correspond to exactly the unit cell of 4H-SiC, ABCB steps in the ABC notation. On a (0001) \bar{C} face (Fig. 1(b)), however, single bilayer-height steps dominate, and the number of bunched steps is relatively small.

Fig. 2 shows the histograms of step height for the surfaces of (a) 6H-SiC and (b) 4H-SiC epilayers grown on a (0001) Si face through observation of more than 200 steps. In 6H-SiC, 88% of steps have three Si-C bilayers (half of a unit cell), and 7% of steps have six Si-C bilayer height (unit cell). However, on 4H-SiC, four bilayer-height (unit cell) steps are the most dominant (66%) and two bilayer-height steps show the second highest probability (19%). Single Si-C bilayer-height steps are relatively few (5% or less) on both 6H- and 4H-SiC.

In Fig. 3, the histograms of step height for the surfaces of (a) 6H-SiC and (b) 4H-SiC epilayers on a (0001) \bar{C} face are shown. In contrast to the bunched steps on a (0001) Si face, single Si-C bilayer-height steps are dominant on a (0001) \bar{C} face for both polytypes, showing probability of 70–80%. A small number of bunched steps have a three or six bilayer-height in 6H-SiC, and a two or four bilayer-height in 4H-SiC. The origin of this striking surface polarity dependence is not known. The migrating species, surface coverage, and exact bond configuration at step edges should be analyzed to reveal the mechanism.

On a (0001) Si face with a 3.5° off-angle, the average terrace width experimentally obtained was 12.4 nm for 6H-SiC and 16.8 nm for 4H-SiC. In spite of the same off-angle, the different average terrace width between 6H-SiC and 4H-SiC originates from the different height of multiple steps. From the point of view of step-flow growth, narrow terraces are preferable. This is crucial in SiC growth, because supersaturation of chemical species (Si species [10]) increases on wider terraces, leading to 3C-SiC nucleation on the terraces. In this sense, 4H-SiC, which shows wider terrace widths, may have a relatively higher probability for 3C-SiC nucleation on the terraces. To overcome this problem, a slightly higher growth temperature would be helpful, since the longer surface diffusion length of adsorbed

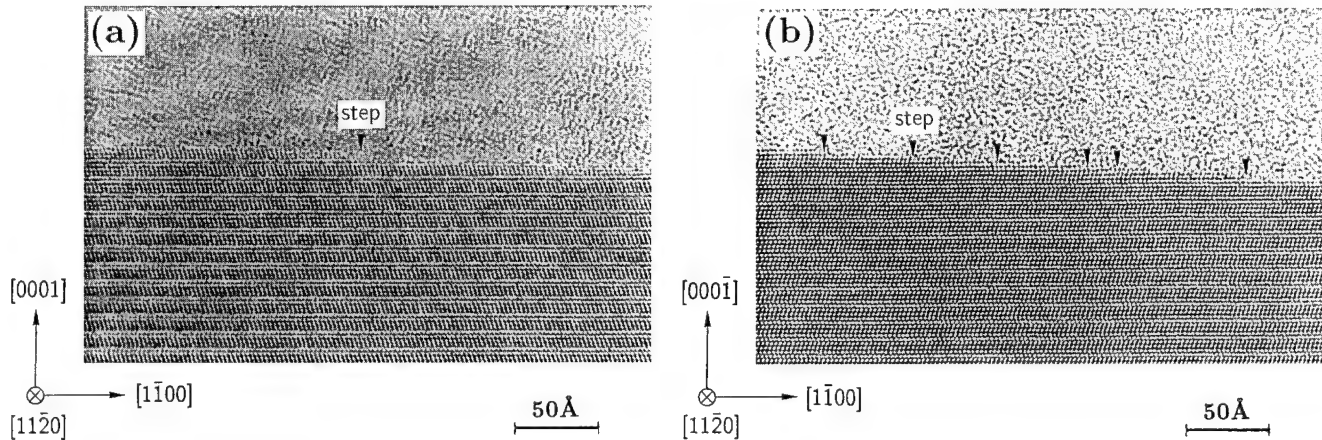


Fig. 1. Typical cross-sectional TEM images for 4H-SiC surfaces grown on: (a) Si and, (b) C faces. Substrates are (0001) Si 3.5° off-oriented toward [11̄20]. Samples are examined along the [12̄10] zone axis.

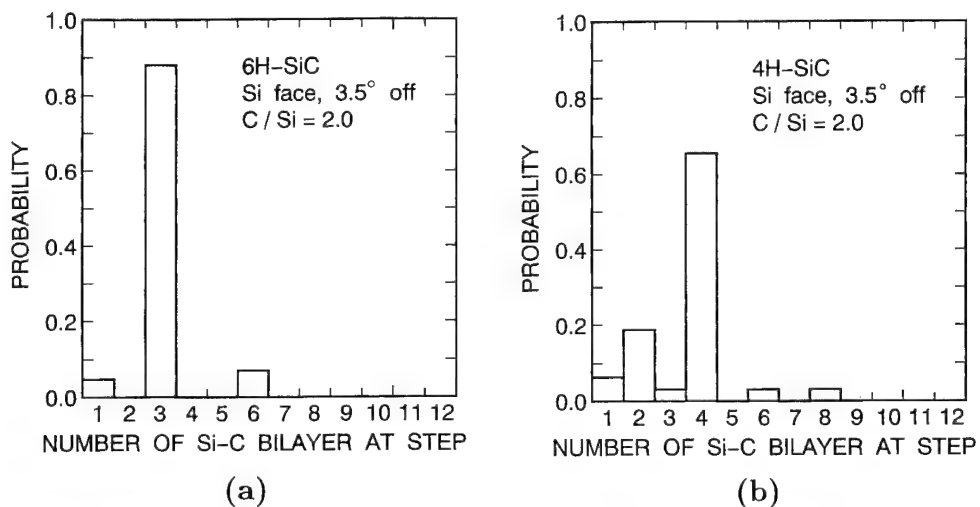


Fig. 2. Histograms of step height for surfaces of: (a) 6H-SiC and (b) 4H-SiC epilayers. Substrates are (0001) Si 3.5° off-oriented toward <11̄20>.

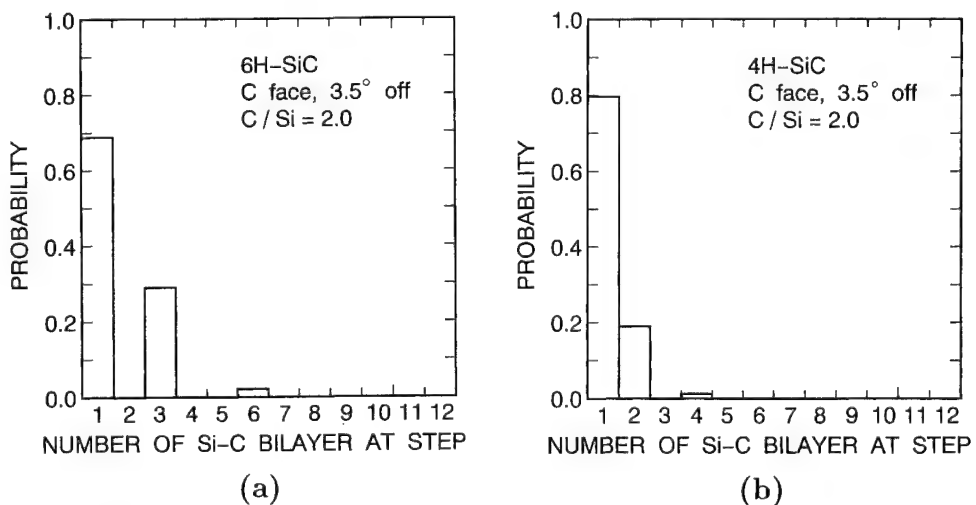


Fig. 3. Histograms of step height for surfaces of: (a) 6H-SiC and (b) 4H-SiC epilayers. Substrates are (000-1)C 3.5° off-oriented toward <11̄20>.

species and lower supersaturation on terraces are expected. Larger off-angles of substrates are also effective in 4H-SiC growth [21]. However, a (0001) C face showed much narrower average terrace width, owing to fewer bunched steps: epilayers grown on a (0001) C face exhibit a very flat surface even for 4H-SiC.

As shown in Figs. 2 and 3, the formation of three or six bilayer-height steps seems to be inherent in 6H-SiC growth, and two or four bilayer-height steps in 4H-SiC growth. Similar results have been reported on 6H-SiC surfaces grown by the Lely method [22] and MBE [23]. The step bunching in SiC, therefore, may be correlated with the surface equilibrium process. Since the surface energy is different for each SiC bilayer plane owing to the peculiar stacking sequence [24], it may lead to a different step velocity between each Si-C bilayer, and causes “structurally induced macrostep formation” [25].

4. In-situ doping of impurities

4.1. Polarity dependence in doping

Fig. 4 shows the C/Si ratio dependence of background doping level in unintentionally doped epilayers. For a C/Si ratio of 2, no significant difference was observed between epilayers on (0001) Si and (0001) C faces. On a (0001) Si face, the donor concentration estimated from capacitance-voltage (C-V) characteristics can be drastically reduced by increasing the C/Si ratio, the lowest value is in the range of 5×10^{13} – 2×10^{14} per cm^3 . On a (0001) C face, however, the donor concentration is not sensitive to the C/Si ratio.

In-situ n-type doping can be easily achieved by the introduction of N_2 during epitaxial growth. The donor concentration increased proportionally with the increase of N_2 flow rate in the wide range on both (0001) Si and (0001) C faces. The doping efficiency of N strongly depends on the C/Si ratio during CVD growth (site-competition epitaxy) [26]. The higher C/Si ratio leads to the lower N concentration. This can be explained by that the higher coverage with C atoms on a growing surface prevents the incorporation of N atoms into epilayers, which substitute at the C site and work as donors.

However, the incorporation of Al and B atoms, which substitute at the Si site, is enhanced under C-rich conditions on a (0001) Si face [26,27]. The addition of trimethyl-aluminum ($\text{TMA:Al(CH}_3\text{)}_3$) is effective for in-situ p-type doping. Although most Al-doped epilayers showed very smooth surfaces, pits and hillocks were observed in heavily doped (Al concentration: 10^{19} per cm^3) samples grown on (0001) C faces. The supply of TMA causes the shift of growth conditions toward C-rich ambience owing to the release of CH_3 species from the mother molecules. The surface migration is suppressed and the two-dimensional nucleation is enhanced under C-rich conditions [15]. Besides, (0001) C faces easily suffer from two-dimensional nucleation, owing to its low critical supersaturation ratio. This may cause the surface roughening of heavily doped epilayers grown on (0001) C faces. The Al acceptor concentration versus the TMA flow rate for a C/Si ratio of 2 is shown in Fig. 5. The acceptor concentration estimated from C-V measurement agreed well with the Al concentration determined by secondary ion mass spectroscopy measurement. The doping efficiency is much higher on a

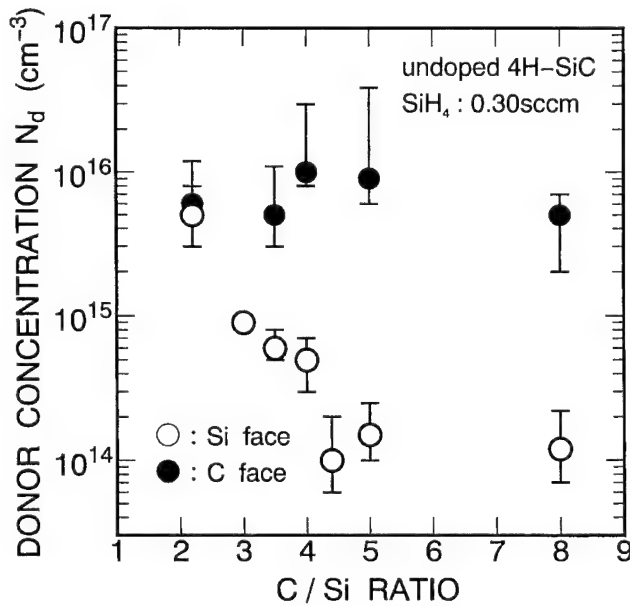


Fig. 4. C/Si ratio dependence of donor concentration for unintentionally doped 4H-SiC epilayers.

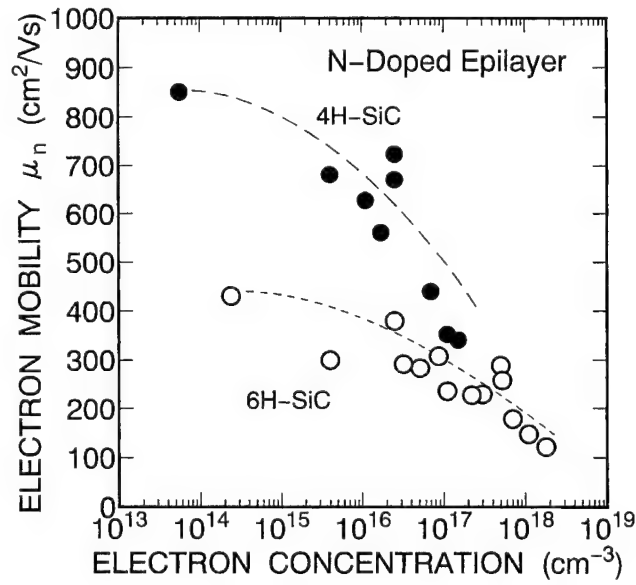


Fig. 5. Electron mobility versus carrier concentration of n-type 6H- and 4H-SiC epilayers at room temperature.

(0001) Si face than that on a (0001̄) C face by a factor of 10–80. On a (0001) Si face, the acceptor concentration increases superlinearly with the TMA supply, which may be caused by the increased effective C/Si ratio under high TMA flow conditions.

4.2. Polytype dependence in doping

4.2.1. n-type doping

Relatively high values of ionization energy for N donors in SiC (80–144 meV in 6H-SiC [28]) cause incomplete activation at room temperature. The activation ratio n/N_d (where n is electron concentration; and N_d is donor concentration) is theoretically estimated as 0.4–0.7 at room temperature, which was confirmed experimentally. Fig. 6 shows the electron mobility at room temperature versus the carrier concentration of 6H- and 4H-SiC epilayers. As is well known, 4H-SiC exhibits electron mobility two times higher than that of 6H-SiC. However, the difference seems to be small for heavily doped layers, as in a previous report [29]. As shown in Fig. 4, very low doped epilayers can be grown on (0001) Si faces under C-rich conditions. For very low doped epilayers grown with a C/Si ratio of 4–5, high electron mobilities of $431 \text{ cm}^2 \text{ Vs}^{-1}$ ($n = 2 \times 10^{14} \text{ per cm}^3$) for 6H-SiC and $851 \text{ cm}^2 \text{ Vs}^{-1}$ ($n = 6 \times 10^{13} \text{ per cm}^3$) for 4H-SiC were obtained at room temperature, the highest values ever reported, to our knowledge. For device applications, 4H-SiC is much more attractive than 6H-SiC owing to its higher electron mobility and smaller anisotropy in mobility [29,30].

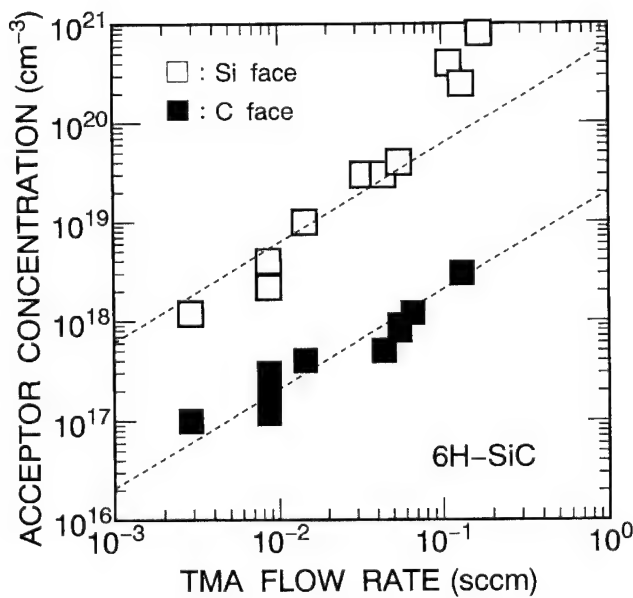


Fig. 6. Al acceptor concentration versus TMA flow rate in Al-doped 6H-SiC epilayers.

4.2.2. p-type doping

Because of a high value of ionization energy for Al acceptors (250 meV) [31], the activation ratio p/N_a (where p is hole concentration; and N_a is acceptor concentration) was as low as 10^{-2} – 10^{-1} at room temperature. However, a very high hole concentration of $4\text{--}6 \times 10^{19} \text{ per cm}^3$ could be achieved for heavily doped epilayers (Al concentration is in the mid 10^{20} per cm^3), which might arise from the decreased ionization energy in heavily doped samples, or from the formation of an impurity band. The lowest p-type resistivity was $0.042 \Omega\text{cm}$ for 6H-SiC and $0.025 \Omega\text{cm}$ for 4H-SiC, obtained on (0001) Si faces.

Fig. 7 shows the hole mobility at room temperature versus the carrier concentration of Al-doped 6H- and 4H-SiC epilayers. The hole mobility is $67 \text{ cm}^2 \text{ Vs}^{-1}$ at $2 \times 10^{16} \text{ per cm}^3$, and $6 \text{ cm}^2 \text{ Vs}^{-1}$ at $1 \times 10^{19} \text{ per cm}^3$ for 6H-SiC. The hole mobility of 4H-SiC seems to be higher than that of 6H-SiC for the same hole concentration.

Another hopeful acceptor is boron (B), which can be easily doped using B_2H_6 gas. Although B doping did not affect surface morphology, the growth rate was reduced by 20–30% in epitaxial growth. The plot of B acceptor concentration versus the B_2H_6 flow rate yields a slope of unity. B-doped samples exhibited high resistivity, which brought difficulties in forming ohmic contacts. This may be ascribed to the high ionization energy of the B acceptor (300–390 meV) [32,33]. The resistivity at room temperature was as high as $520 \Omega\text{cm}$ for a 6H-SiC layer with a boron concentration of $1 \times 10^{17} \text{ per cm}^3$. B-doped layers are known to contain so-called “D-centers”, which are located at $E_V + 0.6 \text{ eV}$, and act as donor-like hole traps [33]. From deep level transient

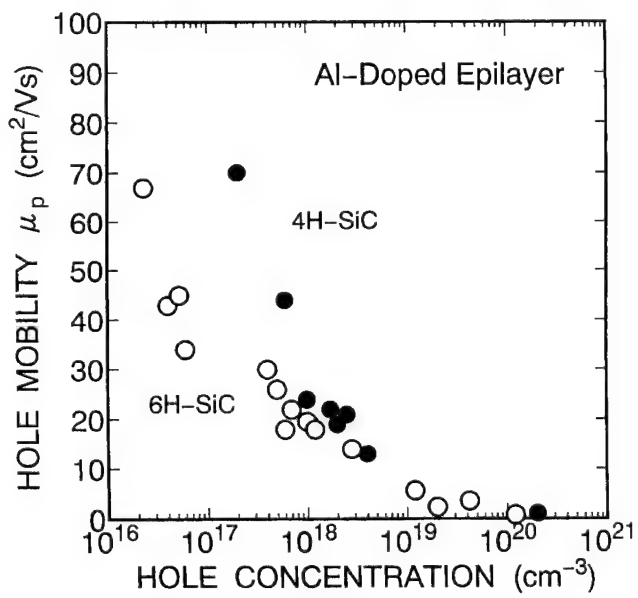


Fig. 7. Hole mobility versus carrier concentration of Al-doped 6H- and 4H-SiC epilayers at room temperature.

spectroscopy measurement for B-doped 6H-SiC epitayers, the D center concentration is lower by two orders of magnitude than the B acceptor concentration (S. Jang, T. Kimoto, H. Matsunami, unpublished data).

5. Conclusions

The dependence of surface polarity in step-controlled epitaxy of 6H- and 4H-SiC on off-oriented {0001} substrates was examined. Step-flow growth is essential to realize polytype replication in epitayers without 3C-SiC inclusions. The step structures of the epitayer surfaces strongly depended on the surface polarity as well as polytypes. Dominant step heights correspond to half (6H-) or a full unit (4H-) cells of the SiC polytypes. The background doping level of epitayers could be reduced to less than 1×10^{14} per cm^3 by the growth under C-rich conditions, by which very high electron mobilities of $431 \text{ cm}^2 \text{ Vs}^{-1}$ for 6H-SiC and $851 \text{ cm}^2 \text{ Vs}^{-1}$ for 4H-SiC were obtained. Deep level analyses revealed that the trap concentration was in the 10^{12} per cm^3 range, indicating very high quality of epitayers. Excellent doping control has been obtained by in-situ doping of a nitrogen donor and aluminum/boron acceptors. The surface polarity dependence and polytype dependence of impurity doping were discussed.

Acknowledgement

The authors wish to express gratitude to Mr. T. Nakata of Ion Engineering Research Institute and Mr. T. Okano of Matsushita Technoresearch, Inc. for TEM analyses. Special thanks are due to Dr. A. Itoh (now Tokyo Institute of Technology) for his contribution to this work. This work was supported by the Ministry of Education, Science and Culture of Japan.

References

- [1] S. Nakashima, H. Matsunami, S. Yoshida, H. Hasima (Eds.) Silicon Carbide and Related Materials 1995, Proceedings of the Sixth International Conference, Kyoto, Japan, 18–21 September, Institute of Physics, Bristol, 1996.
- [2] N. Kuroda, K. Shibahara, W.S. Yoo, S. Nishino, H. Matsunami, Extended Abstracts of the 19th Conference on Solid State Devices and Materials, Tokyo, The Japan Society of Applied Physics, Business Center for Academic Societies, Japan, 1987, p. 227.
- [3] H.S. Kong, J.T. Glass, R.F. Davis, J. Appl. Phys. 64 (1988) 2672.
- [4] J.A. Powell, D.J. Larkin, L.G. Matus, W.J. Choyke, J.L. Bradshaw, L. Henderson, M. Yoganathan, J. Yang, P. Pirouz, Appl. Phys. Lett. 56 (1990) 1442.
- [5] S. Karmann, W. Sutrop, A. Schöner, M. Schadt, C. Haberstroh, F. Engelbrecht, R. Helbig, G. Pensl, R.A. Stein, S. Leibenzeder, J. Appl. Phys. 72 (1992) 5437.
- [6] O. Kordina, A. Henry, C. Hallin, R.C. Glass, A.O. Konstantinov, C. Hemmingsson, N.T. Son, E. Janzen, Mater. Res. Soc. Symp. Proc. 339 (1994) 405.
- [7] A.A. Burk, Jr., D.L. Barrett, H.M. Hobgood, R.R. Siergiej, T.T. Braggins, R.C. Clarke, G.W. Eldridge, C.D. Brandt, D.J. Larkin, J.A. Powell, W.J. Choyke, Silicon Carbide and Related Materials, Proceedings of the Fifth Conference, 1–3 November, 1993, Washington DC, USA, Eds: M.G. Spencer, R.P. Devaty, J.A. Edmond, M. Asif Khan, R. Kaplan and M. Rahman, Institute of Physics, Bristol, 1994, p. 29.
- [8] R. Rupp, P. Lanig, J. Völkel, D. Stephani, J. Cryst. Growth 146 (1995) 37.
- [9] T. Ueda, H. Nishino, H. Matsunami, J. Cryst. Growth 104 (1990) 695.
- [10] T. Kimoto, H. Nishino, W.S. Yoo, H. Matsunami, J. Appl. Phys. 73 (1993) 726.
- [11] T. Kimoto, H. Matsunami, J. Appl. Phys. 75 (1994) 850.
- [12] F.C. Eversteyn, P.J.W. Severin, C.H.J.v.d. Brekel, H.L. Peek, J. Electrochem. Soc. 117 (1970) 925.
- [13] W.K. Burton, N. Cabrera, F.C. Frank, Phil. Trans. Roy. Soc. London A243 (1951) 299.
- [14] T. Kimoto, H. Matsunami, J. Appl. Phys. 76 (1994) 7322.
- [15] T. Kimoto, H. Matsunami, J. Appl. Phys. 78 (1995) 3132.
- [16] J.P. Hirth, G.M. Pound, Condensation and Evaporation, Nucleation and Growth Kinetics, Pergamon Press, Oxford, 1963, Chapter D.
- [17] T. Kimoto, A. Itoh, H. Matsunami, Appl. Phys. Lett. 66 (1995) 3645.
- [18] C. Herring, Phys. Rev. 82 (1951) 87.
- [19] W.A. Tiller, The Science of Crystallization: Microscopic Interfacial Phenomena, Cambridge University Press, Cambridge, 1991, Chapter 2.
- [20] E. Pearson, T. Takai, T. Halicioglu, W.A. Tiller, J. Cryst. Growth 70 (1984) 33.
- [21] V.F. Tsvetkov, S.T. Allen, H.S. Kong, C.H. Carter, Jr., Silicon Carbide and Related Materials 1995, Institute of Physics, Bristol, 1996, p. 17.
- [22] S. Tyc, Silicon Carbide and Related Materials, Proceedings of the Fifth Conference, 1–3 November, 1993, Washington DC, USA, Eds: M.G. Spencer, R.P. Devaty, J.A. Edmond, M. Asif Khan, R. Kaplan and M. Rahman, Institute of Physics, Bristol, 1994, p. 333.
- [23] S. Tanaka, R.S. Kern, R.F. Davis, Appl. Phys. Lett. 65 (1994) 2851.
- [24] V. Heine, C. Cheng, R.J. Needs, J. Am. Ceramic Soc. 74 (1991) 2630.
- [25] T. Kimoto, Ph.D. dissertation, Step controlled epitaxial growth of alpha-SiC and device application, Kyoto University, 1995.
- [26] D.J. Larkin, P.G. Neudeck, J.A. Powell, L.G. Matus, Appl. Phys. Lett. 65 (1994) 1659.
- [27] T. Kimoto, A. Itoh, H. Matsunami, Appl. Phys. Lett. 67 (1995) 2385.
- [28] W. Sutrop, G. Pensl, W.J. Choyke, R. Stein, S. Leibenzeder, J. Appl. Phys. 72 (1992) 3708.
- [29] W.J. Schaffer, G.H. Negley, K.G. Irvine, J.W. Palmour, Mater. Res. Soc. Symp. Proc. 339 (1994) 595.
- [30] M. Schadt, G. Pensl, R.P. Devaty, W.J. Choyke, R. Stein, D. Stephani, Appl. Phys. Lett. 65 (1994) 3120.
- [31] M. Ikeda, H. Matsunami, T. Tanaka, Phys. Rev. B 22 (1980) 2842.
- [32] Yu.A. Vodakov, N. Zhumaev, B.P. Zverev, G.A. Lomakina, E.N. Mokhov, V.G. Oding, V.V. Semenov, Yu.F. Simakhin, Soviet Physics—Semiconductors 11 (1977) 214.
- [33] W. Sutrop, G. Pensl, P. Lanig, Appl. Phys. A51 (1990) 231.

Growth and doping via gas-source molecular beam epitaxy of SiC and SiC/AlN heterostructures and their microstructural and electrical characterization

R.S. Kern ¹, K. Järrendahl, S. Tanaka ², R.F. Davis *

North Carolina State University, Box 7907, Raleigh, NC 27695-7907, USA

Abstract

Gas-source molecular beam epitaxy has been employed to grow thin films of SiC and AlN on vicinal and on-axis 6H-SiC(0001). Growth using the SiH₄-C₂H₄ system resulted in 3C-SiC(111) epilayers under all conditions of reactant gas flow and temperatures. Films of 6H-SiC(0001) were deposited on vicinal 6H-SiC(0001) substrates using the SiH₄-C₂H₄-H₂ system at deposition temperatures ≥ 1350 °C. In situ doping was achieved by intentional introduction of nitrogen and aluminum into the growing crystal.

Monocrystalline AlN was deposited using evaporated Al and ECR plasma derived N or NH₃. Films <50 Å grown on the vicinal substrates had higher defect densities compared to those on the on-axis substrates due to the higher density of inversion boundaries forming at most SiC steps in the former material. Metal/AlN/6H-SiC(0001) thin film heterostructures which had a density of trapped charges as low as of 1×10^{11} cm⁻² at room temperature were prepared without post growth treatment. Superior single crystal AlN/SiC heterostructures were achieved when very thin AlN was deposited on the on-axis substrates. Single phase monocrystalline solid solutions of (AlN)_x(SiC)_{1-x} were deposited between $0.2 \leq x \leq 0.8$. A transition from the zincblende to the wurtzite structure was observed at $x \approx 0.25$. © 1997 Elsevier Science S.A.

Keywords: Silicon carbide; Aluminum nitride; Molecular beam epitaxy; Kinetics

1. Introduction

Molecular beam epitaxy (MBE) has attracted interest for epitaxial SiC [1–5] and AlN [6–12] growth mainly due to the possibilities of a cleaner ambient and lower deposition temperatures.

Several SiC [13,14] and AlN [15–17] deposition studies by gas-source molecular beam epitaxy (GSMBE) have previously been performed in our group. Rowland et al. [13] reported the deposition of monocrystalline 3C-SiC on vicinal 6H-SiC(0001) by GSMBE using a simultaneous supply of C₂H₄ and Si₂H₆ and a growth rate of approx. 100 Å h⁻¹. The films contained double positioning boundaries (DPBs) which formed as a result of 3C-SiC nucleation on terrace sites rather than step sites. Tanaka et al. [14] achieved the first growth of 6H-SiC epilayers on 6H-SiC substrates by stabilizing

step flow growth using low C₂H₄-to-Si₂H₆ gas flow ratios.

Rowland et al. [15,16] and Tanaka et al. [17] used plasma-assisted GSMBE to grow and characterize AlN and the first AlN/SiC heterostructures on vicinal 6H-SiC(0001). High-resolution transmission electron microscopy (HRTEM) images indicated very abrupt interfaces and excellent microstructural quality. Layer-by-layer growth was observed on the on-axis 6H-SiC substrates and DPB formation on vicinal substrates due to island coalescence in the vicinity of the steps on the vicinal SiC surface.

In the following sections, recent research concerned with the growth of SiC [18–21] and AlN [18,22–24] thin films via GSMBE in the authors' laboratory are described.

2. Experimental procedures

A previously described [18,25] GSMBE system was used to deposit SiC and AlN thin films on 6H-SiC(0001)

* Corresponding author.

¹ Present address: Hewlett-Packard Optoelectronics Division, San Jose, CA 95131, USA.

² Present address: The Institute of Physical and Chemical Research (RIKEN), Saitama 351-01, Japan.

substrates. The substrates were cleaned in a 10% HF solution for 5 min, loaded immediately into the growth chamber and further cleaned in situ using a SiH₄ exposure and UHV anneal [18]. Thin films of 3C- and 6H-SiC were deposited on vicinal 6H-SiC(0001) substrates (cut off-axis $3.5 \pm 0.5^\circ$ toward [1120]). Nominally on-axis 6H-SiC(0001) substrates were also used, especially in cases where 3C-SiC(111) was desired. The SiC deposition experiments were performed at 1000–1500 °C in either SiH₄-C₂H₄ or SiH₄-C₂H₄-H₂ environments. Thin films of AlN were deposited on the same type of substrates at temperatures of 900–1300 °C. Two separate sources of nitrogen, namely, molecular N₂ activated by a ECR plasma source and NH₃, were used in conjunction with a standard Al effusion cell operated at 1250 °C. For depositions of (AlN)_x(SiC)_{1-x} solid solutions, C₂H₄ and Si₂H₆ were used as sources for the C and Si, respectively.

The films were structurally analyzed with HRTEM, TEM, in-situ reflection high-energy electron diffraction (RHEED), scanning electron microscopy (SEM), X-ray diffraction (XRD), Auger electron spectroscopy (AES), and secondary ion mass spectrometry (SIMS) [18–20,22,24]. The electrical properties of the deposited films were characterized by Van der Pauw Hall, current–voltage (*I*–*V*) and capacitance–voltage (*C*–*V*) measurements [18,20,21,23,24].

3. Results and discussion

3.1. Deposition of 3C-SiC(111) in a non-hydrogen environment

Epilayer growth using only SiH₄ and C₂H₄ always resulted in films of 3C-SiC(111) [13,14,18–20]. The (♦)-labeled curve in Fig. 1 shows a plot of ln(*R*_g) vs. *T*⁻¹, where *R*_g is the growth rate (Å h⁻¹) and *T* is the temperature (K), for growth on vicinal 6H-SiC(0001) using reactant input flows of 0.75 sccm for SiH₄ and C₂H₄. Analysis of this curve showed that it follows the general Arrhenius equation, $R_g = R_0 \exp(-\Delta H_a/RT)$, where *R*₀ is a pre-exponential factor, ΔH_a is the effective activation energy (kcal mol⁻¹) and *R* is the ideal gas constant (1.987 cal mol⁻¹K⁻¹). From the slope of the curve, the apparent activation energy, ΔH_a , was determined to be 21.9 kcal mol⁻¹. The rate expression describing this data is given by $\ln(R_g) = 12.3 - (11.022/T)$. From the linear shape of the fitted curve and the size of the activation barrier, the reaction appears to be surface reaction limited. The size of the activation barrier was determined to be independent of the partial pressures of the reactants. No change in growth rate was observed for SiH₄ flow rates, *f*_{SiH₄}, of 0.5, 0.75 and 1.0 sccm. These results indicate that the deposition reaction is most likely governed by the

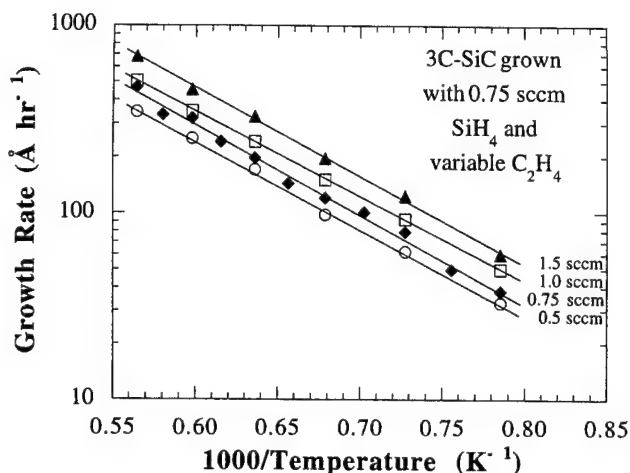


Fig. 1. Plot of growth rate for 3C-SiC(111) films grown at 1000–1500 °C with 0.75 sccm SiH₄, and 0.5, 0.75, 1.0 and 1.5 sccm C₂H₄.

decomposition of C₂H₄ into suitable species to form SiC in the presence of the reaction products from SiH₄.

The C₂H₄ flow rate, *f*_{C₂H₄}, was subsequently varied between 0.5 and 1.5 sccm with *f*_{SiH₄} maintained at 0.75 sccm. The identical slopes in Fig. 1 indicates that the reaction mechanism was unchanged as a function of the C₂H₄ flow rate. Fig. 2 shows a series of plots of ln(*R*_g) vs. ln(*f*_{C₂H₄}) in the range 0.5–1.5 sccm at 1100, 1200 and 1300 °C. The deposition rate as a function of *T* and *f*_{C₂H₄} was determined to be $\ln(R_g) = 12.48 - (11.000/T) + 0.63\ln(f_{C_2H_4})$. Again, the apparent activation barrier for this process was ~22 kcal mol⁻¹. Since the curves were linear over the range studied and had a dependence on the C₂H₄ flow rate, the deposition process appeared to be controlled by surface reactions. The rate of species formation, reaction and desorption from C₂H₄ appeared to be the rate limiting step.

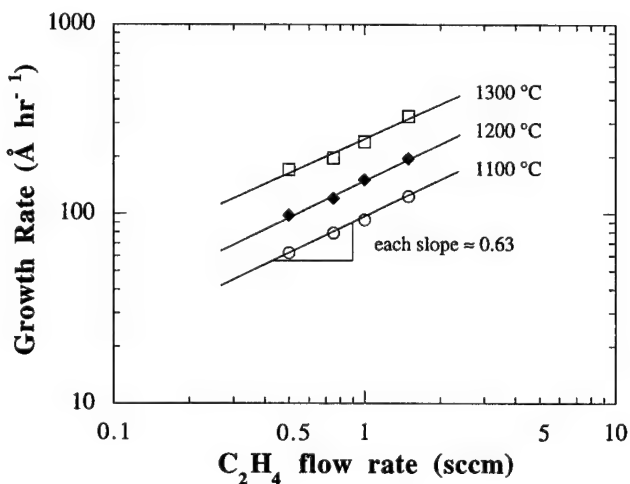


Fig. 2. Plot of ln(*R*_g) vs. ln(*f*_{C₂H₄}) for 3C-SiC(111) films grown at 1100, 1200 and 1300 °C with 0.75 sccm SiH₄ and 0.5–1.5 sccm C₂H₄.

3.2. Deposition of 3C-SiC(111) in a hydrogen ambient

Additions of H₂ (5 sccm flow rate) during the growth of SiC produced several advantageous changes in the resulting films [18–20]. At deposition temperatures <1350 °C, the benefits were increased surface smoothness and a greatly enhanced growth rate of the 3C-SiC films. The activation energy for the films grown with 0.75 sccm SiH₄, 0.75 sccm C₂H₄ and 5 sccm H₂ at 1000–1300 °C was 21.6 kcal mol⁻¹. Thus, the presence of H₂ did not change the magnitude of the barrier over this temperature range. Since the slopes of the curves shown in Fig. 1 and that from this latter study were nearly identical, the reaction mechanism was both apparently unchanged and independent on the input flow of C₂H₄.

The observations are attributed to the presence of H₂ which apparently provided the impetus for at least one of the following processes: (i) adsorption of C₂H₄ onto the surface of the growing film, (ii) sweeping of the unreacted source gas species or unwanted product species from the growth surface and/or (iii) formation of a suitable reactant species in tandem with the decomposition or reaction of C₂H₄ in the presence of H₂.

3.3. Deposition of 6H-SiC(0001) in a hydrogen ambient

Further increases of the deposition temperature (≥ 1350 °C) in a H₂ ambient, resulted in the stabilization of the step flow growth mode, the consequent deposition of 6H-SiC(0001) epilayers, a marked increase in growth rate and an apparent decrease in the activation energy [18–20]. The temperature dependence of the growth rate appeared to be linear on the Arrhenius plot shown in Fig. 3. The activation barrier was determined to be 12.6 kcal mol⁻¹, which is in excellent agreement with values calculated from CVD research (13.0 kcal mol⁻¹) using the same reactant sources, sub-

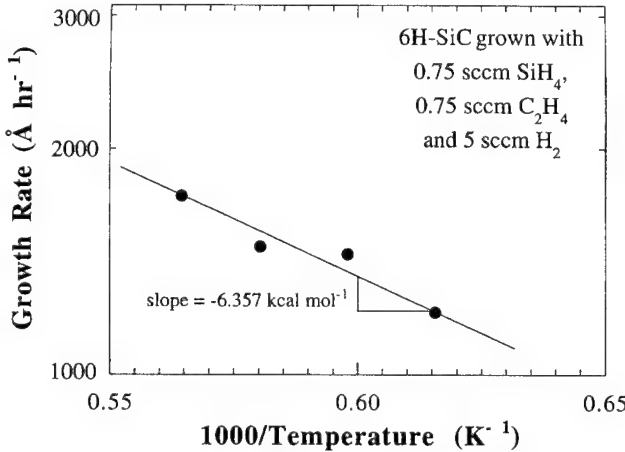


Fig. 3. Plot of growth rate for 6H-SiC(0001) films grown at 1350–1500 °C with 0.75 sccm SiH₄, 0.75 sccm C₂H₄ and 5 sccm H₂.

strate orientation and crystallographic face [26]. Although the growth rate was still strongly dependent on the deposition temperature, the decrease in the value of this activation barrier was an excellent indicator of the effect of the H₂ gas on the gas chemistry, growth kinetics and gas flow dynamics. Limited studies showed that varying the C₂H₄ input from 0.375 to 1.0 sccm did not result in a change in the growth rate. This indicated that the rate controlling factor at these temperatures in the presence in H₂ had most likely changed. It is important to note that growth on both vicinal and on-axis substrates proceeded at approximately the same rate (within 5%) under similar growth conditions. However, 3C-SiC was always produced on the on-axis substrates regardless of growth conditions, because the smaller atomic diffusion distance relative to the distance between steps.

3.4. Doping of 3C- and 6H-SiC films

The presence of the N in SiC grown from the vapor phase is particularly significant, because it is the most shallow donor impurity. Consequently, it was the agent responsible for the n-type character of unintentionally doped SiC films [18,21,20]. Considerable differences in the background atomic nitrogen and electron concentrations in the SiC films was measured when the C₂H₄ flow rate was modulated in the range 0.375–0.75 sccm. Similar to the "site-competition epitaxy" arguments of Larkin et al. [27,28], the N contamination level was significantly decreased by increasing the amount of C₂H₄ delivered in the gas phase. Fig. 4 shows a SIMS profile from a 6H-SiC(0001) film grown at 1400 °C using 0.75 sccm SiH₄, 5 sccm H₂ and a variable C₂H₄ flow. The change in N content with C source supply is very apparent from the abrupt changes that occur in

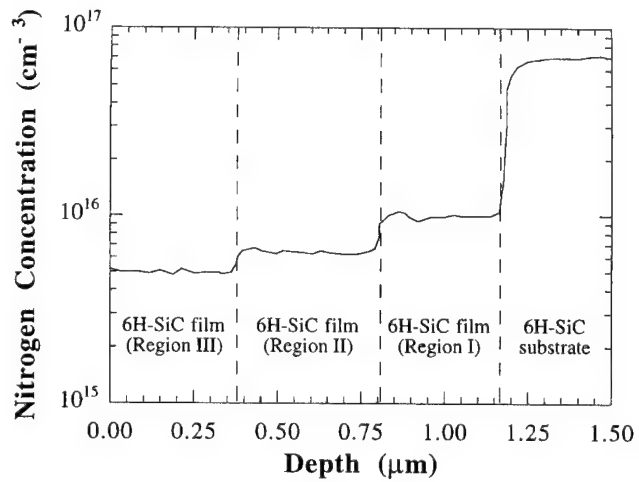


Fig. 4. SIMS profile of a 6H-SiC(0001) film grown at 1400 °C using 0.75 sccm SiH₄, 5 sccm H₂ and a variable C₂H₄ flow (0.375 sccm in Region I, 0.5 sccm in Region II, and 0.75 sccm in Region III).

the N depth profile. A flow of 0.75 sccm C_2H_4 resulted in the incorporation of N at the detection limit for N ($\approx 5 \times 10^{15} \text{ cm}^{-3}$) in the SIMS system. Hall measurements of undoped 6H-SiC films with the lowest atomic nitrogen and electron concentration showed a mobility of $434 \text{ cm}^2 \text{ V}^{-1} \text{ s}^{-1}$.

To study n-type doping of the reactant mixture with the lowest total input of source gases, 0.75 sccm SiH_4 , 0.375 sccm C_2H_4 , and 5 sccm H_2 (for 6H-SiC), was chosen. Donor doping was performed in situ at 1400°C on monocrystalline 6H- and 3C-SiC using both NH_3 (diluted to 300 ppm in H_2) and pure N_2 . Doping in the range $5 \times 10^{15}\text{--}8 \times 10^{17} \text{ cm}^{-3}$ was achieved using the NH_3/H_2 mixture and $1 \times 10^{18}\text{--}4 \times 10^{19} \text{ cm}^{-3}$ with the N_2 additions. Figs. 5(a) and (b) show the electron mobility as a function of electron concentration in the close packed plane for 3C-SiC(111) and 6H-SiC(0001) at room temperature.

Epilayers of 3C- and 6H-SiC were also doped p-type by evaporating Al from a standard MBE effusion cell

during the growth of SiC epilayers. All growth experiments were performed at 1450°C using 0.75 sccm SiH_4 , 0.75 sccm C_2H_4 , and 5 sccm H_2 (for 6H-SiC). The higher C_2H_4 flow rate was used to take advantage of the site-competition process which resulted in a decrease in the concentration of background N, a compensating impurity in p-type SiC. The higher temperature was used in an attempt to aid in dopant activation. Acceptor doping of $2 \times 10^{15}\text{--}8 \times 10^{18} \text{ cm}^{-3}$ was achieved. Figs. 6(a) and (b) show the hole mobility as a function of hole concentration in the close packed plane for 3C-SiC(111) and 6H-SiC(0001) at room temperature.

3.5. Deposition of AlN thin films and Al/AlN/SiC MIS-structures

Thin films of wurtzite structure (2H) AlN were deposited on 6H-SiC substrates [18]. The primary problem encountered using an ECR source as a nitrogen source was the unintentional incorporation of impurity atoms

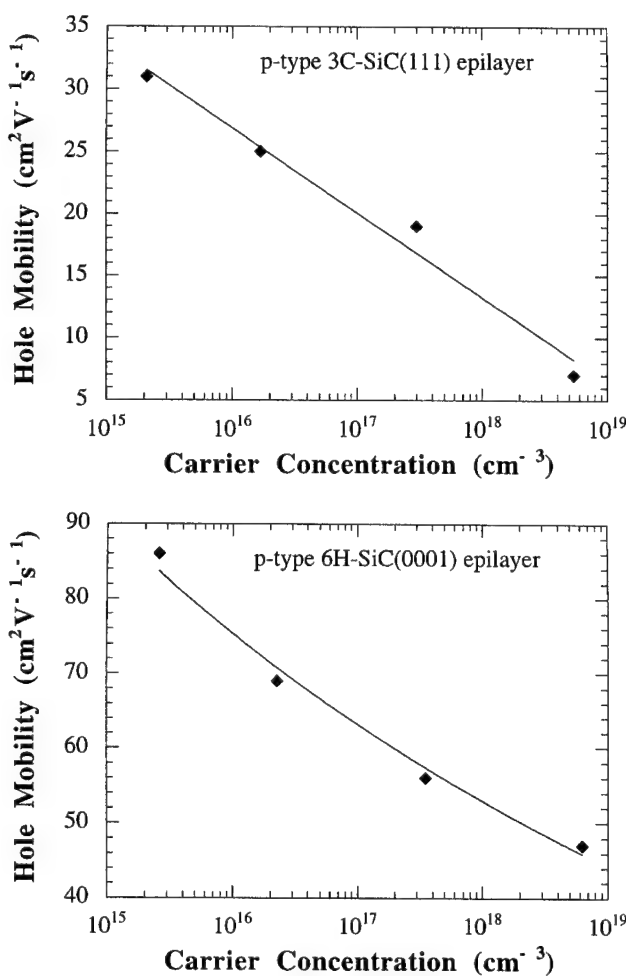
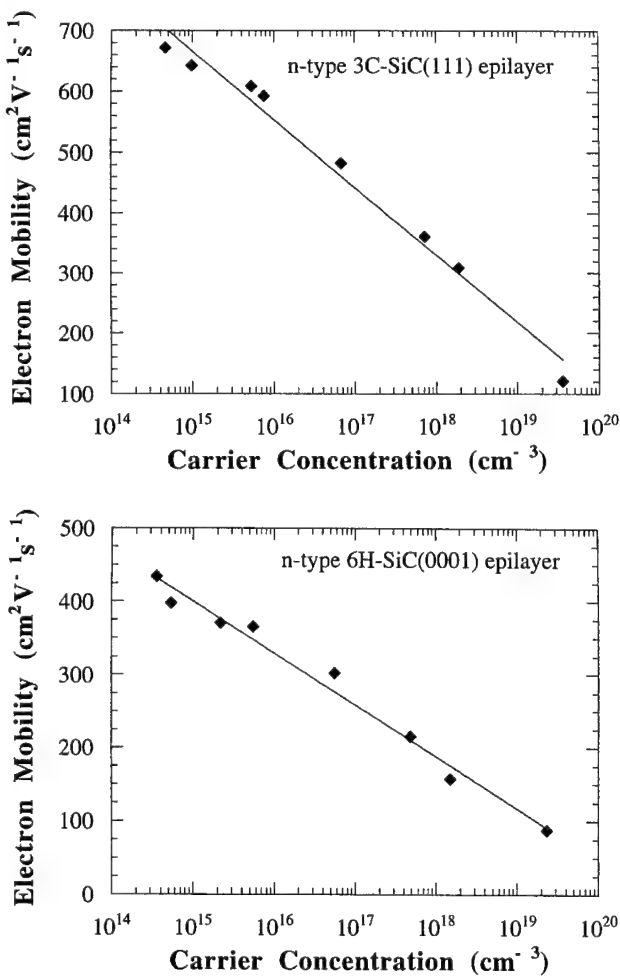


Fig. 5. Room temperature measurements of electron mobility vs. carrier concentration for n-type (a) 3C(111) epilayers and (b) 6H-SiC(0001) epilayers.

Fig. 6. Room temperature measurements of hole mobility vs. carrier concentration for p-type (a) 3C(111) epilayers and (b) 6H-SiC(0001) epilayers.

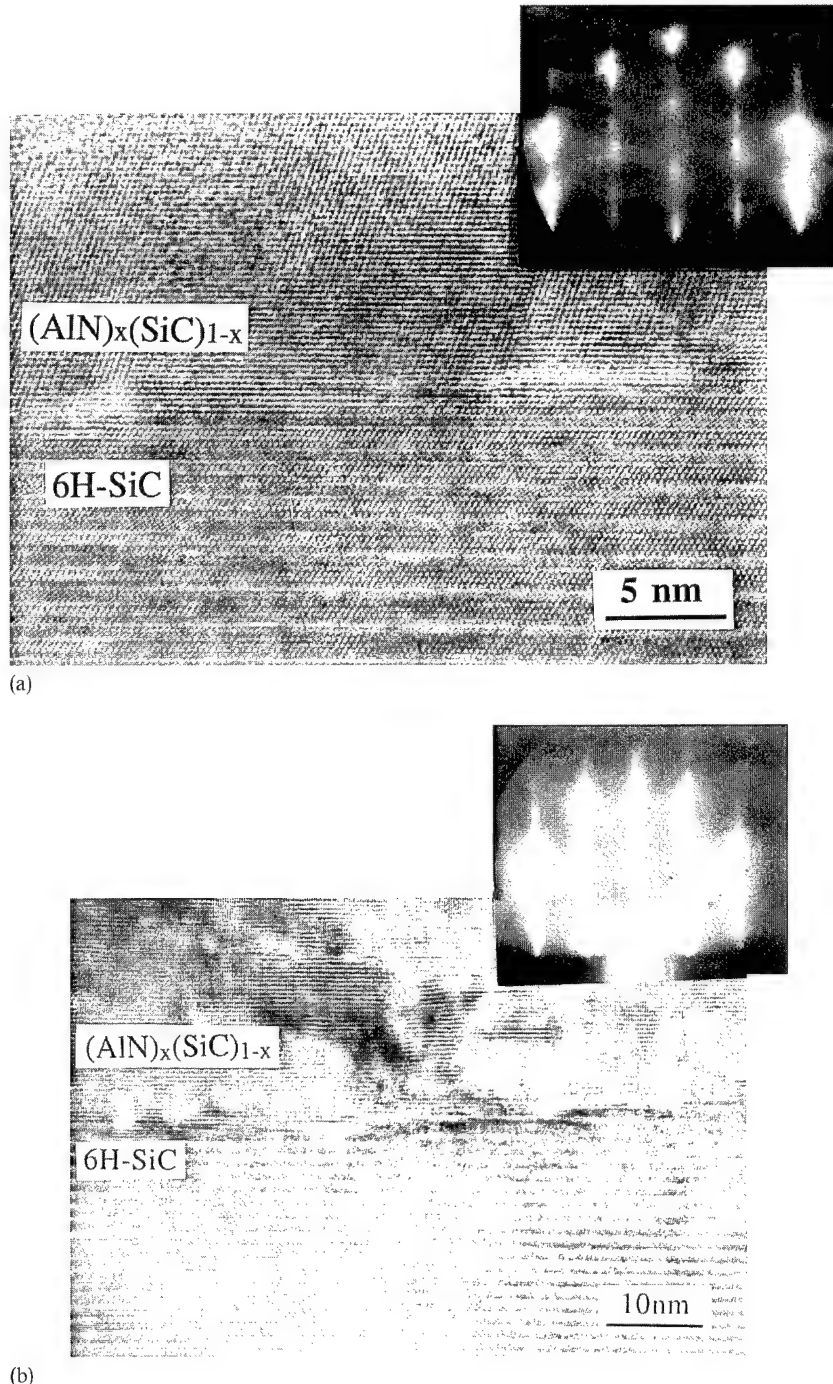


Fig. 7. HRTEM micrographs of (a) a (111)-oriented zincblende $(\text{AlN})_x(\text{SiC})_{1-x}$ film and (b) an (0001)-oriented wurtzite $(\text{AlN})_x(\text{SiC})_{1-x}$ film. The RHEED patterns of the cubic and hexagonal films are taken along the [1 $\bar{1}0$] and [11 $\bar{2}0$] azimuth, respectively.

from the material that made up the liner crucible. Substitution to NH_3 improved film quality and growth rate. Growth rates of about 825 \AA h^{-1} were achieved for films grown at 1050°C using the ECR, whereas, growth rates of about 1000 \AA h^{-1} were obtained for films deposited using NH_3 at 1100°C . With the addition of H_2 , higher growth rates and smoother surfaces were achieved. A comparison of thin (0001) oriented AlN films ($< 50 \text{ \AA}$) grown simultaneously on vicinal and

on-axis 6H-SiC(0001) substrates were made. Films of AlN grown on the vicinal surface exhibited a rough surface, whereas, the films grown on the on-axis substrate possessed a very smooth surface and excellent thickness uniformity, indicative of two-dimensional growth. The achievement of higher quality AlN films in the latter case were due to the low density of surface irregularities (i.e. steps and kinks) on the on-axis substrates. Because of the very low critical thickness of the

AlN epilayers grown on the SiC substrates, the quality of the AlN films thicker than approx. 150 Å did not depend on the substrate. Above this thickness, the misfit/threading dislocations became the dominate defect, and the effect of substrate orientation on crystal quality became of decreasing importance.

The wide band gap and low dielectric constant of AlN permits its use as the gate material in Al/AlN/SiC MIS structures [18,23]. The low lattice mismatch and excellent thermal stability of these materials relative to the SiO₂/SiC system make this a very attractive system for insulated-gate device technology using SiC and, potentially, GaN semiconductor microelectronic devices. The Al/AlN/SiC MIS-structures grown in this research had low interface charge trap densities ($1 \times 10^{11} \text{ cm}^{-2}$) and very small hystereses when swept from deep depletion into accumulation and back. The interface states were negatively charged (acceptor-like) on the Si-face 6H-SiC substrates. Positively charged traps that were attributed to deep level states became the dominant source of interface states and hysteresis when the MIS structures were heated or illuminated under a halogen lamp.

3.6. Growth of AlN/SiC heterostructures and $(\text{AlN})_x(\text{SiC})_{1-x}$ solid solutions

Pseudomorphic heterostructures of wurtzitic AlN and 3C-SiC were grown on vicinal and on-axis 6H-SiC(0001) substrates under a variety of conditions of reactant input, substrate orientation and temperature [18]. The substrate temperature and orientation were determined to affect the growth of both AlN and SiC. To produce SiC films with a low level of defects, layers of AlN having a sub-critical thickness were used. Epilayers of 3C-SiC(111) on these AlN layers had excellent electrical properties with room temperature electron mobilities as high as $721 \text{ cm}^2 \text{ V}^{-1} \text{ s}^{-1}$ for unintentionally doped films grown with a high C₂H₄ flow in order to take advantage of "site-competition epitaxy" [27,28].

Single-phase, monocrystalline $(\text{AlN})_x(\text{SiC})_{1-x}$ solid solutions were deposited [18,24] at 900–1300° using C₂H₄ and Si₂H₆ together with the Al effusion cell and the ECR source. By ranging the composition between $0.2 \leq x \leq 0.8$ both zincblende (3C) and wurtzite (2H) single-phase films were grown with the transition from cubic to hexagonal structure at about $x = 0.25$. Figs. 7(a) and (b) show HRTEM micrographs and RHEED patterns from films with the composition $(\text{AlN})_{0.2}(\text{SiC})_{0.8}$ and $(\text{AlN})_{0.3}(\text{SiC})_{0.7}$, respectively.

4. Summary

Monocrystalline thin films of 3C-SiC(111) were grown by GSMBE on both vicinal and on-axis 6H-SiC(0001) substrates using SiH₄ and C₂H₄. Growth

of homoepitaxial 6H-SiC(0001) and an increase in growth rate were achieved between 1350 and 1500 °C on vicinal 6H-SiC(0001) substrates with the addition of H₂ to the reactants. The epilayers were doped n- or p-type in situ by adding N or Al, respectively, to the processing environment.

Films of AlN were deposited on 6H-SiC(0001) substrates. The high quality of the films allowed the fabrication of metal/AlN/SiC MIS structures and AlN/SiC heterostructures. Single-phase, monocrystalline $(\text{AlN})_x(\text{SiC})_{1-x}$ solid solutions of both zincblende ($0.2 \leq x \leq 0.25$) and wurtzite ($0.25 \leq x \leq 0.8$) structures were also deposited.

Acknowledgement

The authors acknowledge the Office of Naval Research for the sponsorship of this research under Grant No. N00014-92-J-1500 and Cree Research, Inc. for the SiC substrates. K. Järrendahl acknowledges The Swedish Foundation for International Cooperation in Research and Higher Education (STINT) for financial support. We would also like to acknowledge A. Reisman, H.H. Lamb, C. Wolden and M.O. Aboelfotoh of NCSU and J.C. Angus of CWRU for helpful discussions.

References

- [1] S. Kaneda, Y. Sakamoto, T. Mihara, T. Tanaka, *J. Cryst. Growth* 81 (1987) 536.
- [2] T. Yoshinobu, M. Nakayama, H. Shiomi, T. Fuyuki, H. Matsunami, *J. Cryst. Growth* 99 (1990) 520.
- [3] T. Yoshinobu, H. Mitsui, I. Izumikawa, T. Fuyuki, H. Matsunami, *Appl. Phys. Lett.* 60 (1992) 824.
- [4] A. Fissel, U. Kaiser, E. Ducke, B. Schröter, W. Richter, *J. Cryst. Growth* 154 (1995) 72.
- [5] A. Fissel, U. Kaiser, K. Pfennighaus, B. Schröter, W. Richter, *Appl. Phys. Lett.* 68 (1996) 1204.
- [6] M.T. Wauck, D.K. Winslow, *Appl. Phys. Lett.* 13 (1968) 286.
- [7] S. Yoshida, S. Misawa, Y. Fujii, S. Takada, H. Hayakawa, S. Gonda, A. Itoh, *J. Vac. Sci. Technol.* 16 (1979) 990.
- [8] S. Yoshida, S. Misawa, S. Gonda, *Appl. Phys. Lett.* 42 (1983) 427.
- [9] D. Troost, H.-U. Baier, A. Berger, W. Mönnich, *Surf. Sci.* 242 (1991) 324.
- [10] H.-U. Baier, W. Mönnich, *J. Vac. Sci. Technol. B* 10 (1992) 1735.
- [11] M. Miyauchi, Y. Ishikawa, N. Shibata, *Jpn. J. Appl. Phys.* 31 (1992) L1414.
- [12] K.S. Stevens, A. Ohtani, M. Kinniburgh, R. Beresford, *Appl. Phys. Lett.* 65 (1994) 321.
- [13] L.B. Rowland, R.S. Kern, S. Tanaka, R.F. Davis, *J. Mater. Res.* 8 (1993) 2753.
- [14] S. Tanaka, R.S. Kern, R.F. Davis, *Appl. Phys. Lett.* 65 (1994) 2851.
- [15] L.B. Rowland, R.S. Kern, S. Tanaka, R.F. Davis, *J. Mater. Res.* 8 (1993) 2310.

- [16] L.B. Rowland, R.S. Kern, S. Tanaka, R.F. Davis, *Appl. Phys. Lett.* 62 (1993) 3333.
- [17] S. Tanaka, R.S. Kern, R.F. Davis, *Appl. Phys. Lett.* 66 (1995) 37.
- [18] R.S. Kern, Ph.D. Thesis, North Carolina State University, Raleigh, NC, 1996.
- [19] R.S. Kern, S. Tanaka, L.B. Rowland, R.F. Davis, *J. Cryst. Growth.*, submitted.
- [20] R.S. Kern, K. Järrendahl, S. Tanaka, R.F. Davis, *Phys. Stat. Sol. A.*, accepted.
- [21] R.S. Kern, R.F. Davis, *Appl. Phys. Lett.*, accepted.
- [22] R.S. Kern, L.B. Rowland, S. Tanaka, R.F. Davis, *J. Mater. Res.* 8 (1993) 1477.
- [23] M.O. Aboelfotoh, R.S. Kern, S. Tanaka, R.F. Davis, C.I. Harris, *Appl. Phys. Lett.* 69 (1996) 2873.
- [24] R.S. Kern, L.B. Rowland, S. Tanaka, R.F. Davis, *J. Mater. Res.*, submitted.
- [25] L.B. Rowland, S. Tanaka, R.S. Kern, R.F. Davis, in *Amorphous and Crystalline Silicon Carbide IV*, C.Y. Yang, M.M. Rahman, G.L. Harris (Eds.), Springer, Berlin, 1992, p. 84.
- [26] Y.C. Yang, R.F. Davis, *J. Electron. Mater.* 20 (1991) 869.
- [27] D.J. Larkin, P.G. Neudeck, J.A. Powell, L.G. Matus, *Appl. Phys. Lett.* 65 (1994) 1659.
- [28] D.J. Larkin, S.G. Sridhara, R.P. Devaty, W.J. Choyke, *J. Electron. Mater.* 24 (1995) 289.

High quality 4H-SiC grown on various substrate orientations

A. Henry ^{a,b,*}, I.G. Ivanov ^a, T. Egilsson ^a, C. Hallin ^a, A. Ellison ^a, O. Kordina ^{a,b},
U. Lindefelt ^{a,b}, E. Janzén ^a

^a Linköping University, Department of Physics and Measurement Technology, 581 83 Linköping, Sweden

^b ABB Corporate Research, 721 78 Västerås, Sweden

Abstract

Growth of 4H epilayers has been achieved by chemical vapour deposition on various substrate orientations which were on-(0001) oriented, off axis (3.5° and 8°-off towards the (11̄20) direction) and a-cut, both (11̄20) and (10̄10)-oriented material. Various characterisation techniques have been used to assess the epilayer quality such as optical microscopy, X-ray diffraction, and mainly photoluminescence spectroscopy. © 1997 Elsevier Science S.A.

Keywords: 4H-SiC; c-Axis; a-Axis; Photoluminescence

1. Introduction

SiC currently attracts a growing interest owing to its large potential as a power device material. High-voltage bipolar devices require thick low-doped epitaxial layers with long carrier lifetimes, and are most conveniently grown by chemical vapour deposition (CVD) [1–4]. The study of epitaxy on various crystal orientations of SiC helps the understanding of the growth mechanisms and facilitates device development. Certain material properties differ for the distinct crystal faces and one face could be more or less desirable for a special device application. Previous works on 6H-SiC report [5,6] a lower quality on the (10̄10)-oriented material compared with the (11̄20). We present a study on 4H-SiC, since this polytype has shown to be more suited as power device material than 6H. Various characterisation techniques are used such as optical microscopy, X-ray diffraction and mainly photoluminescence (PL) spectroscopy.

2. Experiment

The samples used in this study are CVD epitaxial films grown in a hot-wall reactor with a SiC coated graphite susceptor [1,2]. The following substrate ori-

tations of the n-type 4H polytype were used: (1) (0001) oriented c-cut (a) on-axis, (b) 3.5°- and (c) 8°-off from the c-axis towards the (11̄20), direction; and (2) a-cut material (a) (11̄20); and (b) (10̄10)-oriented substrates grown by the modified Lely method. The growths were performed by passing reactive gases (silane and propane diluted to 5% in H₂) through the susceptor inside which the substrates were placed. Hydrogen was used as the carrier gas. The growth temperature (T_g) was varied from 1450 to 1650 °C, the C/Si ratio from 1.5 to 3 and the growth rate (R_g) from 1.5 to 3 μm/h. A hydrogen etch prior to growth was performed at the growth temperature for a long time (15–30 min) in order to improve the substrate surface as much as possible [7]. It should be noted that some of the samples used in this study were intentionally doped n-type in the 10¹⁶ cm⁻³ range and thus, no free exciton (FE or I) related line could be observed in the PL spectra. However, the background doping concentration in our reactor is readily low: samples with doping levels less than 5 × 10¹⁴ cm⁻³ are grown reproducibly.

To control the morphology of the epilayers, optical microscopy with Normaski optics was used. X-ray diffraction (XRD) measurements were performed on a Philips MRD 1880/HR diffractometer [8].

Low-temperature photoluminescence spectra were recorded at about 2 K, using the 275 nm or the double-frequency line of the 488 nm (thus 244 nm) of an Ar⁺-ion laser as the excitation source. The luminescence

* Corresponding author. Fax: 46 13 14 23 37; e-mail: ahy@ifm.liu.se

was dispersed by a SPEX 1404 0.85-m double monochromator, fitted with two 1200 grooves/mm gratings blazed at 5000 Å and detected by a UV-sensitive Hamamatsu photomultiplier tube operating in a photon-counting mode. The usual geometry used to record the PL spectra is very close to the so-called backscattering geometry (see Fig. 1) and only photons with $E \perp c$ polarisation can be detected, where E denotes the polarisation vector of the photon. However, with a rectangular geometry (Fig. 1b) photons with both $E \perp c$ or $E // c$ can be detected and selected by means of a polariser. The emission from the surface was blocked with a mass of Ag paste, as indicated in Fig. 1b.

3. Results

Three 4H-SiC, 10 µm thick, epilayers were grown on three different c-cut substrate orientations: on-axis, 3.5°- and 8°-off, at the same time, thus with the same growth conditions ($T_g = 1600$ °C, $C/Si = 2$ and R_g approx. 2 µm/h). Mosaic patterns and boundaries of 3C-inclusions and 4H material were observed with optical microscopy on the on-axis sample, whereas few triangles were seen from the 3.5°-off epilayer. The 8°-off grown material showed a specular good surface with very few defects.

Fig. 2 shows typical XRD spectra of these three samples. The present rocking curves are recorded in triple-axis mode, and thus allow polytype identification from the related lattice parameter change [9]. A very intense 4H-SiC (0004) peak could be observed from all three samples. However, 3C inclusions could be detected through the 3C-SiC (111) peak for the on-axis sample, and more weakly for the 3.5°-off sample.

These observations are confirmed by the PL results obtained on these samples. For the on-axis epilayer, strong 3C-related PL lines could be observed on some

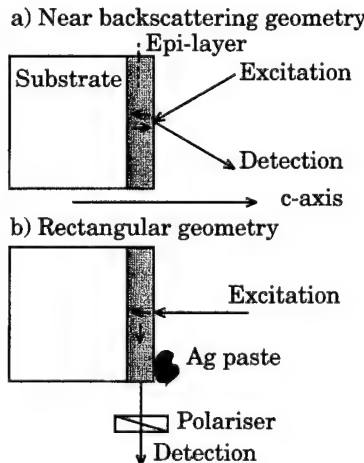


Fig. 1. Schematic representation of the experimental PL conditions.

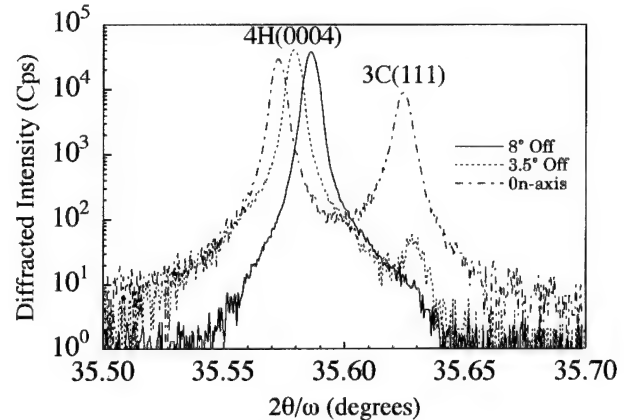


Fig. 2. X-ray diffraction rocking curves recorded for on-axis, 3.5°- and 8°-off 10 µm thick n-type 4H-epilayers grown on c-cut substrates.

parts of the samples (Fig. 3(a)), whereas 4H-related PL lines were observed on the other parts. The purity of the 3C-inclusions, which were in a very small proportion compared with the 4H, was extremely high, showing

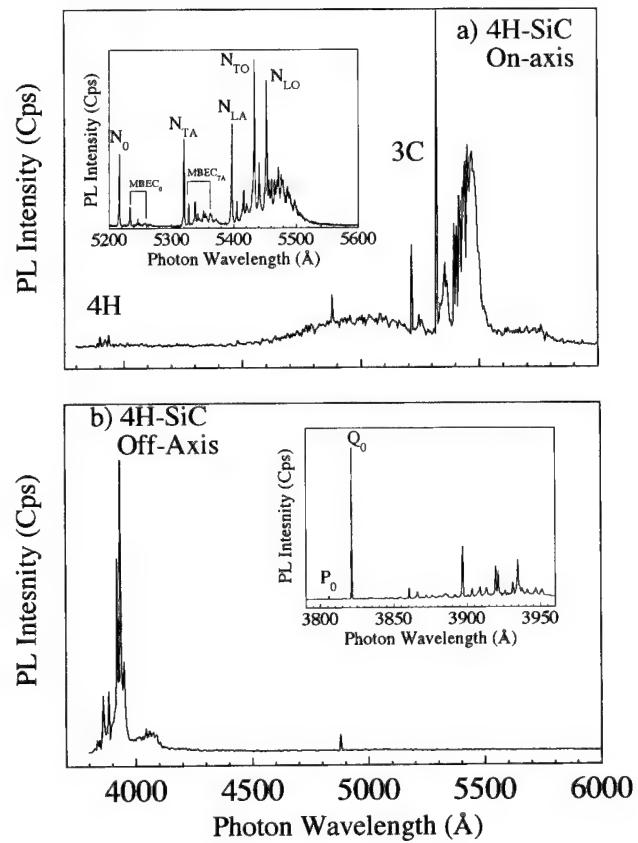


Fig. 3. PL spectra showing: (a) 3C related luminescence from the on-axis epilayer; and (b) 4H luminescence from the off-axis material. The insert in the both cases shows the near band gap emission. The multi-bound excitons (MBEC) are marked in the zero-phonon and TA phonon regions of the 3C nitrogen BE. The PL spectrum (a) was observed only from a few parts of the on-axis material, whereas the majority of the material shows PL spectra as the spectrum (b) which was recorded for 3.5°-off material.

multi-bound exciton (MBEC) lines of the N donor-bound exciton (BE) (see insert of Fig. 3(a)). No donor–acceptor pair or other deep emissions were observed, were only intense near band gap emission without the contribution of the Al-acceptor BE, as can be seen in Fig. 3. For the spectra recorded on the off-axis materials, as well as those showing 4H-related luminescence from the on-axis material, very intense nitrogen BE are detected with very sharp lines (less than our spectral resolution of 0.4 Å) without broadening. These samples were doped in the 10^{16} cm^{-3} range, and thus no FE lines could be observed.

By varying the growth conditions, samples showing either strong FE or BE related lines in the PL spectra, can be grown. For instance, if $T_g = 1550^\circ\text{C}$, $R_g = 3 \mu\text{m/h}$, and the C/Si is ≥ 3 , the samples may be compensated n-type or even p-type. To be able to obtain samples showing only N donor BE, N_2 gas needs to be added during growth in combination with a very low C/Si ratio.

Fig. 4(a) and (b) show the polarised PL spectra of FE replicas and the BE replicas, respectively, for the two possible polarisations. By comparing very carefully these spectra we found 11 phonon replicas with the $E \perp c$ polarisation and 11 phonon replicas with the $E // c$ polarisation. It should be noted here that the zero-phonon

lines P_0 and Q_0 of the BE are observed to be polarised perpendicular to c ($E \perp c$). We would also like to point out that for the $E \perp c$ polarisation, the 76.4 meV phonon replica is the dominating one, as it is often observed for the near backscattering geometry, whereas for the $E // c$ polarisation, it is the 94.7 meV phonon replica which is the most intense. For 6H-SiC, the most intense phonon replica for $E \perp c$ is the 77 meV, whereas for $E // c$ it is the 95 meV from the TO region. The results for the phonon replica energies of FE and BE in the case of 4H are summarised and compared with values from the literature, where only BE lines were considered [10,11] in Table 1. These results are in agreement with theoretical polarisation selection rules if the conduction band minimum in 4H-SiC is at the M-point of the Brillouin zone (BZ). At this point the 24 phonons can be classified by the irreducible representations of the so-called vibrational representation:

$$\Gamma_M = 8M_1 + 4M_2 + 4M_3 + 8M_4, \quad (1)$$

where M_1 , M_2 , M_3 and M_4 are the irreducible representations of the group C_{2v} of the wavevector at the M-point [12]. A group-theoretical analysis was carried out to find the polarisation selection rules leading to the results: (i) the polarisation selection rules are the same for the FE and BE described within the effective mass approximation; (ii) 12 phonon replicas are polarised $\perp c$,

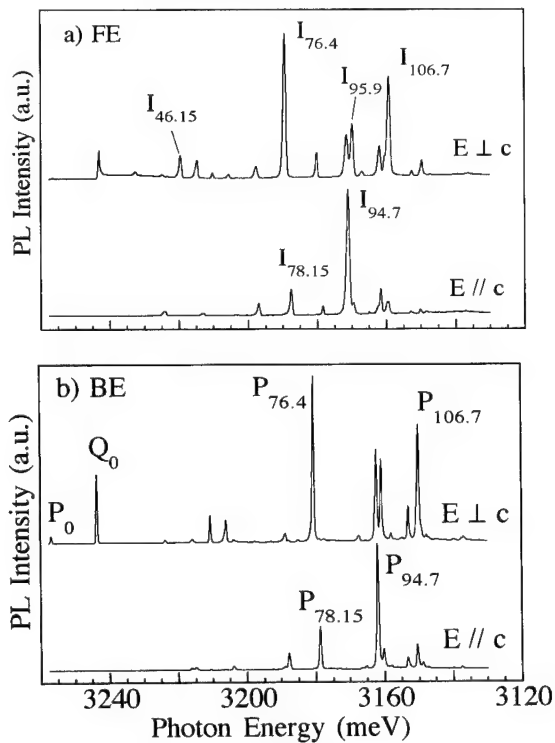
4H - SiC, $T = 2\text{K}$ 

Fig. 4. PL spectra recorded at 2 K from 30 μm -thick 4H epilayers with dominant (a) FE phonon replicas; and (b) BE-related lines for the two possible polarisations.

Table 1
Phonon replicas energies as determined from the PL data

Ref. [12]	Ref. [11]	Our data
33.5 (TA1)	33.0	33.05 ($E \perp c$)
11	36.5	36.7 ($E // c$)
37.2 (TA1)	40.6	40.8 ($E // c$)
41.4 (TA2)	41.0	41.0 ($E \perp c$)
42.4 (TA2)	41.7	41.9 ($E // c$)
46.7 (TA1)	46.1	46.15 ($E \perp c$)
51.4 (TA2)	50.8	50.75 ($E \perp c$)
53.4 (TA2)	52.7	52.7 ($E // c$)
68.7 (LA)	67.8	68.1 ($E \perp c$)
69.7 (LA)	68.7	68.7 ($E // c$)
76.9 (LA)	76.6	76.4 ($E \perp c$)
78.8 (LA)	78.5	78.15 ($E // c$)
95 (TO)	—	94.45 ($E \perp c$)
—	—	94.7 ($E // c$)
96.1	96.1	95.9 ($E \perp c$)
96.7 (TO)	97.3	96.6 ($E // c$)
—	97.8	—
—	99.1	98.8 ($E \perp c$)
—	100.3	—
—	101.6	—
104 (LO)	—	103.5 ($E // c$)
104.3 (LO)	—	103.9 ($E \perp c$)
—	105.6	106.2 ($E // c$)
107 (LO)	106.3	106.7 ($E \perp c$)
—	108.2	—
107.4 (LO)	108.7	109.0 ($E // c$)

whereas 12 are //c; and (iii) the neutral donor state has a Γ_4 symmetry in the double-group C_{3v} .

The understanding of the polarisation study of c-axis material is very important for the characterisation of a-cut material. We expect to observe both E//c and E \perp c phonon replicas in a PL spectrum from an a-cut sample recorded in the near backscattering geometry.

Growth on a-cut material was thus attempted. The first grown epilayers showed very bad morphology mainly due to the poor quality of the substrate, and no XRD signal could be observed from these samples. The PL spectra showed, however, near band gap emission but with very low intensity compared with c-axis samples. For the (10 $\bar{1}$ 0) oriented samples the observed lines were not only weak in intensity but also broad, underlining the poor quality of this layer. By increasing the time of the hydrogen etch prior the growth, better layers with significantly better morphology were grown with observation of the (11 $\bar{2}$ 0) XRD peak. Very sharp lines could be observed in the PL spectra. As expected, the 94.7 meV phonon replica for both FE and BE are the most intense phonon replicas observed in the PL spectrum of the (11 $\bar{2}$ 0) (Fig. 5(a)). This epilayer was found to have a net carrier concentration of $3 \times 10^{14} \text{ cm}^{-3}$, as determined from capacitance–voltage (C–V) measurements. The morphology of the (10 $\bar{1}$ 0)-oriented sample was observed to be of worse quality with more imperfections and defects. The growth of 4H on (10 $\bar{1}$ 0)-oriented substrates appears to be more difficult and sensitive to substrate imperfections, as is normally observed also when 6H-SiC is grown on this substrate orientation [5]. These facts are confirmed by the PL spectrum where the 94.7 meV replica is still the most intense and where the 76.4 meV replica is also observed with a high intensity.

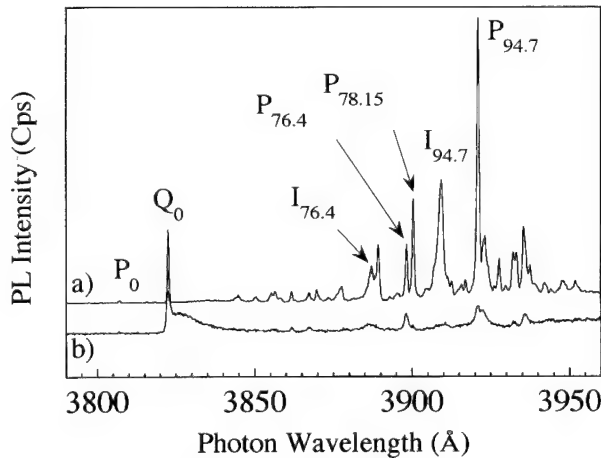


Fig. 5. PL spectra of 18 μm thick a-cut (a) (11 $\bar{2}$ 0)-; and (b) (10 $\bar{1}$ 0)-oriented materials.

4. Summary

High-quality growth for 4H thick epilayers is reported and characterised with various techniques. The quality on (11 $\bar{2}$ 0) and (10 $\bar{1}$ 0)-oriented substrates is confirmed by PL. Line widths of the PL lines from the (11 $\bar{2}$ 0) grown epilayers are comparable with those of (0001)-oriented CVD material. The PL spectra of the a-cut samples show both E \perp c and E//c phonon replicas, whereas in the (0001)-orientated 4H, only the E \perp c replicas are observed.

Acknowledgement

Financial support of this work was provided by the Swedish Natural Science Research Council (NFR), the Swedish Council for Engineering Sciences (TFR), the Swedish Board for Industrial and Technical Development (NUTEK), the NUTEK/NFR Material Consortium on Thin Film Growth, and the NUTEK/Asea Brown Boveri (ABB) Power Device Program.

References

- [1] E. Janzén, O. Kordina, Inst. Phys. Conf. Ser. No. 142 (1996) 653.
- [2] O. Kordina, C. Hallin, R.C. Glass, A. Henry, E. Janzén, Inst. Phys. Conf. Ser. 137 (1994) 41.
- [3] A.A. Burke Jr., L.B. Rowland, A.K. Agarwal, S. Sriram, R.C. Glass, C.D. Brandt, Inst. Phys. Conf. Ser. 142 (1996) 201.
- [4] T. Kimoto, A. Itoh, H. Matsumi, S. Sridhara, L.L. Clemen, R.P. Devaty, W.J. Choyke, T. Dalibor, C. Peppermüller, G. Pensl, Inst. Phys. Conf. Ser. 142 (1996) 393.
- [5] A.A. Burke Jr., D.L. Barrett, H.M. Hobgood, R.R. Siergiej, T.T. Braggins, R.C. Clarke, G.W. Eldridge, C.D. Brandt, D.J. Larkin, J.A. Powell, W.J. Choyke, Inst. Phys. Conf. Ser. 137 (1994) 29.
- [6] L.L. Clemen, R.P. Devaty, M.F. MacMillan, W.J. Choyke, A.A. Burke Jr., D.L. Barrett, H.M. Hobgood, D.J. Larkin, J.A. Powell, Inst. Phys. Conf. Ser. 137 (1994) 147.
- [7] C. Hallin, A.S. Bakin, F. Owman, P. Mårtensson, O. Kordina, E. Janzén, Inst. Phys. Conf. Ser. 142 (1996) 613.
- [8] P.F. Fewster, N.L. Andrew, J. Appl. Cryst. 28 (1995) 451.
- [9] Gmelin Handbook of Inorganic Chemistry, (Springer-Verlag, Berlin), Si Suppl. Vol. B2—Silicon Carbide, 1984, p. 8.
- [10] W.J. Choyke, R.P. Devaty, L.L. Clemen, M.F. MacMillan, M. Yoganathan, G. Pensl, Inst. Phys. Conf. Ser. No 142 (1996) 257.
- [11] L. Patrick, W.J. Choyke, D.R. Hamilton, Phys. Rev 137 (1965) A1515.
- [12] G. Koster et al., Proprieties of the Thirty-point Groups, MIT Press, Cambridge, Massachusetts, 1969.

Hydrogen incorporation in epitaxial layers of 4H- and 6H-silicon carbide grown by vapor phase epitaxy

Adolf Schöner ^{a,*}, Kurt Rottner ^a, Nils Nordell ^a, Margareta Linnarsson ^b,
Christian Peppermüller ^c, Reinhard Helbig ^c

^a IMC, P.O. Box 1084, S-16421 Kista, Sweden

^b Royal Institute of Technology, Department of Solid State Electronics, Kista, Sweden

^c Lehrstuhl für Angewandte Physik, Universität Erlangen-Nürnberg, Nürnberg, Germany

Abstract

The incorporation of hydrogen during vapor phase epitaxy was investigated using secondary ion mass spectroscopy, low temperature photoluminescence, and capacitance–voltage measurements. It was found that hydrogen incorporation is strongly dependent on the concentration of the acceptor dopants aluminum and boron, regardless of changes in the doping concentration caused by varying the concentration ratio between carbon and silicon or the dopant precursor flow. An electrical passivation of the acceptor dopants was found and could be reduced by annealing at temperatures above 1000 °C. At the same anneal temperature hydrogen-related photoluminescence was considerably reduced and the diffusion of hydrogen was detected. © 1997 Elsevier Science S.A.

Keywords: Hydrogen incorporation; 6H-, 4H-SiC; SiC vapor phase epitaxy; Al-, B-doping

1. Introduction

The intrinsic material properties of silicon carbide (SiC) motivate the development of a new generation of high power and high frequency devices, and new devices that operate at high temperatures and in aggressive environments. To fabricate these next generation devices reproducible control of the dopant and impurity incorporation is crucial.

Hydrogen (H) passivation of electrically active shallow and deep impurities is known from Si and III–V-compound semiconductors [1]. For SiC the passivation mechanisms are less well known, although H is present in epitaxial growth processes. Here H₂ is the most commonly used carrier gas and growth precursors like silane (SiH₄) and propane (C₃H₈) contain H. Therefore, the dissociation of the precursor and the carrier gas molecules leads to the presence of highly reactive atomic H at growth temperatures of around 1500 °C.

Recently the electrical passivation of impurities by H has been confirmed for SiC [2,3]. Hence the incorporation and annealing behavior of H needs to be studied

carefully, in order to understand the electrical properties and the thermal stability of epitaxially grown device material.

We investigated the incorporation and electrical passivation effects of H in 4H- and 6H-SiC epilayers grown by vapor phase epitaxy (VPE). The layers were characterized by secondary ion mass spectroscopy (SIMS), low temperature photoluminescence (LTPL), and capacitance–voltage (C–V) measurements.

2. Experimental

The growth of the epitaxial films was carried out in a horizontal reactor for vapor phase epitaxy (VPE), for details see Ref. [4]. Besides the standard precursors silane (SiH₄) and propane (C₃H₈), trimethylaluminum (TMAI) for aluminum (Al) and diborane (B₂H₆) for boron (B) doping were used to achieve p-type conductivity. For n-type layers nitrogen gas (N₂) was the dopant precursor. Palladium purified H₂ was the carrier gas and the SiH₄ flow was fixed to 2.2 sccm, giving a growth rate of around 2.5 μm h⁻¹. The growth temperature was

* Corresponding author.

varied between 1550 and 1620 °C, and the C:Si ratio between 1 and 4.

The atomic doping concentration was measured by SIMS using a CAMECA ims 4f instrument. The Al and B profiles were obtained with an O_2^+ ion beam and detection of $^{27}Al^+$ and $^{11}B^+$, respectively. The detection limit for Al and B was better than $5 \times 10^{14} \text{ cm}^{-3}$. The H concentration profiles were detected with a Cs^+ primary ion beam and detection of $^1H^-$ with a sensitivity limit of $1 \times 10^{18} \text{ cm}^{-3}$.

The LTPL spectra were obtained at a temperature of 1.9 K with a 40 mW HeCd laser operating at a wavelength of 325 nm used for the excitation. The detection system included a 0.75 m Spex-monochromator (1200 lines/mm, blazed at 500 nm) together with a Thorn-EMI 9635QD bialkali photomultiplier, giving a wavelength resolution of approx. 0.5 Å at a slit width of 50 μm.

For *CV*-measurements 100 nm thick nickel or titanium Schottky contacts were formed by electron beam evaporation through a shadow mask. The capacitance was measured with a Boonton 7200 capacitance meter using a frequency of 1 MHz and an AC-voltage of 100 mV.

3. Results

3.1. Atomic H incorporation measured by SIMS

The doping concentration in VPE growth can be controlled either by the dopant precursor flow or the C:Si ratio. In order to study the incorporation of atomic H as a function of the precursor flow or the C:Si ratio, epitaxial layers of both 4H- and 6H-SiC were grown with stair-like Al- and B-doped structures. A high acceptor concentration ($>1 \times 10^{18} \text{ cm}^{-3}$ for B, $>1 \times 10^{19} \text{ cm}^{-3}$ for Al) was chosen, to be able to detect a variation in the H concentration above the background level of around $1 \times 10^{18} \text{ cm}^{-3}$ of the SIMS instrument.

SIMS profiles for the detection of Al and H are shown in Fig. 1, where the precursor flow was used to change the Al concentration every 20 min of growth. We were not able to detect any significant difference between the two SiC polytypes investigated, as shown as an example in Fig. 1 for the Al profile. From Fig. 1 it can be seen that the incorporation of H changed according to the variations in Al doping. After a heat treatment in an argon (Ar) atmosphere at 1200 °C for 30 min, a H step profile could hardly be seen and the H concentration at the highest doped step was reduced by a factor of 3.

Studies like those for Al doping have also been performed for B-doped epilayers. The B stair-like structures have been grown by varying the B concentration using the B_2H_6 flow (Fig. 2) or the C:Si ratio (not shown). In both cases the H concentration profile follows the B doping profile. In contrast to the Al doping,

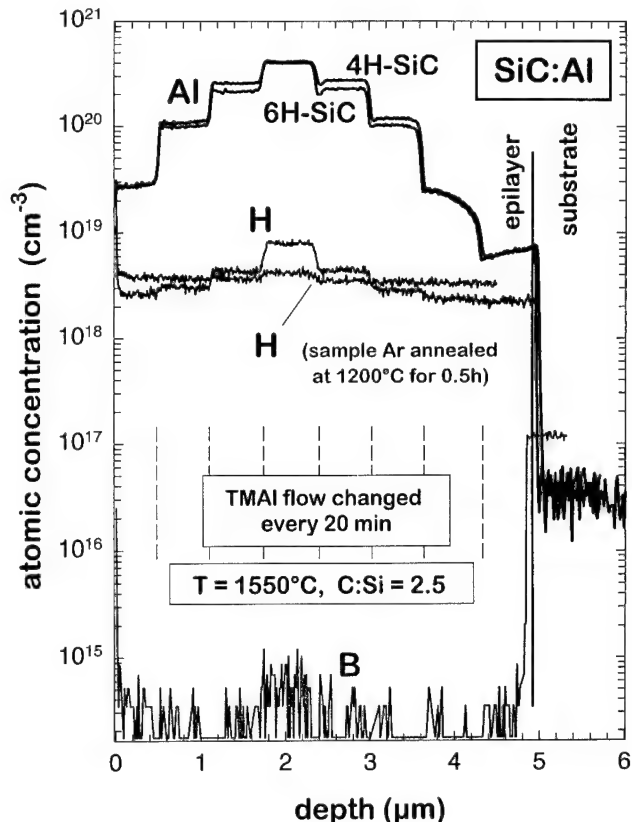


Fig. 1. SIMS concentration profiles for aluminum (Al), boron (B) and hydrogen (H) in stair-like structured Al-doped 4H- and 6H-SiC epilayers. The Al doping concentration was varied by changing the precursor (TMAI) flow at a growth temperature of 1550 °C and a C:Si ratio of 2.5.

the incorporated H concentration is higher and saturates at around $1 \times 10^{19} \text{ cm}^{-3}$, which indicates that an incorporation limit for H is reached. Furthermore, we observed a decrease in the H concentration with depth for each step in the epilayer.

For comparison we simultaneously monitored both acceptor dopants (Al and B), and the corresponding SIMS profiles are included in Fig. 1 and Fig. 2. The concentration of B in the Al-doped epilayers and of Al in the B-doped ones is close to the SIMS detection limit.

3.2. Thermal stability of H related luminescence

H related luminescence (denoted as H-lines in the following) was investigated in the 1970s by Choyke et al. [5,6]. In this study we used the H-lines with the highest intensity in the LTPL-spectra (H_1 , H_2 , H_1^S , and H_2^S in 4H-SiC and H_1 , H_2 , H_3 , and H_3^S in 6H-SiC) to examine the thermal stability of the H incorporation. It was suggested that a H atom bound to a C at a Si vacancy would give this H LTPL-spectrum [5].

As H was not detected in our N-doped n-type SiC epilayers, we grew Al- and B-doped 4H- and 6H-SiC epilayers to investigate the thermal stability. The layers

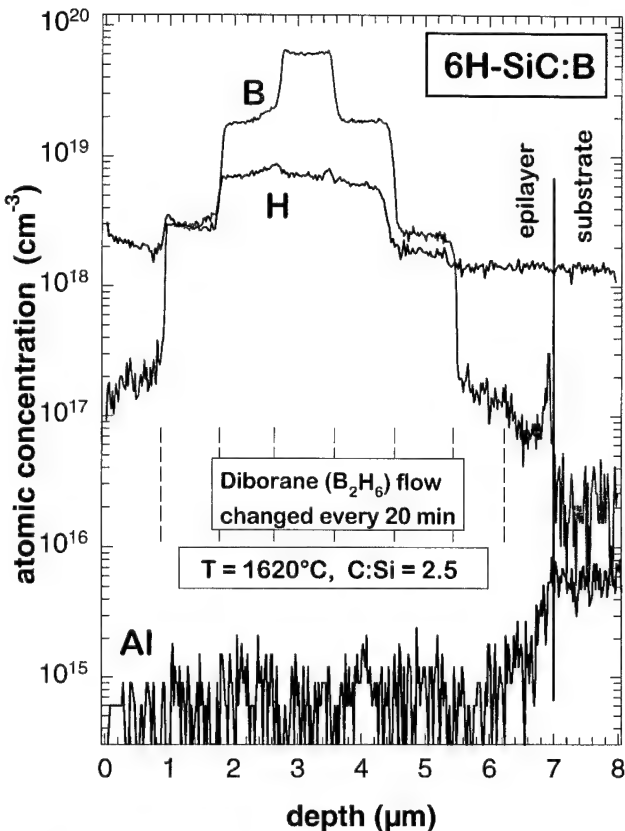


Fig. 2. SIMS concentration profiles for aluminum (Al), boron (B) and hydrogen (H) in a stair-like structured B-doped 6H-SiC epilayer. The B doping concentration was varied by changing the precursor (diborane B₂H₆) flow at a growth temperature of 1620 °C and a C:Si ratio of 2.5.

were divided into six pieces, one piece was kept as a reference and the other five were annealed in an argon atmosphere for 20 min at temperatures of 600, 800, 1000, 1200 and 1600 °C, respectively. LTPL-spectra of the grown B-doped and annealed 6H-SiC samples are shown in Fig. 3 for the wavelength range where the

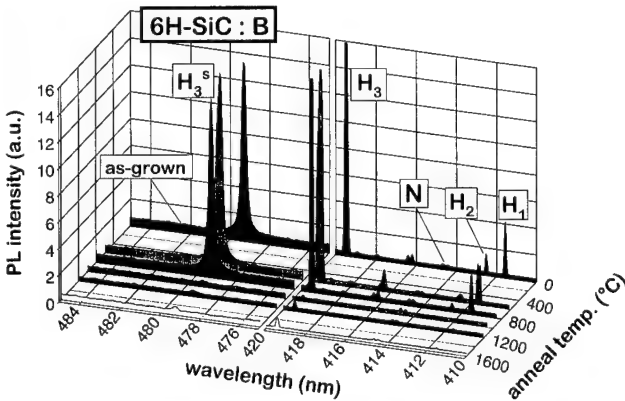


Fig. 3. Low temperature photoluminescence spectra of as-grown and (at different temperatures) annealed samples of a B-doped 6H-SiC epilayer.

H-lines appear. No difference in anneal behavior between Al- and B-doping or between the polytypes was observed and no new luminescence lines of for example B-H- or Al-H complexes were detected. In all cases, a drastic decrease in the intensity of the H-lines was seen at an anneal temperature of 1000 °C. For higher anneal temperatures the intensity of the H-lines remains stable at this low level.

3.3. Hydrogen passivation of the aluminum acceptor

To investigate electrical passivation effects in SiC we used the same Al-doped samples as for the LTPL studies. In order to obtain the net doping concentration as a function of the anneal temperature CV-measurements on Schottky diodes were performed. As seen in Fig. 4 the net doping concentration increased by 30% in this particular sample series when the samples were annealed at temperatures above 1000 °C. This increase is monotonous and larger than the inaccuracy of around 10% for the CV-measurements, which indicates that it is a true effect.

4. Discussion

In our investigation we found a strong dependence between the incorporation of H and the number of acceptors in the epitaxially grown layer. We were able

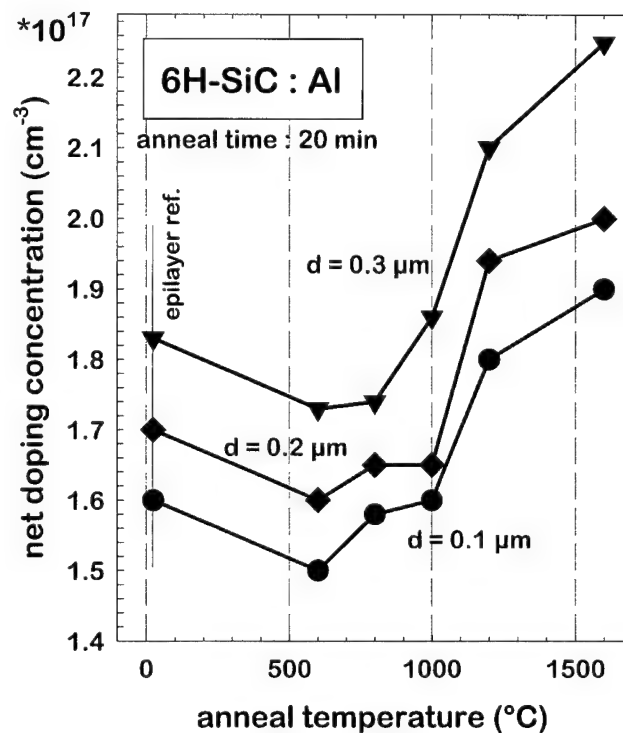


Fig. 4. Net doping concentration in dependence of the anneal temperature of an Al-doped 6H-SiC epilayer obtained by capacitance–voltage measurements for three different depths in the layer.

to reproduce the results of Larkin et al. [2], where the incorporation of H into B-doped 6H-SiC epilayers using the C:Si ratio to change the doping concentration was studied. In addition we have shown, that the incorporation of H was independent of the acceptor dopant (Al or B) and the same qualitative dependency occurs when either the precursor flow or the C:Si ratio was used to vary the acceptor doping concentration. As no H signature could be detected in our N-doped epilayers, Figs. 1 and 2 lead to the conclusion that a high H incorporation is preferentially seen when acceptor impurities are present. The reason for this is most probably that H is incorporated with the acceptor dopant by Al–H and B–H complexes which remain from the used acceptor dopant precursors.

After heat treatment at a temperature of 1200 °C for 30 min in Ar the atomic concentration of H equalized at an intermediate level, when compared to the non annealed sample and a stair-like structure was evened out. This is most probably due to H diffusion in the crystal as recently demonstrated on implanted samples annealed at various temperatures [7].

We found a strong decrease in the intensity of the H-lines at anneal temperatures over 1000 °C. This finding is in agreement with infra-red absorption measurements [8], where C–H bond-related absorption lines observed in as-grown epilayers disappeared after heat treatment at 950 °C.

The presence of H in the p-type epilayers results in electrical passivation of impurities, as observed in other semiconductors [1] and for SiC [3]. As the concentration of compensating donors in our layers was found to be in the order of $1 \times 10^{14} \text{ cm}^{-3}$ [4], the increase in net doping concentration after annealing at 1000 °C is most likely due to electrical passivation of the acceptors by H. For n-type SiC we did not observe a similar increase in net doping concentration during Ar anneal. Together with the fact that no H incorporation was found in the n-type epilayers, this indicates that H is not influencing the donor concentration in epitaxially grown material. This is in contrary to results given in Ref. [3], where after annealing in H_2 atmosphere at a temperature

between 1500 and 1700 °C, and a H pressure of 10 bar a passivation of N donors was observed.

5. Conclusion

The incorporation of H into SiC during epitaxial growth seems to be mainly related to the presence of acceptor impurities. Independent of the actual shallow acceptor dopant (Al or B) used, the H concentration increased with increase of the acceptor concentration, where both a change in precursor flow and in the C:Si ratio at constant precursor flow gave similar results. H passivates electrically active acceptors to some extent, whereas a passivation of donors was not observed. The H concentration in the epilayers and the electrical passivation of acceptors can be reduced by heat treatments in Ar atmosphere at temperatures above 1000 °C.

Acknowledgement

The authors gratefully acknowledge financial support by Asea Brown Boveri and the Swedish National Board for Industrial and Technical Development (NUTEK).

References

- [1] R.K. Willardsen, A.C. Beer, in: J.I. Pankove, N.M. Johnson (Eds.), *Hydrogen in Semiconductors*, vol. 34, Academic Press, San Diego, 1991.
- [2] D.J. Larkin, S.G. Sridhara, R.P. Devaty, W.J. Choyke, *J. Electrochem. Mater.* 24 (4) (1995) 289–294.
- [3] F. Gendron, L.M. Porter, C. Porte, A. Bringuir, *Appl. Phys. Lett.* 67 (9) (1995) 1253–1255.
- [4] N. Nordell, A. Schöner, S.G. Andersson, *J. Electrochem. Soc.* 143 (9) (1996) 2910–2919.
- [5] L. Patrick, W.J. Choyke, *Phys. Rev. B* 8 (4) (1973) 1660–1669.
- [6] W.J. Choyke, L. Patrick, *Phys. Rev. B* 9 (8) (1974) 3214–3219.
- [7] M.K. Linnarsson, J.P. Doyle, B.G. Svensson, *MRS Spring Meeting*, San Francisco, 1996, *MRS Symposium Proceedings Series*, No.423.
- [8] K. Rottner, R. Helbig, *Appl. Phys. A* 59 (1994) 427–429.

The origin of 3C polytype inclusions in epitaxial layers of silicon carbide grown by chemical vapour deposition

C. Hallin ^a, A.O. Konstantinov ^a, B. Pécz ^{b,*}, O. Kordina ^{a,c}, E. Janzén ^a

^a Department of Physics and Measurement Technology, Linköping University, S-581 83 Linköping, Sweden

^b Research Institute for Physics of the Hungarian Academy of Sciences, P.O.Box 76, H-1325 Budapest, Hungary

^c ABB Corporate Research, S-721 78 Västerås, Sweden

Abstract

Formation of 3C silicon carbide (SiC) inclusions in 4H SiC epitaxial layers has been investigated using defect revealing techniques and transmission electron microscopy. The nucleation mechanism of 3C is shown to relate to the formation of triangular stacking faults (TSFs) induced by substrate imperfections and surface defects. The TSFs modify the surface morphology by forming large (0001) surface terraces. A high local supersaturation at the TSF regions results in the spontaneous nucleation of 3C, in a manner similar to that which occurs on on-axis SiC substrates. Depending on the defect that gives rise to the TSF, the 3C inclusions may be completely overgrown by 4H polytype only leaving a striation at the edge. © 1997 Elsevier Science S.A.

Keywords: SiC; Epitaxy; Stacking fault; Transmission electron microscopy (TEM)

1. Introduction

Recent advances in epitaxial growth of SiC using chemical vapour deposition (CVD) have brought down the background doping to within the 10^{14} cm^{-3} range, and the minority carrier lifetimes up to several microseconds [1,2]. Such a material could ensure fabrication of high power high temperature devices. However, the substrate quality leaves much to be desired resulting in a high defect density in the device structures. In the present paper we study triangular defects, a common type of imperfection in epitaxial layers of 4H SiC. We show that these defects are related to the formation of 3C, the cubic polytype of SiC.

2. Experimental

Epitaxial growth was carried out in an atmospheric pressure hot-wall CVD reactor with a SiC-coated susceptor [3]. Silane and propane were used as precursor gases. The growth temperature was in the range 1450–1600 °C. The substrates were (0001) Si-face off-axis (3.5° towards $\langle 11\bar{2}0 \rangle$) wafers grown using the

modified-Lely technique [4]. They were cleaned by organic solvents and hydrogen-etched at the growth temperature prior to growth. The structure of the imperfections was investigated by optical and scanning electron microscopy using defect revealing techniques, and by cross-section transmission microscopy (XTEM).

3. Results and discussion

When compared to 6H epitaxial layers of 4H-SiC appear to be more given to 3C formation, a simultaneous epitaxial growth onto 4H and 6H substrates usually results in a much higher 3C inclusion density on 4H. Both the substrate imperfections and the growth regimes are important for the nucleation of 3C. The 3C inclusion density is much more pronounced at low growth temperatures and at high growth rates. Those observations are in agreement with the results reported by Kong et al. [5] and Kimoto and Matsunami [6] for 3C inclusions in 6H-SiC. The semi-quantitative model of Kimoto and Matsunami [6] explains the effect in terms of competition between the step-flow growth due to adatom accommodation on surface step ledges and the spontaneous two-dimensional (2D) nucleation of 3C at the surface terraces. The 2D nuclei of SiC spontaneously nucleated

* Corresponding author.

on low-index {0001} crystal planes typically do not follow the polytype structure of the substrate, rather they crystallise in the structure of 3C instead. If growth occurs via flow of the surface steps due to the off-orientation angle, the layer reproduces the substrate polytype. The material transport along the surface requires a certain supersaturation, and follows a parabolic dependence on surface step period for a simple model of surface adatom transport [6, 7]. If either the growth temperature is too low or the growth rate too high the maximum supersaturation will exceed the 2D nucleation threshold and 3C-SiC will be formed.

We found that the growth temperature and growth rate are not the only process parameters which affect the 3C inclusion density, the C/Si ratio also appears to be very important. A combination of a high growth rate, i.e. high silane flow, and a high C/Si ratio results in a dramatic increase of 3C inclusion densities, particularly at low growth temperatures.

Thin epi-layers were grown at 1500 and 1550 °C with a growth rate of 3 μm/h and C/Si ~ 2. A high density of large triangular pits appeared on the 4H SiC epi-layer grown at 1500 °C, see Fig. 1. However, the epi-layer grown at 1550 °C showed a much lower concentration. The triangular regions expand in the close-packed directions [2̄1̄0] and [1̄2̄0], but the [11̄20], [10̄10], and [01̄10] directions also occur. The 6H SiC epi-layer grown at 1500 °C shows very few triangular defects and those that do occur have a slightly different character compared to those on the 4H surface. They do not grow beyond a certain size, instead, the triangular region is displaced laterally in the growth direction of the advancing steps. Behind the triangular region terraced growth appears. Investigation of thicker 6H epi-layers showed that the triangular regions may vary in size during the displacement, though, not too abruptly.

To reveal the inclusion structure inside the triangular region as viewed from the top the samples were oxidised. Many of the triangles appeared to be completely filled with 3C while many other have mixed growth of 3C and 4H inside the region, see Fig. 1. However, no 3C was revealed in the 6H epi-layer.

The interface between 4H and 3C was investigated by removing the 3C using polytype-selective photo-electrochemical etching. Because of the difference in bandgap energy the low-bandgap 3C polytype can be selectively etched in solutions of fluorides with a blue light (in this case the 458 nm line of an Ar-laser) photo excitation. The interface surface was flat and the inclination-angle was settled at ~3.5° from the epi-layer surface by investigation of a sample cross-section. Thus, the initial triangle surface was on-axis.

We investigated the effect of mechanical damage on 3C formation in 4H epitaxial layers following the experiments performed by Powell et al. on 6H [8]. The marks of a diamond scriber appear to be preferential sites of 3C nucleation on 4H-SiC. Damage-induced and self-nucleated inclusions of 3C are of the same size and of nearly the same shape. That suggests a common formation mechanism, therefore, the self-nucleated 3C regions most probably originate from some highly strained regions in the substrate.

Potassium hydroxide (KOH) is an etchant with a high selectivity for defects [9, 10], and it was used here to obtain more information about the triangular defects. The 4H epi-layers grown at 1500 and 1550 °C were etched for 2 min at approximately 500 °C. Four different kinds of etch-pits appeared, hexagonal with a pointed bottom, hexagonally shaped holes, 'shell-like', and pits with round or irregular shape. It was deduced that hexagonally shaped holes relate to micropipes (screw with hollow core), etch-pits with pointed bottoms to screw and edge dislocation, and shell-like pits to slip dislocation in the basal plane [9, 10]. The round or irregular etch-pits are due to surface damage caused by for example, cutting and lapping. An etch-pit appeared at the top of all indented triangular regions, some with a hexagonal pit with a pointed bottom and the others with a rounded triangular or a more irregular shape. It could also be concluded that triangles with only 3C growth inside the area most often had an etch-pit related to a dislocation at the top, while most of the triangles with mixed growth inside had an etch-pit related to a shallow defect. Most of the triangular defects in the epi-layer surface grown at 1550 °C were related to a dislocation and showed only 3C inside the region.

The above results suggest that the triangular shaped morphology defects, which may result in 3C formation, are actually induced by a crystal imperfection within the hexagonal SiC material, which either appears in the epitaxial layers or is already present in the substrate.

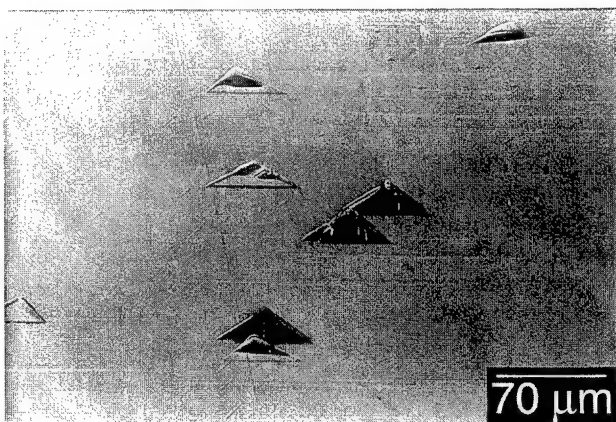


Fig. 1. Photomicrograph of the morphology of a 1 μm epitaxial layer grown at 1500 °C on a 4H-SiC substrate. The epi-layer was oxidised after growth to reveal 3C inclusions, 3C appears as dark areas in the photograph.

For sublimation growth the triangular indentations like those shown in Fig. 1 have been identified by Morkhov et al. [11] using X-ray topography. The development of large triangular on-axis regions occurs as a result of formation of triangular stacking faults (TSFs). A TSF has a structure, very similar to that of a 3C inclusion, except that the material within the triangular domain is a crystal twin of the same polytype as the substrate. Twinning occurs as a result of a glide along {0001} crystal planes as induced by substrate defects.

To investigate whether the similar stacking faults are present in our triangular defects, cross-sectional samples of the layer regions in the vicinity of the 3C inclusion origin point were prepared. Fig. 2 shows an TEM-image of a sample examined along the [1̄100] zone axis. At the lower interface between 4H and 3C, the 4H stacking sequence has been interrupted and continued into a 3C stacking sequence. Thus, the triangular defects are stacking faults due to a glide in the (0001) plane. We can also see that the 3C sequence has, for some reason, changed to a twinned sequence just after the first stacking fault. After about 80 nm the 3C stacking sequence shifted perfectly to the 4H stacking sequence again, this

is actually a triangular domain where the 3C has been overgrown by 4H.

The triangular stacking fault will give rise to development of an on-axis region due to a suppression of conventional step-flow growth within the domain. The suppression occurs as a result of the twin being incoherent with the rest of the crystal. The twin domain boundaries are energetically unfavourable places for adatom accommodation because of the strain at the boundary region. A certain supersaturation threshold is required for the growth either at the triangle apex and at the domain walls. However, adatom accommodation onto growth steps outside the domain does not require any threshold supersaturation, therefore some adsorbed species can either migrate out from the domain and deposit at a step or be re-evaporated. The development of a large on-axis region results in an increased supersaturation and may cause 2D nucleation of 3C.

Inside the expanding TSF domain 3C-SiC nucleated very early during growth at 1500 °C. Whether 3C would continue to grow or 4H would take over seems to be dependent on what kind of defect gave rise to the TSF. An indentation from a heavy load for example, introduces a large number of dislocations into a deep region from where we will have plastic deformation [12]. The presence of dislocations and stress may give rise to disordered stacking and polytypic transformation [13,14]. A 4H-SiC stacking sequence at the edges of the TSF region, particularly close to the defect centre, has low probability, rather 3C-SiC will grow from the edges and by 2D nucleation when the supersaturation is high enough. 3C growth can proceed layer by layer and will expand laterally by step flow growth, see Fig. 3(a). TSFs caused by shallow defects, for example aggregated contaminant adatoms, seem to be more of a problem when growing at lower temperatures and high C/Si ratios. The increase of 3C inclusions will be even more dramatic if we increase the silane flow, and thereby the increase the growth rate, at the same time. For the epi-layers grown at 1500°C mixed growth was commonly observed where the two polytypes had filled different regions of the TSF domain. However, what could be observed after 1 μm growth is a dominance of 4H, and from longer growths under similar conditions the situation shown in Fig. 3(b) is the most probable. The 4H poly-

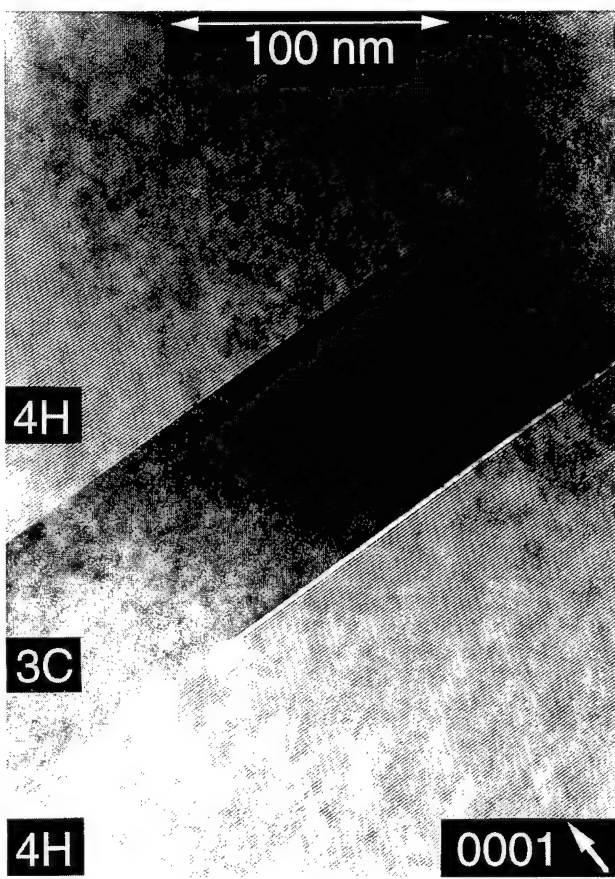


Fig. 2. Cross-sectional TEM image of a 4H-SiC epitaxial layer with a 3C-SiC inclusion. Image is taken in the vicinity of the 3C inclusion origin point. The sample is examined along the [1̄100] zone axis.

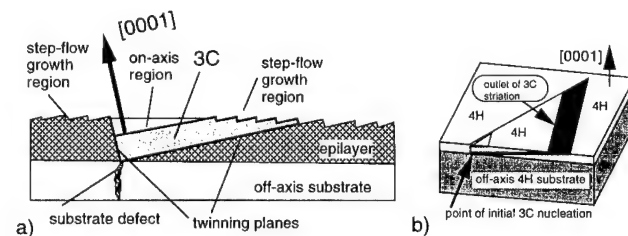


Fig. 3. The structure of (a) bulk inclusion and (b) striations of 3C as established by results of present study.

type will cover the 3C polytype only leaving a small striation at the open end of the TSF visible. The XTEM image in Fig. 2 was taken from a TSF domain with this growth character proving the existence of embedded 3C layers in the 4H epi-layers. This was also revealed by polytype-selective etching where thin free-hanging 4H-films could be seen in cross-section when investigated by SEM.

6H epi-layers grown under the same conditions as the 4H epi-layers on as-received samples did not show 3C inclusions, although the on-axis region could be quite large and comparable to sizes where 4H TSFs showed 3C inclusions. However, 3C inclusions were visible in 6H epi-layers using lower growth temperatures. This suggests that the TSF energy is higher in 6H epi-layers compared with 4H, thereby increasing the critical supersaturation ratio for 2D nucleation. This could also explain the less extended TSF domains in 6H epi-layers having a stronger attractive force between the partials.

In conclusion, we investigated the formation of cubic inclusions in epitaxial layers of 4H and 6H SiC. The 3C inclusion formation is much more pronounced for 4H than for 6H. We established the structure of 3C inclusions in 4H and demonstrated that a common type of morphology imperfection, large triangular defects, is related to 3C formation. The study of 3C formation suggests an involvement of stacking faults in hexagonal material. The stacking faults promote development of large on-axis terraces resulting in a region with high local supersaturation. The formation of 3C at these regions occurs via spontaneous 2D nucleation and growth from the triangle apex.

Acknowledgement

The work has been supported by TFR, NUTEK/NFR Materials Consortium on Thin Film Growth, the NUTEK/ABB Silicon Carbide Power Device Research Project, COPERNICUS project No. CP940603, and the Royal Swedish Academy of Sciences.

References

- [1] E. Janzén, O. Kordina, Inst. Phys. Conf. Series 142 (1996) 653.
- [2] A.A. Burk, L.B. Rowland, A.K. Agarwal, S. Sriram, R.C. Glass, C.D. Brandt, Inst. Phys. Conf. Series 142 (1996) 201.
- [3] O. Kordina, C. Hallin, R.C. Glass, A. Henry, E. Janzén, Inst. Phys. Conf. Series 137 (1993) 37.
- [4] CREE Research Inc, Durham NC 27713, USA
- [5] H.S. Kong, J.T. Glass, R.F. Davis, J. Appl. Phys. 64 (1988) 2672.
- [6] T. Kimoto, H. Matsunami, J. Appl. Phys. 75 (1994) 850.
- [7] W.K. Burton, N. Cabrera, F.C. Frank, Phil. Trans. Roy. Soc. A243 (1951) 299.
- [8] J.A. Powell, D.J. Larkin, J.B. Petit, J.H. Edgar, in: Amorphic and Crystalline Silicon Carbide IV, Springer Proceedings in Physics, 71, Springer, Berlin, 1992 p. 23.
- [9] K. Koga, Y. Fujikawa, Y. Ueda, T. Yamaguchi, in: Amorphic and Crystalline Silicon Carbide IV, Springer Proceedings in Physics, 71, Springer, Berlin, 1992, p. 96.
- [10] J. Takahashi, M. Kanaya, Y. Fujiwara, J. Cryst. Growth 135 (1994) 61.
- [11] E.N. Morkov, I.L. Shulpina, A.S. Tregubova, Yu.A. Vodakov, Cryst. Res. Technol. 16 (1981) 879.
- [12] K. Maeda, K. Suzuki, S. Fujita, M. Ichihara, S. Hyodo, Phil. Mag. A 57 (1988) 573.
- [13] P. Pirouz, Inst. Phys. Conf. Series 104 (1989) 49.
- [14] J.A. Powell, H.A. Will, J. Appl. Phys. 43 (1972) 1400.



ELSEVIER

SiC and group III nitride growth in MOVPE production reactors

R. Beccard ^{a,*}, D. Schmitz ^a, E.G. Woelk ^b, G. Strauch ^a, H. Jürgensen ^a

^a AIXTRON GmbH, Kackertstr. 15-17, D-52072 Aachen, Germany

^b AIXTRON Inc., 1569 Barclay Blvd, Buffalo Grove, IL 60089, USA

Abstract

In this study a range of MOVPE systems for high temperature epitaxial growth processes, such as SiC and group III nitrides, is presented. It is shown that extensive modelling of the heat transfer, gas flow and reactant depletion has led to highly efficient reactors that provide the capability for uniform growth of binary and ternary material systems at temperatures up to 1600 °C in single- and multi wafer configurations. Experimental results of various layers are presented to prove the availability of state-of-the-art process technology in production-scale systems. © 1997 Elsevier Science S.A.

Keywords: MOCVD; Nitride; SiC; Modelling

1. Introduction

Silicon carbide is currently gaining much attention as a material for high temperature, high speed and high power devices. However, fabricating epitaxial SiC films is still a challenge since very high growth temperatures (up to 1600 °C) have to be used. These require carefully adapted reactor design to ensure laminar flow conditions and controlled depletion of the reactants inside the reactor.

Similar considerations are valid for the group III nitrides (AlN, GaN, InN and their alloys). These materials are also grown at high deposition temperatures (up to 1300 °C). Furthermore, the heterostructures of these materials typically require abrupt changes in growth temperature. In general, both nitrides and SiC are similar in their challenges to growth equipment.

This study uses a family of high temperature reactors to grow SiC and nitrides. Extensive modelling was used in order to find the optimum reactor geometry. Thus an optimization of uniformity and efficiency, and a minimization of undesired parasitic reactions was obtained.

2. Experimental

Growth experiments performed in an AIX 200/4 series two-flow horizontal laminar flow CVD reactor provided

the basis for the numerical calculations of the optimization of this reactor type, as well as the reactor and process design for the high temperature Planetary Reactor®.

The reactor consists of a double-walled, water-cooled outer quartz reactor and a rectangular inner quartz liner tube in which the gas reaction takes place. The reactor is designed to sustain CVD processes in the pressure range 10–1000 mbar. The susceptor which is inductively heated can handle one wafer of up to 4 in. diameter rotated using the Gas Foil Rotation® technique.

Fig. 1 shows a cross-section of the Multiwafer Planetary Reactor® chamber. To obtain the required uniformity of material film each individual substrate is rotated around its centre axis similar to in the linear flow channel reactor described above [1]. The seven satellite disks, each with one 2 in. wafer, are also rotated around the inlet to provide total symmetry in the growth chamber for all wafers.

The reactor is able to sustain a susceptor temperature of 1600 °C by inductive heating which makes it suitable for the growth of SiC where temperatures in the range of 1400–1600 °C are required [2]. The susceptor temperature is measured by means of a pyrometer.

In MOVPE having control over the temperature of the reactor's inner walls has been found to be crucial. In the case of the Planetary Reactor®, this is simply the ceiling of the reactor chamber, a plate of fused quartz above the susceptor. The temperature can be controlled by adjusting the gas composition between the ceiling

* Corresponding author.

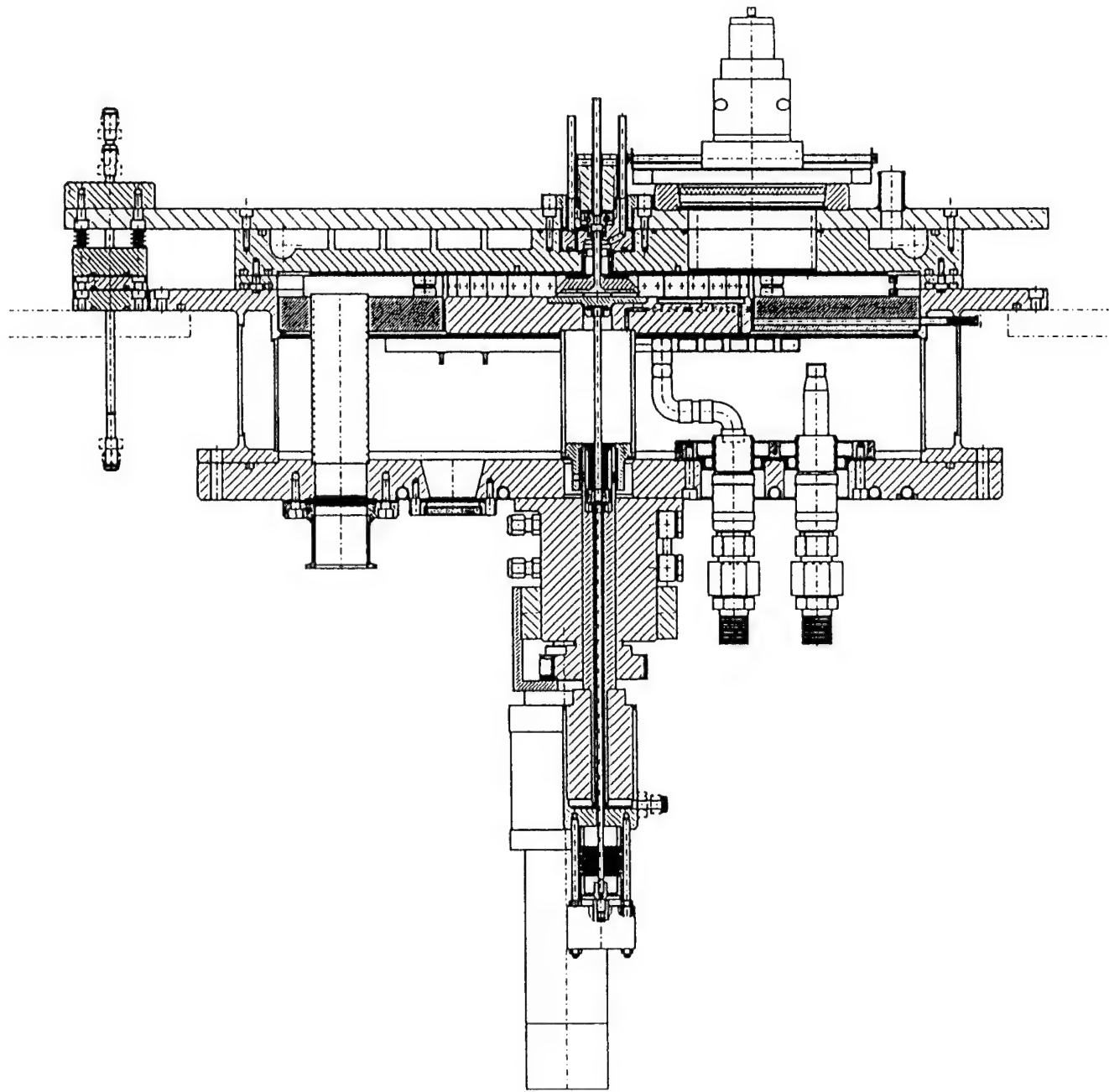


Fig. 1. Cross-sectional view of the high temperature Planetary Reactor®.

and the water cooled reactor top, thus regulating the thermal conductivity between the plate and the heat sink. This technique has worked for all materials grown in this type of reactor so far and greatly reduces the deposition [3].

In both reactors the two-flow gas inlet introduces the metalorganic precursors keeping them separate from the ammonia in the GaN system, or in the case of SiC growth keeping the silicon precursor away from the carbon source gas flow. Thus pre-reactions are avoided and tuning of the two separate gas flows can be used to

adjust the deposition uniformity over the rotating substrate.

For the GaN material growth, NH₃ with semiconductor purity and conventional Ga- and Al-precursors was used. Pd-diffused H₂ or N₂ was used as a carrier gas. Most experiments were performed on basal plane Al₂O₃. Typical total flow rates for the growth experiments are 6.5 and 13 slm at reactor cell pressures of 10 and 50 mbar, respectively. In the case of SiC growth, 3C-SiC layers were deposited on Si (100, 111) substrates and 6H-SiC substrates. For growth on Si the well known

Growth rate of GaN vs 1/Td

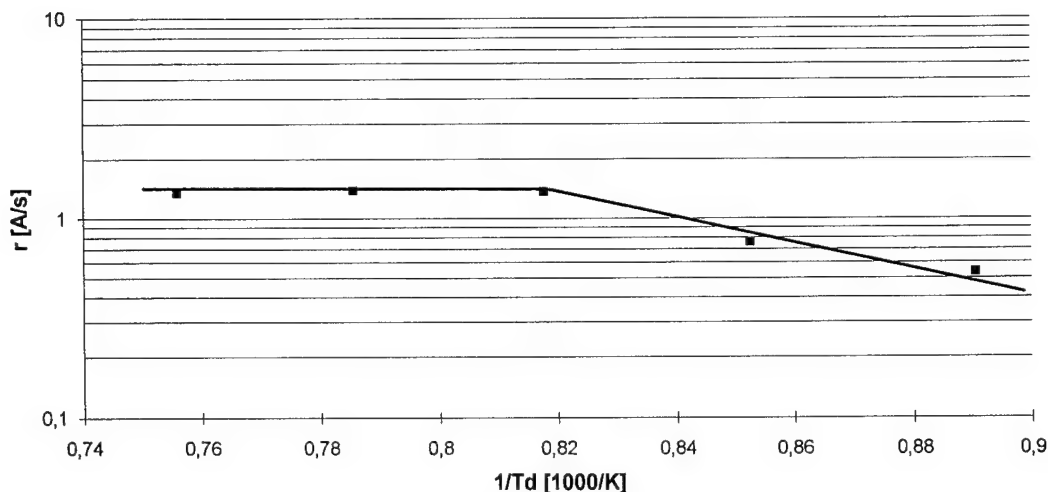


Fig. 2. Growth rate of GaN versus $1/T_d$ (AIX 200/4).

carbonization techniques were used. SiH_2Cl_4 and C_2H_4 were used as process gases. The substrate temperature was varied between 1200 and 1390 °C; when using SiH_4 and C_3H_8 temperatures up to 1700 °C were employed.

3. Modelling

Extensive modelling was performed to study the dependence of the growth rate on key process parameters, such as temperature, pressure, input partial pressure of TMG and ammonia, and the total flow rate. A two-dimensional model was used as described in Ref. [4]. The results for the linear channel reactor are shown first. It can be seen that homogeneous decomposition of TMG near the growing surface is almost completed under the conditions used.

Fig. 2 shows the growth rate versus the deposition temperature of GaN in the linear channel reactor. The excellent agreement between the calculated and experimental growth rate distribution along the flow direction in the reactor has been published elsewhere [5]. Initial data with wafer rotation gave a growth rate uniformity of $\pm 4\%$. By further optimization a uniformity of $\pm 1.5\%$ is achievable.

All considerations concerning the linear horizontal two-flow reactor can be transferred to the mass production Planetary Reactor® family. Thus several pieces of information are obtained from the simulations, the most important being that the gas phase in the reactor with the susceptor at 1100 °C is laminar and stable. Fig. 3 shows the concentration of trimethylgallium (TMGa), monomethylgallium (MMGa), and Ga vapour as a function of the radius. The flux of MMGa

originating from the TMGa decomposition is assumed to govern the growth rate. As seen in Fig. 3(b), the MMGa gradient decreases linearly along the radius. Similar results were also found in the simulations of a smaller horizontal reactor which were in good agreement with the actual growth runs [5].

Both the modelling and the experiments show that the thermal management of heat transfer can be handled by the predicted Planetary Reactor® design. The temperature of the reactor ceiling can be adjusted to allow optimum and reproducible deposition conditions. Temperature uniformities at 1600 °C on 2 in. substrates that are better than $\pm 5\text{ }^\circ\text{C}$ have been measured. The calculated streamlines at 1000 mbar and 50 mbar are free from any vortices from the centre toward the outer radius. Further, the model clearly points out the advantage of this geometrical concept in the Planetary Reactor® which, even at high-temperature growth, linearizes the depletion behaviour rather than compensating depletion effects while giving the best achievable efficiency on wafers, as often seen in the conventional III-V material system.

4. Results

Trimethylgallium and trimethylindium in a purified nitrogen carrier gas were used for the growth of $\text{Ga}(\text{In})\text{N}$ together with purified ammonia. The growth temperature for the 500 Å buffer layer was 600 °C, the temperatures for the GaN layer were 1050–1100 °C. By using growth initiation and buffer layer growth, excellent layer properties of GaN were obtained. Using optimized conditions, GaN with an X-ray 0002 peak FWHM of

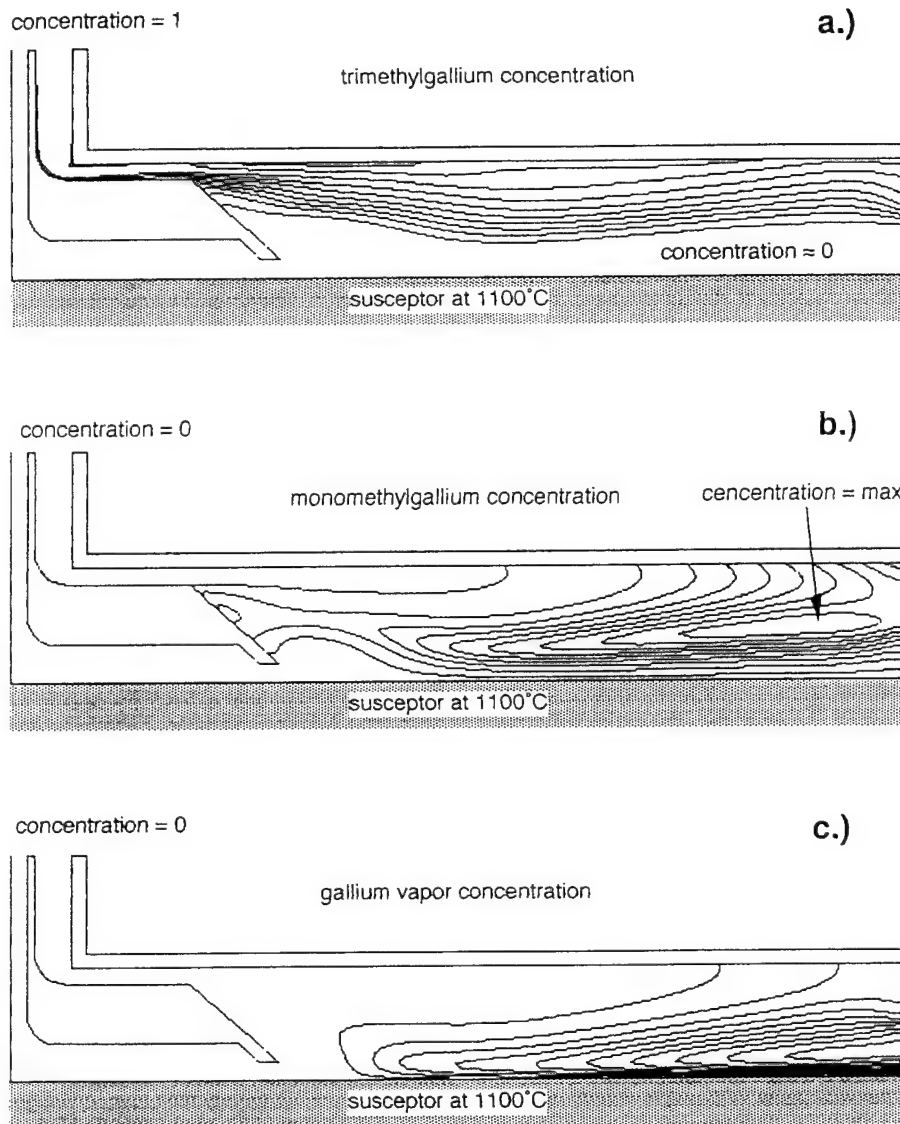


Fig. 3. Concentrations of TMGa (a), MMGa (b), and gallium vapour (c) in the reactor.

approximately 30 arcs was obtained. PL results show values of 50 meV FWHM.

In order to grow the p-doped layers necessary for LED and laser production, Mg-doping has been used employing Cp_2Mg [6].

Growth of SiC on Si also shows excellent layer properties. The X-ray analysis reveals a strong texture. Beside the main high-intensity peak, reflexes with lower intensities have been registered. X-ray diffraction clearly shows the existence of additional 3C-SiC modifications, SEM analysis shows a smooth surface.

In the Planetary Reactor® the following growth parameters were used: pressure 100 mbar, total flow 14.1 slm, ammonia flow 4 slm and TMGa $267 \mu\text{mol min}^{-1}$. At these conditions a growth rate of $1.3 \mu\text{m h}^{-1}$ was observed. Higher TMGa flows yield higher growth rates. The simulated growth rate is shown

in Fig. 4 along with the actual growth rate. The total flow consumption of 21 min^{-1} per wafer is minimal compared to any other multiwafer MOCVD reactor described in the literature so far.

The material films were characterized by Hall, X-ray and photoluminescence (PL) measurements. The mapping of the full width at half maximum (FWHM) of the X-ray peak of a GaInN film with an indium content of $\sim 5\%$ and a thickness of $0.3 \mu\text{m}$ shows a variation of less than ± 150 arc s. PL mappings reveal similar results; GaInN PL uniformities across a 2 in. wafer are better than 3 nm.

5. Summary

In this paper it is shown that material systems like GaN and SiC which require high temperature MOVPE

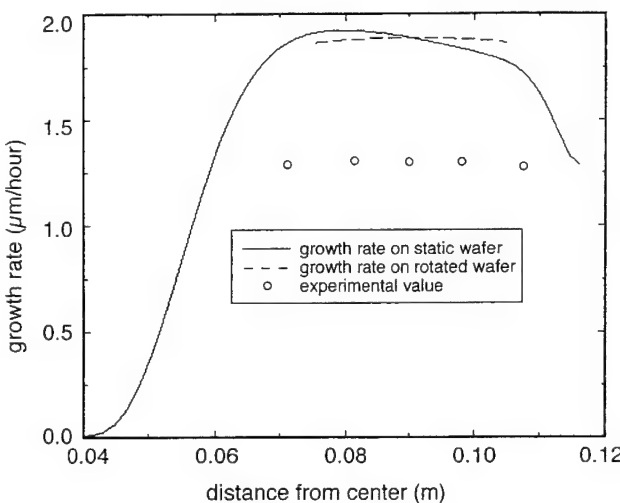


Fig. 4. Simulated and observed growth rates in the reactor.

reactors can be grown successfully. A two-flow reactor concept is required to separate the precursors until shortly before the growth area on the susceptor. Simulation has shown how to optimize the reactor geometry to guarantee high quality deposition. Using the Planetary Reactor® concept, multiwafer mass production of SiC and GaN is possible and available on the market. Modelling has shown that high quality and high efficiency layers can be deposited across large areas. Temperature uniformities at 1600 °C on 2 in. substrates of better than ± 5 °C have been obtained. Currently a number of these 7 × 2 in. reactors are used to scale-up production quantities for both material systems.

Acknowledgement

The authors would like to acknowledge Prof. Razeghi's group, Center of Quantum Devices, Northwestern University; Dr Makarov, Institut für Strömungsmechanik, Erlangen; and also E. Niemann, D. Leidich, Daimler Benz AG, Frankfurt, for providing their modelling and experimental growth results for this paper.

References

- [1] P.M. Frijlink, A new versatile, large size MOVPE reactor, *J. Cryst. Growth* 93 (1988) 207–215.
- [2] BurkA.A., Jr., L.B. Rowland, Reduction of unintentional aluminum spikes at SiC vapor phase epitaxial layer/substrate interfaces, *Appl. Phys. Lett.* 68 (1996) 382–384.
- [3] P.M. Frijlink, Epitaxial Reactor having a wall which is protected from deposits, United States Patent No 5,027,746 July 2, 1991.
- [4] T. Bergunde, M. Dauelsberg, Yu. Egorov, L. Kadinski, Yu.N. Makarov, M. Schäfer, G. Strauch, M. Weyers, Algorithms and models for simulation of MOCVD of III-V layers in the planetary reactor, in: H. Ryssel, P. Pichler (Eds.), *Simulation of Semiconductor Devices and Processes*, vol. 6, Springer Wien, New York, 1995.
- [5] M. Dauelsberg, L. Kadinski, Yu. N. Makarov, E. Woelk, G. Strauch, D. Schmitz, H. Juergensen, GaN-MOVPE: Correlation between computer modeling and experimental data, *Proceedings of the 6th International Conference on Silicon Carbide and Related Materials*, Kyoto, September 18–21, 1995 (in press).
- [6] P. Kung, X. Zhang, E. Bigan, M. Razeghi, A. Saxler, Low pressure metalorganic chemical vapor deposition of high quality AlN and GaN thin films on sapphire and silicon substrates, *Proceedings of SPIE Photonics West*, San José, February 4–10, 1995 (in press).

Growth of SiC films obtained by LPCVD

M.T. Clavaguera-Mora ^{a,*}, J. Rodríguez-Viejo ^a, Z. El Felk ^a, E. Hurtós ^a, S. Berberich ^a, J. Stoemenos ^b, N. Clavaguera ^c

^a Grup de Física de Materials I, Departament de Física, Universitat Autònoma de Barcelona, 08193-Bellaterra, Spain

^b Physics Department, Aristotle University of Thessaloniki, 54006 Thessaloniki, Greece

^c Grup de Física de l'Estat Sòlid, Departament ECM, Facultat de Física, Universitat de Barcelona, Diagonal 647, 08028-Barcelona, Spain

Abstract

This paper reports the results of a systematic study of the influence of deposition conditions on the morphology of films grown using a tetramethylsilane $\text{Si}(\text{CH}_3)_4$ precursor in a hot-wall, low pressure, chemical vapor deposition system at the temperature range 900–1150 °C. Most of the SiC films were deposited on a thin a- SiO_2 layer, thermally grown on Si(001) wafers. Characterization of the SiC films was performed by X-ray diffraction, scanning and transmission electron microscopy, ellipsometry, profilometry, electron microprobe analysis with a wavelength dispersive spectrometry detection system, and X-ray photoelectron spectroscopy. The results obtained on the kinetics of growth concern the change in the growth rate and the evolution of the preferential [111] orientation of the polycrystalline films with the deposition conditions. The general characteristics of the polycrystalline films are their columnar structure, which is related with the very strong [111] preferred orientation, and the formation of microtwins, having the twin planes perpendicular to the direction of growth. © 1997 Elsevier Science S.A.

Keywords: Poly-SiC; LPCVD; Metal-organic precursors; Microtwins development

1. Introduction

SiC is a good candidate for electronic application at high temperatures because it combines excellent semiconducting properties and high thermal conductivity with intrinsic resistance to oxidation and creep [1,2]. The growth of poly-SiC by metalorganic low pressure chemical vapor deposition (LPCVD) in a hot-wall reactor is of considerable interest due to the reduction of impurities inside grain boundaries and the deposition over large distances [3,4]. In the present study we concentrate on the influence of deposition conditions on the morphology of films deposited on (001) Si wafers, prepared from a mixture of tetramethylsilane (TMS), $\text{Si}(\text{CH}_3)_4$, in H_2 . A thin a- SiO_2 layer was thermally grown on the Si substrate prior to deposition to avoid strain development due to the 20% mismatch lattice and the 8% difference in thermal expansion coefficients of the substrate and the overgrown layer.

2. Experimental details

The deposition system, is shown schematically in Fig. 1. The furnace consists of a hot-wall tubular quartz reactor with a large (≈ 60 cm) isothermal (± 5 °C) zone. The gas handling system uses pneumatically operated valves and electronic mass flow meters, every gas line

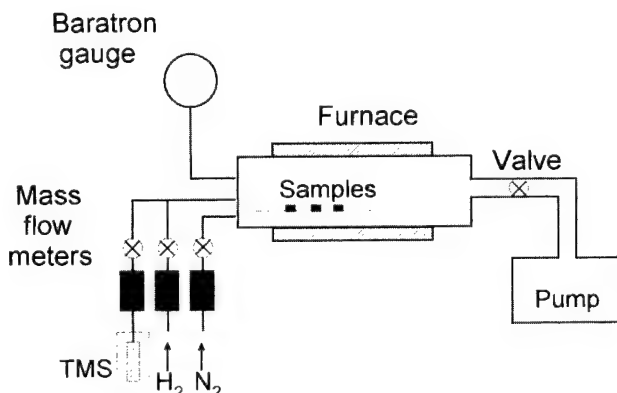


Fig. 1. Experimental set-up of the hot-wall LPCVD reactor.

* Corresponding author.

being connected in a run/vent configuration. The substrates used were 2 in. Si(100) wafers p-type with a resistivity of $1\Omega\text{ cm}$. Prior to the deposition the wafers were treated by a $\text{H}_2\text{SO}_4 + \text{H}_2\text{O}_2$ mixture followed by HF etching, thoroughly rinsed with deionized water and then dried with N_2 . The SiO_2 thickness of the thermally grown interlayer film ranges between 60 and 3000 Å. The growth parameters used during the process were: total pressure: 0.5–1.5 Torr, TMS flow: 0.5–15 sccm, H_2 flow: 1–2 slm, deposition time: 30–240 min and temperature 900–1150 °C. After deposition, samples were cooled to room temperature at a rate of 5 °C/min in a N_2 atmosphere.

3. Results and discussion

Characterization of SiC films was performed by X-ray diffraction (XRD) using Cu K_α radiation, scanning electron microscopy (SEM), transmission electron microscopy (TEM), ellipsometry, profilometry, electron microprobe analysis with a wavelength dispersive spectrometry detection system (EPMA/WDS) and X-ray photoelectron spectroscopy (XPS). Fig. 2 shows some details of the microstructures obtained by TEM. Films grown at 900–980 °C are amorphous with nanocrystals of mean grain size 10 nm and have smooth surfaces. Surface profilometry measurements give a root mean square roughness (RMS) of ≈ 6 nm. At 1000–1150 °C

polycrystalline β -SiC is formed, the growth being mostly columnar after an induction period where crystallites nucleate on the substrate forming equiaxed grains. The diameter of the cylindrical crystallites, arranged parallel to the growth direction, increases with deposition temperature and film thickness. They form rounded hillocks at the film surface. Consequently, the surface RMS increases with the development of preferred orientation along the [111] direction of β -SiC. It is quite high, ranging from 70 to 100 nm depending on the temperature and film thickness. The crystallites show micro-twins having their twin planes perpendicular to the direction of growth even at the deposition temperature of 1000 °C [5]. This is attributed to the very low adatom mobility in conjunction with the high number of atoms which may be incorporated per unit area on the [111] planes at low energy sites.

Amorphous films are defective in Si. When they are deposited at 900 °C their Si content is 40 at% and this increases up to the stoichiometric value with deposition temperature, as shown by EPMA/WDS. Differences between polycrystalline and amorphous films are clearly seen in the XPS spectra. The C 1s and Si 2p peaks of two samples deposited at similar total pressure, TMS and H_2 flows, but different temperature are shown in Fig. 3. The most striking difference is the disappearance of the graphite peak [6] in the C 1s spectrum at 283.9 eV (FWHM = 1.9 eV) in the poly-SiC films. The main peak has been identified as an Si–C bond. The FWHM are

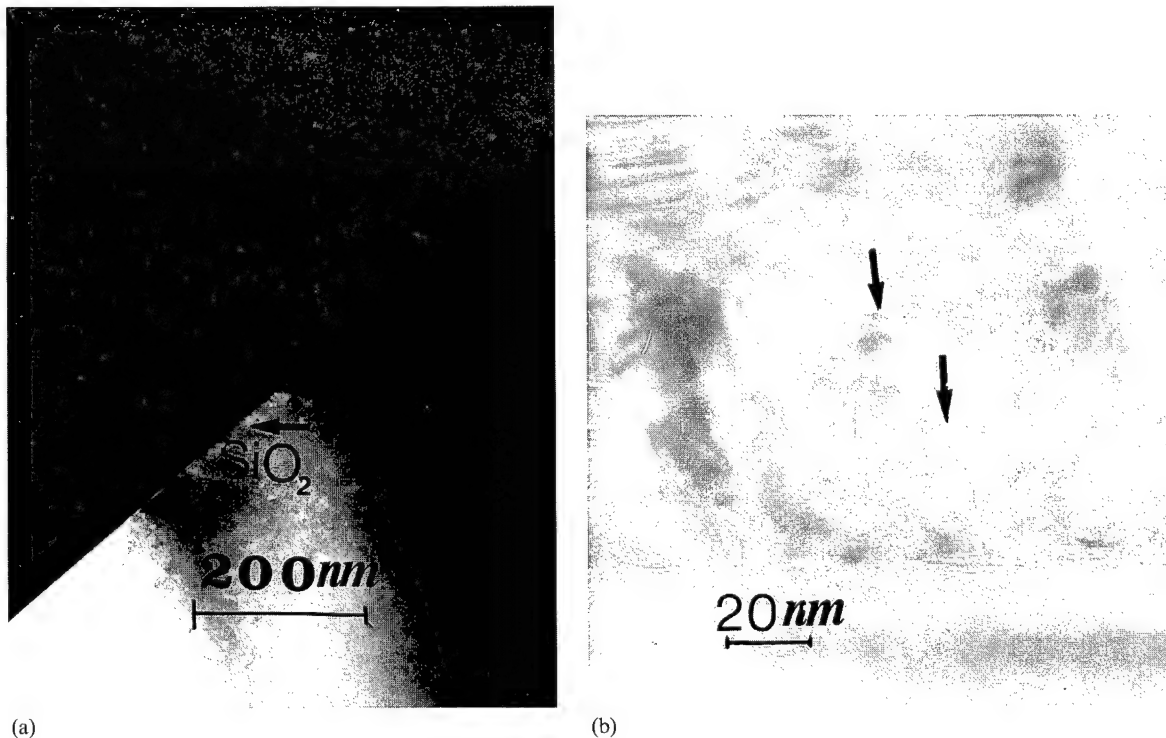


Fig. 2. Cross-section TEM micrographs. (a) Dark-field image focalized on [111] reflection of a film deposited at 915 °C, showing the Si/SiO_2 interface (between arrows) and nanocrystals. (b) Bright-field image of a film deposited at 1130 °C; arrows show cavities between grains.

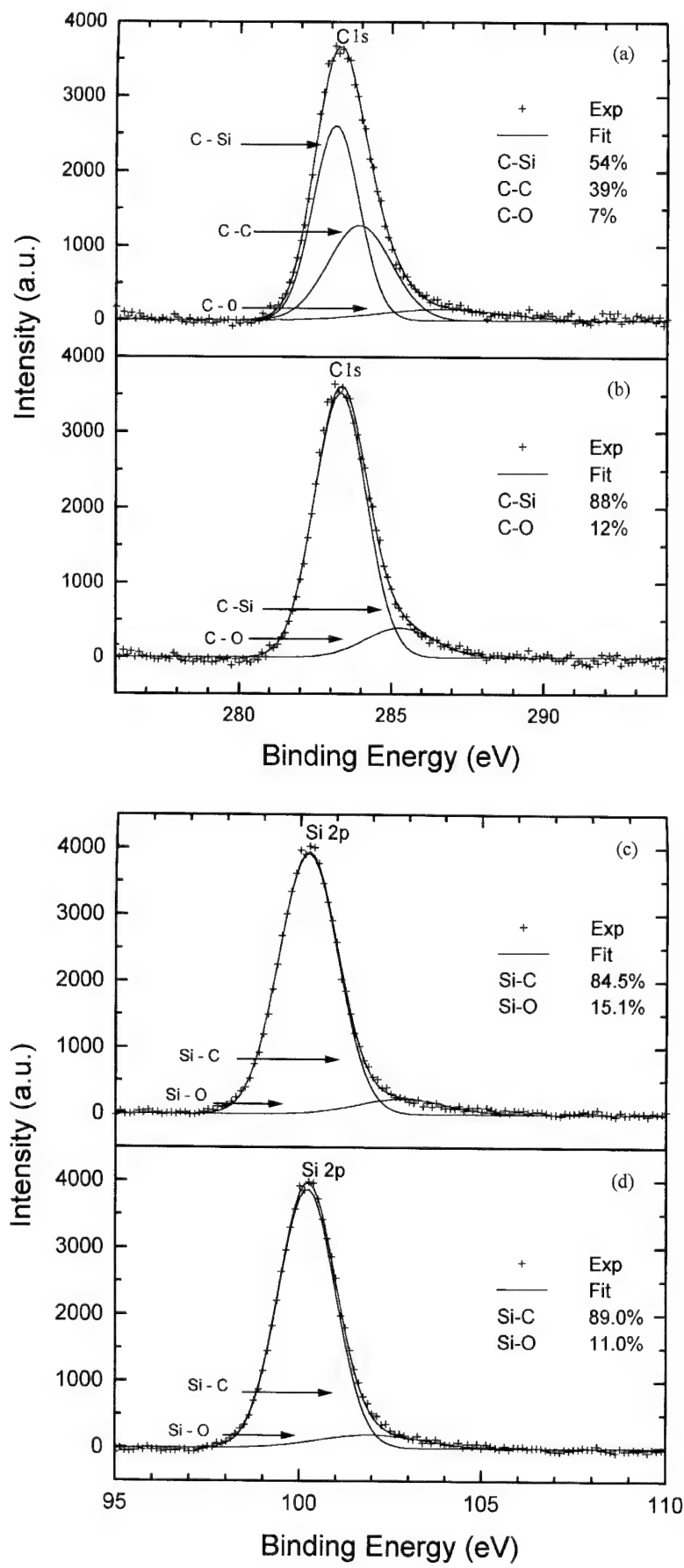


Fig. 3. Analysis of the XPS spectra: C 1s peak of (a) film grown at 915 °C, (b) grown at 1130 °C, and Si 2p peak of (c) film grown at 915 °C and (d) grown at 1130 °C.

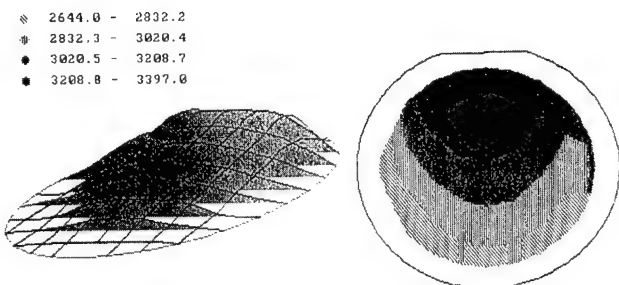


Fig. 4. Ellipsometric mapping of an SiC film.

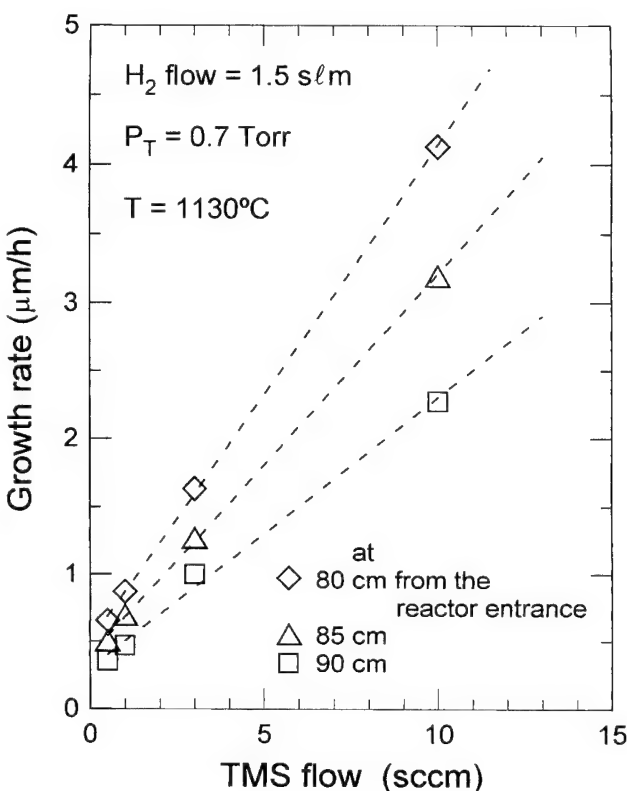


Fig. 5. Growth rate versus TMS flow at several wafer positions from the reactor entrance.

≈10% higher for the amorphous films than for the poly-SiC ones due to the disordered network. In some of the samples peaks arising from C or Si bonded to oxygen are seen due to native oxidation or contamination.

The film thickness increases linearly with the deposition time, independently of the growth conditions. The thickness uniformity of the wafers is fairly good. Fig. 4 shows an ellipsometric mapping obtained with 50 points when measuring a SiC film whose mean thickness is about 15 μm from edge to edge. Fringes are produced by the interference of the free SiC surface with the interface. Thickness differences between consecutive fringes correspond to about 0.1 μm.

Fig. 5 shows the dependence of the growth rate, J , on the wafer location in the reactor for a fixed H₂ flow and

different values of TMS flow. As expected, there is a linear increase of J with the TMS flow. In addition, J decreases on successive wafers located at increasing distance from the reactor entrance. This decrease is due to an important TMS depletion along the reactor produced by the deposition on the previous wafers and on the hot reactor walls.

The apparent activation energy of growth is (1.4±0.1) eV. This value of the activation energy remains constant irrespective of: the H₂ to TMS flow ratio, the crystallinity of the film and the thickness of the SiO₂ interlayer. The linearity of the film thickness with both deposition time and TMS flow, as well as the film thickness uniformity and the high activation energy value support the finding that growth is controlled by some surface mechanism. Also, J increases with the TMS to H₂ flow ratio, for a fixed total pressure. Since the strong preferred orientation of the crystalline growth is related to the generation of microtwins, it permits a fast incorporation of the atoms in the crystal lattice resulting in a reduction of the free energy of the system and creating large twinned grains.

4. Conclusions

The main conclusions with respect to the growth of films from TMS/H₂ by LPCVD process deduced from the experimental study are:

- (1) Amorphous (with nanocrystalline inclusions dispersed in the matrix) films incorporate an excess of C with respect to stoichiometry. Nanocrystals exhibit no preferred orientation.
- (2) Polycrystalline films have the β-type structure and develop [111] orientation.
- (3) Planar defects are generated perpendicular to the direction of growth. They are microtwins which facilitate growth.
- (4) The surface reaction-controlled growth rate has an activation energy of 1.4±0.1 eV.
- (5) The surface roughness and preferential orientation increase with film thickness, deposition temperature and TMS versus H₂ flow ratio.

Acknowledgement

Authors are indebted to the 'Serveis Científico-Tècnics' of the University of Barcelona for the XRD, EPMA/WDS and XPS analysis. Financial support from CEE BRITE/EURAM by Contract No BRE-CT92-0211, from CIRIT by Project No GRQ-2.048 and from CICYT by Project No MAT95-0875 is acknowledged.

References

- [1] R.F. David, G. Kelner, J.W. Palmour, J.A. Edmond, Proc. IEEE 79 (1991) 677.
- [2] J. Rodriguez, N. Clavaguera, Z. El Felk, M.T. Clavaguera-Mora, G. Arnaud, J. Camasel, J. Pascual, S. Berberich, J. Millán, Mater. Sci. Technol. 12 (1996) 98–101.
- [3] K.K. Schuegraf (Ed.), *Handbook of Thin Film Deposition*, Noyes Publishers, Park Ridge, 1988.
- [4] I. Golecki, F. Reidinger, J. Marti, Appl. Phys. Lett. 60 (1992) 1703.
- [5] J. Rodríguez Viejo, J. Soemenos, N. Clavaguera, M.T. Clavaguera-Mora, J. Cryst. Growth 155 (1995) 214.
- [6] A. Tabata, S. Fujii, Y. Suzuki, T. Mizutani, M. Leda, J. Appl. Physics 23 (1990) 316.

Chemical conversion of Si to SiC by solid source MBE and RTCVD

J. Pezoldt *, V. Cimalla, Th. Stauden, G. Ecke, G. Eichhorn, F. Scharmann, D. Schipanski

TU Ilmenau, Institut für Festkörperelektronik, Postfach 100565, 98684 Ilmenau, Germany

Abstract

The carbonization of (111)Si surfaces exposed to a sublimed carbon molecular beam with carbon fluxes varying ca two orders of magnitude at substrate temperatures between 700 and 1050°C was studied. The structural and morphological evolution was investigated in comparison to the growth under RTCVD conditions. Two different polytype structures, 3C- and 2H-SiC, were grown on 4" (111)Si wafers. Generally in the investigated parameter range carbonized layers formed by RTCVD have a better crystallinity and a smoother surface. © 1997 Elsevier Science S.A.

Keywords: Molecular beam epitaxy; Polytypism; Reflection high energy electron diffraction; Silicon carbide

1. Introduction

Carbonization is a classical process to form silicon carbide on silicon. It is commonly used to form the buffer layer in different growth techniques [chemical vapour deposition (CVD) [1], rapid thermal chemical vapour deposition (RTCVD) [2], molecular beam epitaxy (MBE) [3,4] etc.], acting as a pseudo-substrate for the further growth process. Up to now for carbonization by solid sources only few attempts have been reported and only one systematic investigation about the nucleation and growth process on (100)Si has been carried out [5].

The aim of this work was the comparative study of the carbonization process in a wide range of carbon fluxes, substrate temperatures and growth times using two different growth techniques RTCVD and solid source MBE. These two methods were compared regarding morphological and structural evolution on (111)Si.

2. Experimental

In the case of RTCVD the substrates were cleaned wet chemically and by in situ H₂ annealing. The carbonization in propane diluted in hydrogen at atmospheric pressure is as described in Refs [6,7].

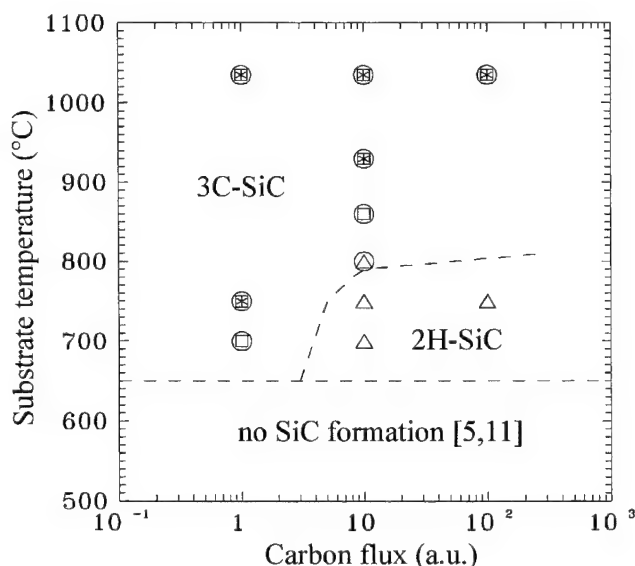


Fig. 1. Kinetic phase diagram for solid source MBE carbonization at 10 min processing time: ○, twinned (111)3C-SiC; □, (110)3C-SiC; *, (311)3C-SiC; △, 2H-SiC.

The carbonization of (111)Si 4" wafers by carbon molecular beams was carried out in a UMS 500 Balzers MBE system with base pressure of 8×10^{-11} mbar during the deposition process the pressure was in the range of 10^{-9} mbar. The cleaning and deposition process were monitored by in situ reflection high energy electron diffraction (RHEED). Pyrolytic graphite was used as the C source. The carbon was evaporated using an electron beam evaporator. The flux (CF) was controlled

* Corresponding author. Tel.: 49 3677 691669; Fax: 49 3677 691674; e-mail: Pezoldt@e-technik.tu-ilmenau.de

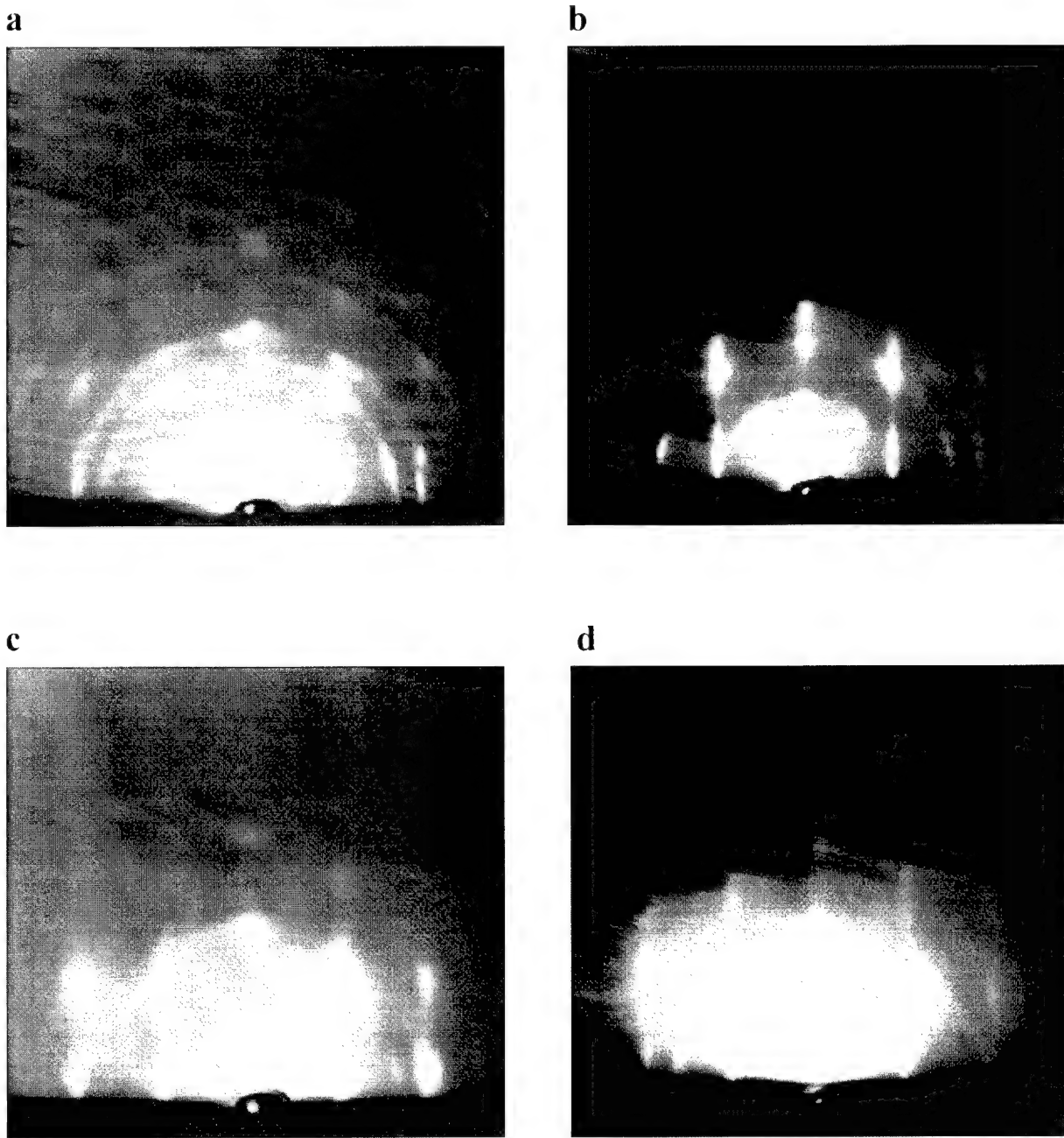


Fig. 2. RHEED pattern from SiC samples grown at: (a) 930°C, CF = 10 a.u., 10 min; (b) 860°C, CF = 10 a.u., 10 min; (c) 750°C, CF = 10 a.u., 10 min, (d) 750°C, CF = 1 a.u., 10 min.

by a quadrupole mass spectrometer and varied over two orders of magnitude. The substrate temperature was in the range of 700–1100°C. Prior to the deposition process the silicon wafers were cleaned in a Balzers PCCM plasma module in a low energy hydrogen plasma without a wet cleaning procedure [8,9]. After transferring the wafer into the reaction chamber a first heating step at 750°C was carried out for 5 min to eliminate the incorporated hydrogen and etching damage. A following second annealing step at 1050°C for 10 min was used to remove the carbon contamination which was formed during the

first stage of the *in situ* cleaning procedure. Cooling down the substrate to 700°C the 7×7 (111)Si surface reconstruction remained without any additional diffraction spots in the RHEED pattern, indicative of the cleanliness of the substrate surface. The substrate was then reheated to the process temperature and the carbon beam was allowed to carbonize the silicon surface.

The SiC layers were characterized by *ex situ* RHEED, ellipsometry, optical microscopy, atomic force microscopy (AFM), Auger electron spectroscopy (AES) and X-ray diffraction.

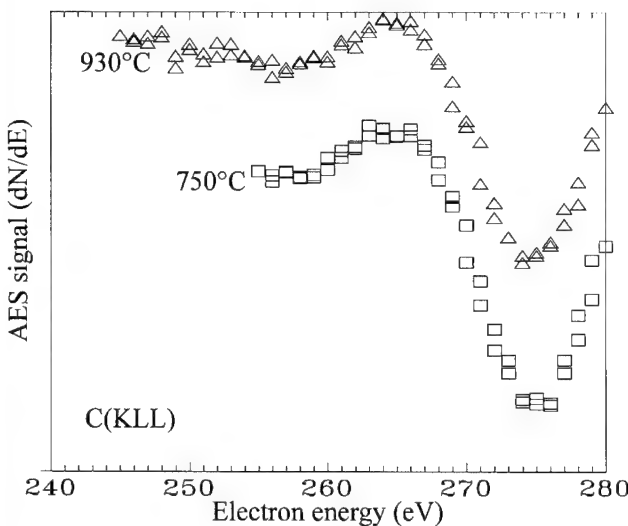


Fig. 3. C(KLL) peaks of the carbonized (111)Si wafers having different polytype structures: 750°C 2H-SiC layer; 930°C 3C-SiC layer.

3. Results and discussion

The obtained kinetic phase diagram as a function of carbon flux and substrate temperature and corresponding typical RHEED pattern are shown in Figs. 1 and 2. For substrate temperatures $> 850^\circ\text{C}$ and independent on the carbon flux the RHEED pattern consists of sharp spots and rings indicative for a very rough surface and the evidence of non-oriented crystallites [Fig. 2(a)]. The analysis of the diffraction pattern revealed the existence of 3C-SiC with three different orientations. The main orientation is (111)SiC with $(\bar{1}\bar{1}\bar{1})\text{SiC}$ twins. The second orientation is the $\langle 110 \rangle$ growth direction. As a third orientation the $\langle 311 \rangle$ direction was identified, but only weakly present. These observations correspond to the growth orientation obtained in carbonized layers grown on (111)Si in the case of RTCVD at heating-up velocities $> 100 \text{ K s}^{-1}$, where an initial layer formation during the heating-up of the substrate was suppressed [10]. These agree well with the results of Zekentes et al. [11].

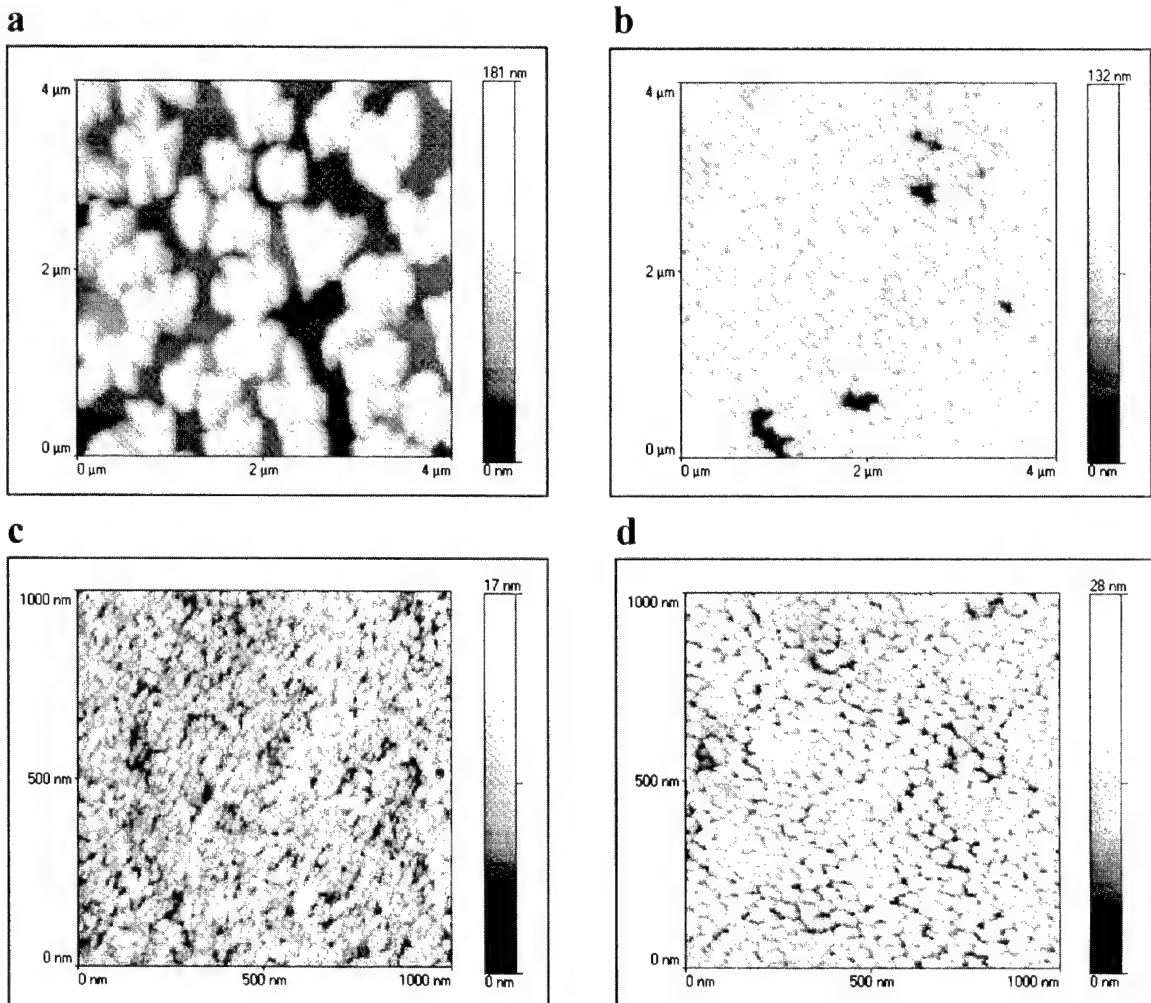


Fig. 4. AFM images for different growth conditions: (a) 1035°C, CF = 10 a.u., 10 min; (b) 930°C, CF = 10 a.u., 10 min; (c) 750°C, CF = 10 a.u., 10 min; (d) 750°C, CF = 1 a.u., 10 min.

With decreasing substrate temperature the 3C-SiC diffraction spots elongates perpendicular to the RHEED pattern horizon, caused by the smoother growing surface [Fig. 2(b)]. In the temperature range between 800 and 900°C the $\langle 311 \rangle$ growth orientation could not be detected. At carbonization temperatures $< 800^\circ\text{C}$ and high carbon fluxes the RHEED pictures indicate the growth of 2H-SiC silicon carbide [Figs. 1 and 2(c)]. The evidence of this structure was confirmed by additional X-ray diffraction measurements using the thin film analyser of the SIEMENS D 500 TF diffractometer. In the case of carbon fluxes < 10 a.u. (see Fig. 1) between 700 and 800°C only the growth of 3C-SiC was observed [Fig. 2(d)]. In all cases the AES spectra revealed a clear carbide peak (Fig. 3). This corresponds to the critical temperature (650°C) necessary for the formation of SiC by solid source MBE [11]. Under RTCVD conditions using propane we observed a SiC formation only at temperatures $> 1050^\circ\text{C}$. This is caused by the necessary decomposition of the hydrocarbons and is in agreement with the observations by Steckl and Li [12]. The critical temperature can be lowered using higher reactive hydrocarbons and lower pressures [12].

The island density and the mean grain size as well as the morphological evolution were investigated by AFM. At high growth temperatures the AFM observations revealed isolated islands with irregular shapes [Fig. 4(a)]. With an increasing deposition time the coalescence of these islands occurs, forming a discontinuous rough SiC film with a high density of diffusion channels for further material transport. With decreasing substrate temperature the island density increases and the mean grain size decreases [Figs. 4(a–c) and 5]. A similar behaviour was observed increasing the carbon flux [Fig. 4(c and d)]. Increasing island density results in more regular shaped islands. These dependencies are

in agreement with the common theories of crystal growth [13,14] and similar to the growth behaviour observed on (100)Si [5]. At the lowest investigated temperature no grains could be separated. The typical increasing of the grain density with the carbon impingement was also found for the carbonization under RTCVD conditions [15]. Here the nucleation density have shown a linear dependence on the propane concentration in the flowing hydrogen. The grain size increases slightly with the processing time by lateral overgrowth. However, both values, grain size and density, have not shown such a distinct temperature behaviour in the investigated temperature range (1100 – 1300°C).

The surface roughness decreases drastically with decreasing substrate temperature (Fig. 6) leading to the formation of smooth films which was also confirmed by RHEED analysis. This morphology was similar to the RTCVD carbonized silicon at very high propane concentrations ($> 0.15\%$) despite different crystal structures. On the contrary, however, over the whole parameter range we found no carbon accumulation at the SiC surface, neither for the highest carbon flux which corresponds to an effective carbon pressure, where a saturation in the growth was observed in the case of acetylene ($> 10^{-5}$ Torr, see Mogab and Leamy [16]).

This behaviour results in clear differences in the growth kinetics. This is similar to the increase of the initial growth rate with an increasing carbon supply. This rate is much higher in the case of RTCVD, which is simply caused by the higher temperatures and effective carbon fluxes. For the RTCVD carbonization a saturation was always found, differing only in the saturation thickness and time [7]. As earlier the saturation set in the better the crystal structure of the SiC film. On the contrary the growth rate under MBE conditions has shown only a weakly decreasing progressing growth

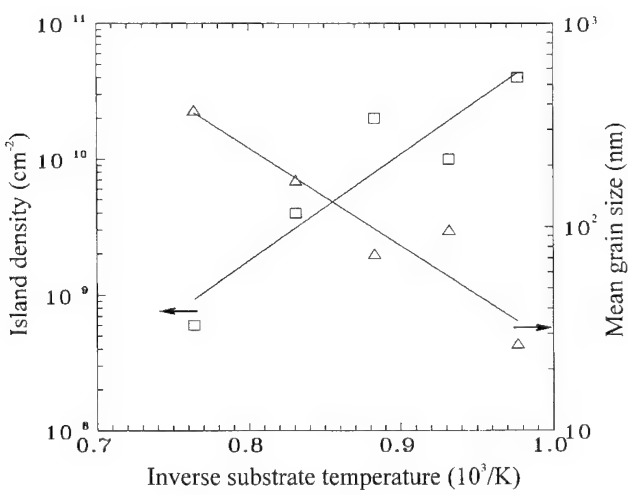


Fig. 5. Nucleation density and mean grain size versus inverse substrate temperature at carbon flux rates 10 a.u.: □, island density; △, mean grain size.

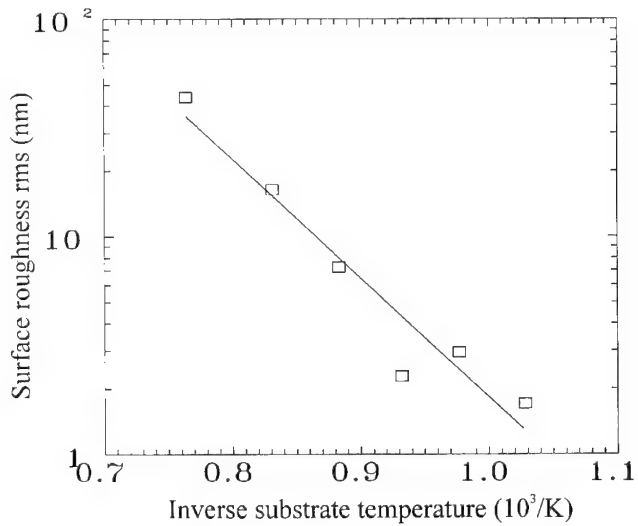


Fig. 6. Surface roughness versus inverse substrate temperature at carbon flux rates 10 a.u.

rate. A similar behaviour was observed by Rimai et al. [17] using laser ablation for the carbon supply. This indicates the existence of open diffusion paths for further silicon transport to the growing SiC surface and consequently differences in the growth mechanism. The preferred Si out-diffusion led to the void formation and non-epitaxial SiC grain growth. An important factor for this behaviour should be the different carbon supersaturation at the growing surface, and consequently the nucleation density. However, the existing deviations to the carbonization using hydrocarbons as carbon sources [16] show the role of hydrogen to the lateral growth and coalescence behaviour during SiC growth.

4. Conclusion

In the investigated parameter range carbonized layers formed by RTCVD have a better crystallinity and a smoother surface. However, solid source MBE is suitable for the formation of large area thin silicon carbide layers having different polytypes structures (3C- and 2H-SiC). To use this silicon carbide layer as a buffer layer for the following epitaxial growth the development of methods for sealing-off the open diffusion paths to prevent void formation beneath the epitaxial layer is necessary.

Acknowledgement

The authors would like to thank O. Nennewitz and

H. Romanus for X-ray diffraction measurements and Dr L. Spieß for providing AFM, XRD facilities.

References

- [1] H. Matsunami, S. Nishino, H. Ono, IEEE Trans. Electron Dev. 28 (1981) 1235.
- [2] A.I. Steckl, J.P. Li, IEEE Trans. Electron Dev. 39 (1992) 64.
- [3] T. Yoshinobu, H. Mitsui, Y. Tarui, T. Fuyuki, H. Matsunami, J. Appl. Phys. 72 (1992) 2006.
- [4] G.L. Zhou, Z. Ma, M.E. Lin, T.C. Shen, L.H. Allen, H. Morkoç, J. Cryst. Growth 134 (1993) 167.
- [5] K. Zekentes, V. Papaioannou, B. Pecz, J. Stoemenos, J. Cryst. Growth 157 (1995) 392.
- [6] V. Cimalla, J. Pezoldt, G. Ecke, H. Rößler, G. Eichhorn, J. Phys. IV, Colloq. C5 (suppl.) J. Phys. II 5 (1995) C5-863.
- [7] V. Cimalla, K.V. Karagodina, J. Pezoldt, G. Eichhorn, Mater. Sci. Eng. B29 (1995) 170.
- [8] J. Ramm, E. Beck and A. Zueger, Mater. Res. Soc. Symp. Proc., 220 (1991) 15.
- [9] J. Ramm, E. Beck, A. Zueger, A. Domman and R.E. Pixley, Thin Solid Films, 228 (1993) 23.
- [10] V. Cimalla, J. Pezoldt, Mater. Res. Soc. Symp. Proc. 355 (1995) 332.
- [11] K. Zekentes, R. Callec, K. Tsagaraki, B. Sagnes, G. Arnaud, J. Pascual, J. Camassel, Mater. Sci. Eng. B29 (1995) 138.
- [12] A.J. Steckl, J.P. Li, Mater. Res. Soc. Symp. Proc. 242 (1992) 537.
- [13] J.P. Hirth, G.M. Pound, Condensation and Evaporation, Pergamon Press, Oxford, 1963.
- [14] A van der Drift, Philips Res. Rep. 2 (1967) 269.
- [15] H. Romanus, V. Cimalla, A. Kromka, L. Spieß, J. Pezoldt, Mater. Sci. Eng. B (1997) to be published.
- [16] C.J. Mogab, H.J. Leamy, J. Appl. Phys. 45 (3) (1974) 1075.
- [17] L. Rimai, R. Ager, W.H. Weber, J. Hangas, A. Samman, W. Zhu, J. Appl. Phys. 77 (1995) 6601.

Hexagonal and cubic SiC thin films on SiC deposited by solid source MBE

Andreas Fissel, Kay Pfennighaus, Ute Kaiser, Bernd Schröter, Wolfgang Richter *

Friedrich-Schiller-Universität Jena, Institut für Festkörperphysik, Max-Wien-Platz 1, D-07743 Jena, Germany

Abstract

Epitaxial growth of SiC on SiC was realized between 900 and 1100 °C by means of solid-source molecular beam epitaxy. In general, our results show that the growth mode is strongly influenced on the surface stoichiometry. In case of Si-stabilized surfaces, showing 3-fold superstructures, films grow layer-by-layer via two-dimensional nucleation even at relatively low temperatures (<1000 °C). RHEED investigations of the epitaxial growth on 3C-SiC(100) show that a layer by layer growth is achieved at $T > 925$ °C and $R < 100$ nm h $^{-1}$. The activation energy of nucleation was determined to be 5.3 eV. The film structure was found to be dependent on the deposition mode. In the case of continuous deposition the films consist of a mixture of the cubic and hexagonal polytypes. The films grown by an alternating flux supply controlled to an atomic level using $(\sqrt{3} \times \sqrt{3})$ - and (1×1) -surface superstructures were dominantly of 6H-SiC. In case of the Si-rich (3×3) -superstructure actually the cubic polytype has been grown. Therefore, we assume that the formation of a certain superstructure stabilizes the nucleation of a special polytype.

© 1997 Elsevier Science S.A.

Keywords: Silicon carbide; Molecular beam epitaxy

1. Introduction

SiC is an interesting wide-band-gap semiconductor material. One of the most promising properties of SiC is the occurrence of different structures (polytypes) in this material with different physical properties, such as the band gap and carrier mobilities. Therefore, it may be possible to build devices consisting of one semiconducting material only with confined electrons in a two dimensional gas [1] by different stacking of atomic SiC layers. Because of changing stacking sequences along the c-axis, the growth of such structures is possible in the $<0001>$ direction, however it demands definite nucleation conditions. In this context, epitaxial films of SiC in the [0001] orientation with a definite layer structure are of interest. Molecular beam epitaxy (MBE) is an attractive method to prepare such structures because of the controlled deposition process within an atomic layer range.

In general, different SiC-polytypes have been grown at high growth temperatures ($T > 1800$ °C) near the thermodynamical equilibrium in dependence of the

growth rate and the temperature by means of CVD and sublimation growth (see e.g. [2]).

In a medium temperature range ($T < 1800$ °C) the growth is performed under non-equilibrium conditions. Growth by nucleation in this case results preferentially in the growth of the cubic polytype. However, a reproduction of substrate polytype has been realized by a “step-controlled epitaxy” under selected conditions by an advantageous selection of growth rate and temperature as well as the off-orientation of the substrate [3].

Recently we found by MBE growth of SiC that at low temperatures ($T < 1000$ °C) different polytypes can be grown as well [4,5]. The reason for that may be the occurrence of thermodynamically stable surface phases, so called superstructures, on the SiC surface which are dependent on the coverage and substrate temperature.

In our studies surface superstructures on SiC(0001) have been investigated and, moreover, SiC films have been grown under surface-stabilized conditions using different superstructures. The surface-stabilized conditions were realized by an alternating deposition of silicon and carbon.

RHEED investigations have been performed to select the optimum growth conditions and to investigate the influence of increasing Si adlayer thicknesses in dependence on the temperature.

* Corresponding author.

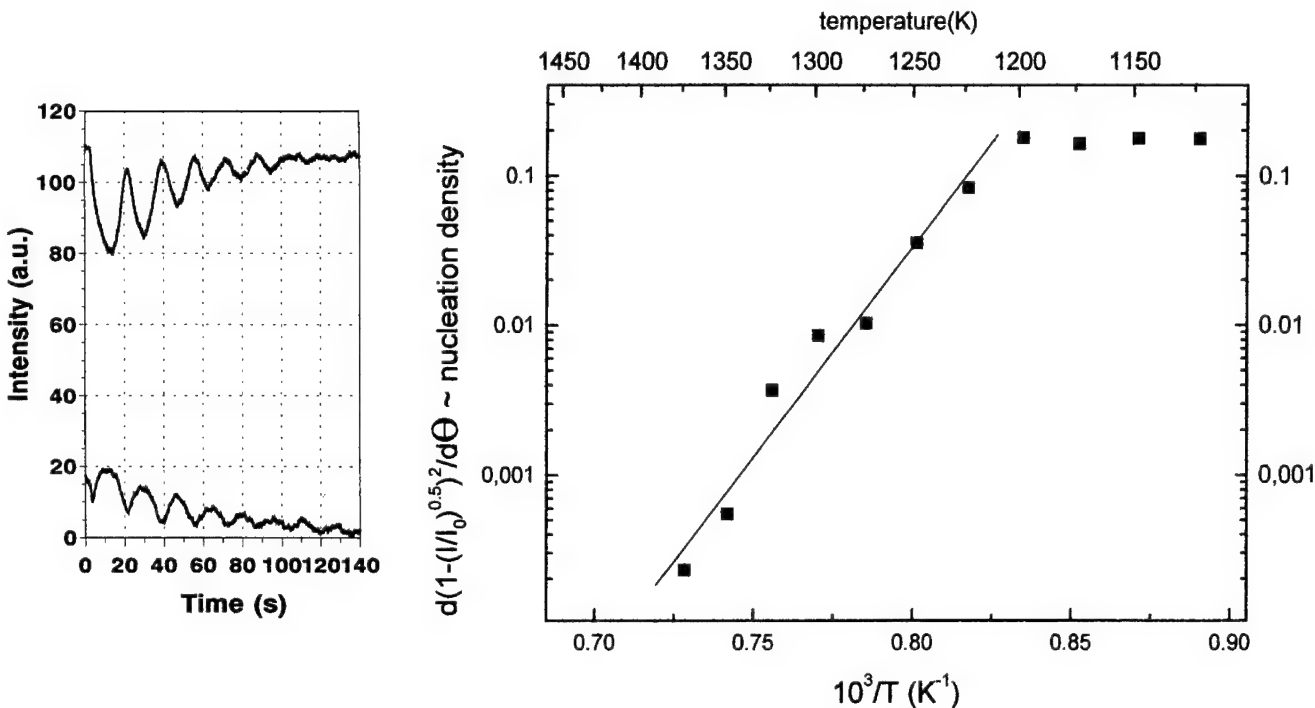


Fig. 1. RHEED measurements of the SiC MBE-growth on CVD-grown 3C-SiC(100): (a) intensity oscillations of the specular beam (upper curve) and the diffuse background (lower curve) at 900 °C (growth rate: about 60 nm h⁻¹); (b) dependence of the specular beam intensity in the capture range 0.1 < Θ < 0.35 monolayers between 1100 and 1400 K. The ascent corresponds to an activation energy of 5.3 eV between 1200 and 1400 K. (I_0 RHEED intensity before growth, I RHEED intensity during growth, Θ monolayer coverage, T temperature).

2. Experimental conditions

The SiC films were grown between 900 and 1100 °C in a RIBER-EVA 32 MBE system. The source materials of high-purity Si and high-purity C were evaporated separately by means of electron beam guns. Substrates used were on-axis and 3–4° off-axis SiC(0001) wafers from Cree Research Inc., samples prepared from on-axis and 2–5° off-axis (0001) Acheson-grown crystals, and 3C-SiC films CVD-grown on Si(100).

The MBE growth mode, the surface morphology, and the structure were investigated by in situ reflection high-energy electron diffraction (RHEED) and ex situ by transmission electron microscopy (TEM) at 200 kV and 400 kV acceleration voltage and atomic force microscopy (AFM). Low-energy electron diffraction (LEED) experiments have been performed to investigate surface superstructures. Ex situ Auger electron spectroscopy (AES) measurements were done to clarify the stoichiometry, the impurities, and the depth profile of the film.

3. Results

3.1. RHEED intensity investigations of MBE growth of SiC on 3C-SiC(100)

The RHEED intensity is very sensitive to morphological changes of the surface, such as changes of nucleation

density [6]. Therefore, investigations of RHEED intensities especially of the specular beam can give information concerning the nucleation or adatom mobility. Such investigations have been performed for the growth of SiC on SiC(100), where, in the onset of growth, RHEED intensity oscillations were found (Fig. 1(a)) corresponding to a SiC monolayer growth in each oscillation period. This indicates a layer-by-layer growth via two-dimensional nucleation. Additionally, we investigated the drop of the RHEED intensity just after the growth started, where the growth is mainly determined by nucleation. The drop of the intensity has been analysed using a simple scattering theory [7]. From the results presented in Fig. 1(b), it is clearly seen that at temperatures <1200 K the drop of the RHEED intensity is nearly temperature independent likely due to a non-thermally activated motion of adatoms. Growth at this temperatures results in the development of rough and highly defective films. At $T > 1200$ K the nucleation is strongly activated and an energy barrier of 5.3 eV was found from the slope of the curve in Fig. 1(b). This value corresponds to the diffusion barrier of carbon on SiC [8]. In this temperature range films can grow layer-by-layer [4].

3.2. LEED investigations of surface phases on 6H-SiC(0001)

During our investigation of surface superstructures on SiC(0001) we found the (3 × 3), a (1 × 1), a Si-rich

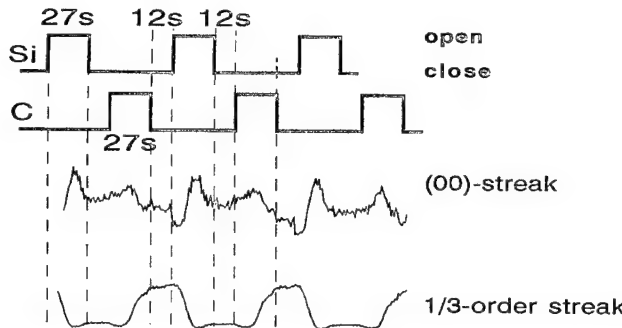


Fig. 2. Sequence of source supply (upper part) and the corresponding RHEED intensity oscillations (lower part) of the (00) streak and the 1/3-order streak during MEE-growth of SiC on vicinal 6H-SiC(0001).

$(\sqrt{3} \times \sqrt{3})R30^\circ$, a (1×1) again, a C-rich $(\sqrt{3} \times \sqrt{3})R30^\circ$ - and a C-rich $(6\sqrt{3} \times 6\sqrt{3})R30^\circ$ -superstructure. (The order corresponds to the decreasing amount of Si on the surface.) We have concentrated our investigations on the Si-rich $(\sqrt{3} \times \sqrt{3})R30^\circ$ - and (3×3) -superstructures, which are formed by an ordered 1/3 Si-monolayer and 2 Si-monolayers coverage, respectively.

3.3. Surface-stabilized growth on SiC(0001)

Recently, growth of SiC on 3C-SiC(100) by atomic layer epitaxy using different surface structures has attracted considerable attention [9,10]. In our experiments alternating deposition of Si and C has been performed on the Si-rich SiC(0001)- $(\sqrt{3} \times \sqrt{3})R30^\circ$ and on the (3×3) -surface by switching the flux supply by computer controlled automatic valve operation. Shutter sequences were adjusted to deposit approximately one monolayer per supply. Between each deposition step the sample was annealed for a certain time (up to an almost constant RHEED intensity) to improve the adatom ordering at the surface. The atomic level control of the surface stabilization was realized by recording the RHEED intensities of both the (00) streak and an 1/3-order streak resulting from superstructures on the SiC-surfaces. Exposing the $(\sqrt{3} \times \sqrt{3})R30^\circ$ -surface to Si, the surface transforms to a (1×1) structure and the $(\sqrt{3} \times \sqrt{3})R30^\circ$ -superstructure recurs during deposition of one ML carbon. As seen in Fig. 2, oscillations of the RHEED intensities were measured during alternating deposition. In continuous deposition of SiC on SiC(0001) no RHEED oscillations occur [4]. This indicates an accurate layer-by-layer growth in case of alternating deposition.

A comparison of cross-sectional TEM investigations of layers grown by continuous and alternate deposition shows the difference in the structure. Whereas there is a high amount of different polytypes in continuously grown SiC layers [4,5], the alternately grown epilayers are predominantly of 6H polytype, as seen in Fig. 3. From the image examined in the $\langle 11-20 \rangle$ direction for

the edge-on foils it is seen that to a small extent 3C is embedded within the 6H-phases as well. Additionally, microtwins appear inclined at approx. 70° to the (0001)-surface. These microtwins extending into the growing 6H-film were found to be formed within the cubic inclusions. Furthermore, the occurrence of 3C-SiC within the film corresponds to deviations from regular monolayer growth as indicated by a damping of the RHEED 1/3-order streak intensity.

The controlled deposition on the (0001)-surface using the (3×3) -superstructure is much more difficult than on the $(\sqrt{3} \times \sqrt{3})R30^\circ$ -surface because of the higher Si coverage. Only a few additional Si atoms can lead to a very rapid clustering of Si on the surface as it was investigated by RHEED. The Si-bulk pattern occurs already after the deposition of a submonolayer Si on the Si-rich (3×3) -superstructure at $T > 700$ °C indicating the growth of large Si-clusters on the surface. During further growth these clusters carbonize and the result is a rough surface. Therefore, any Si clustering has to be avoided by a very accurate monolayer deposition. Further work is, however, required to get the process stable for many deposition cycles. In first successful experiments [11] on the Si-rich (3×3) -surface only 3C-SiC has been grown.

4. Summary and conclusions

For SiC MBE growth we found that the substrate temperature has to be higher than 925 °C and the growth rate lower than $0.1 \mu\text{m h}^{-1}$. An activation barrier for the SiC nucleation of 5.3 eV was determined. Moreover, deposition under surface-stabilized conditions using the $(\sqrt{3} \times \sqrt{3})R30^\circ$ - and the (1×1) -surface superstructures results in the growth of preferentially the 6H polytype, whereas in case of the (3×3) -superstructure 3C-SiC has been grown. However, the cubic structure also appears at any deviation from the surface stabilized layer-by-layer growth.

Because the superstructures are stable only up to temperatures of about 1000 °C, for the growth of special SiC-polytypes via nucleation there exists only a small window between 925 and 1000 °C. The variety of polytype formation mechanisms at this low temperature may be wide and discussed elsewhere [12]. Up to now the question of mechanisms which are really responsible for the occurrence and the change of polytypes at low temperature MBE growth cannot be fully answered.

More accurate measurements recently performed [A. Fissel, H. Oehme, K. Pfennighaus, W. Richter, Surf. Sci. (in press) [13]] yield nucleation activation energies of 0.77 eV for $T < 1200$ K and 3.9 eV for $T > 1200$ K.

Recent investigations suggest ordered Si-coverage for the (3×3) -superstructure in the range between 11/9 and

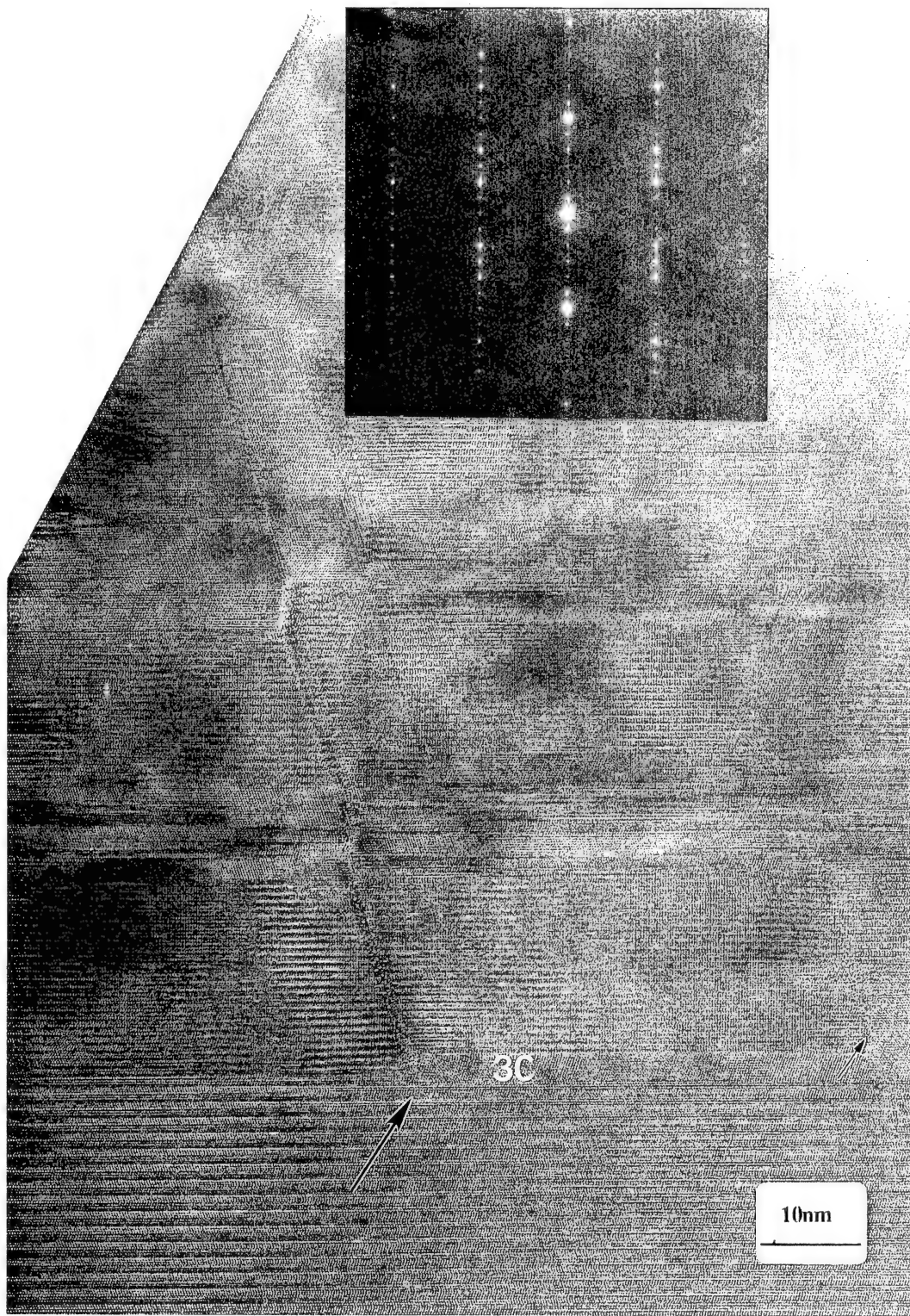


Fig. 3. Cross-sectional high resolution TEM image of 6H-SiC on vicinal 6H-SiC(0001) substrate grown by an alternate supply at 930 °C using the $(\sqrt{3} \times \sqrt{3})R30^\circ$ -superstructure. The large arrow indicates a surface step at the film–substrate interface with a small amount of 3C embedded within the 6H-SiC, the short arrow denotes a microtwin. The inset shows the diffraction pattern of the grown 6H-SiC film.

13/9 ML [see H.A. Kulakov, G. Henn, B. Bullemer, *Surf. Sci.* 346 (1996) 49 [14]; J. Furthmüller, F. Bechstedt, A. Fissel, P. Käckell, K. Pfennighaus, W. Richter, B. Schröter, Ext. Abstract Int. Conf. Silicon Carbide, III-nitrides and Related Materials, 1997, Stockholm [15]].

Acknowledgement

The work was supported by the Sonderforschungsbereich 196 (project A03) of the Deutsche Forschungsgemeinschaft and the British-German ARC (project 313-ARC-VII). The authors gratefully acknowledge P. Brown (Cambridge University) for the high resolution TEM work.

References

- [1] F. Bechstedt, P. Käckell, *Phys. Rev. Lett.* 75 (1995) 2180.
- [2] Yu.M. Tairov, V.F. Tsvetkov, *Prog. Cryst. Growth Character.* 7 (1983) 111.
- [3] T. Kimoto, H. Nishino, W.S. Yoo, H. Matsunami, *J. Appl. Phys.* 73 (1993) 726.
- [4] A. Fissel, U. Kaiser, E. Ducke, B. Schröter, W. Richter, *J. Cryst. Growth* 154 (1995) 72.
- [5] A. Fissel, U. Kaiser, K. Pfennighaus, E. Ducke, B. Schröter, W. Richter, *Inst. Phys. Conf. Ser.* 142 (1996) 121.
- [6] T. Shitara, D.D. Vvedensky, M.R. Wilby, J. Zhang, J.H. Neave, B.A. Joyce, *Phys. Rev. B* 46 (1992) 6815.
- [7] G. Rosenfeld, N.N. Lipkin, W. Wulfhekel, J. Kliewer, K. Morgenstern, B. Poelsema, G. Comsa, *Appl. Phys. A* 61 (1995) 455.
- [8] T. Takai, T. Halicioglu, W.A. Tiller, *Surf. Sci.* 164 (1985) 327.
- [9] T. Fuyuki, T. Yoshinobu, H. Matsunami, *Thin Solid Films* 225 (1993) 225.
- [10] S. Hara, T. Meguro, Y. Aoyagi, M. Kawai, S. Misawa, E. Sakuma, M. Yoshida, *Thin Solid Films* 225 (1993) 240.
- [11] A. Fissel, K. Pfennighaus, U. Kaiser, B. Schröter, W. Richter, unpublished.
- [12] A. Fissel, K. Pfennighaus, U. Kaiser, B. Schröter, W. Richter, *Proc. E-MRS 1996 Spring Meeting, Strasbourg, Mater. Sci Eng. B*, 46 (1997) 324–328.
- [13] A. Fissel, H. Oehme, K. Pfennighaus, W. Richter, *Surf. Sci.* (in press).
- [14] H.A. Kulakov, G. Henn, B. Bullemer, *Surf. Sci.* 346 (1996) 49.
- [15] J. Furthmüller, F. Bechstedt, A. Fissel, P. Käckell, K. Pfennighaus, W. Richter, B. Schröter, Ext. Abstract Int. Conf. Silicon Carbide, III-nitrides and Related Materials, 1997, Stockholm.

Hydrogen-, boron-, and hydrogen-boron-related low temperature photoluminescence of 6H-SiC

C. Peppermüller ^{a,*}, Adolf Schöner ^b, Kurt Rottner ^b, R. Helbig ^a

^a Institute of Applied Physics, University of Erlangen-Nürnberg, Staudtstr. 7 A3, D-91058 Erlangen, Germany

^b Industrial Microelectronics Center (IMC), P.O. Box 1084, Isafjordsgatan 22, S-16421 Kista, Sweden

Received 21 March 1997 accepted 24 April 1997

Abstract

An investigation of the low temperature ($T < 2$ K) photoluminescence (LTPL) of boron-, hydrogen-, and boron together with hydrogen-doped SiC was done. We used n-type samples of the polytype 6H. After the implantation of boron and annealing at 1700 °C, we detected three new LTPL emission lines close to a wavelength of 4205 Å. After the implantation of hydrogen into the boron-implanted samples, we detected another single line at 4183 Å, while the lines at 4205 Å disappeared. In samples with a higher dose of boron, phonon replica of the 4183 Å emission line were detected and two vibrational modes affiliated to the defect were identified (86 and 118 meV). The investigation of boron-doped CVD layers revealed intense hydrogen correlated LTPL emission. © 1997 Elsevier Science S.A.

Keywords: SiC; Photoluminescence; Boron; Hydrogen

1. Introduction

The development of electronic devices based on SiC requires a better knowledge of impurities and defects in this material. The influence of hydrogen on the electrical and optical properties of SiC is an important issue, because hydrogen is present at high concentrations during the CVD growth of epilayers. Furthermore, as described in Ref. [1], hydrogen is expected to be an efficient passivator for impurities, as in many other semiconductors. To obtain planar structures for devices, up to now only ion implantation has been used because of the low diffusion coefficients of dopants in SiC. For p-type doping, aluminium and boron are widely used as acceptor impurities; for MOS structures, boron is preferred (to avoid possible problems with aluminium at the SiC–SiO₂ interface). We used low temperature photoluminescence (LTPL) to detect the presence of hydrogen, the behaviour of implanted boron after annealing, and the interaction between boron and hydrogen in 6H-SiC. To obtain well-defined concentration profiles of boron and hydrogen, ion implantation was used conducted by the computer simulation pro-

gram TRIM to calculate the implantation profiles and to maximize the overlap of the boron- and the hydrogen concentration profiles.

2. Sample preparation

Different samples (all n-type 6H-SiC) were prepared both from commercially available material (n-type 6H-SiC wafers from Cree Research, net doping concentration $N_D - N_A \approx 5 \cdot 10^{17} \text{ cm}^{-3}$) and from epitaxial layers grown at IMC using the CVD technique ($N_D - N_A \approx 10^{16} \text{ cm}^{-3}$) on similar substrates. Each of these samples was divided into four parts (a)–(d), some into five (a)–(e). Part (a) was used as reference. Parts (b) and (d) were implanted with boron at an energy of 350 keV, a dose of $1 \cdot 10^{14} \text{ cm}^{-2}$, leading to a concentration maximum of $n_B = 1 \cdot 10^{18} \text{ cm}^{-3}$ at a depth of 0.6 μm and annealed at 1700 °C for 30 min in argon atmosphere. Parts (c) and (d) were then implanted with hydrogen ($1 \cdot 10^{14} \text{ cm}^{-2}$, 80 keV, leading to $5 \cdot 10^{18} \text{ cm}^{-3}$ at 0.6 μm); no annealing was done after the hydrogen implantation. Part (e) was first implanted with a higher dose of boron ($5 \cdot 10^{14} \text{ cm}^{-2}$), annealed at 1700 °C for 30 min, implanted with hydrogen ($1 \cdot 10^{14} \text{ cm}^{-2}$) and afterwards annealed at 600 °C for 5 min.

* Corresponding author. Fax: 49 9131 858423;
e-mail: christian.peppermuller@rzmail.uni-erlangen.de

3. Experimental set-up

LTPL measurements were done using a He–Cd laser operating at a wavelength of 325 nm and 40 mW power for excitation. The samples were immersed in superfluid helium in a bath cryostat at a temperature of 1.9 K. Two filters were used to avoid the detection of laser plasma emission lines (Schott, UG11) and to suppress the scattered UV light (Schott, GG13). Wavelength selection was done using a Czerny-Turner-monochromator (Spex 1700-III) with a 1200/mm grating blazed at 5000 Å and slit widths of 50 µm, giving a resolution of 0.55 Å. A S20 type photomultiplier and photon counting electronics were used for detection. Spectral intensity corrections were neither done nor were necessary, because of the limited wavelength interval investigated.

4. Experimental results

Fig. 1 shows the LTPL spectra of parts (a)–(c) of a Cree substrate. Part (a) shows the usual LTPL spectrum of n-type 6H-SiC consisting of the emission lines of excitons recombining at a neutral nitrogen donor. This spectrum is described in detail in Ref. [2]. Fig. 1(b) shows the LTPL spectrum of the boron-implanted and

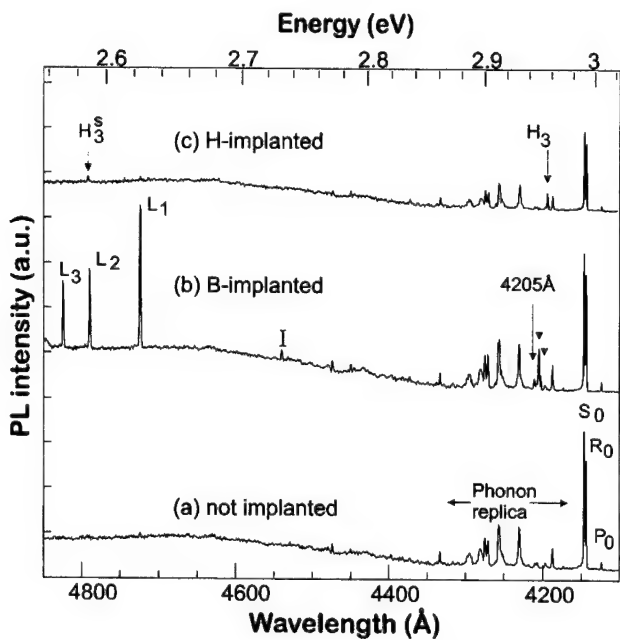


Fig. 1. LTPL spectra at a temperature of 1.9 K of a sample: (a) as grown; the lines marked as “ P_0 ”, “ R_0 ”, “ S_0 ” and “Phonon replica” are due to excitons recombining at neutral nitrogen. (b) Spectrum of the part that was boron-implanted and annealed at 1700 °C. Boron-implantation defect lines are marked by “4205 Å”. The “L” lines are the D_1 defect emission lines, the “I” line originates from radiative recombination at another defect. (c) Spectrum of the hydrogen-implanted part. The lines H_3 and H_3^* are known as hydrogen-related LTPL emission lines.

annealed part of this sample. The LTPL emission lines L_1 , L_2 , and L_3 are due to the D_1 -defect that appears usually after annealing of ion-implanted samples [3–5]. A line labelled “I” was observed in former experiments after aluminium and chromium implantations and is probably the low temperature form of a line described in Ref. [6]. Additionally, we detected a shorter-wavelength emission located at 4205 Å (three lines). These emission lines seem to be specific for the implantation of boron, because we did not detect these lines in samples implanted with different elements (e.g. Al, He, Ti). Fig. 1(c) shows the LTPL emission of part (c). The lines H_3 and H_3^* are attributed to a defect in which hydrogen is bound to carbon [7–10], because the energy difference of the emission lines of 369 meV corresponds to the energy of the C–H stretch mode in SiC detected by IR absorption spectroscopy [11]. The H-correlated luminescence was detected only in some of the samples, while all the other LTPL emission lines described in this paper were found to be sample-independent. Fig. 2 finally shows the spectrum of part (e) that was both implanted with boron and hydrogen and showed the same emission lines as part (d) (not shown here), but with much higher intensity. The boron-related emission at 4205 Å was not detected but another single emission line at 4183 Å was detected, together with its phonon replica and vibrational modes.

Further LTPL measurements were done on CVD grown layers that were doped with boron during the growth (a detailed description is given elsewhere by Schöner et al.). The spectrum of one of those samples is shown in Fig. 3. As described in Ref. [12], we detected

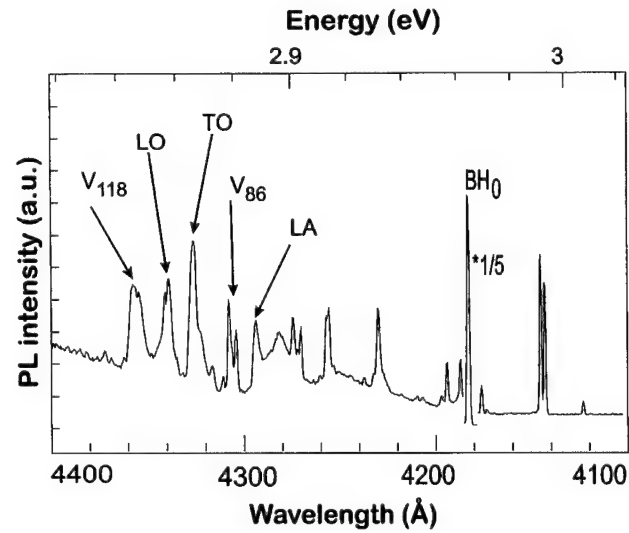


Fig. 2. LTPL spectrum at 1.9 K of a sample implanted with a high dose of boron, annealed at 1700 °C, implanted with hydrogen and annealed at 600 °C. The spectrum shows one emission line BH_0 (intensity reduced 5 times) and its phonon replica together with two vibrational modes (called V with their energy as index). Lines not labelled originate from excitons recombining at a neutral nitrogen donor.

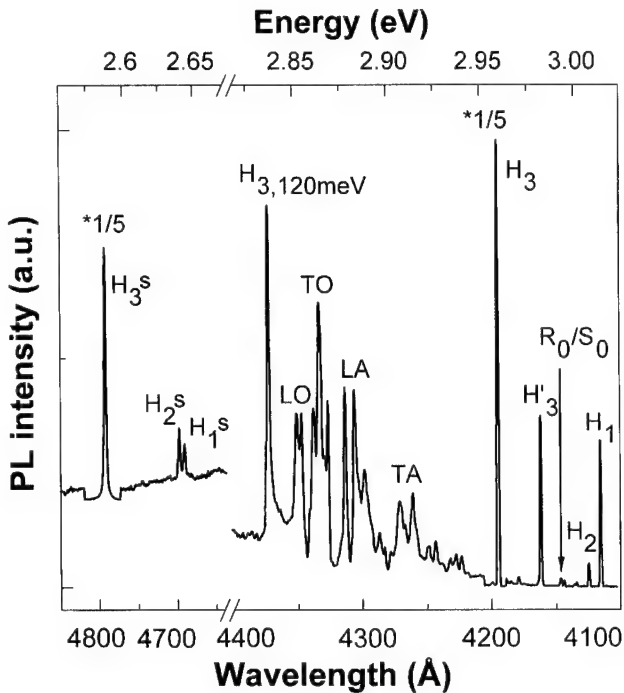


Fig. 3. LTPL spectrum at 1.9 K of a boron-doped CVD epilayer. The intense lines are hydrogen-correlated and named "H". H_3 and H'_3 are 5 times as intense as plotted. Lines labelled " R_0 "; " S_0 " originate from excitons recombining at a neutral nitrogen donor. Besides the phonon replica of H_3 (labelled TA, LA, TO, LO) there are some local modes (not labelled) [8].

intense hydrogen-correlated LTPL emission; neither the 4183 nor the 4205 Å LTPL emissions were detected. The spectra did not change after the additional implantation of hydrogen into the epilayers.

5. Discussion

The implantation of boron into 6H-SiC leads to two different defects that are detected by their different radiative recombination. First, the D_1 -defect is detected as usual after implantations of ions and subsequent annealing. This defect has been known for a long time in SiC [3,4] and not discussed here. Second, there is another defect responsible for emission at a shorter wavelength. The nature of this defect has to be examined by other experiments, but we think that it includes boron and some radiation-induced defect, because the

defect is detected only after the implantation of boron, but not after implantations of other elements or in the CVD grown boron-doped epilayers. After additional implantation of hydrogen into the boron-implanted samples, the defect-related LTPL emission moves to shorter wavelengths. Therefore, we have some evidence that the LTPL active boron-implantation related defect center has unsaturated bonds or includes a vacancy.

The observation of strong hydrogen-correlated LTPL emission of boron-doped CVD layers in Ref. [12] and in our experiments suggests that either (a) boron induces unsaturated carbon bonds during the growth; (b) that boron is part of the defect center leading to the hydrogen-correlated LTPL; or (c) that the B_2H_6 used for the boron doping was not cracked completely at the SiC surface during the CVD growth at high temperatures (about 1550 °C).

Acknowledgement

The authors would like to thank all members of IMC Stockholm and of the Institute of Applied Physics, Erlangen, for help in preparing the samples (implantation and annealing). Part of the work was financed by the Swedish National Board for Industrial and Technical Development (NUTEK) and the German Ministry for Education, Science, Research and Technology (BMBF, MATFO-program).

References

- [1] F. Gendron, L.M. Porter, C. Porte, E. Bringuer, *Appl. Phys. Lett.* 67 (9) (1995) 1253.
- [2] W.J. Choyke, L. Patrick, *Phys. Rev.* 117 (1960) 1430.
- [3] V.V. Makarov, N.N. Petrov, *Sov. Phys. Sol. State* 8 (1966) 1272.
- [4] L. Patrick, W.J. Choyke, *Phys. Rev.* B5 (1972) 3253.
- [5] T. Dalibor, C. Peppermüller, G. Pensl, S. Sridhara, R.P. Devaty, W.J. Choyke, A. Itoh, T. Kimoto, H. Matsunami, *Inst. Phys. Conf. Ser.* No. 142 (1995) 517.
- [6] V.V. Kodrau, V.V. Makarov, *Sov. Phys. Semicond.* 15 (1981) 813.
- [7] W.J. Choyke, L. Patrick, *Phys. Rev.* 29 (1972) 355.
- [8] L. Patrick, W.J. Choyke, *Phys. Rev.* B8 (1973) 1660.
- [9] W.J. Choyke, L. Patrick, *Phys. Rev.* B10 (1974) 2554.
- [10] L.L. Clemen, R.P. Devaty, W.J. Choyke, BurkA.A., Jr., D.J. Larkin, J.A. Powell, *Inst. Phys. Conf. Ser.* No. 137 (1993) 227.
- [11] K. Rottner, R. Helbig, *Appl. Phys. A* 59 (1994) 427.
- [12] D.J. Larkin, S.G. Sridhara, R.P. Devaty, W.J. Choyke, *J. Electron. Mat.* 24 (1995) 289.

Carrier lifetimes in SiC, studied by time resolved photoluminescence spectroscopy

J.P. Bergman ^{a,b}

^a Department of Physics and Measurement Technology, Linköping University, 581 83 Linköping, Sweden

^b Corporate Research, 721 78 Västerås, Sweden

Abstract

Recent results regarding the time decay of carrier and exciton recombination in different SiC polytypes are presented. The recombination of bound excitons, bound both at the nitrogen donor and at the Al acceptor, is extremely fast in 4H- and 6H-SiC. These are therefore dominated by efficient non-radiative recombinations, assumed to be a phonon-less Auger process. In high quality epitaxial layers where the free exciton is present, all decay times are determined by the free exciton lifetime. Typically the free exciton also dominates recombination at intermediate temperatures, while the measured time decay at high temperatures is determined by the minority carrier lifetime.

A significant improvement in the minority carrier lifetime of 4H-SiC in particular has been obtained over the past two years, with values as high as 2 μ s. The minority carrier lifetime is probably determined by capture at unidentified deep levels. © 1997 Elsevier Science S.A.

Keywords: SiC; Bound excitation; Time resolved; Minority carrier lifetime

1. Introduction

For many years photoluminescence (PL) has been an important experimental technique for the study of SiC [1]. Photoluminescence has been used mainly to study the presence and properties of excitons bound at different defects. In recent years PL has also been used to determine the doping levels in high quality n-type epitaxial layers by comparison of the relative intensities between free and bound exciton PL emissions at low temperatures [2].

Time resolved PL measurements (TRPL) complement normal PL studies. By exciting with a pulsed laser and observing the luminescence decay which occurs after excitation further information about the recombination process is obtained. This can be used at low temperatures (as in normal PL) to study the recombination properties of the different bound exciton (BE) emissions, and also at high temperatures to observe the PL decay related to the lifetime of the minority carriers. This is an important material parameter for SiC, a semiconductor intended for power device applications.

A few years ago only a few studies of time resolved PL on SiC had been published [3–5]. But in recent years improvements in epitaxial crystal growth have meant

that better samples are available, and more detailed studies can be performed. This is especially true for the minority carrier lifetime observed at room temperature [6,7].

In this paper we present a compilation of the results obtained over recent years using time resolved PL. We will specifically describe the time decay of the dominating BE recombination observed at low temperatures in the 4H- and 6H-polytype. We will also show results indicating the recent increase in the room temperature minority carrier lifetime in high quality epitaxial layers.

2. Experimental

The samples used in this study were grown in a hot-wall chemical vapor deposition (CVD) type reactor, previously described in Ref. [8], using the silane–propane–hydrogen system on n⁺ 6H-SiC or 4H-SiC (0001) oriented substrates with an off-axis cut of 3.5° towards the [11–20] direction. The reactive gases silane and propane are initially diluted to 5% in hydrogen in the gas bottle and further diluted prior to entry into the cell by a massive flow of purified hydrogen.

The samples were excited using pulsed excitation from a dye laser synchronously pumped by a mode locked Ar-ion laser. The light pulses, with a duration of less than 10 ps and a wavelength of ~ 680 nm were frequency doubled by a LiIO₃ crystal to a wavelength of ~ 340 nm (3.65 eV). The frequency-doubled average power was below 1 mW and the repetition rate of the pulses was varied between 10 and 0.15 MHz, using a cavity dumper attached to the dye laser (Fig. 1).

Low temperature (2–300 K) measurements were performed in a combined bath and flow He cryostat. The luminescence from the sample was dispersed by a 0.6 m double monochromator. The high temperature measurements (300–600 K) were performed in normal atmosphere with the sample placed on a heater element. In this case the luminescence was dispersed by a 0.25 m single monochromator. In both cases, the luminescence was detected by a photon counting photomultiplier tube. Using a time-correlated photon counting technique, the luminescence decay could be measured with a time resolution of better than 200 ps (Fig. 2).

3. Experimental results

In typical samples of all studied polytypes (4H and 6H) the bound excitons (BE) at the neutral nitrogen donor dominate the spectrum at low temperatures. The nitrogen donors have, depending on the polytype, several different equivalent sites which together with the phonon coupling give a characteristic set of sharp emission lines. The measured values for the decay time

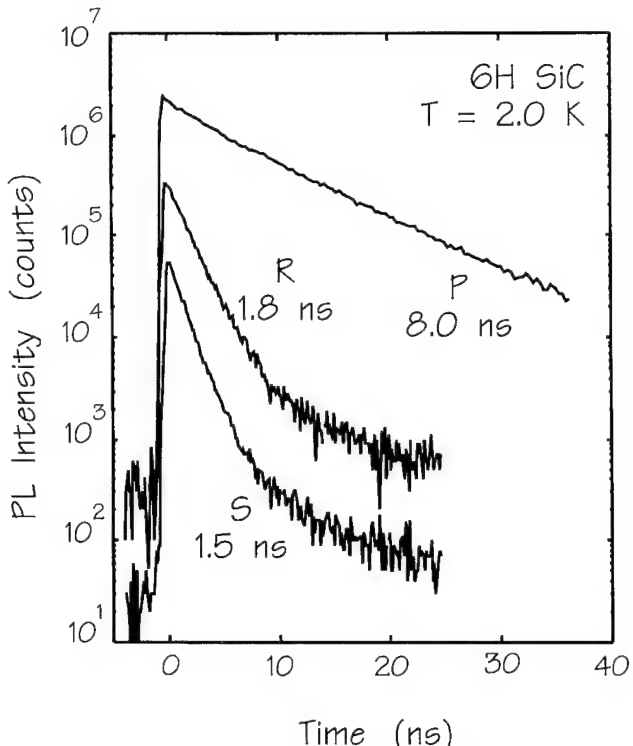


Fig. 2. Decay curves of the three different nitrogen-bound excitons in 6H-SiC.

of these nitrogen BE are 1.5 ± 0.1 ns, 1.8 ± 0.1 ns and 8.0 ± 0.5 ns for the three different BEs in 6H, and 9.5 ± 1.0 ns and 48.5 ± 4 ns for the two different excitons observed in 4H. These decay times are relatively fast for a material with an indirect band gap such as SiC, and it is clear that the radiative transition is not the dominant recombination process. A clear dependence between the observed decay times and the binding energy of the corresponding donor level has been reported previously [9]. This dependence has also been observed for similar BE in Si [10] and is consistent with a recombination dominated by a phonon-less Auger process. We believe that this is also the dominant process in SiC [9].

This dependence between the decay time and the donor binding energy is a consequence of the overlap of the wavefunctions in momentum space between the three different particles in the neutral BE. A faster decay time is observed for the exciton bound to the Al acceptor observed in p-type 6H-SiC (Fig. 3). In 4H-SiC the corresponding decay time is even faster and is below the time resolution of 200 ps for the measurement. Similar behaviour is observed for the Ga acceptor in both 6H- and 4H-SiC, with a decay faster than 250 ps, at 2 K [11]. This was also observed previously in Si [10] for acceptor BEs and further demonstrates the effective non-radiative Auger process.

In high quality epitaxial samples the FE is also

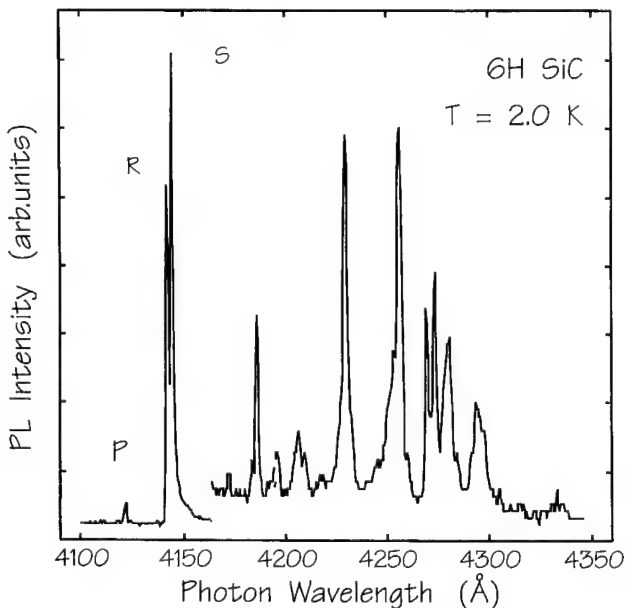


Fig. 1. Photoluminescence at low temperatures from SiC:6H. The spectrum is dominated by the recombination of the exciton bound at the neutral nitrogen donor.

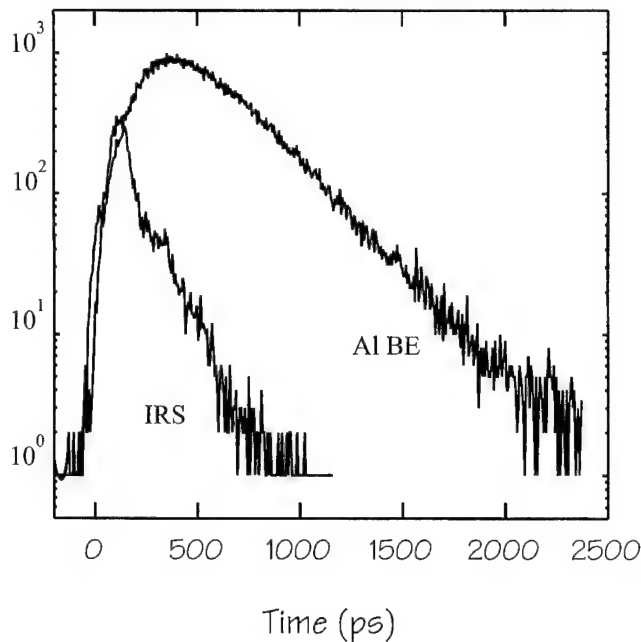


Fig. 3. Decay curve of the Al BE in 6H-SiC.

observed, together with the nitrogen BE, at low temperatures. In such cases the observed decay time of all exciton emissions is determined by the lifetime of the FE, if this is longer than the effective decay time of the BE. The FE recombination dominates the spectrum at elevated temperatures when the BEs are thermally quenched. The observed decay time of the FE increases with temperature when the recombination channel which corresponds to the capture of the FE to the defect disappears.

At room temperature the band gap PL is dominated by a single emission at approx. 3.0 eV and 3.2 eV for 6H and 4H, respectively. In both cases there is a weaker shoulder at an energy of approx. 0.1 eV lower, as seen in Fig. 4. The recombination process responsible for this emission has not been definitely identified, due to its broad spectral shape. It could be either a FE recombination, a free-to-bound emission with a shallow donor or acceptor level, or maybe a band-to-band recombination together with different phonons. In any case, the different levels within this energy range should be thermalized at room temperature and the observed decay time of the PL emission must be determined by the lifetime of the minority carriers, which for all our measurements are the holes. It should be noted that the PL emission observed is not the dominant recombination process in SiC. The dominant recombination mechanism is instead assumed to be a non-radiative capture of carriers by mid-gap defects. Only a minor part of the recombination is radiative and can be observed as PL close to the band gap.

Great care should be taken to determine that this band edge emission is present and dominates the PL

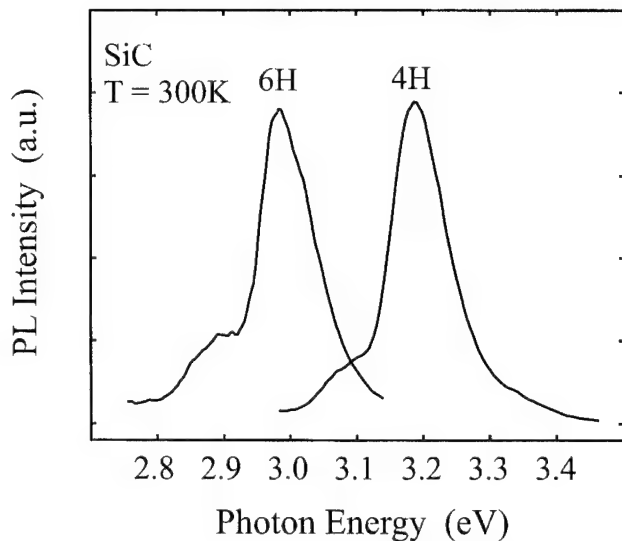


Fig. 4. Room temperature PL of 6H- and 4H-SiC epitaxial layers, showing the band edge emission over which the minority carrier lifetime is measured.

spectra. In SiC samples with higher defect concentration the PL emission is dominated instead by the high energy wing of the donor acceptor pair (DAP) or the free-to-bound recombination, and usually no distinct band edge emission is observed. In this case the observed decay time will not be related to the minority carriers but will instead be determined by the recombination time of the DAP. The measured decay will normally be longer and with the DAP recombination be typical nonexponential, wavelength dependent behaviour.

Fig. 5 shows the decay curves of 6H-SiC and 4H-SiC epitaxial layers. These samples were grown in the same growth run and any difference in minority carrier lifetime

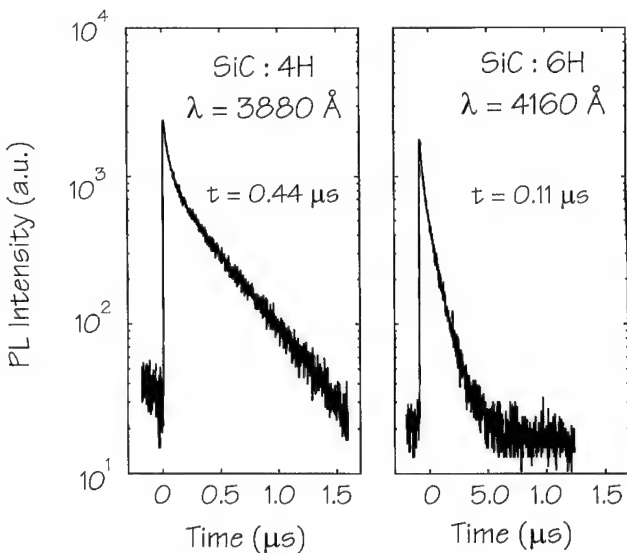


Fig. 5. Decay curves at room temperature of the emission band shown in Fig. 4. The minority carrier lifetime is significantly shorter in the 6H layer as compared to the 4H layer.

cannot be explained by differences in growth conditions. As can be seen, the lifetime is significantly shorter for the 6H layer than for the 4H layer. This is in no way a unique result of this growth run but is the normal outcome of an experiment such as this.

Previously we observed a weak correlation between the decay time and the nitrogen doping concentration in the sample [6]. This dependence is probably not related directly to the doping or carrier concentration, but to the general quality of the epitaxial layer.

Another strong correlation between observed minority carrier lifetime and epitaxial layer thickness has also been observed, as shown in Fig. 6. There may be two different explanations for this dependence; firstly, the quality of the epitaxial layer increases continuously with increasing thickness; secondly, the deep levels, that are assumed to be responsible for the non-radiative recombination, which limits the minority carrier lifetime, are present with a higher concentration close to the interface between the epitaxial layer and the substrate. The highest observed value for the minority carrier lifetime is 2.1 μ s, in a sample that was approximately 60 μ m thick.

The temperature dependence of the minority carrier lifetime in this sample is shown in Fig. 7, measured at two different spots on a 4H wafer. The increase in the measured decay time is expected for a process determined by the lifetime of the minority carrier. A lack of such temperature dependence, or an inverse dependence, has previously been reported [4] and is most likely due to thermal emission of holes from deep levels, which have trapped the photoexcited minority carriers. The minority carrier lifetime at 500 K, which is a tentative

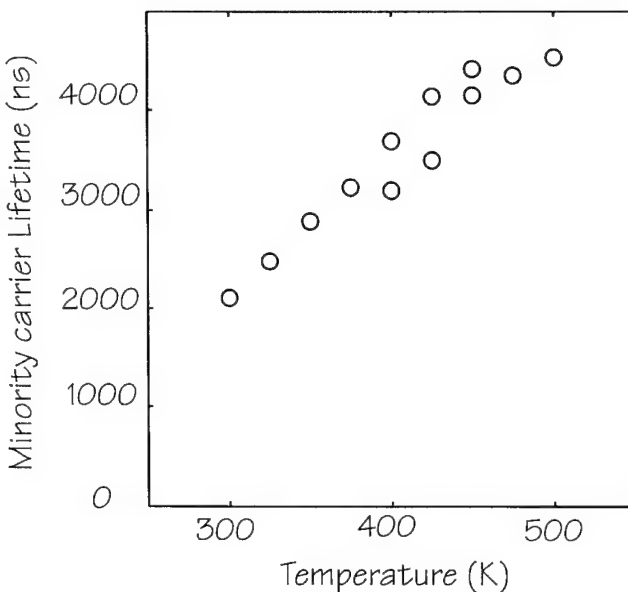


Fig. 7. Temperature dependence of the minority carrier lifetime, from two different points at a wafer.

operating temperature for a SiC power device, is close to 5 μ s.

To investigate this measured the PL decay time using different photon energies of the excitation light. By varying the wavelength of the laser between 310 and 350 nm, we were able to change the absorption length and hence create carriers at different concentrations and at different depths in the epitaxial layer. We also prepared samples with different doping profiles at the interface or at the surface to inhibit the diffusion of minority carriers to the interface or surface, respectively. In none of these cases did we observe any difference in measured minority carrier lifetime from the normal fluctuation between each sample. This indicates that the dominant non-radiative recombination channel is evenly distributed in the epi layer, and is not dominated by recombinations at the interface or surface.

4. Summary

We have shown that time resolved PL is an effective technique for the study of optical recombinations in SiC. We measured the PL decay time for nitrogen- and aluminium-bound excitons in different polytypes. The fast decay observed is attributed to an efficient non-radiative Auger process. The minority carrier lifetimes were also measured at room temperature using time resolved PL. An increase in the lifetime, specially in the 4H polytype, has been observed during recent years. The maximum observed minority carrier lifetime was longer than 2 μ s. The single most important factor that determines the observed lifetime is the thickness of the epitaxial layers.

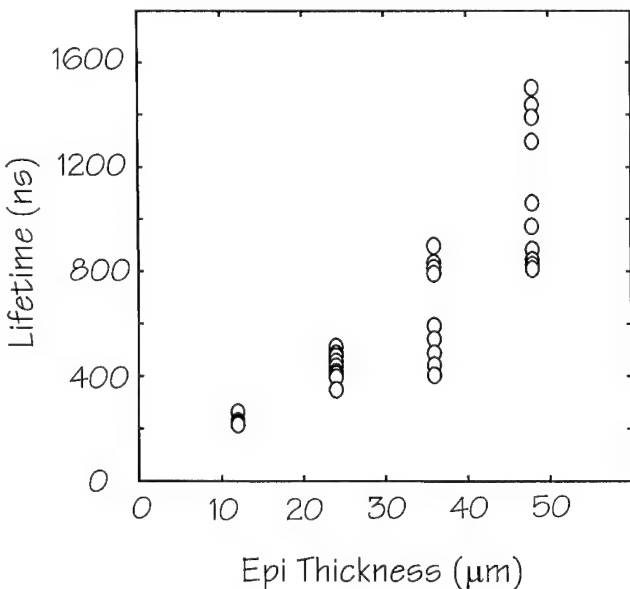


Fig. 6. Observed minority carrier lifetime in epitaxial samples with different thickness. The different values for each sample originate from measurements on different places on the wafer.

References

- [1] W.J. Choyke, Diamond and Related Materials (this proceedings).
- [2] A. Henry, O. Kordina, C. Hallin, C. Hemmingsson, E. Janzen, *Appl. Phys. Lett.* 65 (1994) 2457.
- [3] A.V. Naumov, V.I. Sankin, *Sov. Phys. Semicond.* 23 (1989) 630.
- [4] M.M. Anikin, A.S. Zubrilov, A.A. Lebedev, A.P. Strelchuk, A.E. Cherenkov, *Sov. Phys. Semicond.* 25 (1991) 289.
- [5] A.M. Danishevskii, A.Yu. Rogachev, *Semiconductors* 30 (9) (1996).
- [6] O. Kordina, J.P. Bergman, A. Henry, E. Janzen, *Appl. Phys. Lett.* 66 (1995) 189.
- [7] O. Kordina, J.P. Bergman, C. Hallin, E. Janzen, *Appl. Phys. Lett.* 69 (1996) 679.
- [8] O. Kordina, A. Henry, J.P. Bergman, N.T. Son, W.M. Chen, C. Hallin, E. Janzen, *Appl. Phys. Lett.* 66 (1995) 1373.
- [9] J.P. Bergman, C.I. Harris, O. Kordina, A. Henry, E. Janzen, *Phys. Rev. B* 50 (1994) 8305.
- [10] N.T. Son, E. Sörman, W.M. Chen, O. Kordina, B. Monemar, E. Janzen, *Appl. Phys. Lett.* 65 (1994) 2687.
- [11] W. Schmid, *Phys. Stat. Solids* 84 (1977) 529.

Analysis of transport properties of β -SiC films: determination of donor density and compensation ratio

S. Contreras *, C. Dezauzier, P. Thomas, J.L. Robert

G.E.S, cc074, UM2-CNRS, 34095 Montpellier, cedex 5, France

Abstract

In this paper we present an interpretation of the electrical behavior of n-type β -silicon carbide films deposited on silicon. The Hall effect and mobility behaviors were consistently analysed as a function of temperature in order to determine the donor concentration, the compensation ratio and the ionization energy of impurities in the SiC films. The model takes into account the parallel conduction at the interface and the role of the substrate. The role of the compensation ratio on the electrical properties is clearly demonstrated — for the more weakly doped sample, we found a value of E_D which compares well to the one determined by optical spectroscopy. © 1997 Elsevier Science S.A.

Keywords: β -SiC; Hall effect; High temperature

1. Introduction

Many authors have been interested in the analysis of the temperature dependence of the Hall coefficient in β -SiC [1,2] and from the results, have deduced the activation energy of the main dopants (N, Al). However, fewer papers have been devoted to a full understanding of the Hall coefficient and mobility changes versus temperature. Susuki et al. [3] investigated both undoped and n-doped films within the temperature range 70–1000 K. They deduced the values of the donor and acceptor concentrations (N_D , N_A) from the temperature dependence of the carrier concentration. However, the results seem to be questionable since the impurity compensation ratio N_A/N_D is significantly different to the one estimated in the same series of samples using the mobility temperature dependence [4]. Tachibana et al. also performed measurements up to 1000 K [5] but the method they used to determine the compensation ratio is again doubtful, since it is based only on carrier concentration analysis.

In this work, we present measurements of the resistivity and Hall effect performed on various CVD-grown, undoped and nitrogen-doped n-type β -SiC films deposited on on-axis silicon substrates. Taking into account both the measured carrier concentration and the mobil-

ity, the impurity density and the compensation ratio of the deposited films have been deduced.

2. Experimental details

The β -SiC films were deposited on Si (100) substrates (Table 1). Sample B was non-intentionally doped. Samples A and C were n-type. Two of the samples (B and C) were grown using off-axis orientations of Si (100) with inclinations of 4° towards the $\langle 011 \rangle$ direction for sample B and 3.5° for sample C.

The electrical properties of the epitaxial layers were investigated for the temperature range 4.2–1000 K, using the standard four contacts Van der Pauw technique, without removal of the substrate. When analysing the data, we took into account the magnetoconductivity correction factor, C_H , which depends on the sample geometry and the probe positions [6]. In our case C_H was about 0.75.

3. Results

The Hall carrier concentration versus temperature is shown in Fig. 1. Three different regions are clearly visible. At low temperatures (region 1), the material behaves like a degenerate semiconductor. In this tempe-

* Corresponding author.

Table 1

Samples' characteristics, donor concentrations N_D , compensating acceptor concentrations N_A , donor ionization energies E_D and interface layer parameters (e_2 , n_2 , μ_2) obtained by the fitting procedure

Sample	Thickness (μm)	Nominal value of net density of donors* ($\times 10^{17} \text{ cm}^{-3}$)	E_D (meV)	N_D ($\times 10^{17} \text{ cm}^{-3}$)	N_A ($\times 10^{17} \text{ cm}^{-3}$)	N_A/N_D	e_2 (Å)	μ_2 (cm^2/Vs)	n_2 ($\times 10^{18} \text{ cm}^{-3}$)
A	5.35	1.8	45	1.8	0.1	0.05	50	25	15
B	6.1	NID	33	3	1.5	0.5	50	70	3.5
C	2.8	0.35	28	3.3	3.13	0.94	50	3	2

*This value is given by the sample's supplier.

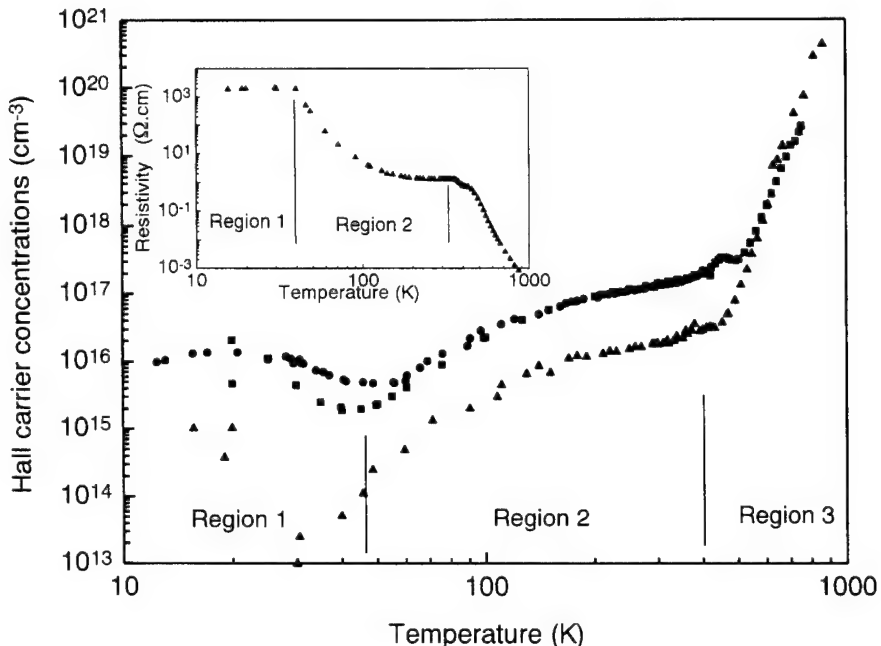


Fig. 1. Temperature dependences of the Hall carrier concentrations for sample A (■), sample B (◆) and sample C (▲). The inset shows the temperature dependence of the resistivity for sample C.

ture range, the Hall coefficient remains constant. In the temperature range 40–400 K (region 2), the carrier concentration first increases, and then saturates. Above 400 K (region 3), it increases drastically.

This situation is very similar to the one encountered on SOS (silicon on sapphire) films [7] and, taking into account the full series of results, it is impossible to explain those observed if only the conduction mechanism which occurs in the SiC film is considered. There is obviously a highly doped transition layer, with a very low mobility, located at the Si/SiC interface. This is clearly shown in Fig. 1 (inset) in which the resistivity shows metallic behavior at low temperature. In this region, the Hall carrier concentration, determined with the total thickness of the layer, is much lower than that existing at the interface layer. To account for this metallic behavior, the carrier concentration must be larger than the critical concentration determined at the metal–non metal transition (i.e. $\gg 10^{18} \text{ cm}^{-3}$). The corresponding transition layer thickness must be much less

than 100 Å and be comparable to the carbonization layer measured by TEM (20–50 Å) [8].

In the high temperature range (region 3), a parallel conduction appears due to the existence of a strong leakage current, inducing an apparent increase of the carrier concentration. In other words, in this temperature range, the conduction is governed by the intrinsic carriers present in the silicon substrate and not in the SiC layer (the measured activation energy being strictly equal to half the Si energy gap).

The electrical properties of the 3C-SiC films only appear in the intermediate temperature range (40–450 K: region 2) in which the parallel conduction process is negligible. In this region we are not able to make any correlation between the electrical behavior and the substrate orientation.

The Hall mobility versus temperature, is plotted in Fig. 2. It increases below 50 K, passes through a maximum and then decreases around room temperature. It is worth noticing that the mobility of sample C, which

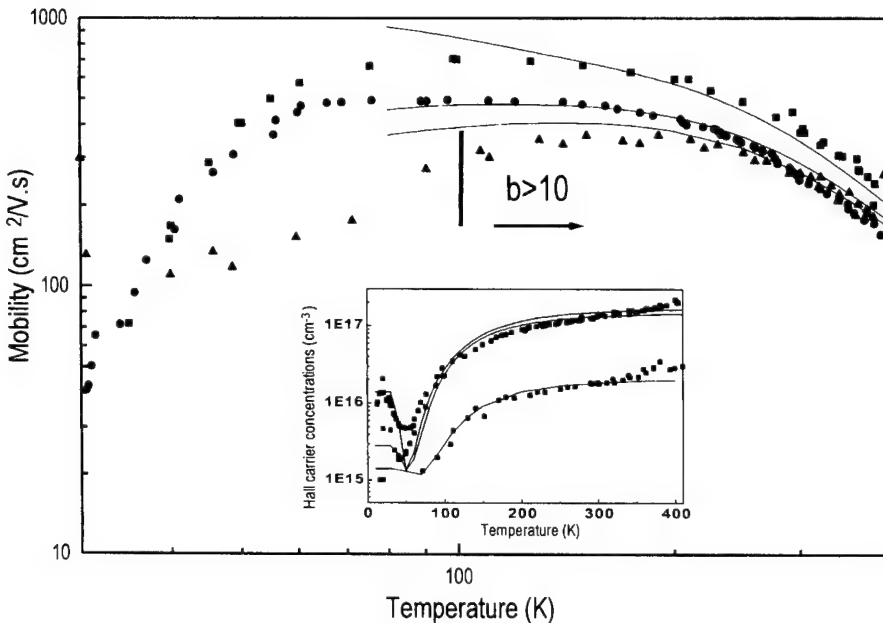


Fig. 2. Temperature dependences of the Hall mobilities for sample A (■), sample B (◆) and sample C (▲). The inset shows the variation of the Hall carrier concentrations versus temperature. The solid lines are theoretical calculations.

has the lowest carrier concentration, is always lower than that of samples A and B. This can only be explained by a large difference in the compensation ratio.

4. Discussion

In order to account for the experimental data collected in the range 40–400 K, we have only to concentrate on two parallel conducting layers: (i) the SiC film (e_1 , n_1 , μ_1) and (ii) the interface layer (e_2 , n_2 , μ_2). Concerning the SiC/Si transition layer, we used the thickness e_2 as determined by TEM. The value of the mobility in this layer is deduced from the ratio R_H/ρ and depends on the value of e_2 .

In the case of the SiC film, the carrier concentration n_1 in the non-degenerate material, obeys the following relation:

$$\frac{n_1(n_1 + N_A)}{N_D - N_A - n_1} = \frac{N_c}{g} \exp \frac{-E_D}{KT}$$

where g is the degeneracy factor, N_c the density of states in the conduction band and E_D the activation energy of the impurity states.

When all impurities have been ionized, the carrier density is equal to $N_D - N_A$. This value is deduced from the Hall carrier concentration in the exhaustion regime (i.e. at the transition between regions 2 and 3, see Fig. 1).

Because of the uncertainty in the experimental Hall coefficients, several pairs of E_D and $N_D - N_A$ values can be used to fit the Hall carrier concentration. For a given pair, the fit of n_H leads to a single value of N_A/N_D :

consequently, N_D and N_A must be chosen in order to obtain the best agreement between experimental and theoretical mobility values.

To compute the mobility, we consider the following scattering processes [9–11]

- (1) deformation potential and acoustic phonons scattering,
- (2) piezoelectric, non polar and polar optical phonons scattering,
- (3) neutral impurities scattering, and
- (4) ionized impurities scattering.

Each process is characterized by a relaxation time τ_i ; the final mobility is deduced from the mean value of the relaxation time $\langle \tau \rangle$ using: $\frac{1}{\tau} = \sum \frac{1}{\tau_i}$. In the temperature range 40–400 K, our results show that the acoustic phonon scattering and ionized impurity scattering are the most important. The ionized impurity scattering mode is usually described by the Brooks–Herring formula:

$$1/\tau_{\text{imp}} = \left(\frac{1}{16\pi} \right) \times e^4 \times N_i \times \epsilon^{-2} \times (2m)^{-1/2} \times E^{-3/2} \times f(b)$$

where:

$$f(b) = \ln(1+b) - b/(1+b)$$

with

$$b = \left(\frac{128\pi^2}{h^2} \right) m^* E L^2$$

L being the mean free path and

$$N_i = n + 2N_A$$

The Brooks–Herring formula is only valid in the framework of the first Born approximation when the electron wavelength (K_F) is shorter than the screening length. This leads to the condition $b \gg 1$. In the case of SiC the electron mobility is not very high and, as the temperature is lowered, when ionized impurity scattering plays a dominant role, the condition $b \gg 1$ is not satisfied. Moore [12] considered this problem in detail and obtained a general formula:

$$\mu_{imp} = \frac{\mu_{BH}}{1 + \delta\sigma}$$

which includes the quantum corrections $\delta\sigma$ to the Brooks–Herring expression. These corrections have been experimentally determined for $b > 10$ [13], in agreement with the theory. The fit of our experimental results has been made in the framework of this model, in the temperature range 100–400 K which corresponds to such values of b .

The procedure consists of self-consistent analysis of the electrical properties of the samples. The donor concentrations, compensating acceptor concentrations, donor ionization energies and interface layer parameters (e_2 , n_2 , μ_2) obtained from the fitting procedure are given in Table 1. In Fig. 2, the solid lines correspond to theoretical calculations of the Hall concentration and Hall mobility.

Two important results can be noticed. First, as expected from the Pearson and Bardeen model for hydrogenic donors [14], we observe a decrease in the activation energy of the donor level when the total density of the impurities increases. For the purest sample, this activation energy is close to that determined by PL measurements [15]. As a result, the ambiguity already mentioned between the transport and optical measurements fails. Second, as expected, the compensation ratio is much higher in sample C than the values found for the other samples.

Moreover, the compensation ratio is very low for sample A. This indicates that it is difficult to consider

an other mechanism which could play a role in the scattering processes in this temperature range. This allows us to consider that scattering by dislocation is not efficient in the present case.

5. Conclusion

We have shown that careful analysis of both the Hall effect and mobility in 3C-SiC films is necessary to fully understand their electrical behavior. The compensation ratio plays an important role and its determination is an absolute necessity if conclusions about the quality of the material are to be made. The activation energy E_D of the donor decreases as the impurity density increases and, for the first time, we obtain an agreement with the electrical and optical values of E_D for the less heavily doped sample.

References

- [1] K. Sasaki, E. Sakuma, S. Misawa, S. Yoshida, S. Gonda, *Appl. Phys. Lett.* 45 (1) (1984) 72.
- [2] B. Segall, S.A. Alterovitz, E.J. Haugland, L.G. Matus, *Appl. Phys. Lett.* 50 (21) (1987) 1533.
- [3] A. Suzuki, A. Uemoto, M. Shigeta, K. Furukawa, S. Nakajima, *Appl. Phys. Lett.* 49 (1986) 450.
- [4] A. Suzuki, A. Ogura, K. Furukawa, Y. Fuji, M. Shigeta, S. Nakajima, *J. Appl. Phys.* 64 (5) (1988) 2818.
- [5] T. Tachibana, H.S. Kong, Y.C. Chong, R.F. Davis, *J. Appl. Phys.* 67 (1990) 6375–6381.
- [6] M.A. Green, M.W. Gun, *Solid State Electr.* 15 (1972) 577.
- [7] J.L. Robert, J.M. Dusseau, P. Girard, J. Sicart, *J. Appl. Phys.* 54 (4) (1983) 1903.
- [8] N. Becourt, J.L. Ponthenier, A.M. Papon, C. Jaussaud, *Physica B* 185 (1993) 79–83.
- [9] H.J. van Daal, Mobility of charge carriers in silicon carbide, Philips Research Report, Suppl. 3, 1965, p. 48.
- [10] R. Kaplin, R.J. Wagner, *Solid State Commun.* 55 (1985) 55.
- [11] R.C. Marshall, J.W. Faust, C.E. Ryan (Eds.), *Silicon Carbide — 1973*, University of South Carolina, Columbia, SC, 1974, p. 668.
- [12] E.J. Moore, *Phys. Rev.* 160 (1967) 607.
- [13] W. Zawadzki, Mechanisms of electron scattering in semiconductors, in: T.S. Moss (Ed.), *Handbook on semiconductors*, vol. 1, 1982, p. 713.
- [14] W. Schokley, *Electrons and holes in semiconductors*, D. Van Nostrand Company, Inc., Princeton, New Jersey, 1950, p. 228.
- [15] P.J. Dean, W.J. Choyke, L. Patrick, *J. Lumin.* 15 (1977) 299.

Radiation-induced defect centers in 4H silicon carbide

Thomas Dalibor ^{a,*}, Gerhard Pensl ^a, Tsunenobu Kimoto ^b, Hiroyuki Matsunami ^b,
Shankar Sridhara ^c, Robert P. Devaty ^c, Wolfgang J. Choyke ^c

^a Institute of Applied Physics, University of Erlangen-Nürnberg, Staudtstraße 7, D-91058 Erlangen, Germany

^b Department of Electrical Engineering, Kyoto University, Kyoto 606-01, Japan

^c Department of Physics and Astronomy, University of Pittsburgh, Pittsburgh, PA 15260, USA

Abstract

Deep level transient spectroscopy (DLTS) and low temperature photoluminescence (LTPL) were applied to investigate radiation-induced defect centers and their thermal stability in 4H silicon carbide (SiC) epilayers grown by chemical vapor deposition (CVD). The epilayers were implanted with He⁺ ions and annealed at different temperatures. Several deep defect levels were monitored with DLTS in the 4H polytype. The correlation of these centers with photoluminescence lines is discussed with respect to appropriate annealing steps. © 1997 Elsevier Science S.A.

Keywords: Deep level transient spectroscopy; Low temperature photoluminescence; Radiation-induced deep defect centers; Thermal stability; 4H silicon carbide

1. Introduction

The fabrication of electronic devices based on the wide-bandgap semiconductor silicon carbide (SiC) requires the control of various processing techniques from epilayer growth to etching, oxidation, contact preparation and doping. Owing to very small diffusion coefficients leading to undesirably high temperatures for doping by diffusion [1], ion implantation and subsequent annealing are the favored techniques for n- and p-type doping of SiC. Recent progress in implantation of nitrogen (N) [2], phosphorus (P) [3], aluminum (Al) [4] and boron (B) [5] shows the feasibility of achieving n- or p-type conductivity in SiC epilayers grown by chemical vapor deposition (CVD). However, these reports mainly focus on the electrical activation of the dopants and the structural characterization of the implanted layer, rather than on electrically active radiation-induced defect centers and their thermal stability. Deep level transient spectroscopy (DLTS) investigations have been carried out by Doyle et al. [6] on electron-irradiated n-type 4H SiC and by Dalibor et al. [7] on ion-implanted n-type 4H SiC. The optical properties of radiation-induced defects were characterized by Choyke

with low temperature photoluminescence (LTPL) (see e.g. [8]).

It is the purpose of this paper to present a detailed study of radiation-induced defect centers and their thermal stability in 4H SiC monitored by DLTS and LTPL.

2. Experimental

The 4H SiC epilayers used were grown by atmospheric pressure CVD in a silane (SiH₄)–propane (C₃H₈)–hydrogen (H₂) system on n-type 4H SiC {0001} substrates 4° off toward <1120> [9]. The thickness of the epilayers was ~8 μm; growth temperature and C:Si ratio in the source gas flow were 1500 °C and 3.0, respectively. Nickel (Ni) Schottky contacts with a diameter of 0.7 mm were prepared on top of the epilayers for C–V and DLTS measurements. Large-area ohmic contacts were fabricated on the backside of the substrates by evaporating Ni and subsequent annealing at 1050 °C. The net doping concentration of unintentionally n-type doped as-grown epilayers was about (1–2) · 10¹⁶ cm⁻³. To achieve a rectangular damage profile to a depth of 1.6 μm, we conducted a six-fold He⁺-implantation with an integral fluence of 9 · 10¹⁰ cm⁻² resulting in a mean vacancy concentration of 4.5 · 10¹⁶ cm⁻³ as calculated by the TRIM cascade

* Corresponding author. Tel: +(49)-9131-858426;
Fax: +(49)-9131-858423.

program. The anneals were performed either in a rapid isothermal annealing system (1000 °C anneal) under vacuum ($5 \cdot 10^{-5}$ mbar) or in a furnace with a closed SiC crucible (1400 °C anneal) under argon atmosphere. DLTS measurements were carried out in a temperature range from 80 to 700 K with a reverse bias of –8 V, a filling pulse bias of –0.5 V and a filling pulse width of 20 ms using a fast computer-controlled system described in Ref. [10]. For LTPL measurements at $T=2$ K, the samples were excited either with a He–Cd laser ($\lambda=325$ nm) or a frequency doubled Ar⁺ laser (FRED, $\lambda=244$ nm). The spectra were recorded with a liquid nitrogen cooled CCD array on a Fast-Fastie spectrometer with an 1800 l/mm grating blazed at 4000 Å.

3. Experimental results and discussion

Figs. 1a and b show DLTS and LTPL spectra of an n-type 4H SiC CVD epilayer subsequent to different processing steps. The trap parameters of the observed defect centers are summarized in Table 1. In the DLTS spectrum of the as-grown sample (solid curve, magnified by a factor of 10), we only observed one level at E_C –(0.63–0.68) eV (the energy range is caused by assuming $\sigma=\text{const.}$ and $\sigma \propto T^{-2}$ for the temperature dependence of the capture cross-section, respectively) attributed to the Z_1 -center [7] at a concentration of $2 \cdot 10^{13} \text{ cm}^{-3}$. A small L_1 line due to the D_1 -defect is observed in the LTPL spectrum of the as-grown sample (magnified by a factor of 20).

After implantation of the epilayer with He⁺ ions and an anneal at 430 °C occurring during the DLTS measurement up to this temperature, several new peaks arise in the DLTS spectrum (dashed curve in Fig. 1(a)). The concentration of the Z_1 -center increases to about $4 \cdot 10^{15} \text{ cm}^{-3}$, which has to be considered only as a rough estimate since the Z_1 peak is obviously overlapped by a second peak not resolved by our measurement. Furthermore, it is possible that the long tail to the low temperature edge of this double peak contains another two peaks at $T \approx 210$ K and $T \approx 135$ K. At higher temperatures, three additional features can be detected: a double peak around $T \approx 450$ K at a concentration of about $2 \cdot 10^{15} \text{ cm}^{-3}$ termed $RD_{1/2}$, which could not be resolved by our measurement and two peaks at $T \approx 560$ K (concentration equal to $2 \cdot 10^{15} \text{ cm}^{-3}$) and $T \approx 660$ K (concentration equal to $4 \cdot 10^{15} \text{ cm}^{-3}$) labeled as RD_3 and RD_4 , respectively. An Arrhenius plot evaluation results in ionization energies of (0.89–0.97), (0.98–1.08) and (1.49–1.60) eV for $RD_{1/2}$ (treated as a single peak in the evaluation), RD_3 and RD_4 , respectively; the capture cross sections for electrons are ($7 \cdot 10^{-16}$ – $5 \cdot 10^{-15}$), ($5 \cdot 10^{-17}$ – $3 \cdot 10^{-16}$) and

(1 – 9) $\cdot 10^{-14} \text{ cm}^2$. The LTPL spectrum (see Fig. 1b) taken after He⁺-implantation and anneal at 430 °C is dominated by two lines at 4310.5 and 4347.7 Å. In addition, the L_1 line is increased compared with the as-grown spectrum and several further lines appear in the wavelength ranges 4270–4310 Å, 4325–4375 Å and 4410–4450 Å.

Annealing at 1000 °C for 10 min causes significant changes in the DLTS and LTPL spectra. The Z_1 -center is now the dominating feature in the DLTS spectrum (dot-dashed curve in Fig. 1(a)) with a concentration of $4 \cdot 10^{15} \text{ cm}^{-3}$. The peak, which has overlapped the Z_1 peak in the as-implanted and annealed at 430 °C state, disappeared, as can be seen from the reduced width of the Z_1 peak. Moreover, two new features are resolved on the low temperature side of the Z_1 peak: a double peak at $T \approx 110$ /135 K at a concentration of about $1 \cdot 10^{14} \text{ cm}^{-3}$ and a single peak at $T \approx 210$ K at a concentration of $3 \cdot 10^{14} \text{ cm}^{-3}$. Ionization energies of (0.19–0.21) eV (for the peak at $T \approx 135$ K; the shoulder at $T \approx 110$ K could not be evaluated) and of (0.31–0.35) eV and capture cross-sections for electrons of ($1 \cdot 10^{-17}$ – $1 \cdot 10^{-16}$) cm^2 and of ($2 \cdot 10^{-17}$ – $1 \cdot 10^{-16}$) cm^2 are obtained from an Arrhenius plot evaluation for these peaks. $RD_{1/2}$, RD_3 and RD_4 are reduced with respect to their concentrations by about one order of magnitude by the anneal at 1000 °C. The L_1 line (reduced by a factor of 10 in Fig. 1(b)) and its phonon-replica (4340–4470 Å) with the local mode at 4400 Å are dominating the LTPL spectrum after the anneal at 1000 °C for 10 min. However, several smaller lines in the wavelength range between 4275 and 4350 Å are still observable, especially the lines at 4310.7 and 4346.0 Å. In addition, a new feature around 4250 Å appears in the spectrum after the 1000 °C-anneal.

A further anneal at 1400 °C for 10 min leads to a reduction of deep levels observable in the DLTS spectrum (dot-dot-dashed curve in Fig. 1(a)). RD_3 and RD_4 disappeared as well as the peak at $T \approx 210$ K. The concentration of the Z_1 -center is decreased to about $3 \cdot 10^{14} \text{ cm}^{-3}$; the peak at $T \approx 135$ K and $RD_{1/2}$ are detected at concentrations of $\sim 4 \cdot 10^{13} \text{ cm}^{-3}$. The number of lines in the LTPL spectrum (Fig. 1(b)) is also reduced. Although with a lower intensity compared with the 1000 °C-anneal spectrum, the L_1 line and its phonon-replica still dominate after the anneal at 1400 °C. The lines in the wavelength range between 4275 and 4350 Å, especially those at 4310.7 and 4346.0 Å, disappeared. Besides L_1 only the feature at 4250 Å survived the anneal; its line shape looks different compared with the 1000 °C-anneal spectrum.

The implantation of n-type 4H SiC CVD epilayers with He⁺ ions introduces several energetically deep levels in the bandgap of this polytype. Only one defect center, the Z_1 -center, is present at a rather low concentration in the epilayers prior to implantation. The

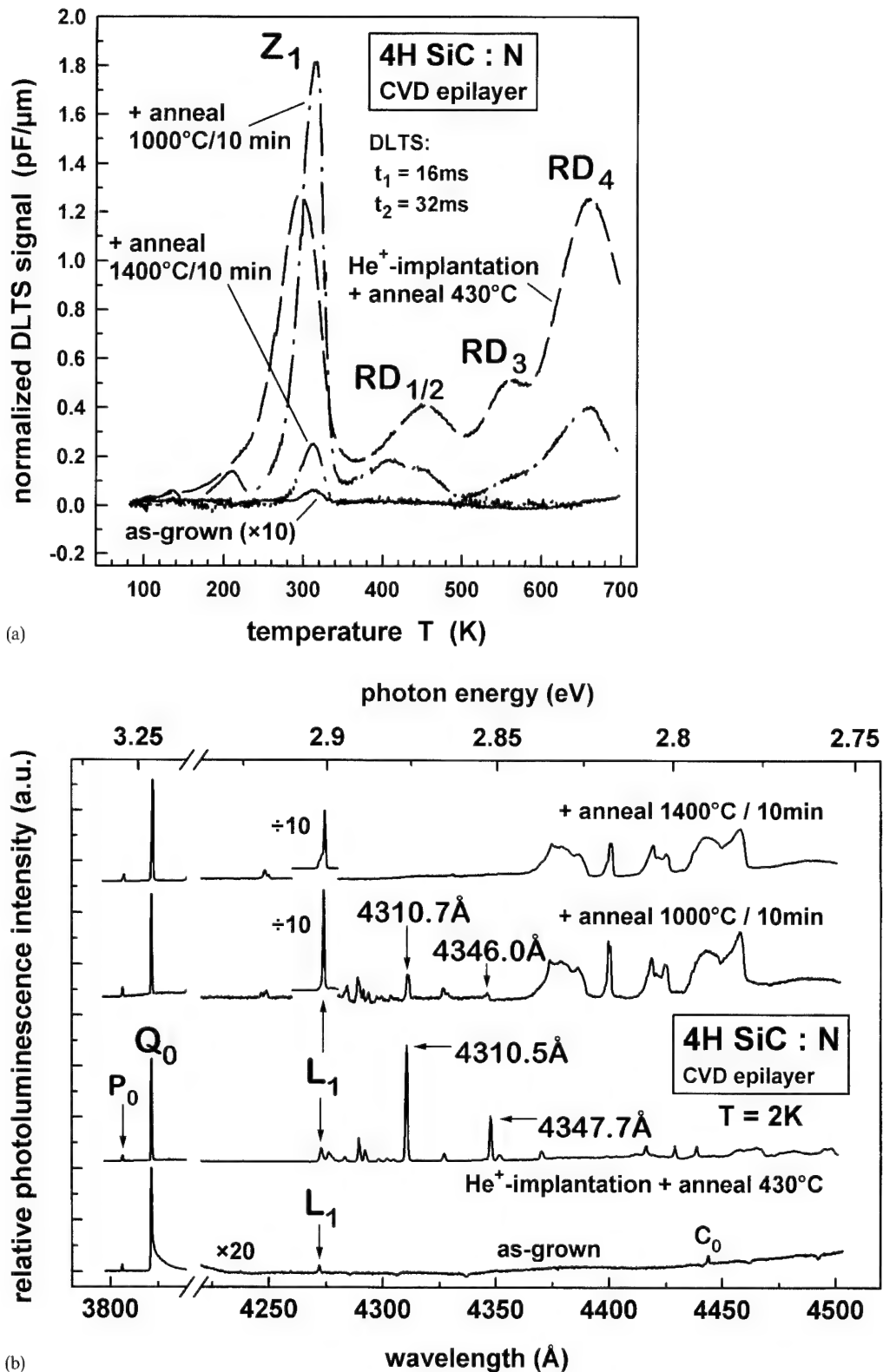


Fig. 1. (a) Normalized DLTS spectra (time window $t_1/t_2 = 16/32$ ms) taken on an n-type 4H SiC as-grown CVD epilayer (solid curve, magnified by a factor of 10) and subsequent to He⁺-implantation and anneals at 430°C (dashed curve), 1000°C for 10 min (dot-dashed curve) and 1400°C for 10 min (dot-dot-dashed curve), respectively. (b) LTPL spectra taken at $T = 2\text{ K}$ on an n-type 4H SiC as-grown CVD epilayer (excited with a He-Cd laser) and subsequent to He⁺-implantation and anneals at 430°C , 1000°C for 10 min and 1400°C for 10 min (excited with a frequency doubled Ar⁺ laser), respectively.

Table 1

Trap parameters of radiation-induced defect centers in n-type 4H SiC CVD epilayers as obtained from an Arrhenius plot evaluation (assuming $\sigma = \text{const.}$ and $\sigma \propto T^{-2}$ for the temperature dependence of the capture cross-section, respectively)

Peak temperature ($t_1/t_2 = 16/32\text{ ms}$)	Center	Ionization energy (eV)	Capture cross section (cm^2)	Concentration (cm^{-3})
135 K		0.19–0.21	$1 \cdot 10^{-17}$ – $1 \cdot 10^{-16}$	$1 \cdot 10^{14}$ (1000 °C anneal) $4 \cdot 10^{13}$ (1400 °C anneal)
210 K		0.31–0.35	$2 \cdot 10^{-17}$ – $1 \cdot 10^{-16}$	$3 \cdot 10^{14}$ (1000 °C anneal)
310 K	Z_1	0.63–0.68	$3 \cdot 10^{-15}$ – $2 \cdot 10^{-14}$	$2 \cdot 10^{13}$ (as-grown) $4 \cdot 10^{15}$ (430 °C anneal) $4 \cdot 10^{15}$ (1000 °C anneal) $3 \cdot 10^{14}$ (1400 °C anneal)
450 K	$RD_{1/2}$	0.89–0.97	$7 \cdot 10^{-16}$ – $5 \cdot 10^{-15}$	$2 \cdot 10^{15}$ (430 °C anneal) $2 \cdot 10^{14}$ (1000 °C anneal) $4 \cdot 10^{13}$ (1400 °C anneal)
560 K	RD_3	0.98–1.08	$5 \cdot 10^{-17}$ – $3 \cdot 10^{-16}$	$2 \cdot 10^{15}$ (430 °C anneal) $4 \cdot 10^{14}$ (1000 °C anneal)
660 K	RD_4	1.49–1.60	$1 \cdot 10^{-14}$ – $9 \cdot 10^{-14}$	$4 \cdot 10^{15}$ (430 °C anneal) $4 \cdot 10^{14}$ (1000 °C anneal)

Z_1 -center is a thermally stable (up to at least 2015 °C) acceptor-like defect center and is discussed in terms of a divacancy in a previous publication [7]. To reveal the charge state of the other radiation-induced deep levels, we conducted double-correlated DLTS (DDLTS) investigations. Fig. 2 depicts the DDLTS signal as a function of temperature for different electric fields applied. The electric field varies for each peak by about a factor of three in a range from $6 \cdot 10^4$ to $2 \cdot 10^5 \text{ V/cm}$. As can be seen in Fig. 2, the position of the peak temperature does not change with different applied electric fields. This means that the ionization energies of the centers are

independent of the electric field suggesting that the overlapping peak of Z_1 , $RD_{1/2}$, RD_3 and RD_4 correspond to acceptor-like defect centers. For future experiments, a stronger variation of electric fields would be desirable to strengthen this indication.

The energetically shallower level overlapping the Z_1 -center already anneals out at temperatures below 1000 °C. This suggests that both levels are due to different defect centers and do not belong to the same defect center residing at inequivalent lattice sites. The most interesting feature is the RD_4 -center with its energy level at E_C -(1.49–1.60) eV close to mid-bandgap. Its rather high capture cross-section for electrons of about $5 \cdot 10^{-14} \text{ cm}^2$ may enable this center to act as an efficient recombination center in ion-implanted 4H SiC. We would like to point out that the RD_4 -center and the LTPL lines at ~ 4311 and $\sim 4347 \text{ \AA}$ (4347.7 and 4346.0 Å, respectively) show a similar behavior in terms of their generation and annealing. The LTPL line at $\sim 4311 \text{ \AA}$ has previously been assigned to the D_1 -defect in 4H SiC by Haberstroh et al. [11] and has been termed L_2 . Since the thermal stability of the 4311 Å line is completely different compared with the L_1 line in 4H SiC and to the L lines in the other polytypes, we suggest that this line does not belong to the D_1 -defect.

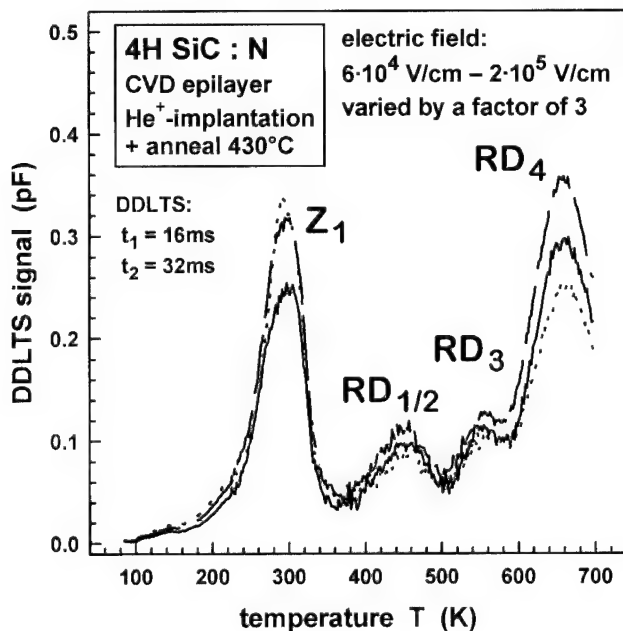


Fig. 2. DDLTS spectra (time window $t_1/t_2 = 16/32\text{ ms}$) taken on an n-type 4H SiC CVD epilayer subsequent to He^+ -implantation and anneal at 430 °C for three different applied electric fields ranging from $6 \cdot 10^4$ to $2 \cdot 10^5 \text{ V/cm}$.

Acknowledgement

The support of this work by the Ministry of Education, Science and Culture of Japan, by the German Science Foundation (Sonderforschungsbereich 292) and by the German Bundesministerium für Bildung, Wissenschaft, Forschung und Technologie (BMBF) is gratefully acknowledged.

References

- [1] Yu.A. Vodakov, E.N. Mokhov, in: R.C. Marshall, J.W. Faust Jr., C.E. Ryan (Eds.), *Silicon Carbide—1973*, University of South Carolina Press, South Carolina, 1974, p. 508.
- [2] T. Kimoto, A. Itoh, H. Matsunami, T. Nakata, M. Watanabe, *J. Electron. Mat.* 24 (1995) 235.
- [3] T. Troffer, C. Peppermüller, G. Pensl, K. Rottner, A. Schöner, *J. Appl. Phys.* 80 (1996) 3739.
- [4] T. Kimoto, A. Itoh, H. Matsunami, T. Nakata, M. Watanabe, *J. Electron. Mat.* 25 (1996) 879.
- [5] T. Troffer, Ch. Häßler, G. Pensl, K. Hözlein, H. Mitlehner, J. Völkl, *Inst. Phys. Conf. Ser.* No. 142 (1996) 281.
- [6] J.P. Doyle, M.O. Aboelfotoh, M.K. Linnarsson, B.G. Svensson, A. Schöner, N. Nordell, C. Harris, J.L. Lindström, E. Janzén, C. Hemmingsson, *MRS Symp. Proc. Ser.* Vol. 423 (1996) 519.
- [7] T. Dalibor, C. Peppermüller, G. Pensl, S. Sridhara, R.P. Devaty, W.J. Choyke, A. Itoh, T. Kimoto, H. Matsunami, *Inst. Phys. Conf. Ser.* No. 142 (1996) 517.
- [8] W.J. Choyke, *NATO ASI Series Vol.* 185 (1989) 563.
- [9] T. Kimoto, A. Itoh, H. Matsunami, S. Sridhara, L.L. Clemen, R.P. Devaty, W.J. Choyke, T. Dalibor, C. Peppermüller, G. Pensl, *Appl. Phys. Lett.* 67 (1995) 2833.
- [10] K. Hözlein, G. Pensl, M. Schulz, P. Stolz, *Rev. Sci. Instrum.* 57 (1986) 1373.
- [11] Ch. Haberstroh, R. Helbig, R.A. Stein, *J. Appl. Phys.* 76 (1994) 509.

Thermal properties of β -SiC epitaxial layers between 150 °C and 500 °C measured by using microstructures

C. Wagner *, G. Krötz

Forschung und Technik, Daimler-Benz AG, Postfach 80 04 65, 81663 München, Germany

Abstract

The heat conductivity and the thermal diffusion velocity of LPCVD grown, nominally undoped epitaxial SiC layers on silicon were determined from 150 °C to 500 °C. A novel arrangement of micromachined SiC bridges was used to measure these quantities with little calculation effort. The thermal conductivity was derived from the temperature difference and the heat flow over a SiC micro bridge. The heat diffusion velocity was obtained from the phase shift between the temperature modulation induced at one side of the SiC micro bridge and detected at the other, respectively. The temperature distribution of the SiC microstructure was measured by a thermal imaging system. © 1997 Elsevier Science S.A.

Keywords: Heat diffusion; Thermal conductivity; High temperature; SiC

1. Introduction

SiC is usually known as an attractive wide bandgap material for high temperature and high power electronics. The chemical inertness and good elastic behaviour even at high temperatures also make it a good candidate for microsensor applications in harsh environments [1]. In particular, microsensor concepts based on silicon substrates can be improved by using epitaxial SiC. For thermal simulations of those sensors reliable data on the thermal properties are necessary. These partly exist for poly-crystalline bulk SiC [2] but are not available for thin layers of epitaxial SiC. For the latter the thermal data are not expected to be the same as for bulk material, as for example the influence of surfaces could increase with decreasing sample size or crystal quality decrease because of lattice mismatch and interface defects.

2. Sample design and preparation

In the case of macroscopic samples sticks are the standard structures for determining thermal quantities [3]. For microstructures an imitation very similar to those sticks are bridges [4]. Fig. 1 shows a photograph

and a schematic sectional view of the novel sample design used in this work. It consists of four identical bridges namely heater, reference heater, heat sink and symmetrical heat sink. Each of these four bridges can be heated by evaporated conductors which are isolated electrically by an underlying oxide. The heater and the heat sink are connected by a SiC bridge without any add-on layer, called the transfer bridge. The thermal properties of the latter have been determined.

The arrangement has some advantages especially compared to heated membranes [5,6]:

- (1) A thin, narrow microbridge can be treated as one-dimensional. The calculation then becomes less effort.
- (2) The heat Q which flows across the transfer bridge and defines the thermal conductivity (see Eq. (1)) can be measured easily and with high accuracy. By comparing the heater bridge with an almost identical reference bridge several uncertainties can be eliminated: e.g. the unknown heat transfer between metallization and SiC layer, thermal losses across the frame to the substrate as well as at the electric contacts or radiation losses along the metallizations.
- (3) The hot parts of the microstructure are localized. They do not influence the temperature sensitive areas of the chip like wire bonds or chip fixation. Thus measurements up to very high temperatures can be realized.

* Corresponding author.

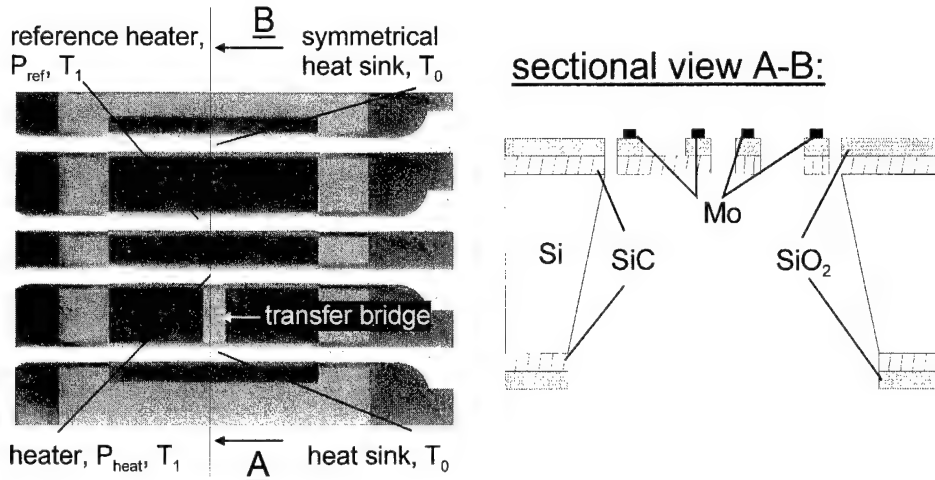


Fig. 1. SiC microstructure for measurements of thermal conductivity heat diffusion velocity: (a) photograph, (b) schematic sectional view.

(4) Heater and heat sink can be heated separately. If the difference between the temperatures is small the thermal properties can be treated as constants.

Most of the SiC microstructure preparation steps are standard micromachining processes [7] and only specific features will be described in detail:

Nominally undoped β -SiC was grown at 1100 °C on both sides of the substrate up to a thickness of 2.5 μm . Details of the applied low temperature LPCVD process working with methyl-silane as a precursor are described elsewhere [8]. The SiC epitaxial layers were thermally oxidized by a standard wet oxidation process to obtain an electrical isolation against the subsequent metallization. To structure the SiC epitaxial layers a PECVD etching process was developed [9]. As metallization for the heaters' molybdenum was used because of its high melting point, a similar thermal expansion coefficient as SiC ($\approx 5.5 \times 10^{-6} \text{ K}$ at 500 K compared to $\approx 4.3 \times 10^{-6} \text{ K}$ respectively [10]) and because it exhibits a good adhesion to the underlying oxide. In a final process step free standing bridges were realized by anisotropic etching of the Si-substrate in KOH. Special substrate holders were used to protect the metallized side of the sample during the etching process.

3. Experimental setup

For all measurement procedures described below it is mandatory to measure the exact temperature at multiple points of the SiC microstructure. To avoid disturbances by convection the sample was placed in a vacuum chamber. An IR imaging system was used to record the temperature distribution on top of the microstructure with an optical and interpolated resolution of 100 and 25 μm , respectively. The emissivity of each structure was determined in a separate vacuum chamber where the

chip was mounted on a heating chuck. A comparison of the temperature of the chuck and the temperature measured by the IR system yielded the emissivity.

The heating power of the different heater bridges and heat sinks were determined by measuring the voltage drop U at a resistor R_0 connected in series to the resistors of the bridges itself. The heating power was calculated from $P = U \times I$ where $I = U/R_0$.

For measuring phase shifts in the case of diffusivity measurements the time resolving measurement mode of the IR imaging system was used.

4. Measurement procedures

4.1. Heat conductivity

To measure the heat conductivity the heater and the reference heater were heated to T_1 and the heat sink and the symmetrical heat sink to T_0 . As the heater has thermal losses over the transfer bridge, the heating power P_{heat} is higher than that of the reference heater P_{ref} . All other losses, except for radiation losses of the transfer bridge, are eliminated by comparison of the heater and reference heater: $\Delta P = P_{heat} - P_{ref}$. This difference is used to calculate the heat conductivity κ from [11]:

$$\frac{\Delta P}{A} = -\kappa \cdot \text{grad}T \quad (1)$$

where A is the cross-section of the transfer bridge. For temperatures higher than 400 °C it is necessary to consider radiation losses of the transfer bridge. For small temperature differences the temperature profile along the bridge can be assumed to be linear. The resulting radiation loss can be calculated according to the radia-

tion law of Stefan–Boltzmann [12] and added as a simple correction term: $Q' = Q - P_{\text{rad}}$.

4.2. Heat diffusion velocity

To measure the heat diffusion velocity a sinusoidally modulated heating power was applied to the heater (Fig. 3). The heat flow across the transfer bridge causes a phase shifted temperature variation between two observation points. The phase shift ϕ depends on their distance l , the wave period t and the thermal diffusion velocity α [3]. From this relation α can be derived:

$$\alpha = \frac{\pi \cdot l^2}{\tau \cdot \phi^2} \quad (2)$$

5. Results

5.1. Heat conductivity

Fig. 2 shows an IR image of the temperature distribution of the SiC microstructure given in Fig. 1b. The sample is in thermal equilibrium and a constant temperature gradient is applied over the transfer bridge (600 μm long, 2.5 μm thick, 200 μm wide). From Fig. 2 and similar results for other temperatures the temperature gradient along the transfer bridge was extracted. Together with the electrically measured heat transfer Q the thermal conductivity was determined according to Eq. (1) and assigned to the related average temperature across the transfer bridge. As a result Fig. 4(a) shows the thermal conductivity in dependence of the temperature.

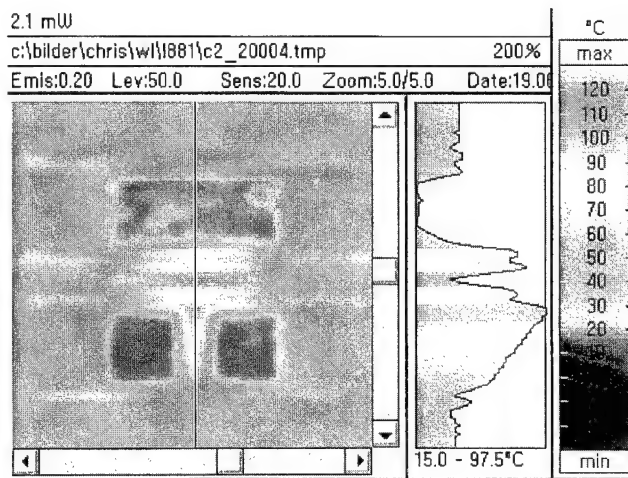


Fig. 2. Thermographic image of the heated microstructure shown in Fig. 1.

5.2. Heat diffusion velocity

Fig. 3 shows the temperature variation of the transfer bridge taken by the IR imaging system when a sinusoidally modulated heating power is applied to the heater. In the main figure each horizontal line indicates the temperature gradient across the transfer bridge within the scanning time per line of 4.1 ms. The lower curve in Fig. 3 shows the gradient in x - y -notation for the indicated line. The sine wave depicted on the left-hand side shows the temperature variation near the heat sink, the right curve near the heater. Evaluation of these two sine waves yields a phase shift. From Eq. (2) the thermal diffusion can be derived. As related temperature the time averaged temperature of the heater was taken. Fig. 4(b) shows the heat diffusion velocity determined for various temperatures.

6. Discussion

Thermal conductivity and heat diffusivity data of LPCVD grown SiC layers on silicon were measured up to temperatures of 500 °C. In comparison to data measured with macroscopic samples [2] the heat conductivity is found to be 1.2 times smaller than expected. This may be due to varying crystal quality (doping and impurity effects, interface defects because of lattice mismatch of epitaxial β-SiC on [100]-Si-substrate) as well as to increasing surface to bulk ratios. In order to distinguish and to quantify these surface and material influences additional samples with bridges of different surface to volume ratios must be investigated. The thermal diffusivity shows the expected $1/T$ dependence because for high temperatures the number of phonons, and therefore

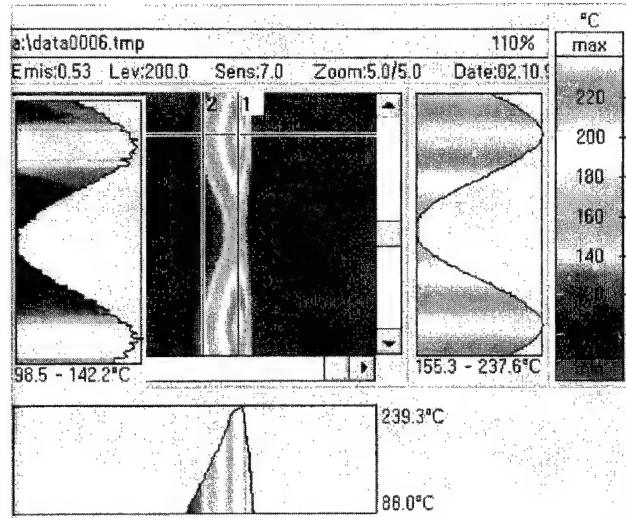


Fig. 3. Time resolved thermographic image of the transfer bridge heated by a sinusoidally modulated current.

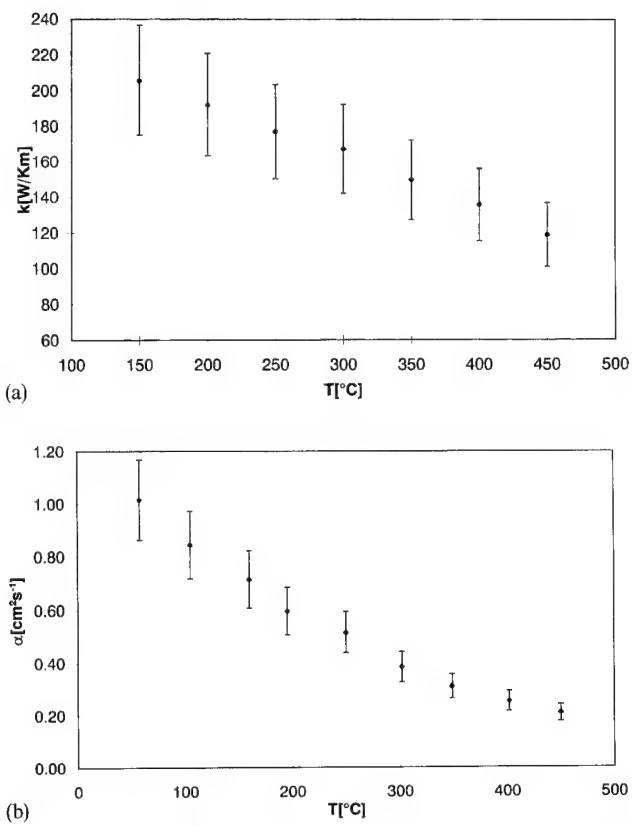


Fig. 4. Results: (a) Heat conductivity and (b) heat diffusion velocity of LPCVD grown β -SiC on silicon in dependence on the temperature.

the phonon collision rate, increases proportionally with T [11].

Acknowledgement

Part of this work has been supported by the BMBF within the project named HOMSIC.

References

- [1] G. Krötz, Ch. Wagner, W. Legner, H. Sonntag, H. Müller, G. Müller, Institute of Physics Conference Series No. 142, Chap. 4, 1996, p. 829.
- [2] Morton International, Woburn, MA, Technical Bulletin # 107.
- [3] Y.S. Touloukian, C.Y. Ho, Thermophysical Properties of Matter, The TPRC Data Series, IFI Plenum Data Corp., New York, Thermal Diffusivity, vol. 10, 1973.
- [4] C.H. Mastrangelo, Yu-Chong Tai, R.S. Muller, Sensors and Actuators, A21–A23 (1990) 856–860.
- [5] C. Wagner, G. Krötz, H. Sonntag, H. Müller, W. Hellmich, G. Müller, Transducers '95, Eurosensors IX, Stockholm, Digest of Technical Papers, vol. 2, 280-A11, p. 194.
- [6] E. Jansen, O. Dorsch, E. Obermeier, W. Kulisch, Diamond Relat. Mater. 5 (6–8) (1996) 644.
- [7] S.M. Sze (Ed.), VLSI Technology, McGraw-Hill, Singapore, 1985.
- [8] G. Krötz, W. Legner, G. Müller, H.W. Grueninger, L. Smith, B. Leese, A. Jones, S. Rushworth, Material Science and Engineering B29 (1995) 154.
- [9] C. Richter, K. Esperthshuber, C. Wagner, M. Eickhoff, G. Krötz, E-MRS Spring Meeting, Strasbourg, 1996.
- [10] G.A. Slack, S.F. Bartram, J. Appl. Phys. 46 (1) (1975) 89.
- [11] C. Kittel, Introduction to Solid State Physics, 3rd edition, New York, 1967.
- [12] N.W. Ashcroft, N.D. Mermin, Solid State Physics, International Edition, Japan, 1981.

Valence band dispersion of hexagonal SiC

G. Wellenhofer, U. Rössler *

Institut für Theoretische Physik der Universität Regensburg, 93040 Regensburg, Germany

Abstract

We describe the spin-dependent electronic dispersion close to the valence band maximum of 2H-, 4H-, and 6H-SiC. Using spin-independent band structure calculations within the density functional theory (DFT) in the local density approximation (LDA) we determine all parameters of the invariant Hamiltonian for the valence bands of the hexagonal polytypes except for the value of the spin-orbit coupling which we take from experimental data. Based on this spin-dependent valence band structure and alternatively on the spin-independent DFT-LDA dispersion we calculate the density of states with the quadratic tetrahedron method and compare it to the density of states related to parabolic valence bands. Finally, we calculate the carrier density for different acceptor levels and acceptor densities and determine their temperature dependence. © 1997 Elsevier Science S.A.

Keywords: Electronic band structure; Spin orbit interaction; Carrier density of pSiC

1. Introduction

The valence band structure of a semiconductor is prerequisite for studying the motion of holes and the calculation of carrier densities. Its knowledge is thus important, e.g. in order to design semiconductor devices. At present, there are only a few calculations for SiC which provide information about the valence band structure such as the effective hole masses [1,2] or the crystal field splitting parameter A_{cr} [2–4]. Moreover, as the electronic states close to the valence band maximum at the Γ point have non-negligible probability density close to the constituent atoms these states are split due to the spin-orbit interaction [1]. Although, for SiC the influence of the spin-orbit interaction on the valence band dispersion is considered to be small (because both Si and C are light elements) we want to analyze this effect on hexagonal SiC. Based on spin-independent ab initio calculations within the density functional theory (DFT) in the local density approximation (LDA) we determine the parameters of an invariant Hamiltonian [5,6]. The spin-orbit parameter A_{so} is taken from experimental data. The dispersion obtained from this Hamiltonian is used to calculate the density of states (DOS) with the quadratic tetrahedron method [7] and the carrier concentration for different acceptor levels and acceptor densities.

2. Theory

In our DFT-LDA calculations for the valence band structure of hexagonal SiC we apply the same approach as in previous work on structural and electronic properties of SiC [8]. We use a plane wave expansion, the parameterization of Perdew and Zunger for the exchange-correlation potential [9], and the method of Martins and Troullier for generating soft pseudopotentials [10]. \mathbf{k} -space integration is performed with 12 special points [11] in the irreducible part of the Brillouin zone. Details about the determination of the lattice parameters can be found in [8]. The obtained valence band structure of SiC is used in order to determine constants entering the invariant Hamiltonian which in addition contains also the spin-orbit interaction.

The invariant Hamiltonian [5,6] for the three topmost valence bands in crystals with hexagonal symmetry which considers terms up to second order in \mathbf{k} and the spin-orbit interaction contains seven mass parameters A_i ($i=1-7$) and three energy splitting parameters A_i ($i=1-3$). A_1 can be identified with the crystal field splitting A_{cr} and A_2 and A_3 are related to the energy splitting induced by the spin-orbit interaction. Without the spin-orbit interaction ($A_2=A_3=0$) the valence band dispersion reads—in the case of $A_1>0$ —for the directions parallel \parallel and perpendicular \perp to the k_z -axis and for the (101) direction (denoted by xz)

* Corresponding author.

$$E_{hh}(k_\perp) = \Delta_1 + k_\perp^2(A_2 + A_4 - A_5) \quad (1)$$

$$E_\pm(k_\perp) = \frac{1}{2} \left\{ \Delta_1 + k_\perp^2(2A_2 + A_4 + A_5) \right. \\ \left. \pm \sqrt{\Delta_1^2 + k_\perp^2(8A_7^2 + 2A_4\Delta_1 + 2A_5\Delta_1) + k_\perp^4(A_4 + A_5)^2} \right\}$$

$$E_{hh(lh)}(k_\parallel) = \Delta_1 + k_\parallel^2(A_1 + A_3)$$

$$E_{\text{split}}(k_\parallel) = k_\parallel^2 A_1$$

$$E_{hh}(k_{xz}) = \Delta_1 + \frac{1}{2}k_{xz}^2(A_1 + A_2 + A_3 + A_4 - A_5)$$

$$E_\pm(k_{xz}) = \frac{1}{2} \left\{ \Delta_1 + \frac{1}{2}k_{xz}^2(2A_1 + 2A_2 + A_3 + A_4 + A_5) \right. \\ \left. \pm \sqrt{\Delta_1^2 + k_{xz}^2(4A_7^2 + \Delta_1(A_3 + A_4 + A_5))} \right\}$$

The subscripts hh, lh and split refer to the heavy hole, light hole and crystal field split-off bands, the subscript \pm means lh (+) and split (−), respectively. Including the spin-orbit interaction, these bands are denoted with decreasing order of energy by A , B , and C , respectively.

Including spin-orbit interaction ($\Delta_2 = \Delta_3 \neq 0$) the energy differences $E_A - E_B$ and $E_A - E_C$ at $\mathbf{k}=0$ only depend on the energy splitting parameters Δ_i . Identifying Δ_1 with Δ_{cr} and using the cubic approximation $\Delta_2 = \Delta_3 = 1/3\Delta_{so}$ [5,6] we can expand these differences in second order of Δ_{so}/Δ_{cr}

$$E_A - E_B = \frac{2}{3}\Delta_{so} - \frac{2}{9}(\Delta_{so}^2)/(\Delta_{cr}^2)\Delta_{cr},$$

$$E_A - E_C = \Delta_{cr} + \frac{1}{3}\Delta_{so} + \frac{2}{9}(\Delta_{so}^2)/(\Delta_{cr}^2)\Delta_{cr}$$

because Δ_{so} is much smaller than Δ_{cr} . Experimental values for Δ_{so} in hexagonal and rhombohedral SiC of about 7 meV [12–15] are used as the value of the spin-orbit interaction in the invariant Hamiltonian. Thus, all constants of this Hamiltonian are determined and the valence band dispersion and the DOS including the spin-orbit interaction can be studied.

Concerning the calculation of carrier densities for p-SiC we assume that the number of holes is determined by thermal equilibrium between the density of ionized acceptors N_a^- and the density of holes p in the valence bands, $N_a^- = p$. Both carrier densities are ruled by the Fermi function f

$$N_a^- = N_a f_\mu^g(E_a, T); p = \int_{-\infty}^{E_V} D(E)(1-f_\mu(E, T)) \quad (2)$$

with

$$f_\mu^g(E, T) = \frac{1}{1+ge^{(E-\mu)/(kBT)}} \text{ and } f_\mu(E, T) = \frac{1}{1+e^{(E-\mu)/(kBT)}}$$

The Fermi distribution of the acceptor level is modi-

fied by the factor $g=4$ which takes a four-fold degeneracy of the acceptor level ($E_A \approx E_B$) into account [16]. Here, μ is the chemical potential. N_a is the acceptor density, E_V the valence band maximum, and E_a the acceptor level. It turns out that for $g=2$ (assuming a two-fold degeneracy of the acceptor level because $E_A > E_B$) the carrier concentrations is increased by most a factor of $\sqrt{2}$ at a given temperature.

3. Results

By fitting the expressions of Eq. (1) to our DFT-LDA band structure (an example is shown for 6H-SiC in Fig. 1(c), dotted lines) we obtain the parameters $\Delta_1 \dots \Delta_7$ and $\Delta_1 = \Delta_{cr}$ of Table 1. The mass parameters $A_1 \dots A_6$ of the hexagonal polytypes are very close to each other. The mass parameter A_7 (which was not set to zero as in a similar study for AlN and GaN [6])

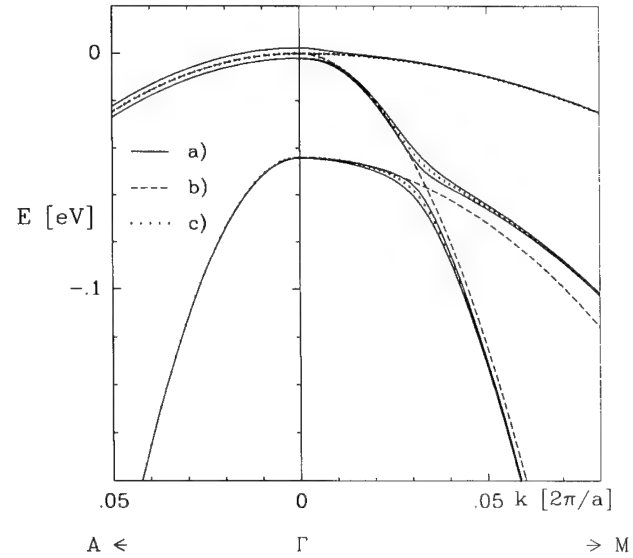


Fig. 1. Valence band dispersion of 6H-SiC. (a) Invariant theory, (b) parabolic approximation, (c) DFT-LDA.

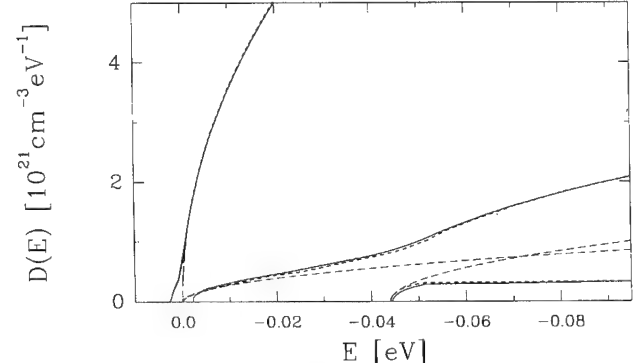


Fig. 2. Density of states of 6H-SiC. Solid lines: invariant theory, dotted lines: DFT-LDA, dashed lines: parabolic approximation.

Table 1

1-Dimensionless mass parameters A_i and crystal field splitting A_{cr} in meV of 2H-, 4H-, and 6H-SiC

	A_1	A_2	A_3	A_4	A_5	A_6	A_7	A_{cr}
2H-SiC	-4.83	-0.576	4.18	-1.24	-1.41	-1.49	0.0232	144
4H-SiC	-4.76	-0.628	4.14	-1.11	-1.45	-1.49	0.0127	74
6H-SiC	-4.76	-0.590	4.14	-1.15	-1.50	-1.34	0.0119	44

increases with the hexagonality parameter h . The value for the crystal field splitting A_{cr} scales almost linearly with h .

The dashed lines in Fig. 1 show the parabolic approximation to the expressions of Eq. (1) which allow to define band masses in terms of $A_1 \dots A_7$ and A_1 . These masses which are sometimes quoted in the literature [2,6] are shown in Table 2 (the masses of Ref. [2], however, do not reflect the hexagonal symmetry, e.g. different masses are given for the directions ΓM and ΓK). They should not be mixed with effective hole masses representing the curvature of the real valence bands close to the valence band maximum as they are obtained without considering the spin-orbit interaction [17]. As can be seen in Fig. 1 the parabolic dispersion (dashed lines (b)), however, is pretty close to case (c) (DFT-LDA calculations without spin-orbit interaction) and case (a) (solid lines, obtained by diagonalizing the invariant Hamiltonian including the spin-orbit interaction) except for the anticrossing and the topmost part close to the valence band maximum. The solid lines in

Fig. 1 show the removal of spin degeneracy in the second and third valence band along ΓM .

The DOS of 6H-SiC for the valence bands A, B, and C calculated with the quadratic tetrahedron method is depicted in Fig. 2. The spin degeneracy due to time reversal symmetry is considered. Solid (dotted) lines are obtained from calculations based on the invariant theory (DFT-LDA) and dashed lines from effective mass approximation. Except for energies near the band edges the DFT-LDA densities of states are close to the densities including the spin-orbit interaction. While the DOS of the A band follows a square-root dependence (dashed and dotted lines coincide) we find for the B and C bands deviations of the DOS in the parabolic approximation (dashed lines) from DFT-LDA results and invariant theory due to the neglect of the anticrossing effect. Taking the sum of the DOS of band B and C, however, this deviation is less significant. Beyond the k -and energy range presented in Fig. 1 we continue the DOS with a slope, given by the mean curvature of the DFT-LDA valence bands. The parabolic approxima-

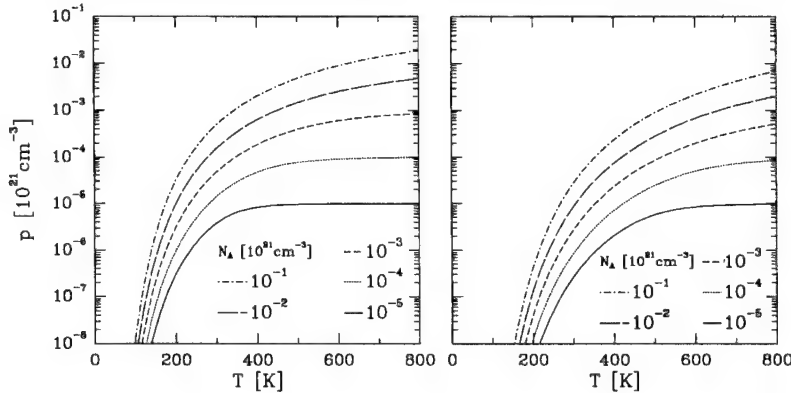


Fig. 3. Carrier density for acceptor levels 250 meV (left part of the figure) and 400 meV (right part of the figure) above the valence band maximum for different acceptor densities.

Table 2

Spin-independent effective hole masses and their relation to the mass parameters A_i

	2H-SiC	4H-SiC	6H-SiC
$m_{hh;hh}^{\parallel}/m_0 = (-A_1 - A_3)^{-1}$	1.5	1.6	1.6
$m_{\text{split}}^{\parallel}/m_0 = (-A_1)^{-1}$	0.20	0.21	0.21
$m_{hh}^{\perp}/m_0 = (-A_2 - A_4 + A_5)^{-1}$	2.4	3.6	4.1
$m_{lh}^{\perp}/m_0 = (-A_2 - A_4 - A_5 - 2A_7^2/A_1)^{-1}$	0.32	0.33	0.32
$m_{\text{split}}^{\perp}/m_0 = (-A_2 + 2A_7^2/A_1)^{-1}$	1.5	1.6	1.4

tion, i.e. the effective masses (Table 2) are in excellent agreement with this mean curvature for bands B and C. However, the slope of band A for the direction perpendicular to the k_z -axis becomes smaller with decreasing energy. Therefore, the carrier densities using the parabolic approximation overestimate the carrier densities given by the DOS described above. Between 200 and 800 K, the differences are smaller than 4%, 6% and 9% for acceptor densities 10^{16} , 10^{18} and 10^{20} cm^{-3} , respectively. In Fig. 3 we show the temperature dependent carrier density of 6H-SiC for acceptor levels 250

and 400 meV above the valence band maximum calculated from the DOS including spin-orbit interaction (solid lines of Fig. 2). In order to analyze the temperature dependence of the carrier concentration we define the temperature $T_{1/2}$ at which half of the acceptors is excited. The closer the acceptor level is to the valence band maximum and the smaller the acceptor density the lower is this temperature $T_{1/2}$. For $E_a = 250$ meV it increases for densities 10^{16} , 10^{17} , 10^{18} , 10^{19} , and 10^{20} cm $^{-3}$ from 320, 410, 555, 825, to 1410 K and for $E_a = 400$ meV for the same densities from 325, 610, 800, 1150 to 1875 K. These numbers are changed by less than 5 K if the DFT-LDA density of states or the DOS referring to parabolic approximated bands are used. This accounts for the reliability of both approximations.

References

- [1] M. Willatzen, M. Cardona, N.E. Christensen, Phys. Rev. B 51 (1995) 13150.
- [2] P. Käckell, B. Wenzien, F. Bechstedt, Phys. Rev. B 50 (1994) 10761.
- [3] C.H. Park, B.-H. Cheong, K.-H. Lee, K.J. Chang, Phys. Rev. B 49 (1994) 4485.
- [4] A. Qteish, V. Heine, R.J. Needs, Phys. Rev. B 45 (1992) 6534.
- [5] G.L. Bir, G.E. Pikus, Symmetry and Strain-induced Effects in Semiconductors, Wiley, New York, 1974.
- [6] M. Suzuki, T. Uenoyama, A. Yanase, Phys. Rev. B 52 (1995) 8132.
- [7] M.H. Boon, M.S. Methfessel, F.M. Müller, J. Phys. C 19 (1986) 5337.
- [8] K. Karch, G. Wellenhofer, P. Pavone, U. Rössler, D. Strauch, in Proceedings of International Conference on Physics of Semiconductors, D.J. Lockwood (Ed.), World Scientific, Singapore, 1995, p. 401. G. Wellenhofer, U. Rössler, Solid State Commun., 96 (1995) 887. G. Wellenhofer, K. Karch, P. Pavone, U. Rössler, D. Strauch, Phys. Rev. B 53 (1996) 6071. G. Wellenhofer, U. Rössler, in SiC and Related Materials 1995, S. Nakashima, H. Matsunami, S. Yoshida, H. Harima (Eds.), IOPP, Bristol, Philadelphia, 1996, p. 297 and 301.
- [9] J.P. Perdew, A. Zunger, Phys. Rev. B 23 (1981) 5048.
- [10] N. Martins, J.L. Troullier, Phys. Rev. B 43 (1991) 1993.
- [11] D.J. Chadi, M.L. Cohen, Phys. Rev. B 8 (1973) 5747.
- [12] G.B. Dubrovskii, V.I. Sankin, Fizika Tverdogo Tela 14 (1972) 1200.
- [13] R.G. Humphreys, D. Bimberg, W.J. Choyke, Proc. 15th Int. Conf. Physics of Semiconductors, Kyoto, in J. Phys. Soc. Japan Suppl. A 49 (1980) 519.
- [14] R.G. Humphreys, D. Bimberg, W.J. Choyke, Solid State Commun. 39 (1981) 163.
- [15] F. Engelbrecht, J. Zeman, G. Wellenhofer, C. Peppermüller, R. Helbig, G. Martinez, U. Rössler, Phys. Rev. B, in press.
- [16] S.M. Sze, Physics of Semiconductor Devices, Wiley, New York, Chichester, Brisbone, Toronto, Singapore, 1981.
- [17] We would like to emphasize that the mass obtained from the slope along \mathbf{k} differs from the cyclotron mass observed for a magnetic field $\mathbf{B} \parallel \mathbf{k}$ due to the anisotropy of the valence band dispersion (e.g. U.Rössler, Solid State Commun., 65 (1988) 1279).



ELSEVIER

Diamond and Related Materials 6 (1997) 1346–1348

**DIAMOND
AND
RELATED
MATERIALS**

Polytypism and surface structure of SiC

P. Käckell *, J. Furthmüller, F. Bechstedt

*Friedrich-Schiller-Universität Jena, Institut für Festkörpertheorie und Theoretische Optik, Max-Wien-Platz 1,
D-07743 Jena, Germany*

Abstract

Within the framework of density functional theory (DFT) in the local density approximation (LDA) using ultrasoft Vanderbilt pseudopotentials in a plane wave basis we investigate the atomic and electronic structure of 3C SiC(111) and n H SiC(0001) surfaces (1×1 and $\sqrt{3} \times \sqrt{3}$ reconstructions) and of 3C SiC(001̄) surfaces (2×2 reconstructions). Since (111)/(0001) is the natural growth direction, the 3C SiC(111)/ n H SiC(0001) surfaces are of special interest. Atomic geometries of various reconstructions, their relative stability and their electronic structure (surface band structure) are discussed. The theoretical results are compared with available experiments. © 1997 Elsevier Science S.A.

Keywords: Silicon carbide; Surface structure; Theory; First principles calculations

1. Introduction

The understanding of the atomic structure and the electronic (chemical) properties of SiC surfaces is one key ingredient for understanding crystal growth processes. A controlled growth of high quality SiC layers of a defined polytype by homo- and heteroepitaxy is of fundamental interest for many special electronic or optoelectronic applications of SiC (e.g. growth of heterostructures, integrated optical/optoelectronic devices). The interpretation of experimental data is often complicated and ambiguous. Hence there is a need for supplementary theoretical investigations. Parameter-free DFT-LDA calculations serve as a powerful high-quality tool to investigate the atomic and electronic structure of SiC surfaces. In this paper we like to give a short overview of recent results obtained for $\sqrt{3} \times \sqrt{3}$ (and 1×1) reconstructions of Si-terminated 3C SiC(111) and n H SiC(0001) surfaces with additional Si overlayers as well as for 2×2 reconstructions of clean and hydrogenated C-terminated 3C SiC(001̄) surfaces.

2. Theoretical framework

The theoretical framework of our investigations was the density functional theory in the local density approximation. Explicitly we used the Vienna Ab initio Simulation Package (VASP) [1–4] developed at the TU Wien. For our calculations we used (two different)

ultrasoft Vanderbilt pseudopotentials [5] in a plane wave basis corresponding to a cutoff energy of about 20 Ry for the 3C SiC(001̄) surfaces and about 13.2 Ry for the 3C SiC(111)/ n H SiC(0001) surfaces. Our surfaces were modelled by repeated slab geometries using the primitive surface unit cell. For the 3C SiC(001̄) surface we used slabs consisting of 8 layers of atoms and a vacuum region between the slabs being about 6 atomic layers thick (for clean surfaces). For the 3C SiC(111) surfaces we used slabs with 6 double layers of atoms and a vacuum of about the same thickness in the case of a clean surface (less for adsorbate structure). In all cases the atoms of the one half of the slab (which is of no interest) were kept fixed in their ideal bulk positions and all dangling bonds of the corresponding surface were always saturated with hydrogen in order to minimize spurious interactions or charge transfers between the two slab surfaces. For the Brillouin zone sampling we used 16 k -points in the half of the Brillouin zone for the 3C SiC(001̄)(2×2) surfaces and 8 k -points in the half of the Brillouin zone for the 3C SiC(111)/ n H SiC(0001) ($\sqrt{3} \times \sqrt{3}$) surfaces. Tests with more k -points have been performed and we obtained no significant changes in our results.

3. Results and discussion**3.1. C-terminated 3C SiC(001̄) $c(2 \times 2)$ surfaces**

The main results for this surface have already been published elsewhere [6], the aim of the investigation

* Corresponding author.

was to clarify the nature and bonding of the $c(2\times 2)$ reconstruction of C-terminated 3C SiC(001) surfaces. Two possible models were suggested: a staggered C-dimer arrangement with C–C double bonds and C_2 groups with C–C triple bonds in Si bridge sites. By comparing photoelectron spectroscopy data with the calculated surface band structures it could be shown that the triple bonded C_2 groups in the Si-bridges should be the experimentally observed structure. The calculated total energies also favor this model (though the energy differences are very small). Counting the number of C–C, Si–C and Si–Si bonds of these two structures one would expect the opposite result (C–C bonds stronger than C–Si bonds stronger than Si–Si bonds). However, elastic effects might also play a significant role (the C_2 groups fit very well into the Si-bridges whereas the staggered C-dimers introduce a relatively large surface stress). It seems that the C_2 group structure is also kept if one hydrogenizes the surface though after hydrogenization the staggered dimer model should become energetically more favorable. Our suspicion is that (maybe due to large barriers) the primarily formed hydrogenated C_2 groups remain in a metastable state.

3.2. Si-terminated 3C SiC(111) ($\sqrt{3}\times\sqrt{3}$ R30°) surfaces

In many experimental studies a typical finding is that one observes a 3×3 reconstruction for very Si-rich surfaces [7–11]. After depletion of some few Si one observes sometimes a structure exhibiting a diffuse 1×1 LEED pattern [8–11]. The origin of this “unreconstructed” surface is yet absolutely unclear. After depletion of further Si one finally ends up with a $\sqrt{3}\times\sqrt{3}$ reconstruction [7–11] which is commonly attributed to a T_4 -site Si-adatom structure [12,13].

We have investigated the atomic structure and the stability of Si- and C-covered Si-terminated 3C SiC(111) surfaces of varying stoichiometry. In order to investigate possible polytypism effects we performed also calculations for 2H SiC(0001) surfaces. The general outcome was that the qualitative picture does not change at all when changing the underlying polytype (therefore we will focus only on the 3C SiC(111) surfaces here). There are small quantitative changes (of maximum order 0.1 eV) in the relative surface energies.

A cubic termination is always favorable over a hexagonal termination. The energy differences between the surfaces with cubic and hexagonal termination become as a crude rule of thumb the smaller the larger the adsorbate coverage. However, there remains always an energy difference of larger about 0.1 eV in favor of a cubic termination. From this we suspect that the selection mechanism determining which polytype is finally grown might be quite complicated. Our calculations

performed at $T=0$ K alone can surely not provide any final information. Inclusion of finite temperature effects is essential for the real understanding of SiC growth and especially of the polytype selection mechanism. Hence we cannot yet discuss such subtle details here. Anyway, we like to demonstrate that a first crude understanding of SiC growth can already be achieved.

Fig. 1 shows the phase diagram for a small selection of possible models for the $\sqrt{3}\times\sqrt{3}$ reconstruction of 3C SiC/nH SiC(0001) surfaces. Over a wide range of Si chemical potentials a T_4 -site Si-adatom structure is clearly favored (in full agreement with previous theoretical work [12]). Only for very Si-rich environments one finds more stable Si-rich structures which can be characterized as Si-adatoms adsorbed on an additional Si-overlayer covering a Si-terminated surface. Though the work on these higher Si-coverages is still in progress the preliminary results point towards a certain “energetical flatness” of the surface, i.e. it seems that there exists no such clear preference for a special adsorption site as in the case of clean surfaces (energy differences of order 0.1 eV between different structures to be compared with 0.5 eV energy difference between the T_4 - and the H_3 -site Si-adatom on the clean surface). So we expect (at least at higher temperatures) some strong structural fluctuations destroying any long-range order, i.e. we suspect that these Si-rich surfaces are related to the sometimes observed “ 1×1 ” structure (the diffuse

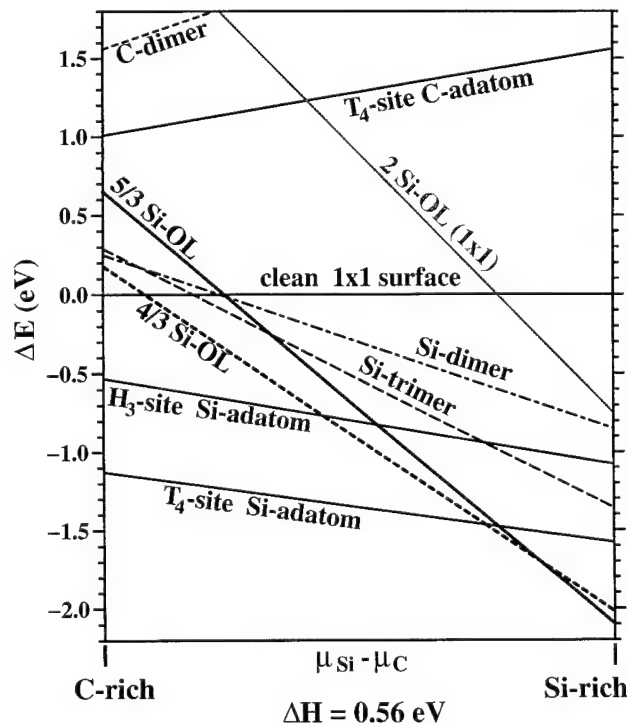


Fig. 1. Phase diagram of possible models of $\sqrt{3}\times\sqrt{3}$ surface structures as a function of the Si (C) chemical potential.

LEED pattern [11] clearly supports the picture of a “disordered” or strongly fluctuating surface).

Furthermore this phase diagram clearly shows that in general the adsorption of Si is clearly favored over the adsorption of C on less Si-rich surfaces. Only for Si-rich surfaces the adsorption of C becomes more and more favorable (at least for more C-rich environments—compare the energetical positions of the Si-rich surface with 4/3 Si-overlayers and of the Si-adatom structure corresponding to 1/3 Si overayers on a clean Si-terminated surface which would be obtained after adsorbing one monolayer of C on the surface with 4/3 Si overayers—there is now a substantial energy gain when adsorbing C). So generally some “two-step” growth mechanism for SiC can be expected (at least if no contaminants of surfactants are present). First one has to expect that some Si overayers grow on a clean/Si-poor surface and it is very hard or even impossible to adsorb C (first step). After reaching a Si-rich surface the adsorption of C becomes then very easy (at least for more C-rich environments) so that finally a Si-overlayer can be transformed into a Si–C bilayer, i.e. finally SiC has been grown (second step). This is consistent with a recent experimental finding of an experimental group [8–11] that very good MBE growth can be achieved if one first grows a very Si-rich surface out of a Si-poor surface (detected by the development of a 3×3 or 1×1 LEED pattern) and then switching (as a second step) to more C-rich conditions finally growing SiC by carbonization of the Si-rich surface (ending up with an again Si-poor surface detected by the observation of a $\sqrt{3} \times \sqrt{3}$ LEED pattern). The incorporation of C seems to be easiest for 3×3 reconstructed surfaces. The very details (on which paths can C reach its final “sub-surface” adsorption site, which barriers have to be overcome, how does all precisely depend on the stoichiometry etc?) have still to be clarified by future work. However, a first qualitative understanding of possible growth scenarios is already possible.

It should be noted that (contrary to the findings described above) one cannot rule out a possible scenario where first C-rich surfaces can be grown which are then enriched with Si. Of course we have only discussed “clean” conditions here (without any presence of surfactants/contaminants). It might be possible that for example the presence of large amounts of H (CVD growth) could change the picture (i.e. stabilisation of C-rich surfaces over Si-rich surfaces due to the higher strength of the C–H bond compared to the Si–H bond). Some future work shall also be dedicated to this important question. Furthermore, one should also note that extremely C-rich surfaces have not been included in this

work (i.e. we do not know where they would appear in the phase diagram).

4. Conclusions

We have shown that triple bonded C_2 groups in Si-bridges are the favorite model for the $c(2 \times 2)$ reconstruction of C-terminated 3C SiC(001) surfaces. Our results for the 3C SiC(111) surface clearly confirm recent findings that a T_4 -site Si-adatom model is the favorite model for the $\sqrt{3} \times \sqrt{3}$ reconstruction of Si-terminated (111) surfaces. For very Si-rich conditions one finds more stable structures (order 4/3 to 5/3 overayers of additional Si adsorbed) which might be related to a sometimes observed “ 1×1 ” structure (randomly distributed adatoms on a Si overlayer). Some first crude understanding of SiC growth can be achieved (“two-step” mechanism) though the very details have still to be clarified.

Acknowledgement

This work was supported by the “Deutsche Forschungsgemeinschaft” within the framework of the “Sonderforschungsbereich 196” (project A8). We thank Bernd Schröter and Andreas Fissel for many helpful discussions. We also gratefully acknowledge the collaboration with Georg Kresse and Jürgen Hafner at the University of Technology in Vienna.

References

- [1] G. Kresse, J. Hafner, Phys. Rev. B 47 (1993) RC558.
- [2] G. Kresse, PhD Thesis, TU Wien 1993.
- [3] G. Kresse, J. Furthmüller, Comput. Mat. Sci. 6 (1996) 15.
- [4] G. Kresse, J. Furthmüller, Phys. Rev. B 54 (1996) in press.
- [5] D. Vanderbilt, Phys. Rev. B 41 (1990) 7892.
- [6] P. Käckell, J. Furthmüller, F. Bechstedt, G. Kresse, J. Hafner, Phys. Rev. B 54 (1996) in press.
- [7] R. Kaplan, Surf. Sci. 215 (1989) 111.
- [8] A. Fissel, U. Kaiser, E. Ducke, B. Schröter, W. Richter, J. Crystal Growth 154 (1995) 72.
- [9] A. Fissel, U. Kaiser, K. Pfennighaus, B. Schröter, W. Richter, Appl. Phys. Lett. 68 (1996) 1204.
- [10] A. Fissel, U. Kaiser, K. Pfennighaus, E. Ducke, B. Schröter, W. Richter, Proc. of Silicon Carbide and Related Materials 1995 Conference, Kyoto, Japan, Inst. of Phys. Conf. Ser. No. 142, IOP, 1996, Chapter 1, p. 121.
- [11] B. Schröter, A. Fissel, private communication.
- [12] J.E. Northrup, J. Neugebauer, Phys. Rev. B 52 (1995) 17001.
- [13] F. Owman, P. Martensson, Surf. Sci. 330 (1995) L639.

Structure and morphology of SiC surfaces studied by LEED, AES, HREELS and STM

U. Starke *, J. Bernhardt, M. Franke, J. Schardt, K. Heinz

Lehrstuhl für Festkörperphysik, Universität Erlangen-Nürnberg, Staudtstraße 7, 91058 Erlangen, Germany

Abstract

Low energy electron diffraction, Auger electron spectroscopy, high resolution electron energy loss spectroscopy and scanning tunnelling microscopy investigations used for structure and morphology determinations of different hexagonal SiC surfaces are presented. The analyses include sample orientation, layer stacking, step morphology, layer spacings as well as the species and coordination of surface terminating adatoms. The samples were prepared ex situ and investigated without further treatment. Predominant ABCACB stacking is found for 6H-SiC(0001) corresponding to a triple step morphology. The surface is covered by hydroxyl species bound to the topmost Si atoms. The surface of a 3C-SiC(111) sample was found to be covered by oxygen on only 50% of the available Si sites. On both surfaces the first bilayer is slightly compressed on an otherwise bulk-like geometry. 6H-SiC(0001) exhibits a single step morphology in agreement with the mixed stacking found on the surface. All three possible surface stacking sequences are present in equal amounts. © 1997 Elsevier Science S.A.

Keywords: Low-energy electron diffraction; Morphology; Silicon carbide; Surface structure

1. Introduction

The physical properties of silicon carbide make it a promising semiconductor material for new applications such as high power and high frequency devices or electronics in high temperature environments. Still the difficulties in growing SiC material of sufficient crystalline and electronic quality have so far prevented a vast commercial development. It is apparent that the surface structure of the substrate plays an important role for the crystallization process. The natural growth plane of SiC is a hexagonal bilayer consisting of alternating Si and C atoms in tetrahedral bond coordination which is the (0001) plane in hexagonal SiC crystals and the (111) plane of the cubic modification. The different polytypes are distinguished by the sequence of linearly stacked and mutually rotated hexagonal bilayers. For a specific polytype surface, different termination domains are feasible distinguished by the topmost stacking sequence. In Fig. 1 the different stacking sequences for 6H and 3C polytypes and the termination possibilities for a 6H surface are shown. The analysis of the surface stacking is a major part of the present study. In addition we

address the distinction between the two possible crystal orientations as well as the determination of surface layer geometries and the identification of possible adatoms and their sites applying scanning tunnelling microscopy (STM), high resolution electron energy loss spectroscopy (HREELS), Auger electron spectroscopy (AES) and quantitative low energy electron diffraction (LEED). In a previous study of 6H-SiC(0001) we found large steps of multiple triple bilayer height, equivalent to odd or even numbers of half 6H unit cells, and the layer stacking sequence could be determined to be ABCACB [1,2]. In the present study we present a refined analysis of this 6H-SiC(0001) allowing for mixtures of domains with different surface termination. Additionally, new results of the hexagonal surfaces of other samples of different polytype and different polarity, that is, 6H-SiC(0001), 4H-SiC(0001) and 3C-SiC(111) are given.

2. Experimental

Samples of either bulk grown Lely material or CVD grown homoepitaxial films were prepared involving dry oxidation, chemical cleaning steps and HF treatment

* Corresponding author. Fax 49 9131 858400;
e-mail: ustarke@fkp.physik.uni-erlangen.de

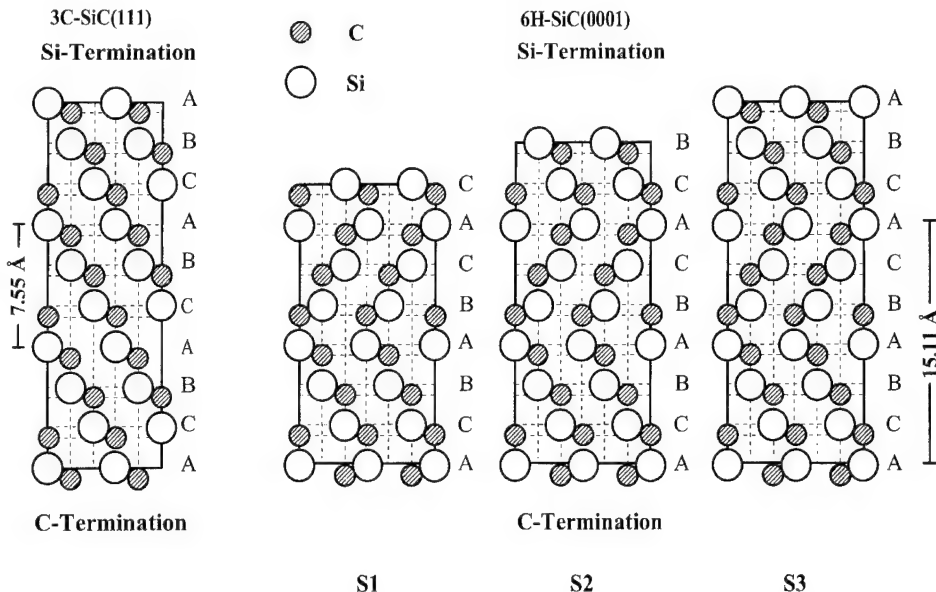


Fig. 1. Cross-sectional view of the linear stacking present in the cubic (3C) polytype (β -SiC) and three different stacking sequences possible at the surface of the 6H polytype. The different surface terminations are labelled according to the depth of the orientation change (S1, CACBABC; S2, BCACBAB; and S3, ABCACBA).

[3]. The 3C-SiC sample used was an epitaxial film grown in (111) orientation on Si(111). By a fast transfer into vacuum recontamination and oxidation of the sample surfaces could be kept to a minimum. In ultra-high vacuum we used different techniques to investigate the surface structure. AES was used to determine the stoichiometry of the surface as well as the presence of adatoms. The complete atomic surface structure was analysed using quantitative LEED. The lateral surface periodicity is immediately related to the periodicity of the diffraction pattern. Atomic positions can be accurately determined by analysing the spot intensities by means of fitting experimental intensity spectra to spectra obtained from model calculations [4,5]. The best-fit model was identified by minimizing the Pendry R -factor [6] calculated between the experimental and theoretical data. Additional information about the nature of dangling bond saturating ad-species was gathered using HREELS to detect their vibrational modes. Finally, STM was used to monitor the step morphology of the surfaces in real space.

3. Surface structure analysis

Immediately after the chemical treatment all samples showed a well ordered LEED pattern. This was found with and without oxidation included in the preparation treatment and was regardless whether 50% HF or buffered NH_4F (pH 7.8) was used. The surface periodicity as judged from the diffraction angles corresponds to the SiC bilayer structure for all polytypes and preparation procedures. Hexagonal and cubic samples can easily

be distinguished by the symmetry of their LEED pattern when the primary electron beam is aligned normal to the surface. A single domain of a specific layer stacking always exhibits three-fold surface symmetry. This gives rise to a three-fold diffraction pattern, where for example, within first order diffraction two groups of three spots, that is, the (10), (1̄1) and (01̄) and the (01), (1̄0) and (11̄) have different intensities. This is indeed the case for the cubic modification which contains only linearly stacked bilayers. However, on surfaces of hexagonal polytype we expect equally weighted domains rotated by 60° with respect to each other illuminated simultaneously by the electron beam. Their intensities add giving rise to the observed six-fold rotational symmetry. Fig. 2 demonstrates this symmetry difference between a 3C-SiC(111) and a 6H-SiC(0001) LEED pattern.

Information about the chemical composition of the surfaces was obtained from AES. We observe oxygen for all ex situ prepared samples. Unfortunately, the Si and C signal does not accurately reflect the SiC stoichiometry due to contamination before the sample transfer. Therefore, the surface polarity, that is, whether (0001) or (0001̄) orientation applies, cannot be determined by AES. Yet, LEED intensity versus energy spectra are very different for the two crystal sides as demonstrated in Fig. 3(a) and therefore can be used as an experimental fingerprint.

As mentioned above, the surface of a 6H-sample may be terminated by three different topmost layer stacking sequences (see Fig. 1), equivalent to different cuts in the ABCACBA... stacking of the crystal. From a new, detailed intensity analysis of LEED diffraction spots of

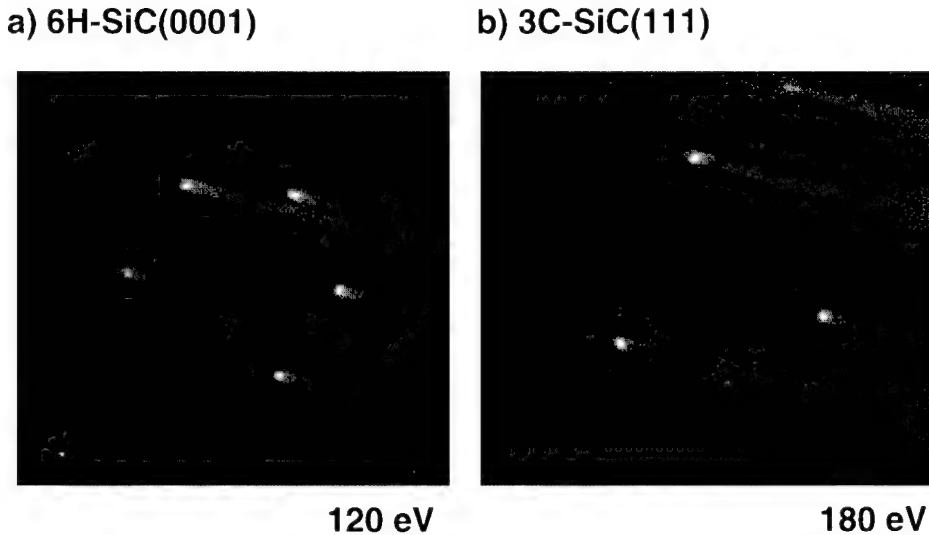


Fig. 2. LEED pattern for a 3C-SiC(111) and a 6H-SiC(0001) sample acquired with normal electron incidence.

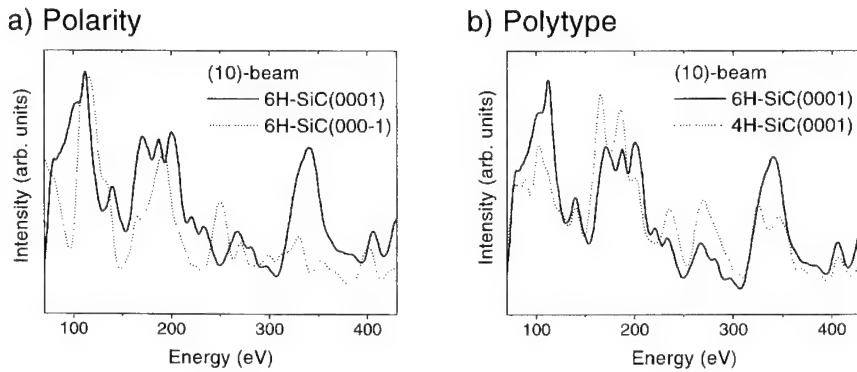


Fig. 3. Experimental LEED intensity spectra of the (10) beam of a silicon (0001) and carbon (000̄1) terminated 6H-SiC sample.

the 6H-SiC(0001) sample we identify the “A” layers to be the predominant (80%) surface layer (S3 stacking in Fig. 1), in agreement with the $n \times 3$ bilayer step heights found in STM [1,7]. An additional layer of oxygen on top of the topmost silicon atoms (the so-called T1 site) was also found in the LEED analysis (bondlength $d_{\text{Si}-\text{O}} = 1.66 \text{ \AA}$). This oxygen obviously represents the hydroxyl species that were detected by vibrational analysis using HREELS [1]. The presence of OH-groups is consistent with the pronounced electron beam sensitivity of the samples causing the LEED pattern to disappear after a few minutes of measurement. The topmost bilayer is compressed to $d_{11} = 0.55 \text{ \AA}$ due to the anisotropic bond coordination of the topmost silicon atom, accompanied by an expansion of the spacing between the first two bilayers ($D_{12} = 1.94 \text{ \AA}$). Other atomic distances were determined to be similar to the geometry in a bulk crystal ($d_{\text{nm}} = 0.63 \text{ \AA}$, $D_{\text{nm}} = 1.89 \text{ \AA}$). Further details of the LEED analysis can be found elsewhere [8]. Experimental intensity spectra of 6H- and 4H-SiC(0001) shown in Fig. 3(b) are not as different as observed for different surface polarities, cf Fig. 3(a). This holds in

particular when a mixture of surface terminating domains is present as shown in our previous theoretical study [2]. A structure analysis of the 4H-SiC(0001) sample has been published elsewhere [9].

On the 3C-SiC sample the linear stacking sequence of the bulk crystal structure is found to extend up to the surface. The three-fold symmetry of the LEED pattern indicates that the crystal contains exclusively a single stacking orientation which is quantitatively corroborated by the intensity analysis. The oxygen found in AES is again bonded in T1 geometry ($d_{\text{Si}-\text{O}} = 1.61 \text{ \AA}$), yet with the oxygen layer incomplete – only 50% of the available Si atoms are covered by adatoms. There is no compression of the topmost bilayer. As in the case of 6H all other layer spacings are unrelaxed.

On the 6H-SiC(0001) surface a predominant stacking sequence ABCACB was found in accordance with step bunching observed by STM. To the contrary, on the 6H-SiC(0001) surface all possible stacking sequences are present in equal amounts as determined by the LEED analysis. A model with a domain mixture yields a far better R -factor ($R_p = 0.20$) than any single domain

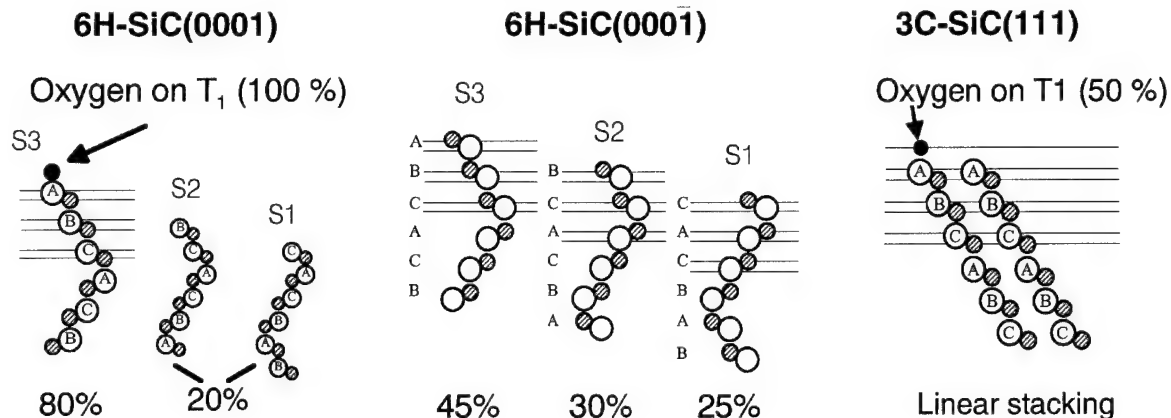


Fig. 4. Surface stacking sequence and adatom coordination obtained from the analyses of 6H-SiC(0001), 6H-SiC(000̄1) and 3C-SiC(111).

model ($R_p > 0.35$). This result indicates a single step morphology for the carbon rich orientation. Different from the other surfaces investigated in this study, on SiC(0001) no oxygen could be found in the diffraction analysis. Possibly, the oxygen detected by AES is disordered or confined to step sites. The topmost bilayer is compressed for all three stacking domains by values between 0.10 and 0.16 Å, while deeper layers are again unrelaxed.

4. Discussion

Using quantitative LEED in combination with AES, HREELS and STM the atomic structures of hexagonal 6H- and 3C-SiC surfaces were analysed. Work for 4H-SiC has been completed recently [9]. In agreement with recent transmission electron microscopy work [10,11], different step morphologies were found for the two orientations of 6H-SiC, that is, triple steps on the (0001) and single steps on the (0001̄) surface. Oxygen is present on all samples after the ex situ preparation. However, it seems that only on the Si orientation the adatoms are positioned in well defined and ordered sites. A summary of the three surface structures with respect to stacking sequences and adatom sites is given in Fig. 4.

LEED can be used as a fingerprinting technique to determine certain aspects of the SiC surface geometry. In particular, the distinction between hexagonal and cubic modifications is possible from the pattern symmetry, while spot intensity spectra can clearly identify the orientation of the sample. The surface stacking sequence can be determined in a full LEED analysis. However,

the intensity differences between different hexagonal polytypes are small and may not allow for an experimental fingerprint distinction.

Acknowledgement

We would like to thank R. Helbig (University of Erlangen), and A. Schöner and N. Nordell (IMC, Kista, Sweden) for providing the different SiC film samples. The work carried out was supported by Deutsche Forschungsgemeinschaft (DFG) through SFB 292. U.S. gratefully acknowledges additional support by DFG (Sta 315/4-2).

References

- [1] U. Starke, C. Bram, P.-R. Steiner, W. Hartner, L. Hammer, K. Heinz, K. Müller, *Appl. Surf. Sci.* 89 (1995) 175.
- [2] J. Schardt, C. Bram, S. Müller, U. Starke, K. Heinz, K. Müller, *Surf. Sci.* 337 (1995) 232.
- [3] W. Kern, D.A. Puotinen, *RCA Review* 31 (1970) 187.
- [4] J.B. Pendry, *Low Energy Electron Diffraction*, Academic Press, London, 1974.
- [5] K. Heinz, *Prog. Surf. Sci.* 27 (1988) 239.
- [6] J.B. Pendry, *J. Phys. C* 13 (1980) 937.
- [7] U. Starke, J. Schardt, P.-R. Steiner, W. Hartner, S. Müller, L. Hammer, K. Heinz, K. Müller, in: P. Varga, F. Aumayr (Eds.), *Proceedings: Symposium on Surface Science 3S'95*, Institut für Allg. Physik, TU Wien, Wien, 1995, p. 11.
- [8] J. Schardt, U. Starke, J. Bernhardt, K. Heinz, *Surf. Rev. Lett.* accepted.
- [9] U. Starke, J. Schardt, M. Franke, *Appl. Phys. A*, accepted.
- [10] T. Kimoto, H. Matsunami, *J. Appl. Phys.* 76 (1994) 7322.
- [11] H. Matsunami, private communication.

Investigation of modified 3C SiC(100) surfaces by surface-sensitive techniques

T. Balster ^a, F.S. Tautz ^a, H. Ibach ^b, J.A. Schaefer ^{a,*}

^a Institut für Physik, TU Ilmenau, PF 100565, D-98684 Ilmenau, Germany

^b Institut für Grenzflächenphysik und Vakuumphysik, Forschungszentrum Jülich GmbH, D-52425 Jülich, Germany

Abstract

We studied 3C-SiC(100) surfaces with various reconstructions by high-resolution electron energy-loss spectroscopy (HREELS), Auger electron spectroscopy (AES), X-ray photoelectron spectroscopy (XPS) and low-energy electron diffraction (LEED). After annealing at 1325 K oxygen desorbs and a Si-terminated (2 × 1) surface is obtained. Subsequent annealing at higher temperatures leads to the sublimation of Si, which results in a carbon-rich c(2 × 2) surface. We exposed (2 × 1) and c(2 × 2) surfaces to atomic hydrogen, and were able to observe the H–Si–H stretching vibration on silicon carbide. © 1997 Elsevier Science S.A.

Keywords: Vibrational spectroscopy; Chemical bonding; Surface characterization; Atomic structure

1. Introduction

SiC, with its outstanding electrical and thermal properties (i.e. its wide band gap, high saturation drift velocity and thermal conductivity), has a great importance in science and technology. In this work we prepared 3C-SiC(100) surfaces by annealing with and without silicon flux. Surfaces were then exposed to atomic hydrogen, using it as an extremely surface-sensitive probe of the atomic structure and stoichiometry in a subsequent HREELS experiment.

2. Experimental

The experiments were partly performed in a UHV chamber equipped with LEED facilities, an electron gun, a Mg/Al X-ray source and a hemispherical analyser for AES and XPS, and partly in a second chamber equipped with an HREELS spectrometer, a cylindrical mirror analyzer (CMA) for Auger measurements, and LEED optics. The base pressure in both chambers was better than 7×10^{-11} Torr, rising up to 2×10^{-8} Torr during sample annealing. The XPS spectra were taken at normal emission. The energy scale was referenced to

the Au 4f level of gold foil mounted on the sample holder. The intensity of the XPS spectra was evaluated by integrating the whole peak after background subtraction according to Shirley [1]. For AES, a primary electron beam energy of 3 keV was used. The Auger spectra were taken with the hemispherical analyser in the constant retardation mode, and subsequently differentiated numerically. LEED pictures were observed at primary beam energies between 60 and 130 eV and stored with a video LEED system. The HREELS spectra were observed at an angle of incidence of 54° with respect to the surface normal. Primary electron energies between 5 and 20 eV were used. The resolution of the spectrometer was set to 40 cm^{-1} (5 meV) in straight-through position.

The 2.5×10^{18} and $4.8 \times 10^{16} \text{ cm}^{-3}$ n-type SiC(100) samples were purchased from Cree Research Inc. These were 3 μm films grown epitaxially on Si(100) substrates. After rinsing in methanol and drying in argon, samples were transferred via load locks into the UHV systems. Sample heating for surface preparation [2] was achieved by electron bombardment. Temperature control was provided by an optical pyrometer. Samples were annealed for 3 min at the temperatures shown in the figures, followed by a gradual decrease of the heating power over a period of 6 min. All experiments were performed at room temperature.

In some cases, surfaces were conditioned by annealing

* Corresponding author. Fax: +49 3677 693205;
e-mail: schaefer@physik.tu-ilmenau.de

in a Si flux [3]. For this purpose, a Si wafer ($0.6 \times 1.8 \text{ cm}^2$) was resistively heated to 1475 K. The deposition rate at a distance of approximately 4 cm from the sample was measured as one monolayer per minute. The sample was heated to 1275 K and kept in the Si flux for 3 min. After this exposure the sample was annealed for a further 3 min and cooled over a period of 6 min. Additional annealing cycles at higher temperatures were performed without the Si flux, as described above.

We exposed $c(2 \times 2)$ - and (2×1) -reconstructed SiC(100) surfaces to atomic hydrogen. For this purpose, molecular hydrogen was introduced into the chamber via a leak valve. The molecules dissociated at a hot tungsten filament ($T=2300 \text{ K}$) placed at a distance of 4 cm in line of sight of the sample.

3. Results and discussion

3.1. Annealing without Si flux

As built in, samples show a (1×1) structure with satellites at the first 1/5th order position. Given the shape of the Si L_{2,3}VV signal, we can deduce that this surface is covered by a silicon suboxide (SiO_x). Also, the Si L_{2,3}VV transition is shifted to lower kinetic energies (as compared to Si in a SiC environment), which is characteristic for this oxidation stage of silicon [4]. After annealing at 1275 K the satellites in the LEED structure have vanished, but no significant changes in the O KLL/C KVV or the Si L_{2,3}VV/C KVV intensity ratio occur (not shown here). This can be interpreted as thermal disordering of the oxide layer. The intensity ratio of O KLL/C KVV is reduced after annealing at 1325 K. At the same time, the reconstruction changes to (2×1) in two domains with diffuse half-order spots. The Si L_{2,3}VV/C KVV ratio increases and reaches its maximum of 3.8 at an annealing temperature of 1400 K. This supports the notion that oxygen bonds to silicon, because after the desorption of oxygen the uppermost Si layer contributes to the intensity of the unshifted Si L_{2,3}VV transition in the SiC environment. At still higher temperatures the reconstruction changes to $c(2 \times 2)$, the Si L_{2,3}VV/C KVV ratio simultaneously decreasing to a minimal value of around 1.6 at 1475 K. The higher-order spots become more distinct with higher annealing temperatures. The reduction of the Si/C Auger ratio can be explained by sublimation of Si from the surface. The $c(2 \times 2)$ reconstruction is known to be terminated with a monolayer of carbon [5]. This is borne out by the observation of a second C 1s peak at a shifted binding energy of 284.6 eV which is characteristic of carbon–carbon bonds, in addition to the peak at a binding energy of 283.1 eV which is characteristic of C in SiC (not shown here).

We now turn to our HREELS results. We measured

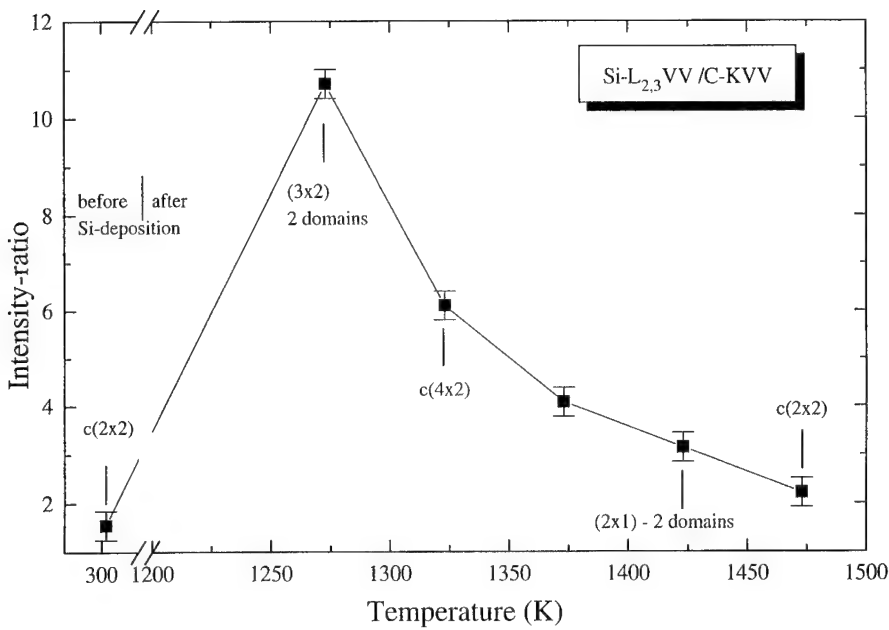
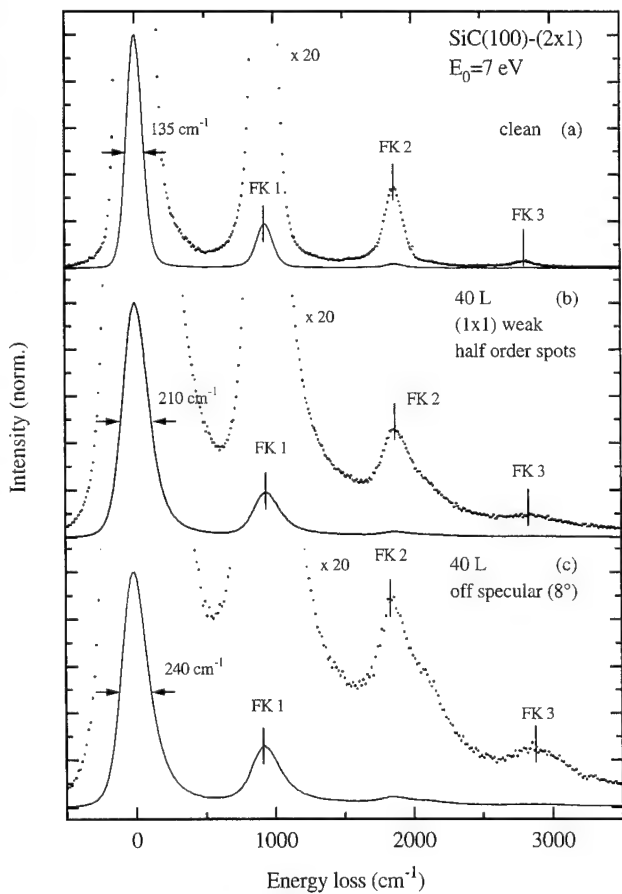
loss features at 945 cm^{-1} (118 meV), 1890 cm^{-1} (236 meV) and 2835 cm^{-1} (354 meV), which can be assigned to the optical surface phonon (Fuchs–Kliewer phonon) and its multiple losses. These frequencies are in good agreement with values at the 3C-Si(111) and 4H/6H-Si(0001) surfaces reported in Ref. [6], 6H-SiC(0001) in Ref. [7], and 3C-SiC(001) reported in Refs. [2,8]. Additionally, at 430 cm^{-1} (54 meV) and 1175 cm^{-1} (147 meV) two different modes of Si–O–Si stretching vibrations occur (not shown here). The frequency of 1175 cm^{-1} can be identified with the asymmetric Si–O–Si stretching mode [9,10]. The peak at 430 cm^{-1} corresponds to a second type of stretching vibration [9,10] which is degenerate with the Si–O–Si wagging mode. The current results on SiC(100) are thus in good agreement with earlier observations on Si(100). It should be mentioned that both Si–O–Si peaks have disappeared after annealing at 1325 K, the temperature around which the intensity ratio O KLL/C KVV is also reduced. The FWHM of the elastically reflected beam increases and reaches its maximum of 190 cm^{-1} (24 meV) after annealing at 1275 K. This is in good agreement with LEED data, implying a disordering of the oxide at this temperature, as mentioned above. At higher annealing temperatures, the FWHM decreases again to 156 cm^{-1} . The intensity of the Fuchs–Kliewer phonon increases relative to the oxygen-covered surface.

3.2. Annealing after deposition of silicon

Starting from the $c(2 \times 2)$ -reconstructed surface, annealing in Si flux at 1275 K makes the C–C bonded peak in the C 1s spectrum disappear. The sample exhibits a (3×2) LEED structure in two domains, the intensity ratio Si L_{2,3}VV/C KVV being at its maximum value of 10.8 (Fig. 1). This structure is known to correspond to a 1.33 monolayer Si-terminated surface [11]. Indeed, the Si 2p peak shows an additional shoulder due to Si in a Si environment. After successive annealing steps the intensity ratio Si L_{2,3}VV/C KVV is reduced again, and reaches a minimum value of 2.3 at 1475 K. In LEED, several surface reconstructions can be observed with rising annealing temperatures (see Fig. 1 for details). Both the $c(4 \times 2)$ and the (2×1) structures are commonly interpreted as representing 1 ML Si-terminated surfaces [11,12]. However, in our investigations all samples show differing surface stoichiometries for these two reconstructions. We note that in a recent theoretical investigation by Sabisch et al. [13] it is claimed that a C-terminated (2×1) reconstruction is energetically favoured over a Si-terminated (2×1) reconstruction.

3.3. Exposure of a (2×1) -reconstructed surface to atomic hydrogen

Fig. 2 shows HREELS spectra for the clean and 40 L hydrogen-exposed SiC (2×1) surfaces. As compared to

Fig. 1. AES Si $L_{2,3}$ VV/C KVV intensity ratio after Si deposition and annealing.Fig. 2. HREELS spectra ($E_0 = 7$ eV) of the SiC(100)-(2x1) surface (a) before and (b, c) after 40 L hydrogen exposure. FK 1–FK 3 are Fuchs–Kliewer phonons. The shoulders on the high energy side of FK 2 in (b) and (c) correspond to the Si–H vibration.

the oxygen-free (1×1) surface, one notices a sharper elastic peak (135 versus 156 cm^{-1}) and lower-intensity Fuchs–Kliewer phonons for the (2×1)-reconstructed surface in Fig. 2(a). Turning to the hydrogen-covered specimens in Figs. 2(b) and (c), one notices a drastic increase of the FWHM of the elastic peak and a simultaneous loss of surface reconstruction in the LEED pattern, which reverts to (1×1). The most notable change, however, is the appearance of a shoulder on the high energy side of the peak denoted FK2. Fitting FK2 and the new structure yields peak positions at 1875 and 2120 cm^{-1} , respectively, in the case of off-specular detection (Fig. 3). The fitting in Fig. 3 was accomplished using two folded Gaussian–Lorentzian peaks, the FWHM of which was determined by the width of the elastically reflected intensity. The frequency of 2120 cm^{-1} is in good agreement with the well-known H–Si–H dihydride stretching mode on Si(100) substrates [14–16], and is therefore assigned to the corresponding dihydride mode on H/SiC(100)-(1×1). To the best of our knowledge, this vibrational mode has been observed for the first time in HREELS on SiC substrates. It confirms that the clean (2×1)-reconstructed surface is indeed Si-terminated. Further results will be published elsewhere.

3.4. Exposure of a $c(2 \times 2)$ -reconstructed surface to atomic hydrogen

The $c(2 \times 2)$ reconstruction was prepared as described above. After exposure to 10^3 Langmuir

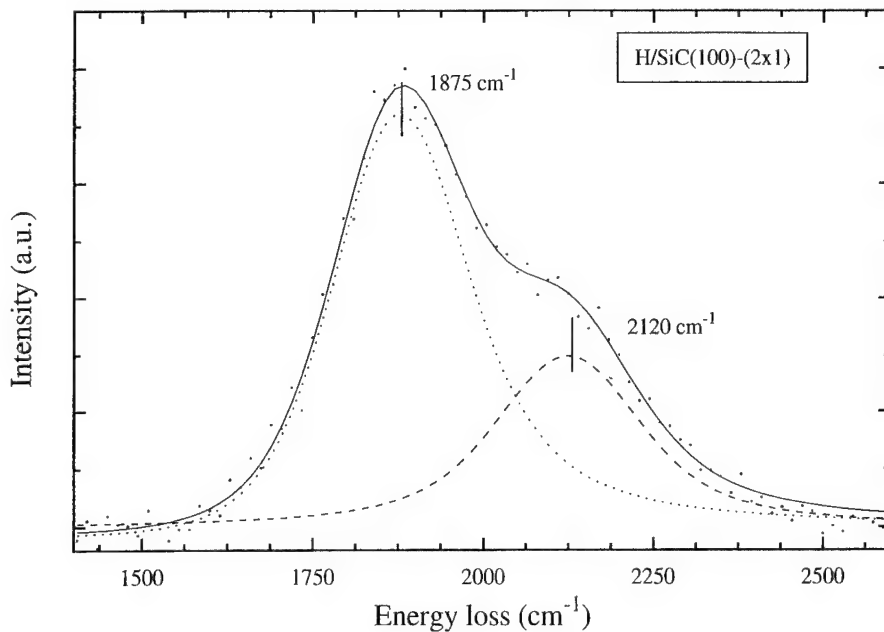


Fig. 3. Results of peak fitting procedure as described in the text for the spectrum of Fig. 2c (8° off-specular detection on 40 L hydrogen-covered surface). The peaks at 1875 and 2120 cm⁻¹ correspond to FK 2 and the Si-H stretching vibration, respectively.

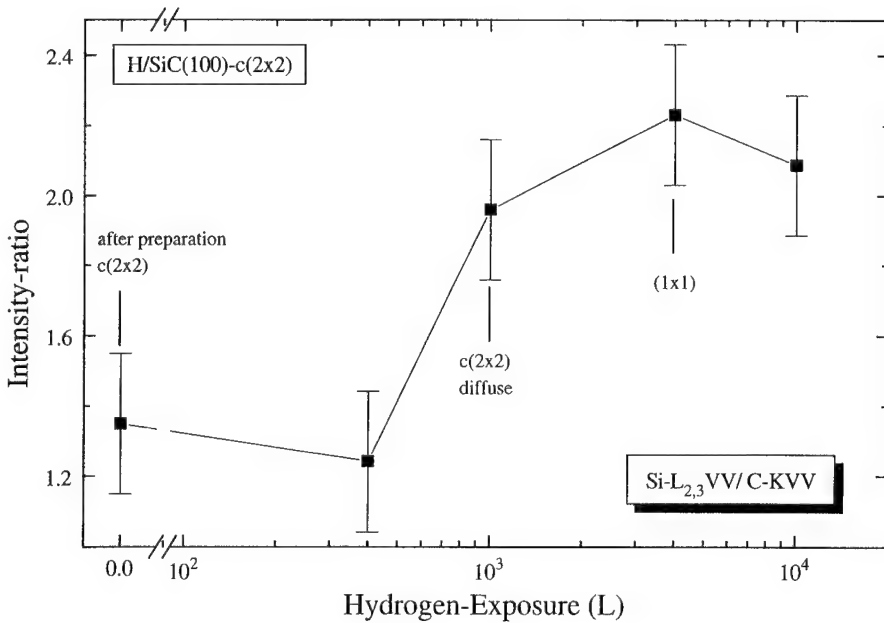


Fig. 4. AES Si L_{2,3}VV/C KVV intensity ratio with increasing hydrogen exposure.

hydrogen the intensity ratio Si L_{2,3}VV/C KVV has risen to 2.0 (Fig. 4), the c(2×2) LEED pattern simultaneously becoming increasingly diffuse. At an exposure of 4×10³ L, the surface reverts to (1×1). This behaviour can be interpreted by the conjecture that up to approximately 10³ L exposure a monohydride forms, thus retaining the surface reconstruction. Beyond this threshold, hydrogen breaks up the bonds responsible

for the reconstruction, and a dihydride with its characteristic (1×1) pattern ensues. For higher exposures, the intensity ratio Si L_{2,3}VV/C KVV increases to a value of 2.2, then remains constant within the error limits. This rise could be interpreted as the removal of carbon due to some etching reaction. However, more work on this point is needed, and will be undertaken in the future.

4. Summary

In this paper we have presented new results pertaining to the adsorption of hydrogen on the 3C-SiC(100) surface. Various reconstructions of the 3C-SiC(100) surface have been obtained by annealing SiC(100) surfaces with or without Si flux. After exposing a (2×1) surface to 40 L hydrogen, we have observed the H–Si–H stretching mode of a (1×1) dihydride phase on 3C-SiC(100). Furthermore, exposing a C-terminated c(2×2) surface to atomic hydrogen, we observed a reduction of the carbon content of the surface in Auger electron spectroscopy, possibly indicating etching reactions.

Acknowledgement

This work was supported by the Deutsche Forschungsgemeinschaft and the Landesgraduiertenförderung Thüringen. We also wish to acknowledge helpful discussions with Dr. S. Lehwald and D. Bruchmann.

References

- [1] D.A. Shirley, Phys. Rev. B 5 (1972) 4709.
- [2] M. Dayan, J. Vac. Sci. Technol. A 4 (1986) 38.
- [3] R. Kaplan, Surf. Sci. 215 (1989) 111.
- [4] B. Carriere, J.P. Deville, Surf. Sci. 80 (1979) 278.
- [5] J.M. Powers, A. Wander, M.A. Van Hove, G.A. Somorjai, Phys. Rev. B 44 (1991) 11159.
- [6] H. Nienhaus, T.U. Kampen, W. Mönch, Surf. Sci. 324 (1995) L328.
- [7] U. Starke, Ch. Bram, P.-R. Steiner, W. Hartner, L. Hammer, K. Heinz, K. Müller, Appl. Surf. Sci. 89 (1995) 175.
- [8] M. Dayan, Surf. Sci. 149 (1985) L33.
- [9] J.A. Schaefer, W. Göpel, Surf. Sci. 155 (1985) 535.
- [10] J.A. Schaefer, J. Electron Spectrosc. Relat. Phenom. 44 (1987) 163.
- [11] S. Hara, W.F. Slijkerman, J.F. van der Veen, I. Ohdomari, S. Misawa, E. Sakuda, S. Yoshida, Surf. Sci. 260 (1992) L196.
- [12] J.M. Powers, A. Wander, M.A. Van Hove, G.A. Somorjai, Surf. Sci. 260 (1992) L7.
- [13] M. Sabisch, P. Krüger, A. Mazur, M. Rohlfing, J. Pollmann, Phys. Rev. B 53 (1996) 1.
- [14] F. Stucki, J.A. Schaefer, J. Anderson, G.J. Lapeyre, W. Göpel, Solid State Commun. 47 (1983) 795.
- [15] J.A. Schaefer, F. Stucki, J. Anderson, G.J. Lapeyre, W. Göpel, Surf. Sci. 140 (1984) 207.
- [16] J.A. Schaefer, Trends Vacuum Sci. Technol. 1 (1993) 417.

Angle resolved photoemission and the band structure of 6H-SiC

M. Hollering ^{a,*}, A. Ziegler ^a, R. Graupner ^a, B. Mattern ^a, L. Ley ^a, A.P.J. Stampfl ^b, J.D. Riley ^b,
R.C.G. Leckey ^b

^a Institut für Technische Physik, Universität Erlangen-Nürnberg, 91058 Erlangen, Germany

^b Department of Physics, La Trobe University, Victoria 3083, Australia

Abstract

Well ordered, unreconstructed, C-terminated surfaces of 6H-SiC(000̄1) were obtained after treatment with a hydrogen microwave plasma. From angle resolved photoemission spectra (ARPES) measured at normal emission for photon energies between 40 and 60 eV valence band energies at the Γ and A critical points of the hexagonal Brillouin zone of 6H-SiC are derived. The boundaries of the ionic gap (9.3 and 10.5 eV) and the total valence band width of 15.5 eV are determined using X-ray excited photoemission spectra. The results are compared with pertinent band structure calculations. © 1997 Elsevier Science S.A.

Keywords: 6H-SiC; Electronic states; Photoelectron spectroscopy

1. Introduction

Silicon carbide (SiC) belongs to a class of materials that emerges on account of their unique properties as a new breed of semiconductors for high power applications which can be operated under adverse environmental conditions such as at high temperature or under high levels of radiation. The 6H polytype of SiC is a well suited candidate in this respect since it displays a thermal conductivity of $3.6 \text{ W cm}^{-1} \text{ K}$ [1], a high breakdown field of $10\,640 \times N_D^{0.142} \text{ V cm}^{-1}$ [2], where N_D is the donor concentration, and has an indirect gap of 3.0 eV [3]. A number of investigations dealing with the surface properties of this material have recently been reported. Little experimental work, however, has been published concerning the electronic band structure. The exception appears to be the recent work of Johansson et al. [4]. In the present paper the results of angle resolved photoemission measurements on the C-terminated unreconstructed surface of 6H-SiC(000̄1) are reported and critical points of the bulk band structure are derived.

2. Experimental

Angle resolved photoemission measurements were performed at the Berlin synchrotron radiation source

(BESSY) in the photon energy range 40–60 eV. The overall energy resolution was 0.25 eV and the angular resolution $\pm 1^\circ$. Angle integrated core and valence band spectra were also performed with a resolution of 0.5 eV using monochromatized Al $K\alpha$ X-rays (XPS, $h\nu = 1486.6 \text{ eV}$). In ultra-high vacuum (UHV) sample temperatures were determined by measuring the temperature of the Ta sample holder with an infra-red pyrometer. The $6 \times 6 \text{ mm}^2$ sample was cut from a 6H-SiC boule (Cree Research Inc.) such that the [0001] direction was perpendicular to the surface. After mechanical polishing, the C-terminated surface was plasma etched in a hydrogen microwave plasma (power 500 W, H_2 pressure $5 \times 10^3 \text{ Pa}$, H_2 mass flow 100 sccm, sample temperature $\sim 800^\circ\text{C}$) for ca 30 min, dipped in diluted HF (5% in deionized water), and transferred into the spectrometer which had a base pressure of $5 \times 10^{-8} \text{ Pa}$. After a 5 min annealing at 700°C a stoichiometric and well ordered (1×1) surface was obtained as judged by XPS. Low energy electron diffraction (LEED) gave a sharp (1×1) pattern with a low background down to electron energies of 30 eV thus confirming the ordered, bulk truncated nature of the sample surface. C 1s, Si 2p and O 1s core level spectra essentially reveal a contamination free stoichiometric surface. An oxygen contamination amounting approximately to an equivalent coverage of one monolayer is ascribed to oxidized areas localized in deep scratches that remained after mechanical polishing

* Corresponding author.

and could not be removed in the course of the plasma treatment.

3. Results and discussion

Fig. 1 shows the angle integrated XPS valence band spectrum of the 6H-SiC crystal. In SiC both Si and C are tetrahedrally coordinated by atoms of the opposite kind, and the structure of the 6H-polypeptide differs from the corresponding zincblende (ZB) structure only with respect to the stacking order of the SiC double layers along [111] or the equivalent [0001] direction. Therefore, due to their close structural similarity it is expected that the density of states (DOS) corresponds to the canonical three peaked DOS of III-V and II-VI compounds [5]. States in the topmost 7 eV are essentially due to the C 2p orbital; the peak at 8 eV can be identified as being of mixed C 2p–Si 3s bonding character, and the broader maximum III around 13 eV is of mixed Si 3s–C 2s character having more weight on the C 2s level [6]. Of course, the spectral features as measured differ from the DOS on account of varying photoemission cross-sections and a lifetime broadening that increases approximately quadratically with binding energy [7]. It is nevertheless possible to derive some salient energies from this spectrum.

Regions I and II are separated from III by the so-called ionic gap. Taking the finite resolution of our measurements and the lifetime broadening into account we place the boundaries of this gap at 9.3 and 10.5 eV, respectively. The uncertainty in these values is estimated to be no more than ± 0.1 eV. The total band width is estimated as 15.5 ± 0.2 eV when the valence band maximum is defined via the extrapolation of the leading edge of the spectrum to the base line.

Fig. 2 shows a series of angle resolved valence band

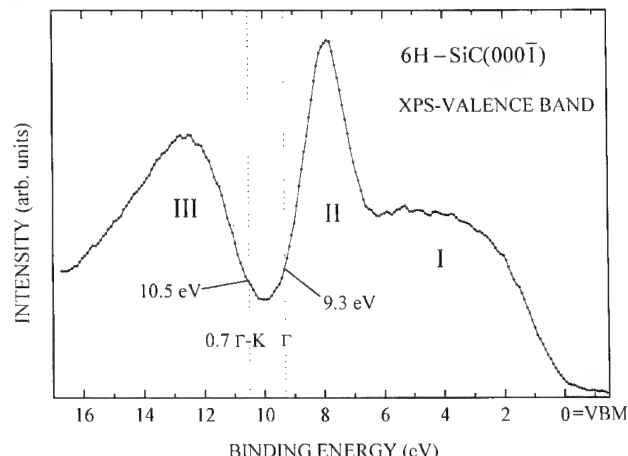


Fig. 1. XPS valence band spectrum. The binding energy is referred to the valence band maximum. The labels I, II and III indicate states with different atomic character as explained in the text.

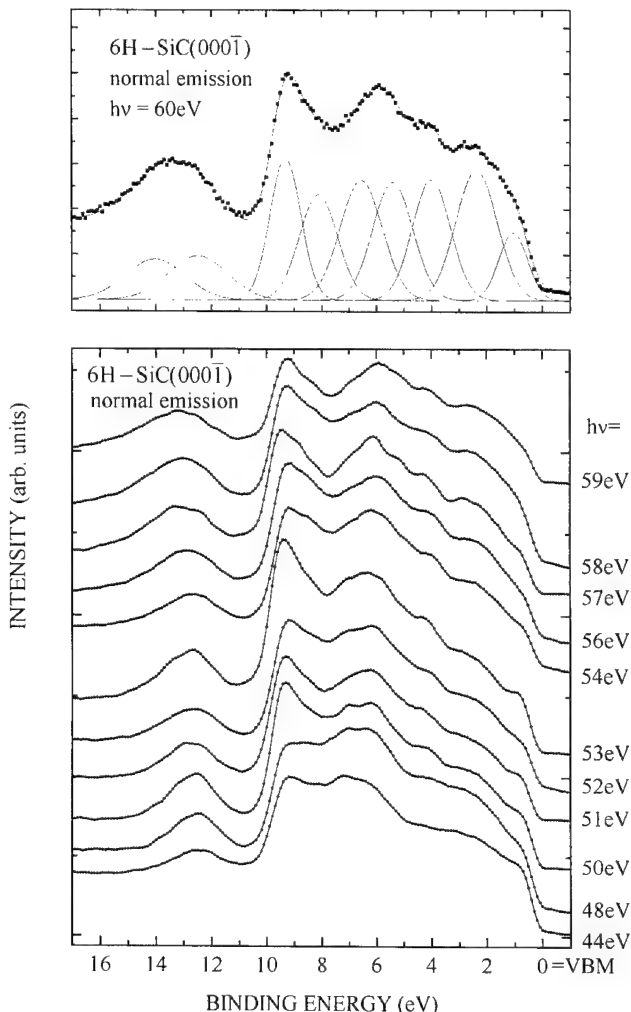


Fig. 2. Normal emission valence band spectra for different photon energies $h\nu$. For the normal emission spectrum at $h\nu=60$ eV there is shown a least squares fit with Gaussian curves. Not shown is an also fitted cubic background.

spectra recorded at normal emission for photon energies between 44 and 60 eV. The structures in these spectra are much sharper than those in the angle integrated data and furthermore vary in intensity with photon energy as expected for direct transitions from different regions in k -space; in fact, all direct transitions are restricted to wave vectors with components ($k_{\parallel}=0, k_{\perp}$) with k_{\perp} lying along the crystallographic [0001] direction. The k_{\perp} component for a particular peak and photon energy in Fig. 2 can be calculated if one makes the usual assumptions of direct, that is, k -conserving, transitions and of free electron final states: $k_{\perp}=\sqrt{2m(E_{\text{kin}}-V_0)/\hbar}$, where $E_{\text{kin}}=h\nu-E_i-\Phi_0$ is the kinetic energy of photoelectrons from a transition with initial energy E_i , Φ_0 is the photoemission threshold, m is the free electron mass, and V_0 is the so-called inner potential which here is defined with respect to the vacuum level. From this kind of analysis the band dispersion along [0001], that is,

between the high symmetry points Γ and A of the hexagonal Brillouin zone can in principle be determined for the occupied valence states.

To this end we have determined the peak positions in the spectra of Fig. 2 either via minima in their second derivatives or through least squares fits. The result was always the same: there is no dispersion of peak positions with photon energies and thus with k_{\perp} .

Lack of dispersion may occur when the unit cell is small and contains many bands as is the case for SiC. Peaks in the spectra would generally reflect an average over many transitions and therefore may reasonably be approximated by the DOS. In Fig. 3 we have plotted the average peak positions as derived from our measurements together with the results of two band structure calculations for 6H-SiC along Γ - A [8, 9]. According to both calculations parts of the band structure along Γ - A can be understood simply by folding the corresponding ZB bands along Γ - L , the [111] direction, back into the Γ - A [0001] direction. This holds in particular for the strongly dispersing split-off band which is twofold degenerate and spans the range from the valence band maximum to the upper boundary of the ionic gap at Γ (equivalent to L in the ZB structure) and again for the s-like band from Γ to Γ (equivalent to Γ - L in ZB) below the ionic gap. These are the only bands which can contribute to the measured spectra for binding energies beyond ~ 1.5 eV. Between VBM and 1.5 eV a

multitude of p-like bands are present which are not shown in Fig. 3.

Both calculations were performed using the Kohn-Sham density functional formalism within the local density approximation (LDA). The one on the left of Fig. 3 is a quasiparticle calculation (QP) and should thus in principle be more appropriate for the interpretation of photoemission data. Indeed, a better agreement with experiment is found as far as the width of the upper half (p and s-p bands) of the band structure is concerned: 9.4 eV for QP versus 8.8 eV for LDA and 9.3 eV from experiment. However, the width of the ionic gap is with 2.4 eV grossly overestimated in the QP calculation whereas the LDA calculation reproduces this quantity reasonably well: 1.3 eV versus the experimental value of 1.2 ± 0.1 eV. For the remainder of the experimental structure a match between peak positions and critical point energies at Γ and A appears to be the most reasonable interpretation with the exception of the peak at 5.6 eV, which is ascribed to emission from the O 2p lone pair orbital. This is more clearly shown in Fig. 4 where we have plotted the experimental peak positions in an extended zone scheme along k_{\perp} superimposed on the two band structures. The extension was chosen so as to correspond to the equivalent ZB structure along that direction. The peak energies are plotted at positions of k_{\perp} which correspond alternately to the Γ and A points in the original hexagonal BZ. It is obvious that

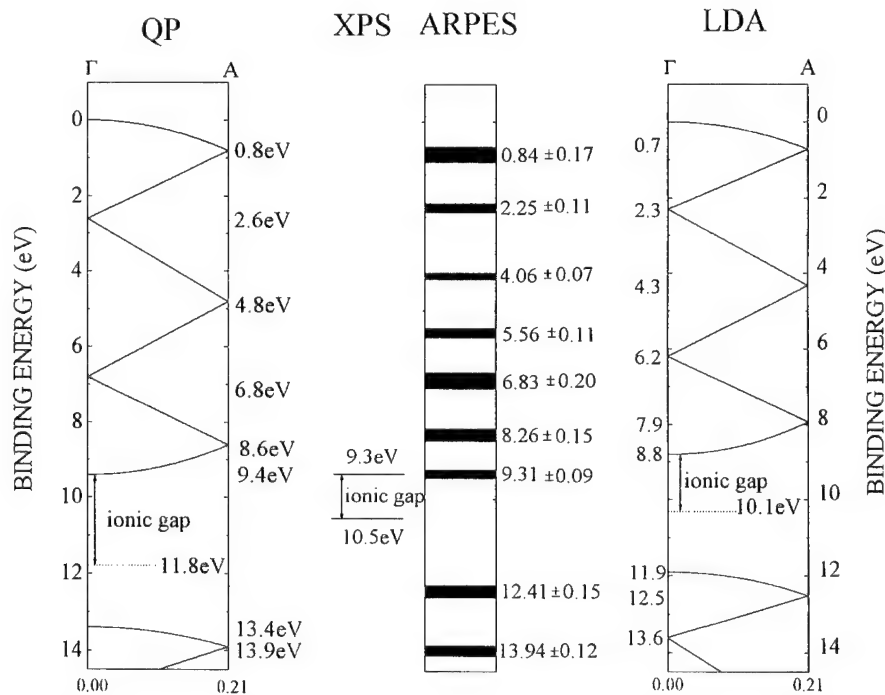


Fig. 3. Comparison of binding energies at the critical points Γ and A as determined by a quasiparticle calculation (QP) [9], by a calculation using the Kohn-Sham formalism in the LDA [8], and by photoelectron spectroscopy in normal emission (ARPES, this work). The width of the lines in the ARPES column indicates the statistical fluctuations of the fitted binding energy values. Also included in this figure are the boundaries of the ionic gap as determined by XPS.

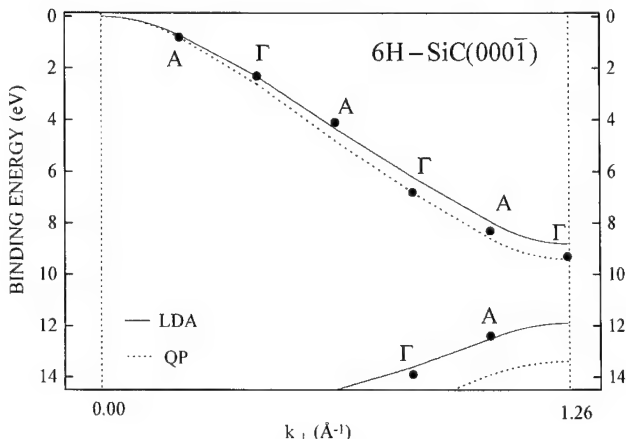


Fig. 4. Experimental peak positions of normal emission spectra plotted in an extended zone scheme. Also shown are calculated band structures (LDA, [8]; QP, [9]). Γ and A denote critical points of the volume Brillouin zone (BZ) of 6H-SiC.

in this way all critical points are covered experimentally with the exception of the VBM and the topmost point of the s-like band starting at ~ 12 eV. Both are expected to have vanishing k -space volume. Moreover, the agreement with the LDA calculation is seen to be overall very good with the exception of states near the bottom of the upper band as mentioned earlier. Note that the ionic gap does not correspond to the band gap at Γ ($k_{\perp}=1.26 \text{ \AA}^{-1}$ in the extended zone scheme) as might be construed from Fig. 3. The lower edge of the ionic gap is rather defined by states with k -vector ca 70% of the way from Γ to K .

4. Summary

We succeeded in preparing well ordered 6H-SiC (000̄1) surfaces by a hydrogen plasma treatment in a microwave discharge with only small amounts of oxygen located in scratches left over from mechanical polishing and therefore not disturbing the smooth crystalline parts

of the surface. From angle integrated XPS valence band spectra we derived the boundaries of the ionic gap as 9.3 and 10.5 eV, and the total bandwidth as 15.5 ± 0.2 eV, respectively. Binding energies of the bulk valence band at the critical points Γ and A of the BZ could be derived from UPS valence band spectra taken along normal emission. These values are in good agreement with theoretical computations (QP [9], LDA [8]).

Acknowledgement

This work was supported by the Deutsche Forschungsgemeinschaft through SFB 292 and the Bundesministerium für Bildung, Forschung, Wissenschaft und Technologie, Contract No. 05 622 WEA 7. We would like to thank the staff of BESSY, especially Dr Walter Braun, for their help during the experiments, and Magdalena Sabisch for her band structure calculations. We also acknowledge the help of Reinhard Stöckel and Klemens Janischowsky who performed the hydrogen plasma preparation.

References

- [1] E.A. Burgemeister, W. von Münch, E. Pettenpaul, J. Appl. Phys. 50 (1979) 5790.
- [2] B.J. Baliga, Springer Proc. Phys. (Germany) 71 (1992) 305.
- [3] W. Choyke, D.R. Hamilton, L. Patrick, Phys. Rev. A 133 (1964) 1163.
- [4] L.I. Johansson, F. Owman, P. Mårtensson, Surf. Sci. 360 (1996) L478.
- [5] L. Ley, R.A. Pollack, F.R. McFeely, S.P. Kowalczyk, D.A. Shirley, Phys. Rev. B 9 (1974) 600.
- [6] L.I. Johansson, F. Owman, P. Mårtensson, C. Persson, U. Lindfèlt, Phys. Rev. B 53 (1996) 13803.
- [7] J. Schäfer, J. Ristein, R. Graupner, L. Ley, U. Stephan, T. Frauenheim, V.S. Veerasamy, G.A.J. Amaralunga, M. Weiler, H. Ehrhardt, Phys. Rev. B 53 (1996) 7762.
- [8] M. Sabisch, Ph.D thesis, Münster, Germany, 1996.
- [9] B. Wenzien, P. Käckell, F. Bechstedt, Phys. Rev. B 52 (1995) 10897.

Topology of twin junctions in epitaxial β -SiC

V. Papaioannou ^a, Ph. Komninou ^a, G.P. Dimitrakopoulos ^a, K. Zekentes ^b, B. Pecz ^c,
Th. Karakostas ^a, J. Stoemenos ^{a,*}

^a Aristotle University of Thessaloniki, Department of Physics, Solid State Section, 540 06 Thessaloniki, Greece

^b Foundation of Research and Technology, Heraklio, Crete, Greece

^c Research Institute for Technical Physics, Hungarian Academy of Sciences, P.O. Box 76, H-1325 Budapest, Hungary

Abstract

The island growth of β -SiC on vicinal (001) Si is studied by HREM and AFM. The initial nuclei have the morphology of tetragonal pyramids. Growth proceeds by a dendritic mechanism resulting in a large density of primary twins and stacking faults. The density of planar defects is reduced dramatically with increasing distance from the substrate. Mutual twin annihilation was studied taking into account interfacial connectivity principles developed recently. The secondary defects that are geometrically necessary for such a mechanism were identified. It has been shown that, for the formation of closed defect topologies, junction lines of planar defects are introduced. This has been verified using computer simulation of HREM images. © 1997 Elsevier Science S.A.

Keywords: Planar defects; Interfacial connectivity; Epitaxial β -SiC

1. Introduction

Material behaviour depends strongly on the internal interfaces such as grain and twin boundaries. The spatial distribution and coexistence of these are subject to the interfacial connectivity principles [1,2]. In this paper the topology of twins in β -SiC grown epitaxially on (001) Si by MBE is investigated. A possible mechanism of twin annihilation, based on experimental observations is proposed. The films were characterised by HREM and AFM.

2. Experimental observations

β -SiC films were grown on (001) Si by MBE. A detailed description of the process is given elsewhere [3]. At early island growth, SiC islands having the morphology of tetragonal pyramids form, with their bases along the in-plane $\langle 110 \rangle$ directions (Fig. 1). Their surfaces are {111} close-packed planes in order to reduce surface energy; at their facet junctions, ledges are often observed which act as sites of preferential adsorption [4]. Growth proceeds by a dendritic mechanism until

island coalescence. As a consequence, a large density of stacking faults and micro-twins emerging from the Si/SiC interface are observed (Fig. 2(a)). These relieve some of the lattice mismatch (20%) by locally destroying the epitaxic orientation; the rest of the relaxation is introduced by misfit dislocations. However, at greater thickness, the planar defects seem to terminate and the film becomes almost monocrystalline [4].

3. Crystallographic analysis and discussion

β -SiC crystallises with the sphalerite structure. In accordance with its symmetry, {111} pyramids are polar with alternating polarity in each facet; the change of polarity is accompanied by the introduction of demisteps at the facet junctions, which promote the dendritic growth by acting as nucleation sites for ledges [4]. The primary (P) twins observed near the Si/SiC interface grow during epitaxial deposition until stopped by another interface or an array of line defects. Therefore, a {111} twin can meet with another of same type but different orientation. In this case, a strain field is formed for which relaxation is only possible via the introduction of a secondary (S) twin segment or the equivalent array of line defects. The junction line of the three twins is a

* Corresponding author.

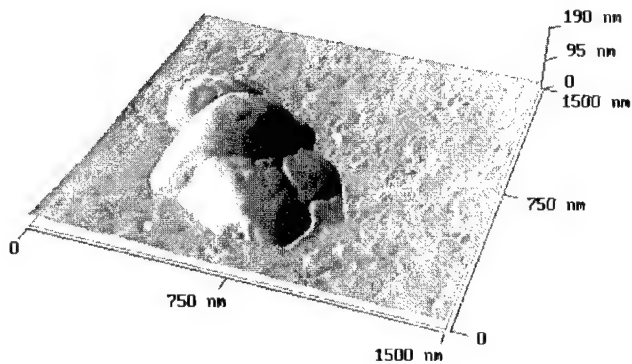
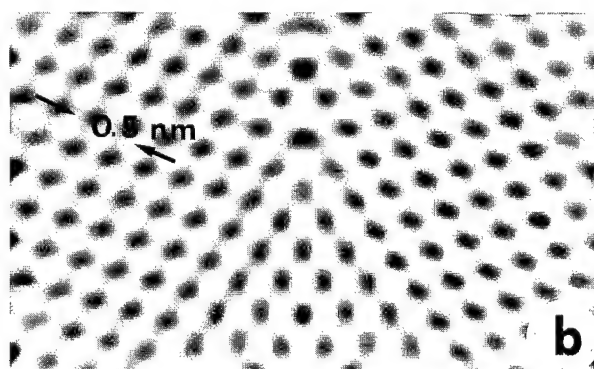
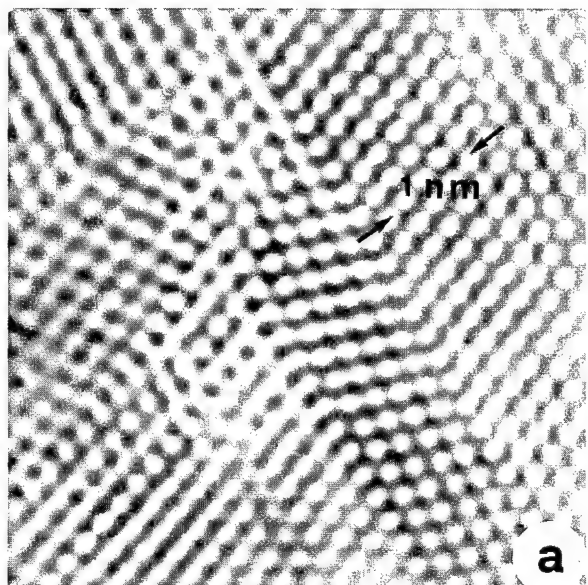
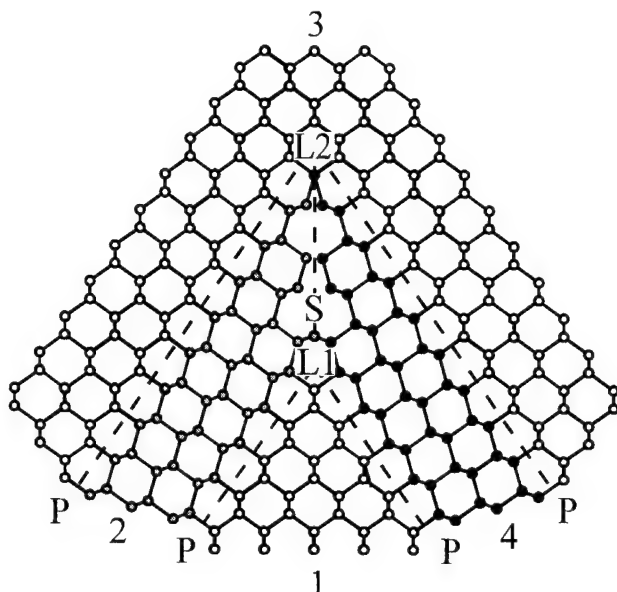


Fig. 1. AFM image of pyramidal SiC islands.

Fig. 2. (a) Cross-sectional HREM image of the epitaxic SiC along $\langle 110 \rangle$. The micrograph exhibits pyramidal twin arrangements and triple junctions. (b) HREM image simulation of one junction line.

triple junction and two such lines are illustrated schematically in Fig. 3. The P twins form initially on the faces of the pyramidal islands, while the S one propagates outwards. In Fig. 3, distinct atomic species are not

Fig. 3. Triple junctions each composed of two primary (P) and one secondary (S) twin boundary (numbers denote distinct crystals). The junction lines (L1, L2) are along the projection direction, i.e. along a $\langle 110 \rangle$ direction in the epitaxic interface. Colouring denotes distinct crystal orientations.

indicated; instead colouring has been used to show distinct orientation relationships of the crystals. Consideration of the interaction with Inversion Domain Boundaries leads to a number of feasible configurations, given elsewhere [4]. Both junction lines in Fig. 3 can be obtained from the same trichromatic complex and hence are symmetry related as explained elsewhere [2]. Such a crystallographic analysis can be used to predict the possible configurations that permit twin annihilation via mutual interaction, as explained below.

According to the observations, twin annihilation occurs for both P and S twins; this can be achieved by nested twin topologies comprising arrangements such as illustrated in Fig. 3, whereby two junction lines are involved. This configuration achieves twin annihilation for the case of the P twins being located on opposite faces of the initial pyramid (i.e. P twins intersecting at acute angle). As shown, a small segment of S twin connects the two junction lines. Fig. 2(a) is the experimental image corresponding to this configuration and similar observations have been made in other diamond-based deposited materials (e.g. [5]). In order to clarify the existence of junction lines, HREM image simulations of an unrelaxed model of one junction line were carried out using the multislice program of the EMS package [6]. The image is shown in Fig. 2(b). Good qualitative agreement is obtained as can be seen by comparing the experimental and simulated images of Figs. 2(a) and (b) respectively.

In the more general case, twinning is expected on all surfaces of the initial nuclei, so that twins may impinge

at obtuse angles, i.e. corresponding to adjacent pyramid faces. For this case, the nested topology corresponds to a hyperpolyhedron [7] as shown in Fig. 4(a) whereby the outer and inner pyramids are made of P twin boundaries and they are interconnected by segments of S twins. Such configurations may be found complete or

partial. In accordance with the above topology is also an elongated prismatic arrangement (Fig. 4(b)) where the two pairs of P twins form an acute angle. The existence of prismatic nuclei is possible due to the difference in energy between {111} surfaces of different polarity [8]. It should be noted that configurations as in Fig. 4 cannot give clear HREM images due to the complexity of their structure. Thus only slices as the one of Fig. 2 can be observed.

4. Conclusions

In this paper nuclei and twins of β -SiC are crystallographically studied. It has been discussed that the tetragonal pyramids exhibit demisteps that can play an important role in film growth. The decrease of twins via mutual annihilation can contribute to the formation of an almost monocrystalline film. Using interfacial connectivity principles, it has been shown that closed twin topologies near the Si/SiC interface can be due to junctions lines. This mechanism can contribute to the reduction of the density of the twins. The secondary defects which result from these topologies are analysed. HREM observations support the existence of these models.

Acknowledgement

The authors gratefully acknowledge support by: EU mobility contract no. ERBCHRX-CT94-0467 (G.P.D., Ph.K. and Th.K.), and EU BRITE EURAM no. BRE2-CT92-0211 (K.Z., V.P. and J.S.).

References

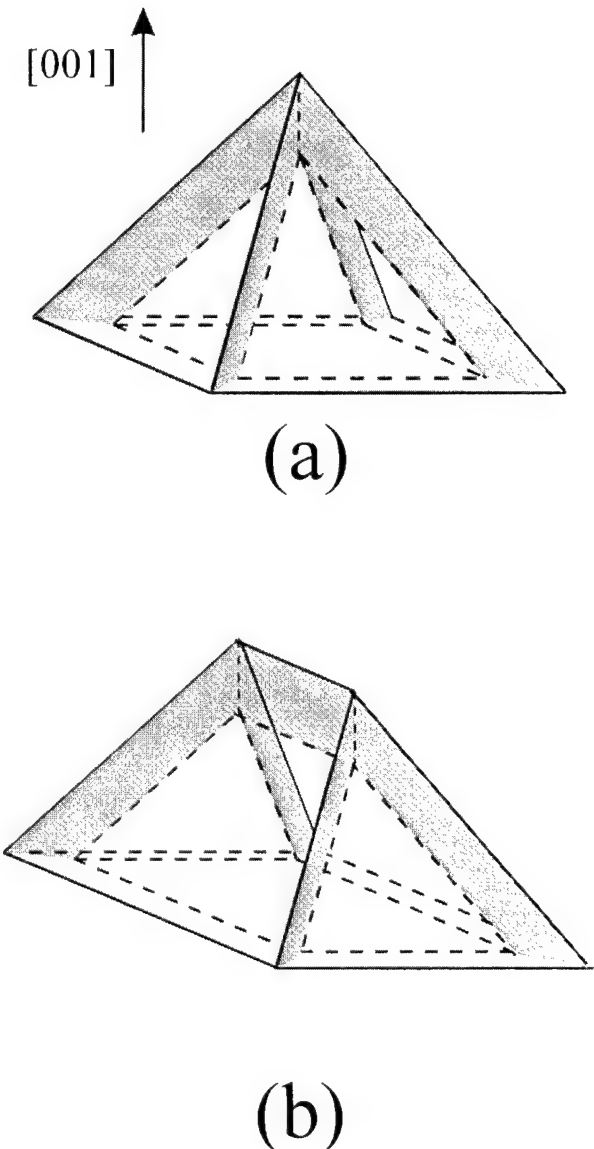


Fig. 4. (a) Nested pyramidal topology. The primary twin boundaries are the faces of the pyramids, while the secondary twin boundaries are shaded. (b) Nested prismatic topology.

- [1] V. Randle, *Acta Metall. Mater.* 42 (1994) 1769.
- [2] G.P. Dimitrakopoulos, Th. Karakostas, *Acta Cryst. A* 52 (1996) 62.
- [3] K. Zekentes, V. Papaioannou, B. Pecz, J. Stoemenos, *J. Cryst. Growth* 157 (1995) 392.
- [4] G.P. Dimitrakopoulos, Ph. Komninos, K. Zekentes, V. Papaioannou, J. Stoemenos, Th. Karakostas, *J. Mech. Beh. Mater.* 7 (1996) 51.
- [5] D. Shechtman, J.L. Hutchison, L.H. Robins, E.N. Farabaugh, A. Feldman, *J. Mater. Res.* 8 (1993) 473.
- [6] P. Stadelmann, *Ultramicroscopy* 21 (1987) 131.
- [7] M.A. Fortes, *Acta Metall.* 34 (1986) 33.
- [8] F. Ernst, P. Pirouz, *J. Mater. Res.* 4 (1989) 834.

Micropipe defects and voids at β -SiC/Si(100) interfaces

R. Scholz ^{a,*}, U. Gösele ^a, E. Niemann ^b, D. Leidich ^b, F. Wischmeyer ^b

^a Max-Planck-Institut für Mikrostrukturphysik, Weinberg 2, D-06120 Halle, Germany

^b Daimler-Benz Forschungsinstitut, D-60528 Frankfurt/Main, Germany

Abstract

The application of an uncommon silicon substrate pretreatment and a carbonization procedure without temperature ramp in a CVD reactor was found to create a new kind of defect besides the usual voids at β -SiC/Si(100) interfaces. SiC-covered micropipes of minute size and of high area densities evolve into the substrate by Si outdiffusion and simultaneous ingrowth of SiC. Results of our systematic investigations of micropipes and voids, obtained mainly by transmission electron microscopy (TEM), are summarized. The micropipe formation is obviously determined by very specific conditions such as, e.g., a high density of SiC nuclei at high carbonization temperatures. Recent new results demonstrate that micropipes together with voids can also develop in carbonization experiments during a relatively slow temperature rise at very low hydrocarbon concentrations. © 1997 Elsevier Science S.A.

Keywords: Carbonization; Silicon carbide; Micropipes; Electron microscopy

1. Introduction

Various deposition methods and numerous variations of experimental parameters have been applied over the last 30 years in order to grow epitaxial β -SiC layers on silicon substrates or to improve layer and interface qualities. Disturbing defects at interfaces SiC/Si well known but difficult to prevent are planar defects of high density in the grown SiC layer arising from the large lattice mismatch, and pyramidal voids within the substrate created by silicon outdiffusion. The formation of voids in CVD carbonization processes seemed to be widely understood in relation to SiC nucleation and layer growth, depending on the hydrocarbon concentration in the reaction gas [1]. Voids described in the literature were directly observed mainly by light or scanning electron microscopy (SEM) [1–4]. Recently [5], using TEM as a method of higher local resolution, in addition to the usual voids a new kind of silicon outdiffusion defect was identified at β -SiC/Si interfaces: micropipes which form by Si outdiffusion and simultaneous ingrowth of SiC. In order to elucidate the reasons for their formation, and of the coexistence of micropipes and voids, short-time carbonization experiments were

carried out. Details of the results and discussions will be given in a forthcoming paper [6]. Here, the essential statements of our observations and interpretations are summarized and discussed in conjunction with the results from some additional experiments.

2. Experiments

On a SiC-coated graphite susceptor within a CVD reactor, (100) Si substrates, 2–4° off-axis, were treated in the following sequence: (i) pretreatment with a H_2 flow of 3.5 slm at 1300 °C for 1 h and subsequent cleaning by H_2 and HCl . (ii) Carbonization with 20 sccm C_2H_4 in 3.5 slm H_2 for 1 min, or less, after the substrate was at high temperatures (1220 °C and 1300 °C, respectively). Total gas pressures of 20 and 80 mbar, resp., were chosen. (iii) In most cases, layer growth followed with C_2H_4 and $SiCl_2H_2$ in H_2 .

In a recent new series of experiments the hydrogen pretreatment was drastically reduced to 5 min at 1000 °C without additional HCl cleaning. Carbonization was initiated during a temperature rise of 200 °C/min. C_3H_8 was used instead of C_2H_4 with very low concentrations in H_2 .

TEM investigations were carried out on different kinds of cross-section and planar specimens using

* Corresponding author. Fax: 49 345 5511 223; e-mail: roscholz@mpi-halle.mpg.de

JEM-4000EX and JEM-100C electron microscopes at 400 and 100 kV, respectively. Complementary SEM investigations on wafer surfaces were made, especially after short-time carbonization experiments.

3. Results

The new micropipes were first detected under SiC layers formed by carbonization and subsequent layer growth. Studying cross-sections under different imaging conditions revealed the pipe nature and a certain nanocrystalline SiC content within the pipes along their walls. Within the substrate, often pipes were detected with bubble-like bulges at their ends. Pipes of different diameters between about 10 and 30 nm were observed after temperature and total gas pressure as carbonization parameters had been varied. The area densities of micropipes were much higher than those of voids, which were occasionally detected in cross-sections. Micropipes were also found protruding from the inner {111} walls of pyramidal voids. The pipes there were always longer and of larger diameter than those under the SiC layer in the respective sample.

The SiC skeleton of micropipes below SiC layers could be imaged in different ways after the surrounding silicon was etched off. In thin cross-section specimens the pipe SiC was then freely hanging down from the SiC layer. Fig. 1 shows a respective example with a high density of pipes partly superimposed near the interface. The figure also shows a pyramidal void with longer pipes connected at the walls. It is obvious also that the inner void walls are coated with a thin SiC layer. Etching free the micropipes under thin SiC layers of planar specimens allowed one to image the lateral distribution of pipes and to determine their area density. Fig. 2 is a plan view image taken at relatively large overfocus. It shows micropipes of high density (about $2 \times 10^{10} \text{ cm}^{-2}$) and, at the top, a group of entangled micropipes at a void. The voids of our samples were relatively small with edge lengths between about 60 and 250 nm.

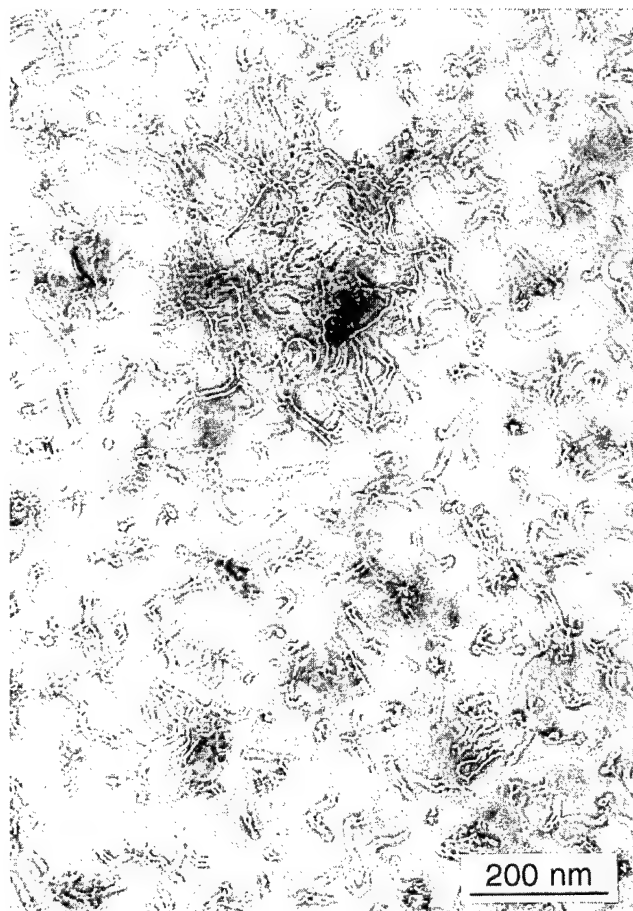


Fig. 2. Plan view (at overfocus) of a thin SiC layer with SiC micropipes interconnected. Above, there is a group of entangled micropipes located at a void.

Short-time carbonization experiments were carried out without further layer growth to elucidate the reasons for micropipe and void formation. After 10 s of carbonization, the initial shapes of micropipes with open SiC-covered craters at the top were found, in addition to voids smaller than before. The voids were already widely bridged by the thin SiC layer grown. Neither SiC growth nor pipe development was detected at the inner void walls. Fig. 3 indicates these structural features. SEM

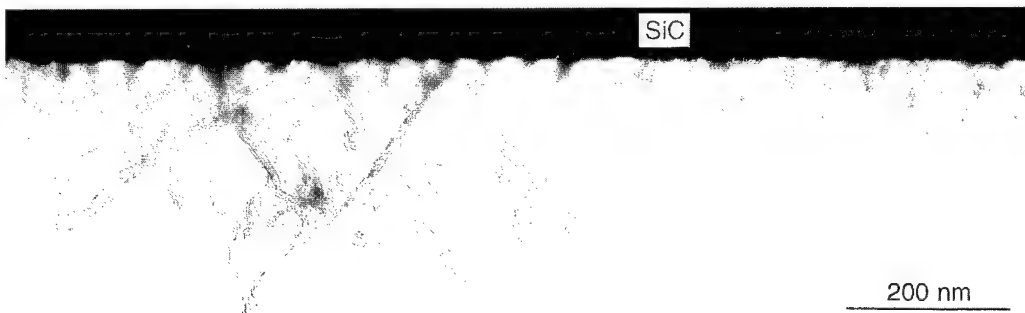


Fig. 1. SiC material of micropipes and of a pyramidal void under a continuous SiC layer after the chemical removal of the surrounding silicon of a cross-section specimen.

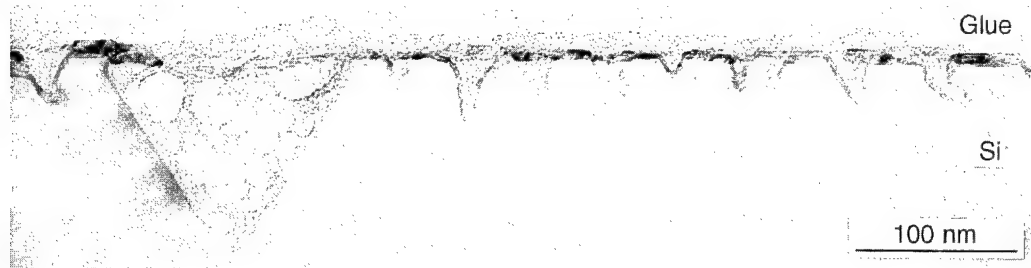


Fig. 3. Cross-section image of a thin SiC layer on Si with initial shapes of micropipes and of one pyramidal void grown during carbonization with C_2H_4 for 10 s at 1220 °C.

imaging of the specimen surface revealed a dense island structure in an advanced coalescence state, and cavities between the islands fitting in size and density to craters at micropipes, and to pipe densities. From this surface structure an extremely high initial nucleation density was concluded, which, however, was not consistent with the carbonization conditions applied, i.e., at high temperatures without a usual temperature ramp. The high nucleation density, which obviously was related to the micropipe density, was attributed to the surface state of the silicon substrates after pretreatment.

Planar and cross-section investigations of substrate surfaces after pretreatments revealed a high density of SiC precipitates in partly epitaxial and non-epitaxial relationship to the substrate. The density of SiC nuclei on the substrate surface was of the same order as the micropipe densities after carbonization. Cross-section studies revealed a certain surface roughness of the substrate, in addition to the SiC nuclei.

The first results from a new series of carbonization experiments mentioned in Section 2 indicate that micropipes (again together with voids) can also develop under these conditions, without SiC nuclei preexisting. Fig. 4 shows micropipes and voids grown during a temperature ramp to 1320 °C and carbonization for 60 s, resulting in pipes of increasing diameter and finally with faceted bulges at their ends. In a subsequent paper it will be shown that the formation of micropipes and of voids can be fully prevented.

4. Discussion

The observations clearly point out that micropipes develop by Si outdiffusion and simultaneous ingrowth of SiC, whereas voids remain empty during Si outdiffusion, being bridged by the SiC layer grown. A model of micropipe formation, explaining a micropipe radius to arise from two diffusion processes, is described elsewhere [5,6]. Variations of the micropipe diameters by changes in the carbonization conditions, the formation of bulges at the end of micropipes and other details of our observations can be interpreted by this model.

A prerequisite to the formation of micropipes is the combination of a high density of SiC nuclei with high carbonization temperatures. The SiC precipitates are assumed to form during our uncommon glow pretreatment of substrates in hydrogen on a carbon-containing susceptor (see Ref. [6]).

The specific prerequisites at substrate surfaces leading to the development of voids are still not completely understood. One possible explanation is discussed in Ref. [6]. However, frequent observations of micropipe features superimposed on areas of voids point to a certain connection of the two processes of defect formation.

Acknowledgement

The authors are grateful to Mrs S. Hopfe and B. Lausch for the skilful preparation of numerous TEM specimens.

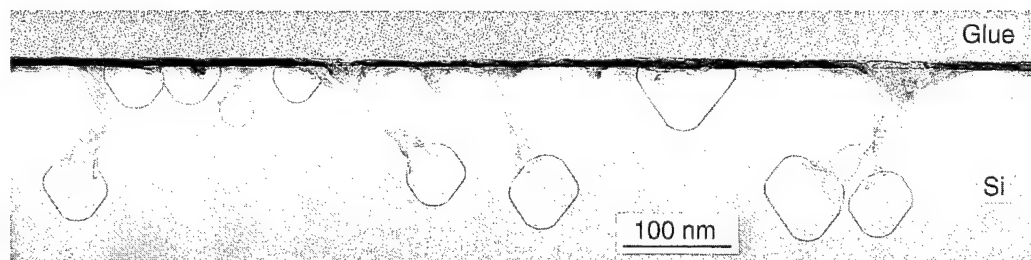


Fig. 4. Cross-section image of a SiC/Si interface and interconnected voids and micropipes with bulges created by C_3H_8 flow during a relatively slow temperature ramp to 1320 °C and further carbonization for 60 s.

References

- [1] J.P. Li, A.J. Steckl, *J. Electrochem. Soc.* 142 (1995) 634.
- [2] A.J. Steckl, J.P. Li, *IEEE Trans. Electron Devices* 39 (1992) 64.
- [3] A. Addamiano, J.A. Sprague, *Appl. Phys. Lett.* 44 (1984) 525.
- [4] H.J. Kim, R.F. Davis, X.B. Cox, R.W. Linton, *J. Electrochem. Soc.* 134 (1987) 2269.
- [5] R. Scholz, U. Gösele, E. Niemann, D. Leidich, *Appl. Phys. Lett.* 67 (1995) 1453.
- [6] R. Scholz, U. Gösele, E. Niemann, F. Wischmeyer, *Appl. Phys. A* 64 (1997) 115.

Wafer warpage, crystal bending and interface properties of 4H-SiC epi-wafers

A. Ellison ^{a,*}, H. Radamson ^a, M. Tuominen ^{a,b}, S. Milita ^c, C. Hallin ^a, A. Henry ^{a,d},
O. Kordina ^{b,d}, T. Tuomi ^e, R. Yakimova ^{a,b}, R. Madar ^f, E. Janzén ^a

^a Department of Physics and Measurement Technology, Linköping University, S-581 83 Linköping, Sweden

^b Okmetic Ltd, P.O. Box 44, FIN-02631 Espoo, Finland

^c European Synchrotron Radiation Facility, BP 220, F-38 043 Grenoble, France

^d ABB Corporate Research, S-721 78 Västeras, Sweden

^e Optoelectronics Laboratory, Helsinki University of Technology, FIN-02150 Espoo, Finland

^f LMGP (CNRS-INPG) ENSPG, BP 46, F-38 402 St-Martin-d'Hères, France

Abstract

The relationship between the warpage of 4H-SiC CVD grown epi-wafers with crystal bending and substrate properties is investigated. The wafer surface preparation before and after epitaxy is found to affect both long range properties such as the wafer flatness and to some extent local properties such as the epi-substrate interface. Structural characterisation is carried out using X-ray diffraction techniques and KOH etching. © 1997 Elsevier Science S.A.

Keywords: X-ray diffraction; Topography; Bending; Interface

1. Introduction

The high figures of merit of silicon carbide are currently driving increased developments in device processing. Even during the development stage on 1.3 in. substrates, the processing of full wafers demands a wafer flatness which can tolerate micron or sub-micron optical lithography patterning. This is especially true for high-frequency and high-power transistor applications. Also, the final quality of the SiC epilayers is expected to be influenced, to a certain extent, by substrate defects and surface preparation before epitaxy. Structural properties, such as the bending and interface quality, of epitaxial layers grown by chemical vapour deposition (CVD) therefore need to be addressed.

2. Experimental procedure

Investigations were carried out on commercial (Cree Research Inc.) 4H (0001) wafers, 350–450 µm thick,

either single (Si-face) or double-side polished, with n-type doping in the high 10^{18} cm^{-3} range. The substrates used for epitaxy of low-doped (10^{15} cm^{-3} range) layers were Si-face, off-axis, the growth being performed in a hot-wall CVD reactor at 1550 °C, using propane and silane precursors diluted in a hydrogen carrier gas flow [1].

Substrate and epilayer crystalline defects were imaged by white beam synchrotron X-ray projection topography, combining transmission and section geometries. Measurements allowing high spatial resolution were carried out at the European Synchrotron Radiation Facility using HR Kodak film. The wafer flatness was measured with either a Dektak profilometer or with a micro-interferometer from Fisba Optik using a HeNe (633 nm) laser. X-ray diffraction (XRD) rocking curves of symmetrical (0004) reflections were measured with a Philips MRD 1880/HR diffractometer (Cu anode) using the triple-axis geometry [2]. The crystal curvature was measured by the shift of the peak centroid of ω rocking curves (sensitive to lattice plane tilts and bending) with the position of the incident beam along an in situ oriented $\langle 11\bar{2}0 \rangle$ diameter of the wafer.

* Corresponding author.

3. Results

3.1. Long range properties: crystal bending and wafer warpage

The warpage of 1.3 in. epi-wafers (low doped 15–30 μm thick epilayer, ground backside) typically ranges from 5 to 12 μm (Fig. 1) and depends on the backside preparation before CVD growth (concave towards Si-face for polished backside before epitaxy, convex or “horse-saddle” for ground backside). XRD mapping reveals a strong, non-uniform, crystal bending with a curvature radius, measured in the center of the wafer, of typically 5–15 m (Fig. 2). Unlike their direction (towards Si-face), the magnitude of the crystal bending and the wafer warpage are found to be not simply correlated (see Figs. 1 and 2), which suggests that the substrate structural properties and preparation prior to, and after, CVD growth play an important role. Epilayer thickness variation as a cause of warpage is excluded, being typically one order of magnitude less than the observed epi-surface flatness variation. In particular, XRD rocking curves mapped out before and after epitaxy show that, in as-grown epi-wafers, the crystal bending and the mosaicity are inherited from the substrate. The quality of the substrate prior to epitaxy therefore requires more attention.

3.1.1. Crystal bending

Investigations carried out on several samples show that crystal bending and warpage depend strongly on the origin of the substrate, together with its preparation. For commercial n-type 4H wafers from Cree Research Inc., the mean basal crystallographic plane bending is found to be oriented systematically towards the Si-face,

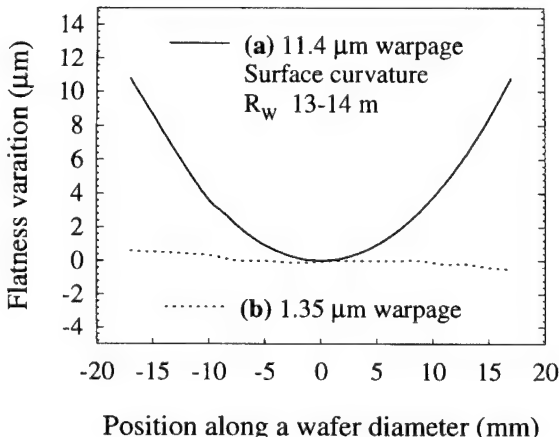


Fig. 1. Wafer flatness measured by profilometer on a 15 μm thick 4H CVD epilayer grown on the Si-face of a double side polished substrate: (a) as-grown, after backside grinding, (b) after backside re-polishing. The uniformity of the flatness was in both cases confirmed by micro-interferometry measurements.

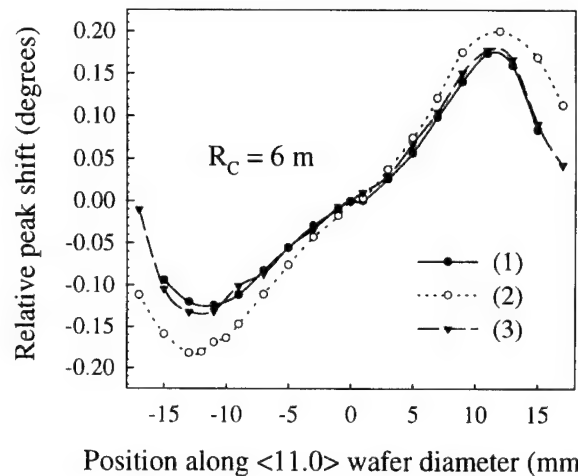


Fig. 2. Bending of lattice planes measured on the Si-face of the same wafer as Fig. 1. The centroid of XRD ω rocking curves from the (0004) reflection are plotted versus the position of the incident beam along a $\langle 11\bar{2}0 \rangle$ wafer diameter. The curvature radius R_C is determined in the linear region of the curve. The bending of the as-grown epilayer (1) is similar to the one of the as-received substrate, and is oriented towards the Si-face. It is increased after backside grinding (2), whereas re-polishing of the backside (3) allows to regain the initial bending.

whether measured on the Si- or C-face. The magnitude of the bending varies from substrate to substrate, but exhibits the same shape on substrates cut from the same boule.

X-ray transmission topographs taken from such 4H-SiC wafers revealed domain boundaries similar to the ones recently reported by Takahashi et al. [3], the domain walls containing a high density of edge dislocations with Burger vector mainly in $\langle 11\bar{2}0 \rangle$ directions. As mosaicity effects and crystal bending, the size of domain walls was observed to increase from the center to the periphery of the substrate. We relate the crystal bending and the domain structure to a polygonization of the crystal, the stresses introduced by the growth process, or its environment, relaxing into polygonized low-angle domains linked to the non-uniform crystal bending. Since polygonization requires glide and climb of dislocations, it is a temperature activated process, most probably occurring during bulk growth, the mosaic structure, together with a non-uniform bending, being inherited by the sliced substrate.

Owing to these results, together with the fact that the ductile–brittle transition is reported to occur between 800 and 1000 °C [4], it can be assumed that the level of intrinsic stresses present in the substrates will increase their sensitivity to warp during epitaxy and other processing steps.

3.1.2. Wafer warpage

In particular, the magnitude of wafer warpage and crystal bending is found to be strongly affected by the wafer's backside preparation. Fine polishing of the

ground backside of as-delivered one side (Si-face) polished wafers was shown to improve both the crystal and surface curvatures: warpage was found to be reduced by a factor of 8–10, whereas deviation in crystal bending is decreased (in our best case from 5 down to 80 m in the center of the wafer), but remains non linear.

A similar influence is observed for the epi-wafer. In particular, during CVD growth, the wafer is placed on a SiC-coated graphite susceptor, therefore a several hours long run leads to a substantial sublimation of the low-doped SiC coating on the substrate's backside. Vertical devices require this high resistivity layer to be removed and this can be done using 40–45 µm diamond grinding disks. Even when starting with a flat substrate (double-side polished), the epi-face warpage, together with the magnitude of the crystal bending, is found to be increased by this backside grinding (Fig. 1(a)). Re-polishing the ground backside again leads to improved flatness (Fig. 1(b)), while the epilayer's crystal bending regains exactly the shape of the as-grown sample (Fig. 2). Thus, the warpage of SiC wafers results from a convolution of the surface preparation and intrinsic properties inherited from the bulk growth process, the rather high defect content present in the substrates easily enabling them to deform plastically.

3.2. Localized properties: substrate–epilayer interface

Surface preparation before epitaxy, in particular polishing, is expected to affect not only long range properties such as warpage, but also the substrate–epilayer interface. To clarify this, the structural quality of a 60 µm thick CVD layer grown on an off-axis (3.5° towards $\langle 11\bar{2}0 \rangle$) 4H substrate was investigated by X-ray projection topography combining transmission and section geometries. The low-doped n^- -layer was grown after in situ hydrogen etching [5], on a n^+ substrate.

The main defects imaged in transmission topographs are basal plane dislocations with either $\langle 11\bar{2}0 \rangle$ (0001) or $\langle \bar{1}010 \rangle$ (0001) families slip systems, similar to those reported earlier in 6H M-Lely grown material [6]. Section topographs were taken perpendicular to the step-flow direction, i.e. along a $\langle \bar{1}010 \rangle$ direction. In the $(\bar{1}011)$ reflection (Fig. 3(a)), the substrate is characterised by strong and rather complex, non-resolved contrast features, whereas in some areas the epilayer shows a more uniform (light grey) contrast. Defects imaged in the epilayer appear as either dot-like features (D), resulting from dislocation lines intersected by the section [7] or zig-zag shaped lines (PF), mostly originating from the epi-substrate interface, which in kinematical contrast, are related to planar faults. Similar layer versus substrate contrast is observed in other $(h0\bar{h}l)$ reflections. This strong contrast difference in the $(10\bar{1}l)$ reflections can be explained by the nature of the defects: the imaged dislocations have a Burger vector component parallel

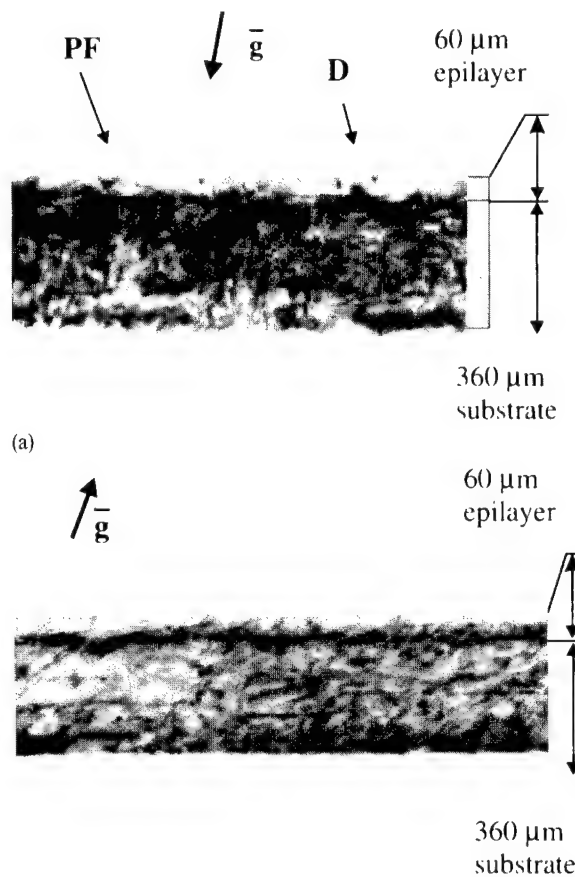


Fig. 3. (a) $(1\bar{0}1)$ reflection of a section topograph of a 60 µm thick epilayer grown on a 3.5° off-axis. The sample was inclined 60° from the incident beam to increase the spatial resolution necessary to image the epilayer (upper part of the section), showing in this reflection a lighter contrast than the substrate. (b) $(11\bar{2}4)$ reflection of the same section topograph as Fig. 3(a).

to $\langle 10\bar{1}0 \rangle$, and therefore correspond for one part to partial dislocations in the hexagonal lattice. Insufficient temperature activation during CVD growth [8] or interaction with the step-flow growth mechanism may explain their reduced content in the layer.

However, the contrast level and difference between the epilayer and the underlying substrate are reduced in $(11\bar{2}l)$ reflections (e.g. $(11\bar{2}4)$ reflection, Fig. 3(b)). Straight lines originating from stacking faults are imaged in the substrate. In addition, strong contrast lines along the growth interface are observed in several areas. These features do not form a uniform boundary at the interface, but are closely spaced, showing that they may be associated with defects localized at the interface, rather than with a uniform strain field resulting from the n^+/n^- doping difference (3–4 orders of magnitude). Since the density of imaged defects is higher at the interface than in the substrate, they shall be related to the quality of the surface before epitaxy. We attribute them to the polishing damaged layer. Polishing damage

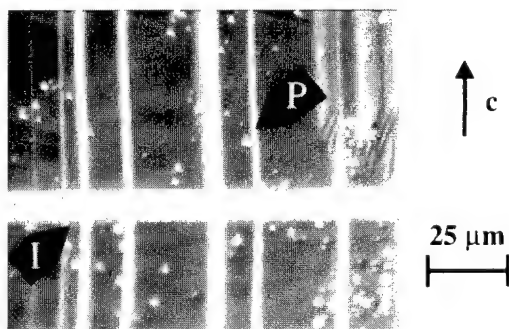


Fig. 4. Interference contrast micrograph of a cleaved n^-/n^+ epi-wafer ($10\bar{1}0$)-like surface etched for 3 min in KOH (480°C). The selective etching at the interface leads to a horizontal contrast band (I) whose width extends with increased etching time. Pyramidal etch pits (P) pointing towards the Si face are revealed both in the substrate and the epilayer. The vertical stripes originate from the cleavage.

has been reported to extend up to a few microns beneath the surface [9] and was therefore not fully eliminated by the pre-growth hydrogen etching (which in the present case removed a $0.1\ \mu\text{m}$ surface layer [6]). This explanation is supported by the similar contrast visible in the bottom of the section, corresponding to the wafer backside, which has been re-polished after epitaxy (kinematic contrast).

3.2.1. KOH etching of cleaved epi-wafers

In order to further assess the crystalline defect distribution between the epilayer and the underlying substrate, the surface of epiwafers sections, either as-cleaved or polished down to $1\ \mu\text{m}$ diamond slurry, were etched with molten KOH (480°C). When observed under a Nomarski contrast microscope after etching, the sections revealed an extremely uniform straight band extending along the entire epilayer–substrate interface (as confirmed from observation of the low-doped layer which appeared semi-transparent in the transmission mode). This feature, observable only under Nomarski contrast, results from a selectively etched groove located at the interface (Fig. 4), which under repeated etching extends into the underlying substrate at a rate of roughly $4\ \mu\text{m}\ \text{min}^{-1}$. When similar etching is performed on a cleavage of a low-doped (10^{15} range) CVD layer grown on a n^+ buffer layer, preferential etching is observed only at the n^-/n^+ interface, not at the n^+ -buffer/ n^+ -substrate interface. The observed interface etching can thus be assigned to the doping-difference induced electric field or to the lattice mismatch ($\Delta a/a \approx 10^{-4}$) [10], weaker bonding resulting from high impurity content favoring a preferential etching into the higher doped crystal regions.

In addition, the KOH etching reveals pyramidal shaped features pointing towards the (0001) Si face both in the substrate and in the epilayer. Being absent before etching and extending in size with increasing etch time,

these features are assigned to etch pits resulting from dislocations lines intersecting the $\{1\bar{1}00\}$ type surface of the section. The morphology of the pyramidal etch pits can be related to the crystal's structure: as etching on c -faces leads mainly to hexagonal pits, the point group symmetry of α -SiC polytypes is expected to lead to pyramid shaped pits on a -faces [11].

Section topographs revealed a slightly reduced defect content in the epilayer; whereas the density and size distribution of the pyramidal etch pits observed in the same epilayer are, in most cases, the image of the nearby region of the substrate. This may be due to the differing nature of the dislocations revealed by the two techniques, and requires further investigation.

4. Conclusion

Crystal bending and wafer warpage are shown to be affected both by the bulk growth process and the wafer preparation, mainly polishing. The tilt component of the lattice plane bending is related to a polygonization of the crystal into low-angle tilt boundaries. This degree of imperfection favors the wafers capacity to warp, thus making it essential to optimize processing steps in terms of surface preparation. Warpage of 1.3 in. epi-wafers can be reduced down to $1\text{--}3\ \mu\text{m}$ by backside re-polishing after epitaxy. Surface preparation also affects the epi/substrate interface through localized defects resulting from the polishing damaged layer, while the n^+/n^- doping difference induces a selective KOH etching.

Acknowledgement

The authors are grateful to the support of the TMR Programme of the European Commission (contract no ERBFMBICT960728). We thank Drs J. Baruchel and Dr J. Härtwig for the beam time at ESRF (application HC544). This work was supported by TFR, NUTEK/NFR Material Consortium on Thin Film growth and the NUTEK/ABB Power Device Programme.

References

- [1] O. Kordina, C. Hallin, R.C. Glass, A. Henry, E. Janzén, Inst. Phys. Conf. Series 137 (1994) 41–44.
- [2] P.F. Fewster, J. Appl. Crystallogr. 24 (1991) 178–183.
- [3] J. Takahashi, N. Ohtani, M. Kanaya, Inst. Phys. Conf. Series 142 (1996) 445–448.
- [4] K. Maeda et al., Phil. Mag. A, 57 (4) (1988) 573–592.
- [5] C. Hallin, A.S. Bakin, F. Owman, P. Mårtensson, O. Kordina, E. Janzén, Inst. Phys. Conf. Series 142 (1996) 613–616.

- [6] M. Dudley et al., *J. Phys.*, D 28 (1995) A63–A68.
- [7] H. Klapper, *Diffraction and Imaging Techniques in Material Science*, vol. 2, Springer, Berlin, 1991, pp. 109–162.
- [8] S. Wang, M. Dudley, C.H. Carter, H.S. Song, *Mater. Res. Soc. Symp. Proc.* 339 (1994) 735–740.
- [9] W. Qian, M. Skowronski, G. Augustine, R.C. Glass, H.McD. Hobgood, R.H. Hopkins, *J. Electrochem. Soc.* 142 (12) (1995) 4290–4294.
- [10] Gmelin Handbook of Inorganic Chemistry, Si Suppl., vol. B2 (Silicon Carbide), 1984, p. 18.
- [11] K. Sangwal, *Etching of Crystals*, North-Holland Physics Publishing, Amsterdam, 1987 p. 303.

Nonlinear optical mapping of 3C-inclusions in 6H-SiC-epilayers

C. Meyer *, G. Lüpke, E. Stein von Kamienski, A. Götz, H. Kurz

Institute für Halbleitertechnik II, RWTH Aachen, 52056 Aachen, Germany

Abstract

Optical second-harmonic generation (SHG) is shown to be a powerful technique for identifying different polytypes of SiC-films deposited on 6H-SiC substrates. The rotational anisotropy of the SHG radiation reflected from homo-epitaxially grown 6H-SiC epilayers provides a clear fingerprint of microcrystalline inclusions of 3C-SiC. The large dynamic range of the SHG response of more than one order of magnitude between different SiC polytypes allows a fast nondestructive mapping of SiC wafer surfaces with a lateral resolution in the μm -regime. © 1997 Elsevier Science S.A.

Keywords: Nondestructive testing; Second harmonic generation; Thin films

1. Introduction

Implementing high-temperature, high-frequency, and high-power electronic devices, as well as GaN blue lasers on SiC substrates depends critically on the quality of the material available. Although active and passive devices have been fabricated on homo-epitaxially grown 6H-SiC films [1,2], their performance is limited by defects, such as micropipes, microfacets, and crystalline inclusions of different polytypes. 6H-SiC epilayers grown at a high growth temperature reveal a high density of stacking faults and antiphase boundaries [3]. On the other hand, a low growth temperature favors the inclusion of 3C-SiC islands in the 6H-SiC film [4]. Experimental approaches to detect inclusions of different SiC polytypes include the growth of oxides on the epilayer making use of different growth rates of the polytypes [5] and white beam synchotron topographic analysis methods [6]. However, the development of new epitaxial growth processes requires fast and reliable in situ measurement techniques.

In this paper, we demonstrate the capability of optical second-harmonic generation (SHG) for detecting different SiC-polytypes. SHG is a known powerful tool for probing surfaces and interfaces of centrosymmetric media [7,8], and has been used for studying the formation of antiphase domains in epitaxial layers of compound semiconductors, such as GaP [9], and GaSe films

[10], and Si_mGe_n superlattices [11], all grown on Si substrates. Recently, Galeckas et al. investigated the SHG rotational anisotropy (RA-SHG) from 3C-SiC films on Si(001) to probe the crystalline order, and detected the presence of (111)-oriented 3C-SiC micro-areas [12]. RA-SHG which is defined by the nonlinear susceptibility tensor $\chi^{(2)}$ and its relation to structural symmetry is the key feature for identifying various SiC-polytypes. In this work, RA-SHG measurements from different polytypes, such as 4H-, 6H-, and 3C-SiC are presented, and the method is applied for spatially resolved mapping of 3C-SiC inclusions in 6H-SiC epilayers.

2. Theoretical background and experiments

The tensorial characteristic of $\chi^{(2)}$ gives rise to a RA-SHG response from SiC wafers rotated about its surface normal. The RA-SHG Intensity, $I^{(2\omega)}(\phi)$, as a function of the sample azimuthal angle ϕ can be written in the electric dipole approximation as a truncated Fourier expansion:

$$I^{(2\omega)}(\phi) \propto |\chi^{(2)} E^{(\omega)} E^{(\omega)}|^2 = \left| \sum_{m=0}^3 c_m \cos[m(\phi + \phi_m)] \right|^2 I^{(\omega)^2}, \quad (1)$$

where the complex c_m are given by the appropriate elements of $\chi^{(2)}$ multiplied by Fresnel coefficients. The phase angles ϕ_m denote the relative phases of the aniso-

* Corresponding author. Tel: +49 241 807895; Fax: +49 241 8888246; e-mail: meyer@basl.rwth-aachen.de

tropic c_m and $E^{(\omega)}$ and $I^{(\omega)}$ denote the electric field and intensity of the excitation at the fundamental frequency ω . The c_m coefficients of the RA-SHG response reflect the symmetry of the crystal surface. For example, a three-fold symmetric crystal, such as 3C-SiC cut parallel to the (111) plane or rhomboedrally polytypes oriented in the (0001) direction exhibit a three-fold symmetry component c_3 in the SHG anisotropy according to Eq. (1). On the other hand, a six-fold rotational anisotropy expected for 6H-SiC(0001) does not show up in the SHG anisotropy, because a third rank tensor such as $\chi^{(2)}$ can only reveal a symmetry up to three-fold. The six-fold symmetry gives rise to an isotropic SHG contribution c_0 . A vicinal surface causes an additional one-fold symmetry contribution, represented by c_1 in Eq. (1). A special case holds for crystals of the zincblende-structure, such as 3C-SiC. For this crystal class, $\chi^{(2)}$ consists of only one independent tensor element $\chi_{14}^{(2)}$ [13]. Therefore the rotational anisotropy can be calculated for each crystal orientation by transforming $\chi^{(2)}$ into the beam coordinate system, allowing the crystal orientation of 3C-SiC surfaces to be determined [14].

The commercially-available samples (CREE Research Inc.) consist of a 5-μm-thick 4H- or 6H-SiC film homoepitaxially grown on substrates cut with a misorientation angle α of nominally 3–4° toward [11̄20] away from the [0001] direction. The 3C-SiC epilayer was grown on a vicinal Si(001) surface oriented 3.5° toward [11̄2]. For RA-SHG measurements, we used a passively mode-locked titanium:sapphire laser generating 100 fs pulses at a repetition rate of 75.6 MHz. The p -polarized laser beam tunable over a wavelength range of 730–810 nm is focused on the sample surface to a spot size of about 10 μm at a 45° angle of incidence [15]. The reflected p -polarized SHG signal is separated from the reflected fundamental radiation using a prism and glass filters, and is detected by a single photon counting device. The sample is mounted on a xy translation and ϕ rotation stage for spatially resolved RA-SHG measurements. A computer is used to control sample movement and data acquisition.

3. Results and discussion

Fig. 1 shows the RA-SHG response from 3 different polytypes measured at a beam intensity of 10 mW at a wavelength of 760 nm. The two upper curves show the RA-SHG signal from the hexagonal 6H and 4H samples. Both curves exhibit only an isotropic and one-fold component expected for a surface misoriented from the crystal six-fold symmetry direction. The lower curve reveals the rotational anisotropy of a 3C-SiC film grown on vicinal Si(001). The expected two-fold symmetry of the RA-SHG electric field is documented by the four peaks of $I^{(2\omega)}(\phi)$. Additionally, the misorientation leads

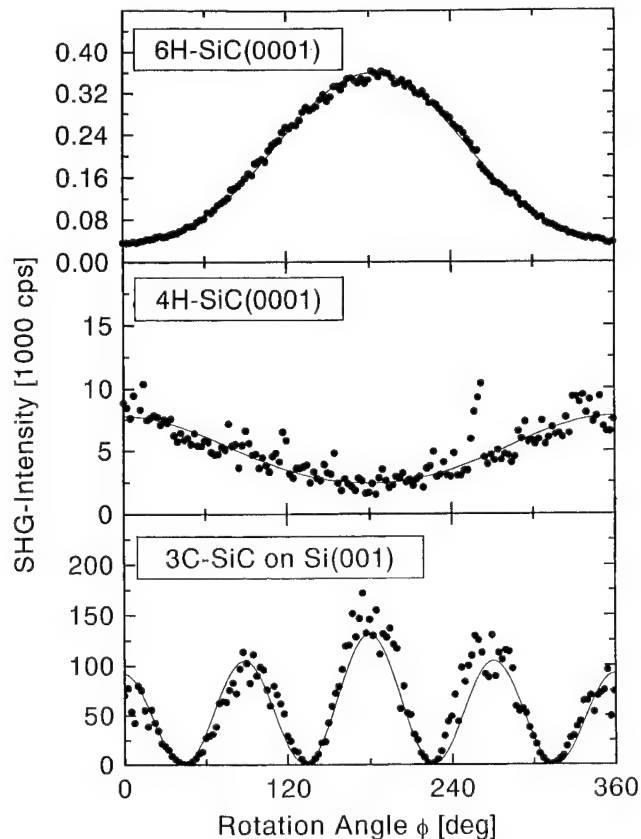


Fig. 1. RA-SHG from different SiC polytypes.

to an interfering one-fold contribution. Note the large difference of more than one order of magnitude between the maximum RA-SHG response from 6H-, 4H-, and 3C-SiC, allowing a fast mapping of these polytypes in homoepitaxially grown SiC films.

Fig. 2 displays an xy scan of a 2 mm × 2 mm surface area of a 6H-SiC epilayer using 30 mW incident radiation at 730 nm wavelength. The film reveals a wide variety of defects, such as micropipes and facets also visible under an optical microscope. A few facets, exhibiting no SHG signal due to beam deflection away from the detector, show up as dark nearly triangular regions in Fig. 2. On the left-hand side of the scan, two bright spots labelled (A) and (B) appear, where the SHG intensity exceeds the background signal from 6H-SiC by more than a factor of 10. To investigate the structure of these spots, two SHG images have been taken at a higher spatial resolution at two different azimuthal orientations ϕ of the sample. The result is shown in Fig. 3. These high-resolution images reveal microareas with straight edges inclined by $\Delta\phi = 30^\circ$. The size of these regions lies in the range of 30–50 μm. The two SHG scans taken at different orientations manifest the structural difference between the microareas and the 6H-SiC film. The streaks shown in (Fig. 4) are also visible under an optical microscope, whereas the microareas cannot be distinguished from the adjacent 6H-SiC.

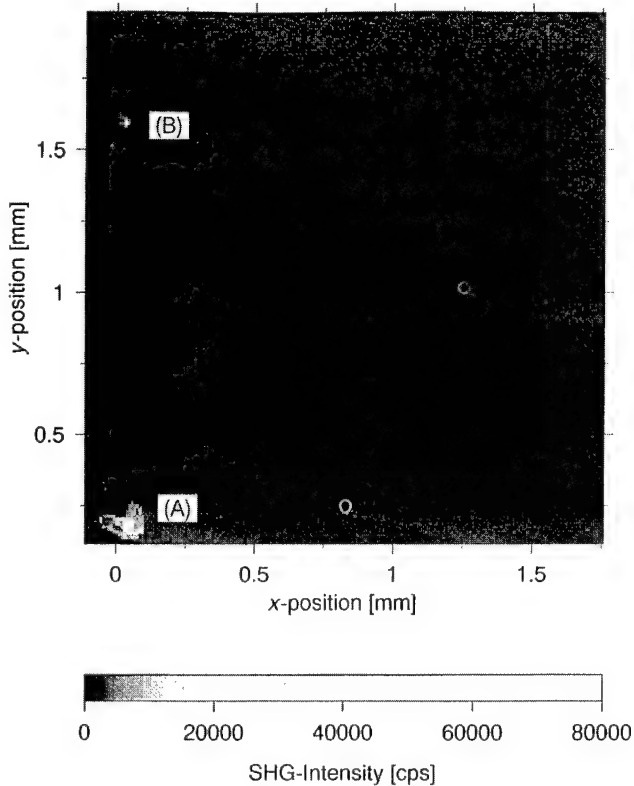


Fig. 2. Scan of a $\sim 2 \text{ mm} \times 2 \text{ mm}$ surface area. The scanning time was about 40 min for 200×200 points.

To determine the RA-SHG of the microareas, additional xy scans were performed at a variety of different sample orientations ϕ and the data were averaged over the regions labelled I and II in Fig. 3, respectively. The rotational anisotropy shows a clear three-fold symmetry, as displayed in Fig. 5(b) and (c). This excludes a hexagonal polytype for the inclusions. To identify the polytype in the regions I and II, we calculated the RA-SHG from 3C-SiC, which is determined by the Fourier coefficients c_m as defined in Eq. (1). Therefore the only nonvanishing $\chi^{(2)}$ tensor element, $\chi_{14}^{(2)}$ is transformed into the beam coordinate system as outlined by Bottomley et al. [14].

The solid lines in Fig. 5(a) and (b) represent theoretical predictions of $I^{(2\omega)}(\phi)$ from zincblende-type microcrystallites for polar and azimuthal misorientation angles $\alpha = 3.5^\circ$, and $\beta = -25.61^\circ$ and $+34.37^\circ$ with respect to the cubic [111]- and [112]-direction, respectively. Refractive indices of $n(\omega) = 2.616$ and $n(2\omega) = 2.817$ for the fundamental and second harmonic light were used for the calculation [16]. The agreement between theoretical curve and experimental data is excellent using only a scaling factor which is identical within $< 1\%$ for both microareas. This clearly identifies the inclusions as 3C-SiC microcrystallites of different azimuthal misorientation. The difference between β values of the two areas is exactly 60° as one would expect for

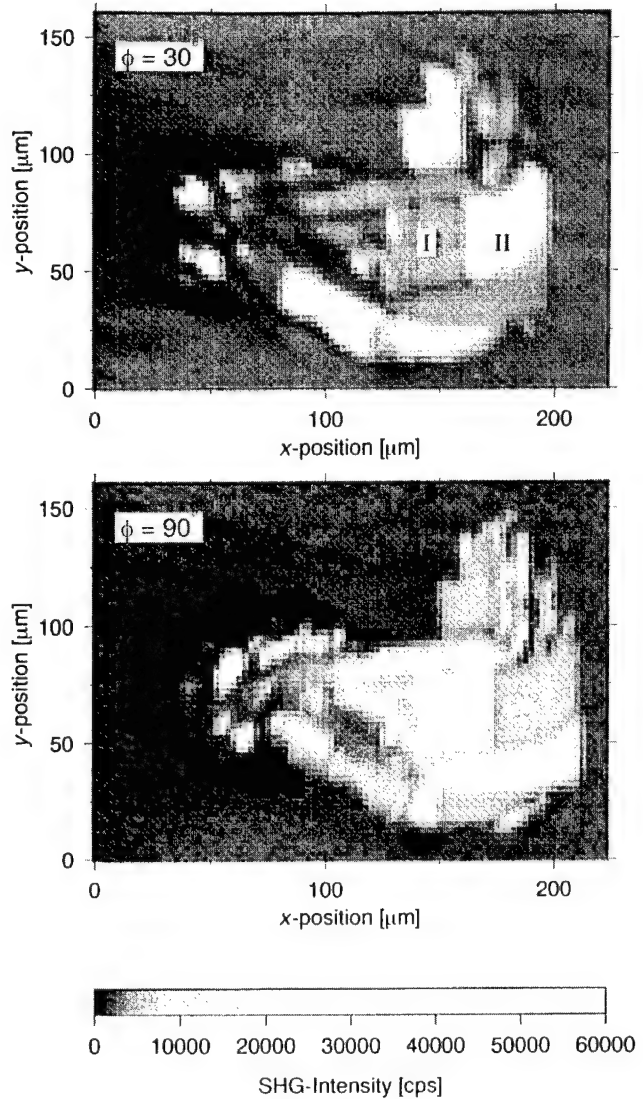


Fig. 3. Scans of area (A) in Fig. 2 taken at two different azimuthal angles. The scanning time for each image is approximately 8 min.

a lattice-matched cubic crystal with three-fold symmetry on a six-fold-symmetric substrate. The [112] direction of the cubic crystal corresponds to either the [1120] or the [1210] direction of the 6H substrate. From the β values of the inclusions the azimuthal misorientation of the substrate can be determined to be 4.4° away from the [1120] direction.

Because of the large difference of more than one order of magnitude in the SHG response from different polytypes, sampling times of only 20 ms per data point are required. The image shown in Fig. 2 consisting of a 200×200 data array with a spacing of $9.375 \mu\text{m}$ has been taken in about 40 min. Positioning required 12 min, which can be reduced further by using a faster positioning system. The use of an optical imaging tool for monitoring the SHG reflection from a larger surface area will also reduce measurement time [17].

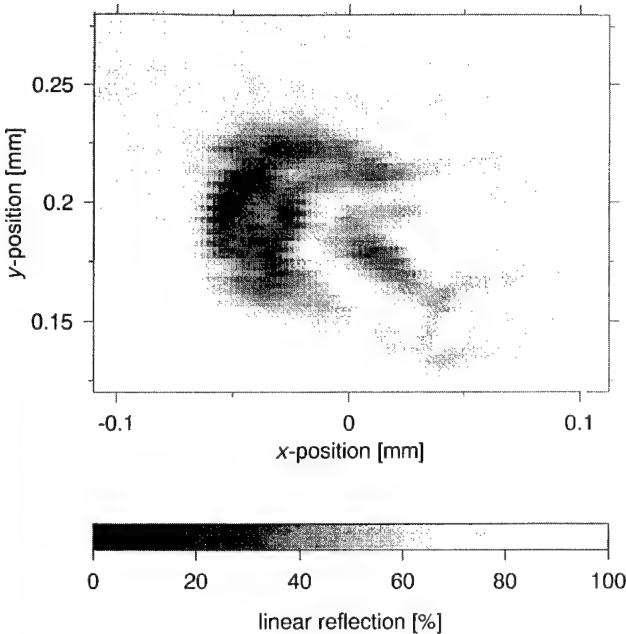


Fig. 4. Linear optical scan of the area shown in Fig. 3.

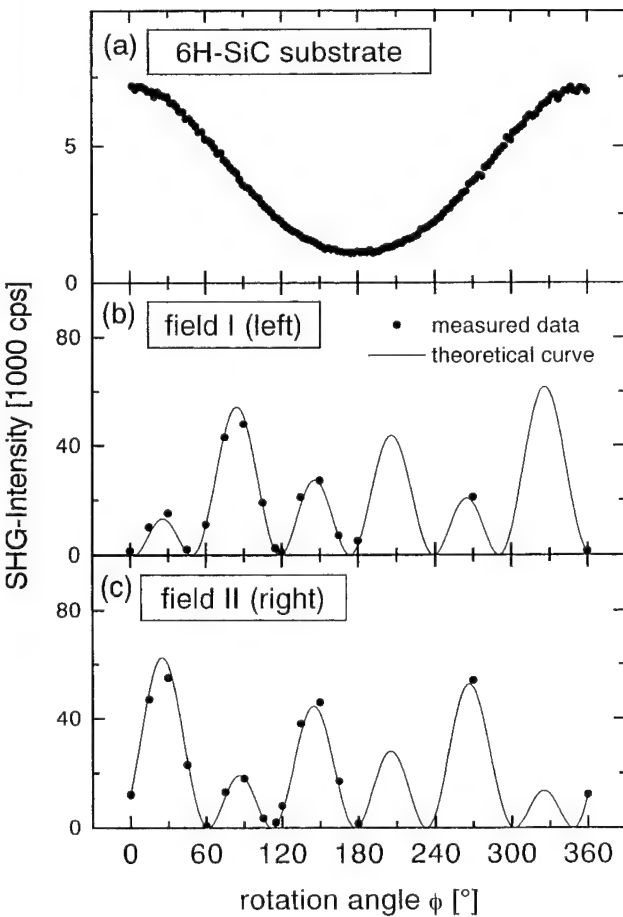


Fig. 5. SHG intensity from different crystalline microareas shown in Fig. 3. The upper curve shows the undisturbed 6H-SiC, the two lower curves show the areas labelled I and II in Fig. 3, respectively.

4. Conclusion

A nonlinear optical mapping tool based on spatially resolved SHG has been demonstrated for detecting different silicon carbide polytypes. Inclusions of 3C-SiC microcrystallites in a 6H-SiC epilayer could be spatially mapped within reasonable measurement times. By RA-SHG measurements, the inclusions could be undoubtedly identified as 3C-SiC and their crystalline orientation could be determined. The huge signal dynamic between different polytypes allows polytypes of similar crystal structure, such as 4H- and 6H-SiC, to be easily distinguished by their SHG response. Since optical SHG mapping is noninvasive and rapid, it can be used as an in situ growth control of SiC epilayer.

Acknowledgement

This work was partially supported by the BMBF (contract number 01 BM 302) and by the DFG (contract number Ku540/13).

References

- [1] R.F. Davis, G. Kelner, M. Shur, J.W. Palmour, J.A. Edmond, Proc. IEEE 79 (1991) 677.
- [2] K. Shibara, T. Saito, S. Nishino, H. Matsunami, IEEE Electr. Dev. Lett. EDL 7 (1986) 692.
- [3] K. Shibara, S. Nishino, H. Matsunami, J. Cryst. Growth 78 (1986) 538.
- [4] Y.C. Wang, R.F. Davis, J. Electr. Mater. 20 (1991) 869.
- [5] J.A. Powell, J.B. Petit, J.H. Edgar, I.G. Jenkins, L.G. Matus, J.W. Yang, P. Pirouz, W.J. Choyke, L. Clemen, M. Yoganathan, Appl. Phys. Lett. 59 (1991) 333.
- [6] M. Dudlea, W. Huang, S. Wang, J.A. Powell, P. Neudeck, C. Fazi, J. Phys. D: Appl. Phys. 28 (1995) A56.
- [7] Y.R. Shen, Nature 337 (1989) 519.
- [8] T.F. Heinz, Second-order nonlinear optical effects at surfaces and interfaces, in: Nonlinear Surface Electromagnetic Phenomena, H.-E. Ponath, G. Stegeman (Eds.), ch. 5, pp. 353–416, Elsevier Science B.V., 1991.
- [9] C. Meyer, G. Lüpke, Z.G. Lü, A. Götz, H. Kurz, G. Lucovsky, J. Vac. Sci. Technol. B 14 (1996) 3107.
- [10] J. Amzallag, H. Benisty, S. Debrus, M. May, M. Eddrief, A. Bourdon, A. Chevy, N. Piccioli, Appl. Phys. Lett. 66 (1995) 982.
- [11] D.J. Bottomley, G. Lüpke, M.L. Legerwood, X.Q. Zhou, H.M. van Driel, Appl. Phys. Lett. 63 (1993) 2324.
- [12] A. Galekas, M. Petrauskas, Q. Wahab, M. Willander, Nucl. Instr. Methods in Phys. Res. B 65 (1992) 357.
- [13] Y.R. Shen, The Principles of Nonlinear Optics, John Wiley and Sons, New York, 1984.
- [14] D.J. Bottomley, G. Lüpke, J.G. Mihaychuk, H.M. van Driel, J. Appl. Phys. 74 (1993) 6072.
- [15] C. Meyer, G. Lüpke, E. Stein von Kamienski, A. Götz, H. Kurz, Appl. Phys. Lett. (1996), in press.
- [16] E.D. Palik, Handbook of Optical Constants of Solids, Academic Press, New York, 1985.
- [17] M. Flörsheimer, H. Loosser, M. Küpfer, P. Günter, Thin Solid Films 244 (1994) 1001.

Deep luminescent centres in electron-irradiated 6H SiC

N.T. Son *, E. Sörman, M. Singh, W.M. Chen, C. Hallin, O. Kordina, B. Monemar,
J.L. Lindström, E. Janzén

Department of Physics and Measurement Technology, Linköping University, S-581 83, Linköping, Sweden

Abstract

We report on our observation of several new photoluminescence (PL) spectra in electron-irradiated 6H SiC. In addition to the vacancy-related PL spectrum ranging from 1.36 to 1.44 eV, four other spectra with no-phonon lines in the regions of 0.9983–1.0738 eV, 1.0878–1.1342 eV and 1.3563–1.3711 eV were detected in 6H SiC. These luminescent centres are rather thermally stable. From the formation and annealing behaviour, these centres were suggested to be complexes, of which some involve a silicon vacancy. © 1997 Elsevier Science S.A.

Keywords: SiC; Electron irradiation; Defects; Photoluminescence; Deep levels; Vacancy complexes

1. Introduction

In semiconductors, vacancies and interstitials are created during high-energy particle bombardment. In a binary compound semiconductor such as SiC, anti-sites defects can also be formed. Under high temperature annealing, these primary defects become mobile and interact with other intrinsic defects or impurities to form complexes. Radiation-induced defects are often found to be associated with deep level states in the energy gap of semiconductors. Some of these are carrier traps, while others act as recombination centres, and both have a strong influence on the electrical and optical properties of the material. The creation of these recombination centres, either non-radiative or radiative, will lead to a considerable reduction of the carrier lifetime in the semiconductors. Such radiation defects, therefore, have been used for lifetime control in semiconductor bipolar devices. In some semiconductors, such as silicon, the vacancy and interstitial are mobile at temperatures well below room temperature, and hence, the properties of the material are mainly influenced by the secondary defects, i.e. their associated complex defects. In SiC, however, primary defects are stable at room temperature and will also be important for device applications. In some common polytypes such as 3C and 6H SiC, the negatively charged silicon vacancy had been detected by

electron spin resonance (ESR) as early as 1970 [1], but was identified only recently [2,3], when high quality crystals became available. Secondary defects in SiC are thermally stable, and in some cases, also luminescent active. In the past, photoluminescence (PL) was extensively used to study radiation-induced luminescent centres, but mainly in the visible region [4]. Recently, several vacancy-related defects were detected by PL and optically detected magnetic resonance (ODMR) in the near-infrared region of irradiated 3C [5] and 6H [6] polytypes. In this paper, we report our observation of several new PL spectra in the region of 0.98–1.45 eV in electron-irradiated 6H SiC.

2. Samples and equipment

Samples used in this work are 6H SiC epitaxial films grown by chemical vapour deposition (CVD), including low-doped n-type and aluminium compensated p-type [7] material. The net donor concentration is in the mid 10^{14} to 10^{16} cm^{-3} range. The typical thickness of the films is about 10–15 μm. Samples were irradiated by 2.5 MeV electrons at room temperature with doses ranging from 5×10^{13} to 10^{18} cm^{-2} . PL measurements were performed on a BOMEM DA3 Fourier transform spectrometer optimised for the region 0.7–1.6 eV. Luminescence emissions were detected using a cooled North-Coast germanium photo-diode. The sample tem-

* Corresponding author. Fax: 46-13-142337; e-mail: son@ifm.liu.se

perature could be varied from 5 K to room temperature using a He gas flow cryostat. The annealing time of the samples in nitrogen gas flow is typically 10 min at each temperature.

3. Results

In as-grown 6H SiC samples, through the range 0.7 to 1.6 eV, only the PL spectrum of vanadium was observed, as can be seen in Fig. 1(a). Irradiation with doses below 10^{15} cm^{-2} does not change the picture of near-infrared PL, but introduces the well-known D₁ and D₂ luminescence bands [4] in the visible region. With higher doses of irradiation, several PL bands can be detected in the region of 0.98–1.45 eV, while the PL from vanadium is almost quenched (Fig. 1(b)). The intensity of these PL bands increases rapidly with increasing the dose of irradiation from 10^{16} to 10^{17} cm^{-2} . Higher doses lead to a creation of a number of PL lines in the regions 0.998–1.135 eV and 1.356–1.372 eV (Fig. 1(b)). The PL band with three NPLs at 1.368, 1.398 and 1.434 eV is related to the spin triplet states of the silicon vacancy, as identified by ODMR [6]. As can be seen from Fig. 1(b), in the region 0.98–1.135 eV, several sharp lines were observed. These

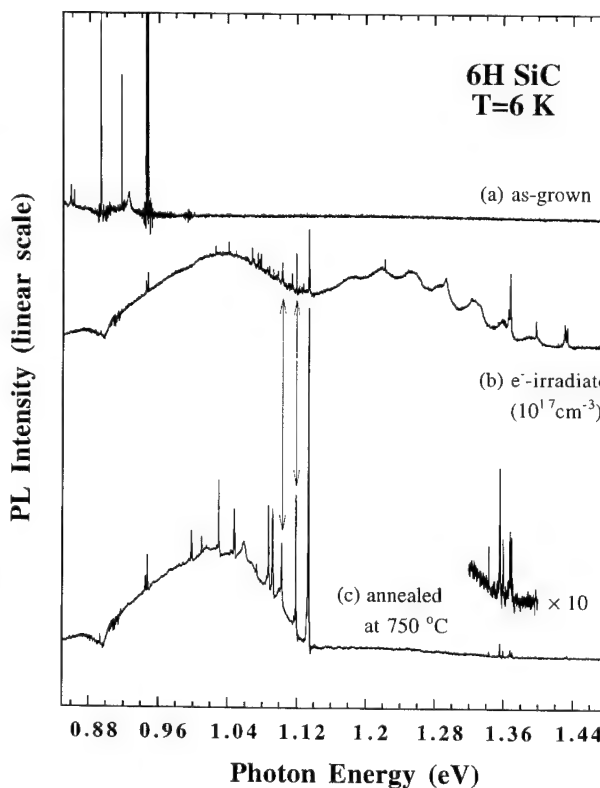


Fig. 1. PL spectra observed at 6 K in 6H SiC epitaxial layers: (a) as-grown; (b) irradiated by 2.5 MeV electrons with a dose of 10^{17} cm^{-2} , and (c) annealing at 750°C. The resolution is 0.25 meV.

lines appear differently in different samples, indicating that they are not all from the same defect. After annealing at 750 °C, the silicon vacancy-related PL band disappears together with its broad phonon band (Figs. 1(c) and 2). In the region 0.98–1.14 eV, some lines are also annealed out at this temperature, while the others become much stronger and a new group of four lines appears at 0.98–1.05 eV (Figs. 1(c) and 2). In annealed, p-type samples, only a PL band with five NPLs at the region 1.0878–1.1342 eV was detected, while in the n-type samples a deeper band with six NPLs (0.9983–1.0783 eV) was also observed (Fig. 2(a)). The energy position for these lines is indicated in Fig. 2(a). In the n-type samples, several new NPLs are also observed between 1.3563 and 1.3711 eV (the inset in Fig. 1(c)). After a short anneal at 960 °C, three lines can still be detected. Two of these are shown to be a doublet (Fig. 3(a)).

4. Discussion

Before annealing, three NPLs at 1.1031, 1.1195 and 1.1342 eV are dominating in this region, while the other two lines at 1.0878 and 1.0923 eV can hardly be seen (Fig. 1(b)). After annealing, these two lines appeared and the intensity ratios between the other three lines (1.1031–1.1342 eV) changed. It seems that these five NPLs belong to two similar defects. The behaviour of these five NPLs with annealing (above 750 °C) is very

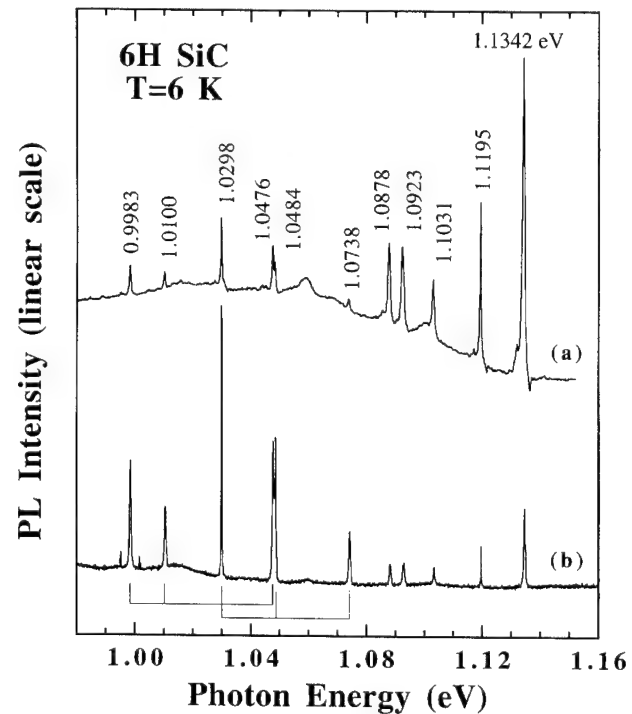


Fig. 2. (a) High resolution (0.06 meV) PL spectra of the same sample as shown in Fig. 1(c); (b) the same PL spectra after annealing at 960 °C. The numbers indicate the energy positions of the lines in eV.

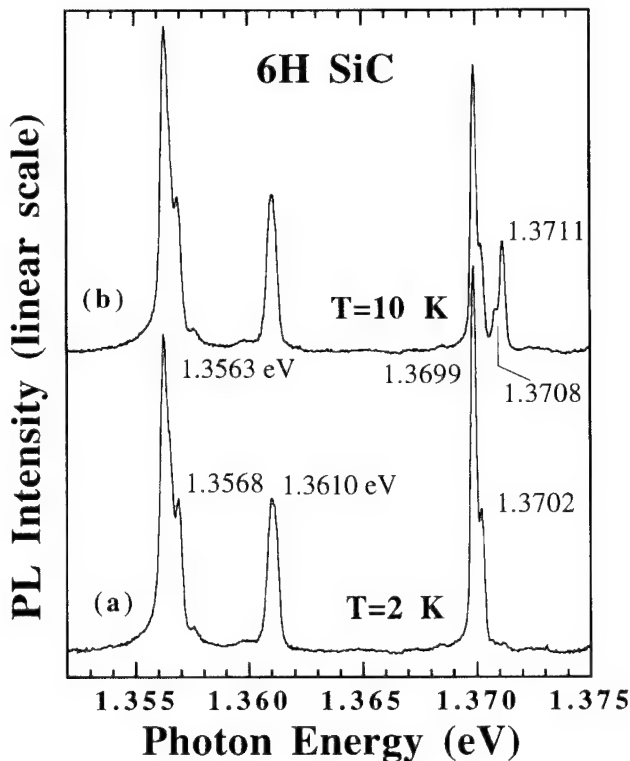


Fig. 3. Details of the PL band at 1.3563–1.3711 eV in n-type, electron-irradiated 6H SiC after annealing at 960 °C: (a) measured at 2 K; and (b) at 10 K. The energy positions of the lines are indicated in eV.

similar. This PL band only becomes clear in the structure and gets stronger when the silicon vacancy-related PL band at 1.434 eV [6] starts annealing out (700–750 °C). Annealing with temperatures above 750 °C leads to a decrease in intensity of this band. The spectrum still survives at temperatures closed to 1200 °C. This annealing behaviour indicates that this PL band is probably related to complex defects involving a silicon vacancy. These NPLs are very sharp and show no broadening effect or decreasing in intensity when increasing the temperature from 6 to 77 K. For such a deep centre, sharp PL lines are usually due to either excitonic transitions or internal transitions of the defect. In the case of a bound exciton, the NPLs are often shown to be split under a magnetic field. However, our preliminary data from the Zeeman effect experiments showed no splitting of any line, except a small energy shift of the 1.1342 eV line. The available data seem to indicate that these lines may be due to the transitions between the excited states and the ground state of a defect. For a substitutional impurity or a vacancy in 6H SiC, the PL spectrum usually consists of three NPLs (or three groups of NPLs in the case of the energy states are split by low-symmetry crystal field) corresponding to three different inequivalent sites of the lattice. It is possible that three NPLs at 1.1031, 1.1195 and 1.1342 eV belong to one defect. The other also gives rise to two NPLs,

overlapping with the 1.1195 and 1.1342 eV lines, and two other lines at 1.0878 and 1.0923 eV, corresponding to the third inequivalent site of the 6H SiC lattice. No optically detected magnetic resonance (ODMR) signal was detected via this PL band. The defects giving rise to this PL band may not be paramagnetic centres.

With increasing annealing temperature above 750 °C, the PL band at 0.9983–1.0738 eV is increased. From the intensity ratios between these NPLs from different samples and at different annealing temperatures, it seems that these lines belong to two different centres. A tentative assignment of these NPLs is indicated in Fig. 2(b). The formation and annealing behaviour of these centres suggest that they are complex defects. This PL band appears to be extremely weak in high purity n-type epilayers and is not observed in p-type samples. The involvement of the impurities (e.g. nitrogen) in these defects, therefore, may be considered.

Temperature dependence studies of the near-midgap PL band (1.3563–1.3711 eV) were carried out in the range 2–130 K. Figs. 3(a) and 3(b) show the spectrum recorded at 2 and 10 K. At temperatures above 2 K, a new doublet appears (1.3708 and 1.3711 eV). With increasing temperature, this new line increases in intensity while the 1.3699 eV line decreases. The temperature dependence of these two doublets is very similar to that of a triplet-singlet structure. At temperatures above 100 K, only the line at 1.3563 eV survives. Since this PL band can only be observed after annealing and is stable at high temperatures, it is probably related to a complex defect. These three lines/group of lines may be attributed to the same defect at three inequivalent sites of the 6H SiC lattice.

In summary, we have observed several new near-infrared PL spectra in electron-irradiated 6H SiC after annealing. From the formation and their annealing behaviour, these spectra are suggested to be related to complex centres. All the spectra are shown to be very complicated in structure, and therefore, at this stage the assignment of the lines and the electronic structure of these centres are preliminary.

References

- [1] L.A.S. de Balona, J.H.N. Loubser, *J. Phys. C* 3 (1970) 2344.
- [2] H. Itoh, M. Yoshikawa, I. Nashiyama, S. Misawa, H. Okumura, S. Yoshida, *IEEE Trans. Nucl. Sci.* 37 (1990) 1732.
- [3] J. Schneider, K. Maier, *Physica B* 185 (1993) 199.
- [4] W.J. Choyke, *Inst. Phys. Conf. Ser.* 31 (1977) 58.
- [5] N.T. Son, E. Sörman, W.M. Chen, M. Singh, C. Hallin, O. Kordina, B. Monemar, E. Janzén, J.L. Lindström, *J. Appl. Phys.* 79 (1996) 3784.
- [6] E. Sörman, N.T. Son, W.M. Chen, J.L. Lindström, O. Kordina, E. Janzén, in: M. Scheffler and R. Zimmermann (Eds.), *The physics of semiconductors* Word Scientific, Singapore, 1996) p. 2649.
- [7] O. Kordina, PhD thesis, Linköping 1994.

Optically detected magnetic resonance studies of defects in 3C SiC epitaxial layers

N.T. Son *, E. Sörman, W.M. Chen, C. Hallin, O. Kordina, B Monemar, E. Janzén

Department of Physics and Measurement Technology, Linköping University, S-581 83 Linköping, Sweden

Abstract

Optically detected magnetic resonance (ODMR) was used to study defects in 3C SiC epitaxial layers grown at high temperatures (1550 °C) by chemical vapour deposition on a free-standing 3C SiC film substrate. An isotropic, very broad and asymmetric ODMR line was observed under ultraviolet light excitation. This line is shown to be due to the overlapping of two different isotropic spectra, as revealed by magnetic field modulation measurements. Both spectra can be described by an effective electron spin $S=1/2$. The higher field line with a g -value of 2.006 may be related to a silicon vacancy. Using below bandgap excitation, the lower field spectrum ($g=2.012$) was found to have a triplet structure which could be due to the hyperfine of ^{14}N . This defect is related to a new photoluminescence band in the region of 1.1–1.58 eV. © 1997 Elsevier Science S.A.

Keywords: SiC thin films; Defects; ODMR; Photoluminescence

1. Introduction

Single crystals of 3C SiC are often grown epitaxially by chemical vapour deposition (CVD) on Si substrates. However, owing to the large mismatch of about 20% in lattice constants between Si and 3C SiC, a high density of dislocations and other structural defects are usually present in such films. The mismatch-induced strain may be partly relieved by dislocations and defects but will still affect the quality of the film during the growth. Therefore, for growing high quality films, free-standing 3C SiC film substrates would be desirable. Using 3C SiC substrates, one can grow at higher temperatures which helps to increase the mobility and surface diffusion of atoms during growth, and hence, to reduce structural defects. A higher growth rate is assured while achieving the same quality. The possible introduction of electronic defects during growth at high temperatures with high growth rates has not, however, been studied.

Photoluminescence (PL) is one of the most common techniques being used for characterisation of semiconductors, especially 3C SiC epitaxial films. The quality of 3C SiC films is often evaluated based on information obtained from the PL spectra of the nitrogen-bound exciton and other intrinsic defects in the visible region,

e.g. the D₁ and G centres [1]. In the past, defects in as-grown 3C SiC were extensively studied by PL, but only in the visible region. Very little is known about defects associated with PL in the near-infrared region. Such deep level defects often play an important role in carrier recombination and strongly influence the optical and electrical properties of the material. The carrier recombination processes are sometimes spin-dependent and can be studied by optically detected magnetic resonance (ODMR). In this work, we used ODMR and PL to investigate deep level defects introduced into 3C SiC epitaxial layers during growth at high temperatures (1550 °C) by CVD on free-standing 3C SiC film substrates. The PL and ODMR results of two defects observed in such a film are presented.

2. Experimental details

The 3C SiC film was first grown on a Si(100) substrate at 1250 °C by CVD up to a thickness of about 15 μm [2], then the silicon substrate was removed by chemical etching. Pieces of free-standing films with a size of about 5 × 5 mm² were used as substrates for CVD growth of 3C SiC layers at 1550 °C. The ODMR measurements were performed on a modified Bruker

* Corresponding author. Fax: 46-13-142337; e-mail: son@ifm.liu.se

ER-200D X-band (approx. 9.22 GHz) electron spin resonance spectrometer using a TE₀₁₁ cylindrical microwave cavity with optical access. The sample temperature can be varied from 5 K to room temperature using a helium gas flow cryostat. The film was glued directly on a quartz exchangeable sample holder with one of the <011> directions along the vertical axis. The rotation of the magnetic field in the (011) plane could be achieved by rotating the sample holder. The ultraviolet (UV) light (351.1–363.8 nm) or the 514 nm line of an ion argon laser was used for above-bandgap excitation. For below-bandgap excitation, a tuneable Ti-doped sapphire laser was used. In the ODMR experiments, different emissions were selected using optical filters and were collected by a North Coast cooled Ge detector. The PL measurements were carried out at temperatures below 2 K using a He bath cryostat and a SPEX-1404 double grating monochromator.

3. Results and discussion

In the 3C SiC films grown on Si substrates at 1250 °C, the PL emission from the nitrogen-bound exciton is dominating in the visible region [2]. In such films, no signal was observed in ODMR by monitoring different PL emissions. After regrowth by CVD at 1550 °C, the PL spectrum of the nitrogen-bound exciton showed very sharp lines (approx. 1.3 meV full width at half-maximum) at the expected energy positions [2]. These are indications of strain-free layers with a low density of structural defects [1]. In addition, two new near-infrared PL bands were observed. One of these consisted of several sharp no-phonon lines at 1.453, 1.484 and 1.578 eV and their lattice phonon replicas (Fig. 1). The other ranged from 0.8 eV to 1.1 eV. This deep PL band is not related to the defects described in this paper and hence will not be discussed here. The PL spectrum shown in Fig. 1 was recorded with below-bandgap light excitation (760 nm). The same structure of this band was also observed under UV excitation, but the signals were weaker owing to a smaller excitation depth of the UV light.

In this regrown film, an isotropic and broad ODMR line was detected. As can be seen from Fig. 2(a), the asymmetric and broad (approx. 2.3 mT at half-maximum) line, as observed under UV excitation seems to be due to the overlapping of several ODMR lines. However, the line shape remains unchanged with varying temperature or modulation frequency. At X-band frequency the spectrum is isotropic. The *g*-value at the peak position is *g*=2.006. The observed PL spectrum of the nitrogen bound exciton with very sharp lines indicates that the broad line width of the ODMR spectrum is clearly not due to the strain in the film. The

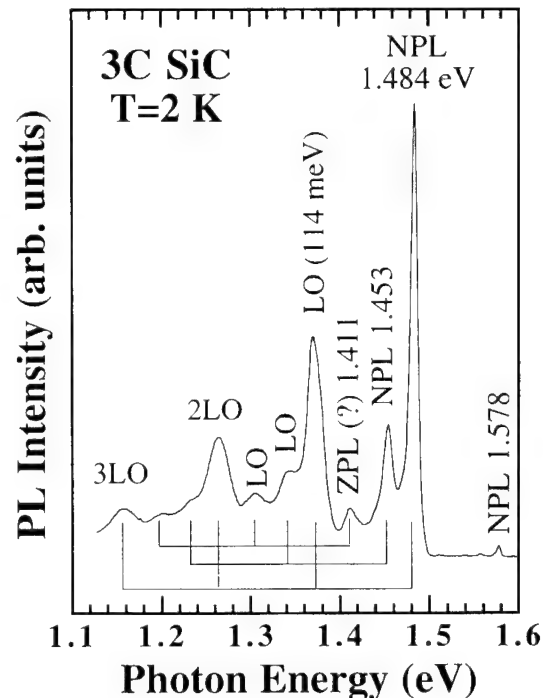


Fig. 1. The PL band recorded at 2 K, under near-infrared excitation (760 nm) in a 3C SiC layer grown on a free-standing 3C SiC film substrate by CVD at 1550 °C.

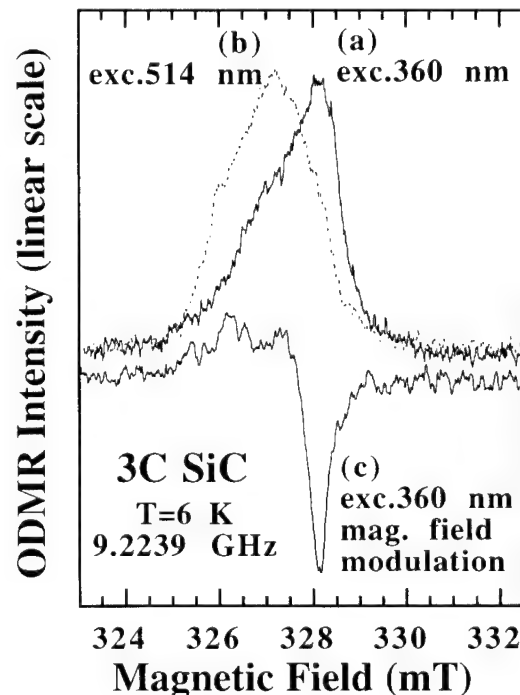


Fig. 2. The ODMR spectrum observed in the same sample as shown in Fig. 1 with different excitation: (a) 360 nm; and (b) 514 nm; and (c) with magnetic field modulation (10 G).

spectral dependence studies using different bandpass filters show that the ODMR spectrum can be observed

as a positive signal when detecting different PL emissions in the near-infrared region (780–1700 nm).

Fig. 2(b) shows the ODMR spectrum observed under green light excitation (514 nm). The line shape now becomes symmetric and the ODMR peak moves to a lower magnetic field, corresponding to a *g*-value of 2.012. This experimental fact indicates that there are probably two different defects giving rise to two isotropic ODMR spectra, which are overlapping owing to a small difference in *g*-value. The defect related to the high field part of the spectrum in Fig. 2(a) is more efficiently excited by the UV light than the 514 nm laser line, while both excitation sources are equally sufficient for the defect associated with the low field part. Moreover, the green light (514 nm) can penetrate deeper into the film and excite a larger volume of the sample. As a result, under the 514 nm line excitation, the high field side of the spectrum, which is favoured by the UV excitation, decreases, while the low field component increases and becomes dominant. This explains the shift of the ODMR peak towards the lower field and the change of the line shape (Fig. 2(b)). In this case, the spectrum seems to be attributed mainly to one defect. However, the line width of about 2.3 mT is unusually broad, which is probably due to an unresolved structure.

The ODMR measurements with magnetic field modulation, which often provides a higher resolution than the conventional MW modulated experiments, have been performed. As shown in Fig. 2(c), the broad line now decomposes into several components with the strongest one at the same magnetic field position as the ODMR peak in Fig. 2(a). Some weak structures were observed at lower magnetic fields. Thus, the high field side of the broad ODMR line in Fig. 2(a) is due to a defect which has an isotropic *g*-value of 2.006, while the low field part arises from a different ODMR centre. However, a part of this structure is still overlapping with the strong peak and it is therefore not possible to draw any further conclusion.

As shown above, one of these defects is favoured by UV excitation, so in order to selectively excite only one defect, ODMR experiments with near-infrared excitation (760 nm) were carried out. As can be seen in Fig. 3, the ODMR peak with *g*=2.006 is not detected. The signal in this case is rather weak, but a structure of three lines with an estimated separation of about 9–10 G can be recognised (Fig. 3). The structure is not well resolved, even with such separation. It may partly be due to the broadening by high MW power (200 mW) which was required to observe the ODMR signal. In 3C SiC, a triplet structure of a nitrogen-related ODMR spectrum would have three lines of equal intensity. In this case, the observed structure, where the middle line is much stronger, does not fit to the hyperfine interaction of nitrogen, unless there is another isotropic ODMR line with the same *g*-value also present. This seems

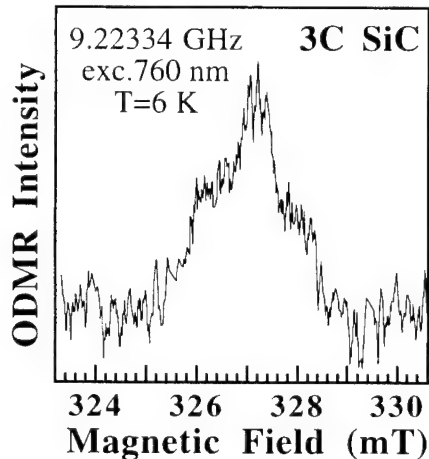


Fig. 3. The ODMR spectrum observed under near-infrared excitation (760 nm).

possible since under near-infrared excitation, several PL lines which are from different defects were observed (Fig. 1). A positive ODMR signal observed in this case must be related to this PL band. Unfortunately, the ODMR signal is too weak for a spectral dependence study using a monochromator, so the assignment of particular lines of that PL band being related to this ODMR defect was not possible.

The defect giving rise to the strong ODMR line with *g*=2.006 is probably an intrinsic defect. Within experimental errors, its *g*-value is identical to that of the L2 centre (2.0061), which is observed in electron-irradiated 3C SiC and is suggested to be related to a silicon vacancy [3]. It is possible that the no-phonon line related to the L2 centre (1.121 eV) [3] is present but is obscured by the two new strong PL bands in this region.

In summary, we have revealed two different ODMR defects in 3C SiC layers grown by CVD at 1550 °C on free-standing 3C SiC film substrates. Nitrogen is probably involved in one of these defects, which has an isotropic *g*-value of 2.012 and gives rise to the PL band in the region of 1.45–1.58 eV, while the other defect may be related to a silicon vacancy. These two deep level defects are introduced or enhanced during growth at moderately high temperatures.

Acknowledgement

Financial support for this work was provided by the Wenner-Gren Center Foundation for Scientific Research, the Swedish Board for Industrial and

Technical Development (NUTEK), the Swedish Council for Engineering Sciences (TFR), the Swedish National Science Research Council (NFR), the NUTEK/NFR Materials Consortium on Thin Film Growth and the NUTEK/Asea Brown Boveri (ABB) Power Device Research Project.

References

- [1] W.J. Choyke, Z.C. Feng, J.A. Powell, *J. Appl. Phys.* 64 (1988) 3163.
- [2] O. Kordina et al, *J. Crystal Growth* 154 (1995) 303.
- [3] N.T. Son et al, *J. Appl. Phys.* 79 (1996) 3784.

Optical investigation of thick 3C–SiC layers deposited on bulk silicon by CVD

J.M. Bluet ^{a,*}, J. Camassel ^a, L.A. Falkovsky ^{a,b}, A. Leycuras ^c

^a Groupe d'Etudes des Semiconducteurs, cc074 UM2-CNRS, 34095 Montpellier, cedex 5, France

^b L.D. Landau Institute for Theoretical Physics, Russian Academy of Sciences, Kosyginia 2, Moscow 117 334, Russia

^c Centre de Recherche sur l'Hétéroépitaxie et ses Applications, CNRS, Rue Bernard Gregory, 06560 Valbonne, France

Abstract

Thick (up to 25 µm) SiC layers deposited on silicon have been probed by micro-Raman spectroscopy and infrared reflectivity measurement. The Raman spectra collected on the edge of the sample show a large strain relaxation when moving from the interface region to the free surface of the sample. The IR reflectivity measurements evidence a finite roughness of the Si/SiC interface and about 10% dispersion in the layer thickness homogeneity. © 1997 Elsevier Science S.A.

Keywords: 3C–SiC heteroepitaxy; Roughness; Epitaxial layer uniformity; Strain relaxation

1. Introduction

The fabrication of thick (~20 µm or more) epitaxial layers of 3C–SiC deposited on SOI (Silicon On Insulator) is a goal for micro-sensor applications working in harsh (high temperature, space, radioactive and/or chemically corrosive) environments [1,2]. Considering the cost of available 6H–SiC (or the lack of reproducible 3C–SiC) substrates, this appears interesting also for producing large area-compliant substrate which could be used in the hetero-epitaxial deposition of GaN on silicon [3].

The main characteristic of SiC on SOI is to allow at the same time a better strain relaxation within the complete SiC/silicon wafer system [4] and, versus temperature, improved electrical properties [5,6]. The purpose now is to produce device quality films at the industrial level [7,8]. To this end, the growth technology has still to be optimized and fast, non-destructive, optical techniques are required. Of course, in order to compare with 3C–SiC deposited on bulk silicon wafers, a prerequisite is to investigate the corresponding material. This is done in this work. Using only Raman scattering and infrared (IR) reflectivity measurements, we show that the relaxation of the residual stress, the roughness of

the interfaces and the homogeneity of the as-grown layers can be easily probed.

2. Experimental results and discussion

Four different samples have been considered. All consisted of thick 3C–SiC layers deposited by CVD on silicon, at 1400 °C. We have used propane and silane as active species and changed slightly the carbonization conditions from sample A to samples B, C and D. For additional information, see Ref. [9].

We first started by using a confocal micro-Raman spectrometer (Jobin–Yvon) equipped with a CCD camera. The excitation was provided by the 514 nm line of an argon–krypton laser. The sample was oriented in such a way that, focusing in the backscattering configuration on a {110} cleaved face with ~1 µm laser spot, we could easily probe the SiC layers at various distances from the interface. We display in Fig. 1 the results collected on sample A (18 µm thick).

We have found the following:
(1) near the interface (Fig. 1(a)), a sizeable splitting of the two transverse TO(X') and TO(Z) modes resolves clearly. The frequency splitting reduces significantly when moving 1 µm away from the interface (Fig. 1(b)) and, then, decreases more

* Corresponding author. Fax: 04 67 14 37 60.

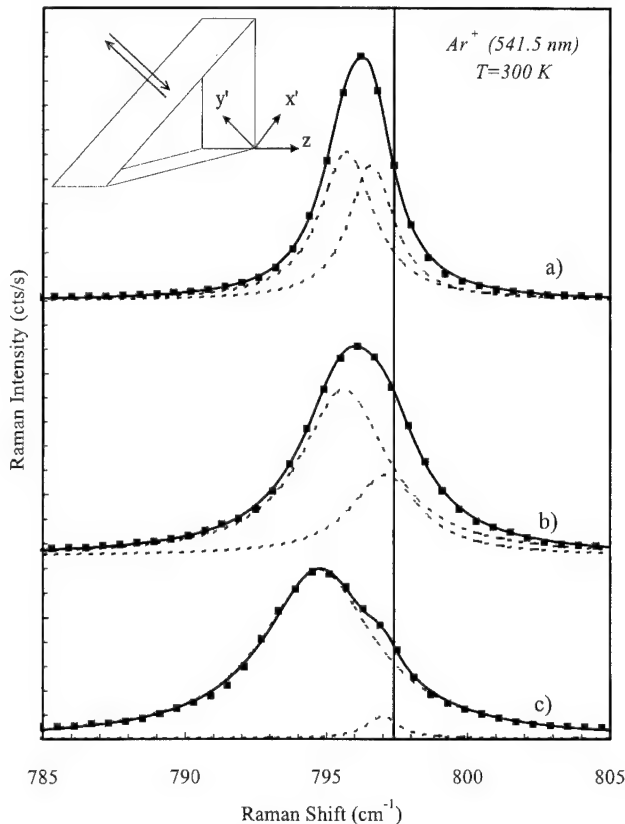


Fig. 1. TO mode frequencies resolved in sample A: (a) near the interface; (b) 1 μm away from the Si/SiC interface; and (c) 2 μm away from the Si/SiC interface. The square symbols represent experimental data. Dashed lines are TO(Z) and TO(X') contributions. Full line gives the sum of the two contributions. The vertical line indicates the bulk material value. Inserted is the back-scattering geometry used in the experiments. Also shown is the corresponding system of rectangular (X' , Y') and Z) axes.

slowly. At 2 μm (Fig. 1(c)) it is still about 1 cm^{-1} . It only becomes unnoticeable after 5 μm ;

- (2) performing an analysis of the experimental spectra in terms of Lorentzian shapes, we get the series of results listed in Table 1. They show clearly that both the magnitude and the relaxation of the interface splitting associated with the two TO frequencies varies from sample to sample. The splitting is larger (but relaxes faster) for sample A carbonized at 1400 °C under a weak propane flux, and smaller (but with less relaxation) for samples B, C and D carbonized at 1380 °C under a larger propane flux;
- (3) similar effects are found in the LO phonon range or concern the silicon substrate. Detailed investigations have been done and will result in a forthcoming paper [10].

Since we now have experimental evidence of a sizeable strain relaxation within the SiC layers, a prerequisite to obtain more quantitative information is to determine accurately the unstrained phonon frequencies. This was done using two different, but mainly strain free, “bulk”

Table 1
Raman lines position and stress-induced splitting of the two SiC (TO₁-TO₂)-like frequencies

Sample	Focal point	ω_{TO1} (cm^{-1})	ω_{TO2} (cm^{-1})	$\Delta(\omega_{\text{TO}})$ (cm^{-1})	ω_{LO} (cm^{-1})
A	Interface	794.5	796.8	2.3	971.9
	1 μm from interface	795.8	796.9	1.1	972.5
	5 μm from interface	797.4	—	—	973.3
B	Interface	794.8	796.5	1.7	—
	1 μm from interface	795.2	796.6	1.4	971.9
	5 μm from interface	795.9	796.9	1	972.3
C	Interface	795.3	797.2	1.9	971.8
	1 μm from interface	795.3	796.4	1.1	971.8
	5 μm from interface	795.4	796.3	0.9	972.4
D	Interface	794.7	796.4	1.7	971.9
	1 μm from interface	795.3	796.9	1.3	972.3
	5 μm from interface	795.8	796.9	1.1	972.6

3C-SiC samples. The first was an epitaxial layer of the 3C variety deposited on a 6H-SiC substrate using the SSM technique. The other was a 4 mm^2 inclusion of 3C polytype in a 6H ingot, produced by the modified Lely method under non-equilibrium conditions. In both cases the doping level did not exceed 10^{17} cm^{-3} and the LO shift arising from the effect of phonon-plasmon coupling could not be larger than 0.5 cm^{-1} . We obtain $797.5 (\pm 0.1) \text{ cm}^{-1}$ for the pure 3C-SiC TO mode and $973.5 (\pm 0.6) \text{ cm}^{-1}$ for the LO one.

With respect to these absolute values, all SiC modes shift to lower energy. This is clear from Fig. 1, where the bulk TO frequency has been shown as a full line. This occurs, of course, because the strain experienced by the SiC layer is tensile. As previously stated, we have found qualitatively similar results, but opposite in sign and much less intense, in silicon. They evidence the compressive strain which does exist in the bulk material wafer: similar to the case of the epitaxial layer, it is maximum at the interface and decreases when moving toward the bulk of the wafer.

As regards the IR reflectivity measurements, performed on the two series of samples, interesting and complementary data have been found. Depending on the sample under investigation, we observed in the range $800\text{--}1000 \text{ cm}^{-1}$ a well developed Reststrahlen band with typically 98% reflectivity amplitude (samples B, C and D) or a double structure with a small weakly allowed component close to the LO frequency (sample A). This is shown in Fig. 2. An oscillator fit analysis indicates that the new component has a very weak oscillator strength (typically 10^{-3} times the strength of the allowed 795 cm^{-1} component) and, because it resolves more clearly on sample A (where both the stress-induced splitting at the Si/SiC interface and the relaxation effect are stronger) we believe again in a stress-induced effect.

The calculation predicts also a strong interference pattern (with about 30% reflectivity changes in the range

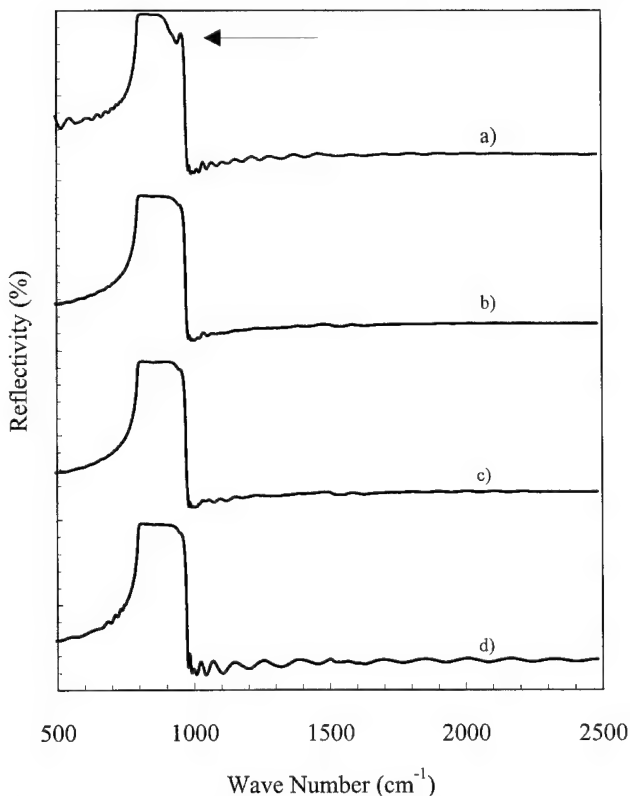


Fig. 2. Infrared reflectivity spectra collected on samples A, B, C and D, respectively. Notice the weak mode (arrow) which resolves on sample A near the LO frequency. This occurs because of the larger stress relaxation noticed in this case.

1100 and 5000 cm⁻¹). This is obviously not found. To account for such a discrepancy, the simplest way is to introduce a finite surface and/or interface roughness. Both effects, which scatter the incident light, must result in a loss of amplitude of (i) specular reflectivity; and (ii) the interference pattern [11]. Fitting the experimental data, we could get typical values of 70 nm at the top SiC surface and 1 μm at the lower Si/SiC interface. The comparison with the experimental spectra was satisfactory but, even if we could obtain very good agreement, two problems remained:

- (1) the amplitude of the interference pattern which appears near the Reststrahlen band was largely overestimated in the theoretical calculation;
- (2) the estimated interface roughness (1 μm) was also far too large when comparing with the TEM data collected on a typical sample [9].

To solve these discrepancies, we considered the loss in light coherency which arises when a finite distribution of layer thickness exists within the area probed by the IR beam. Since only a well defined thickness can correspond with a (well defined) interference figure, all fringes must vanish when averaging over different values. Indeed, assuming a gaussian distribution of thickness, we could calculate reasonable (final) spectra and obtain

Table 2
Growth parameters deduced for the four SiC layers investigated in this work from the analysis of IR reflectivity spectra

Sample	A	B	C	D
Γ (cm ⁻¹)	3	2	2	2
Thickness (μm)	18	25	21	11.3
Homogeneity (μm)	1.5	2.2	2	1.2
Surface roughness (nm)	25	75	78	70
Si/Si interface roughness (nm)	300	350	400	300

information about the macroscopic (large scale) roughness associated with the growth process. All results concerning the four different samples have been reported in Table 2. We find that while the Si/SiC roughness is of the order of 350 (± 50) nm, each time the thickness homogeneity is 10% of the final average value. The main difference noticed in this case between sample A and samples B, C and D is the surface roughness. Like the interfacial strain, it seems to correlate with the carbonization conditions.

3. Conclusion

Investigating a series of thick SiC layers grown on silicon substrates, we have shown that micro-Raman spectroscopy performed on the sample edge reveals strain in both the SiC layer and the bulk Si wafer. The strain relaxes when moving away from the interface. The IR reflectivity measurements confirm the strain relaxation and demonstrate either a surprisingly large roughness, both at the Si/SiC interface and the free SiC surface, or a lack of layer thickness uniformity. Maintaining the Si/SiC roughness at a reasonable level, they suggest a 10% dispersion in the final values of thickness probed by the IR beam.

References

- [1] J.C. Pazik, G. Kelner, N. Bottka, Appl. Phys. Lett. 58 (1991) 1419.
- [2] A.J. Steckl, C. Yuan, Q.-Y. Tong, U. Gosele, M.J. Loboda, J. Electrochem. Soc. 141 (1994) L66.
- [3] Z. Yang, F. Guarin, I.W. Tao, W.I. Wang, S.S. Iyer, J. Vac. Sci. Technol. B13 (1995) 789.
- [4] J. Camassel, C. Dezaudier, L. DiCioccio, J. Stoemenos, J.M. Bluet, S. Contreras, J.L. Robert, T. Billon, Inst. Phys. Conf. Series 142 (1996) 453.
- [5] J.-M. Bluet, S. Contreras, J. Camassel, J.-L. Robert, L. Di Cioccio, W. Reichert, R. Lossy, E. Obermeier, J. Stoemenos, Proc. E-MRS'96 Spring Meeting, Symposium A (to be published in Mat. Science and Eng. B)
- [6] W. Reichert, R. Lossy, J.-M. Gonzales Sirgo, E. Obermeier, J. Stoemenos, Inst. Phys. Conf. Series 142 (1996) 129.
- [7] SBIR 95-1 Solicitation, Proposal 08.02-6000
- [8] Brite-Euram 3 Call, Proposal BE 96-3339
- [9] A. Leycuras, this conference; also see: Leycuras, Applied Physics Letters (in press) and references therein.
- [10] L. Falkovsky, J. Camassel, J.M. Bluet, Phys. Rev. B 55, Rapid Comm. (in press).
- [11] H.E. Bennett, J.O. Porteus, J. Opt. Soc. Am. 51 (1960) 123–129.



ELSEVIER

Characterization of electrically active deep level defects in 4H and 6H SiC

J.P. Doyle ^{a,*}, M.O. Aboelfotoh ^a, B.G. Svensson ^a, A. Schöner ^b, N. Nordell ^b

^a Royal Institute of Technology, Solid State Electronics, P.O. Box E229, S-164 40 Kista-Stockholm, Sweden

^b Industrial Microelectronics Center, P.O. Box 1084, S-164 21 Kista-Stockholm, Sweden

Abstract

Electrically active deep level defects have been characterized in n-type 6H- and 4H-SiC utilizing deep level transient spectroscopy (DLTS). In both polytypes, defects are observed in the as-grown state. In 6H-SiC two levels in the energy gap at 0.34 and 0.41 eV below the conduction band edge (E_c) are suggested as being intrinsic in nature as their concentration increases after 2 MeV electron irradiation. Additionally, a level 0.51 eV below E_c observed after electron or deuterium irradiation anneals out completely below 300 °C. In as-grown epitaxial layers of the 4H-SiC polytype, a level 0.70 eV below E_c is found with a capture cross-section of $4 \times 10^{-14} \text{ cm}^2$ and a concentration at or below $1 \times 10^{13} \text{ cm}^{-3}$ exhibits acceptor-like behavior. Secondary ion mass spectrometry (SIMS) profiling reveals no evidence for Ti, V, or Cr incorporation into the epitaxial layers above $\approx 10^{13} \text{ cm}^{-3}$. © 1997 Elsevier Science S.A.

Keywords: Defects; SIMS; DLTS; Deep levels

1. Introduction

Defects and impurities in semiconducting materials can result in efficient recombination centers or carrier traps leading to a reduction in, for example, the carrier lifetime. The identification and control of as-grown defects becomes important as the elimination or control of these levels is required for device technology to progress. In this work, as-grown layers of both 6H and 4H polytypes were characterized through the use of deep level transient spectroscopy (DLTS), secondary ion mass spectrometry (SIMS), electron and ion beam irradiation, and thermal annealing in order to shed some light on the origin of these levels.

2. Experimental

Vapor phase epitaxy (VPE) was used to grow both 4H and 6H n-type epitaxial layers with doping concentrations ranging from 1×10^{15} to $2 \times 10^{16} \text{ cm}^{-3}$. In all cases the dopant was nitrogen. Characterization was performed on layers either grown by a previously described process [1,2] or on samples obtained from Cree Research Inc [3].

Deep level transient spectroscopy measurements were conducted using rate windows ranging from $(100 \text{ ms})^{-1}$ to $(3.2 \text{ s})^{-1}$ in the temperature range 77–365 K. The experimental set-up has been previously described [4]. In the determination of the capture cross-section of the levels we assume a T^2 -correction to account for the temperature dependence of the effective density of states in the conduction band and the electron velocity.

Secondary ion mass spectroscopy measurements were performed using a Cameca IMS 4f microanalyzer utilizing an O_2^+ ion beam. Through the aid of ion implanted standards, we obtained sensitivities of $< 10^{14} \text{ cm}^{-3}$ for V and Ti and $< 10^{13} \text{ cm}^{-3}$ for Cr.

Electron irradiation was performed at room temperature with the samples held against a water-cooled block which kept them at a temperature below 30 °C. The electron energy was 2 MeV with the dose in the range 1×10^{15} to $1 \times 10^{16} \text{ cm}^{-2}$. Annealing of the samples was conducted in a furnace continuously flushed with nitrogen in the temperature range between 300 and 1000 °C.

3. Results

As shown in Fig. 1, electron irradiation results in a number of electrically active deep levels which have been

* Corresponding author.

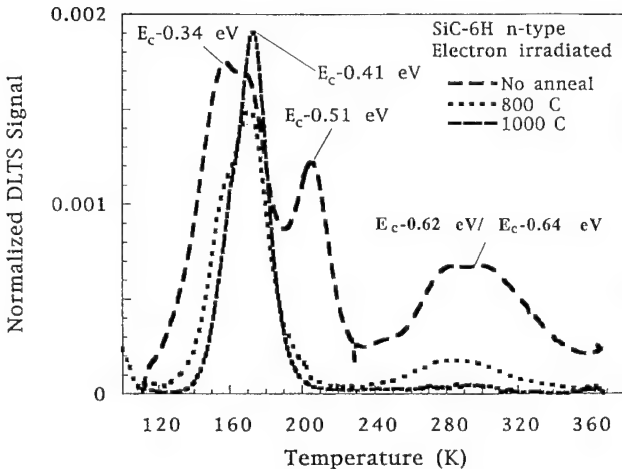


Fig. 1. DLTS spectra of electron irradiated SiC-6H n-type epitaxial layer. The doping concentration and electron dose were approximately $2 \times 10^{16} \text{ cm}^{-3}$ and $1 \times 10^{16} \text{ cm}^{-2}$, respectively, although in the case of the 1000°C annealed sample the electron beam dose was somewhat higher. Maximum defect concentrations: 0.34 eV and 0.41 eV levels: $2.2 \times 10^{14} \text{ cm}^{-3}$; 0.51 eV: $1.5 \times 10^{14} \text{ cm}^{-3}$; 0.62/0.64 eV: $8 \times 10^{13} \text{ cm}^{-3}$.

reported previously [5,6]. However, after an 800°C anneal for 30 min, a significant reduction in the levels at 0.62 eV (capture cross-section: $1 \times 10^{-16} \text{ cm}^2$) and 0.64 eV ($1 \times 10^{-17} \text{ cm}^2$) below the conduction band edge (E_c) is observed along with the complete removal of the $E_c - 0.51 \text{ eV}$ ($2 \times 10^{-14} \text{ cm}^2$) level. In addition, the $E_c - 0.34 \text{ eV}$ ($6 \times 10^{-16} \text{ cm}^2$) and $E_c - 0.41 \text{ eV}$ ($3 \times 10^{-14} \text{ cm}^2$) levels are also found to be reduced with the $E_c - 0.34 \text{ eV}$ level annealing at a faster rate. After a 1000°C anneal we observe that the $E_c - 0.62 \text{ eV}$ and $E_c - 0.64 \text{ eV}$ levels are completely annealed while the $E_c - 0.34 \text{ eV}$ and $E_c - 0.41 \text{ eV}$ levels remain, with the $E_c - 0.34 \text{ eV}$ level just visible as a kink on the low temperature side of the $E_c - 0.41 \text{ eV}$ level. Note that the higher signal from these two levels is due to the slightly higher electron dose when compared with the as-grown and 800°C conditions which were taken from the same sample. The result is consistent with that observed in as-grown material where only these lower energy levels remain as plotted in Fig. 2. Note that the spectra are identical except for the intensity of the peaks, a sign of the higher defect concentration in the electron beam irradiated sample even after the 1000°C anneal.

As transition metals are ubiquitous to bulk grown samples especially Ti, Cr and V a SIMS analysis of a 6H-SiC epilayer is shown in Fig. 3. We find that the concentration of V and Ti is less than the detection limit which has been determined to be less than $1 \times 10^{14} \text{ cm}^{-3}$ while that for Cr is below $1 \times 10^{13} \text{ cm}^{-3}$.

The results of deuterium implantation shown in the DLTS spectra of Fig. 4 reveal the same basic trend as discussed earlier for electron irradiated samples. It should be noted that the damage introduced by the relatively moderate dose causes a significant amount of donor compensation which complicates the observability

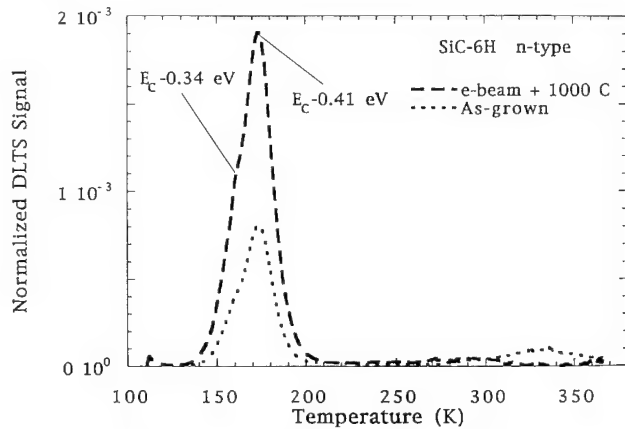


Fig. 2. A comparison of the as-grown ($1.6 \times 10^{13} \text{ cm}^{-3}$) deep level defects and after a $1 \times 10^{15} \text{ cm}^{-2}$ electron irradiation dose and thermal annealing ($4 \times 10^{13} \text{ cm}^{-3}$).

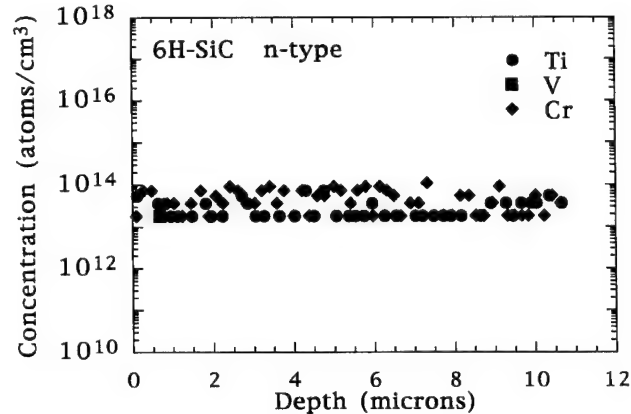


Fig. 3. SIMS analysis for Ti, V, and Cr using O_2^+ ion sputtering.

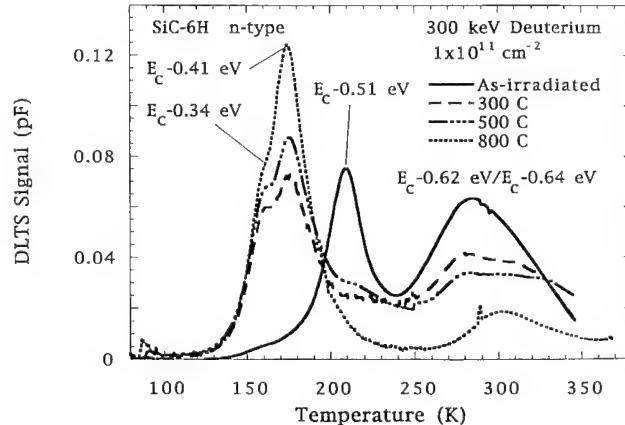


Fig. 4. DLTS spectra after deuterium ion implantation and thermal annealing. Maximum defect concentrations: 0.34 eV: $1.7 \times 10^{14} \text{ cm}^{-3}$; 0.41 eV: $2.5 \times 10^{14} \text{ cm}^{-3}$; $0.62/0.64 \text{ eV}$: $1.4 \times 10^{14} \text{ cm}^{-3}$.

of deep level traps especially at lower temperatures. Additionally, an accurate determination of the maximum trap concentration is not possible as the compensation does not allow us to fully probe the implantation end-of-range region where the highest concentration of defects are located. However, annealing at 300°C results

in a partial restoration of the lattice structure as reflected by the observability of all defect levels except for the level at $E_c - 0.51$ eV which is completely eliminated. Additionally we observe a large decrease in the $E_c - 0.62$ eV and $E_c - 0.64$ eV levels. It should be noted that the increasing signal strength for the $E_c - 0.34$ eV and $E_c - 0.41$ eV levels is the result of a decreasing compensation of the donor levels as the crystal is annealed. Interestingly the compensation of the donor by deuterium implantation damage is found to be much greater in SiC than in Si for an equivalent dose and energy.

In 4H-SiC only a single level is observed at $E_c - 0.70$ eV (4×10^{-14} cm 2) in as-grown material with a concentration of $\approx 1 \times 10^{13}$ cm $^{-3}$. The level is observed to be acceptor-like from the lack of a Poole–Frenkel shift as the electric field is varied as shown in Fig. 5. Secondary ion mass spectrometry analysis was identical to that for the 6H epitaxial layer with Ti, V, and Cr below the detection limit shown in Fig. 3.

4. Discussion

The DLTS data on as-grown and irradiated SiC coupled with the SIMS analysis for the common bulk grown contaminants, provided strong evidence that the as-grown defects are not the result of metallic impurities but are intrinsic in nature (i.e. vacancies and/or Si and C interstitials and combinations thereof). Additionally, the annealing of 6H-SiC irradiated samples with the resulting decrease in the $E_c - 0.51$ eV, $E_c - 0.62$ eV, and $E_c - 0.64$ eV levels is consistent with that usually observed in as-grown samples, that is only the $E_c - 0.34$ eV and $E_c - 0.41$ eV levels are present although the concentrations are typically in the low 10 13 cm $^{-3}$ range. Early DLTS 6H-SiC studies of Lely grown bulk samples and epitaxial layers grown by LPE (liquid phase

epitaxy) reported the $E_c - 0.62$ eV and $E_c - 0.64$ eV levels (so-called Z₁/Z₂ centers) with the epitaxial layers requiring electron or ion irradiation in order to observe the level [5,7]. Unfortunately, there was no mention of a chemical characterization of these samples. The levels were also reported to have a thermal stability up to 1700 °C. The same levels observed in this work, however, are annealed out after a 1000 °C anneal for 30 min. One possible explanation is the presence of impurities in the sample with a position in the electronic bandgap near to the Z₁/Z₂ center. Recent work has shown that V incorporated into bulk grown samples introduces a level in the bandgap at $E_c - 0.66$ eV, very near to the Z₁/Z₂ center [8].

In the case of 4H-SiC, our initial speculation for the single level observed in as-grown material centered upon impurities. These are likely to be transition metals particularly in the recent work on the identification of a Cr deep level at $E_c - 0.74$ eV through the use of radioactive ion implantation [9]. However, SIMS analysis revealed that the concentration of Cr in the epitaxial layers was below 1 × 10 13 cm $^{-3}$, which is near to the measured defect concentration.

Additionally, after electron irradiation where two levels at $E_c - 0.62$ eV (4×10^{-14} cm 2) and $E_c - 0.68$ eV (5×10^{-15} cm 2) are produced [6], we find that the $E_c - 0.70$ eV level evolves from these levels after low temperature thermal treatment. In contrast, Kimoto *et al.* [10] observed the levels at 0.62 and 0.68 eV in as-grown epitaxial layers. The transformation can occur at room temperature as well as after long periods of time. After the transformation, the $E_c - 0.70$ eV level is found to be stable. Although the origin of this effect is currently under more detailed study, it appears that carbon may be involved. In silicon, the high mobility of interstitial carbon can result in the formation of unstable electrically active defects at room temperature. The initial position of a deep level in the electronic bandgap associated with

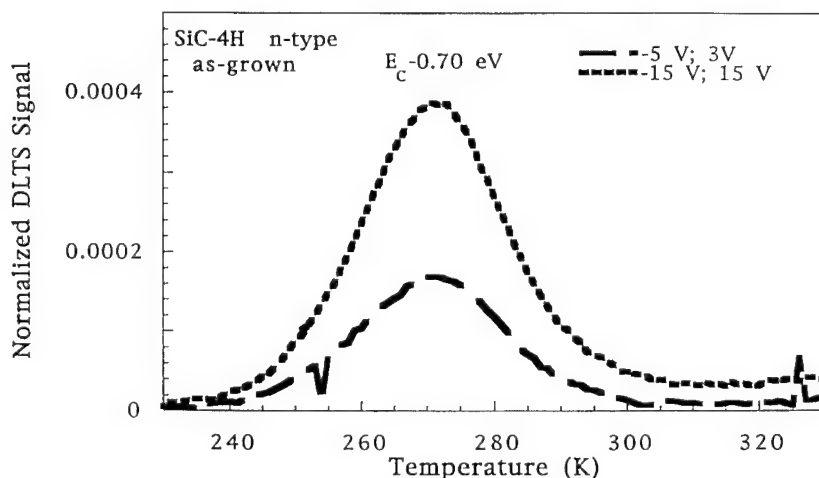


Fig. 5. As-grown SiC-4H sample under differing electric fields. Concentration of the level was measured to be 1×10^{13} cm $^{-3}$.

carbon is observed to decrease with the increasing concentration of a new level correlated to the decreasing level [11]. The new level produced in this transformation is also found to be stable.

5. Conclusion

In both 6H and 4H epitaxial layers in this study, the observed deep levels are found to be intrinsic defects (i.e. vacancies and/or interstitials and combinations thereof) and not the result of transition metal impurities of Ti, V, or Cr. The most stable defects are located in the electronic bandgap at $E_c - 0.34$ eV and $E_c - 0.41$ eV consistent with that observed in the as-grown state. The level at $E_c - 0.51$ eV is found to anneal out completely at or below 300 °C while the defects at $E_c - 0.62$ eV and $E_c - 0.64$ eV are found to anneal out at or below 1000 °C. In 4H-SiC, the level at $E_c - 0.70$ eV is found to be the most stable consistent with the as-grown case. The unstable nature of the $E_c - 0.62$ eV and $E_c - 0.68$ eV levels at room temperature may be related to carbon.

References

- [1] N. Nordell, S.G. Andersson, A. Schöner, Inst. Phys. Conf. Series 142 (1996) 81.
- [2] O. Kordina, C. Hallin, R.C. Glass, A. Henry, E. Janzén, Inst. Phys. Conf. Series 137 (1993) 41.
- [3] Cree Research Inc. Meridian Parkway, Durham, N.C., USA
- [4] B.G. Svensson, K.H. Ryden, B.M.S. Lewerentz, J. Appl. Phys. 66 (1989) 1699.
- [5] G. Pensl, W.J. Choyke, Phys. B 185 (1993) 264.
- [6] J.P. Doyle, M.O. Aboelfotoh, M.K. Linnarsson, B.G. Svensson, A. Schöner, N. Nordell, C. Harris, J.L. Lindström, E. Janzén, C. Hemmingsson, Proceedings of the 1996 Spring MRS Meeting, San Francisco, CA (in press).
- [7] H. Zhang, Ph.D. Thesis, Erlangen University, Germany, 1990.
- [8] J. Jenny, M. Skowronski, W.C. Mitchel, H.M. Hobgood, R.C. Glass, G. Augustine, R.H. Hopkins, Appl. Phys. Lett. 68 (1996) 1963.
- [9] N. Achtinger, W. Witthuhn, Proceedings of the E-MRS 1996 Spring Meeting, Session A (in press)
- [10] T. Kimoto, A. Itoh, H. Matsunami, S. Sridhara, L.L. Clemen, R.P. Devaty, W.J. Choyke, T. Dalibor, C. Peppermuller, G. Pensl, Appl. Phys. Lett. 67 (1995) 2833.
- [11] A.K. Tipping, R.C. Newman, Semicond. Sci. Technol. 2 (1987) 315.

High field/high temperature performance of semi-insulating silicon carbide

T.S. Sudarshan ^{a,*}, G. Gradinaru ^a, G. Korony ^a, S.A. Gradinaru ^b, W. Mitchel ^c

^a Department of Electrical and Computer Engineering, University of South Carolina, Columbia, SC 29208, USA

^b SC Governor's School for Science and Mathematics, Hartsville, SC 29550, USA

^c WL/MLPO Bldg. 651, 3005 P St. Ste 6, Wright-Patterson AFB, OH 45433-7707, USA

Abstract

The influence of ambient temperature (295–730 K) and pulsed electric fields (0.5–80 kV/cm) on the electrical properties of high resistivity single-crystal 6H-SiC is reported. It is shown that the resistivity of the undoped 6H-SiC varies strongly, with the ambient temperature following a temperature/field function dominated by an exponential factor containing the activation (ionization) energy of residual boron of 0.35 eV. The dominant activation energy of semi-insulating Vanadium-compensated material (6H-SiC:V) varies with the ambient temperature, increasing from approx. 0 eV at 295–320 K to approx. 0.8 eV at T>600 K. This result can explain the viability of insulating 6H-SiC as a substrate for next-generation high temperature power microwave integrated circuits based on large bandgap semiconductors. © 1997 Elsevier Science S.A.

Keywords: Silicon carbide; Resistivity; Temperature; Electronic field

1. Introduction

Silicon carbide is a highly promising semiconductor material for high temperature (600–900 K) electronic applications [1–3]. Along with various electronic active devices, SiC is a serious contender as a semi-insulating or insulating substrate for next-generation high temperature/high power/high density microwave integrated circuits, based on large bandgap semiconductors (GaN and SiC). In the past few years high resistivity undoped and V-compensated single crystal 6H-SiC have been produced [4]. A severe limitation of these materials is the significant decrease of their electrical resistivity (ρ) with an increase in the ambient temperature (T) [4,5]. In the present work the electrical resistivity of 6H-SiC is measured directly in a pulsed regime in function of the applied field and ambient temperature.

27.5 kΩcm, and two types of 6H-SiC:V ($\rho_0=165$ kΩcm and $\rho_0=10^{11}$ – 10^{12} Ωcm) were investigated using lateral MSM structures with a 0.64 mm gap and rounded NiCr/Au contacts (Fig. 1a). A resistive heater (Fig. 1b) and a thermocouple control the device temperature. All tests were performed in vacuum (approx. 5×10^{-4} Pa). Simultaneous time–voltage [V(t)], current [I(t)], and light emission signal [VIS(t)] characteristics were obtained at different temperatures, starting with room temperature ($T_0=295$ K) with relatively small steps (10–20 K) up to approx. 730 K. The pulsed electric field was applied also in small steps (0.5–1 kV/cm) starting at approx. 0.5 kV/cm up to approx. 80 kV/cm, depending on the ambient temperature and maximum current density. Rectangular voltage pulses of approx. 2 μs duration were applied for semi-insulating and insulating 6H-SiC in order to separate the displacement current component from the total current.

2. Experimental

Three types of undoped 6H-SiC having the room temperature and low field resistivity (ρ_0) of 1.1, 4.5, and

3. Results

The I–V (peak-to-peak) and corresponding J–E characteristics at $T=\text{constant}$ are fairly linear up to large fields for all undoped types of 6H-SiC and for the

* Corresponding author. Fax: 1 803 777 8045;
e-mail: sudarsha@charlie.ece.sc.edu

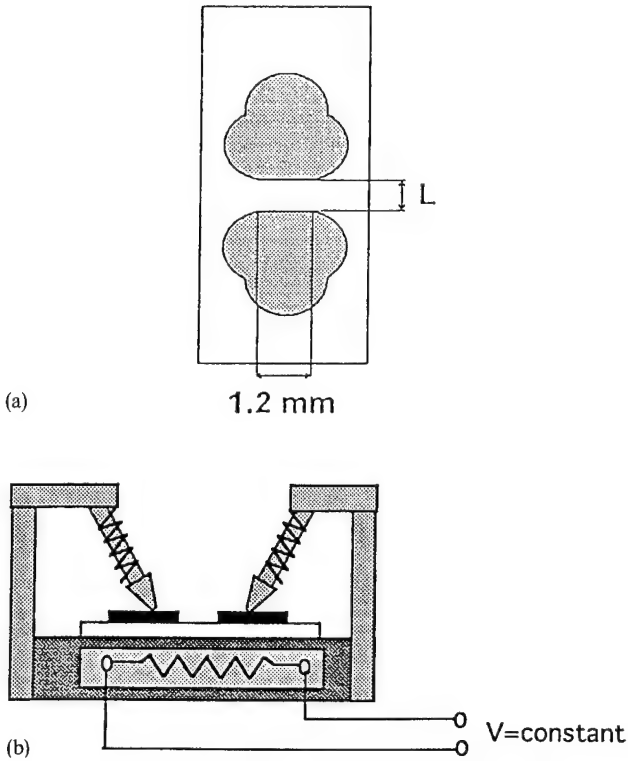


Fig. 1. Lateral MSM test device geometry (a) and the high field probe system with heater (b).

165 k Ω cm 6H-SiC:V, indicating the dominant ohmic character of the electrical response. Note that the second type of 6H-SiC:V was practically insulating, behaving at room temperature like quartz ($\rho_0 \geq 10^{14} \Omega\text{cm}$).

With $\rho = E/J$, the experimental variation $\rho = f(E)$ at $T = \text{constant}$ is obtained for each material. Then, experimental characteristics $\rho = f(T)$ at $E = \text{constant}$ and Arrhenius plots $\log \rho = f(1000/T)$ at $E = \text{constant}$ are produced. Examples of such experimental characteristics are presented for the 4.5 k Ω cm undoped 6H-SiC in Figs. 2 and 3 and for the 165 k Ω cm 6H-SiC:V in Figs. 4 and 5. Note that the theoretical characteristics (solid lines) in Figs. 2 and 3 will be discussed later.

A significant difference in the electrical response of undoped V-compensated 6H-SiC to a temperature/field stress is observed. For all undoped SiC, the resistivity strongly decreases with temperature following a general exponential law. By increasing the device temperature above room temperature by $\Delta T = 10, 50, 225$ and 430 K, ρ decreases from ρ_0 by a factor of 2, 10, 100, and 450, respectively. For the V-compensated material, ρ is approx. constant for $\Delta T = 10–20$ K above room temperature and then decreases only by approx. 35% for $\Delta T = 50$ K. However, for $T > 500$ K, ρ decreases with a larger rate in 6H-SiC:V than in the undoped material. Consequently, a quasi-linear Arrhenius plot at low fields for the undoped material is obtained (Fig. 3), but a non-linear one for the 6H-SiC:V (Fig. 5).

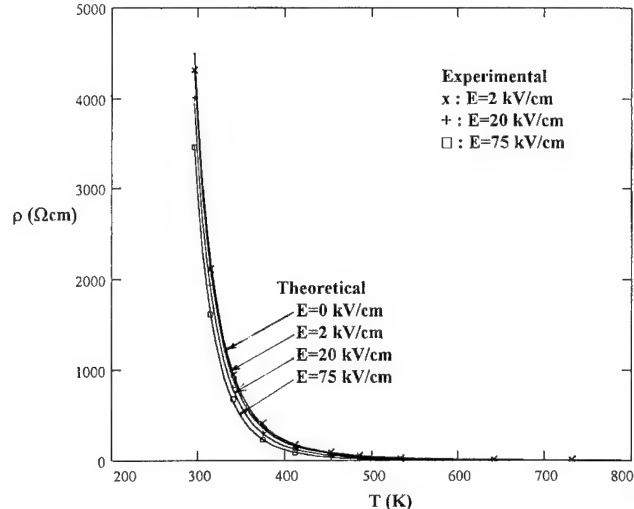


Fig. 2. Experimental and theoretical resistivity-temperature characteristics at $E = \text{constant}$ for the 4.5 k Ω cm undoped 6H-SiC.

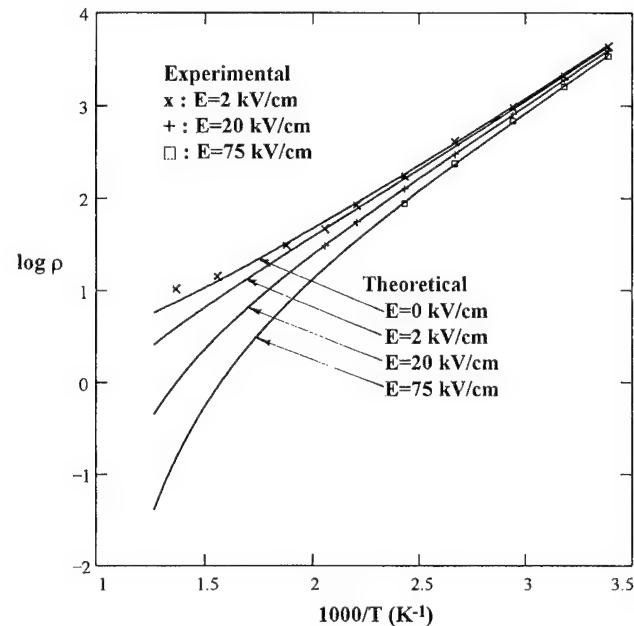


Fig. 3. Experimental and theoretical $\log \rho = f(1000/T)$ characteristics at $E = \text{constant}$ for the 4.5 k Ω cm undoped 6H-SiC.

The field influence on ρ is also different for the undoped and V-doped 6H-SiC. For the undoped material E induces a significant decrease (approx. 40%) of ρ only at $T > 500$ K, for low fields (0.5–5 kV/cm), while for 6H-SiC:V, ρ decreases strongly at lower temperatures (295–350 K) and very low fields (0.5–2.5 kV/cm).

4. Discussion

For p-type 6H-SiC, the resistivity may be approximated by $\rho = 1/q\mu_p p$, where q is the electron charge, μ_p

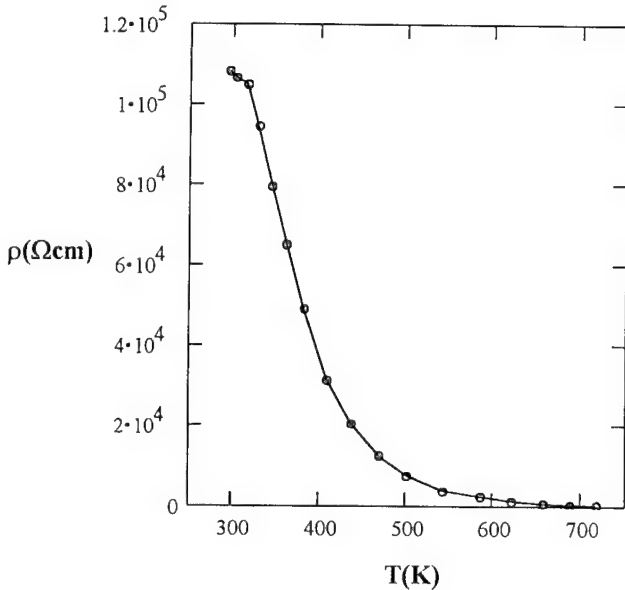


Fig. 4. Experimental resistivity-temperature variation at $E=10$ kV/cm for the 165 $\text{k}\Omega\text{cm}$ 6H-SiC:V.

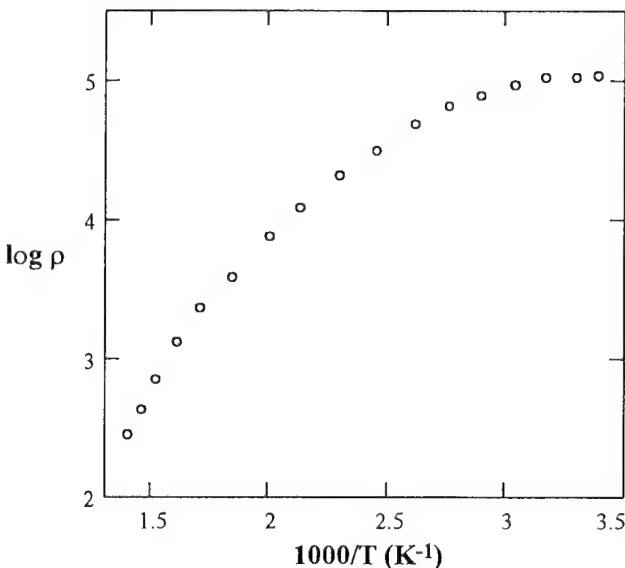


Fig. 5. Experimental Arrhenius plot at $E=10$ kV/cm for the 165 $\text{k}\Omega\text{cm}$ 6H-SiC:V.

is the hole mobility, and p is the hole concentration. Consequently, the $\rho=f(T,E)$ variation is directly related to $\mu_p(T,E)$ and $p(T,E)$ correlations. Considering a single acceptor level in 6H-SiC, $p \propto \exp(-E_a/kT)$ and $\mu_p \propto T^{-2}$ Ref. [6]; using the reference constant ρ_0 , the $\rho(T)$ function at zero or very low fields is:

$$\rho(T)=\rho_0(T/T_0)^2 \exp[(E_a/kT)-(E_a/kT_0)] \quad (1)$$

We observed that, using Eq. (1) in a representation $\log \rho=f(1000/T)$ (Arrhenius plot), the value of E_a should be corrected with a $+2 kT$ term compared with the result from a general form $\rho(T)=C \exp(E_a/kT)$, as

used in different reports [4,5]. We found the experimental data at low field ($E=2$ kV/cm), for all undoped 6H-SiC, a value $E_a=0.35$ eV which corresponds to the most reliable value of the boron level in 6H-SiC [4,7].

The field influences the resistivity of p-type 6H-SiC only through carrier concentration, because the mobility (μ_p) is constant up to ~ 150 kV/cm [8]. A field-assisted thermal ionization process, described first by Frenkel [9] is believed to take place in this case. However, the Frenkel function $\omega(E,T)=q(qE/\pi K_s \epsilon_0)^{1/2}/kT$ (K_s =relative permittivity and ϵ_0 =vacuum permittivity), was modified according to our results as $\gamma(E,T)=\omega(E,T)/10(T_0/T)^4$, resulting in a general $\rho(T,E)$ expression which we propose for a single or dominant impurity level in p-type 6H-SiC:

$$\rho(T,E)=\rho_0(T/T_0)^2 \exp[(E_a/kT) - (E_a/kT_0)] \exp[-\gamma(E,T)] \quad (2)$$

Using Eq. (2) we have obtained the theoretical characteristics (solid lines) $\rho=f(E)$ at $T=\text{constant}$, $\rho=f(T)$ at $E=\text{constant}$ (Fig. 2), and $\log \rho=f(1000/T)$ at $E=\text{constant}$ (Fig. 3). For all types of undoped 6H-SiC, as shown in Figs. 2 and 3 for the 4.5 $\text{k}\Omega\text{cm}$ sample, the theoretical characteristics correspond very well to experimental ones for $E_a=0.35$ eV, especially in the 295–600 K range. For $T>600$ K, additional processes cause a reduction of ρ at low fields larger than that predicted by Eq. (2). We can conclude that all types of high resistivity undoped 6H-SiC are dominated by residual boron introduced during the growth process [4].

In contrast, owing to the compensation process being gradually affected by the device temperature in the V-compensated material, the resultant activation energy changes with the temperature, as indicated in Fig. 5. The resultant E_a increases from approx. 0 eV at $T=295\text{--}320$ K to about 0.8 eV for $T\geq 600$ K. Note that for $T\geq 600$ K the Arrhenius characteristic in Fig. 5 becomes a straight line with a slope corresponding to a non-corrected $E_a=0.67$ eV, very similar to the value (0.66 eV) reported recently [5]. However, owing to the correction ($+2 kT$) imposed by the factor $(T_0/T)^2$ introduced by the mobility in $\rho(T,E)$ variation, we obtained $E_a=0.8$ eV in 6H-SiC:V at $T\geq 600$ K, which was proposed as a V-acceptor level in 6H-SiC [5]. The compensation process in 6H-SiC:V should take place between three main levels: V-donor ($E_a=1.35$ eV beneath E_v), V-acceptor ($E_a=0.8$ eV beneath E_v), and B-acceptor ($E_a=0.35$ eV above E_v). Near room temperature (295–320 K) the compensation is very effective, indicating a negligible resultant activation energy. Between 320 and 600 K, E_a increases to ~ 0.8 eV and maintains this value for $T>600$ K, suggesting the dominance of the V-acceptor level at high temperatures.

The above results can better explain the behavior of insulating 6H-SiC:V than the recently reported fixed

E_a values (1.48 or 0.66 eV) [4,5]. In lateral MSM structures, considering our current sensitivity ($\sim 20 \mu\text{A}$), the material resistivity exceeds $10^8 \Omega\text{cm}$ for large ambient temperatures ($T=700 \text{ K}$) and applied fields ($E=80 \text{ kV/cm}$). As shown in Fig. 5, a variable E_a may result in a reduction of ρ by only about 10^3 between 295 and 700 K, leading to a $\rho_0=10^{11}\text{--}10^{12} \Omega\text{cm}$ of the insulating material, more acceptable than $\rho>10^{15} \Omega\text{cm}$ required by a fixed E_a [4]. However, in vertical 6H-SiC:V MSM devices, at room temperature and moderate fields (20–50 kV/cm), ρ decreases to $\sim 10^7 \Omega\text{cm}$, indicating a large increase in the current density. We believe that this process is due to the presence of micropipes in the material, which activate easily in parallel fields (vertical devices), but are insensitive to perpendicular fields (lateral devices) [10].

5. Conclusions

The strong influence of the ambient temperature and the applied electric field on the electrical resistivity of undoped and V-compensated 6H-SiC was demonstrated by direct measurements of the resistivity in lateral MSM devices in pulsed regime. The resistivity variation of the undoped 6H-SiC with ambient temperature is mainly dominated by the boron acceptor level, with $E_a=0.35 \text{ eV}$ making it impractical for high temperature microwave integrated circuits. The field influence was well described for the undoped material by a modified Frenkel function. A clear variation of the activation energy with the ambient temperature was observed in the V-compensated material, resulting in very large

resistivity at high ambient temperatures. The results of lateral MSM devices, with no micropipe activation at high temperatures and high fields, prove the viability of insulating 6H-SiC:V for high temperature power microwave integrated circuits based on large bandgap semiconductors.

Acknowledgement

We are grateful to Dr Dwight Duston and Dr Kepi Wu of BMDO/TRI for their encouragement and support of this research.

References

- [1] R.F. Davis, G. Kelner, M. Shur, J.M. Palmour, J.A. Edmond, Proceedings IEEE 79 (1991) 677.
- [2] M. Bhatnagar, B.J. Baliga, IEEE Trans. Electron Devices 40 (1993) 645.
- [3] M. Shur, B. Gelmont, C. Saavedra-Munoz, G. Kelner, Inst. Phys. Conf. Ser. No. 137 (1993) 465–470.
- [4] H.M. Hobgood, R.C. Glass, G. Augustine, R.H. Hopkins, J.R. Jenny, M. Skowronski, W.C. Mitchel, M. Roth, Appl. Phys. Lett. 66 (1995) 1364.
- [5] J.R. Jenny, J. Skowronski, W.C. Mitchel, H.M. Hobgood, R.C. Glass, G. Augustine, R.H. Hopkins, Appl. Phys. Lett. 68 (1996) 1963.
- [6] M. Yamanaka, H. Daimon, E. Sakuma, S. Mishawa, S. Yoshida, J. Appl. Phys. 61 (1987) 599.
- [7] W. Sutrop, G. Pensl, P. Lanig, Appl. Phys. A 51 (1990) 231.
- [8] R.J. Trew, J.-B. Yan, P. Mock, Proceedings IEEE 79 (1991) 598.
- [9] J. Frenkel, Tech. Phys. (USSR) 5, 685 (1938) and Phys. Rev. 54 (1938) 647.
- [10] T.S. Sudarshan, G. Gradinaru, G. Korony, W.C. Mitchel, R.H. Hopkins, J. Electr. Mat. 25 (1996) 893.

OBIC studies on 6H-SiC Schottky rectifiers with different surface pretreatments

Manfred Frischholz ^{a,*}, Kurt Rottner ^a, Adolf Schöner ^a, Thomas Dalibor ^b, Gerhard Pensl ^b

^a IMC, P.O. Box 1084, S-164 25 Stockholm-Kista, Sweden

^b Lehrstuhl für Angewandte Physik, Universität Erlangen-Nürnberg, D-91058 Erlangen, Germany

Abstract

The influence of different surface treatments on the device characteristics of Schottky rectifiers was investigated. Prior to the formation of Schottky barrier contacts the SiC surface was either thermally annealed in hydrogen, etched using O₂ or CF₄/Ar/H₂ as reactive gases or Ar sputtered. Differences in reverse current densities of several orders of magnitude for different surface treatments were observed. The effective device area was determined by the optical beam induced current (OBIC) technique. The results confirm that the effective device area is given by the area of the metal contact and the additional area of the surface charge induced depletion layer. Our results indicate the importance of an optimized surface treatment in order to control the quality and the area of the surface region for achieving optimum device performance. © 1997 Elsevier Science S.A.

Keywords: OBIC; Schottky contacts; Surface pretreatment; 6H-SiC

1. Introduction

The high breakdown electric field strength of SiC makes it one of the most promising candidates to replace silicon in power semiconductor applications. However, in order to utilize the advantage in electric field strength over other materials a proper design of the junction termination is crucial to reduce the surface electric field to prevent premature breakdown at the surface and to be able to use established passivation schemes developed for silicon power devices.

Experimentally observed breakdown voltage of SiC rectifiers exceed the value predicted by 2-D numerical device simulations and approach the value of the parallel plane case for both, SiC p-n mesa diodes [1] and Schottky diodes [2]. In these previous studies the authors found evidence for negative surface charge on n-type and positive surface charge on p-type 6H-SiC, respectively. The surface charge led to a significantly increased lateral depletion layer width which was mapped using optical beam induced current (OBIC: the abbreviation will be used throughout the text for both the method and the photocurrent as long as it is clear from the context). The increase of the surface depletion layer

width causes a reduction in the surface electric field thus increasing the breakdown voltage. This was observed on as-grown and processed surfaces as well, however, differently pronounced. The presence of surface charge has a large impact on the design of any junction termination. Therefore it is important to obtain a comprehensive understanding of the mechanism by which the surface charge is formed and its process dependence. Using Schottky contacts instead of p-n mesa diodes for the present study made it possible to study as-grown SiC surfaces and to study the influence of typical processes used in device processing. In this work we concentrated on studying the influence of different surface treatments on the device characteristics of Schottky rectifiers in order to be able to control the surface charge density.

2. Experimental procedures

Commercially available n-type 6H SiC substrates (3.5° off-oriented) with a doping concentration of $7 \times 10^{17} \text{ cm}^{-3}$ from Cree Inc. were used. CVD layers (n-type, $5 \times 10^{15} \text{ cm}^{-3}$, 10 μm) were grown on the Si face.

The SiC surface was then exposed to four different processes: (1) thermally annealed in hydrogen at atmo-

* Corresponding author. Tel: +46 8 752 1061; Fax: +46 8 750 5430.

spheric pressure at 1500 °C; (2) plasma etched, using O₂ (50 sccm, 700 mTorr, 200 W); (3) RIE etched using a CF₄/Ar/H₂ (50/5/5 sccm, 15 mTorr, 100 W); (4) sputtered with Ar (ion current density: 0.5 mA cm⁻², ion energy: 100 eV). The process time was 15 min for all processes (in the following the samples will be referred to as H, O, RIE and Ar sample, respectively).

Prior to the formation of Schottky contacts the samples were cleaned and residual oxide was removed by an HF etch. Schottky contacts were formed by thermal evaporation of Au using a shadow mask ($\varnothing = 0.2$ mm) at a background pressure of 2×10^{-7} mbar. For the large area ohmic backside contact Al was deposited by electron-beam evaporation. The devices were characterized by current–voltage measurements and OBIC.

The OBIC technique is a method to study surface electric fields in power devices, as first demonstrated by Lindsay [3] in 1979. The technique involves measuring the current caused by a light beam focused onto the sample. If the energy of the light used for illumination is larger than the bandgap of the material electron–hole pairs are generated within the sample. In the presence of an electric field electrons and holes are separated before they can recombine and result in a current flow through the device. By measuring the spatial variation of the photocurrent a mapping of the depletion layer can be accomplished. A schematic view of the set-up is shown in Fig. 1. Because of the band gap of SiC we used monochromatic light from a 100 W mercury arc lamp in combination with interference filters (bandwidth 5 nm) for the UV mercury spectral lines. The plasma arc spot of the mercury lamp is imaged onto a pinhole aperture. The aperture acts as a well defined point light

source which is then reimaged onto the sample surface using a microscope with a long working distance objective. The spot size achieved with our set-up is approximately 15 µm in diameter. The penetration depth ($1/\alpha$, with the absorption coefficient α) in 6H-SiC is about 14 µm for 3.4 eV photons [4]. A lock-in technique was used in order to separate the photocurrent from the dark current and for increased sensitivity. The light beam was mechanically chopped ($f = 70$ Hz). A more detailed description of the set-up can be found in [5].

3. Experimental results

3.1. Electrical measurements

The current–voltage characteristics of the Schottky diodes for different surface treatments are shown in Fig. 2. Differences in reverse current densities of several orders of magnitude are observed for different surface treatments indicating a large influence of surface treatment on the electrical characteristics of devices. The lowest current is observed for the O sample. Uniformity of current–voltage characteristics over as-grown samples is poor (two contacts denoted as #1 and #4 in Fig. 2). A similar non-uniform behavior is found for the hydrogen annealed sample, while the characteristics of the O, RIE and the Ar samples are uniform over the samples.

3.2. Optical beam induced current (OBIC) measurements

Using the OBIC technique for spatially resolved measurements of the photocurrent we determined the effective

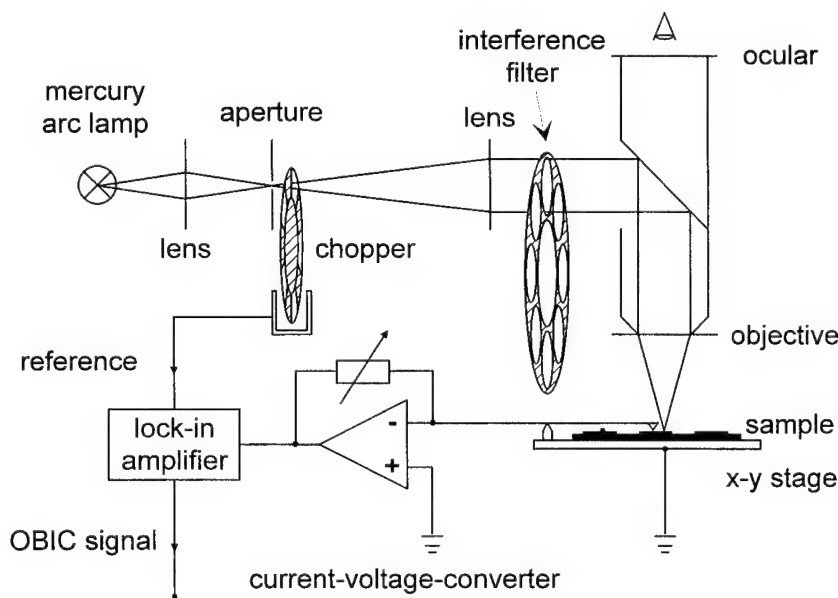


Fig. 1. Schematic view of the OBIC set-up.

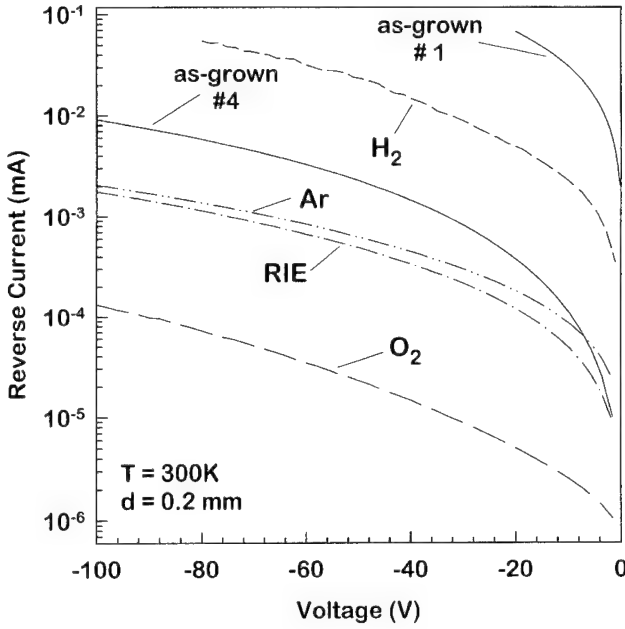


Fig. 2. Reverse current as a function of voltage for different surface treatments. The as-grown sample shows a non-uniform behavior of the contacts over the sample area (indicated by the two contacts #1 and #4), also the H_2 annealed sample (not shown here), while for the other samples all the contacts showed the same behavior.

area contributing to the electrical characteristics of the device. To account for non-symmetric behavior four line scans per contact in different directions (as shown in Fig. 3(a)) were used for the evaluation. The slope of the OBIC was extrapolated to the noise level on each side of the contact to determine the diameter of the surface depletion layer. Fig. 3 illustrates this procedure: a gray-scale encoded OBIC map for the RIE sample is shown in Fig. 3(a); the contact area and dashed lines represent-

ing the line scans are superimposed. Fig. 3(b) shows the corresponding OBIC profiles. The decrease of the OBIC in the center of the diode is due to the opaque metal contact. Current suppression there is incomplete owing to light reflected from the microscope objective reaching the surface field region at the contact edge. For each of the samples several contacts were evaluated except for the H sample, where high leakage currents prevented OBIC measurements on most of the contacts. Diameters obtained from these profiles are summarized in Table 1. For all surface treatments we observe a very large depletion layer width along the surface. The as-grown sample shows the largest spread of the diameter as can be seen from the larger standard deviation. As it has already been in the case in the reverse characteristic of the Schottky diodes (Fig. 2) Ar and RIE samples show little difference. The O sample has approximately the same surface depletion layer width as the RIE and Ar samples.

The behavior of the surface depletion layer width for different surface treatments is also reflected in the maximum photocurrent observed on the samples, as seen in Table 1. Remarkably the O sample lies closer to the as-grown and H sample than to the RIE or Ar samples. If grouped in the two groups as suggested by this finding, the surface depletion width and maximum photocurrent show the same general trend.

4. Discussion

The results of our measurements show a large influence of the surface preparation on the reverse characteristics of Schottky contacts where the currents vary over three orders of magnitude for different surface prepara-

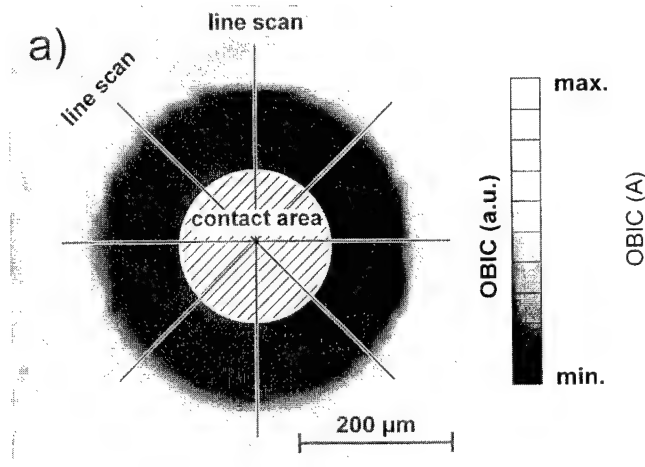


Fig. 3. Illustration of the procedure to extract the diameter of the surface depletion region from the OBIC measurement. (a) OBIC image of RIE-etched sample (wavelength 365 nm, bias voltage 1 V), superimposed is the contact area and the four line scans used for the extraction procedure. (b) OBIC as a function of the distance from the center of the contact.

Table 1
Summary of OBIC results: diameters of the surface depletion region—the division in groups I and II is explained in the text—and the maximum optical beam induced current for the different processes

	I			II	
	as-grown	O ₂ etched	H ₂ annealed	Ar sputtered	RIE etched
Diameter (μm)	632 \pm 41	505 \pm 22	450 \pm 4	503 \pm 18	490 \pm 13
Max. OBIC (pA)	0.92	0.37	0.17	102	51

tion processes. Samples with lower reverse currents show also a higher OBIC.

On all samples large surface depletion layer widths were observed. Without assuming the presence of surface charge depletion layer widths calculated for a Schottky contact at the corresponding voltage are considerably smaller than those observed experimentally. The diffusion length in SiC (typically less than a few μm) is too small to account for the observed depletion layer widths and its influence can be neglected for this consideration.

These data are, however, in agreement with previous results on Schottky diodes and mesa p–n junction diodes [1,2], where it was concluded that surface charges are responsible for the observed enlarged depletion layer width. From the value of the breakdown voltage we estimated a surface charge density in the range of 3×10^{12} – $1 \times 10^{13} \text{ cm}^{-2}$ [2]. For the present study we have chosen a relatively high doping concentration in order to minimize the influence of the increased depletion layer area on the reverse current of Schottky diodes, since a previous study has shown that for samples with low doping concentrations the lateral increase in depletion layer width was so pronounced that it caused an interconnection of several Schottky diodes on the sample and thus made it impossible to characterize individual devices without significant contributions from neighboring devices [1].

The observed difference in surface depletion width implies that the effective device area is given by the area of the metal contact alone and by the additional depletion layer area its size strongly depending on the surface treatment. As is evident from our data the quality of

the surface region determines the reverse characteristic of the Schottky diodes. Considering the additional contribution from the adjacent surface region to the device characteristic it is even more fundamental to find an appropriate surface treatment for optimum device performance. Using plasma assisted etch processes, e.g. RIE, O₂ or Ar-sputter etching, the reverse current of Schottky diodes is reduced by 1–2 orders of magnitude as compared to diodes prepared on as-grown and hydrogen-annealed surfaces, respectively.

Acknowledgement

The authors gratefully acknowledge financial support by Asea Brown Boveri and the Swedish National Board for Industrial and Technical Development (NUTEK).

References

- [1] K. Rottner, A. Schöner, M. Frischholz, R. Helbig, MRS Spring Meeting, San Francisco, 1996, MRS Symp. Proc. Series., Vol. 423, in press.
- [2] K. Rottner, S. Savage, J. Andre, L. Ramberg, M. Frischholz, R. Helbig, in Silicon Carbide and Related Materials 1995, Proc. 6th Int. Conf. on Silicon Carbide and Related Materials 1995, Kyoto, Japan, S. Nakashima, H. Matsunami, S. Yoshida, H. Harima (Eds.), Inst. Phys. Conf. Ser. No. 142, Bristol and Philadelphia, 1996, p. 721.
- [3] S.M. Lindsay, Phys. Stat. Sol. A 53 (1979) 311.
- [4] W.J. Choyke, L. Patrick, Phys. Rev. 172 (1968) 769.
- [5] M. Frischholz, Th. Mandel, R. Helbig, A. Hammerschmidt, G. Schmidt, Appl. Surf. Sci. 65-66 (1993) 784.

SiC device technology: remaining issues

J.W. Palmour *, L.A. Lipkin, R. Singh, D.B. Slater, Jr, A.V. Suvorov, C.H. Carter, Jr

Cree Research, Inc., 4022 Stirrup Creek Drive, Suite 322, Durham, NC 27703, USA

Abstract

Some of the key remaining issues facing SiC device technology for power devices and high temperature devices are discussed. Research on improving the oxide/SiC interface quality has shown that a low temperature re-oxidation step yields interface trap densities of $1 \times 10^{11} \text{ cm}^{-2} \text{ eV}^{-1}$, resulting in a high SiC MOSFET channel mobility of $72 \text{ cm}^2/\text{V}\cdot\text{sec}$. Device lifetimes for SiC n-channel MOSFETs have been increased to as much as 5 years at 350°C , and time-dependent dielectric breakdown of oxides on p-type SiC have lifetimes >700 years at $2 \text{ MV}/\text{cm}$ and 350°C . Sheet resistivities for p⁺ of $<10 \text{ k}\Omega/\text{sq}$. and p-type contact resistivities less than $10^{-5} \Omega\cdot\text{cm}^2$ have been obtained using high temperature Al⁺ ion implantation processes. These processes have been used to fabricate the first SiC CMOS circuits, with an operational amplifier having a gain $>10^5$. High voltage termination techniques have improved Schottky diode yield, as well as that of mesa devices such as 4.2 kW, 700 V thyristors. The defect densities of SiC substrates has also been improved, with recent 4H-SiC wafers having a micropipe density of 1.8 cm^{-2} .

© 1997 Elsevier Science S.A.

Keywords: Oxide interface; SiC; Micropipes; Schottky diodes; Ion implantation; Thyristors; CMOS

1. Introduction

Silicon carbide technology has made tremendous strides in the last 5–7 years, with a variety of encouraging device and circuit demonstrations. The commercial availability of relatively large, high quality wafers of the 6H and 4H polytypes of SiC for device development has facilitated these exciting breakthroughs in laboratories throughout the world. These have occurred in numerous application areas, including high power devices, high temperature devices, and high power/high frequency devices. However, there are still a number of factors that are limiting the commercialization of devices in these areas. Some of the areas receiving the most attention currently are insulator/SiC interface quality, high temperature reliability, high voltage terminations, and ion implantation. Another area of major concern is the micropipe defect density in the SiC wafers, particularly for those interested in making high power vertical devices. This paper discusses efforts in these areas and the impact of the processes on the devices of interest.

2. Oxide quality and reliability

One of the biggest advantages of SiC over other wide bandgap materials is the ability to grow a thermal oxide, as in the case of silicon. However, there is still much improvement required in the interface quality of thermal oxides grown on SiC before its full potential can be exploited. In particular, high interface trap densities (D_{it}) on p-type SiC, result in low channel mobilities for SiC n-channel MOSFETs. However, it has recently been demonstrated that thermal oxides grown on p-type 6H-SiC were significantly improved with a combination of low oxidation temperature (1050°C) followed by a 950°C re-oxidation anneal. Experimental results have shown that the interface state densities decreased with decreasing wet oxidation temperature, as shown in Fig. 1. By growing the bulk of the oxide at low temperature, and then finishing the growth in wet O₂ at a still lower temperature, even further improvement can be made. Fig. 2 shows the effect of this “re-oxidation” annealing on oxide layers grown at 1050°C in wet O₂. Using this process, interface state densities of $1.0 \times 10^{11} \text{ cm}^{-2} \text{ eV}^{-1}$ have been achieved [1]. This improved process produced the highest SiC surface channel mobility, $72 \text{ cm}^2/\text{V}\cdot\text{s}$, reported to date for 6H-SiC MOSFETs. It is believed that further reductions

* Corresponding author. Tel: 1 (919) 361-4770; Fax: 1 (919) 361-2266;
e-mail: john_palmour@cree.com

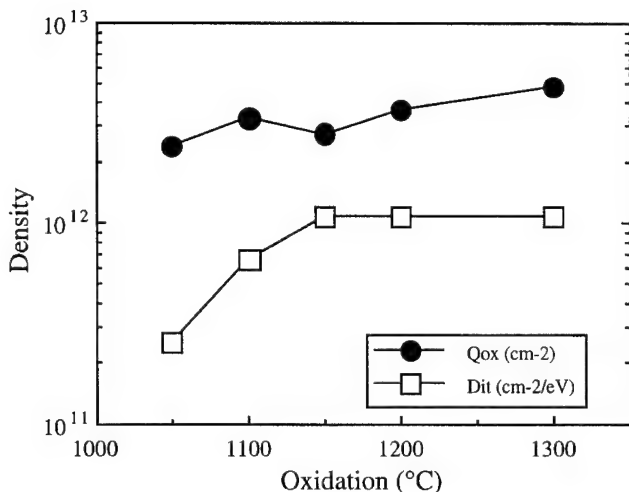


Fig. 1. Net oxide charge and interface state densities for samples oxidized in wet O_2 across the usable temperature range.

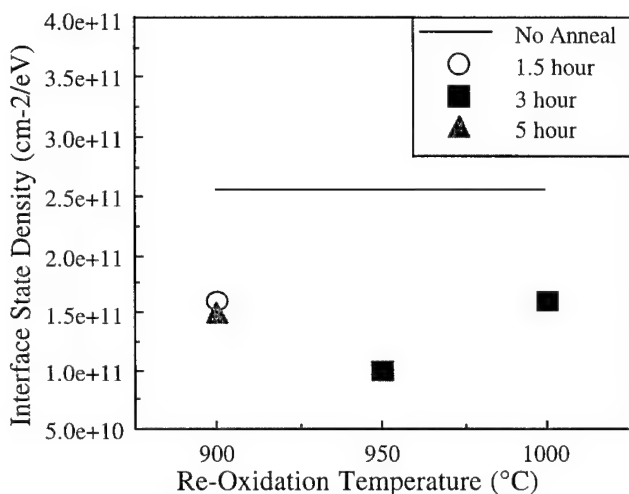


Fig. 2. Comparison of the interface state densities on oxides grown in wet O_2 at 1050 °C then re-oxidized in wet O_2 at 900, 950 or 1000 °C.

in D_{it} as well as the oxide charge (Q_{ox}) by about a factor of 5 must be achieved to make these devices commercially viable.

Oxide reliability is another area of concern for SiC devices. At high fields and high temperatures, SiO_2 layers have been reported to have poor lifetimes [2]. However, recent work has begun to show some promise. As oxide quality and device processing techniques improve, the lifetimes have been significantly increased. Time-dependent dielectric breakdown (TDDB) results indicate that thermal oxides grown on p-type SiC have lifetimes as high as 700 years at 2 MV/cm and 350 °C, as shown in Fig. 3 [3]. However, samples fabricated on heavily doped material demonstrate a reduced high temperature lifetime. Additionally, TDDB data on SiO_2 on n-type SiC show much worse lifetimes, indicating an area of concern to be studied more thoroughly [2]. Device lifetimes measured on n-channel MOSFETs

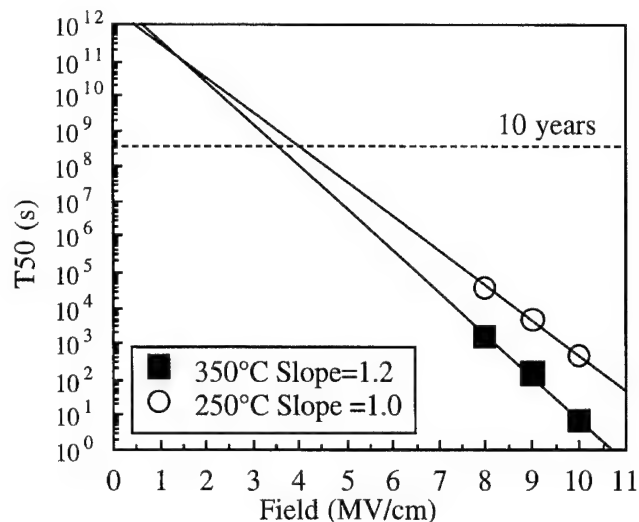


Fig. 3. TDDB data on MOS capacitors on p-type 6H-SiC oxidized in wet O_2 at 1150 °C.

have also shown a large increase, with devices operating in air at 350 °C for > 70 h without failure. The projected lifetime for these n-channel MOSFETs is about 5 years at 350 °C, and is projected to be even longer for p-channel MOSFETs.

3. Ion implantation processes

The area of ion implantation of dopants into SiC has also begun to receive increased attention because of its importance to power devices and high temperature circuits. Reliable, low resistance N^+ implants seem to be relatively easily attained through the use of high temperature implantation (500–800 °C) followed by high temperature annealing (1500 °C) [4]. While the N^+ results have been encouraging, reliable processes for Al^+ for p-type ion implantation have been more difficult to obtain. The best results reported to date have followed the same high temperature trends as was seen for N^+ implantation, although it appears that even higher implantation and annealing temperatures are required [5]. Implantation temperatures in the range of 500–1000 °C and annealing temperatures in the range of 1000–1650 °C have been successfully used [6,7]. Recent efforts at Cree with similar conditions have resulted in significant increases in the dopant activation and reduction of sheet resistivities of Al^+ implanted layers. Sheet resistivities less than 10 k Ω /sq. and p-type contact resistivities less than 10^{-5} $\Omega\text{-cm}^2$ have been obtained for Al implants into n-type 6H-SiC.

As a demonstration of the benefit of ion implantation processes in SiC, we have fabricated the first CMOS circuits reported in SiC [8], using 6H-SiC enhancement-mode MOSFETs. The n-channel MOSFET devices were fabricated in a lightly doped p-type epitaxial layer,

grown on a p-type 6H-SiC substrate. The complementary p-channel devices were fabricated in n-type wells formed by ion implanting nitrogen into the epitaxial layer through a mask. The source and drain of the n-channel and p-channel devices were also formed by ion implanting N^+ and Al^+ , respectively. Some of the CMOS circuits demonstrated were 17 stage CMOS ring oscillators and a CMOS operational amplifier with an open loop gain of greater than 10 000 (80 dB). The DC transfer curve for a 6H-SiC CMOS opamp is shown in Fig. 4. The input offset voltage was 95 mV.

4. High voltage terminations

While a number of demonstrations of high voltage devices have been made in SiC, most of these have relied on the use of dielectric liquids or gases to prevent premature failures at low voltages. For commercially viable devices, high voltage termination techniques must be developed that allow for standard packaging of parts and allow higher temperature operation without the use of dielectric media. Efforts are now underway to develop these terminations. Promising results have been obtained with the use of field plates [9], self-aligned amorphizing implants [10], porous SiC [11], and boron implants [12] for Schottky diodes.

In this study, we examined a variety of termination designs for Schottky diodes in order to optimize for 700–800 V operation. Diodes were fabricated with Al^+ ion implanted guard rings under the periphery of the Schottky contact, others had a field plate that extended over an oxide at the Schottky periphery, some had single ion implanted floating field rings spaced 2–4 μm away from the Schottky periphery, while others had dual concentric implanted floating field rings. Another variation was to have the floating field ring implanted into the bottom of an etched trench, thereby placing the ring deeper in the material. Both the single and dual trench implanted field rings were fabricated. Some of the devices were also fabricated with no edge termination to act as standards for the experiment. Finally, the edge radius was varied, with 50, 100, and 150 μm radii being

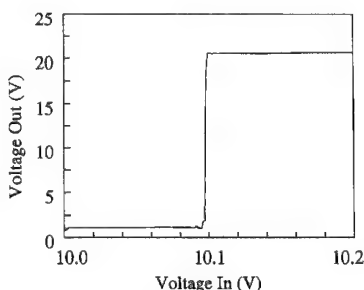


Fig. 4. The open loop DC transfer characteristic of the SiC CMOS operational amplifier. The open loop gain was >10 000 (>80 dB).

fabricated for each of the designs. The doping of the 4H-SiC epilayer was in the range of $8\text{--}10 \times 10^{15} \text{ cm}^{-3}$ and the thickness was 13 μm . Both platinum and titanium Schottky metals were used.

The variation of the average breakdown voltage of the Schottky diodes with these various termination techniques is shown in Fig. 5. The most obvious trend observed is that the breakdown voltage improves significantly with increasing edge radius, for all planar termination techniques investigated. This is an expected result because the increased edge radius moves the field boundary condition from spherical to a more cylindrical field, with less field crowding. Guard ring termination was more effective than unterminated, while field plate termination was even more effective. The single and dual floating field rings, and the single and dual trench implanted floating field rings were all similar in their effectiveness. It can be seen that the highest average breakdown of 580 V corresponds to the single ion implanted floating field ring with the 150 μm edge radius, versus an average breakdown of 115 V for unterminated devices. The highest voltage diode observed (805 V) used the single ion implanted floating field ring.

The effectiveness of mesa terminated devices has also been improved. Previously, we have not been able to measure mesa terminated devices at voltages higher than 300–400 V without immersing them in FluorinertTM 1, a dielectric liquid, to prevent arcing. This approach, or the use of dielectric gases, has also been used by others to obtain high voltage operation of mesa terminated devices [13]. However, by using a combination of thick (2–3 μm) deposited SiO_2 and subsequently deposited layers of solid polyimide passivant, we increased the blocking voltage to >700 V without the use of FluorinertTM. This mesa passivation was applied to npnp 4H-SiC thyristors. Relatively large area devices ($6.0 \times 10^{-3} \text{ cm}^2$) with this passivation blocked over 700 V without the use of Fluorinert in both forward and reverse bias and were capable of carrying 6 A (1000 A/cm²) of forward current at about 3.7 V forward voltage drop. This is the highest power switching device (4.2 kW) reported to date for SiC.

While this is an improvement in measured voltage in air, these devices could still be taken to higher voltages when immersed in dielectric media. The highest voltage operation achieved was 900 V when immersed in FluorinertTM, as shown in Fig. 6. The forward breakover voltage could be reduced with a negative gate trigger current. The forward breakover voltage (in the lower-left quadrant) was reduced to less than 30 V with a gate current of -3.5 mA (1.1 A/cm²). The forward current for this device was 2.0 A, with a voltage drop of 3.93 V, corresponding to a current density of 625 A/cm². The cathode leakage current at a forward blocking voltage

¹FluorinertTM is a registered trademark of the 3M Company.

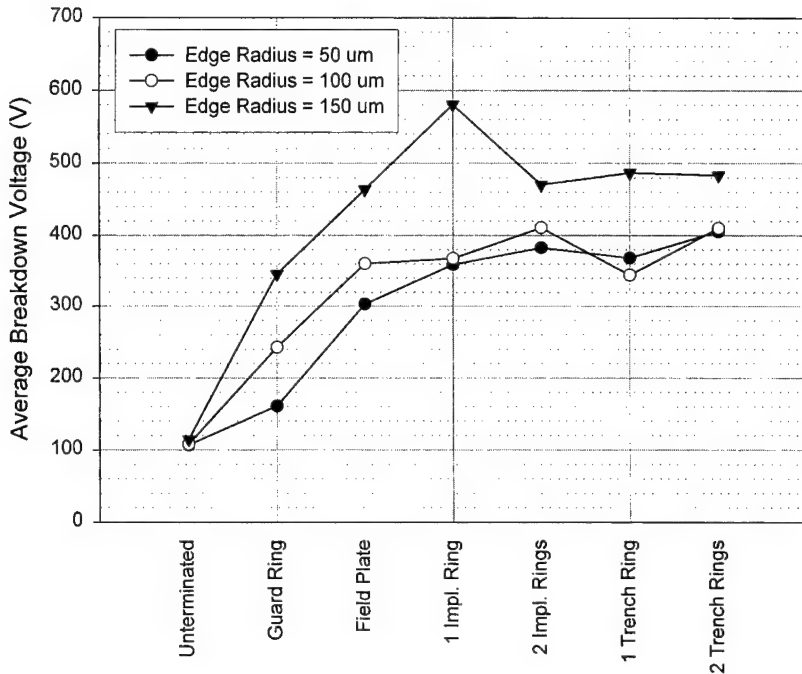


Fig. 5. The variation of average breakdown voltage of 4H-SiC Schottky barrier diodes with various termination techniques and diode edge radii.

of -800 V was only 22 nA at 27 °C, yielding an on-off ratio of about 10^8 .

5. SiC material quality

Finally, one of the most important areas for SiC power devices still depends on material quality issues. High power devices ($1\text{--}100$ A) have large active areas

that must withstand high electric fields, so the wafer size and defect density of SiC is a key factor to the commercial success of this technology. One of the most important defects currently limiting the production of large area power devices in SiC is the “micropipe” defect, which causes device failures at high fields [14]. The diameters of the micropipes can vary depending on the growth conditions and formation mechanism but are typically $0.5\text{--}10$ μm in diameter [15]. These defects are fatal for many kinds of devices, and especially for high voltage power devices. Silicon carbide wafers have traditionally had rather high densities ($100\text{--}500$ cm^{-2}) of micropipes but recent 4H-SiC wafers at Cree have micropipe densities as low as 3.5 cm^{-2} [15]. A digitized image of an etched 30 mm 4H SiC wafer which has 13 micropipes or 1.8 cm^{-2} is shown in Fig. 7. It is important to note that the micropipes are not evenly distributed throughout the wafer. Some rather large areas which are free from micropipes can be found. In fact, the center 25 mm of the wafer in Fig. 7 only has two micropipes, a density of only 0.4 cm^{-2} . These levels must be reduced to <1 cm^{-2} in production quantities for viable power devices. We believe that micropipe densities can be rapidly decreased over the next few years and possibly eliminated in $3\text{--}4$ years.

6. Conclusions

Four of the major issues remaining for the successful commercialization of SiC have been discussed. These issues concern SiC/SiO₂ interface quality and high tem-

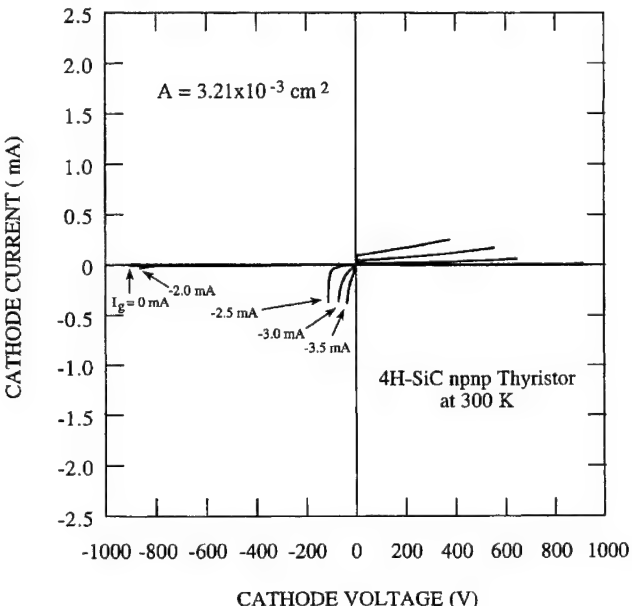


Fig. 6. Forward and reverse bias I-V characteristics of a 900 V 4H-SiC npnp thyristor, immersed in Fluorinert™.

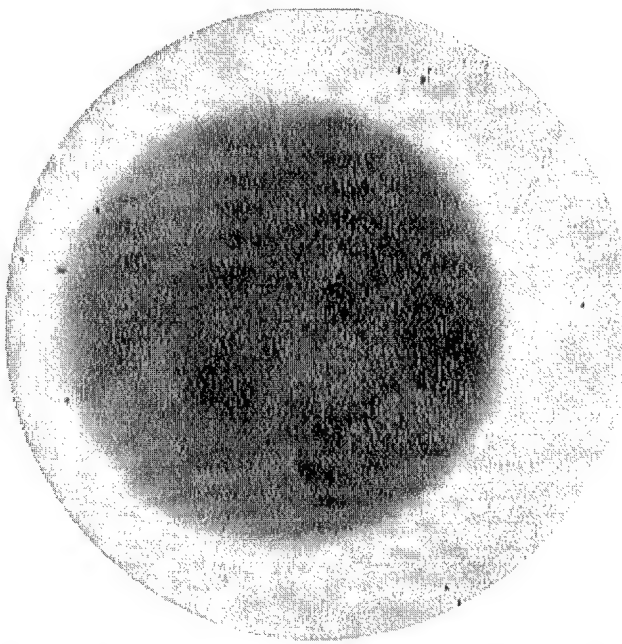


Fig. 7. Digitized micrograph of an etched 30 mm 4H-SiC wafer which has 13 micropipes, or 1.8 cm^{-2} . The darkness in the center is due to doping variation across the wafer.

perature reliability, ion implantation (particularly for the formation of p^+ regions), high voltage termination techniques, and material quality. The interface quality of SiO_2 on SiC can be improved to $1 \times 10^{11} \text{ cm}^{-2} \text{ eV}^{-1}$ using a low temperature “re-oxidation” anneal. This process has resulted in 6H-SiC MOSFET channel mobilities as high as $72 \text{ cm}^2/\text{V}\cdot\text{s}$. The high temperature reliability of n-channel MOSFETs has been improved to as much as 5 years at 350°C , and the upper bound on what is achievable is the range of 700 years, based on high temperature TDDB data. The use of high temperature ion implantation, followed by higher temperature annealing has allowed the first demonstration of a viable SiC CMOS technology, with an operational amplifier having a gain of 10^5 . However, further work on reducing the p^+ sheet resistivities, and improving the repeatability of the process is required. Using ion implantation technology, high voltage termination techniques are beginning to show promise for SiC, with single floating field rings giving good results for 4H-SiC Schottky diodes in

the 500–800 V range. Mesa terminated devices have also been improved, with a 700 V, 6 A thyristor being demonstrated in air without the use of dielectric media. Finally, major strides have been made in reducing the micropipe density in SiC wafers, with a density as low as 1.8 cm^{-2} being demonstrated. While great progress has been demonstrated, much more work remains in each of these areas to enable the commercial success of SiC high temperature and high power devices.

References

- [1] L.A. Lipkin, J.W. Palmour, *J. Electronic Mater.* 25 (1996) 909.
- [2] D.M. Brown, M. Ghezzo, J. Kretchmer, V. Krishnamurthy, G. Michon, G. Gati, in: D.B. King, F.V. Thome (Eds), *Trans. Second High Temp. Electronics Conf.*, Sandia National Labs, Albuquerque, NM, 1996, pp. XI-17.
- [3] L.A. Lipkin, J.W. Palmour, J.S. Suehle, in: D.B. King, F.V. Thome (Eds), *Trans. Third High Temp. Electronics Conf.*, Sandia National Labs, Albuquerque, NM, 1996, p. XIV-15.
- [4] N. Inoue, A. Itoh, T. Kimoto, H. Matsunami, T. Nakata, M. Watanabe, *Inst. Phys. Conf. Ser.* 142 (1996) 525.
- [5] A.V. Suvorov, P.A. Ivanov, Y.V. Morozenko, V.N. Makarov, Abstracts of Third All-Union Conference on Wide-Gap Semiconductors, (in Russian), Mahachkala, USSR, 10–12 September 1986, pp. 28.
- [6] M.V. Rao, P. Griffiths, J. Gardner, O.W. Holland, M. Ghezzo, J. Kretchmer, G. Kelner, J.A. Freitas, Jr., *J. Electronic Mater.* 25 (1996) 75.
- [7] J.R. Flemish, K. Xie, H. Du, S.P. Withrow, *J. Electrochem. Soc.* 142 (1995) L144.
- [8] D.B. Slater, Jr., G.M. Johnson, L.A. Lipkin, A.V. Suvorov, J.W. Palmour, Abstracts of 54th Device Research Conf., IEEE, Piscataway, NJ, 1996, p. 162.
- [9] M. Bhatnagar, H. Nakanishi, S. Bothra, P.K. McLarty, B.J. Baliga, 5th Int'l. Symp. on Power Semicond. Devices and ICs, IEEE, Piscataway, NJ, 1993, p. 89.
- [10] D. Alok, B.J. Baliga, M. Kothandaraman, P.K. McLarty, *Inst. Phys. Conf. Ser.* 142 (1996) 565.
- [11] C.I. Harris, A.O. Konstaninov, C. Hallin, E. Janzén, *Appl. Phys. Lett.* 66 (1995) 1501.
- [12] A. Itoh, T. Kimoto, H. Matsunami, Proc. of 1995 7th Int'l. Symp. on Power Semicond. Devices and ICs, IEEE, Piscataway, NJ, 1995, p. 101.
- [13] P.G. Neudeck, D.J. Larkin, J.A. Powell, L.G. Matus, *Appl. Phys. Lett.* 64 (1994) 1386.
- [14] P.G. Neudeck, J.A. Powell, *IEEE Electron Device Lett.* 15 (1994) 63.
- [15] V.F. Tsvetkov, S.T. Allen, H.S. Kong, C.H. Carter, Jr., *Inst. Phys. Conf. Ser.* 142 (1996) 17.

Silicon carbide for microwave power applications

Christian Brylinski *

Thomson CSF LCR, Domaine de Corbeville, 91404 Orsay, Cedex, France

Abstract

Microwave power emission has entered into the citizen's daily life, pushing towards ever increasing availability and decreasing prices for both personal terminal and base station equipment. By lifting threshold limits in operating temperatures, power density and impedance matching capabilities, SiC is expected to bring a technological breakthrough in the RF and microwave high power amplification area.

Competitors to SiC could be diamond or III-N materials. However, diamond or BN technologies are far from maturity. III-N materials deposited on sapphire have shown promising small signal results but a thermally conductive substrate will be needed for high power devices and the most obvious candidate is SiC.

Preferred device structures on SiC will probably be MOSFET and HBT. Presently, the MOS interface still suffers from very poor channel mobility and HBT is only emerging. Therefore, the only published results today refer to Static Induction Transistors (SIT), JFETs or MESFETs. Westinghouse SIT microwave amplification results in the UHF (more than 1 kW at 600 MHz) and in the S-band (36 W pulse at 3 GHz) are impressive.

On the MESFET side, encouraging power results in the (2–4 W) range have been obtained at Westinghouse, Cree/Motorola, and Thomson, although only Westinghouse has been successful yet in using semi-insulating substrates. © 1997 Elsevier Science S.A.

Keywords: Silicon carbide; Microwave power

1. Introduction: microwave power amplification

Electromagnetic power emission applications now expand into customers' daily lives with the following areas of applications:

- (1) information transmission in free space, including radio and TV broadcast, satellite transmissions, classical and cellular telephone;
- (2) remote imaging, object detection (and jamming), including all kinds of radars for air traffic control, aeroplane and missile detection, meteorology, collision avoidance;
- (3) heating for industrial processes and home microwave ovens.

In all cases, the core function is amplification the basic principle of which is energy conversion from a DC supply source into a high field electromagnetic signal with controlled frequency spectrum. The main evolution trends are frequency increase, owing to spectrum crowd-

ing, power emission increase, and most crucially, volume, weight and cost decrease.

Convenient cost analysis of the related industrial activity must refer to the whole equipment or system which is split primarily into amplification unit, small signal information processing and infrastructure. The amplification unit of free-space communication or detection equipment and systems today represents 30–50% of the overall fabrication cost.

Tubes and solid-state devices still compete as active devices. There exists an extremely wide variety of vacuum tube devices covering the whole electromagnetic spectrum with very high efficiency but rather low lifetimes owing to incompletely solved cathode limitations. Also, tube amplifiers need high-voltage supply, high vacuum atmosphere and individual precise mechanical adjustment.

However, solid-state chip prices can be made very low for large series but solid-state circuit prices increase fast with output power, owing to the necessary adaptation networks associated with the low output impedance of existing devices.

Indeed, vacuum is an excellent medium for

* Corresponding author. Tel: +33 1 69339251; Fax: +33 1 69330866.

electromagnetic energy conversion at high power levels. Semiconductors exhibit intrinsic power density limitations. The two main ones are the electrical breakdown and the electron velocity saturation. The ultimate figure of merit related to those physical properties is the Johnson figure of merit (JFM) as detailed in Section 2.

Small power applications, i.e. cellular telephone personal terminals, are perfectly covered by the present solid-state devices. Only the technology complexity and the available lithography resolution decide whether silicon or GaAs is the best choice. When power increases, the number of elementary solid state devices needed increases. Coupling of those elementary devices requires expensive passive networks and, for high power levels, the tube cost is inferior to the solid-state solution one. A typical case is that of today's microwave oven magnetron tube source.

Additionally, silicon existing microwave power devices (bipolar or MOS) do not work over a 200–250 °C active layer temperature. Their use in large power amplifiers implies the building of a heavy cooling infrastructure. The availability of devices based on wide band-gap semiconductors is expected to result in a displacement of the solid-state/tube applications border and a dramatic reduction (30–50%) of the costs for the present solid-state high power systems (base stations) by cumulative cost reductions on design, passive circuitry and infrastructure.

2. Solid state ultimate performance: frequency/power/output impedance compromise: the Johnson limit

The JFM applies to comparisons of the ultimate possibilities of semiconducting materials used in electron transit devices. This device family covers all kinds of transistors and transit-time diodes (Gunn) but excludes avalanche mode devices such as IMPATT diodes. JFM gives a link between the basic significant physical properties of the material and the main operational parameters of the ultimate elementary device: frequency, power and output impedance.

The mechanism under this limitation lies in the principle of operation of the elementary high-frequency amplifier stage whose usual basic circuit is shown on Fig. 1. Such an amplifier stage works as a cycling converter.

In a first phase of the cycle, power supply energy is converted into electrostatic energy stored inside the gate/anode capacitor.

Then, in a second phase, this energy is transferred by electrical conduction to the load by performing a controlled discharge of the capacitor.

Two kinds of limitations restrict the converted power flow. Firstly, since the storage capacitor dielectric is the

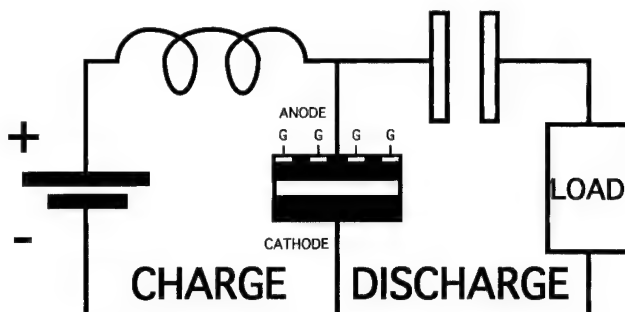


Fig. 1. Basic microwave amplifier circuit.

semiconducting medium, the electrostatic energy density is expressed as $1/2 \cdot \epsilon \cdot E^2$ and the maximum energy density is obtained when E equals the breakdown field E_b in some area of the device. So, the maximum converted power is proportional to E_b^2 .

As a second limitation, the discharge time cannot exceed roughly half of the cycle period, leaving enough time to properly charge the capacitor. This discharge time corresponds to the delay necessary for carriers to reach the anode after they get out of the gate influence zone.

In a semiconductor, for such a carrier transit, the saturation velocity limit v_s cannot be exceeded, with some velocity overshoot (a factor of 2 is a maximum) possible for very short distances in direct band-gap semiconductors. Therefore, for operation at a given frequency, the carrier transit length, which is also the dielectric thickness of the storage capacitor, cannot exceed a maximum value. As a consequence of the breakdown field limit, maximum voltage swing is also limited which induces a subsequent limitation of the doping level. Therefore, there is only one free parameter left to adjust the optimum device (device giving maximum power) global size: its transverse section area.

Increasing this section area gives greater volume to store and convert energy, hence higher converted power but it also increases the average electric charge current flowing through the device. Since the maximum voltage is fixed, an increase of the converted power gives a subsequent decrease of the output impedance.

In summary, JFM states that, for any transit electron device (excluding avalanche modes), the power \times (frequency) $^2 \times$ output impedance (real part) product is proportional the product of $(E_b v_s)^2$ which is purely a material related factor.

For a given application, the frequency is imposed, and impedance of an elementary device must stay in a range compatible with the load one (typically an antenna) or the transmission lines characteristic impedance. Classical antennae and lines characteristic impedances stay within the 20–300 ohm range. Devices able to deliver power directly to the load impedance can be naturally operated with simple one- or two-element

adaptation cells. Presently, owing to the relatively low breakdown field value of all actually available semiconductors (germanium, silicon, GaAs and InP exhibit $E_b < 0.5 \text{ MV cm}^{-1}$), most solid-state high power devices exhibit natural output impedance levels well below that of the lines and antennas. An example, output impedance real part of a typical 100 W silicon device at 1 GHz lays around 1 ohm. Therefore its adaptation requires a complex passive reactive network. Complexity, losses and band-narrowness increase dramatically with the impedance mismatch. This results in expensive, heavy, voluminous circuits and systems.

3. Thermal issues

Higher power density is the key to more compact and cheaper circuits and electronic functions. In the way towards higher power density, only in the case of short pulses mode applications JFM limit becomes the main limitation.

This mode essentially covers specific professional electronics needs (mainly radars). For devices working in a CW mode, which cover nearly all consumer electronics applications, thermal limitations arise before electric ones.

The thermal limitation is particularly stringent in semiconducting materials, because of the non-linear behavior of their thermal conduction. Thermal conductivity decreases rapidly with temperature and so the heat dissipation is a self-impeding process. The use of a substrate with better thermal conductivity (K) raises the possible power density (P) with a P improvement much greater than the K one.

In standard bipolar transistors, emitter current injection is a temperature activated process and thermal runaway naturally occurs. The threshold of this runaway process depends heavily on the device thermal resistance. Two ways to prevent those phenomena are substrate thinning and emitter ballasting.

In HBT transistors, the situation is slightly better owing to current gain thermal deactivation, but there exists a spatial thermal runaway effect (also called “crunch” effect) which tends to concentrate all the current in the hotter part of the transistor.

This is one reason why field effect transistors, which do not exhibit any thermal runaway problem, are often preferred.

In the far future, the most probable evolution will be towards the use of polycrystalline (or maybe monocrystalline) diamond substrate and the bonding of wafers or chips on it.

At present, SiC substrates, with K values much over those of classical materials such as Si or GaAs, will represent a clear progress in the thermal behavior of devices. With SiC RT thermal conductivity nearing that

of copper, substrate thinning will probably not be necessary or even useful.

However, thermal resistance improvement for a given geometry, expected to lie around a factor of 5–8, will be lower than the electrical improvement. For CW applications, it is expected that optimizing device geometry will require respect of a thermally driven compromise inducing larger spacing between fingers and/or elementary finger size reduction, especially for the high power density structures such as HBT.

4. Semiconducting material choice

Regardless of any other parasitic limitation factors which we will describe later, materials with highest possible JFM would be preferred. As a natural trend, materials made out of lighter chemical elements (low atomic number) exhibit much higher breakdown fields, thermal conductivity and slightly higher saturation velocities.

At a first glance, “extra-light” semiconductors such as diamond or boron nitrides may be considered as the ultimate choice for making high-frequency power devices. However, as yet, diamond monocrystals are only available in very small wafers within a few square millimeters size, at very high prices.

Moreover, no effective n-type dopant has been identified and the only p-type dopant, boron, gives a deep acceptor level with $E^* = 0.36 \text{ eV}$ which means that electrical activity of B dopants is less than 1% at room temperature. Dopant electrical activity also varies a lot with increasing temperature which means that the temperature range for optimum operation of a given device will be narrow. This is expected to bring a severe limitation of the interest of such a technology. Little is known today on monocrystalline BN but on the one hand, its crystal growth remains very difficult, and on the other hand, problems with depth of doping impurities levels are expected to be similar to the diamond case.

Just a step lower in the scale of “lightness” come materials such as SiC and GaN. SiC substrates and epitaxial layers are now commercially available, although wafer prices are very high and quality has still to be improved for large volume production of power devices. GaN and related compounds (III-Ns) are presently thoroughly investigated, mainly for visible-UV light emission and detection, but also for microwave amplification purposes.

One of the main problems remaining with III-N is the absence of matched substrate [1]. Although sapphire does not exhibit exactly the same crystal lattice as GaN and presents a lattice parameter mismatch of around 15%, GaN epitaxy on sapphire is still the most successful today with high volumes of LEDs commercialized and impressive small signal microwave performances

published for MESFETs [2], HEMTs or MISFETs [3–5]. However, on the one hand, sapphire has a low thermal conductivity, even lower than that of GaAs, which makes it unusable for making real power devices and moreover, GaN layers on it still exhibit a very high density of crystal defects (typically more than 10^7 per cm^2) which reduces the usable breakdown field. Published GaN devices exhibit very limited breakdown voltage and no high power emission results are available on GaN-based devices today.

Wafer bonding technologies may be a long-term solution to this kind of thermal problem, but much more promising appears to be the use of a SiC substrate with a much closer similarity to crystal lattice, lower lattice parameter mismatch, high thermal conductivity, and now commercially available as conductive or prototype semi-insulating 30–35 mm diameter wafers. GaN epitaxy on SiC is still tricky and GaN/SiC device results are still inferior to GaN/sapphire ones, but one can hope that this is only a technical problem which will be solved soon.

From this point of view, these are good reasons to say that the two best candidates (GaN and SiC) as semiconducting materials for the next generation of microwave power devices will both preferably be made on a SiC substrate.

This first choice stage related only to criteria referring to the basic intrinsic device ultimate possibilities and regardless of technology. In real devices, many parasitic passive elements embed the core characteristics. Technology refinement is the way to reduce those parasitic influences. Lithography resolution choice results from a compromise between acceptable cost/yield and parasitic element values. Capacitance is one kind of ubiquitous parasite. Series resistance and inductance are the main other ones. Miller capacitance between device anode and gate electrodes and cathode series inductance are generally the most deleterious to microwave performances.

Connection capacitances can be very significantly reduced by the use of semi-insulating substrates. This has accounted for a large part of the success of GaAs compared to silicon in higher frequency microwave applications.

Access resistances depend on lithography resolution but also on carrier mobility. Regarding electron mobility, standard III-V behaves better than SiC or III-N, which are roughly similar to silicon. Regarding holes, III-N seems to be the worst, followed by SiC and III-V far inferior to silicon or diamond (see Table 1). As a conclusion on the material choice, it is expected that SiC or GaN will allow much higher emitted power than Si or classical III-V compounds at a given frequency but they will also require a more refined technology in order not to let parasitic terms degrade the power gain, conversion efficiency and impedance levels.

Table 1

Measured or expected properties of semiconducting material relative to the silicon reference

	Si	GaAs	SiC	GaN	C
E_b	1	1.2	10	10	20
v_s	1	0.8	2	2	2
JFM	1	1.5	400	400	>2000
μ_e	1	6	0.8	1	1,5
μ_h	1	0.5	0.1	0.02	3
Thermal conductivity (K)	1	0.3	3	1–2	15

5. Device structure choice for SiC microwave power technology

The choice of optimum device structure and geometry is crucial in several ways. In a first approach, it is a way to maximize amplifier performances, minimize energy losses and allow the best possible tuning according to the signal source and the load. All this has to be performed in a wide range of temperature and under the pressure of many other practical operating constraints. In a second stage, it is a way to minimize fabrication costs and allow delivery of devices with adequate life-time.

Very restricted in the early years of solid state technology, the panel of potentially feasible devices is now rather extended. In the coming paragraph, we will review existing structures and discuss issues related to their adaptation to SiC.

5.1. Vertical versus horizontal

Transistor device structures divide primarily into “vertical” ones with current flowing perpendicular to the substrate plane and “horizontal” ones with current flowing parallel (see Fig. 2 and Fig. 3). Generally, for vertical devices such as bipolar junction transistors, U, V or D-MOS, static induction transistors (SIT), the substrate is conductive (as conductive as possible). Current flows through the whole substrate thickness and anode contact is taken on its back side.

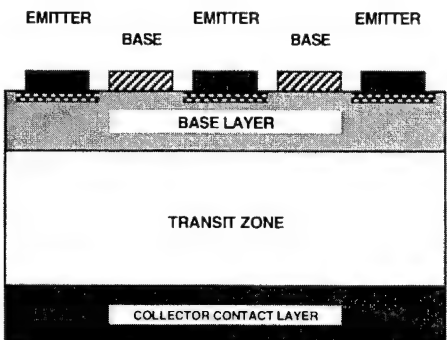
For horizontal devices (see Fig. 3), such as laterally depleted MOSFETs (LD-MOS), MESFETs, JFETs, HEMTs, the cathode and anode are set as an alternate interdigital finger array. Each must be isolated (DC and RF) from its neighbours and so, insulating substrate is highly preferred.

Advantages of vertical structures compared to horizontal ones are:

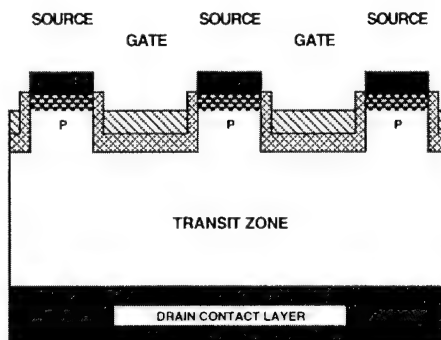
- (1) Possibility of a back side contact which implies only a two electrode connectic topology on the upper side of the substrate. There is no necessary crossing between the upper side electrodes. Getting a comparable situation for horizontal devices requires both insulating substrate and via-holes technology.

bipolar structures

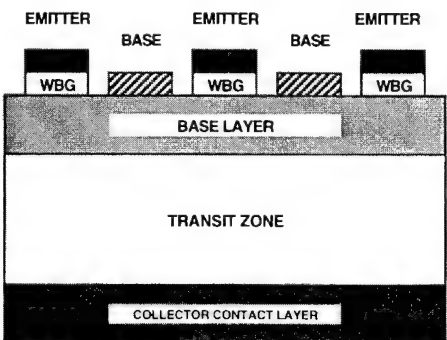
(2.a) BJT

*field effect structures*

(2.c) U-MOS



(2.b) HBT



(2.d) SIT

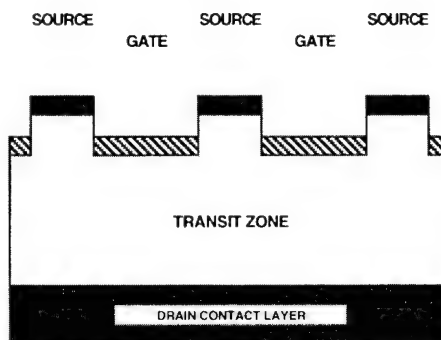


Fig. 2. Examples of the main “vertical” topologies: (a) bipolar junction transistor (BJT); (b) heterojunction bipolar transistor (HBT); (c) vertical metal oxide semiconductor transistor (U MOS); and (d) static induction transistor (SIT).

- (2) Plate-like carrier transit zone with rather homogeneous field distribution (Horizontal devices are much more likely to generate two- or three-dimensional effects leading to high-field spots).
- (3) Less exposure of the device active area to air and hence, lower sensitivity to possible surface traps and charging effects.

Their main drawbacks related to vertical structures on conductive substrate are:

- (1) the large capacitances of connections lines and pads with the conductive substrate;
- (2) necessary insertion of an electrically insulating layer between back contact and ground as back contact is connected to the anode, which enhances the device thermal resistance.

5.2. Connectics

On an insulating substrate with backside metallization, conduction wires with normal width (30–300 μ)

constitute electromagnetic transmission lines exhibiting characteristic impedance around 50 ohms, which makes it possible to realize microwave monolithic integrated circuits. The three electrodes on the upper side have to be connected making it mandatory either to use via-holes, to cross the substrate and connect cathode or gate electrode to the ground, or to make bridges in order to organize low-capacitance electrode crossing.

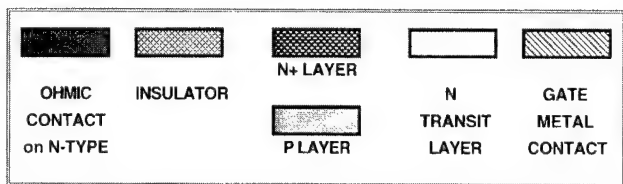
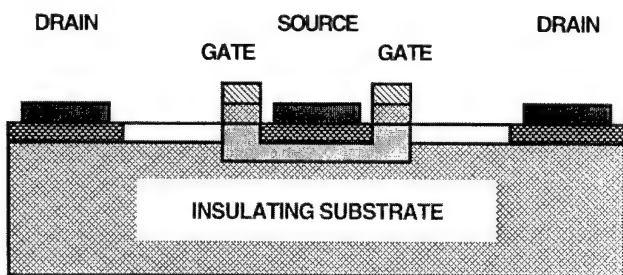
Air bridges are more difficult to make but exhibit the lowest possible parasitic crossing capacitances. Via-holes allow the minimization of cathode inductance. However, via-holes on SiC substrates will require hundreds of microns SiC etching, for which an industrial process has not been demonstrated yet.

5.3. Current control

For the control of the electric current flow inside the transistor, despite some work on exotic quantum structures, only the two classical basic configurations are really in use today:

- (1) bipolar structure (examples on Fig. 2(a) and

(3.a) LD-MOS



(3.b) MES

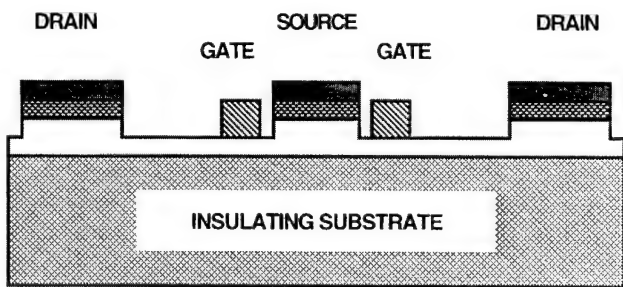


Fig. 3. Examples of “horizontal” topologies: (a) laterally depleted metal oxide semiconductor transistor (LD-MOS); and (b) metal semiconductor transistor (MESFET).

Fig. 2(b) in which minority carriers are injected from the emitter into the conductive base layer that they have to cross before entering the transit zone; (2) field effect structure in which the gate is placed along side the current flow channel (its electrostatic potential controls the channel width and/or the mobile carriers density).

5.4. Bipolar structures

Bipolar transistors have long been the only solid-state devices available for high-frequency power operation.

The bipolar current control is the most efficient that can be obtained in any device, since carriers migrate through the gate conductive layer to reach the transit zone.

So, the transistor intrinsic transconductance is the highest possible, although it is current and temperature dependent and generally limited by the parasitic access resistance in all power amplifier configurations.

However, input impedance levels are very low, typically far under the 1 ohm level, which makes it mandatory to use complex input adaptation cell networks. The carrier transit zone topology is nearly plate-like making electric field distribution very homogeneous, giving maximum possible voltage handling capability, often close to the theoretical limit in real devices.

5.5. Bipolar junction transistor

The classical silicon bipolar junction transistor (BJT) (Fig. 2(a)) without heterojunction is a vertical structure made on conductive substrate with alternate base and emitter fingers on the upper side (schematic view on Fig. 2(a)). Practical realisation have been available from 0 to 3 GHz. Emitter and base doped zones layers are generally made by diffusion into the collector epitaxial layer and so, this technology cannot be translated today to SiC. Anyway, this is not a high performance structure since it exhibits additional limitations owing to carrier injection from the base into the emitter. Doping levels have to be adjusted far from the optimum to conserve reasonable current gain.

Therefore, global intrinsic device performance compromise is blocked at a level far inferior to the JFM limit and further from it as the operating frequency goes higher. Moreover, unavoidable losses happen in relation with to the use of conductive substrates. Although explored in the early days of SiC devices research, SiC BJT is certainly no longer considered to be one of the best routes to microwave power devices.

5.6. Heterojunction bipolar transistors

In heterojunction bipolar transistors (HBTs: Fig. 2(b)), the emitter hetero-interface blocks carrier diffusion from the base and allows much higher base doping levels only limited by the base material restrictions (dopant solubility limit, recombination centers density, hence allowing an extreme reduction of the series base access resistance. Global level of performance can come very close to the JFM limit. HBT is the technology which gives the highest operation frequency for a given lithography resolution.

As an example, comparable performance at 10 GHz can be obtained using 0.5 µm gate length MESFETs or HEMTs, or 2 µm emitter HBT transistors. The highest difficulty is in the material structure. Present realisations include essentially the following assemblies: Si emitter/SiGe strained base technology on silicon, AlGaAs/GaAs or GaInP/GaAs matched emitter on GaAs substrate, and InP/GaInAs or InAlAs/GaInAs on InP substrate. The availability of semi-insulating III-V substrates makes it easier to realise low loss matching

circuits. This is a rare example of a vertical structure on a semi-insulating substrate. However, its technology is much less mature than for BJT and the reliability of the present devices is still questionable.

HBT is certainly a favored direction for the future SiC-based microwave power devices. Emitter heterojunction could be either established between different polytypes or between SiC and a III-N material such as GaN. Polytype transition control and GaN/SiC direct epitaxy of defect-free material with controlled doping profiles are still challenging goals for the next few years without predictable issue. Although GaN/SiC HBT with good static current gain has been published two years ago [13], published voltage handling capabilities were low and no microwave data have been made available since. In case of failure of the two already mentioned types of heterojunction, structures with AlGaN emitter on GaN base, collector and contact sub-collector layers will certainly be tried because they are potentially less sensitive to hetero-interface problems.

5.7. MOS

The most popular device for silicon microwave power technology today is the n-channel inversion MOS transistor; until recently, most silicon power MOS used vertical structure with inversion MOS channels on p-type localised either on edges of NPN ridges (V or U MOS, see Fig. 2(c)), or on the surface of localised double diffused/implanted NPN islands (DMOS). The recently developed horizontal laterally depleted silicon LD-MOS, (Fig. 3(a)) seems to exhibit better global characteristics. Translation to SiC would require good MOS or MIS interfaces on SiC and especially on p-type SiC, which has always been a problem so far. The best n-channel mobilities stay around $50 \text{ cm}^2 \text{ V}^{-1} \text{ s}^{-1}$ [14], instead of approximately 500 for silicon. Recent progress has been made in improving SiC MOS interfaces but has not yet resulted in published microwave power transistors.

In the case of success in finding a good process to make SiC MOS, SiC LD-MOS devices would be one of the most favored devices owing to an isolated gate allowing large negative excursion for class B or C amplifiers and positive DC bias. However, even silicon MOS devices suffer from oxide degradation owing to high-energy carrier injection from the semiconductor. This effect is predicted to be even more stringent in SiC MOS owing to higher electric fields in operation and lower potential barriers at the insulator/semiconductor interface.

So the two silicon champions do not allow any simple and direct translation to silicon carbide and early SiC device research's only choice has been between "exotic" Si-like and GaAs-like structures such as static induction transistors, JFET and MESFET.

6. Static induction transistor

One "exotic" structure presently in use is the so-called static induction transistor, also known as the permeable base transistor, which has periodically appeared and disappeared during the past thirty years of silicon technology. It is a majority carrier vertical field effect structure (see Fig. 2(d)). A network of trenches is etched into an epitaxial or implanted structure with a highly doped top layer. The resulting ribbons define the channel fingers. The sources' ohmic contacts are made on the top of the ribbons. Schottky metal/semiconductor control gates are put at the bottom of the trenches, sometimes extending on the lower parts of their edges. As mentioned before, the vertical structure allows plate-like transit zone topology with quite homogeneous field distribution and reduced surface effects.

However the gate control with reasonable lithography dimensions is highly bi-dimensional and its full optimization looks like a technological nightmare.

To get good control of carrier flow by the gate electrostatic influence, fingers have to be thin. To reduce parasitic Miller capacitance, trenches have also to be as thin as possible. Only devices with very fine lithography can approach JFM limit. With controllable lithography resolution (1 μm trenches), high efficiency (approaching the JFM limit) operation of SIT will be limited to a fraction of a GHz.

An optimized more than 3 GHz operation would require a submicronic (around 0.2 μm) lithography resolution and the associated manufacturing process.

If the dimensions are not fine enough, two deleterious effects will appear. Because of the gate-carriers' distance, channel depletion requires strong gate applied voltage and will impose a doping level reduction, leading to reduced current density and transconductance. The resulting improved linearity is little compensation for these basic drawbacks.

As a second effect, large channel opening (low channel length/height ratio) opens the way to the control of the injected current by the drain potential (dramatic short channel effects) resulting in high output static conductance with "triode-like" characteristics [12], decreasing power gain capabilities in amplifier operation.

Examples of additional problems related to ultimate device optimization are source/gate isolation, edge passivation, gate resistance minimization, and gate positioning in the trench.

As an early SiC RF power device, even a non-optimized SIT/BPT has certainly been a good choice [12]. As the SiC technology gets more mature, it will only stay competitive by going to the most sophisticated lithography and technology. At low frequencies (less than 3 GHz), if passivation problems do not dominate the device performances, we believe that horizontal FETs will exhibit better global performances. At high

frequencies, HBT will probably be preferred, because it allows relaxed lithography dimensions.

However today, it must be emphasized that the SIT/TBP structure is the only one for which true high-power (over 1 kW) amplification has been demonstrated at the laboratory level.

7. MESFET and JFET devices

The other existing early SiC power device structures are field effect ones: mainly horizontal MESFETs and JFETs.

7.1. MESFETs

MESFET experience comes from the III-V world. It is the simplest FET structure which needs only an n-type active layer (Fig. 3(b)) but for which outstanding performances have been predicted [11]. For power devices, the gate has to be placed as near as possible to the source to reduce source access resistance.

The simplest MESFET technology makes use of epitaxial N⁺/N layers. Mesa and recess are first etched and then ohmic contacts and gate Schottky contacts are aligned relatively to the recess edges. Depending on the targeted operation frequency, devices with gate lengths of 2 μm (less than 1 GHz) down to 0.5 μm (greater than 3 GHz) have already been studied [7–10].

7.2. JFETs

JFET topology is very similar to MESFET with the specificity that the gate barrier is a p/n junction. It requires the same technology background together with additional know-how on gate P+ layer, related P+ ohmic contact and N+ ion implantation for making source and drain contacts. This explains why power MESFET technology and results are more advanced than the JFET ones. Following the silicon experience, optimized JFETs may turn out to be more reliable than MESFETs, although the possibility of making Schottky refractory contacts on SiC may make it possible to overcome possible problems related with Schottky repro-

ducibility and reliability often encountered in past silicon MESFET technology trials.

As for other kinds of horizontal devices, interconnections are much easier and less lossy on semi-insulating substrates. Via-holes or air bridges interconnections are a necessity for power multi-finger since three electrodes have to be dispatched. Following GaAs MESFET evolution, planar, implanted and self-aligned technologies are expected to emerge in case of success, in order to lower fabrication costs. Possible variants would be GaN active layer MESFETs and AlGaN/GaN HEMTs most probably on SiC substrates, as mentioned in Section 1. For all these MESFET devices, passivation and reliability issues have still to be clarified and may determine the final choice.

8. SiC power amplification state of the art

Simply, today, all solid state applications over 3 GHz today are GaAs substrate-based and all those below 1 GHz are silicon based. In between, tough competition takes place. At the low frequency end, the “good old” silicon bipolar transistor is progressively replaced by MOS devices giving easier input impedance adaptation.

Inside the MOS category, laterally depleted “horizontal” structures (LD-MOS) are taking over “vertical” structures such as U, V and D-MOS. In the present SiC first approach period, SiC devices are expected to challenge both Si and GaAs microwave power technologies in the RF to S-band spectrum (10 MHz–3 GHz).

At present the best published results for SiC are by Westinghouse/Northrop-Grumman and related to SIT and MESFET transistor (see Table 2). The most impressive is a prototype over 1 kW amplifier [6] made out of many-hundred-watts packaged SIT transistors which are assemblies of selected tens-of-watts cells on several chips. Global performances seem superior to those of silicon-based amplifiers roughly by a factor of three.

JFET results are encouraging, with 1.3 W mm⁻¹ at 0.85 GHz [15] but despite significant early Russian works, only very few teams in the world are still active today in this area.

The other publications are related to MESFETs. The

Table 2
Summary of published SiC microwave power results

What	Who	Substrate type	Power (W)	Frequency (GHz)	Size (mm)	Power added efficiency(%)
SIT	Westinghouse	N+	>1000	0.6	350	
SIT	Westinghouse	N+	36 pulse	3	30	42
MESFET	Westinghouse	S.I.	3.5	6	2	46
MESFET	Cree/Motorola	N+	0.7	1.8	0.33	50
MESFET	Cree/Motorola	N+	0.7	0.85	0.33	60
MESFET	Thomson	N+	1.6	2	1	38
MESFET	Thomson	N+	2	1	4.8	43

highest frequency operation (6 GHz) was demonstrated in 1995, again by Westinghouse/Northrop-Grumman with 3.5 W output power and over 40% power added efficiency [15]. This is on 6H semi-insulating substrates; 4H results are expected soon. Other results are from Cree/Motorola [8,9] and Thomson [10] with devices on conductive substrates. For both, a similar trend is observed: owing to adaptation problems in relation with the conductive substrate, the power density decreases rapidly with the device size. Impressive improvements are expected with the arrival of semi-insulating substrates.

9. Trends for the future

Discrete MESFETs (and possibly JFETs) on SiC substrates should reach soon the 100 W level around 1 GHz and will progressively give competitive performances up to 10 GHz with reasonable gate length (0.3–0.5 µm). MMICs will follow later, when substrate price will go down.

For higher-frequency or low-cost/narrow-band operation, there is a chance that HBT will make a better industrial product. In both cases, choice will be made between purely SiC and mixed SiC/III-N solutions, mainly depending on reliability and fabrication cost issues.

Large-scale commercialisation of SiC based microwave power devices is expected by 2000–2002 when better semi-insulating wafers, at least 2 inches in diameter, will be commercially available.

References

- [1] H. Morkoç, S. Strite, G.B. Gao, M.E. Lin, B. Sverdlov, M. Burns, Large-band-gap SiC, III-V nitride, and II-VI ZnSe-based semiconductor device technologies, *Journal of Applied Physics* 76 (3) (1994).
- [2] S.C. Binari, L.B. Rowland, W. Kruppa, G. Kelner, K. Doverspike, D.K. Gaskill, Microwave performance of GaN MESFETs, *Electron. Lett.* 30 (15) (1994).
- [3] Microwave performance of a 0.25 µm gate AlGaN/GaN heterostructure field-effect transistor, *Appl. Phys. Lett.* 65 (9) (1994).
- [4] A. Özgür, W. Kim, Z. Fan, A. Botchkarev, A. Salvador, S.N. Mohammad, B. Sverdlov, H. Morkoç, High transconductance-normally-off GaN MODFETs, *Electron. Lett.* 31 (16) (1995).
- [5] Q. Chen, M. Asif Khan, J.W. Yang, C.J. Sun, M.S. Shur, H. Park, High transconductance heterostructure field-effect transistors based on AlGaN/GaN, *Appl. Phys. Lett.* 69 (6) (1996).
- [6] A. Morse, P.M. Esker, R.C. Clarke, C.D. Brandt, R.R. Siergiej, A.K. Agarwal, Applications of high power silicon carbide transistors at radar frequencies, *IEEE MTT-S Conference Digest*, 1996, pp. 677–680.
- [7] C.D. Brandt, A.K. Agarwal, G. Augustine, R.R. Baron, A.A. Burk, R.C. Clarke, R.C. Glass, H.M. Hobgood, A.W. Morse, L.B. Rowland, S. Seshadri, R.R. Siergiej, T.J. Smith, S. Sriram, M.C. Driver, R.H. Hopkins, Advances in SiC materials and devices for high frequency applications, *Proceedings of the ICSCRM 95 Conference*, 1995, p. 659.
- [8] C.E. Weitzel, J.W. Palmour, C.H. Carter, K.J. Nordquist, 4H-SiC Mesfets with 2.8 W/mm power density at 1.8 GHz, *IEEE Electron Devices Lett.* 15 (10) (1994).
- [9] S.T. Allen, J.W. Palmour, C.H. Carter, C.E. Weitzel, K.E. Moore, K.J. Nordquist, L.L. Pond III, Silicon Carbide Mesfets with 2 W/mm and 50% P.A.E. at 1.8 GHz, *IEEE MTT-S Conference Digest*, 1996, pp. 677–680.
- [10] O. Noblanc, E. Chartier, C. Arnodo, C. Brylinski, Microwave Power Meset on 4H-SiC, *ECSCRM 96 Conference, Diamond Relat. Mater.* 6 (1997) 1510–1513.
- [11] C. Weitzel, Comparison of SiC, GaAs and Si RF MESFET power densities, *IEEE Electron Devices Lett.* 16 (10) (1995) 451.
- [12] R.R. Siergiej, R.C. Clarke, A.K. Agarwal, C.D. Brandt, A.A. Burk Jr., A. Morse, P.A. Orphanos, High power 4H-SiC static induction transistors, *Proceedings of IEDM 95 Conference*, 1995, pp. 353–356.
- [13] High temperature GaN/SiC heterojunction bipolar transistor with high gain, *IEDM Technical Digest* (1994) 389–394.
- [14] S.C. Binari, L.B. Rowland, W. Kruppa, G. Kelner, Doverspike, D.K., D.K. Gaskill, Critical nature of oxide/interface quality for SiC power devices, *Microelectron. Engng.* 28 (1995) 177–184.
- [15] K. Moore, DC, RF and power performance of 6H-SiC JFETs presented at WOCSEMMAD '95 Conference, New Orleans, 1995.

Aluminium implantation of *p*-SiC for ohmic contacts

L. Spieß ^{a,*}, O. Nennowitz ^a, H. Weishart ^b, J. Lindner ^c, W. Skorupa ^b, H. Romanus ^a,
F. Erler ^a, J. Pezoldt ^d

^a TU Ilmenau, Institut für Werkstoffe, PF 100565, D-98684 Ilmenau, Germany

^b Forschungszentrum Rossendorf eV, PF 510119, D-01314 Dresden, Germany

^c Universität Augsburg, Institut für Physik, Memminger Str. 6, D-86135 Augsburg, Germany

^d TU Ilmenau, Institut für Festkörperelektronik, PF 100565, D-98684 Ilmenau, Germany

Abstract

An important problem is the formation of low-resistance ohmic contacts, especially for *p*-type SiC. The deposition of all known metals onto *p*-type SiC will always result in a depletion *p*-type contact. To obtain an ohmic contact, the depletion zone has to be smaller. This may be achieved by very shallow *p*-dopant implantation. Another aim of this research was to study the structural and chemical changes of the surface, as well as the interface and bulk after implantation, annealing and contact formation. Specific contact resistance of $5 \times 10^{-4} \Omega \text{ cm}^2$ was achieved on *p*-implanted 6H-SiC with Al/Ti metallization. © 1997 Elsevier Science S.A.

Keywords: Atomic force microscopy; Metallization; Ohmic contact; Transmission electron microscopy

1. Introduction

SiC is a promising wide bandgap semiconductor material for active electronic devices. The great potential of SiC as a semiconductor, however, is challenged by the difficulty of controlling the metal contact properties. An important problem lies in creating low-resistance ohmic contacts, especially for *p*-type SiC [1].

It is impossible to fabricate an enhancement *p*-type SiC contact. There is no metal or metal-like material known with a workfunction of about 6 eV. The theoretical band bending that occurs at a metal–semiconductor contact is shown in Fig. 1. This gives rise to the Schottky barrier ϕ_{Bp} . If there are no other effects influencing the metal–semiconductor contact, then ϕ_{Bp} may be written as $\phi_{Bp} = \Phi_s - \Phi_m$.

The application of all known metals to *p*-type SiC will always result in a depletion *p*-type contact. The barrier height depends on the difference between the metal work function and the electron affinity plus the Fermi level of the semiconductor. A depletion zone of holes is observed at the interface. To obtain an ohmic contact, the depletion zone has to be smaller. This may be achieved by very shallow *p*-dopant implantation. This additional doping, however, increases the barrier height

as shown in Fig. 1. A smaller depletion region allows thermionic-field or field emission. Fig. 2 shows the dependence of contact resistance on the hole concentration, using Eq. (1):

$$\rho_c = \frac{k}{qAT} \exp \left\{ \frac{4\pi\sqrt{m\epsilon_s}}{qh} \left(\frac{\Phi_{Bp}}{\sqrt{N_A}} \right) \right. \\ \left. \times \tanh \left[\frac{qh}{4\pi\sqrt{m\epsilon_s}} \left(\frac{\sqrt{N_A}}{kT} \right) \right] \right\}. \quad (1)$$

To obtain a specific contact resistance below $10^{-3} \Omega \text{ cm}^2$ ($T=300 \text{ K}$; $\Phi_{Bp}=0.4 \text{ eV}$) a hole concentration of more than 10^{19} cm^{-3} is necessary. Another problem occurs in SiC because of the high acceptor activation energy (more than 0.2 eV). Only about 1% of the acceptors are ionized at room temperature [2]. One possible way to increase the amount of acceptors is ion implantation.

Another aim of this research was to study the structural and chemical changes of the surface, as well as the interface and bulk after implantation, annealing and contact formation. We performed complex solid state analysis involving atomic force microscopy (AFM), reflection of high energy electron diffraction (RHEED), transmission electron microscopy (TEM) and rutherford backscattering (RBS).

* Corresponding author.

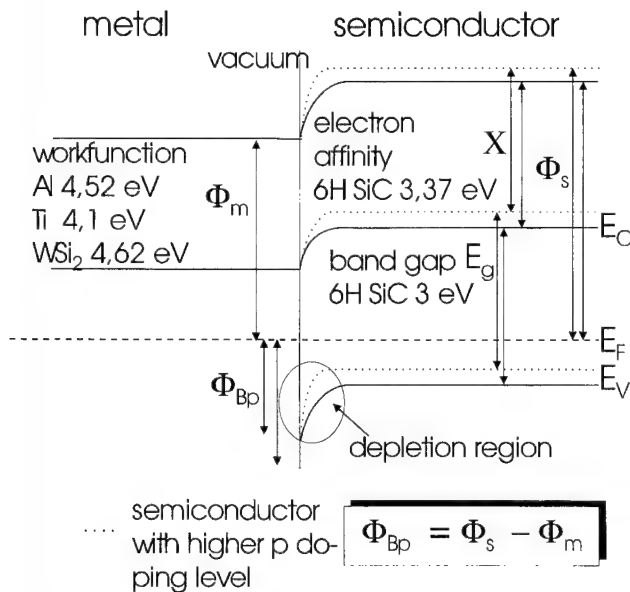


Fig. 1. Theoretical band bending model at a metal–*p*-semiconductor interface.

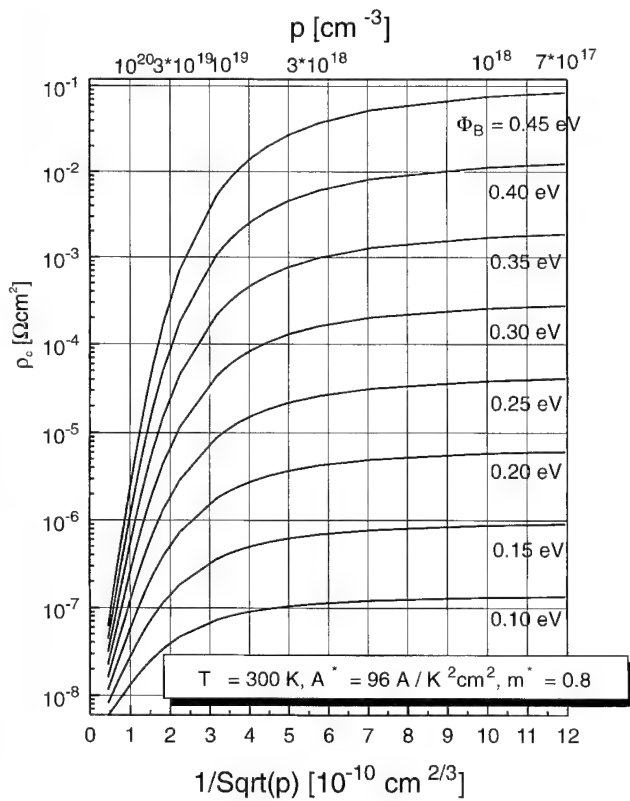


Fig. 2. Calculated contact resistance versus hole concentration.

2. Experimental

In order to increase the acceptor concentration near the surface, an Al implantation with different doses of an implantation energy of 50 keV and room temperature was performed. The theoretical implantation profiles are

shown in Fig. 3. After implantation, the activation of acceptors and the recrystallization of SiC were achieved by annealing at 1650 °C for 20 min in an Argon atmosphere.

RHEED investigations of the near-surface regions were carried out after implantation and after annealing in order to analyse the phase formation resulting from the fabrication process. The damage of the implants was investigated using RBS channeling techniques with 1.6 MeV He⁺ ion energy. The roughness after annealing process was estimated using atomic force microscopy at air and TEM was used to study the microstructure of deeper regions.

Metallization was performed using sputtered Al/Ti. The layer thicknesses were 20 nm Al and 250 nm Ti. A second set of samples was metallized with Tungsten disilicide. WSi₂ layers with a thickness of 400 nm were cosputtered with a stoichiometric ratio Si:W of approximately 2.1:1. In order to form the ohmic contacts, a post implantation annealing was performed at temperatures ranging from 200 to 1100 °C in an Argon atmosphere. The contact resistance was measured at rectangular and circular structures using the transmission line method.

3. Results

The RHEED investigations indicated that the surface damage at implantation is negligible for an implantation dose smaller than $5 \times 10^{14} \text{ cm}^{-2}$, see Fig. 4(a and d). The unannealed sample showed weak 6H-SiC patterns, the annealed sample showed a perfect 6H-SiC pattern including Kikuchi lines. The highest implantation dose resulted in an amorphous region near the surface [Fig. 4(c)]. After annealing, a twinned 3C-SiC RHEED pattern was observed [Fig. 4(f)]. Analysis of the RHEED pattern revealed that a set (111) 3C-SiC twin with a twin plane (111) was formed (Fig. 5).

A smooth surface morphology was observed at the

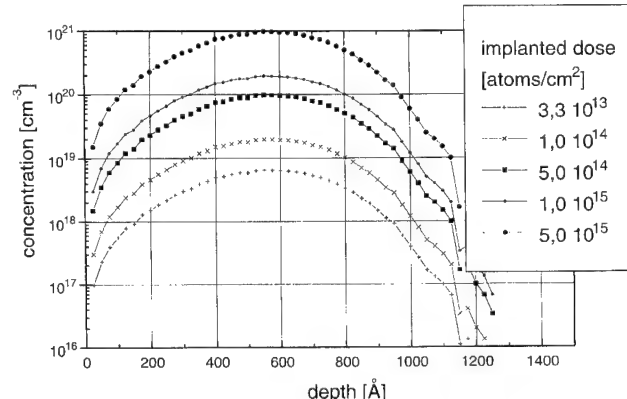


Fig. 3. Implantation profiles calculated using TRIM.

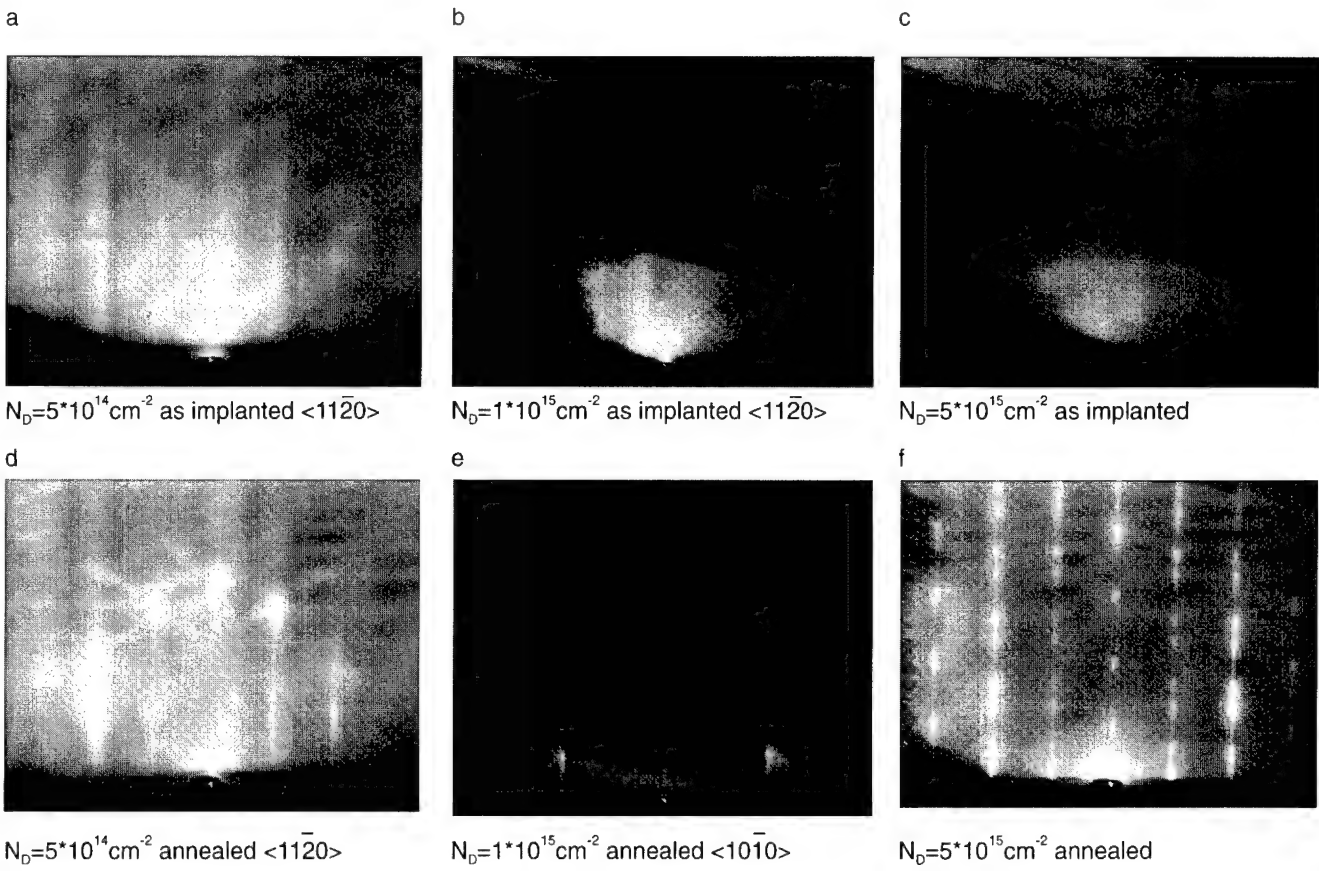


Fig. 4. RHEED patterns: (a) as-implanted $N_{\text{imp}} = 5 \times 10^{14} \text{ cm}^{-2}$; (b) as-implanted $N_{\text{imp}} = 1 \times 10^{15} \text{ cm}^{-2}$; (c) as-implanted $N_{\text{imp}} = 5 \times 10^{15} \text{ cm}^{-2}$; (d) annealed $N_{\text{imp}} = 5 \times 10^{14} \text{ cm}^{-2}$; (e) annealed $N_{\text{imp}} = 1 \times 10^{15} \text{ cm}^{-2}$; (f) annealed $N_{\text{imp}} = 5 \times 10^{15} \text{ cm}^{-2}$.

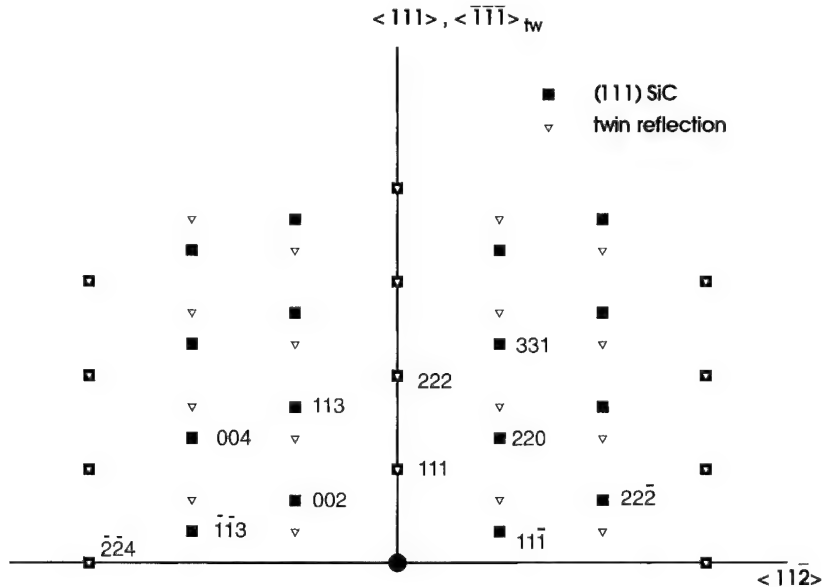


Fig. 5. Theoretical RHEED pattern for (111) 3C SiC twin with plan (111).

as-implanted samples. AFM investigations of the annealed samples showed a smoothing in decrease of the surface roughness with increasing implantation dose; see Table 1. A step structure is observed after annealing;

see Fig. 6. The TEM images showed a perfect surface, but some damage was found in the region of 30 nm under the surface. Two defect regions were found in the sample implanted with a dose of $1 \times 10^{15} \text{ cm}^{-2}$. The

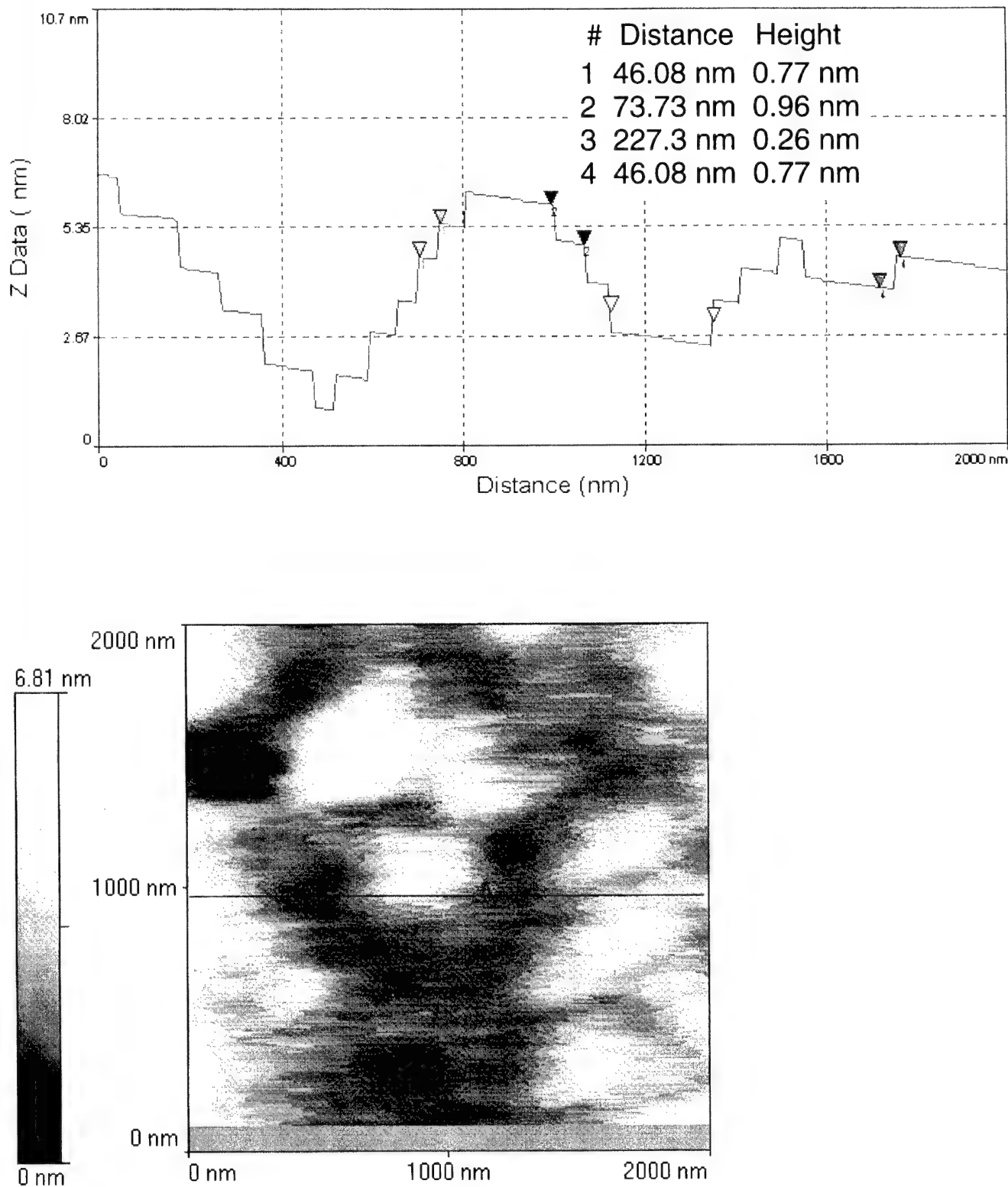


Fig. 6. Surface morphology and step profiles measured using AFM.

shallower of these was observed at the maximum impurity concentration, as calculated by the TRIM program (50 nm), the deeper one at the end of the implantation region (100 nm). Both TEM and AFM investigations

indicated a step formation process during the annealing procedure. The step height ranged from approximately 0.2 to 0.85 nm. Micro beam diffraction in TEM did not indicate the existence of large 3C-SiC particles in the

Table 1

Estimated roughness of implanted and annealed samples using atomic force microscopy

Sample implant dose (cm^{-2})	R_a (nm)	Maximal Height (nm)
Not implanted	1.07	8.85
3.3×10^{13}	0.85	10.4
3.3×10^{14}	0.49	4.4
1.0×10^{15}	0.46	4.0

case of samples with an implantation dose below $2 \times 10^{15} \text{ cm}^{-2}$.

The implanted samples show a lower specific resistance than the non-implanted samples. The specific resistance of SiC is more temperature dependent than that of Si because of the high impurity activation energies. A comparison of the theoretically calculated p -concentrations and the p -concentrations obtained from resistance measurements versus temperature is shown in Fig. 7. The RBS channelling measurements

show that the sample with an implantation dose larger than $1 \times 10^{15} \text{ cm}^{-2}$ is damaged; see Fig. 8.

4. Discussion

The TEM images indicate that some damage is still present. This damage could be dislocations and dislocation loops. With an Al implantation dose of $5.0 \times 10^{15} \text{ cm}^{-2}$, which corresponds to a 10^{21} cm^{-3} Al concentration, an amorphization of the SiC can occur. 3C-SiC is formed during annealing: see the RHEED pattern in Fig. 5. This caused an increase of the surface roughness and a different set of fabrication parameters is required. It was not possible to obtain a good contact measurement in this case. On non-implanted contacts, the lowest specific contact resistance was achieved after annealing at 1100°C ($1.2 \times 10^{-2} \Omega \text{ cm}^2$).

The obtained specific contact resistance for the

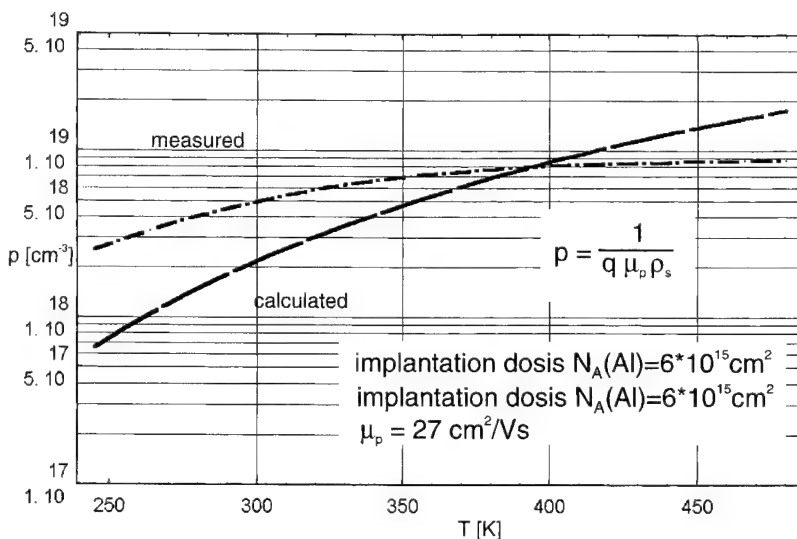


Fig. 7. Calculated p -concentration and p -concentration obtained from resistance measurements versus temperature.

Table 2

Estimated specific contact resistance of Al implanted 6H-SiC samples

Al Doping EPI layer	Contact annealing conditions	Metallization	Al implantation dose (At cm^{-2})					
			3.3×10^{13}	1×10^{14}	3.3×10^{14}	5×10^{14}	1×10^{15}	5×10^{15}
$N_A 1 \times 10^{15} \text{ cm}^{-3}$	Not annealed	Al/Ti	4.5×10^{-1}	1.7×10^{-1}	3.3×10^{-2}		9.7×10^{-3}	
	225 °C	Al/Ti	7.9×10^{-2}	3.1×10^{-2}	3.6×10^{-2}		5.6×10^{-3}	
	500 °C	Al/Ti	2.5×10^{-2}	1.8×10^{-2}	2.0×10^{-2}		5.6×10^{-4}	
$N_A 5 \times 10^{16} \text{ cm}^{-3}$	Not annealed	WSi ₂				X		X
	1050 °C	WSi ₂				X		X
$N_A 7 \times 10^{16} \text{ cm}^{-3}$	Not annealed	WSi ₂					X	
	1050 °C	WSi ₂				X	0.2 at 650 K	X
$N_A 3 \times 10^{18} \text{ cm}^{-3}$	Not annealed	WSi ₂				X		X
	1050 °C	WSi ₂				X		2.0×10^{-2} at 650 K

X = non-ohmic contact behaviour at room temperature.

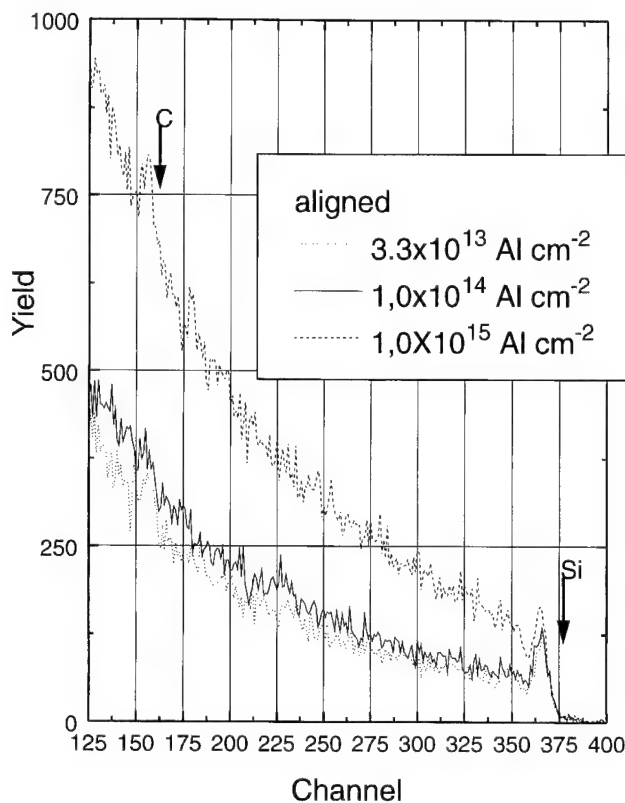


Fig. 8. Channelling RBS spectra.

implanted samples are shown in Table 2. It is obvious that the contact behaviour becomes ohmic with the Al/Ti metallization. WSi₂ metallization created a non-ohmic contact behaviour before and after contact annealing, only at higher operating temperatures is an ohmic character found. It was not possible to estimate the barrier height using current–voltage plots for samples with an implantation dose larger than $1 \times 10^{14} \text{ cm}^{-2}$.

Acknowledgement

This work was supported by the BMBF. The authors would like to thank SIEMENS Erlangen, Dr Völkl for annealing and Mr W. Reibe, Augsburg, for TEM preparation and Mr Röschke for reading the manuscript.

References

- [1] L.M. Porter, R.F. Davis, Mater. Sci. Engng B34 (1995) 83–105.
- [2] L. Spieß, O. Nennewitz, J. Pezoldt, Inst. Phys. Conf. Ser. 142 (1996) 585–588.

Fabrication of high-quality oxides on SiC by remote PECVD

A. Gölz *, S. Groß, R. Janssen, E. Stein von Kamienski, H. Kurz

Institut für Halbleitertechnik, Lehrstuhl II, RWTH Aachen, Sommerfeldstr. 24, D-52074 Aachen, Germany

Abstract

The interface trap density in oxides grown on 6H silicon carbide by remote plasma-enhanced chemical vapor deposition as well as by thermal oxidation is studied. This trap density is found to be drastically reduced by a plasma-assisted PDP (pre-deposition process) in hydrogen. The reduction is stable if a high-temperature annealing step is carried out which excludes a simple passivation by hydrogen. © 1997 Elsevier Science S.A.

Keywords: Pre-deposition processing; Silicon carbide; Thermal oxidation; Remote PECVD

1. Introduction

The high saturation drift velocity and thermal conductivity, and the chemical inertness in harsh environments, makes the wide band-gap semiconductor silicon carbide a promising material for high-power, high-frequency and high-temperature electronics [1]. For MOS-related devices, a high-quality gate insulator is essential. Thermally grown silicon dioxide on 6H silicon carbide reveals electrical properties attractive for gate insulators in SiC-based MOSFETs (metal-oxide-semiconductor field-effect transistor). For some technical applications, e.g. thick field oxides, oxide fabrication by a nonconsumptive method is desirable. Furthermore, surface engineering is expected to have more drastic effects on oxide qualities. For this purpose, we use a two-step remote plasma enhanced chemical vapor deposition (RPECVD) process. The first step consists of a so-called plasma-enhanced PDP (pre-deposition process), where surface engineering is carried out in oxygen or hydrogen plasma. In the second step, an oxide layer is deposited. The two-step RPECVD process has been already used successfully for high-quality oxide deposition on silicon [2,3]. In this study, we describe the results obtained by HFCV (high-frequency capacitance–voltage) measurements on oxides fabricated by RPECVD on 6H silicon carbide, *n*- and *p*-type. The obtained HFCV-data emphasize the crucial role of a PDP. These results are compared with those on thermally grown oxides, where a PDP improves the oxide quality as well.

2. Experimental

The RPECVD method is based on the plasma-enhanced chemical vapor deposition (PECVD) method, but includes technical improvements to reduce the amount of Si–H and Si–OH groups in the oxide layer and to prevent ion damage. This is realized by spatial separation of different reaction steps, especially the fact that the substrate holder is separated from the plasma generation region. For this, an RPECVD-chamber with a 1" substrate holder described elsewhere [3] has been constructed.

For sample preparation, commercially available (Cree Research, Inc.) Si-faced *n*- and *p*-type 6H-SiC epilayers ($\text{doping} \approx 1 \times 10^{16} \text{ cm}^{-3}$) on 6H-SiC substrates are cleaned in acetone and by a standard RCA-clean. The samples are subsequently dipped for 10 s in buffered HF solution, rinsed in distilled water and placed in the chamber at a base pressure of $2 \times 10^{-6} \text{ Pa}$. Before oxidation is carried out, a plasma-assisted pre-deposition processing (PDP) (30 s–20 min) in hydrogen or oxygen is performed. Oxide growth is realized either by the deposition of an oxide layer of about $\approx 25\text{--}30 \text{ nm}$ by RPECVD or by thermal oxidation. As shown below, the low-temperature surface engineering step by the PDP plays an important role to reduce the interface trap density. The PDP and the RPECVD process are run at 200°C and at a pressure of 33 Pa. The gas flows are 100 sccm Ar, 10 sccm O₂ or H₂, and 10 sccm 1% SiH₄ in Ar. Thermal oxidation is carried out in a quartz furnace in dry or wet oxygen at 1150°C . Some samples

* Corresponding author.

are given to a high-temperature annealing step in Ar or forming gas at 1150 °C for 50 min in the quartz tube as well. Finally, they are metallized with aluminum and patterned into MOS-capacitors for electrical characterization.

3. Results and discussion

All results presented in this study are taken from oxides fabricated with molecular oxygen. When nitrous oxide is used for the PDP or the deposition, the oxides show higher defect densities [4]. High-frequency capacitance–voltage (HFCV) measurements at room temperature are used to characterize the MOS-capacitors. From the flat-band voltage V_{fb} the oxide charge density N is derived, which includes not only fixed oxide charges but also interface traps. The latter are frozen in at room temperature and therefore behave like fixed oxide charges. The remaining interface trap density D_{it} is evaluated by the Terman method [5]. To compare different oxides D_{it} is always taken at 300 meV near the valence and conduction band edge for *p*- and *n*-type materials, respectively.

3.1. 6*H* silicon carbide, *n*-type

To investigate the defect densities in the upper half of the band-gap, oxides on *n*-type material have been fabricated. In Fig. 1, HFCV-data taken on oxides on *n*-type 6*H*-SiC are shown before oxide depositions PDP in oxygen has been carried out. Nondistinguishable data are obtained when a PDP in hydrogen is carried out instead. The data from oxides without further treatment after the deposition process still show hysteresis and a shift towards positive voltages indicating an oxide charge and interface trap density of $N \approx 2 \times 10^{12} \text{ cm}^{-2}$ and

$D_{it} \approx 9 \times 10^{11} \text{ eV}^{-1} \text{ cm}^{-2}$, respectively. However, these trap densities can be drastically reduced by annealing in inert argon, nitrogen or even forming gas (10% hydrogen in argon). As can be seen from Fig. 1, the results are nearly the same for all annealing atmospheres. The slope, i.e. the interface trap density, stays approximately the same at $1 \times 10^{11} \text{ eV}^{-1} \text{ cm}^{-2}$. However, a lower flat-band voltage occurs, indicating a reduction of the oxide charge density down to $-7.5 \times 10^{11} \text{ cm}^{-2}$. These encouraging results of defect densities, comparable with those of good thermal oxides [6], prove that oxide fabrication by RPECVD may offer high potentials for MOS-related technologies.

3.2. 6*H* silicon carbide, *p*-type

Investigations on *p*-type 6*H*-SiC are carried out to detect the defect densities in the lower half of the band-gap. For nonannealed oxides on *p*-type SiC, the oxide charge and interface trap density are very high, i.e. $N = 1 \times 10^{13} \text{ cm}^{-2}$ and $D_{it} = 2 \times 10^{13} \text{ eV}^{-1} \text{ cm}^{-2}$. As shown in Fig. 2, a high-temperature (1150 °C) inert gas (argon or nitrogen) annealing step reduces drastically the defect densities. The remaining interface trap density $D_{it} = 6 \times 10^{11} \text{ eV}^{-1} \text{ cm}^{-2}$ is more than one order of magnitude lower than for nonannealed oxides. In comparison with the theoretical CV curve, a large shift towards negative voltages still remains. This indicates an oxide charge density $N = 8 \times 10^{12} \text{ cm}^{-2}$. The obtained defect reduction can be explained by a reorganization of bonds at the interface provoked by the high temperature. This state is stable, i.e. longer annealing does not change this state significantly. In the following we discuss the effects of a low-temperature PDP on the oxide quality. On *p*-type 6*H*-SiC, no PDP or a PDP in oxygen before

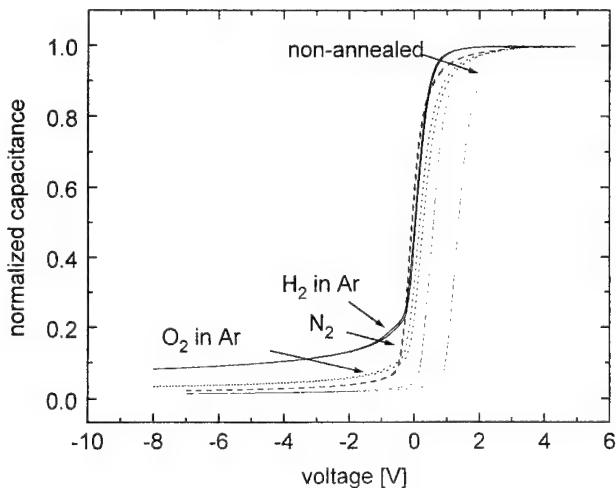


Fig. 1. HFCV data on deposited oxides on *n*-SiC: PDP 30 s in oxygen; annealing at 1150 °C for 50 min in gas ambients as indicated.

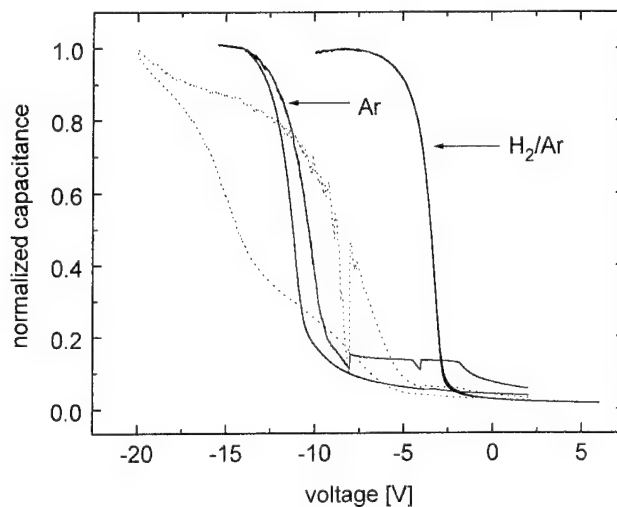


Fig. 2. HFCV data on deposited oxides on *p*-SiC: PDP 20 min in hydrogen; annealing at 1150 °C for 50 min in gas ambients as indicated; dotted line represents as-grown.

deposition provokes high leakage currents indicating high defect densities. This result is different to that reported by Zetterling et al. [8]. For thermal oxidation, they found a reduction of the flat-band voltage of about 50% when the specimen had previously been given into an oxygen plasma.

We found that surface preparation by a low-temperature (200 °C) PDP in hydrogen offers the possibility to reduce drastically the interface trap density, even if a high-temperature annealing step as described above is carried out after the oxide deposition. The effect of the PDP is illustrated in Fig. 3, where calculated D_{it} values for different preclean times are shown. As can be seen, a PDP of 20 min leads to an interface trap density of one order of magnitude lower compared to a PDP of only 30 s. Hydrogen is known to passivate interface traps in thermal oxides as well as in deposited oxides [4,7]. Thus, the first idea is that this defect reduction appears due to a passivation by hydrogen. To compare the effect of hydrogen passivation and the hydrogen PDP, annealing in forming gas (hydrogen in argon) at 1150 °C has been carried out. The result is shown in Fig. 2. The forming gas annealing step leads to a reduction in the oxide charge density and the interface trap density to $N=6.6 \times 10^{11} \text{ cm}^{-2}$ and $D_{it}=4 \times 10^{11} \text{ eV}^{-1} \text{ cm}^{-2}$, respectively. However, if the same high-temperature argon annealing step as after the PDP is carried out, this passivation is completely destroyed, and the same CV data as after an argon anneal are obtained. If a PDP in hydrogen passivated the surface, no effect would be expected to be seen after an argon anneal. This argument indicates that the remaining influence on the interface trap density obtained by applying a hydrogen PDP cannot be explained by a hydrogen passivation at all. The PDP causes a stable change on the interface. Hallin et al. have discussed the effect of applying excited hydrogen on SiC in a CVD

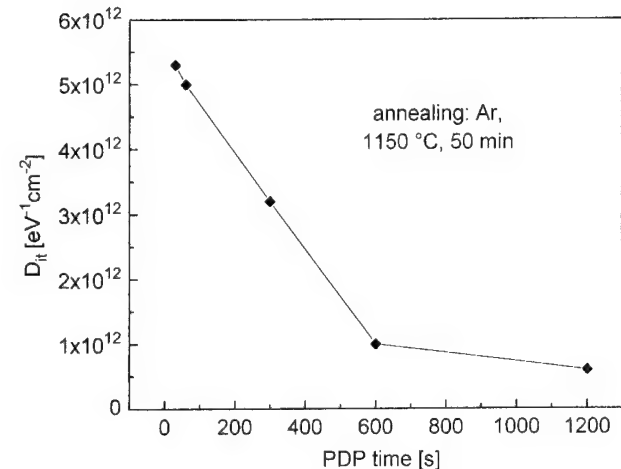


Fig. 3. Interface trap density calculated for oxides on *p*-SiC: PDP in hydrogen, time as indicated; annealing in argon at 1150 °C for 50 min.

process [9]. Using atomic force microscopy, they found that surface roughness decreases owing to hydrogen etching. Although they used high temperatures (1500 °C) in their CVD process, a plasma-assisted PDP with hydrogen excited by a plasma at low temperatures (200 °C) should have similar etching effects. It seems reasonable to assume that this large reduction of the interface trap density found in our CV data is correlated with a reduction of surface roughness.

To investigate the effect of a PDP surface engineering on the defect density of thermal grown oxides, this hydrogen PDP has been carried out before thermal oxidation as well. To avoid surface contamination, after the hydrogen preclean, a thin oxide layer of 2–3 nm is deposited before the specimens are placed in the quartz furnace. For dry oxides annealed in argon at 1150 °C, i.e. non-passivated oxides, the interface trap density is $2 \times 10^{12} \text{ eV}^{-1} \text{ cm}^{-2}$ and $1 \times 10^{12} \text{ eV}^{-1} \text{ cm}^{-2}$ without and with PDP, respectively. For passivated oxides, the PDP shows an effect too. In Fig. 4, HFCV data obtained on oxides fabricated by wet oxidation and forming gas anneal (1150 °C, 50 min) are shown. A reduction in the interface trap density from $7 \times 10^{11} \text{ eV}^{-1} \text{ cm}^{-2}$ to $4 \times 10^{11} \text{ eV}^{-1} \text{ cm}^{-2}$ is obtained when a PDP is carried out. Compared with deposited oxides, the effect is much smaller (about a factor of two compared with one order of magnitude). This can be explained by the fact that the surface structure changes during the consumptive oxidation process. Nevertheless, our results indicate that a low-temperature PDP also has a significant effect on the interface trap density in thermal grown oxides.

4. Conclusions

The presented results show that the plasma-assisted two-step process (pre-deposition process and deposition)

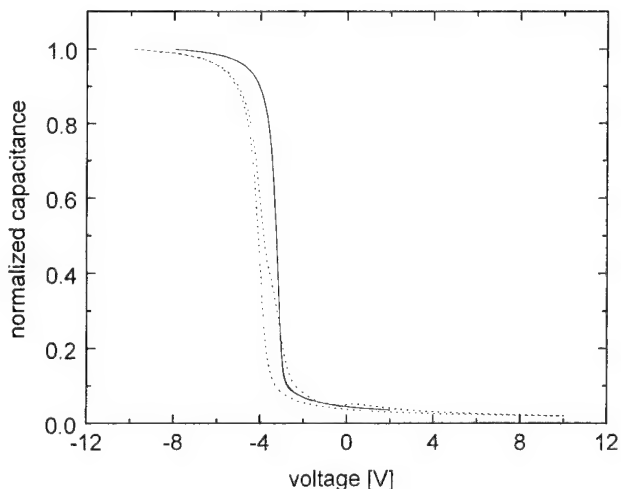


Fig. 4. HFCV data on thermal oxides on *p*-SiCL: PDP in hydrogen; oxidation in wet oxygen at 1150 °C; annealing in forming gas at 1150 °C for 50 min.

in a remote plasma has promising potentials for high-quality oxides on SiC. Oxides can be fabricated by RPECVD with defect densities comparable with thermal oxides, but at much higher growth rates. The surface engineering by a low-temperature PDP particularly improves oxide quality. For deposited as well as for thermal oxides, a reduction in interface traps in the lower half of the band-gap is achieved. For deposited oxides, the effect is more drastic because the well-prepared surface becomes the interface. In addition, this surface preparation is stable against a high-temperature annealing step in an ambient inert gas, which excludes hydrogen passivation to be the reason for the quality improvement.

Acknowledgement

The support by G. Lucovsky, North Carolina State University, USA, to build the Remote PECVD system is gratefully acknowledged. We thank the Bundesministerium für Bildung, Wissenschaft, Forschung und Technologie for financial support.

References

- [1] M. Bhatanagar, B.J. Baliga, IEEE Trans. Elec. Devices 40 (1993) 645.
- [2] G. Lucovsky, Y. Ma, T. Yasuda, C. Silvestre, J.R. Hauser, Jap. J. Appl. Phys. 31 (1992) 4387.
- [3] A. Götz, R. Janssen, E. Stein von Kamienski, H. Kurz, in: H.Z. Massoud, E.H. Pointdexter, C.R. Helms (Eds.), *The Physics and Chemistry of the SiO₂ and the Si–SiO₂ Interface*, The Electrochemical Society, Inc. Proceedings, 96 (1) 753.
- [4] A. Götz, S. Groß, R. Janssen, E. Stein von Kamienski, H. Kurz, Mater. Sci. Engng B 00 (1997) 00–00.
- [5] E.H. Nicollian, J.R. Brews, *MOS (Metal Oxide Semiconductor) Physics and Technology*, Wiley, New York, 1982.
- [6] E. Stein von Kamienski, F. Portheine, A. Götz, H. Kurz, Proceedings of the Sixth International Conference on Silicon Carbide and Related Materials, Kyoto, 1995, p. 641.
- [7] E.G. Stein von Kamienski, C. Leonhard, S. Scharnholz, A. Götz, H. Kurz, Mater. Sci. Engng B 00 (1997) 00–00.
- [8] C.-M. Zetterling, C.I. Harris, M. Östling, V.V. Afanas'ev, Proceedings of the Sixth International Conference on Silicon Carbide and Related Materials, Kyoto, 1995, p. 605.
- [9] C. Hallin, A.S. Bakin, F. Owman, P. Mårtensson, O. Kordina, E. Janzen, Proceedings of the Sixth International Conference on Silicon Carbide and Related Materials, Kyoto, 1995, p. 613

An interface study of vapor-deposited rhenium with the two (0001) polar faces of single crystal 6H-SiC

S. Kennou¹, A. Siokou, I. Dontas, S. Ladas *

Department of Chemical Engineering, University of Patras, and FORTH-ICE-HT, P.O.B. 1414, GR-26500 Rion, Patras, Greece

Abstract

The interfaces formed on the two (0001) polar faces of single crystal n-type 6H-SiC by Re evaporation and subsequent annealing were investigated by X-ray photoelectron spectroscopy (XPS), low energy electron diffraction (LEED) and work function (WF) measurements. Rhenium was deposited from submonolayer up to 2 nm thickness and gradually annealed up to 1100 K. Deposition led to a weakening and eventual disappearance of the 1×1 LEED pattern of the clean surface, an increase of the WF up to the value of metallic Re and the formation of a Schottky barrier with a height of 0.7 ± 0.2 eV for both faces. The Re $4f_{7/2}$ peak binding energy decreased during deposition from approx. 41.1 eV below monolayer coverage, to 40.5 eV for a 2 nm film indicating an island growth of the film. Annealing of the Re films up to 1100 K on both faces led to Re particle coalescence without affecting the low Schottky barrier at the interface, however, there are indications of chemical changes at the interface which could affect the electrical characteristics of the contact. © 1997 Elsevier Science S.A.

Keywords: Silicon carbide; Rhenium; X-ray photoelectron spectroscopy; Work function

1. Introduction

Single-crystal silicon carbide devices are potential candidates for high-temperature applications [1]. In particular, metal/SiC contacts and the resulting Schottky barriers are important for such SiC-based devices. Although the metal/SiC Schottky contact formation at room temperature has been studied in recent years for a large number of metals [2–9], the effect of annealing at higher temperatures on the stability of the metal/SiC contact has been studied for rather few metals, namely Pt, Au, Co, Mo and Ni [3,6–9]. Rhenium is a good candidate for such stability at high temperature because it does not react with SiC at temperatures up to 1400 K, as shown by recent studies of Re films, at thicknesses of up to 300 nm, on n-type β -SiC(001) [10]. On the basis of this thermodynamic inertness one would expect that the electrical behaviour of the Re contact on SiC would be stable with heat treatment, however changes are observed above 750 K which are attributed to minute changes at the interface [11]. In this study, we examined

the early stages of Re/SiC interface formation at room temperature and the influence of annealing up to 1100 K on the interface stability on the two (0001) polar faces of single crystal n-type 6H-SiC, the (0001) (Si-face) and the (0001) (C-face), by using X-ray photoelectron spectroscopy (XPS), work function (WF) measurements and low energy electron diffraction (LEED).

2. Experimental

All measurements were performed in a conventional ultra high vacuum system equipped with XPS, LEED and WF measurement facilities which have been described previously [12]. Single crystal 6H-silicon carbide wafers, both Si-face and C-face, from Cree Research Inc. [13] were used as substrates. The wafers were n-type, nitrogen-doped (3×10^{17} – 3×10^{18} cm $^{-3}$ net doping density) and oriented 3–4° off-axis with respect to the ideal (0001) plane towards the [11-20] direction. Before the samples were mounted into the ultra high vacuum system they were cleaned using the procedure described elsewhere [14]. In the vacuum the crystals were heated up to 900 K to remove volatile compounds. Both clean substrates exhibited a 1×1 hexagonal LEED

* Corresponding author. Tel: +3061 997631/997856; Fax: +3061 993255; e-mail: ladas@iceht.forth.gr

¹ Permanent address: Department of Physics, University of Ioannina, P.O.B.1186, GR-45110 Ioannina, Greece

pattern which was more intense for the C-face. The latter exhibited a Si 2p/C 1s XPS intensity ratio of 0.8 compared with 1.1 for the Si-face. Both faces exhibited a small O 1s peak in the XP spectrum and the Si 2p photopeak showed only traces of an oxidized component. The WF of the clean surface was found 4.5 ± 0.1 eV for both the Si-face and the C-face in agreement with previous measurements [12]. Rhenium was e-beam evaporated from a thoroughly degassed tip at a pressure of 5×10^{-10} mbar and at a deposition rate of 0.2 nm per min. Rhenium was deposited at room temperature at successively increasing amounts up to 2 nm. After each deposition step XPS, LEED and WF measurements were taken. When the surface was covered with 2 nm of Re the crystal was heated for 2 min at successively increasing temperatures up to 1100 K. After each annealing step XPS, LEED and WF measurements were taken again.

3. Results and discussion

Upon Re deposition on both the Si-face and the C-face at room temperature the LEED pattern of the clean surface weakens continuously with increasing background intensity and no new spots are observed. Fig. 1 shows the work function change upon deposition which is the same for the two faces. This similarity between

Si- and C-faces extends over practically the whole range of measurements reported here, therefore in the following only the results for the Si-face will be shown and minor differences will be pointed out when they occur. The WF increases continuously and after ~ 1 nm or 3–4 monolayers of Re evaporation reaches a final value of ~ 5.2 eV, that is close to the value for polycrystalline Re (5.1 eV) [15]. The relatively large amount of Re required to reach WF saturation indicates film growth with cluster formation. This is confirmed with XPS by the binding energy shift of the Re $4f_{7/2}$ core level peak from 41.1 eV at submonolayer deposition to 40.5 eV after 2 nm of Re as shown in Fig. 2. Such a shift is expected for metal cluster formation on a relatively inert substrate [16].

Upon Re deposition at room temperature the C 1s and Si 2p core level peaks from the SiC substrate are attenuated but their shape does not change indicating negligible chemical interaction with deposited Re. The C 1s and Si 2p peaks for the clean substrate and after 2 nm of Re are shown in Figs. 3 and 4 normalized to the same maximum height. The binding energy at the peak maximum shifts slightly and saturates after ~ 1 nm of Re to a value lower by ~ 0.1 eV for both peaks. The Schottky barrier height, Φ_B , for the Re/SiC interface was calculated from the above XPS data using the

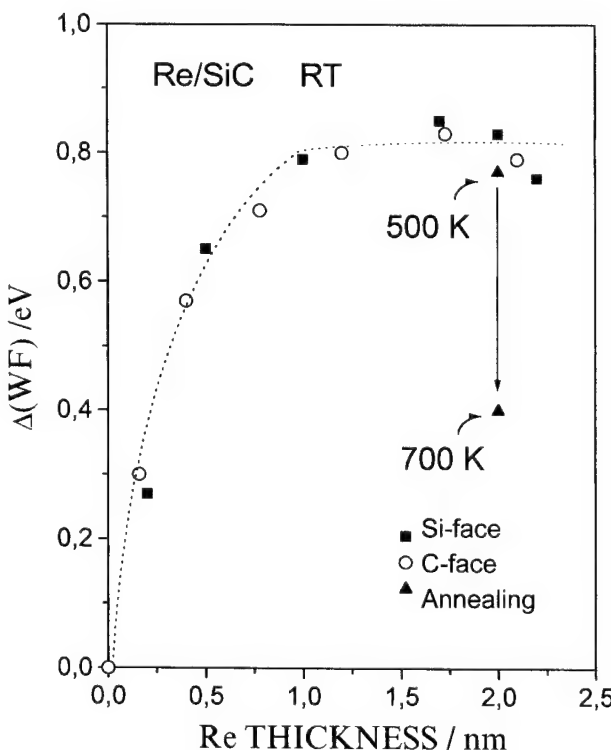


Fig. 1. The variation of the work function with Re deposition on the two polar faces of 6H-SiC at room temperature. The triangles indicate the WF decrease upon annealing a 2 nm Re deposit.

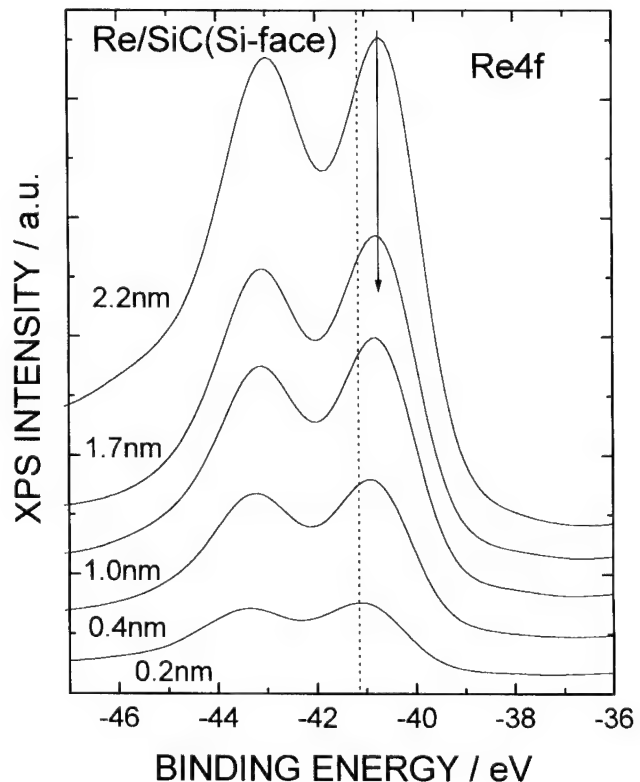


Fig. 2. The Re 4f XPS peaks at successive stages of Re deposition on the Si-face of 6H-SiC. The arrow corresponds to a binding energy of 40.5 eV for the $4f_{7/2}$ state associated with bulk Re metal.

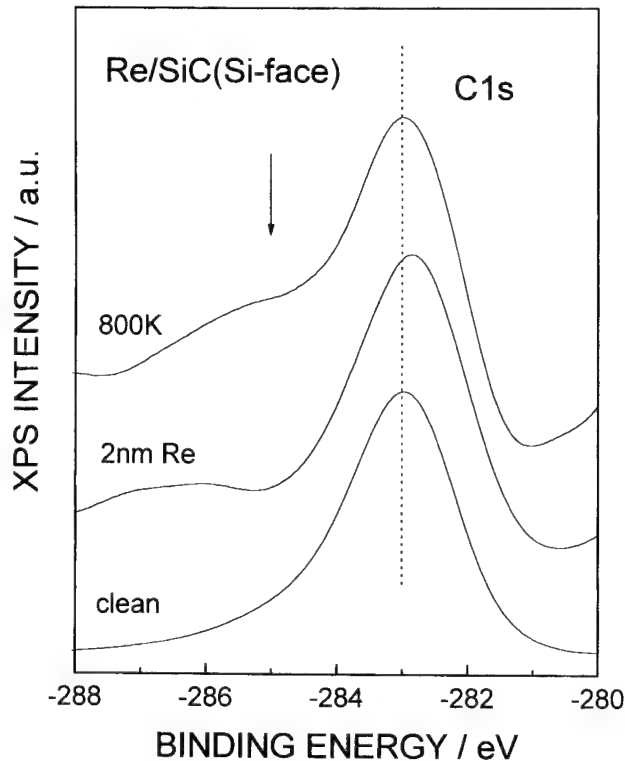


Fig. 3. The C 1s XPS peak at various stages of Re deposition and annealing on the Si-face of 6H-SiC. The arrow indicates increased intensity near 285 eV on the annealed surface arising from free carbon.

method described by Waldrop and co-workers [5]. In brief, $\Phi_B = E_g - E_{fi}$, where $E_g = 3.03$ eV is the 6H-SiC band gap [13] and E_{fi} is the interface Fermi level measured by XPS with respect to the top of the SiC valence band; that is, $E_{fi} = E_{C\ 1s} - (E_{C\ 1s} - E_v)_0$, where the quantity in parentheses is the C 1s to valence-band maximum binding energy difference for the clean SiC. The latter was measured at 280.5 ± 0.1 eV by using valence band data from the clean surface. From the measured C 1s binding energy of 282.8 eV after 2 nm Re deposition (Fig. 3) a Schottky barrier height of 0.7 ± 0.2 eV is obtained for both the Si- and C-faces. This value is lower than that expected if the simple Schottky-Mott model were valid, that is $\Phi_B = \Phi_m - \chi$ where Φ_m is the WF of the metal and χ the semiconductor electron affinity which is ~ 4 eV for 6H-SiC [5]. Furthermore, the Schottky barrier for Re is about the same for the Si- and C-faces (less than ~ 0.2 eV difference), whereas for metals which are close to the Schottky-Mott model, like Pd and Au, the Schottky barrier is different on the two faces. On the C-face, it is, respectively, 0.4 eV higher for Pd and 0.2 eV lower for Au than on the Si-face [5]. Pd and Au have similar WF with Re, therefore the lower Φ_B on Re could be due either to a lower χ for our SiC specimens compared with those in Ref. [5], or to a sheer inadequacy of the simple Schottky-Mott model to describe the complex

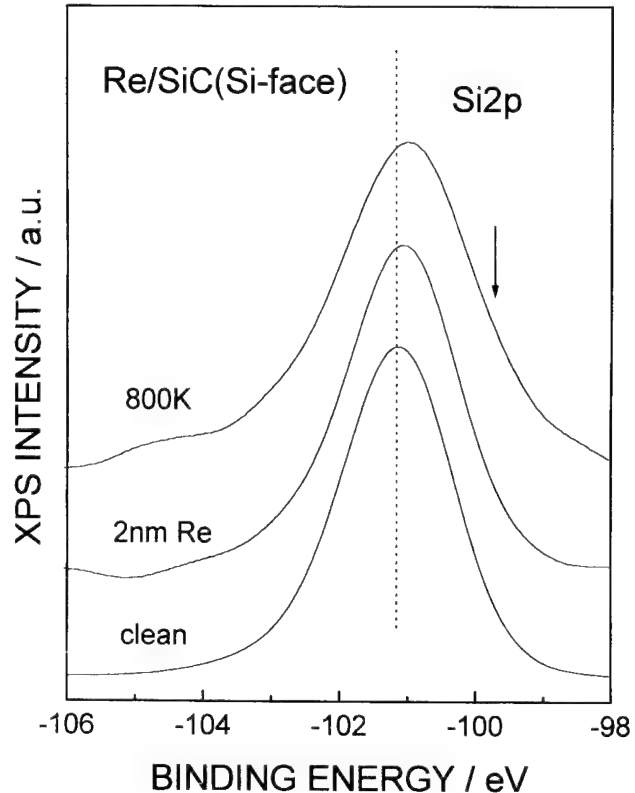


Fig. 4. The Si 2p XPS peak at various stages of Re deposition and annealing on the Si-face of 6H-SiC. The arrow indicates increased intensity near 99.7 eV on the annealed surface arising from elemental Si or ReSi₂.

electronic structure of the metal/6H-SiC interface, as pointed out in Ref. [5]. The former case seems less likely since the cleaning procedures were similar and the composition of the substrate surface before metal evaporation was about the same in this work and in Ref. [5].

Upon annealing of the samples up to 1100 K following 2 nm Re deposition the binding energies of the C 1s and Si 2p peaks do not change (Figs. 3 and 4) hence the Schottky barrier is not affected. This suggests the absence of an extended chemical reaction at the interface, as for example, in the case of Er/SiC [12] where erbium silicide was formed at 900 K and the Schottky barrier increased by 0.4 eV. However, above 700 K there are small changes in the shape of the C 1s and Si 2p peaks, namely the appearance of additional intensity near 99.7 eV for the Si 2p (Fig. 4) and near 285 eV for the C 1s (Fig. 3). The former could be due to elemental Si or traces of ReSi₂ [17] and the latter to free carbon arising from a limited interaction at the interface which is not enough to affect the Schottky barrier but could be related to the changes in the electrical characteristics of Re/SiC contacts alluded to in the Introduction [11]. Annealing up to 600 K does not affect the interface, however it does cause a significant decrease of the WF above 500 K (Fig. 1), which can be attributed to coales-

ence of the Re film into larger particles leading to partial exposure of the substrate surface. This is supported by the LEED pattern, which after annealing again exhibits the 1×1 symmetry of the substrate.

References

- [1] R.F. Davis, G. Kelner, M. Shur, J.W. Palmour, J.A. Edmond, Proc. IEEE 79 (1991) 677.
- [2] V.M. Bermudez, J. Appl. Phys. 63 (10) (1988) 4951.
- [3] N.A. Papanicolaou, A. Christou, M.L. Gipe, J. Appl. Phys. 65 (9) (1989) 3526.
- [4] N. Lundberg, M. Oestling, Appl. Phys. Lett. 63 (22) (1993) 3069.
- [5] J.R. Waldrop, R.W. Grant, Y.C. Wang, R.F. Davis, J. Appl. Phys. 72 (10) (1992) 4757.
- [6] D.E. Ioannou, N.A. Papanicolaou, NordquistP.E., Jr., IEEE Trans., Elect. Devices 34 (1987) 1694.
- [7] N. Lundberg, C.M. Zetterling, M. Oestling, Appl. Surf. Sci. 73 (1993) 316.
- [8] S. Hara, K. Suzuki, A. Furuya, Y. Matsui, Japan. J. Appl. Phys. 29 (1990) L394.
- [9] J. Crofton, P.G. McMulin, J.R. Williams, M.J. Bozack, J. Appl. Phys. 77 (1995) 1317.
- [10] J.S. Chen, E. Kolawa, M.-A. Nicolet, J. Appl. Phys. 75 (2) (1994) 897.
- [11] J.S. Chen, A. Bächli, M.-A. Nicolet, L. Baud, C. Jaussaud, R. Madar, Mater. Sci. Eng. B29 (1995) 185.
- [12] S. Kennou, J. Appl. Phys. 78 (1) (1995) 587.
- [13] Cree Res. Inc., 2810 Meridian Parkway, Suite 176, Durham, NC 27713.
- [14] M.E. Lin, S. Strite, A. Agarwal, A. Salvador, G.L. Zhou, N. Teraguchi, A. Rockett, H. Morkoc, Appl. Phys. Lett. 62 (7) (1993) 702.
- [15] H.B. Michalson, J. Appl. Phys. 48 (1977) 4729.
- [16] W.F. Egelhof, Surf. Sci. Rep. 6 (1987) 253.
- [17] A. Siokou, S. Kennou, S. Ladas, T.A. Nguyen Tan, J.-Y. Veuillen, Surface Science 352–354 (1996) 628.

TEM study of Ni and Ni₂Si ohmic contacts to SiC

B. Pécz ^{a,*}, G. Radnócz ^a, S. Cassette ^b, C. Brylinski ^b, C. Arnodo ^b, O. Noblanc ^b

^a Research Institute for Technical Physics PO Box 76, H-1325 Budapest, Hungary

^b THOMSON-CSF/Laboratoire Central de Recherches, Domaine de Corbeville, 91404 Orsay, Cedex, France

Abstract

The structure of Ni and Si/Ni contacts to SiC was studied by transmission electron microscopy. Annealed Ni/SiC contacts showed ohmic behaviour, but Ni proved to be reactive with SiC resulting in the formation of nickel silicide together with the formation of a high number of voids. Deposition and annealing of Si/Ni multilayer contacts resulted in a void free Ni₂Si contact layer on SiC, while also exhibiting low contact resistivity. © 1997 Elsevier Science S.A.

Keywords: Silicon carbide; Ohmic contacts; Electron microscopy

1. Introduction

Wide-gap SiC is one of the most promising materials for manufacturing high temperature and high power electronic devices. Recently 4H-SiC substrates have become available which are expected to be an excellent alternative to 6H-SiC, due to the former's higher electron mobility. The efficient application of SiC to microwave power devices requires ohmic contacts with low specific contact resistance which are able to withstand high operating temperatures.

2. Experimental details

A 4H-SiC wafer with a heavily doped, 2 μm thick n⁺ epitaxial layer (10^{19} cm^{-3}) was used as a substrate for the Ni contact layer to ensure low contact resistance. Prior to deposition, the sample was cleaned in HF (1%) for 3 min and subsequently etched *in situ* by Ar⁺ ions at 200 eV for 8 min. A Ni layer with a thickness of 150 nm was deposited onto the substrate by high vacuum electron beam evaporation. Annealing was performed in a pure nitrogen ambient at 950 °C for 10 min.

Another set of samples was prepared by depositing Ni and Si multilayers onto n⁺ 6H-SiC ($1-1.8 \times 10^{18} \text{ cm}^{-3}$) by electron beam evaporation at a deposition rate of 0.25 nm s⁻¹. The substrate was

cleaned as above. Si(15 nm)/Ni(16.4 nm)/Si(30 nm)/Ni(32.8 nm)/Si(30 nm)/Ni(32.8 nm) layers were deposited to obtain the overall composition of N₂Si. Samples with the reversed sequence of the Ni/Si layers (e.g. starting with Ni) were also prepared. The Si/Ni contacts on SiC were annealed under the same conditions as the Ni/SiC samples (e.g. at 950 °C in nitrogen).

Cross sectional samples were prepared by ion beam milling. Preparation details of the present samples are given elsewhere [1]. The thinned samples were examined using a Philips CM20 transmission electron microscope operating at 200 kV. EDS (Energy Dispersive System) X-ray analysis was performed by a Ge detector NORAN system attached to the TEM.

3. Results and discussion

3.1. Ni/SiC

As shown in Fig. 1, the as-deposited Ni layer is homogeneous in thickness and exhibits a smooth surface. The Ni layer is of a polycrystalline structure with a typical grain length of ~400 nm. The thickness of the grains is determined by the thickness of the Ni layer. Selected area electron diffraction pattern (SAED) of the Ni layer revealed that the Ni layer possesses a (111) type texture.

The cross-section micrograph of the annealed specimen is shown in Fig. 2. The contact layer substantially increased in thickness and contained a large number of voids (Kirkendall voids). Voids are shown to be present

* Corresponding author. Tel: 36-1-1698-961; Fax: 36-1-1698-037; e-mail: pecz@mufi.hu

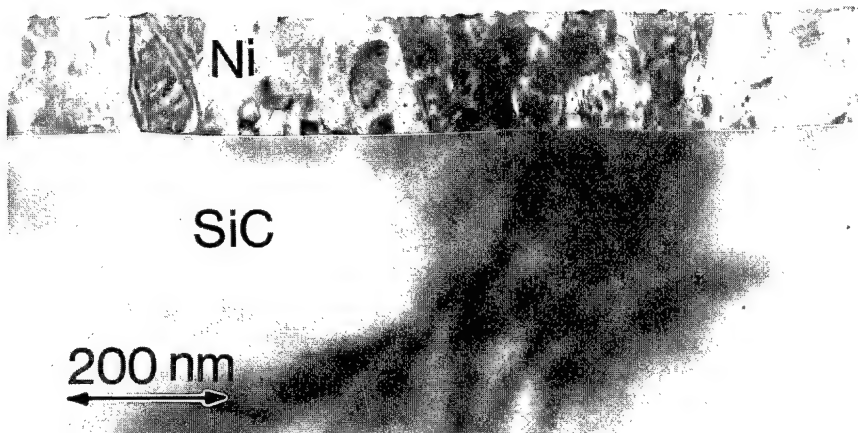


Fig. 1. Cross-section of as-deposited Ni/SiC sample.

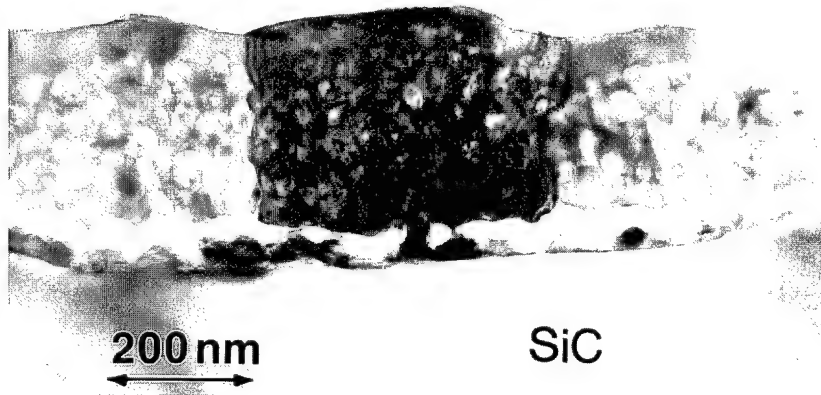


Fig. 2. Cross-section of Ni/SiC sample annealed at 950 °C.

at the original Ni/SiC interface, which corresponds to the white stripe in Fig. 2. The typical length of the grains showed no change and therefore, it was again measured to be ~ 400 nm. The EDS spectrum of the layer (Fig. 3) showed a high silicon content. When the layer was EDS analysed, quantitative measurements showed a 2:1 Ni:Si ratio which indicates that the Ni layer reacted with SiC during the annealing and this resulted in the formation of a polycrystalline Ni_2Si layer.

The Ni_2Si phase was identified by Pai et al. [2] as the only reaction product in the temperature range 700–900 °C, and its formation was also reported [3] later. It is known from Auger depth profiling measurements [4] that carbon is approximately uniformly distributed in the reacted layer and there is no carbon compound present. Our Auger measurements showed the same results with the only difference being that some carbon atoms were segregated to the surface of the specimen from the top region. This agrees well with the results given in Ref. [3].

The presence of large number of voids within the layer suggests that carbon is segregated to the surface

of the voids which is also confirmed by high resolution electron microscopy observations of the authors.

The investigated Ni/4H-SiC contact shows ohmic characteristic after annealing at 950 °C. When the contact resistivity of the annealed specimen is measured by linear TLM (transmission line method) the resulting specific contact resistivity is given [5] to be $3 \times 10^{-6} \Omega\text{cm}^2$. The test structure consisted of a mesa of active material prepared with CHF_3/SF_6 RIE (reactive ion etching), over which identical contacts stripes were patterned. These contacts were 100 μm wide and the distances between them varied from 2 to 32 μm . The electrical performance of these contacts appeared unaffected after aging at 500 °C for 100 h in nitrogen gas.

Our present results show that the total proportion of Ni reacted with SiC resulting in the formation of a polycrystalline Ni_2Si layer. We have also shown that annealed Ni/SiC contacts contain a large number of voids.

3.2. $\text{Ni}_2\text{Si}/\text{SiC}$

Further work was performed to improve the interface morphology by introducing silicon into the deposited

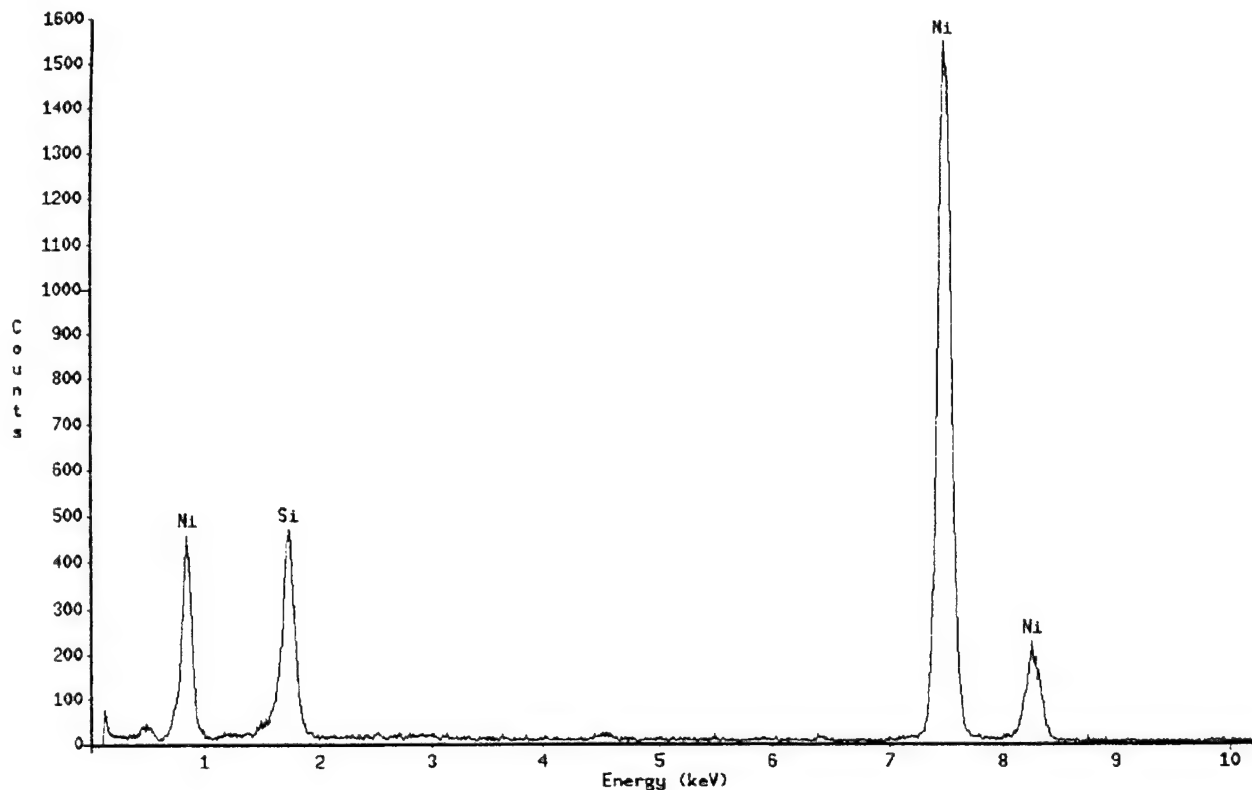


Fig. 3. EDS spectrum of the annealed Ni/SiC contact layer.

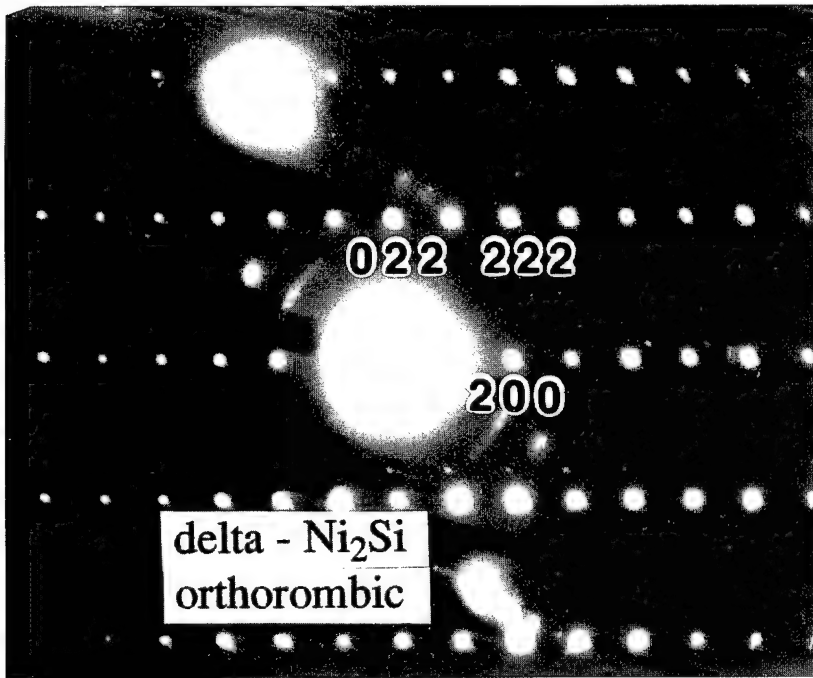


Fig. 4. Indexed selected area diffraction pattern of a Ni₂Si grain.

film to reduce the decomposition of SiC. For this purpose Si and Ni layers were deposited onto SiC successively with the nominal composition of Ni₂Si. After annealing the alloyed layer was identified as ortho-

rhombic Ni₂Si by selected area electron diffraction patterns (Fig. 4). The layer is polycrystalline and the typical length of the grains is 200 nm while their height is limited by the thickness of the whole layer. The annealed

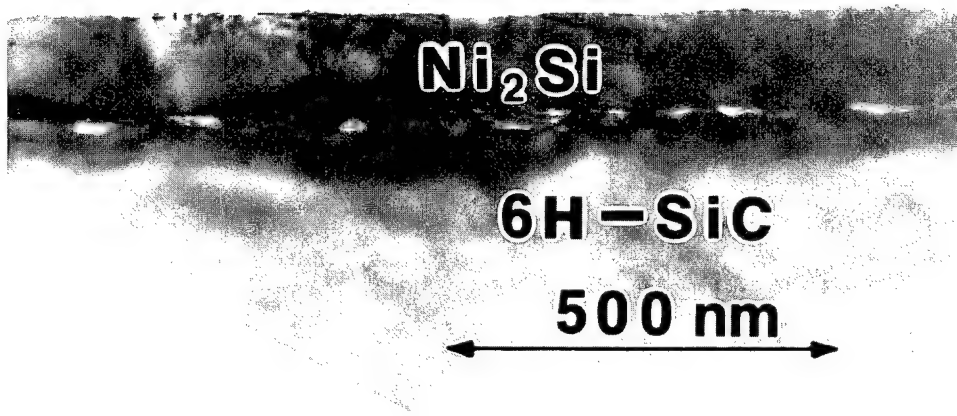


Fig. 5. Cross-section of $\text{Ni}_2\text{Si}/\text{SiC}$ sample annealed at 950°C .

contacts proved to be ohmic and their structure was improved as the contact layer itself did not contain voids (Fig. 5). There are still voids present at the layer/substrate interface even when Si was deposited at first (Fig. 5) during the preparation of Si/Ni multilayers. As expected the number of voids was higher when Ni was deposited at first. The measured specific contact resistivity was an order of magnitude higher than in the case of the annealed Ni/SiC contacts, but the lower doping level of SiC could be responsible for the difference.

4. Conclusion

Ni is very reactive with SiC and in Ni/SiC contacts the annealing leads to the formation of nickel silicide and the contact layer contains many voids while an extremely high number of voids are present at the contact layer–substrate interface. In the present study the Ni_2Si layer was prepared and formation of voids avoided in the contact layer itself although a few voids

are still present at the interface. The formation of those voids could be avoided by the deposition of a thicker Si layer onto the SiC substrate or by the co-deposition of Si and Ni.

Acknowledgement

This work was supported by the COPERNICUS project No. CP940603. G. Vincze is acknowledged for the TEM sample preparation.

References

- [1] Á. Barna, Materials Research Society Symposia and Proceedings Series 254, (1992) 3.
- [2] C.S. Pai, C.M. Hanson, S.S. Lau, J. Appl. Phys. 57 (1985) 618.
- [3] W.F.J. Slijkerman, A.E.M.J. Fischer, J.F. van der Veen, I. Ohdomari, S. Yoshida, S. Misawa, J. Appl. Phys. 66 (1989) 666.
- [4] I. Ohdomari, S. Sha, H. Aochi, T. Chikyow, S. Suzuki, J. Appl. Phys. 62 (1987) 3747.
- [5] C. Arnodo, S. Tyc, F. Wyczisk, C. Brilinsky, 6th International Conference on Silicon Carbide and Related Materials, Kyoto, 1995.

Ion beam assisted deposition of a tungsten compound layer on 6H-silicon carbide

H. Weishart *, V. Heera, W. Matz, W. Skorupa

Forschungszentrum Rossendorf eV, Institut für Ionenstrahlphysik und Materialforschung, Postfach 510119, D-01314 Dresden,
Germany

Abstract

Ion beam assisted deposition (IBAD) as a means of synthesizing a tungsten carbide layer on top of SiC is investigated by Rutherford backscattering (RBS), X-ray diffraction (XRD) and four point probe measurements. Evaporation of tungsten and subsequent implantation of carbon leads to a crystalline layer of tungsten carbide whose resistivity is $1554 \mu\Omega \text{ cm}$. At an implantation dose of $5 \times 10^{17} \text{ C}^+ \text{ cm}^{-2}$, enhanced surface erosion occurs. Simultaneous evaporation of tungsten and implantation of carbon produces a layer of crystalline W_2C mixed with tungsten. The resistivity of this layer is $400 \mu\Omega \text{ cm}$, i.e. only a factor of five higher than that of single crystal W_2C . © 1997 Elsevier Science S.A.

Keywords: Implantation; Silicon Carbide; Tungsten Carbide

1. Introduction

Silicon carbide is an advantageous material for high-temperature semiconductor devices because of its superior properties such as high thermal conductivity, high saturated drift velocity of electrons and wide bandgap [1,2]. High-temperature devices, however, are in need of reliable metallization, which should maintain a low resistivity, good adhesion to the underlying SiC and a high chemical stability at elevated temperatures. Several attempts have been made to achieve such metallization on 6H-SiC [3–10]. Promising contact materials that could meet the above-mentioned requirements are the carbides. In this work, we will investigate the synthesis of tungsten carbide on SiC using ion beam assisted deposition (IBAD).

Fabrication of pure W-carbide contact layers has not yet been reported. Baud et al. have prepared tungsten based contact layers by deposition of pure tungsten on SiC and subsequent annealing [11]. However, these layers have proven to be an inhomogeneous mixture of polycrystalline tungsten silicide, tungsten carbide and tungsten. Earlier investigations of the reaction of a deposited W layer with crystalline SiC [12,13] using Auger electron spectroscopy have shown that the forma-

tion of tungsten carbide and silicide occurs without annealing only at defects within the W–SiC-interfacial region. A complete reaction between SiC and W takes place during annealing above 950°C [11]. We have previously shown that synthesis of tungsten carbide and silicide in SiC at low temperatures is possible by implanting W into the SiC [14,15]. However, this technique still requires high temperatures in order to anneal the implantation-induced damage and to crystallize the new phases.

In this work, we present first results on the synthesis of tungsten carbide by evaporation of tungsten onto a SiC substrate and implantation of C. We investigate the influence of the C dose on the structure of the synthesized layer and determine the crystallinity of the phases so formed. Four point probe measurements give a first elucidation of the electrical properties of the layer.

2. Experimental details

Single crystal *n*-type 6H-SiC from Cree Research, Inc., Durham, NC. served as substrate. Two samples were prepared by evaporation of tungsten onto the substrate and subsequent implantation with C^+ . The first sample had a 50 nm W layer and was implanted to a dose of $2.5 \times 10^{17} \text{ cm}^{-2}$. A dose of $5 \times 10^{17} \text{ cm}^{-2}$ was

* Corresponding author.

used for the second sample which had been covered with 70 nm W for compensation of increased surface erosion. A third sample was prepared by evaporation of 90 nm tungsten at a rate of 0.3 \AA s^{-1} and simultaneous implantation with C^+ at a beam current density of $51 \mu\text{A cm}^{-2}$. All samples were implanted without intentional heating using an energy of 30 keV. The mean projected range of C in tungsten for this energy, according to TRIM91, is 27 nm. Analysis of the W profile and stoichiometry of the synthesized layers was made by Rutherford backscattering spectrometry (RBS) of $1.2 \text{ MeV}^4 \text{ He}^+$. X-ray diffraction (XRD) with grazing incidence was employed to determine the crystalline phases. Four point probe measurements allowed to determine the sheet resistivity.

3. Results and discussion

3.1. Evaporation of tungsten and subsequent implantation

Fig. 1 shows the RBS spectra of samples which have been prepared by evaporation of 50 and 70 nm tungsten, respectively, and subsequent implantation of carbon ions to doses of $2.5 \times 10^{17} \text{ cm}^{-2}$ and $5 \times 10^{17} \text{ cm}^{-2}$, respectively, at an energy of 30 keV. Both samples exhibit a tungsten-rich surface layer, as obvious from the tungsten signals in Fig. 1. A striking feature is that the tungsten signal from the sample initially covered with 50 nm tungsten is more pronounced than that from the sample initially covered with 70 nm tungsten. Simulations reveal that the tungsten rich layer of the sample with 50 nm tungsten is almost twice as thick as that of the sample with 70 nm tungsten. The Si signal

between 600 and 640 keV affirms the existence of a layer of C-rich amorphous SiC beyond the tungsten rich top layer. The thickness of this C-rich amorphous SiC is 100 nm for the sample implanted with $5 \times 10^{17} \text{ cm}^{-2}$ and 74 nm for the sample implanted with $2.5 \times 10^{17} \text{ cm}^{-2}$. The reduced thickness of the tungsten rich region for the sample implanted with $5 \times 10^{17} \text{ cm}^{-2}$ indicates an enhanced surface erosion during implantation. The shift of the interface between the crystalline and amorphous SiC towards the surface with increasing dose is more evidence for enhanced surface erosion of the sample implanted with the higher C dose. Determination of the sputtering yield Y employing the modified Bohdansky formula [16] reveals an increase in Y with increasing C content in the tungsten layer. TRIM calculation indicate a preferential sputtering of tungsten from a W–C target. The C fraction in the near surface region increases during implantation; therefore, surface erosion is enhanced and more C is implanted into the SiC beyond the tungsten layer.

X-ray diffraction patterns of both samples exhibit clear, but significantly broadened, peaks, which indicates the presence of small crystallites. However, the peak broadening and insufficient crystallographic information in the database obstruct a definite attribution to crystalline phases. Best correlation give cubic phases of either $\text{W}_2(\text{C}, \text{O})$ or WC_{1-x} . Nevertheless, the most remarkable point is the formation of a new crystalline phase without any annealing procedure.

Resistivity measurements using the four point probe technique give mean values of the sheet resistivity of $R_s = 409 \Omega \square^{-1}$ and $R_s = 232 \Omega \square^{-1}$ for the samples implanted with $5 \times 10^{17} \text{ cm}^{-2}$ and $2.5 \times 10^{17} \text{ cm}^{-2}$,

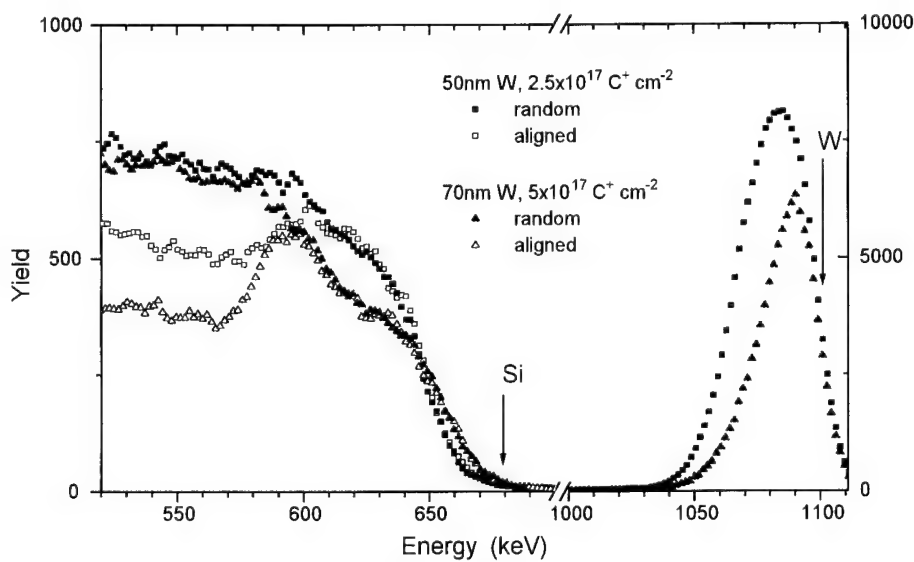


Fig. 1. RBS channelled and random spectra from samples prepared by evaporation of tungsten and subsequent implantation of carbon at 30 keV. The surface edges of W and Si are marked. The sample implanted with $2.5 \times 10^{17} \text{ C}^+ \text{ cm}^{-2}$ has a thicker tungsten rich layer than the sample implanted with $5 \times 10^{17} \text{ C}^+ \text{ cm}^{-2}$. Surface erosion during implantation, therefore, is significant at this dose.

respectively. A resistivity of $\rho = 1554 \mu\Omega \text{ cm}$ is then obtained for both samples.

3.2. Evaporation of tungsten and simultaneous implantation

Fig. 2 shows RBS random and channelled spectra from the sample which has been prepared by evaporation of tungsten at a rate of 0.3 \AA s^{-1} and simultaneous implantation with carbon at a dose rate of $3 \times 10^{14} \text{ cm}^{-2} \text{ s}^{-1}$. The spectra reveal a tungsten-rich layer at the sample surface. The spectrum unambiguously shows a lack of Si in the near surface region. Under this region, a layer consisting of only a small fraction of Si, indicated by the plateau between 590 and 640 keV in Fig. 2, is detected. This layer is produced by the implanted C atoms which have penetrated through the W layer into the SiC because of their high energy. Depth calibration of the RBS spectra gives an average value of 130 nm for the thickness of this C-rich SiC. A comparison of random and aligned RBS signals reveals amorphization of the implanted layer. The slow increase in the Si signal around 660 keV is evidence for implantation induced intermixing of Si, C and W at the initial SiC–W interface.

The X-ray pattern from this sample indicates that crystallites of both pure tungsten and α -W₂C are present in the tungsten-rich layer. The sharp and clear diffraction peaks give evidence of the formation of a crystalline W₂C phase without annealing.

Resistivity measurements using the four point probe technique revealed a mean value for the sheet resistivity of $R_s = 100 \Omega \square^{-1}$. From RBS data, we estimated the thickness of the W containing layer to be approximately

40 nm. A resistivity of $\rho = 400 \mu\Omega \text{ cm}$ was then obtained. This low value compared with the resistivity obtained from the other samples may be due to the presence of pure tungsten within the tungsten carbide, as revealed by XRD.

4. Summary

Synthesis of tungsten carbide by ion beam assisted deposition is feasible. However, an implantation energy of 30 keV is too high for this purpose since at this energy most C atoms penetrate through the evaporated tungsten layer. An implantation dose of more than $2.5 \times 10^{17} \text{ cm}^{-2}$ leads to increased surface erosion, thus resulting in removal of the tungsten. Ion beam mixing occurs at the interface between SiC and the tungsten layer. Crystalline tungsten carbide develops without any annealing process after implantation. The best results with regard to the formation of W₂C and electric resistivity are achieved by simultaneous evaporation of W and implantation of C. The resistivity of such a layer is by only a factor of five higher than that of single crystal W₂C [17].

Acknowledgement

The authors wish to thank Dr R. Yankov for helping remarks, Mr U. Strauch for the support during sample preparation, Dr M. Voelskow for the RBS and Dr D. Panknin for the electric measurements. Our special thanks go to Mrs A. Scholz for her kind help with the XRD analysis.

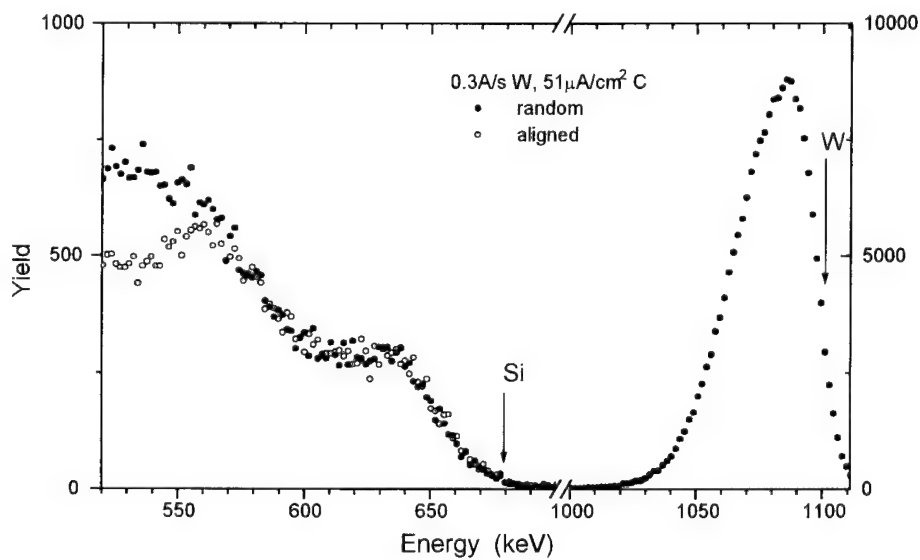


Fig. 2. RBS channeled and random spectra from a sample prepared by evaporation of tungsten at a rate of 0.3 \AA s^{-1} and simultaneous implantation with carbon at a dose rate of $3 \times 10^{14} \text{ cm}^{-2} \text{ s}^{-1}$. The implantation energy of 30 keV causes most of the carbon ions to penetrate through the tungsten layer, thus leading to a broad region of C rich amorphous SiC beyond the tungsten rich layer.

References

- [1] W.E. Nelson, F.A. Halden, A. Rosengreen, *J. Appl. Phys.* 37 (1966) 333.
- [2] G. Pensl, R. Helbig, *Festkörperprobleme/Adv. Solid State Phys.* 30 (1990) 133.
- [3] J.B. Petit, M.V. Zeller, in: T.D. Moustaka, J.I. Pankove, Y. Hamakawa (Eds.), *Wide Band Gap Semiconductors*, MRS Proc. 242, Pittsburgh, PA, 1992, pp. 567–572.
- [4] R.C. Glass, L.M. Spellman, R.F. Davis, *Appl. Phys. Lett.* 59 (1991) 2868.
- [5] M.M. Anikin, M.R. Rastegaeva, A.L. Syrkin, I.V. Chuiko, in: G.L. Harris, M.G. Spencer and C.Y. Yang (Eds.), *Amorphous and Crystalline Silicon Carbide III, and Other Group IV–VI Materials*, Springer Proc. Phys. 56 (1992) 183.
- [6] J. Crofton, J.M. Ferrero, P.A. Barnes, J.R. Williams, M.J. Bozack, C.C. Tin, C.D. Ellis, J.A. Spitznagel, P.G. McMullin, in: C.Y. Yang, M.M. Rahman, G.L. Harris (Eds.), *Amorphous and Crystalline Silicon Carbide IV*, Springer Proc. Phys. 71 (1992) 176.
- [7] V.A. Dmitriev, K. Irvine, M. Spencer, G. Kelner, *Appl. Phys. Lett.* 64 (1994) 318.
- [8] A.K. Chaddha, J.D. Parsons, G.B. Kruaval, *Appl. Phys. Lett.* 66 (1995) 760.
- [9] T. Uemoto, *Jap. J. Appl. Phys.* 34 (1995) L7.
- [10] J. Crofton, P.G. McMullin, J.R. Williams, M.J. Bozack, *J. Appl. Phys.* 77 (1995) 1317.
- [11] L. Baud, C. Jaussaud, R. Madar, C. Bernard, J.S. Chen, M.A. Nicolet, *Mater. Sci. Engng B29* (1995) 126.
- [12] K.M. Geib, C. Wilson, R.G. Long, C.W. Wilmsen, *J. Appl. Phys.* 68 (1990) 2796.
- [13] C. Jacob, S. Nishino, M. Mehregany, P. Pirouz, in: *Silicon Carbide and Related Materials*, Institute of Physics Publishing, Bristol, 1994, p. 247.
- [14] H. Weishart, J. Schöneich, H.-J. Steffen, W. Matz, W. Skorupa, in: D.E. Luzzi, T.F. Heinz, M. Iwaki, D.C. Jacobson (Eds.), *Beam–Solid Interactions for Materials Synthesis and Characterization*, MRS Proc. 354, Pittsburgh, PA, 1995, pp. 177–182.
- [15] H. Weishart, H.-J. Steffen, W. Matz, M. Voelskow, W. Skorupa, *Nucl. Instr. Meth. B112* (1996) 338.
- [16] C. Garcia-Rosales, W. Eckstein, J. Roth, *J. Nucl. Mater.* 218 (1994) 8.
- [17] H.J. Goldschmidt (Ed.), *Interstitial Alloys*, Plenum Press, New York, 1967, p. 88.

Hafnium, cadmium and indium impurities in 4H-SiC observed by perturbed angular correlation spectroscopy

T. Licht ^{a,*}, N. Achtziger ^a, D. Forkel-Wirth ^b, K. Freitag ^c, J. Grillenberger ^a, M. Kaltenhäuser ^a, U. Reislöhner ^a, M. Rüb ^a, M. Uhrmacher ^d, W. Witthuhn ^a, ISOLDE Collaboration^b

^a Institut für Festkörperphysik der Friedrich-Schiller-Universität Jena, D-07743 Jena, Germany

^b CERN/PPE, CH-1211 Geneva 23, Switzerland

^c Institut für Strahlen- und Kernphysik der Universität Bonn, D-53115 Bonn, Germany

^d 2. Physikalisches Institut der Universität Göttingen, D-37073 Göttingen, Germany

Abstract

The annealing behaviour of hafnium impurities in silicon carbide after ion implantation and the formation and stability of complexes of hafnium in 4H-SiC were studied by perturbed angular correlation spectroscopy (PAC) for the first time. Samples of 4H-silicon carbide single crystals were doped with radioactive ^{181}Hf ($t_{1/2}=42.5$ d) and annealed at temperatures of between 600 and 1850 K. After an annealing step at 900 K two axially symmetric electric field gradients (EFGs) were observed oriented along the c-axis of the crystal. Depending on the implantation dose, the fraction of probe atoms exposed to these EFGs increases with the annealing temperature. © 1997 Elsevier Science S.A.

Keywords: Silicon carbide; Hafnium; PAC; Implantation

1. Introduction

In recent years interest has grown in wide band-gap semiconductors like silicon carbide, because of its potential for applications in power device production. Devices built from silicon carbide show very good high temperature resistivity, high chemical and mechanical stability, and high breakdown voltage. Recently improvements in crystal growth techniques have led to the production of epi-layers and bulk materials of higher quality. Doping processes during growth or through implantation have been developed and improved. Although ion implantation is a very well established method, little is known about implantation defects, complex formation and stability in the material.

The role of defects and impurities can be investigated by nuclear probe methods such as EPR, Mössbauer spectroscopy or perturbed angular correlation (PAC) spectroscopy. The study of close probe-defect or impurity pairs by PAC spectroscopy enables direct monitoring of the structure, stability and electronic properties of

complexes formed by defects, impurities or a specific lattice environment.

2. Experimental

Perturbed γ - γ angular correlation spectroscopy (PAC) was used to monitor different complexes formed by the probe atom and impurities or defects. This method allows observation of the nearest lattice surroundings of the probe atoms by the detection of the electric quadrupole moment Q of the probe atom and the electric field gradient (EFG), resulting in a modulation of the PAC spectra. The product of quadrupole moment Q and V_{zz} , the largest component of the EFG, is usually described by the quadrupole coupling constant $v_q = eQV_{zz}/\hbar$. The ratio of the frequency triplet is determined by the asymmetry parameter η of the EFG, and their relative amplitudes depend on the EFG orientation with regard to the crystallographic axis, whereas the absolute amplitude is proportional to the fraction of probe atoms, decorated by trapped defects or impurities. Further information on the theoretical background of this nuclear method is reviewed in Ref. [1]; information

* Corresponding author.

concerning its application to semiconductor research is reviewed in Ref. [2].

In this work we present PAC measurements performed at the ^{181}Ta ($t_{1/2}=10.5$ ns), which is populated by the $7/2^+$ level of ^{181}Hf ($t_{1/2}=42.5$ d). These results are compared with measurements performed at the $5/2^+$ level of the ^{111}Cd ($t_{1/2}=84$ ns), which is populated either by electron capture of ^{111}In ($t_{1/2}=2.83$ d) or by the isomeric transition of ^{111m}Cd ($t_{1/2}=49$ min).

Samples of 4H- (n-type) silicon carbide single crystals were doped with radioactive ^{181}Hf by ion implantation ($E_i=160$ keV) at the ion separator of the University of Bonn. TRIM calculations for these implantation parameters yield a projected range of 43 nm and a straggling of 9 nm [3]. During the first implantation the ratio of active to inactive ions was about 10%. Parallel to the ^{181}Hf implantation, ^{180}Hf and ^{182}Wf are implanted unintentionally. The total number of implanted ions was about $2 \times 10^{13} \text{ cm}^{-2}$. For the second implantation the ratio of active to inactive ions was only about 2–3% resulting in a higher concentration of inactive ions in the sample. Here the implantation dose rises to $1.2 \times 10^{14} \text{ cm}^{-2}$.

After implantation the annealing behaviour of the 4H-SiC samples was investigated by encapsulating the samples in a quartz ampoule in an argon atmosphere and subsequent heating in a furnace. Varying the annealing temperature from 600 to 1850 K and annealing times from some minutes to 1 h lead to no significant loss of radioactive probe atoms. Only at the annealing step at 1850 K was a loss of about 10% of the probe atoms observed. After each step a PAC measurement was taken, to observe the change in the PAC parameters according to the annealing temperature. All these PAC-spectra were taken at room temperature. In the second series the measuring temperature was varied between 30 and 1200 K.

Comparable measurements were performed after implantation of ^{111}In or ^{111m}Cd . Both isotopes decay via the same isomeric $5/2^+$ level of ^{111}Cd . The implantation of the ^{111}In ion into the silicon carbide was performed at the Göttingen IONAS facility using an implantation energy of 400 keV. The ^{111m}Cd isotope was produced at the on line mass separator ISOLDE at CERN. The implantation energy was 60 keV resulting in a cadmium distribution centered at 25 nm beneath the surface [3].

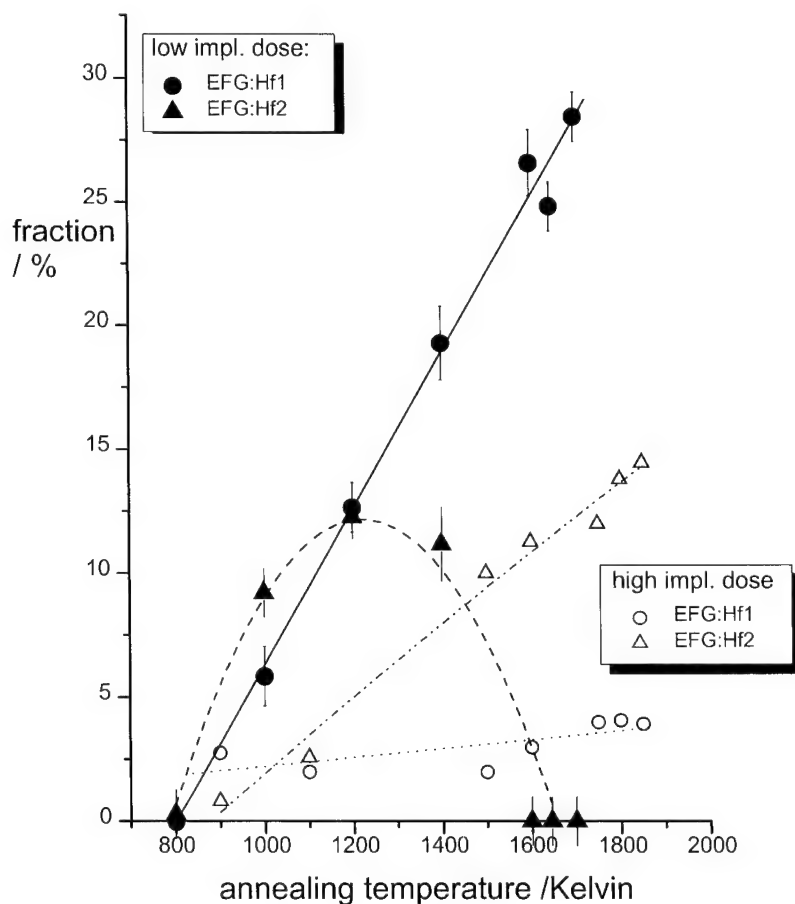


Fig. 1. Dependence of the fraction of decorated probe atoms in 4H-SiC on the annealing temperature and implantation dose after hafnium implantation.

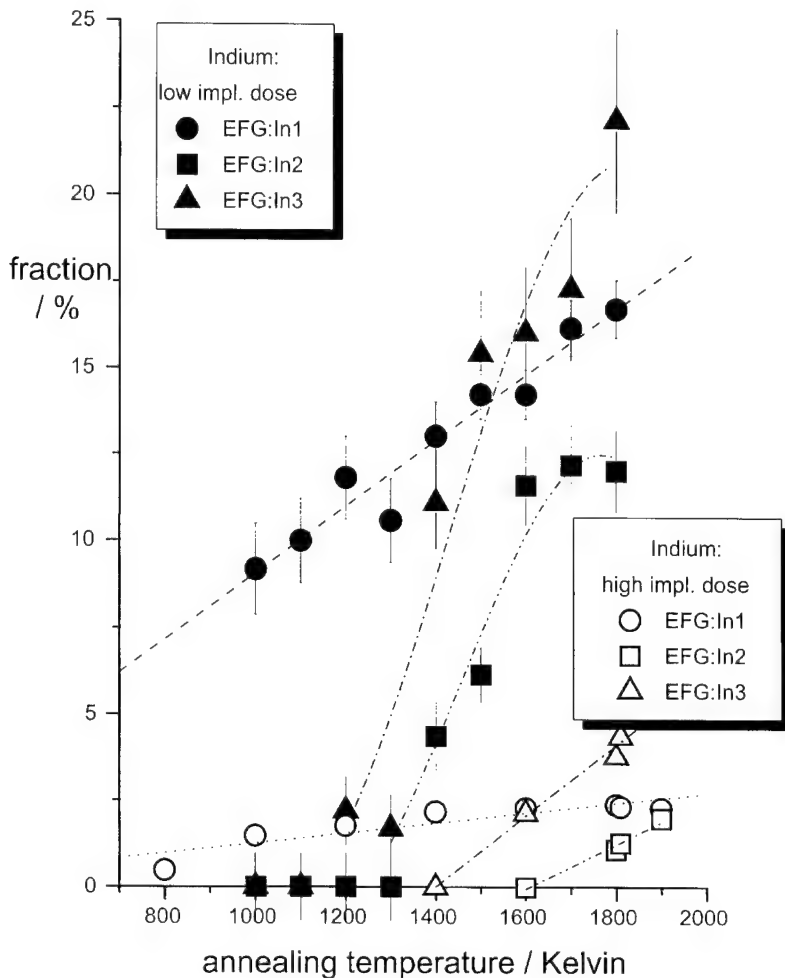


Fig. 2. Dependence of the fraction of decorated probe atoms in 4H-SiC on the annealing temperature and implantation dose after indium implantation.

3. Results and discussion

During the annealing procedure up to two different modulations EFG:Hf1 ($v_q = 602$ MHz; $\eta = 0$) and EFG:Hf2 ($v_q = 485$ MHz; $\eta = 0$) could be found in the PAC-spectra. Both EFGs were already detectable after an annealing temperature of 900 K.

The fraction of the complex EFG:Hf1 increases up to an annealing temperature of 1850 K and the corresponding axially symmetric EFG reveals an orientation along the c-axis of the crystal. Up to 30% of the probe atoms are exposed to this EFG:Hf1 at least (see Fig. 1).

At measuring temperatures, the coupling constant of the probe atoms, which are exposed to EFG:Hf1, decreases from 620 MHz at 77 K to 540 MHz at 1200 K. Between 150 and 300 K no significant change in the PAC parameters could be observed. The fraction at 30 K is only half that at room temperature.

The fraction of the complex characterized by EFG:Hf2 increases by up to 15% at annealing temperatures from 900 to 1200 K. At higher temperatures the

fraction decreases and at 1600 K it is beyond the detection limit for the sample with the lower implantation dose (see Fig. 1).

Another sample with a higher concentration of implanted inactive ions also shows both EFGs. However, at high annealing temperatures the fractions of the EFGs do not reach the level of the low dose implantation. The fraction of probe atoms measuring a disturbed environment is about 80% which is twice the fraction after low dose implantation. The sample implanted with the higher implantation dose shows EFG:Hf2 up to 1850 K without any decrease in the fraction.

EFG:Hf1 is assigned to substitutional probe atoms experiencing the lattice EFG of the crystal which is oriented along the c-axis of the crystal. EFG:Hf2 is interpreted as a complex of probe atoms with a defect produced by the ion implantation. This might be a vacancy, divacancy or interstitial complex. For lower defect concentration (lower implantation dose) this damage was successfully annealed resulting in a decrease

in the fraction of EFG:Hf2. This decrease in EFG:Hf2 is of the same magnitude as the increase in the fraction of EFG:Hf1. This result supports the interpretation of EFG:Hf2 as a defect complex, whereas EFG:Hf1 is a lattice-induced EFG. The higher implantation dose caused lattice damage which was not completely annealed at this temperature. The dominance of EFG:Hf1 supports its interpretation as a defect complex.

PAC investigations of the Hf probe atom are now compared to PAC measurements using the probe atom Cd or In, both measured at the same isomeric level of Cd. Here one EFG is detectable showing a behaviour very similar to EFG:Hf1. This EFG:1 is already detectable after an annealing temperature of 800 K. The fraction of this complex increases up to an annealing temperature of 1800 K showing an axial symmetry tensor oriented along the c-axis of the crystal (see Fig. 2). The coupling constant of this EFG:1 does not change significantly during the whole measuring temperature range. EFG:1 is assigned to substitutional probe atoms experiencing the lattice EFG of the crystal oriented along the c-axis of the crystal.

The two other EFGs are interpreted as complexes of probe atoms with a defect produced by ion implantation. The two different EFGs can be understood because of the two different silicon lattice sites of the probe atoms in 4H-SiC. At high implantation concentrations the annealing behavior of the indium-implanted samples is

very similar to the results for hafnium implantation (see Fig. 1 and Fig. 2). Contrary to the annealing behavior of the EFG:Hf2 observed after low-concentration HF implantation nothing comparable could be measured after In or Cd implantation. The fraction increases up to an annealing temperature of 1600 K and remains constant up to 1900 K. A decrease of the observed fractions could not be observed. This leads to the interpretation of the EFG:2 and 3 as an indium-vacancy complex, which is much more stable up to higher annealing temperatures. A detailed description of the results of the indium and cadmium investigation depending on the nitrogen concentration is given in Ref. [4].

References

- [1] H. Frauenfelder, H.M. Steffen, in: K. Siegbahn (Ed.) *Angular Distribution of Nuclear Radiation in Alpha-, Beta-, and Gamma-ray Spectroscopy*, vol. 2, North Holland, Amsterdam, 1965, p. 997.
- [2] Th. Wichert, N. Achtziger, H. Metzner, R. Sielemann, in: G. Langouche (Ed.) *Hyperfine Interactions in Semiconductors*, North Holland, Amsterdam, 1992.
- [3] J.F. Ziegler, J.P. Biersack, U. Littmark, *The Stopping and Ranges of Ions in Solids*, Pergamon, New York, 1985.
- [4] T. Licht, N. Achtziger, D. Forkel-Wirth, U. Reislöhner, M. Rüb, M. Uhrmacher, W. Witthuhn and ISOLDE Collaboration, Institute of Physics Conference Series No. 142, Chapter 2, 1996. 461-464

Nuclear transmutation doping of 6H-silicon carbide with phosphorous

Hans Heissenstein *, Christian Peppermüller, Reinhard Helbig

Institute of Applied Physics, University of Erlangen-Nürnberg, D-91058 Erlangen, Germany

Abstract

Aluminium doped 6H-SiC epilayers on a p⁺ doped 6H-SiC substrate were irradiated with total neutron doses of $9.4 \times 10^{19} \text{ cm}^{-2}$, $3.5 \times 10^{20} \text{ cm}^{-2}$, and $6.4 \times 10^{20} \text{ cm}^{-2}$ respectively. A donor species is produced by a nuclear reaction involving the decay of ^{31}Si to ^{31}P . The β^- activity after irradiation was measured. The samples were subsequently annealed at a temperature range of between 800 and 1800 °C. The annealing behaviour was studied by Low Temperature Photoluminescence (LTPL), Fourier Transform Infrared Spectroscopy (FTIR), Hall-effect, I-V and C-V measurements. The p type 6H-SiC epilayer was transmuted to n-type by an annealing process which resulted in a p-n junction to the p⁺ substrate. © 1997 Elsevier Science S.A.

Keywords: SiC; pn-junction; Phosphorous; Photoluminescence

1. Introduction

Silicon carbide as a wide band-gap semiconductor material with high thermal conductivity and chemical resistance, is suitable for high power, high frequency electronic devices with high radiation resistance. Until now the commonly used dopants in SiC have been nitrogen as a donor and aluminium as an acceptor. However, in situ doping during crystal growth or epitaxy is difficult to control and not very homogeneous.

Up to now silicon is still the best semiconductor material for high power devices. For this purpose it is homogeneously doped by neutron transmutation doping using phosphorous to get a n-type material (e.g. Refs [1,2]). The implementation of this doping process was a real breakthrough in the development of Si power devices [3]. Phosphorous is also a donor in SiC. Therefore we need to test whether doping SiC by neutron transmutation with phosphorous is useful in obtaining homogeneously doped substrates or layers for new applications. The high nitrogen concentration which is incorporated unintentionally during growth makes the provision of high neutron doses necessary if higher phosphorous concentrations are to be achieved. Since the thermal neutron flux cannot be raised, one has to come along with high portions of fast neutrons, which cause severe damage in the SiC-lattice. It should be

noted that the radiation damage caused by the fast neutrons is the reason for applying an annealing process. The radiation damage due to the nuclear reaction Si→P is very low.

2. Experimental

2.1. Preparation

We used a commercially available wafer (CREE Research Inc.) 3 μm (0001) 6H-SiC epitaxial layer (p-type, $(N_A - N_D) = 5.2 \times 10^{15} \text{ cm}^{-3}$ on a 300 μm thick 6H substrate (p-type, $(N_A - N_D) = 10^{18} \text{ cm}^{-3}$) (Fig. 1). This wafer was cut into six pieces of approx. 5 × 5 mm. The different pieces were then irradiated within a moderated reactor spectrum (Table 1) in the RISÖ-nuclear reactor in Roskilde, Denmark. We irradiated two samples for each of three different periods (Table 1) to obtain three different doping concentrations.

Samples L1, M1, H2 were successively annealed in several steps from 800 to 1800 °C and sample L2 was annealed at 1600 and 1700 °C, each for 30 min. The anneals were carried out in a vacuum for temperatures up to 1000 °C and in an argon atmosphere for higher temperatures. For annealing from 1500 to 1800 °C the samples were mounted in a closed SiC-coated graphite crucible.

* Corresponding author.

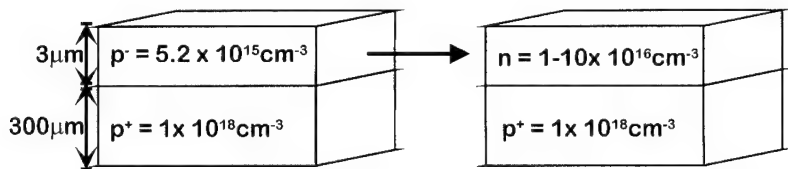


Fig. 1. The used 6H-SiC samples with doping concentrations before and after neutron irradiation (for fluxes etc. see Table 1).

Table 1
Investigated 6H-SiC samples with applied neutron fluxes and resulting doping concentrations

Samples	Irradiation time (days)	Total flux of thermal neutrons in 10^{20} cm^{-2} (67.9% of total flux)	Total flux of fast neutrons in 10^{19} cm^{-2} (24.7% of total flux)	Resultant doping $N_D - N_A (10^{16} \text{ cm}^{-3})$
L	6.75	0.64	2.3	1
M	25.03	2.4	8.7	5
H	46.07	4.4	16	10

2.2. Low temperature photoluminescence (LTPL)

After each annealing step the samples were analysed by LTPL and FTIR. The LTPL equipment is described elsewhere (see the paper by C. Peppermüller et al.; this conference).

2.3. FTIR- measurements

The FTIR-spectra were measured with a Nicolet 740 with Globar source, KBr and Si beam splitters and a DTGS-detector. The measurements were performed at temperatures of 6, 83 and 295 K.

2.4. $I-V$ and $C-V$ and Hall-effect measurements

Following the annealing steps above 1600 °C complementary electrical measurements (Hall-effect, $C-V$, $I-V$) were carried out. To avoid leakage currents at the edges of the samples over the intended p-n junction reactive ion etching (RIE) was used to prepare mesa structures by removing an edge zone of approx. 500 μm width and 5 μm depth. For Hall-effect measurements [4] Ni-contacts in Van der Pauw geometry were evaporated onto the epilayer and processed at 1100 °C by rapid isothermal annealing (RIA). For $C-V$ measurements the Hall contacts were connected with a broad ring of evaporated Ni at least 1 mm in diameter. In the middle of the epilayer a Ni-Schottky contact of 0.8 mm in diameter was prepared. The $C-V$ measurements were done using the four wire method with a HP 4284A bridge.

3. Results

3.1. LTPL measurements

After irradiation all samples were coloured deep black and showed no visible luminescence at the temperature

of liquid nitrogen under excitation of a high pressure mercury arc lamp. The first LTPL emission was detected after 1400 °C annealing. All LTPL-spectra (Fig. 2) show emission due to the D₁-defect centre. This consists of the well known L₁, L₂, L₃ lines [5]. With increasing annealing temperature the intensity distribution of L_{1–3} changes until it becomes similar to that from implanted samples (Fig. 2; [6]). Following annealing at 1600 °C four new emission lines appear at 420.2–421.2 nm. These emission lines are known from phosphorous-implanted samples [6]. They reach their maximum intensity after 1650 °C annealing and the emission disappears after annealing at a temperature of 1800 °C. The intensities of these new lines vary significantly with both the exciting intensity and temperature (Fig. 3(b)). In addition, we detected a line doublet at 443.2 nm, which we interpret as a phonon-replica to the lines described above which are related to the phosphorous transmutation process and a single line at 432.8 nm between annealing temperatures of 1600 and 1700 °C.

3.2. FTIR measurements

The transmission below 2300 cm⁻¹ recovers almost completely during annealing at 1400 °C as does the reflection spectrum, and transmission and reflection become comparable to those from "as grown" SiC. The energy barrier for the "recovery" seems to be rather low, because this process begins with the lowest annealing temperature of 800 °C. The visible transparency of the low doped samples becomes slightly better after 1600 °C annealing (brown colour) and with annealing at 1650 °C changes immediately to a light grey colour. In the region between 250 and 750 cm⁻¹ interference structures grow with successive annealing temperatures. An absorption line is detected at 475 ± 2 cm⁻¹ which increases with neutron dose (Fig. 3(a)), therefore, we

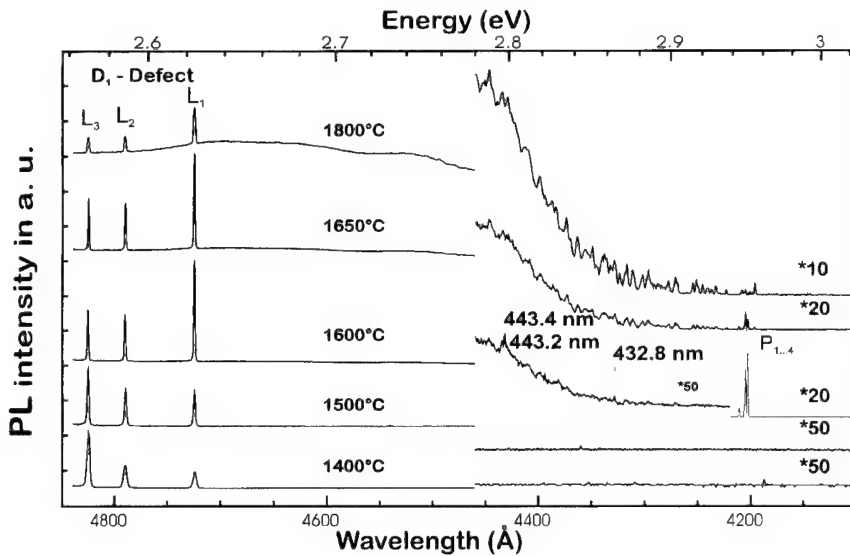


Fig. 2. LTPL spectra of 6H-SiC after neutron irradiation and 1400–1800 °C annealing (for doping by implantation see Ref. [6]).

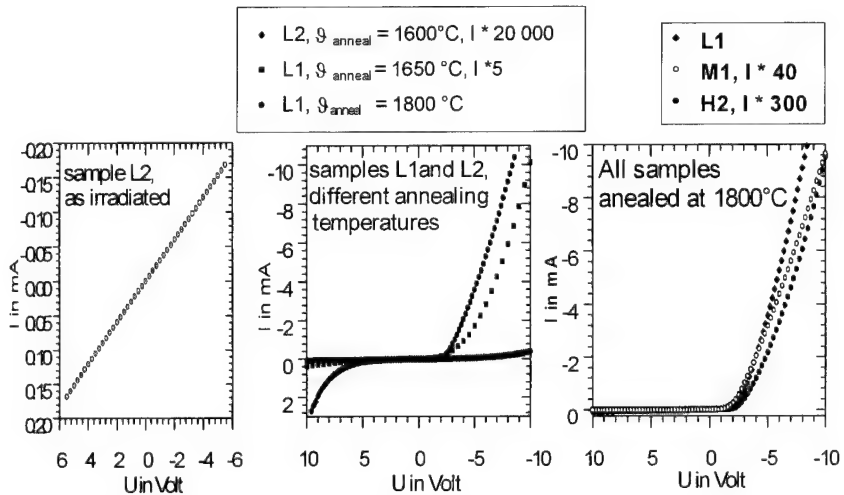


Fig. 3. No rectification and high resistant samples without annealing, showing improving p–n junction with raising temperature. Radiation damage causes the higher resistance of higher dosed samples.

suppose that this absorption is due to a local mode related to the introduced phosphorous defect.

3.3. Electrical measurements

I–*V* measurements of the samples immediately after irradiation show an ohmic behaviour and a resistivity proportional to the neutron dose (Fig. 4(a)). After annealing at 1650 °C the p–n junction in the sample (Fig. 4(b) and (c)) is discernible and the *I*–*V* characteristic of the p–n junction improves with annealing temperature. While the *I*–*V* characteristics of the low doped samples do not change significantly for annealing from 1650 to 1800 °C the more strongly irradiated samples show an increase in the current density in a forward bias direction of more than a factor of 10³.

C–*V* measurements for the sample irradiated with a low dose show a net donor concentration of approximately 5 × 10¹⁵ cm⁻³ evaluated from a Mott–Schottky plot.

Hall-effect data for the n-type epilayer which was produced by neutron transmutation were fitted (Figs. 5(a) and (b)). This fit was based on the assumption that the energies required for ionisation of the three non-equivalent lattice sites may change with C/Si place in 6H-SiC: therefore, we chose twice as many donors with low ionisation energies (k_1, k_2) as with the higher one (h) in analogy with nitrogen.

4. Conclusions

Neutron transmutation doping with phosphorous can also be applied to SiC. The neutron cross-sections of

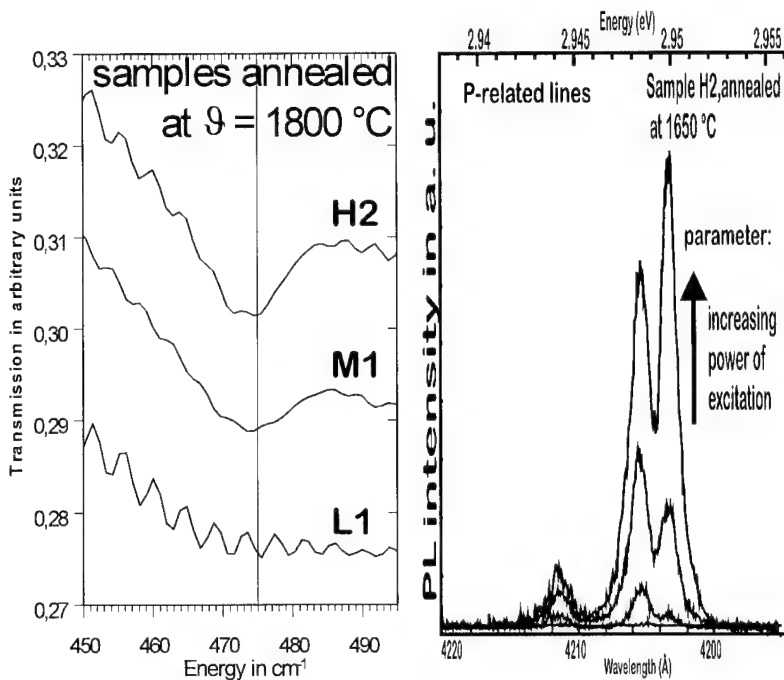


Fig. 4. (a) FTIR transmission of a broad absorption at $475 \pm 2 \text{ cm}^{-1}$ growing with the phosphorous concentration produced by neutron transmutation. (b) The phosphorous-correlated lines are due to defects in the more complicated structure, as demonstrated by the relative intensities of the emission lines for different excitation densities.

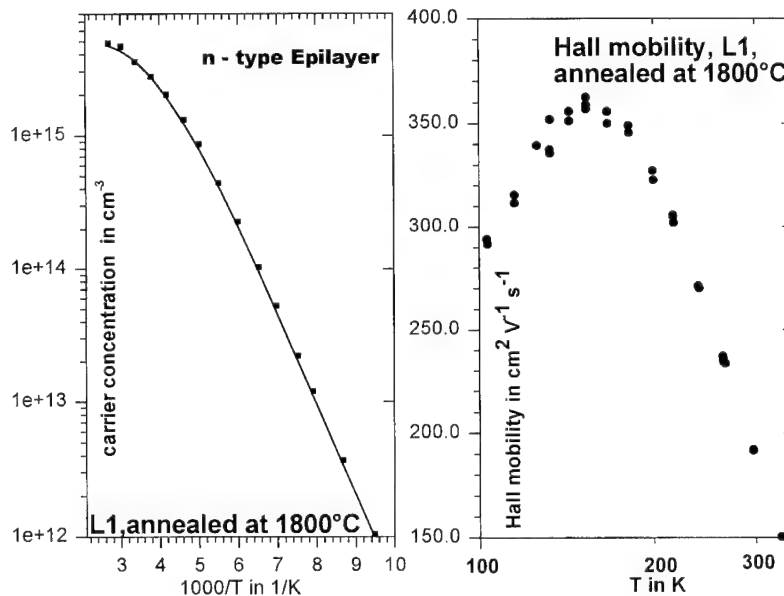


Fig. 5. Hall-effect measurements of the transmuted n-type layer. (a) The analysis of the carrier concentration versus temperature leads to a low energy level: $118.3 \pm 0.87 \text{ meV}$ and a deep energy level: $187.0 \pm 1.8 \text{ meV}$; donor concentration: $1.18 \pm 0.18 \times 10^{16} \text{ cm}^{-3}$; compensation concentration: $6.5 \pm 0.19 \times 10^{15} \text{ cm}^{-3}$. (b) Hall mobility referring to the sample with the concentration given in (a).

C-isotopes are of the same order of magnitude as those for Si but the long half-life of the nuclear reaction ($\text{C} \rightarrow \text{N}$) results in only negligible concentrations of N. There are, however, impurities such as Mg, V and Ti incorporated in SiC which have high cross-sections for nuclear reactions, especially for fast neutrons. From analysis of the energy and momentum conservation of

the ^{31}Si to ^{31}P decay one is able to conclude that the phosphorous atoms produced do not change their lattice sites because of the nuclear reaction.

In our experiments all measurements show considerable radiation damage generated by fast neutrons. Therefore a high temperature annealing has to be applied.

References

- [1] M.S. Schnöller, IEEE Trans. Elect. Dev. ED 21 (5) (1974) 313.
- [2] E.V. Haas, M.S. Schnöller, IEEE Trans. Elect. Dev. ED 23 (8) (1976) 803.
- [3] E. Spenke, p-n Übergänge, Publisher: Springer, Berlin 1979, p. 138.
- [4] R. Schaub, G. Pensl, M. Schulz, C. Holm, Appl. Phys. A34 (1984) 215.
- [5] W.J. Choyke, L. Patrick, Phys. Rev. B5 (1972) 3253.
- [6] T. Troffer, C. Peppermüller, G. Pensl, K. Rottner, A. Schöner, J. Appl. Phys. 80 (7) (1996) 3739–3743.

Investigation of the effects of high temperature implantation and post implantation annealing on the electrical behavior of nitrogen implanted β -SiC films

W. Reichert ^{a,*}, R. Lossy ^a, M. González Sirgo ^a, E. Obermeier ^a, W. Skorupa ^b

^a Technical University of Berlin, Department of Electrical Engineering, Microsensor and Actuator Technology Center, Sekr. TIB 3.1, Gustav-Meyer-Allee 25, D-13355 Berlin, Germany

^b FZ Rossendorf, POB 510119, 01314 Dresden, Germany

Abstract

Nitrogen was implanted into p-type β -SiC at implantation temperatures between 300 K and 1473 K. The implanted samples were characterized by Secondary Ion Mass Spectroscopy (SIMS) and electrically by resistivity and Hall measurements. The analysis was done with as-implanted samples and with samples that were annealed at 1473 K in a nitrogen atmosphere or in a vacuum. The implantation profiles did not show a significant dependence on the implantation temperature whereas the number of active dopants increased when the implantation temperature was raised. The electron mobility was also higher for high implantation temperatures, indicating a decrease in the implantation damage with increasing T_{impl} . As expected for the samples with $T_{\text{impl}} < T_{\text{anneal}}$, the annealing step caused a further rise in the number of electrically active dopants. The trend of electrical activation and the electron mobilities increasing with a higher implantation temperature remained unchanged also after the annealing step. © 1997 Elsevier Science S.A.

Keywords: β -SiC; High temperature nitrogen implantation; Post implantation annealing; Electrical activation

1. Introduction

The material properties that characterize silicon carbide are the wide bandgap, high breakdown electric field, high electron saturation velocity, and high chemical and physical stability. These properties make it a suitable material for high temperature, high power, and high frequency applications as well as for devices to be operated in chemically and radiation harsh environments [1]. For micromechanical applications, e.g. sensors, the cubic polytype is of special interest. Since β -SiC is deposited on Si or SOI (Silicon On Insulator) substrates, the micromachining of the substrate can be done with conventional silicon technology whereas the sensing elements are made of SiC.

Owing to the low diffusion coefficients of the dopants, ion implantation is the only possible technique for area selective doping of SiC. A major problem with ion implantation is the electrical activation of the implanted

dopants in SiC. To achieve high activation the implanted wafers have to be annealed at very high temperatures (1773–1873 K), which is possible with bulk material such as 6H-SiC [2,3]. However, with β -SiC annealing temperatures below the melting point of the Si substrate are necessary. To obtain high electrical activation without annealing at too higher temperatures, the implantation at elevated temperatures is a common method. During this work high temperature implantation of nitrogen in β -SiC and post implantation annealing were analyzed with respect to the electrical behavior of the implanted films.

2. Experimental

Nitrogen was implanted into p-type ($N_A = 2 \times 10^{18} \text{ cm}^{-3}$) β -SiC obtained from CREE Inc., USA. For all samples the implantation energy was 50 keV, the dose was $5 \times 10^{14} \text{ cm}^{-2}$, and the implantation angle was 7° off axis. The implantation temperatures were varied between room temperature (RT)

* Corresponding author. Tel: +49 30 314 72 539; Fax: +49 30 314 72 603.

and $T_{\text{impl}} = 1473 \text{ K}$. The implantation parameters are listed in Table 1. After the implantation the wafers were diced. The first set of samples was analyzed without post implantation annealing while the second set was annealed at $T = 1473 \text{ K}$ (same as highest implantation temperature) for 60 minutes in a nitrogen atmosphere. Two samples, implanted at room temperature and at $T_{\text{impl}} = 1473 \text{ K}$, were also annealed in a vacuum at $T_{\text{a, vac}} = 1473 \text{ K}$ for 30 min with a residual pressure $P_{\text{res}} < 10^{-6} \text{ mbar}$.

The doping profiles were measured by secondary ion mass spectroscopy (SIMS) using negatively charged SiN ions while the electrical characterization was done by resistivity and Hall measurements.

3. Results and Discussion

3.1. Analysis of the Implanted Profiles

The dependence of the doping profile on the implantation temperature was obtained from SIMS measurements. The results of the as-implanted samples showed that the implantation profile is almost independent of the implantation temperature (Fig. 1). Only the tail of the profile implanted at $T_{\text{impl}} = 1473 \text{ K}$ is larger than that of the samples implanted at lower temperatures which indicates diffusion of nitrogen at the highest temperature.

The profile implanted at $T = 673 \text{ K}$ was also analyzed by SIMS after the annealing step in nitrogen at $T_{\text{anneal}} = 1473 \text{ K}$. The profile broadened, i.e. the nitrogen concentration increased towards the surface and the tail became larger. The peak concentration was reduced when compared with the as-implanted sample (Fig. 1). The reason for the broadening of the profile is nitrogen diffusion due to the damage induced into the β -SiC film during the implantation step. This effect is discussed in greater detail in [4].

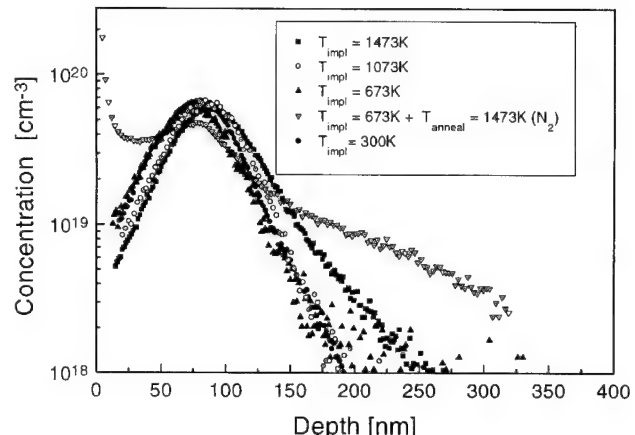


Fig. 1. Implantation (SIMS) profiles of nitrogen implanted in β -SiC at four different temperatures without post implantation annealing compared with a sample annealed at $T = 1473 \text{ K}$ in nitrogen after the implantation process. The implantation energy and dose were 50 keV and $5 \times 10^{14} \text{ cm}^{-2}$, respectively.

3.2. Electrical Characterization

From electrical measurements the resistivity, electrical activation and electron mobilities were determined (Hall method). The electrical characterization of the as-implanted samples showed no n-type doping for implantation temperatures below 1073 K. This is due to the high background p-type doping concentration ($N_A = 2 \times 10^{18} \text{ cm}^{-3}$) of the substrate. Nitrogen implantation into lower doped p-type β -SiC using the same implantation energy and dose showed electrical activations of 0.43% and 1.35% for $T_{\text{impl}} = \text{RT}$ and $T_{\text{impl}} = 673 \text{ K}$, respectively [5]. By increasing the implantation temperature the electrical activation increased from 12% at $T_{\text{impl}} = 1073 \text{ K}$ to 52% at $T_{\text{impl}} = 1473 \text{ K}$.

In Fig. 2 the electrical activation is presented in terms of the activated dose. The electrical characterization of the samples after annealing in nitrogen and vacuum showed a significantly higher number of electrically

Table 1
Implantation conditions

Implantation temperature (K)	Implantation energy (keV)	Implantation dose (cm^{-2})	Implantation time (min)	Total time at implantation temperature (min)
RT	50	5×10^{14}	2.1	—
473	50	5×10^{14}	2.1	17
673	50	5×10^{14}	2.1	12
873	50	5×10^{14}	2.2	7
1073	50	5×10^{14}	6.5	14
1173	50	5×10^{14}	6	13
1273	50	5×10^{14}	6	13
1373	50	5×10^{14}	6	14
1473	50	5×10^{14}	7	15

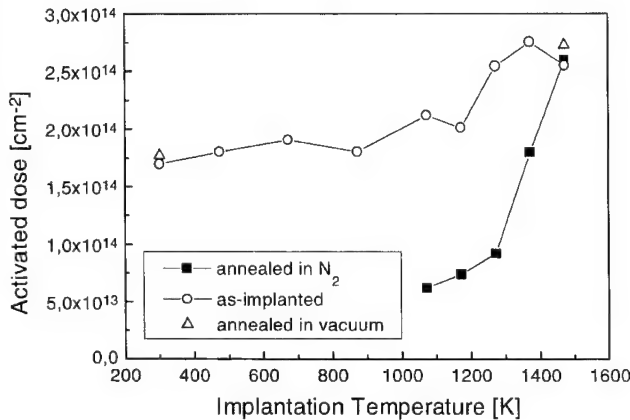


Fig. 2. Activated dose as a function of the implantation temperature for as-implanted and annealed ($T_{\text{anneal}}=1473 \text{ K}$) β -SiC samples. The implanted nitrogen dose was $5 \times 10^{14} \text{ cm}^{-2}$.

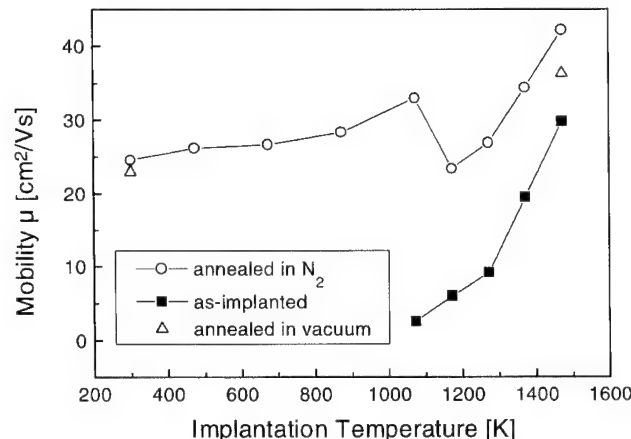


Fig. 3. Electron mobility vs. implantation temperature for as-implanted and annealed ($T_{\text{anneal}}=1473 \text{ K}$), nitrogen doped β -SiC samples. The implantation energy and dose were 50 keV and $5 \times 10^{14} \text{ cm}^{-2}$, respectively.

active dopants as compared to the as-implanted case. However, the activation still showed a dependence on the temperature T_{impl} of the previous implantation step (Fig. 2) and the activation of the sample with $T_{\text{impl}}=T_{\text{anneal}}$ remained essentially the same even though the annealing time after the implantation step (60 min in nitrogen or 30 min in vacuum) was much longer than the annealing time during the implantation process (15 min).

Since most of the annealing was done in a nitrogen atmosphere it cannot be clearly distinguished between an increase in the electrical activation of the implanted dopants owing to the thermal treatment after the implantation, and an increase in the number of dopants due to damage-enhanced diffusion. However, since the two samples annealed in a vacuum show similar results to those annealed in nitrogen it appears likely that most of the increase in electrical activation results from the thermal treatment and not the in-diffusion of nitrogen atoms into the damaged crystal from outside. To clarify this point further annealing experiments are currently being performed.

The electron mobility of the as-implanted samples is in general very low (max. $30 \text{ cm}^2 \text{ V}^{-1} \text{ s}^{-1}$) owing to high compensation. But it increases with increasing implantation temperature (Fig. 3) and therefore with an increasing number of free carriers. Normally the mobility would decrease with increasing carrier concentration. However, if the damage is reduced when the implantation temperature is raised less scattering occurs and therefore the electron mobility is higher. And by raising the implantation temperature, the recrystallization during implantation can be increased as was also shown by Rutherford back scattering (RBS) [5]. However, the implantation damage is also reduced in an annealing step. Therefore the electron mobility is higher when the implanted samples are annealed.

4. Conclusions

The work shows that up to 50% electrical activation of the implanted nitrogen in β -SiC can be obtained without post implantation annealing when the implantation is carried out at 1473 K. Annealing at the same temperature for a longer period of time did not cause a further increase in the electrical activation. However, the mobility values are improved.

The overall trend is that the electrical activation of the implanted nitrogen and the electron mobility increase with increasing implantation temperature for both sets of samples: the as-implanted and the annealed samples. The best results were obtained when the samples were implanted at high temperatures and annealed after the implantation.

Acknowledgement

The work was supported by the Commission of European Communities under the contract number BRE2-CT92-0211. The authors would also like to thank Ch. Wagner from the Daimler-Benz AG for technical assistance.

References

- [1] P.G. Neudeck, J. Electron. Mat. 24 (4) (1995) 283.
- [2] J.A. Freitas, Jr., J. Gardner, M.V. Rao, Inst. Phys. Conf. Ser. No 142, Proceedings of the Sixth Intern. Conf. on Silicon Carbide and Related Materials, Kyoto Japan, 1996, p. 529.
- [3] N. Inoue, A. Itoh, T. Komoto, H. Matsunami, T. Nakata, M. Wanatabe, Inst. Phys. Conf. Ser. No 142, Proceedings of the Sixth Intern. Conf. on Silicon Carbide and Related Materials, Kyoto Japan, 1996, p. 525.
- [4] R. Lossy, W. Reichert, E. Obermeier, W. Skorupa, J. Electron. Mat. 26 (3) (1997) 123.
- [5] R. Lossy, W. Reichert, E. Obermeier, J. Stoemenos, Inst. Phys. Conf. Ser. No 142, Proceedings of the Sixth Intern. Conf. on Silicon Carbide and Related Materials, Kyoto Japan, 1996 p. 553.



ELSEVIER

β-SiC films on SOI substrates for high temperature applications

W. Reichert ^{a,*}, E. Obermeier ^a, J. Stoemenos ^b

^a Technical University of Berlin, Department of Electrical Engineering, Microsensor and Actuator Technology Center, Sekr. TIB 3.1, Gustav-Meyer-Allee 25, D-13355 Berlin, Germany

^b Aristotle University of Thessaloniki, Physics Department, 54006 Thessaloniki, Greece

Abstract

Single crystalline, cubic β-SiC films were deposited by CREE Inc., USA on bonded SOI wafers. The SiC deposition took place under standard conditions used at CREE for deposition on Si wafers, and at deposition temperatures 25 °C and 50 °C below standard deposition conditions to investigate the influence of the deposition temperature on the damage of the buried oxide layer and therefore the insulating capability of that layer.

Transmission electron microscopy (TEM), atomic force microscopy (AFM) and optical microscopy were used for structural analysis of the Silicon Carbide On Insulator (SiCOI) structure. The deposited β-SiC films, the buried SiO₂ layer, and the SiC/Si interface were investigated. First measurements showed similar results for all three deposition temperatures indicating that the deposition temperature is not the only parameter defining the structural and therefore also the electrical quality of the SiCOI wafers. The electrical measurements were performed up to $T=723$ K (current limit of the equipment) and the results showed good electrical insulation of the SiC layer from the Si substrate in the whole temperature range. © 1997 Elsevier Science S.A.

Keywords: β-SiC on SOI; SiCOI; Bonded SOI; High temperature

1. Introduction

Cubic silicon carbide, heteroepitaxially grown on silicon, gives a material system that combines the high temperature capabilities of SiC with the micromachining possibilities of Si. Therefore this material system appears especially interesting for the development of micro-mechanical devices such as microsensors based on membranes, e.g. pressure, gas, and acceleration sensors for operation at high temperatures [1]. However, next to its advantages the SiC/Si system has a major problem. At temperatures greater than approximately 150–200 °C the SiC/Si heterojunction becomes leaky, which results in a current flow through the Si substrate [2]. One approach to minimize or remove this effect is the deposition of thin SiC films on SOI (Silicon On Insulator) substrates. Experiments with SiCOI structures, where β-SiC was grown on SIMOX (Separation by Implanted Oxygen) substrates were very promising since that system allowed higher operating temperatures than the SiC/Si system. However, during the carbonization process cavities were formed in the Si-overlayer that extended to the buried oxide. This damage and the Si

islands in the buried oxide limited the applicability of the SiC/SIMOX system to approximately 300 °C [3]. To obtain electrical insulation of the SiC film from the Si substrate for temperatures higher than 300 °C a better quality SOI substrate with a thermal oxide was used during this work.

2. Experimental

Bonded, (100)-oriented SOI wafers (UNIBOND), obtained from SOITEC, France, have been used for β-SiC deposition since the thermal oxide with its higher density is expected to be a better insulator at high temperatures than an implanted oxide as in the case of SIMOX wafers. The UNIBOND wafers were fabricated using the Smart-Cut® process. The thicknesses of the Si-overlayer and the buried, thermal oxide layer (Box) were 200 nm and 400 nm, respectively (Fig. 1). The substrates used for β-SiC deposition were (100)-oriented and had a size of 20 × 20 mm. The deposited β-SiC films were 2.2 μm thick with an n-type doping concentration of $N_D=3\times 10^{18}\text{ cm}^{-3}$ at room temperature.

After deposition structural characterization of the β-SiC films, the Si-overlayer, the buried SiO₂ layer, and the SiC/Si interface was done by optical microscopy,

* Corresponding author. Tel: +30 31 998 191; Fax: +30 31 214 276.

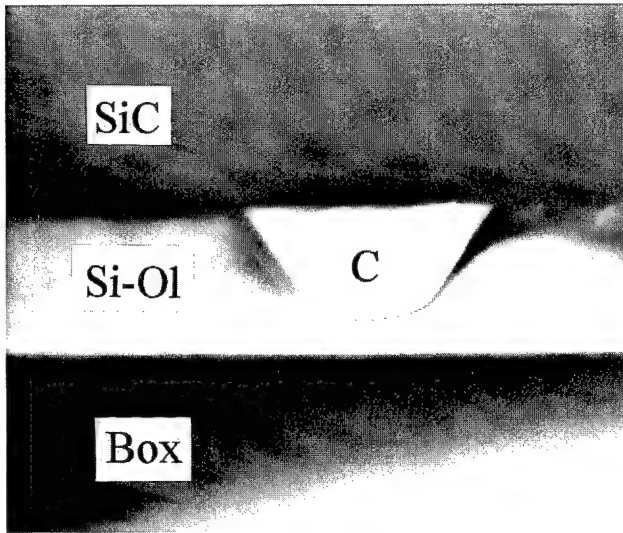


Fig. 1. XTEM micrograph of a SiCOI structure showing a cavity (C) in its initial stage in the Si-overlayer (Si-OI) before touching the buried oxide (Box).

atomic force microscopy (AFM), and transmission electron microscopy (TEM). From electrical measurements using the Hall method the resistivity, free carrier concentration, electron mobility, and the insulating capability of the buried oxide were determined in the temperature range between $T=83$ K and $T=723$ K.

3. Results and discussion

3.1. Structural characterization

For all three deposition temperatures the structural characterization by TEM revealed defect densities of $2\text{--}3 \times 10^9 \text{ cm}^{-2}$ (mainly stacking faults) near the surface of the deposited SiC films that are very close to those observed when β -SiC is deposited on bulk silicon. The analysis also showed that lowering the temperature by 25 °C or 50 °C does not degrade the structural characteristics of the SiC layer. The density of cavities in the silicon overlayer and the SiO_2 layer varies between $1 \times 10^7 \text{ cm}^{-2}$ and $4 \times 10^7 \text{ cm}^{-2}$. Optical microscopy and AFM also showed similar results for all three samples. As expected, the cross section TEM revealed very high defect densities near the SiC/Si interface due to the 21% lattice mismatch.

The cavities in the early stage have the classical morphology of the reversed, truncated tetragonal pyramid frequently observed in bulk silicon near the SiC/Si interface (Fig. 1). However, as they grow the pyramid touches the SiO_2 interface and the shape of the cavity is reversed (Fig. 2). Then the cavity is extended by consuming SiO_2 of the buried layer and the preferred growth direction of the cavities in the SiO_2 seems to be the lateral direction, and not vertical into the oxide

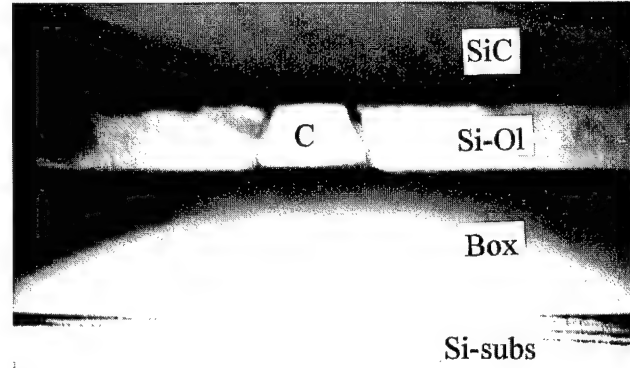


Fig. 2. XTEM micrograph of a SiCOI sample after the growing cavity in the Si-overlayer touched the buried oxide (Box). The cavity reversed its shape from a downward pointing, truncated pyramid to an upward pointing, truncated pyramid.

(Fig. 3). However, the formation of the cavities in the Si/ SiO_2 region needs systematic study.

The same kind of cavities in the Si-overlayer and the buried oxide were observed in the case of a SIMOX substrate [3]. However, the SiC/UNIBOND system has a better quality and higher density thermal oxide, and no small Si islands are present in the SiO_2 layer, as is the case with SIMOX. Therefore a lower overall damage of the SiO_2 layer and a better electrical insulation of the SiC film from the bulk silicon at high temperatures are expected.

3.2. Electrical characterization

From the electrical characterization the sheet resistance, the free carrier concentration, and the electron mobility in the temperature range between $T=83$ K and $T=723$ K have been determined. The sheet resistance versus temperature for β -SiC deposited on Si and UNIBOND substrates under standard deposition temperatures is given in Fig. 4. For temperatures below 525 K the characteristics of the SiC/Si and the SiCOI samples are almost identical. However, for temperatures beyond 525 K the sheet resistance of the SiC/Si sample drops rapidly while the resistance of the SiCOI sample remains essentially unchanged demonstrating the insulating behavior of the buried SiO_2 layer for the SiCOI structure. These results are further confirmed by the temperature dependent Hall measurements. In Fig. 5 the Hall mobility of the electrons vs. temperature is plotted. It shows that at $T>500$ K the mobility characteristics of the SiC/Si and the SiCOI systems separate. While the mobility of the SiCOI system decreases, which is also expected since scattering effects increase in the temperature range above 500 K, the measured mobility of the SiC/Si system increases. This can only be due to a failure of the SiC/Si heterojunction and a current flow through the Si substrate.

First measurements with the samples deposited at

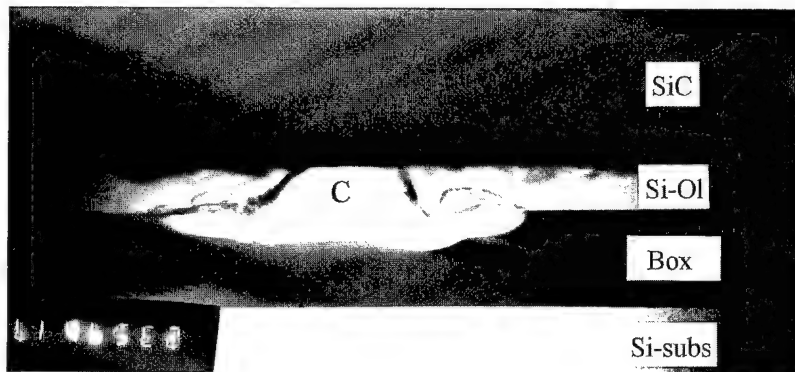


Fig. 3. XTEM micrograph of a structure with a cavity that extended from the silicon overlayer (Si-OI) into the buried oxide (Box). The cavity continues its growth mainly into the lateral direction at the Si-OI/Box interface.

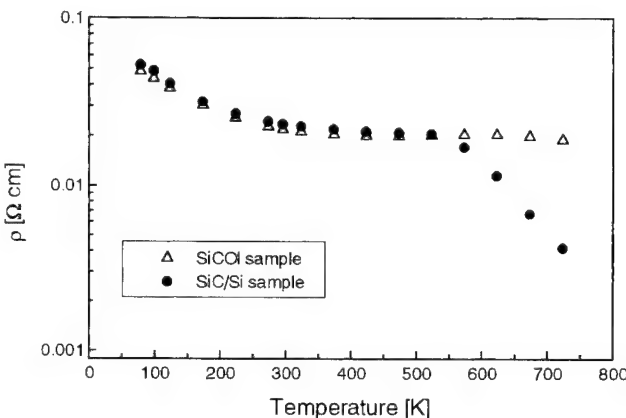


Fig. 4. Resistivity vs. temperature for a SiCOI and a SiC/Si sample. The resistivity of the SiC/Si sample drops at high temperatures due to the substrate effect.

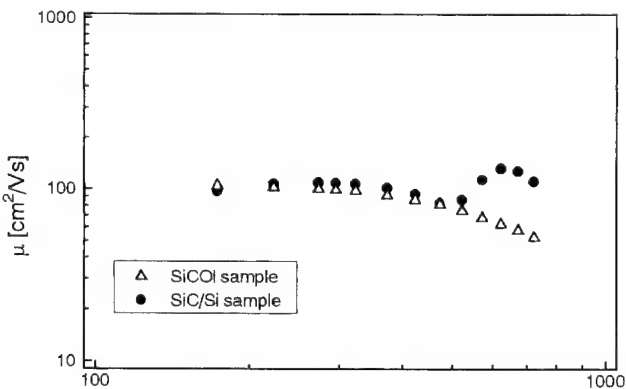


Fig. 5. Electron mobility vs. temperature for a SiCOI and a SiC/Si sample. The mobility measured for the SiC/Si sample increases at high temperatures due to the substrate effect.

$T=25^{\circ}\text{C}$ and $T=50^{\circ}\text{C}$ below standard deposition conditions did not show any improvement as compared to the results shown in Figs. 4 and 5. However, the temperature where the SiCOI material would fail was not reached because 723 K was the maximal operating temperature of the test equipment. Therefore it still needs to be investigated if the lower deposition temperatures

helped to improve the insulating capability of the buried oxide.

4. Conclusions

Even though the degradation process of the buried oxide layer during β -SiC deposition is not well understood so far, it was possible to improve the performance of the SiCOI material by using bonded (UNIBOND) SOI instead of the previously used SIMOX wafers [3]. Due to the better oxide quality compared to SIMOX, not only the temperature, up to which the buried oxide behaved as an insulator was extended (to at least 723 K), but it was also possible to obtain large wafer areas with good electrical separation of the SiC film from the bulk silicon. However, further improvement of the SiCOI substrates is possible, if the growth conditions that are not the same as in the case of SiC/Si are optimized. Therefore a systematic study of the formation of cavities in the SiO_2 layer during the SiC deposition is necessary.

Acknowledgement

The authors would like to thank M. González Sirgo for his assistance during the electrical characterization and V. Papaioannou for performing the atomic force microscopy. The work was supported by the Commission of European Communities under the contract number BRE2-CT92-0211.

References

- [1] G. Krötz, Ch. Wagner, W. Legner, H. Sonntag, H. Müller, G. Müller, Inst. Phys. Conf. Ser. No 142, Proceedings of the Sixth Intern. Conf. on Silicon Carbide and Related Materials, Kyoto Japan, 1995, p. 829.
- [2] A.J. Steckl, C. Yuan, Q.-Y. Tong, U. Gösele, M.J. Loboda, J. Electrochem. Soc. 141 (6) (1994) L166–L168.
- [3] W. Reichert, R. Lossy, J.M. González Sirgo, E. Obermeier, J. Stoenemos, Inst. Phys. Conf. Ser. No 142, Proceedings of the Sixth Intern. Conf. on Silicon Carbide and Related Materials, Kyoto Japan, 1995, p. 129.

Surface chemistry of 6H-SiC(000̄1) after reactive ion etching

N. Sieber *, M. Hollering, L. Ley

Universität Erlangen-Nürnberg, Institut für Technische Physik II, Erwin-Rommel-Straße 1, 91058 Erlangen, Germany

Abstract

X-Ray (Al K α 1486.6 eV) induced core level photoemission spectra of C-terminated 6H-SiC surfaces are reported with the intention to elucidate some of the surface chemistry responsible for the reactive ion etching process in gas mixtures of CHF₃/O₂ as a function of gas composition.

After etching, the SiC surface exhibits a carbonaceous surface layer that is enriched in fluorine solely bonded to C, such that an average stoichiometry of CF_{1.6} is maintained. Despite a dramatic increase in etch rate with the addition of oxygen this layer remains essentially unchanged in stoichiometry while the thickness decreases from 60 Å (at 5% O₂) to 25 Å (20% O₂). Fluorine could be quantitatively removed by annealing at 850°C leaving a graphitic layer on the surface. Oxygen is observed at the SiC–CF_y interface in the form of SiO_z ($z=1\dots2$). © 1997 Elsevier Science S.A.

Keywords: Silicon carbide; Reactive ion etching; Photoelectron spectroscopy

1. Introduction

Nearly all applications of SiC in the form of electronic devices require a structuring of the material. Since most wet chemical methods fail in this respect the method of choice is a dry etching procedure. As a viable treatment the reactive ion etching (RIE) in fluorine containing gas mixtures has been reported in the past [1–5]. It has also been reported that the addition of oxygen enhances the etch rates [2,3,5]. In this contribution we present a study of the surface chemical composition of C-terminated 6H-SiC(000̄1) single crystals after various etching treatments in CHF₃/O₂ plasmas.

2. Experimental

Single crystals of C-terminated 6H-SiC were etched in a conventional parallel plate reactor (area ratio between grounded and powered electrode ca 9:1) with rf-power (13.56 MHz) coupled capacitively to the sample carrying electrode. The surface chemical composition of the sample was measured via core level photoelectron spectroscopy (XPS) with an overall reso-

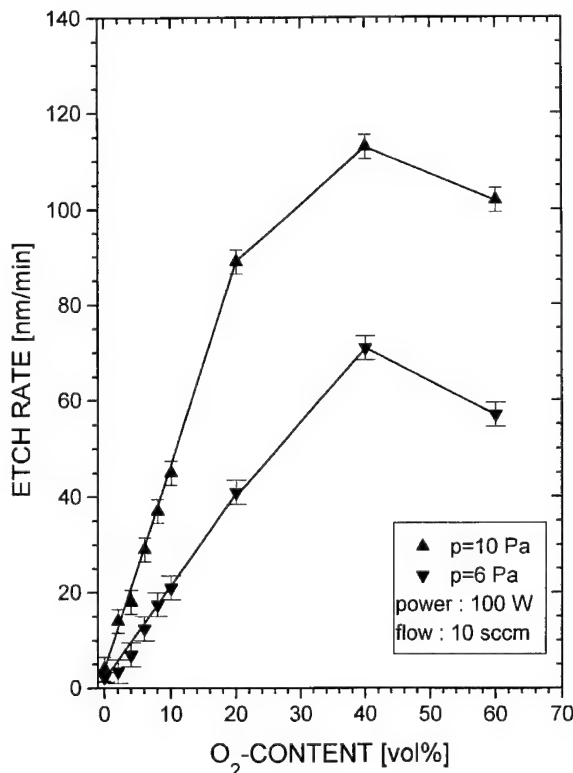


Fig. 1. Etch rates for 6H-SiC(000̄1) for pressures of 6 and 10 Pa as a function of O₂ content in the CHF₃/O₂ gas mixture.

* Corresponding author. Tel.: 49 9131 85-7080; Fax: 49 9131 85-7889; e-mail: sieber@physik.uni-erlangen.de

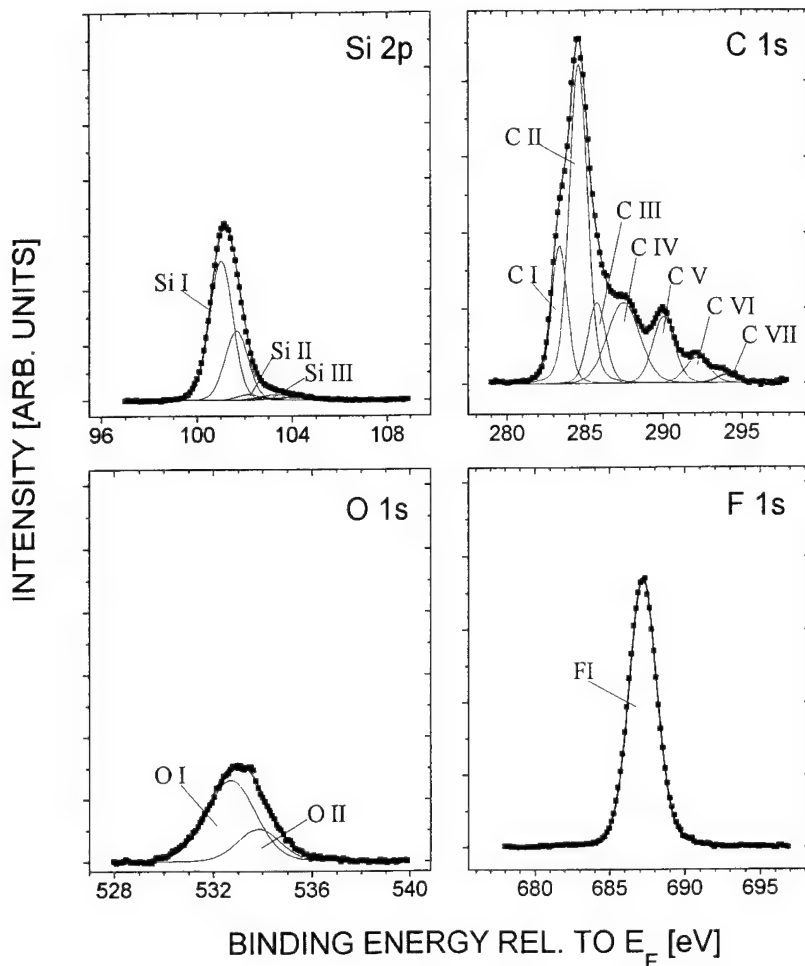


Fig. 2. High resolution core level spectra of all relevant elements after etching 6H-SiC in a CHF_3/O_2 gas mixture with 20 vol% of O_2 for 10 min and at a pressure of 50 Pa. Also shown are the line components used to fit the spectra. The SiII and SiIII peak positions in the Si 2p spectrum are confirmed by other measurements where ca 15 at% of Si is bonded to oxygen.

lution of 0.6 eV using monochromatized Al K α radiation ($h\nu=1486.6$ eV). The relative concentration of a chemical species within the sampling volume was determined from the area under the corresponding XPS line components after appropriate corrections for photoemission cross-sections according to Scofield [6] and for spectrometer sensitivity have been made.

3. Results and discussion

All etch treatments were performed with the sample nominally at room temperature, an rf-power of 100 W, a gas flow of 10 sccm, and pressures of 6 and 10 Pa, respectively, which results in bias voltages on the sample carrying electrode between -625 and -775 V. Fig. 1 shows the etch rate in a gas mixture of CHF_3 and O_2 . Initially the etch rate increases linearly with O_2 content, reaches a maximum of 70 nm min^{-1} at 6 Pa and 110 nm min^{-1} at 10 Pa at an oxygen content of 40 vol%, and drops with higher O_2 content. Without oxygen we

measure etch rates of only about 4 nm min^{-1} . These results agree qualitatively with most previous reports about the beneficial effect of oxygen on the etch rate of SiC using CHF_3 or CF_4 as the main etching agent [2,3,5] despite one report to the contrary [1].

Two sets of core level spectra and their fits which are representative for the ones used to derive the surface chemical composition of the samples after different treatments are shown in Fig. 2 (as etched) and Fig. 3 (after an additional annealing step at 850°C for 10 min). The fits were performed with the constraint that a minimum number of components compatible with the experimental conditions was required to fit all the spectra. The Si 2p lines were fitted using a spin-orbit doublet with a splitting of 0.6 eV and a branching ratio of 2 [7,8].

Most of the line positions and their assignments to a chemical species agree with those given in the literature [9–12]. The SiI and CI components at binding energies of 101.0 ± 0.1 and 283.5 ± 0.1 eV, respectively, are due to SiC. Two further Si components at 102.3 ± 0.1 and

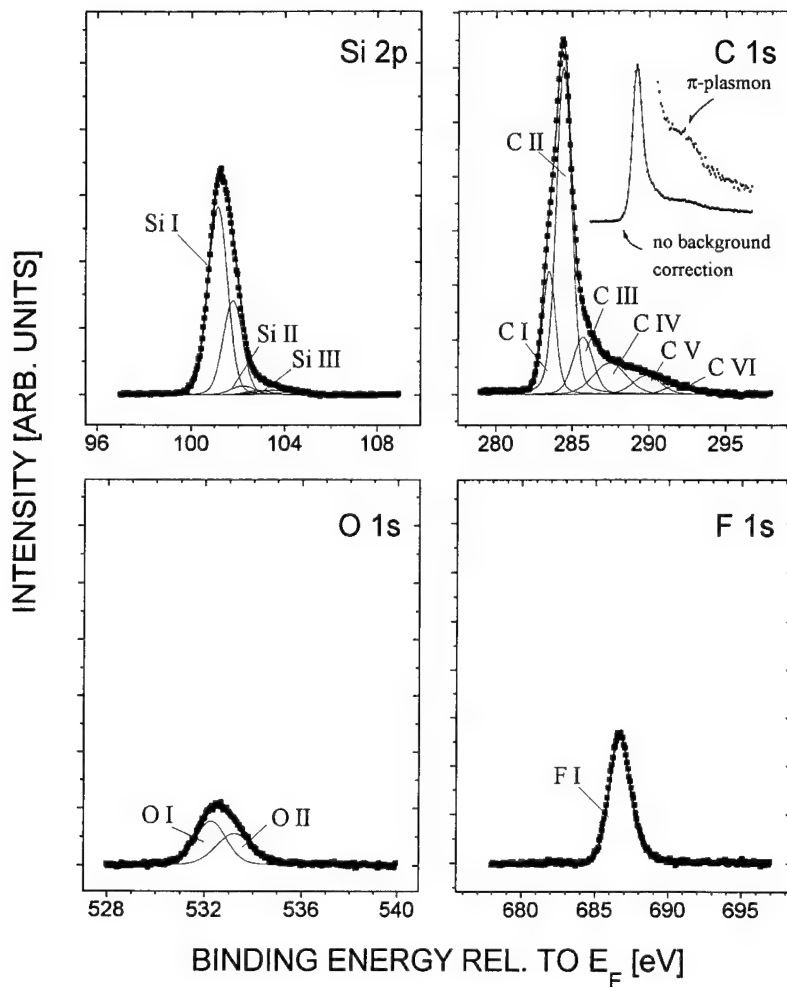


Fig. 3. Core level spectra of the sample of Fig. 2 after annealing at 850°C for 10 min. The deconvolution of the C 1s spectrum was performed after subtracting the π -plasmon loss that dominates the high binding energy side of the C 1s line after annealing as shown in the insert.

103.6 ± 0.2 eV are ascribed to silicon suboxides (SiII) and SiO_2 (SiIII). A binding energy of 284.5 ± 0.2 eV for the CII line (amorphous carbon or graphite) yields adequate fits for all spectra. The CIII component does not represent a chemically different surface species; it rather takes into account the asymmetry of the graphitic CII component. The components CIV through CVII are identified with C atoms bonded to fluorine ($\text{C}-\text{F}_x$, $x=1\dots 4$) at 287.4 ± 0.1 , 290.0 ± 0.1 , 292.2 ± 0.1 and 294.0 ± 0.1 eV, respectively. Finally, we were forced to fit two components of different weight to the rather broad (ca 2.5 eV FWHM) and asymmetrical O 1s line. The one at 533.7 eV (OII) is assigned to $\text{Si}-\text{O}_2$ [9] on account of its intensity variation which parallels the corresponding Si 2p component (SiIII). The other O 1s component (OI) could not be identified unambiguously as yet. On surfaces essentially free of fluorine the C 1s component appropriate for C–O bonds could not be observed in an intensity as required by the corresponding O 1s signal. The F 1s line has a binding energy of 687.2 ± 0.2 eV.

The atomic concentration ratio of SiI and CI which are both ascribed to SiC is generally equal to one independent of surface treatment. The relative concentration of the species corresponding to SiIII and OII is close to two as is expected for SiO_2 . We have applied the analysis of Gruntz et al. [13] to the chemically shifted $\text{C}-\text{F}_x$ ($x=1\dots 4$) components to obtain the concentration of F atoms bonded to carbon, $[\text{F}]_{\text{C} 1s}$. This is to be compared with the F concentration derived from the intensity of the F 1s (FI) component, $[\text{F}]_{\text{F} 1s}$. The fact that this ratio turns out to be 1.0 ± 0.1 in all but a few cases and that the fluorine concentration is given by a single peak implies that F is exclusively bonded to carbon after RIE.

The surface atomic concentrations of C, F, O and Si after RIE are depicted in Fig. 4(a and b) for the two series of etch treatments in which we varied the oxygen content in the gas phase between 0 and 20% for gas pressures of 10 and 50 Pa. Fig. 4(c) corresponds to the samples of Fig. 4(b) after they have been annealed at 850°C for 10 min.

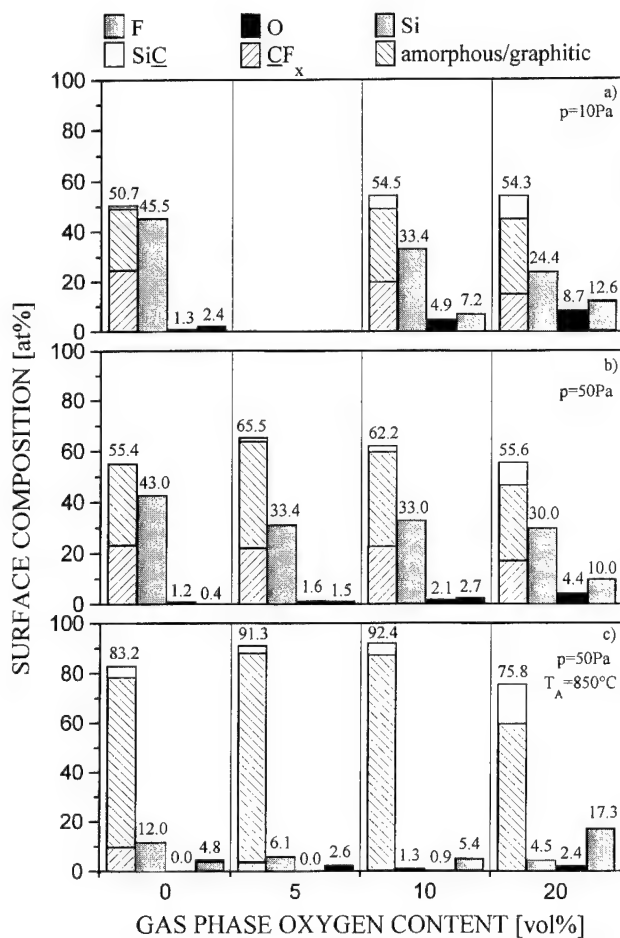


Fig. 4. Survey of the surface chemical composition of 6H-SiC after RIE at (a) 10 and (b) 50 Pa and (c) after annealing at 850°C. The left column of each group displays the total carbon content divided to fractions representing C bonded to silicon, to fluorine and elemental carbon (amorphous or graphitic).

The Si Si 2p analysis shows that in all cases at least 80% of the Si signal is due to SiC with the remainder due to silicon oxides and suboxides. Fluorine is exclusively bonded to carbon in the form of C–F_x ($x=1\dots 4$). The distribution among the different C–F_x configurations depends somewhat on pressure but hardly on oxygen content in the gas phase. Typical relative concentrations of C–F₁:C–F₂:C–F₃:C–F₄ are 18:12:5:1 for 50 Pa and 25:11:4:1 for 10 Pa. This corresponds to average stoichiometries of $y=1.7$ and 1.5 for the fluorinated, amorphous CF_y overlayer. The remainder of the carbon signal is due to the CII/CIII component, that is, amorphous carbon that turns graphitic after heating.

It is evident that the fluorinated carbon layer and the graphitic component dominate the surface composition. As a working model we assume that two kinds of carbon layers are on top of the undisturbed SiC crystal: amorphous/graphitic carbon and CF_y. This model is confirmed and further refined by sputter depth profiling experiments using 5 keV Ar-ions at a current density of

ca 1 $\mu\text{A cm}^{-2}$. The corresponding atom concentrations as a function of sputter time are plotted in Fig. 5(a) for the sample of Fig. 4(b). The C–F_x contribution decays most rapidly uncovering first an amorphous carbon component with a low fluorine concentration and then the stoichiometric SiC substrate after a sputtering time of ca 60 min. This implies that as a result of the RIE the SiC surface is covered with a layer of carbon that is enriched with fluorine at the surface. The thickness of the total carbon layer can be estimated from the ratio of the overlayer carbon signal to the SiC line intensity using the mean free path of the C 1s photoelectrons (~20 Å) [14]. For a sample etched in a CHF₃:O₂ gas mixture of 80:20 and a pressure of 50 Pa we obtain a thickness of ca 24 Å which decreases to ca 17 Å after annealing; the corresponding values for CHF₃:O₂ equal to 95:5 are 60 and 45 Å, respectively. Clearly, the thickness of the carbon layer decreases with oxygen content in the gas phase and appears to be overall reduced for low pressure plasmas possibly on account of the higher bias voltage.

After annealing the fluorine content of all samples is drastically reduced to <10 at% without a concomitant reduction in carbon content. The sputter depth profiling of the annealed sample [Fig. 5(b)] confirms the unaltered structure of the sample surface with a graphitic layer on top of SiC. It furthermore confirms the chemical shift analysis of the Si 2p spectra so far as oxygen is solely bonded to silicon at the graphitic carbon/SiC interface and hardly bonded to carbon at all. The graphitic nature of the C-layer is nicely confirmed by the presence of the π -plasmon as illustrated by the insert of Fig. 3(b).

4. Summary

A detailed investigation of the surface chemical composition of 6H-SiC(0001) after RIE in CHF₃:O₂ gas mixtures yields the following results. After the etching process the surface is covered with an amorphous or graphitic layer of typically 20–60 Å thickness that is enriched in fluorine at the top with an average stoichiometry corresponding to CF_{1.5\dots 1.7}. Small amounts of oxygen between 1 and 10% are bonded preferentially to silicon at the carbon/SiC interface. There is no evidence for a substantial amount of oxygen bonded to carbon. These observations depend only weakly on the oxygen content in the gas phase despite a strong correlation between the latter and the etch rate up to 40 vol% of O₂. Post-etch annealing at 850°C removes the fluorine content almost completely without a substantial loss in the carbon layer which is now clearly graphitic.

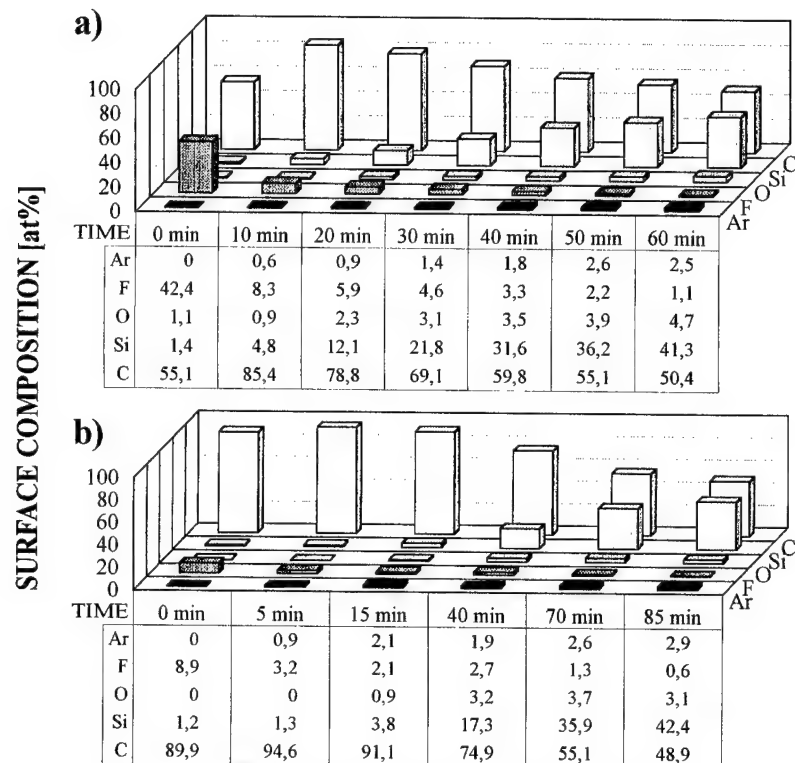


Fig. 5. Surface composition as a function of the Ar-ion sputter time for a sample etched in a pure CHF_3 plasma for 10 min at pressure of 50 Pa (a) before and (b) after annealing at 850°C.

Acknowledgement

This work was supported by the Deutsche Forschungsgemeinschaft through SFB 292 and the Bundesministerium für Bildung, Forschung, Wissenschaft und Technologie, Contract No. 05 622 WEAT. We thank Dr Jürgen Ristein, Anja Ziegler and Ralf Graupner for helpful discussions and Professor Dr. Helbig (Institut für Angewandte Physik) for the permission to use the profilometer for etch step measurements.

References

- [1] J.W. Palmour, R.F. Davis, T.M. Wallett, K.B. Bhasin, *J. Vac. Sci. Technol. A* 4 (1986) 590.
- [2] J. Sugiura, W.-J. Lu, K.C. Cadien, A.J. Steckl, *J. Vac. Sci. Technol. B* 4 (1986) 349.
- [3] R. Padiyath, R.L. Wright, M.I. Chaudhry, S.V. Babu, *Appl. Phys. Lett.* 58 (1991) 1053.
- [4] A.J. Steckl, P.H. Yiu, *Appl. Phys. Lett.* 60 (1992) 1966.
- [5] P.H. Yiu, A.J. Steckl, *Inst. Phys. Conf. Ser.* No. 137, Chap. 3 (1993) 321.
- [6] J.H. Scofield, *J. Electron Spectrosc. Relat. Phenom.* 8 (1976) 129.
- [7] M.L. Shek, *Surf. Sci.* 349 (1996) 317.
- [8] K.L. Håkansson, L.I. Johansson, *Phys. Rev. B* 47 (1993) 10769.
- [9] L.I. Johansson, F. Owman, P. Mårtensson, *Phys. Rev. B* 53 (1996) 1.
- [10] V.M. Bermudez, J.P. Long, *Appl. Phys. Lett.* 66 (1995) 475.
- [11] A.T.S. Wee, Z.C. Feng, H.H. Hng, K.L. Tan, C.C. Tin, R. Hu, R. Coston, *Appl. Surf. Sci.* 81 (1994) 377.
- [12] G. Beamson, D. Briggs, *High Resolution XPS of Organic Polymers*, Wiley, Chichester, 1992.
- [13] K.L. Gruntz, L. Ley, R.L. Johnson, *Phys. Rev. B* 24 (1981) 2069.
- [14] H. Ibach, *Electron Spectroscopy for Surface Analysis*, Springer, Berlin, 1977, p. 1.

Preferential etching of SiC crystals

R. Yakimova ^{a,b,*}, A.-L. Hylén ^a, M. Tuominen ^{a,b}, M. Syväjärvi ^a, E. Janzén ^a

^a Department of Physics and Measurement Technology, Linköping University, 58183 Linköping, Sweden

^b Outokumpu Semitronic AB, 16111 Bromma, Sweden

Abstract

Preferential etching of 6H and 4H SiC in molten KOH is studied at different temperatures as to the etching rate and defect appearance. The effect of etching time on micropipe related etch-pit size is revealed. Optimal etching conditions are suggested in order to gain information on defect type and distribution. © 1997 Elsevier Science S.A.

Keywords: Chemical; Defects; Etching; Preferential; SiC

1. Introduction

Silicon carbide (SiC) is a very attractive material for semiconductor devices working at extreme conditions. High interatomic bonding energy makes it temperature stable and chemically inert. However, difficulties arise when processing SiC because of its outstanding stability. For instance, SiC cannot be etched in chemical solutions that are commonly used to attack preferentially the conventional semiconductors, for example, Si, GaAs, etc. Etching is especially important for revealing structural imperfections in SiC crystals obtained via the sublimation growth method which is known to result in a rather high density of structural defects. Molten KOH ($T > 450^\circ\text{C}$) is most frequently applied to achieve preferential etching of SiC crystals. A limited number of studies have, however, been reported on the etching process and the effect of the etching conditions on the etch patterns produced. In this work we investigate the etch rate and etch pit appearance of SiC treated by molten KOH at different temperatures.

2. Experimental results and discussion

The SiC samples studied were grown with the seeded sublimation technique at Linköping University, but also some commercially available material grown with a

similar technique was investigated (Cree Research, Durham, NC, USA). Both the Si and C terminated faces of 6H and 4H polytype crystals were examined. The samples were on- or slightly off-axis oriented. Since revealing of structural defects via preferential chemical etching demands flat and smooth surfaces, prior to etching, the samples were mechanically polished sufficiently with 1 μm diamond slurry. The etching was carried out in a conventional high-temperature etching set up with KOH in a temperature range of 480–570°C for 1–20 min. The temperature was measured in the vicinity of the crucible placed in the furnace. The samples were initially examined in an optical microscope with Nomarski-interference contrast in order to acquaint with defect appearance on as-polished surfaces and within the volume of the samples. Most attention was focused on micropipes and other defects exhibiting a hexagonal symmetry of the etch patterns. The former can be followed through the wafer in transmission mode while the latter terminate at different depths from the surface. After KOH-etching, the hexagonal symmetry of the defect shape becomes pronounced on the Si-face, where also a lot of dislocation etch pits were revealed. They appear as small hexagonal (sometimes rounded) and shell-like pits that are believed to be screw dislocations running parallel to the c-axis and slip dislocations in the basal plane intersecting vicinal (0001)Si surface, respectively [1]. Very often these defects are gathered around micropipes, Fig. 1(a and b). It was observed that molten KOH attacks the Si-face and the C-face in different ways, the first one being etched preferentially,

* Corresponding author. Tel.: +46 13 282528; Fax: +46 13 142337; e-mail: roy@ifm.liu.se

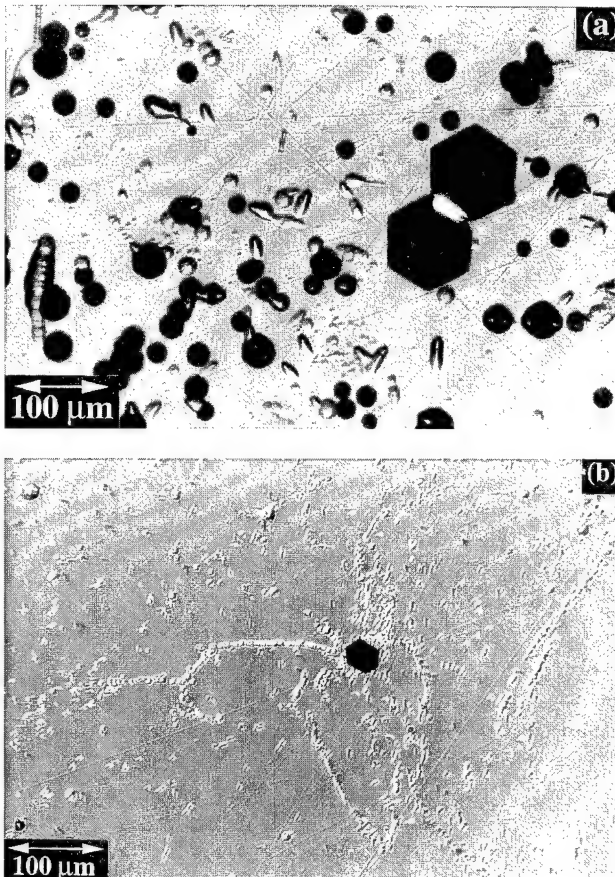


Fig. 1. Defect appearance on Si-face of SiC after etching in molten KOH at 480°C for 5 min: (a) a general view; (b) a micropipe surrounded by dislocations.

whereas the second one is etched isotropically. This suggests different etching rates which can be related to the difference in the surface free energies of the two faces [2]. However, one can still resolve the micropipe outcrop on the C-face but the openings are at least a factor of 10 smaller in size and the shape is round

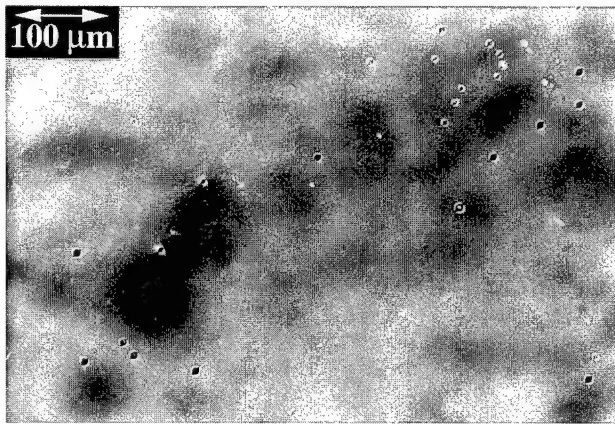


Fig. 2. Defect appearance on C-face (etching conditions as in Fig. 1). The picture is taken in transmission light by focusing on the C-face.

(Fig. 2). This finding is rather interesting as far as micropipe recognition is concerned. The dependence of micropipe related pit-diameter on etching time is shown in Fig. 3. It is linear for the Si-face and sublinear for the C-face, which is due to different mechanisms of pit formation. Similar size dependence for the etch pits on the Si-face has been published in Ref. [3]. It appears that the optimal etching time at 480°C is between 2 and 6 min, depending on the perfection of the crystal. Overetching can cause a merge of neighbouring defects and thus affect the results. On the Si-face we observed three types of hexagonal patterns due to:

- (1) threading micropipes;
- (2) deep (40 μm) and shallow (10 μm) voids; and
- (3) screw dislocations.

Defects of types 1 and 2 have a similar etch pit appearance as to the size (<80 μm), but the type 2 defects have a bottom. For this reason they are believed to be related to micropipes starting and probably stopping at a certain stage of the boule growth. Fig. 4 shows a cross-sectional view of such a striated micropipe. In the insert a top view of the micropipe is seen where the cleavage has been made. Type 3 defects have pointed bottoms and they may be due to screw dislocations. Some times these defects can be followed to the C-face when looking in transmitted light. With increasing temperature the etch pits also become roundish on the Si-face.

The total etch rate (both faces etch) was determined to be ca $2.6 \mu\text{m min}^{-1}$ at 480°C and it is exponentially dependent on the temperature. The weight loss and its temperature dependence was also determined, Fig. 5. It is worth noting that the apparent activation energies of the etching process derived from the Arrhenius plots of these dependencies are quite close, being 12 and 15 kcal mol⁻¹, respectively. These values are much above the energy reported for a diffusion limited etching

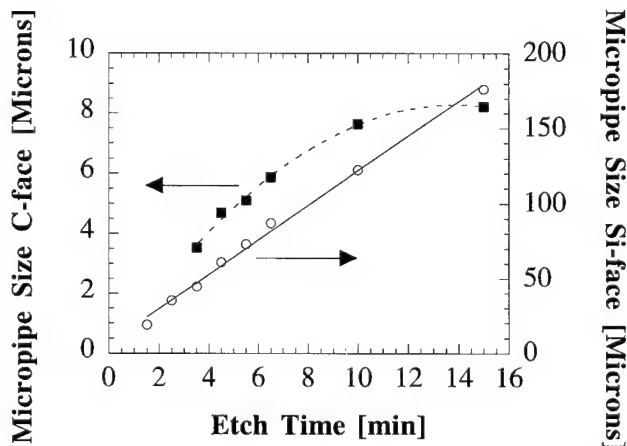


Fig. 3. Micropipe related pit-diameter versus etching time for Si- and C-face.

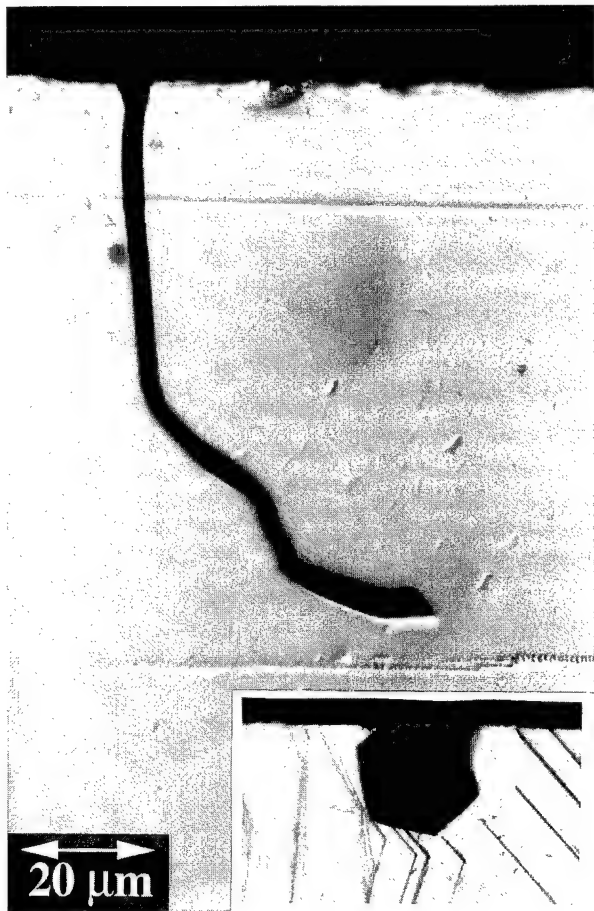


Fig. 4. Cross-sectional view of a striated micropipe; the cleavage is perpendicular to the surface, shown in the insert. The sample is 6H SiC 3.5° off with an epilayer on top.

of compound semiconductors [4], but they are smaller compared to the case of etching SiC in molten salts [5]. No difference was observed when comparing the etching behaviour of 6H and 4H SiC.

3. Conclusion

Preferential etching of SiC in molten KOH can provide information on the type of strain field associated defects. The etch pit size and appearance strongly depend

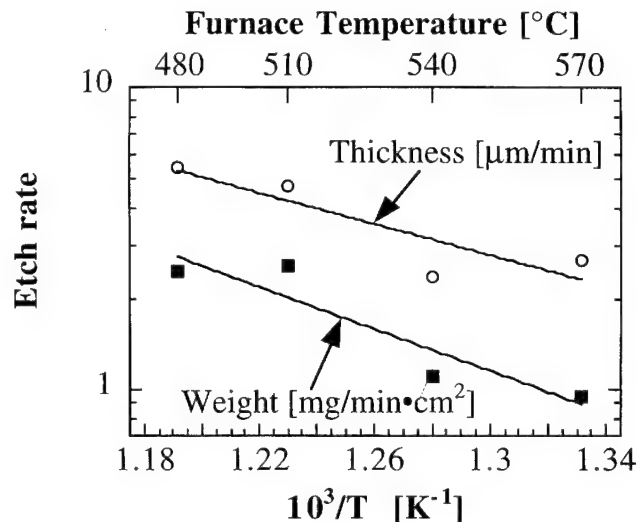


Fig. 5. Temperature dependence of the etch rate evaluated by thickness measurements and weight losses.

on the temperature and etching time. We did not observe etch spirals or hillocks [4]. The etching rate was determined to be ca $2.6 \mu\text{m min}^{-1}$ at 480°C for both cases of side etching. The apparent activation energy of the etching process is suggesting a surface kinetics limited mechanism rather than a diffusion one.

Acknowledgement

This work was financially supported by the Swedish Board for Industrial and Technological Development (NUTEK).

References

- [1] J. Takahashi, M. Kanaya, Y. Fujiwara, *J. Crystal Growth* 135 (1994) 61.
- [2] M. Syväjärvi, R. Yakimova, E. Janzén, *Growth of SiC from liquid phase: wetting and dissolution of SiC*, *Diamond Relat. Mater.* 6 (1997) 1266–1268.
- [3] K. Koga, Y. Fujikawa, Y. Ueda, T. Yamaguchi, *Springer Proc. Phys.* 71 (1992) 96.
- [4] K. Sangwal, *Etching of Crystals: Theory, Experiment and Application*, Elsevier Science B.V., Amsterdam, 1987, p. 260.
- [5] V.J. Jennings, *Mater. Res. Bull.* 4 (1969) 199.

Schottky contact investigation on reactive ion etched 6H α -SiC

G. Constantinidis ^{a,*}, J. Kuzmik ^b, K. Michelakis ^a

^a Foundation for Research and Technology Hellas, P.O. Box 1527, 711 10 Heraklion, Crete, Greece

^b Institute of Electrical Engineering, Slovak Academy of Sciences, Dubravská cesta 9, 842 39 Bratislava, Slovakia

Abstract

Reactive Ion Etching (RIE) was performed on monocrystalline 6H α -SiC samples with CF_4/H_2 -based gas mixtures. Schottky contacts on RIE etched α -SiC were compared with reference Schottky contacts on non-etched α -SiC. © 1997 Elsevier Science S.A.

Keywords: Silicon carbide; Reactive ion etching; Schottky contacts

1. Introduction

Silicon carbide has been attracting considerable attention [1–5] because of its high electron saturation velocity (2.5×10^7 cm/s) and its thermal and chemical stability. These unique physical and electrical properties make SiC a viable material for high power, high frequency and high temperature device applications. Schottky contacts on both α - and β -SiC [2–5] play a key role in devices such as MESFETs and diodes. In the present investigation we report the investigation of Schottky barrier contacts to reactive ion etched (rIE) 6H α -SiC. Schottky contacts on RIE-etched α -SiC were compared with reference Schottky contacts on non-etched α -SiC. The effect of temperature annealing on the properties of the contacts was also investigated.

2. Experimental, results, discussion

The chemical stability of SiC makes device structure patterning difficult. Dry etching remains the main practical technique for SiC removal for device fabrication using conventional photoresist techniques. Reactive Ion Etching (RIE) of SiC is performed with either fluorine-based gases such as CF_4/O_2 , SF_6 , CHF_3/O_2 , CBrF_3 and CCl_2F_2 or chlorine-based gases such as CCl_4/O_2 . RIE of SiC involves both physical and chemical removal processes. It has been shown that residue formation during the etching process can be minimized by

introducing an additive gas such as H_2 to the fluorinated plasmas [6].

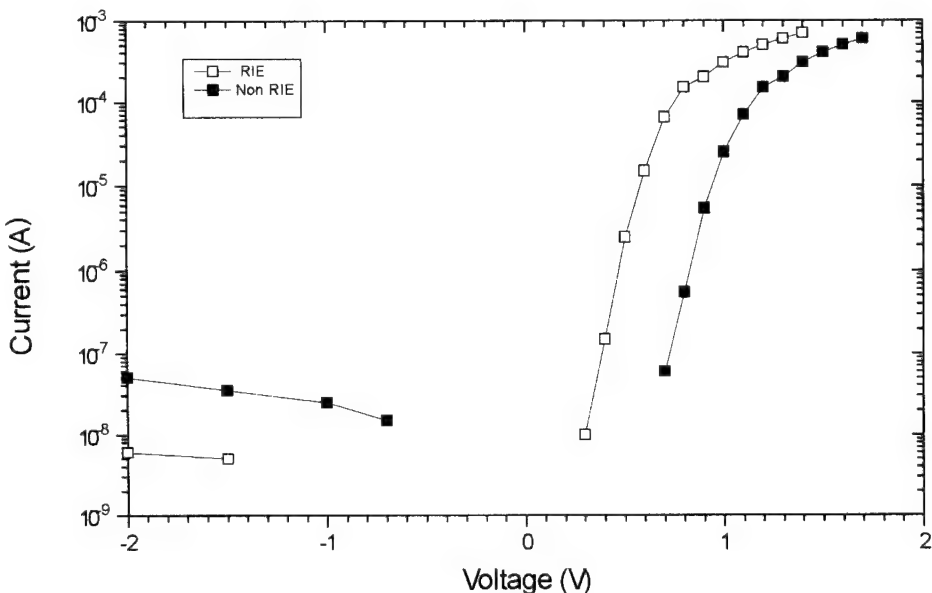
In this investigation the RIE experiment was performed on half the surface (glass mask) of a $10 \mu\text{m}$ thick n-type α -SiC sample in a commercial VPS-1523 dual PECVD/RIE system from Vacutec. The conditions of RIE were: 50 mTorr pressure, 0.29 W/cm^2 plasma power density, 20 sccm of CF_4 and 2 sccm of H_2 flow, respectively. The etching was performed for 10 min and resulted in a very smooth surface and a total etch depth of 150 nm. Then Schottky and ohmic contacts were fabricated on both the RIE-etched, as well as on the non-etched surfaces. The Schottky diode geometry was circular dots, 0.13 mm^2 in area, separated from the ohmic region by an annulus. Pt (50 nm)/Au (200 nm) was the metallization scheme employed for the diodes, while the ohmic contact was Cr (200 nm)/Au (200 nm) (both previously optimized). Both metallizations were fabricated by standard contact photolithography, e-gun evaporation (2×10^{-7} Torr) and lift-off process. Prior to the metallizations, the surface was treated in diluted HF. Rapid thermal annealing (RTA) in argon between 200 and 1000 °C (at 200 °C increments, 10 min duration) was then employed to investigate the behaviour of the diodes. Current–voltage and capacitance–voltage measurements were used for Schottky contact characterization and free carrier density determination. Averages over 5 diodes were taken in each case. Table 1 summarizes the results for the barrier height analysis. Parameters of diodes were calculated according to Ref. [7]. The I – V characteristics of the as-prepared diodes are shown in Fig. 1. Using C – V measurements,

* Corresponding author. Fax: 00 30 81 239735.

Table 1

Barrier height values from $I-V$ and $C-V$ measurements for RIE and non-RIE samples (eV) at various annealing temperatures

RTA Temperature (°C)	Non RIE Φ_b ($I-V$)	RIE Φ_b ($I-V$)	Non RIE Φ_b ($C-V$)	RIE Φ_b ($C-V$)
0	0.96	0.84	1.45	1.10
200	0.94	0.97	1.55	1.45
400	0.98	1.06	1.20	1.75
600	0.92	0.94	—	—
800	1.1	1.04	—	—
1000	1.04	1.14	1.60	2.5

Fig. 1. $I-V$ characteristics of as-prepared Schottky contacts to RIE and non-etched 6H α -SiC.

a free carrier concentration of $7 \times 10^{17} \text{ cm}^{-3}$ and comparable capacitances on both etched and non-etched regions were determined. RIE-related damage due to radiation during the process and plasma-originated species diffusion into SiC is expected to alter the electrical parameters of the material. Zero-biased capacitance (C_0) reflects directly changes in the free carrier concentration near the surface. However, in our investigation there was no substantial difference observed between the C_0 of etched and non-etched samples. Thus, no RIE-related free carrier compensation or passivation effects were observed. The influence of subsequent RTA treatments on the parameters of the diodes is shown in (Fig. 2 and Fig. 3). From the $I-V$ measurements, barrier height $\phi_{b(I-V)}$ dependence on annealing temperature (Fig. 2) exhibits a local maximum at 400 °C with an ideality factor close to the minimum for both etched and non-etched regions. A further increase of $\phi_{b(I-V)}$ was observed for higher annealing temperatures (800, 1000 °C). However, ideality factor evaluation shows contact degradation due to these annealings. This trend correlates with measurement of zero-biased capacitance C_0 dependence shown in Fig. 3. Considerable decrease

of C_0 at 1000 °C RTA was observed, especially for the RIE-treated region. Consequently, the $C-V$ barrier height determination (Fig. 3) led to disagreement with the results of the $I-V$ measurements. This may be explained using a hypothesis similar to Ioannou et al. [4], where from Auger-electron spectroscopy (AES) observations of Schottky contacts on β -SiC, the presence of a thin interfacial layer between the metal and the semiconductor was suggested. Then the ideality factor n and the intercept $\phi_{b(C-V)}$ of the $C^2=f(V)$ plot can be expressed as follows [7]:

$$n = 1 + \epsilon_s / (w(q\sigma D_s + \epsilon_1)), \quad (1)$$

where

 σ is the thickness of the interfacial layer ϵ_1 is the dielectric constant of the interfacial layer ϵ_2 is the dielectric constant of the semiconductor w is the depletion layer width q is the electronic charge D_s is the density of the surface states and

$$\Phi_{b(C-V)} = \Phi_b + \Phi_1, \quad (2)$$

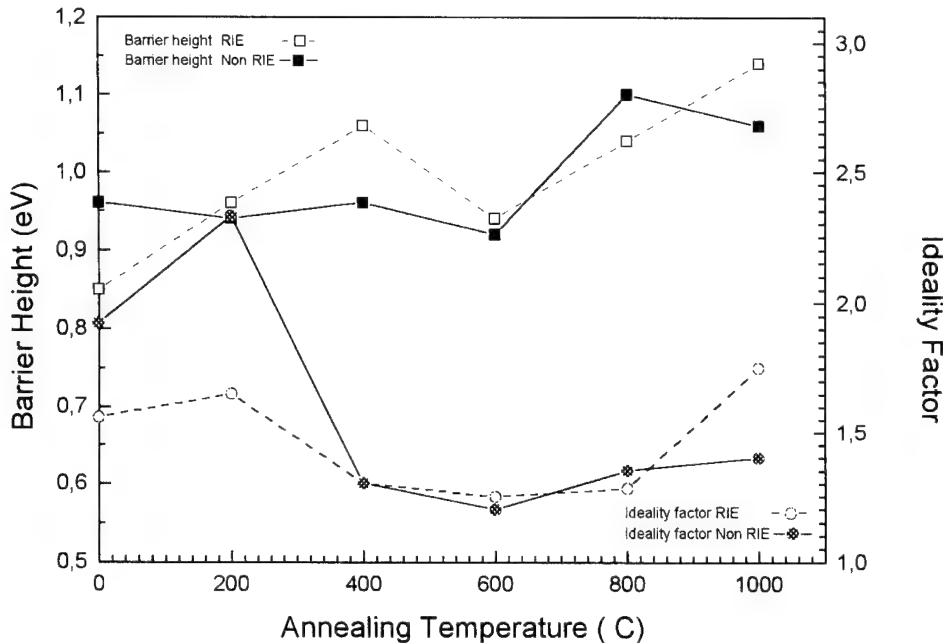


Fig. 2. Ideality factor and barrier height dependence on temperature of annealing, determined from I - V measurements.

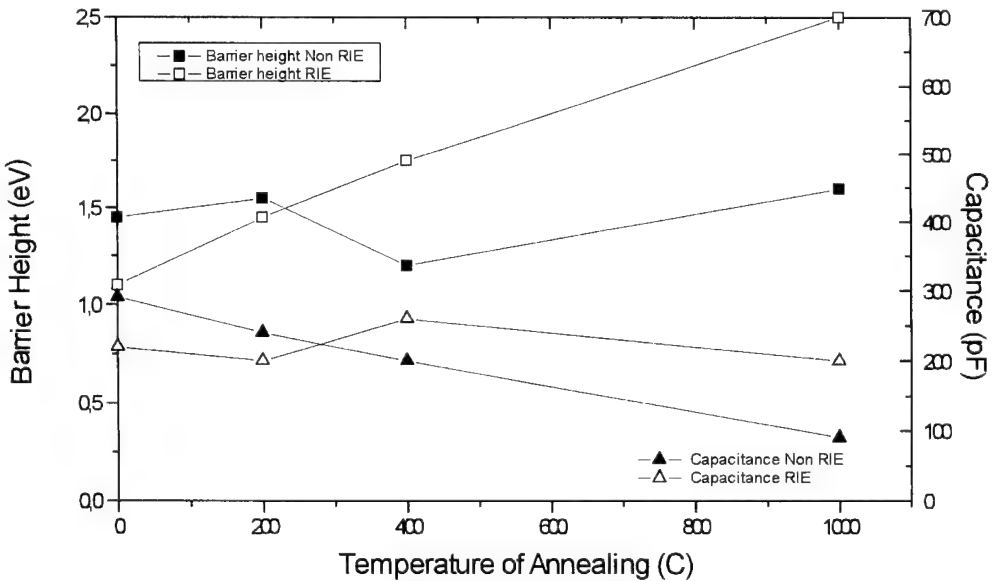


Fig. 3. Zero-biased capacitance and barrier height dependence on temperature of annealing, determined from C - V measurements.

where

$$\Phi_1 = 2\alpha^2 q N_D / \epsilon_s \quad (3)$$

$$\alpha = \sigma \epsilon_s / (\epsilon_1 + q \sigma D_s), \quad (4)$$

where

Φ_1 represents the error of the C - V method in the determination of Φ_b

N_D is the free carrier concentration

Ioannou et al. [4] have observed a strong interdiffusion of species at the metal/ β -SiC interface and an increase

of the interface state density upon RTA annealing. Assuming that similar structural changes occurred in our experiments, an increase of the interface state density could account for the decrease of the ideality factor after RTA at 400 °C (Eq. (1)). On the other hand, this trend may be opposed by the accelerated species interdiffusion and the increase of the interfacial layer after RTA at 1000 °C and can explain the observed changes in n , $\Phi_{b(C-V)}$ and Co (Eqs. (1)–(4)). Our previous AES observation of the RIE-etched surface of β -SiC has revealed the presence of RIE-originated fluorine species. This may

account for the more profound degradation after high-temperature RTA for RIE-based samples.

3. Conclusions

Schottky barrier contacts on RIE-etched 6H α -SiC were investigated. Pt-based diodes after 400 °C/10 min RTA led to the best parameters ($\Phi_{b(I-V)}=0.98$ eV, $n=1.3$) which were comparable to those obtained on reference, non-etched samples. The room temperature barrier height $\Phi_{b(I-V)}$ value of 0.94 eV compares favourably with barrier height values for some other metals [8]. No signs of free carrier compensation or passivation were detected. After high-temperature RTA (1000 °C), degradation of contacts was observed, which was more evident for RIE-treated diodes. The presence of RIE-originated fluorine species on the SiC surface, which may enhance the formation of the thicker metal/semiconductor interfacial layer, could account for it.

Acknowledgement

This work was supported by the CEC Brite–Euram project TECSICA No. 5416.

References

- [1] P.A. Ivanov, V.E. Chelnokov, *Semicond. Sci. Technol.* 7 (1992) 863–880.
- [2] J.R. Waldrop, R.W. Grant, Y.C. Wang, R.F. Davis, *J. Appl. Phys.* 72 (1992) 4757–4760.
- [3] M. Bhatanagar, P.K. McLarty, D.J. Baliga, *IEEE Electron Device Letters* 13 (1992) 501–503.
- [4] D.E. Ioannou, N.A. Papanicolaou, P.E. Norquist, *IEEE Trans. Electron Dev. ED* 34 (1987) 1694–1699.
- [5] N.A. Papanicolaou, A. Christou, L.M. Gipe, *J. Appl. Phys.* 65 (1989) 3526–3530.
- [6] P.H. Yih, V. Saxena, A.J. Steckl, *Inst. Phys. Conf. Ser.* No 142, Chapter 3 (1996) 621–624.
- [7] E.H. Rhoderick, *Metal-Semiconductor Contacts*, Clarendon, Oxford, 1978.
- [8] Y.G. Zhang, X.L. Li, A.Z. Li, A.G. Milnes, *Inst. Phys. Conf. Ser.* No 142, Chapter 4 (1996) 665–668.

Comparative investigation of ECR–RIE patterns on Si and C faces of 6H-SiC using a CF₄/O₂ gas mixture

R. Bonnot ^a, A.L. Syrkin ^{b,*}, G. Lévêque ^c, J.M. Bluet ^b, J. Camassel ^b

^a Atelier de Technologie Microélectronique, UM2 ‘Sciences et Techniques du Languedoc’, 34095 Montpellier, Cedex 5, France

^b Groupe d’Etude des Semiconducteurs, UM2 ‘Sciences et Techniques du Languedoc’ et CNRS, cc074, 34095 Montpellier, Cedex 5, France

^c Laboratoire d’Analyse des Interfaces et de Nanophysique, UM2 ‘Sciences et Techniques du Languedoc’ et CNRS, 34095 Montpellier, Cedex 5, France

Abstract

We report on the relative results of dry etching $\langle 0001 \rangle$ Si-like or $\langle 000\bar{1} \rangle$ C-like oriented faces of bulk natural 6H-SiC Lely crystals. For comparison, a 6H epilayer from Cree Research Inc. was also investigated. In all three cases, the initial and resulting surface morphology has been studied by means of scanning electron and atomic force microscopy. © 1997 Elsevier Science S.A.

Keywords: SiC; RIE; Surface morphology

1. Introduction

Prototype 6H-SiC device technology constantly involves the formation of patterned (mesa) structures on SiC crystal surfaces. To satisfy this requirement, dry etching in a plasma of fluorinated gas species is more appealing. As a consequence, for the last 10 years, many experimental set-up and gas mixtures have been proposed [1–10]. However, in many cases specific problems related to the rough surface of the etched sample have been encountered and no clear technological route has been evidenced.

Recently, we reported on the reactive ion etching (RIE) of 6H-SiC using an electron cyclotron resonance (ECR) plasma and a CF₄/O₂ gas mixture [11]. Good anisotropy and reasonable etch-rate conditions could be found but no detailed investigation of the final (or even initial) surface morphology was done. In this work, we report on the relative results of dry etching either $\langle 0001 \rangle$ Si-like or $\langle 000\bar{1} \rangle$ C-like oriented faces of bulk, natural, 6H-SiC Lely crystals. For comparison, a 6H epilayer from Cree Research Inc. was also investigated. In all three cases, both the initial and resulting surface states have been studied using scanning electron microscopy (SEM) and atomic force microscopy (AFM).

2. Experimental details

We have used a prototype GYGAX 50 reactor, designed by SEMCO Engineering S.A. [12]. The plasma is produced by a 250 W ASTeX compact electron cyclotron resonance (CECR) source operated at 2.45 GHz and diffused downstream into the reactor to the place where the sample has been loaded. The CECR source–sample distance can be adjusted between 10 and 21 cm. A 13.56 MHz r.f. bias is applied to the sample holder.

As already known [13], all ‘natural’ Lely crystals are thin pieces of material already sliced from large single crystals. They have been polished and normally, by naked eye, nothing allows to distinguish the Si from the C face. In this work, such an identification was performed using the following technique. Before processing, the polished crystals were immersed in a molten KOH bath at 550 °C for 30 s. Rinsing in boiling de-ionized water resulted in two different aspects: a uniform polishing–etching of the C face, while small polishing marks still remain on the Si side. Since in both cases similar defects originated from the mechanical polishing treatment, the difference in efficiency and anisotropy of the KOH etching illustrates the difference in chemistry which characterizes the two $\langle 0001 \rangle$ faces. This is the reason why not all defects could be eliminated from the Si side [14].

* Corresponding author.

Table 1

Etch depth and etch rate obtained in this work for different SiC samples. All experimental conditions have been described in the text

	6H-SiC Lely Si-face			6H-SiC Lely C-face	6H-SiC Cree Si-Face
	(a)	(b)	(c)		
Etched depth (μm)	3.1 ± 0.1	3.0 ± 0.1	1.6 ± 0.1	3.2 ± 0.1	3.1 ± 0.1
Etching time (min)	40	40	20	40	40
Etch rate (nm min^{-1})	78 ± 3	75 ± 3	80 ± 5	80 ± 3	78 ± 3

Before loading in the processing chamber, the samples were masked with a 250 nm thick Ni layer deposited by sputtering and patterned using a lift-off lithographic technique. All experiments were carried out using the set of technological parameters defined in [11]: total gas flux 12.5 sccm; ratio of O₂ flux to the total (CF₄+O₂) gas flux 0.4; total pressure 8 mTorr; microwave power 200 W; r.f. power 70 W; ECR source–substrate distance 21 cm. Only the etching time was varied, between 40 and 20 min in the case of Lely samples with Si faces, in order to check for linearity.

After etching the remaining parts of the Ni mask were removed using a HNO₃/CH₃COOH/H₂SO₄ (5:5:2) mixture. The etched depth was then measured using an alpha-step profilometer from TENCOR. Results are listed in Table 1. We have found the following.

(1) Using similar (optimized) etching conditions both the Si and C face of the natural Lely crystals, as well as

the Si face of the epitaxial layer from Cree Research Inc., were etched with identical rates.

(2) The typical value obtained from Table 1 is about 78 nm min⁻¹. This compares well with the result (80 nm min⁻¹) reported in [11].

3. Surface morphology

Clear overviews of the final patterns have been obtained by SEM. A typical example, referring to the Si face of a natural Lely sample, is shown in Fig. 1. Despite the very poor quality of the original mask, it shows clearly that the original geometry was satisfactorily reproduced and that the anisotropy (wall abruptness) appears reasonable. At higher magnification, weak trenching effects manifest and defects appear near the mesa edge. Trenching is a constant problem

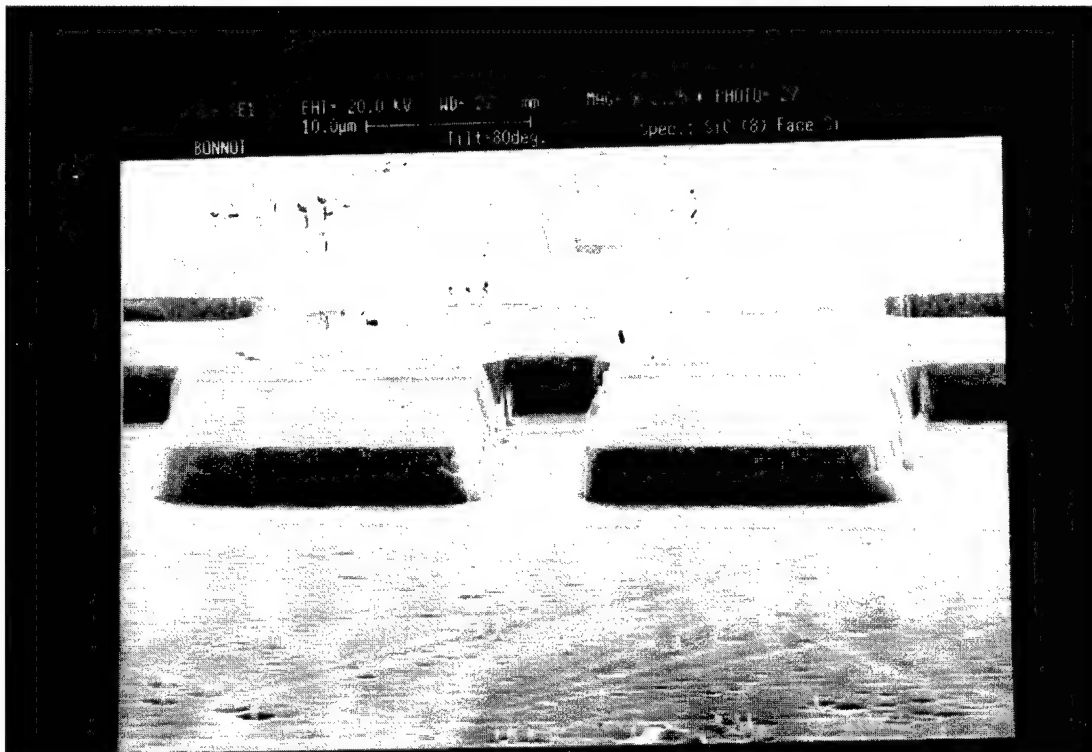


Fig. 1. Patterned Si-face of a natural Lely substrate of 6H-SiC observed by SEM. Magnification is 2250.

Table 2

Summary of RMS roughness obtained in this work by AFM for three different 6H-SiC samples

Sample	Lely C-face	Lely Si-face	CREE Si-face
Surface 25 μm^2	Unetched $2 \pm 0.5 \text{ nm}$	Etched $2 \pm 0.5 \text{ nm}$	Unetched $7 \pm 3 \text{ nm}$
0.5 μm^2	$1.7 \pm 0.2 \text{ nm}$	$1.8 \pm 0.2 \text{ nm}$	Etched $7 \pm 3 \text{ nm}$
		$0.3 \pm 0.1 \text{ nm}$	Unetched $0.5 \pm 0.2 \text{ nm}$
			Etched $0.3 \pm 0.1 \text{ nm}$
			Unetched $0.3 \pm 0.1 \text{ nm}$

with SiC which could not be eliminated up to now. All other effects, which come from mask imperfections and/or defective 'lift off' process, will not be considered further.

One of the most noticeable points is that, in the case of the Lely crystals, the structural difference which separated the initial Si- and C-like faces was well retained

after dry-etching. This is clear from Fig. 1. Because of the difference in surface chemistry already evidenced by the KOH etching, we believe that this evidences (more clearly) a chemical etching mechanism rather than a physical one. This is in very good agreement with the compositional dependence already observed in [11], where changing the O_2 to CF_4 gas ratio from zero to

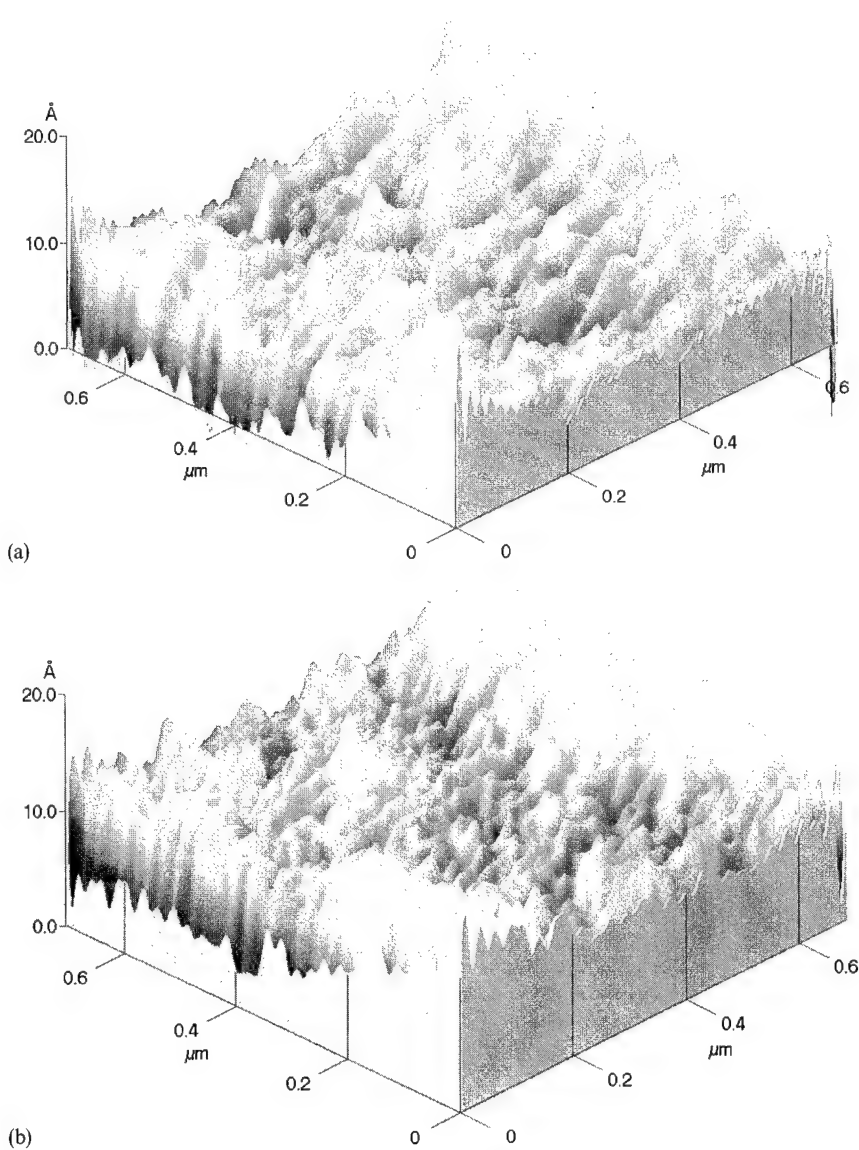


Fig. 2. AFM pictures of a patterned 6H-SiC epitaxial layer from Cree Research Inc: (a) before etching; (b) after dry etching for 40 min. Note that no degradation of the initial surface morphology results from the etching process.

40% increased the rate by a factor of 7. A second interesting point is that, whatever the sample under investigation is, the etched surface appears reasonably free of ‘residues’, ‘grass’ or ‘spikes’. This was not the case in many previous works (see for instance [1–8]).

Using AFM, both the original and final root mean square (RMS) surface roughness could be checked. In many cases we have found that the resulting values differ significantly, depending on the lateral dimensions of the surface under investigation. As a consequence, in Table 2, not only the type of {0001} face and sample under consideration have been indicated but, also, the dimension of the AFM scan. Altogether, this shows the following.

(1) In the case of the C face of the natural Lely crystals, we find almost no difference in the roughness value measured on a $25 \mu\text{m}^2$ or $0.5 \mu\text{m}^2$ scan. It is poor in both cases and falls in the 2 nm range. This is because, at the microscopic level, we find mainly hills and valleys with lateral dimensions of the order of 100 nm. They spread over the complete wafer with a fair uniformity and, whatever is the scan area, no long range perturbation (similar to the series of polishing traces seen in Fig. 1 for a Si face) can be seen.

(2) On the Si-face, the RMS roughness depends strongly on the scan area. In our case, it varied from 7 to 0.3 nm when the AFM scan was reduced from 25 to $0.5 \mu\text{m}^2$. This is because of the presence of large (1 μm wide, 300 Å deep) etch dips. The interesting point is that for smaller scans, i.e. at a more microscopic level, the roughness is much lower than the one observed on the C face.

(3) In both cases of the Si and C faces of the natural Lely crystals, there is almost no change after etching. This means that the process we use is essentially neutral. It does not degrade (or improve) the surface morphology.

(4) Finally, in the case of the epilayer from Cree, we find the results shown in Fig. 2. Quantitatively probing a $25 \mu\text{m}^2$ surface, we find less roughness compared to the one measured on the corresponding Lely material. This is only because less etching dips are found. Indeed, on the $0.5 \mu\text{m}^2$ surface scan both materials appear very similar. After etching, there is again no sizable difference (even if a slight improvement may appear when considering the raw data). Such an effect has not yet been confirmed and would certainly correlate with a finite

difference in microhardness between the two different series of samples.

4. Conclusion

We have shown that one could achieve good anisotropic etching conditions of 6H-SiC using a 60% CF_4 -40% O_2 gas mixture. The typical rate is 78 nm min^{-1} and does not depend on the origin of sample or the type of SiC face under consideration (Si- or C-like). After etching, all surfaces appear mainly defect free, with a typical RMS roughness close to the that of the original material.

References

- [1] I.V. Popov, A.L. Syrkin, V.E. Chelnokov, Sov. Tech. Phys. Lett. 12 (1986) 99.
- [2] P.H. Yih, A.J. Steckl, J. Electrochem. Soc. 142 (1995) 312.
- [3] P.H. Yih, A.J. Steckl, J. Electrochem. Soc. 142 (1995) 2853; also see: P.H. Yih, V. Saxena and A.J. Steckl, Inst. Phys. Conf. Series 142 (1996) 621.
- [4] J.B. Casady, E.D. Luckowski, M. Bozack, D. Sheridan, R.W. Johnson, J.R. Williams, International Conf. on SiC and Related Materials-ICSCRM-95, Kyoto, Japan, 1995 Just. Phys. Conf. Series 142 (1995) 625.
- [5] S. Dohmae, K. Shibahara, S. Nishino, H. Matsunami, Jpn. J. Appl. Phys. 24 (1985) L873.
- [6] J.W. Palmour, R.F. Davis, T.M. Wallett, K.B. Bhasin, J. Vac. Sci. technol. A4 (1986) 590.
- [7] J. Sugiyama, W.-J. Lu, K.C. Cadieu, A.J. Steckl, J. Vac. Sci. technol. B4 (1986) 349.
- [8] R. Padiyath, R.L. Wright, M.I. Chaudhry, S.V. Babu, Appl. Phys. Lett. 58 (1991) 1053.
- [9] J.R. Flemish, K. Xie, J.H. Zhao, Appl. Phys. Lett. 64 (1994) 2315.
- [10] K. Xie, J.R. Flemish, J.H. Zhao, W.R. Buchwald, L. Casas, Appl. Phys. Lett. 67 (1995) 368.
- [11] A.L. Syrkin, J.M. Bluet, J. Camassel, R. Bonnot, Proc. E-MRS spring meeting, Symposium A, High temperature electronics: materials, devices and applications, Strasbourg, 4–7 June 1996, Mater. Sci. and Engng. B 46 (1997) 374–378.
- [12] SEMCO Engineering S.A., 625 rue de la Croix Verte, 34196 MONTPELLIER Cedex 5, France.
- [13] A.L. Syrkin, J.M. Bluet, C. Dezaudier, T. Bretagnon, S. Contreras, J.L. Robert, G. Bastide, J. Camassel, M. Anikin, Inst. Phys. Conf. Series 142 (1996) 189.
- [14] M.M. Anikin, P.A. Ivanov, A.A. Lebedev, S.N. Pytko, A.M. Strel'chuk, A.L. Syrkin, in: Zh.C. Feng (Ed.), Semiconductor Interfaces and Microstructures, World Science, Singapore, 1992, p. 281.

Anisotropic oxidation of silicon carbide

Kai Christiansen^{a,*}, Silke Christiansen^b, Martin Albrecht^b, Horst P. Strunk^b, Reinhard Helbig^a

^a Institute of Applied Physics, University Erlangen–Nürnberg, Staudtstraße 7, A3, D-91058 Erlangen, Germany

^b Institute of Microcharacterization, University Erlangen–Nürnberg, Cauerstraße 6, D-91058 Erlangen, Germany

Abstract

The anisotropy of the thermal oxidation of Silicon Carbide has been investigated. Wet oxidation of a sphere of 6H SiC and dry oxidation of homoepitaxial CVD layers of 4H and 6H SiC were carried out. Afterwards, the oxide thickness and the interfacial structure was analyzed by Rutherford backscattering spectrometry, cross-sectional transmission electron microscopy and high-resolution transmission electron microscopy. After oxidation the sphere showed an impressive image of interference colors in different crystallographic orientations due to different oxide thicknesses. Additional microscopic studies of the oxidized epitaxial layers show a rough interface between SiC and SiO₂. Continuous oxidation of bilayers on a large scale is not observed. © 1997 Elsevier Science S.A.

Keywords: Rutherford backscattering spectrometry; Silicon carbide; Thermal oxidation; Transmission electron microscopy

1. Introduction

Progress in SiC research in recent years has allowed the realization of power electronic devices on SiC. Thermal oxidation is one of the key techniques in processing SiC–metal oxide semiconductor (MOS) structures. A typical class of these devices are U- and V-groove MOS structures. These three-dimensional devices require insulating oxides on faces with crystallographic orientations other than the well investigated Si(0001) and C(0001̄) faces. Therefore a precise knowledge of the oxidation behavior of SiC for different crystallographic planes is necessary, because the breakdown of a MOS device occurs, for example, at the thinnest point of the oxide layer for a study which includes electrical properties (c.f. Ref. [1]). Another important property of an MOS device is the channel mobility. In SiC devices the channel thickness is not more than 50 Å. Thus the interface roughness on the nanometer scale is an important aspect of the oxidation of SiC. In this paper we report oxide thicknesses for various crystallographic orientations as well as transmission electron microscopy (TEM) investigations of the interfacial SiC/SiO₂ structure.

2. Experimental

We used single-crystal material obtained from the modified Lely process for the sphere, and CVD epitaxial layers on Si(0001) and C(0001̄) faces on commercially available (CREE Research Inc.) 4H and 6H substrates. The samples were cleaned by acetone, methanol and a subsequent RCA cleaning process. The sphere was oxidized under wet conditions for 12 h at a temperature of 1100 °C in a gas flow of O₂ saturated with H₂O at 90 °C. The epitaxial layers on the Si face were oxidized under dry conditions for 24 h at a temperature of 1120 °C in a gas flow of O₂, and those on the C face were oxidized for 8 h under the same conditions.

The oxide thicknesses of any orientation of the sphere was determined by Rutherford backscattering spectrometry (RBS). This method allows analysis of the oxide thickness even for curved surfaces, in contrast to other frequently used methods such as ellipsometry or C–V measurements. The RBS measurements were carried out with 2 MeV He⁺ ions on a 2 MV van der Graaff accelerator. The sphere was mounted on a three-axis goniometer and the detector was adjusted under a backscattering angle of $\Phi = 170^\circ$. A detailed description of the experiments has been published elsewhere [2].

The interfacial SiC/SiO₂ structure of the Si(0001) and C(0001̄) faces at 4H and 6H SiC were investigated by cross-sectional transmission electron microscopy

* Corresponding author. Fax: +49 91 31858423;
e-mail: mpap05@rzmail.uni-erlangen.de

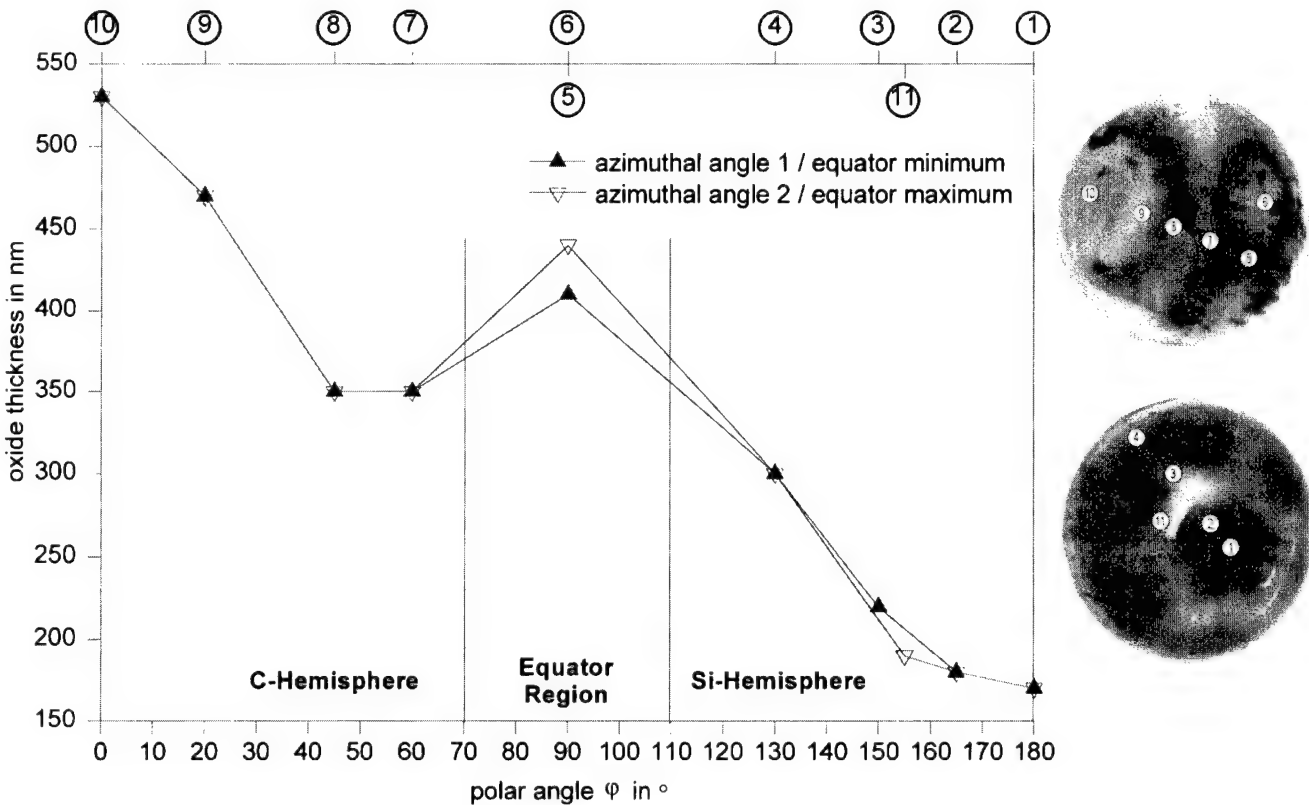


Fig. 1. Oxide thickness versus polar angle for two different azimuthal angles. The different points of the RBS measurement are marked on the optical micrographs of the C hemisphere (with the equatorial region) and the Si hemisphere.

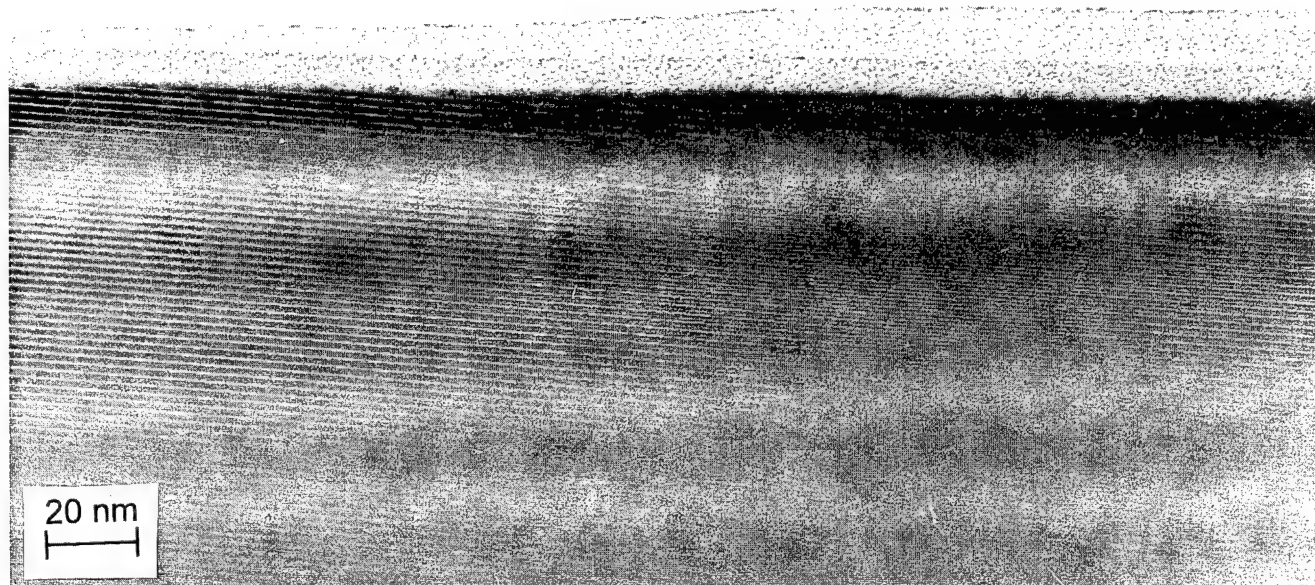
(XTEM) and high-resolution transmission electron microscopy (HRTEM). We used a Philips CM 20 microscope operating at 200 kV for the XTEM studies and a Philips CM 300 UT microscope operating at 300 kV (spherical aberration $C_s = 0.65$ mm, point-to-point resolution 1.72 Å) for the HRTEM studies. The cross-sectional specimens were prepared by conventional mechanical grinding and dimpling, followed by ion milling with Ar^+ to electron transparency in a Gatan Duomill (operating at 4 kV, 1 mA, 13° angle of incidence, nitrogen cooling stage).

3. Results and discussion

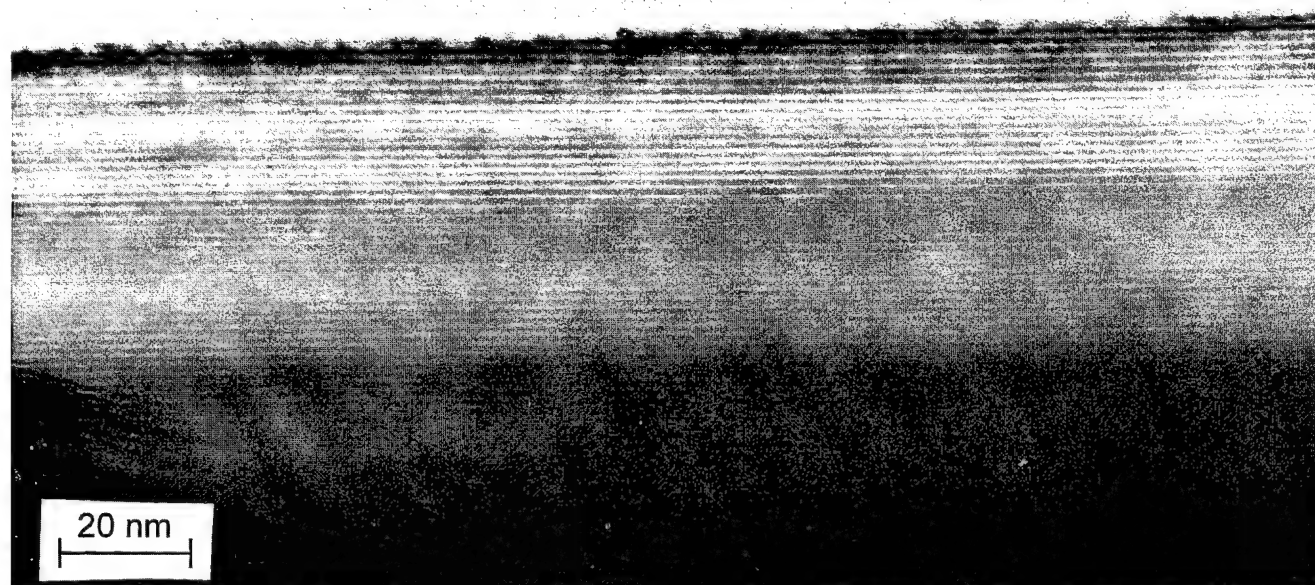
After oxidation the sphere showed a remarkably anisotropic coating with SiO_2 . In analogy to a globe, it is possible to distinguish three different areas on the sphere, i.e. two polar regions and one equatorial zone. From Laue diffraction patterns we could determine the crystallographic orientation of the exposed points of the sphere. The pole with the star-shaped structure can be assigned to the $\text{Si}(0001)$ face and the pole with the concentric contrast rings to the $\text{C}(000\bar{1})$ face. The equatorial zone shows six maxima and six minima in the oxide thickness due to the six-fold symmetry of hexagonal SiC. The maxima correspond to an orientation of

the $(1\bar{1}00)$ type, and the minima correspond to an orientation of the $(11\bar{2}0)$ type. We measured the oxide thickness on several spots of the sphere as a function of the polar angle φ for two different azimuthal angles related to an equatorial maximum and minimum, respectively. The sphere shows decreasing oxide thickness from $\varphi = 0^\circ$ ($\text{C}(000\bar{1})$ pole) to $\varphi = 180^\circ$ ($\text{Si}(0001)$ pole) with an intermediate maximum around $\varphi = 90^\circ$ (c.f. Fig. 1). On the C hemisphere the oxide thickness is independent of the azimuthal angle, while in the equatorial region and on the Si hemisphere a slight difference is observed, dependent on the azimuthal angle. The reason for the different oxidation kinetics are the different activation energies of the oxidation process for the various crystallographic orientations. More detailed discussions of this point have been published elsewhere [2,3].

The interfacial SiC/SiO_2 structure of the 6H samples shows a different behavior for the different crystal faces (c.f. Fig. 2; the undulating oxide surface on both faces is an effect of ion milling). The $\text{C}(000\bar{1})$ face shows a rough interface on the nanometer scale. The roughness can be described as being quasiperiodic, having ripples with an amplitude of about one unit cell of 6H SiC (15 Å) and a wavelength of about 20–60 Å. A continuous oxidation process takes place simultaneously on the whole interface, i.e. the oxidation of Si–C bilayers or in half or full unit-cell steps is not observed. The



(a)



(b)

Fig. 2. XTEM micrographs of the interfacial SiC/SiO_2 structure of a 6H epitaxial layer (3.5° off axis). (a) $\text{Si}(0001)$ face, (b) $\text{C}(0001\bar{1})$ face.

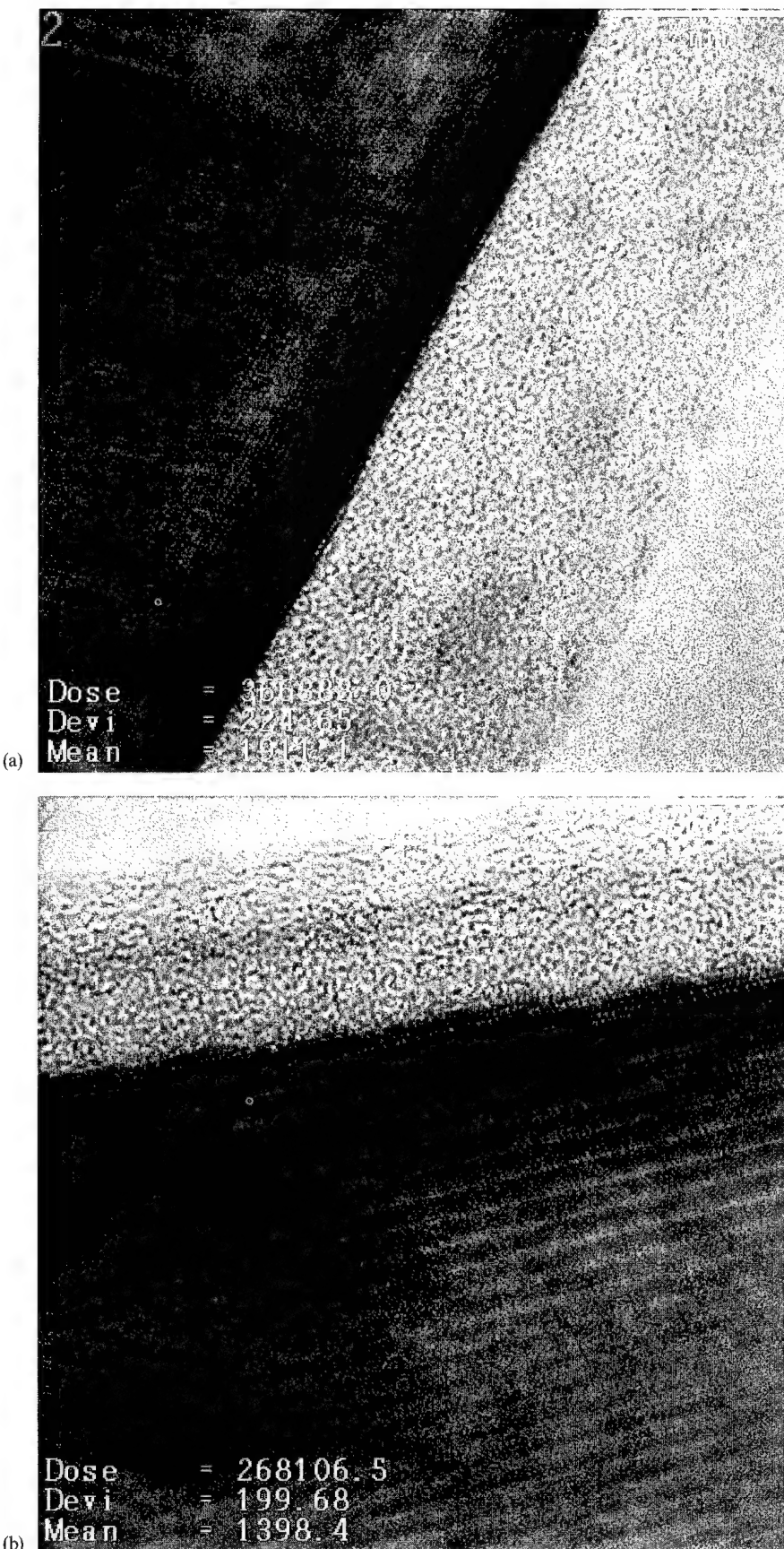


Fig. 3. HRTEM micrographs of the interfacial SiC/SiO₂ structure of a 4H epitaxial layer (3.5° off axis). (a) Si(0001) face, (b) C(000̄1) face.

interface of the Si(0001) face is much smoother, with only a few ripples being visible. However, long-range undulations with a wavelength of some hundred Å and an amplitude of about 10 nm are visible. This property is less distinct on the C(0001̄) face.

In contrast to the 6H samples, the 4H samples exhibit long-range undulation equally on the C and Si faces. The amplitudes and wavelengths of the undulating structures are comparable to those observed on the 6H samples. HRTEM investigations of the SiC/SiO₂ interface (Fig. 3) show distinct interfacial steps on the C and Si faces. A statistical investigation of the step height reveals that essentially half and full unit-cell steps occur and that these are equally represented. The statistic is carried out on an interfacial length of 0.5 μm for each type of specimen.

The occurrence of steps on the surface is a well known and expected process during the growth of epitaxial layers, because of the off-axis orientation of the substrates used in order to avoid defects during epitaxial growth. For the 4H and 6H polytypes it has been reported [4–6] that on the Si face mainly half and full unit-cell steps occur. On the C face single Si–C bilayer steps are observed. In the case of thermal oxidation the reaction on half and full unit-cell steps (i.e. on the hexagonal sites of the unit cell) seems to be most favorable for energetic reasons.

4. Conclusion

The anisotropic oxidation of Silicon Carbide has been investigated. We studied the different oxide thicknesses

on a sphere of 6H SiC. The oxidation rates show an extreme dependence on the crystallographic orientation. The maximum oxidation rate is observed on the C(0001̄) face and the minimum rate on the Si(0001) face. In crystallographic orientations perpendicular to the *c*-axis we observe a structure with six maxima and six minima corresponding to orientations of the (1̄100) and (11̄20) types, respectively.

Additionally, the interfacial SiC/SiO₂ structure of 4H and 6H CVD epitaxial layers on the C and Si faces is investigated. The samples of both polytypes exhibit undulating interfaces on the Si and C faces. On the 4H samples, we observe oxidation in half or full unit-cell steps and on the 6H samples we see ripples with an amplitude of about 15 Å, with a higher density on the C face than on the Si face.

References

- [1] N. Tokura, K. Hara, T. Miyajima, H. Fuma, K. Hara, *Jpn. J. Appl. Phys.* 34 (1995) 5567.
- [2] K. Christiansen, R. Helbig, *J. Appl. Phys.* 79 (1996) 3276.
- [3] K. Ueno, Y. Seki, *Inst. Phys. Conf. Ser.* 142 (1996) 629.
- [4] J. Schardt, C. Bram, S. Müller, U. Starke, K. Heinz, K. Müller, *Surf. Sci.* 389 (1995) 175.
- [5] T. Kimoto, A. Itoh, H. Matsunami, *Inst. Phys. Conf. Ser.* 142 (1996) 241.
- [6] T. Kimoto, A. Itoh, H. Matsunami, *Appl. Phys. Lett.* 66 (1995) 3645.



ELSEVIER

“Carbon cluster model” for electronic states at SiC/SiO₂ interfaces

M. Bassler ^{a,*}, G. Pensl ^a, V. Afanas'ev ^b^a Institute of Applied Physics, University of Erlangen-Nürnberg, Staudtstrasse 7, D-91058 Erlangen, Germany^b KU Leuven, Lab. voor Halfgeleiderfysica, Celestijnenlaan 200D, B-3001 Leuven, Belgium

Abstract

The electronic properties of the SiC/SiO₂ interface are studied for a series of SiC polytypes (3C, 4H, 6H) using various electrical methods and internal photoemission spectroscopy. The energy distribution of states at SiC/SiO₂ interfaces is found to be similar for all the investigated polytypes. The lowest density of states measured at SiC/SiO₂ interfaces is at least one order of magnitude higher than the density of states at Si/SiO₂ interfaces. We have strong indications that this enhancement is caused by residual carbon (graphite-like films, carbon clusters) bonded at the SiC/SiO₂ interface. We propose a “carbon cluster model”, which qualitatively describes the electrical properties of (3C, 4H, 6H)-SiC MOS structures. © 1997 Elsevier Science S.A.

Keywords: SiC/SiO₂-interface; MOS-structure; Density of interface states; Carbon cluster model

1. Introduction

The possibility of growing thermal silicon dioxide (SiO₂) layers on silicon carbide (SiC) is of particular importance in the fabrication of SiC-based MOS devices. However, several groups have recently demonstrated that the density of states at the SiC/SiO₂ interface is higher compared to Si/SiO₂ interfaces [1–5], although the dielectric quality of the SiO₂ layer grown on SiC surfaces is comparable to the quality of SiO₂ layers grown on Si [6]. In this article we determine quantitatively the interface state density of n-/p-type SiC/SiO₂ structures consisting of different SiC polytypes (3C, 4H, 6H) using admittance spectroscopy (AS), constant capacitance-deep level transient spectroscopy (CC-DLTS) and internal photoemission (IPE). Our experiments suggest that carbon is a promising candidate to explain the high interface state density. A “carbon cluster model” is proposed which predicts qualitatively the interface charge of SiC/SiO₂ capacitors for different SiC polytypes.

2. Experimental details

The MOS structures were fabricated by thermal oxidation of Si- (0001) or C-faces (Fig. 1) of different SiC polytypes (3C, 4H, 6H). Prior to oxidation, the SiC samples were exposed to a standard clean (organic

solvents, RCA clean) and for comparison, part of them received in addition an UV-ozone-clean [7].

The oxidation was performed at 1120 °C in dry oxygen for times varying from 2 to 60 h with a post-oxidation anneal in Ar for 1 h at the same temperature. The oxide thickness determined varied from 220 to 2040 Å.

An amorphous hydrogenated carbon (a-C:H) layer with a thickness of 400 Å was deposited on selected MOS structures by plasma-enhanced vapor deposition. The ratio of sp²- and sp³-bonded carbon in these films was varied by changing the substrate bias during deposition. In this way, the optical band gap determined by absorption measurements was varied between 0.7 and 3.0 eV.

In order to monitor the interface states in the band gap of SiC polytypes, we employed admittance spectroscopy (AS, $T=300$ K, $f=100$ Hz to 10 MHz) [8], constant capacitance-deep level transient spectroscopy (CC-DLTS, $T=80$ –700 K, time windows $\Delta t=1$ –64 ms) [9] and internal photoemission spectroscopy (IPE, excitation 150 W Xe discharge lamp) [10].

3. Results and discussion

3.1. Interface state density of different SiC polytypes (3C, 4H, 6H)

Fig. 1 depicts the interface state density of MOS capacitors fabricated on n-/p-type SiC wafers of different SiC

* Corresponding author.

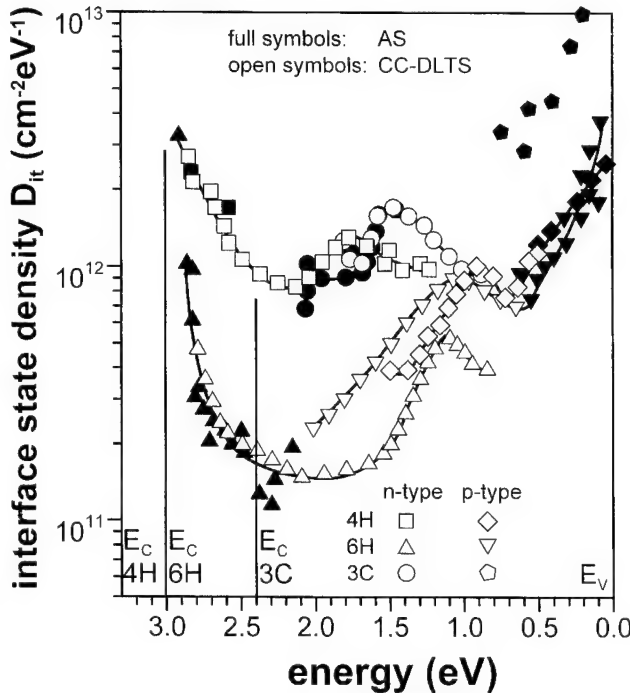


Fig. 1. Energy distribution of interface states for 3C, 4H and 6H SiC as determined from AS (full symbols) and CC-DLTS (open symbols) taken on *p*-type and *n*-type MOS structures.

polytypes (3C, 4H, 6H). Because of the finding in Ref. [11], which revealed that the energy distance between the top of the SiC valence band E_V (SiC) and the bottom of the SiO_2 conduction band E_C (SiO_2) is constant within an accuracy of ± 100 meV for all investigated polytypes (3C, 4H, 6H, 15R: $E_C(\text{SiO}_2) - E_V(\text{SiC}) = 6.0$ eV), we located the zero point of the energy scale at the top of the SiC valence band. Further, we assumed that the applied analysis techniques (CC-DLTS, AS) provides the total density of interface states with a given emission time constant and that there is a clear relation between the emission time constant and the energy position of interface states. The distribution of interface states is qualitatively similar for the investigated polytypes. D_{it} increases towards the band edges $E_V(\text{SiC})$ and $E_C(\text{SiO}_2)$ and reaches a minimum at 2 eV above the valence band; the lowest value of D_{it} is measured for the 6H polytype (approx. $10^{11} \text{ cm}^{-2} \text{ eV}^{-1}$). A particular feature is observed about 1.5 eV above $E_V(\text{SiC})$; there, an increase in D_{it} takes place for all the investigated SiC polytypes independent of the dopant species or doping level. This general observation, and the fact that there is an enhancement of interface states in comparison with the Si/SiO_2 interface by at least one order of magnitude, indicates that a particular defect species is introduced at the SiC/SiO_2 interface.

3.2. Carbon — a candidate for interface states

Several experimental observations favor carbon as a candidate for the enhancement of the density of states

at SiC/SiO_2 interfaces. The carbon may be either present at the surface prior to the oxidation and/or be generated at the SiC/SiO_2 interface during the oxidation process.

As demonstrated in Ref. [7], an UV–ozone-clean of the SiC surface prior to oxidation reduces the density of SiC/SiO_2 interface states in contrast to a standard clean (HF, RCA), which does not remove carbon atoms at the SiC surface.

Also oxidation of a C-face results in a higher density of interface states than the oxidation of a Si-face as demonstrated by the IPE spectra shown in Fig. 2. The photon energy in IPE spectra is, opposite to the energy density of interface states, related to the lower band edge of the SiO_2 conduction band. The threshold ϕ_2 indicating a steep increase of the interface state density (see Fig. 1) is identical for both faces, however, the IPE signal given by the cubic root of the yield, and implying the integral over the interface states, increases more steeply for the C-face than for the Si-face sample.

Angular resolved photoelectron spectroscopy investigations (ARXPS) conducted by Hornetz et al. [12] give evidence for the enrichment of carbon at the interface during the oxidation process. These authors describe the formation of a thin interface oxide layer composed of $\text{Si}_4\text{C}_{4-x}\text{O}_2$ ($X < 2$), which increases with the growing oxide thickness. Our IPE investigations on MOS structures with different oxide thickness confirm this finding. The slope of IPE curves for photon energies greater

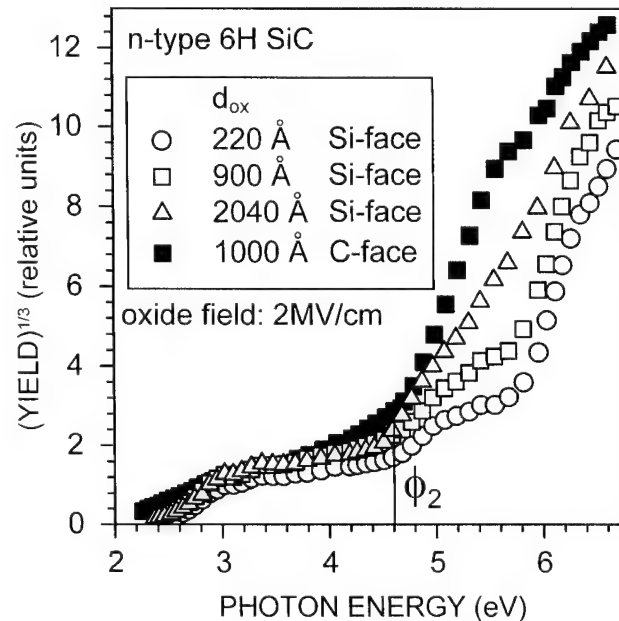


Fig. 2. Spectral curves of IPE from the interface of an *n*-type 6H SiC structure for an oxide field of 2 MV/cm; parameters are the oxide thickness and the polarity: 220 Å (0001) (open circles), 900 Å (0001) (open squares), 2040 Å (0001) (open triangles) and 1000 Å (0001) (filled squares).

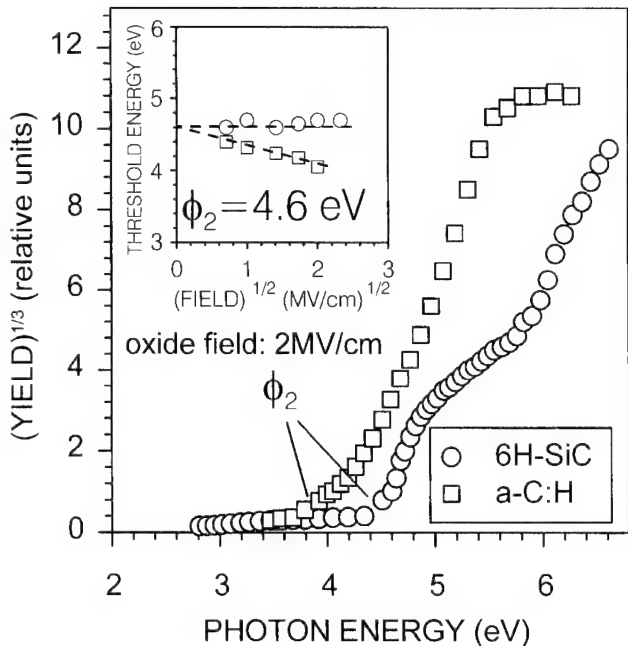


Fig. 3. Spectral curve of IPE from the interface of an *n*-type Si-face 6H SiC/SiO₂ structure (circles) compared with the IPE signal from an a-C:H film deposited on the SiO₂ layer (squares). The inset shows the threshold energy ϕ_2 versus the square root of the applied electric field.

than the threshold for interface states, ϕ_2 increases with growing oxide thickness d_{ox} , as shown in Fig. 2.

A further indication for the presence of carbon at the SiC/SiO₂ interface is demonstrated in Fig. 3. The figure depicts two IPE curves; one taken on a 6H SiC MOS capacitor (open circles) and the second one taken on an a-C:H film (open squares) deposited on the SiO₂ layer of a MOS capacitor; the structure of the a-C:H layer is composed of sp²- and sp³-bonds in such way that its band gap energy is equal to 3 eV. To measure the carbon film related IPE curve, the sign of the bias voltage is inverted [7]. The inset in Fig. 3 shows the threshold ϕ_2 for different electric fields; the value of ϕ_2 extrapolated to zero field is identical for both curves, giving the same electron binding energy of 4.6 eV.

Comparison of both IPE curves shows that the emission from the valence band states of the a-C:H layer arise at the same photon energy as the increase in the IPE signal caused by interface states of the 6H SiC MOS capacitor (see also Ref. [11]). This is a strong hint that the interface states in SiC MOS capacitors (see also the feature at 1.5 eV in Fig. 1) may originate from carbon present at the interface as sp²-bonded carbon clusters. Depending on the size of the clusters they may have a wide band gap, or provide a graphite-like electronic spectrum [13].

3.3. "Carbon cluster model"

Our experimental findings can be sufficiently explained by our proposed "carbon cluster model", which is shown schematically in Fig. 4.

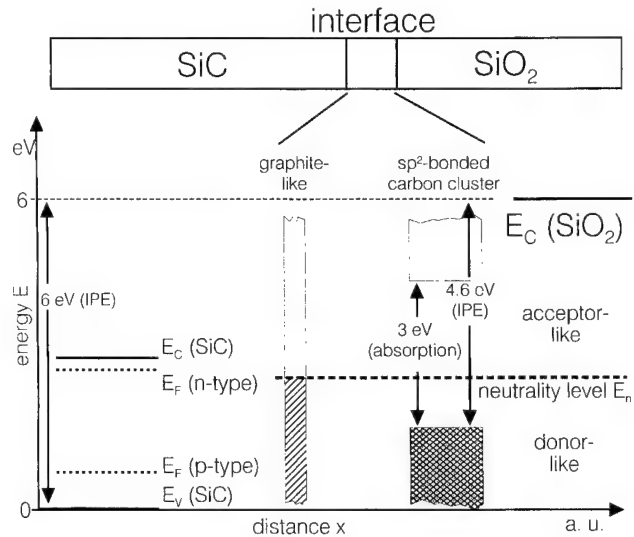


Fig. 4. "Carbon cluster model" for interface states at the SiC/SiO₂ system. The interface states are governed by wide band gap carbon (in our case $E_{gap}=3$ eV) and/or graphite-like carbon clusters.

In the framework of our model, we admit graphite-like films (providing no band gap) and sp²-bonded carbon clusters with a band gap determined by their size ($E_{gap}(\text{cluster})=6/M^{1/2}$ [13], where $M=\text{number of } 6\text{-fold rings in the cluster}$) at the SiC/SiO₂ interface. Thus a graphite layer with, for example, a band gap of 3 eV, as demonstrated in Fig. 3, would on average consist of clusters with 4 rings. We introduce a neutrality level E_n at the interface, which governs the exchange of electrons between the SiC bulk, electrically characterized by the Fermi level E_F , and the interface (E_n). For $E_F > E_n$, electrons will flow from the SiC bulk to the interface and will negatively charge interface states with $E > E_n$ (acceptor-like states); for $E_F < E_n$, electrons will flow from the interface into the SiC bulk and positively charge states with $E < E_n$ (donor-like states). The energy position of the neutrality level E_n can be estimated independently from CV-measurement or from the position of the Fermi level in graphite [14]; its position is estimated to be about 3.5 eV below the SiO₂ conduction band edge.

4. Summary

We proposed a "carbon cluster model" which qualitatively accounts for the observed interface state distribution of SiC/SiO₂ structures. Carbon in form of graphite-like and/or sp²-bonded clusters is a perfect candidate to describe the measured interface states.

Acknowledgement

The authors are grateful to the Deutsche Forschungsgemeinschaft (SFB 292) and the

Bundesministerium für Bildung, Wissenschaft, Forschung und Technologie (BMBF) for support of this work.

References

- [1] T. Billon, E. Bano, L. DiCioccio, T. Ouisse, P. Lassagne, C. Jausand, *Microelect. Eng.* 28 (1995) 193.
- [2] E. Stein von Kamienski, F. Portheine, A. Göltz, H. Kurz, *Inst. Phys. Conf. Series* 142 (1996) 641.
- [3] P. Friedrichs, E.P. Burte, R. Schörner, *J. Appl. Phys.* 79 (1996) 7814.
- [4] L.A. Lipkin, J. Palmour, *J. Elect. Mater.* 25 (1996).
- [5] J.N. Shenoy, J.A. Cooper Jr., M.R. Melloch, *Appl. Phys. Lett.* 68 (1996) 803.
- [6] P. Friedrichs, E.P. Burte, R. Schörner, *Appl. Phys. Lett.* 65 (1994) 1665.
- [7] V.V. Afanas'ev, A. Stesmans, M. Bassler, G. Pensl, M. Schulz, C.I. Harris, *Appl. Phys. Lett.* 68 (1996) 2141.
- [8] E.H. Nicollian, A. Goetzberger, *Bell Systems Technol. J.* 46 (1966) 1055.
- [9] M. Schulz, E. Klausmann, *J. Appl. Phys.* 18 (1979) 169.
- [10] V.K. Adamchuk, V.V. Afanas'ev, *Prog. Surf. Sci.* 41 (1992) 109.
- [11] V.V. Afanas'ev, M. Bassler, G. Pensl, M. Schulz, *J. Appl. Phys.* 79 (1996) 3108.
- [12] B. Hornetz, H.-J. Michel, J. Halbritter, *J. Mater. Res.* 9 (1994) 3088.
- [13] J. Robertson, *J. Non-Cryst. Solids* 137/138 (1991) 825.
- [14] M. de Seta, P. Fiorini, F. Coppola, F. Evangelisti, *J. Non-Cryst. Solids* 137/138 (1991) 867.

Investigation of walk-out phenomena in SiC mesa diodes with $\text{SiO}_2/\text{Si}_3\text{N}_4$ passivation

Zoran Ovuka *, Mietek Bakowski

Industrial Microelectronics Center, P. O. Box 1084, S-164 21 Kista, Sweden

Abstract

The drift or “walk-out” of the breakdown voltage in 6H-SiC mesa diodes passivated by a double layer of 1000 Å SiO_2 and 3000 Å Si_3N_4 was investigated. The drift characteristics of diodes having wet and dry oxide passivation were compared to each other and to diodes subjected to additional hydrogen plasma etching of the SiC surface prior to dry oxidation. The influence of the UV illumination supplied by a HeCd laser of wavelength 325 nm on the walk-out characteristics and on the reverse current was investigated. No significant differences in the amount of drift and saturation level of breakdown voltage was found between the different passivations. However, the saturation level was reached about one order of magnitude faster in the wet oxide. A significant difference was found in the level and time dependence of the reverse current under UV illumination between the wet and dry oxide passivated diodes. The results are consistent with the existence of large concentrations of positive charge and acceptor-type deep interface traps. The walk-out is the result of the acceptor states being filled by hot electrons through the mechanism of avalanche injection. © 1997 Elsevier Science S.A.

Keywords: Walk-out; Mesa diodes; Drift; Oxide passivation

1. Introduction

The high critical electric field of SiC, one order of magnitude higher than for Si, makes it an interesting material for high voltage devices. The realisation of reliable junction termination therefore becomes an issue of particular importance. To date, the same passivation schemes as for silicon are most readily available for SiC devices. Instabilities related to the charge injection and trapping pose a much more serious problem in the case of the SiC/ SiO_2 system due to higher electric fields and lower energy barriers between semiconductor and insulator for both electrons and holes. In order to realise SiC devices using the natural passivants like SiO_2 it is necessary to reduce the electric field at the surface to values comparable to those of Si devices and to improve understanding of the SiC/ SiO_2 system with respect to charge trapping in the interface states and in the interface and bulk traps. One fundamental instability is the frequently observed drift of the breakdown voltage caused by redistribution of the surface charges. This so called walk-out phenomenon can be measured by applying a

constant reverse current and recording the increase of the breakdown voltage as a function of time.

2. Experimental procedures

The diodes were made on Cree p⁺n-n⁺ wafers with doping concentrations of $9 \times 10^{18} \text{ cm}^{-3}$, $6.5 \times 10^{15} \text{ cm}^{-3}$ and $1.5 \times 10^{18} \text{ cm}^{-3}$, respectively. The thicknesses of the epitaxial layers are given in Fig. 1. The walk-out was measured, using a Keithley SMU 237 unit, for

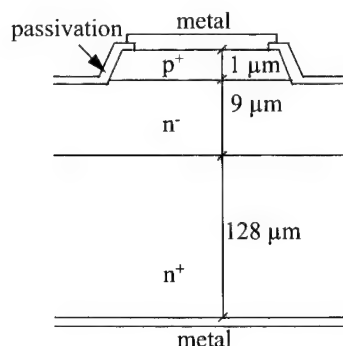


Fig. 1. Cross-section of a mesa diode.

* Corresponding author.

different values of the reverse current as a function of time. In many cases the reverse voltage drift was recorded for up to 10 h. The drift of the reverse voltage and evolution of the reverse current were also measured under DC stress conditions with 400 V applied reverse voltage. Finally the relaxation of the breakdown voltage was measured at room temperature and with zero applied bias on the diodes freshly charged during the walk-out measurements. The measurements were done both with and without UV illumination in order to investigate the influence of the UV on the walk-out phenomena. The UV source was a HeCd laser of wavelength 325 nm. The dry oxide was grown at 1250 °C for a period of 4 h and the wet oxide at 1150 °C for 8 h. A 1 h postoxidation anneal in N₂ at the oxidation temperature was used in both cases. One wafer was subjected to hydrogen plasma etching at 1600 °C for 1 h followed by a 1 h anneal at 1250 °C in Ar prior to dry oxidation.

3. Results

Typical results of walk-out measurements at 2 μA reverse current are shown in Fig. 2. The walk-out saturates faster in the wet oxide. The saturation level is, however, independent of the type of the oxide. Note the relative insensitivity of the walk-out to the UV exposure.

The results of the DC storage measurements at 400 V reverse bias under UV illumination are shown in Fig. 3. Note the dramatic difference in the behaviour of the reverse current between dry and wet oxide.

The results of discharge measurements with and without UV illumination are shown in Fig. 4. There is no significant relaxation of the breakdown voltage shift, in particular the breakdown voltage stays constant in the presence of UV. Without UV some initial relaxation of about 50 V is observed.

4. Discussion

The breakdown voltage drift (walk-out) is very pronounced in SiC mesa diodes [1]. We attribute this to the trapping of hot electrons in the deep acceptor type interface traps. The hot electrons are supplied through the process of avalanche injection [2], which is expected to be more pronounced in SiC as compared to Si. The energy barrier between 6H-SiC and the oxide conduction bands is about 0.25 eV smaller than in the case of Si while the electric field in the interface region is one order of magnitude higher [1,3]. A charge injection process originates close to the edge of the mesa and propagates outwards following the spreading of the space charge due to the new effective charge state of the surface. The oxidised surface is originally positively charged due to the fixed positive charge in the oxide [3]. This charge is gradually compensated by the negative charge due to trapped electrons. No significant differences are observed in that respect between wet and dry oxides. The charge trapping kinetics, as reflected in the time dependence of the reverse voltage drift, differs between the wet and dry oxides. The concentration of the acceptor states, however, as reflected in the saturation level, is comparable. The charge trapped in acceptor states seems to be rather stable and no thermal discharge is observed at temperatures below 250 °C.

A significant difference between wet and dry oxide is observed in the behaviour of the reverse current under UV illumination. The reverse current is about one order of magnitude larger in the wet oxide. Furthermore, it rises with time during DC storage in the wet oxide while it decreases in the case of the dry oxide. The reverse current is determined by the surface generation current and the UV induced photocurrent. Let us assume that the photocurrent responsible for the increase of reverse current in the wet oxide case. This is consistent with the expansion of the space charge region along the surface increasing the carrier generation volume. The possible role of the fast interface states is at the same time

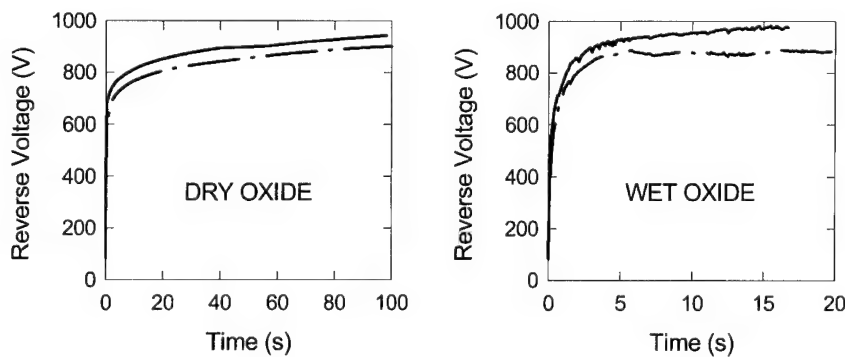


Fig. 2. Walk-out of the breakdown voltage, without (solid line) and with UV illumination (dash-dot line) for dry and wet oxide.

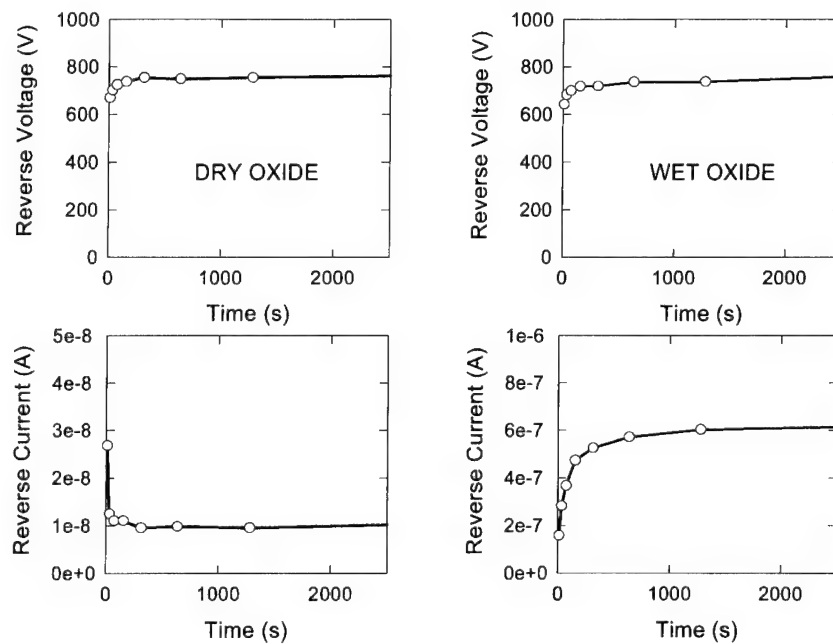


Fig. 3. Evolution of the breakdown voltage and reverse current during DC storage under UV illumination.

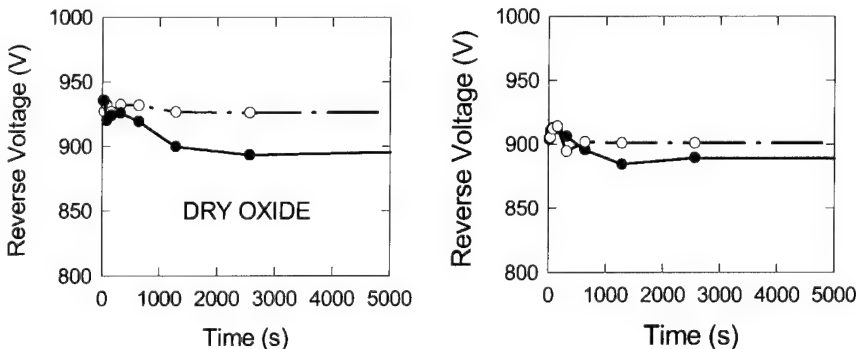


Fig. 4. Relaxation of the breakdown voltage during zero voltage storage at room temperature, with (dash-dot line), and without (solid line) UV illumination.

neglected since their concentration is about one order of magnitude lower in the wet oxide as compared to the dry [4]. This reasoning would be in agreement with OBIC results [5,6]. However, the expansion of the space charge region is equivalent with negative charge build-up and with further increase of the breakdown voltage which is not observed, as can be seen in Fig. 3. An alternative explanation is that the increase in the reverse current is determined by the surface generation component of the current. The reason for this is the increase in surface states concentration at the SiC and wet SiO_2 interface due to trapping of UV-generated holes and dissociation of the SiH bonds (hydrogen depassivation) [7]. This is not observed in the case of dry oxide due to the low concentration of water-related SiH groups.

Interestingly, the walk-out was not affected by UV illumination regardless of the type of the oxide. This

suggests that no generation of the deep acceptor-type states by the UV irradiation is taking place.

5. Conclusions

Trapping of hot electrons supplied by a process of avalanche multiplication is suggested as being responsible for the walk-out of the breakdown voltage in 6H-SiC mesa diodes with wet and dry oxide passivation. The breakdown voltage increases as the fixed positive oxide charge is gradually compensated by the negative charge of electrons trapped in the deep acceptor-type interface traps.

The concentration of the acceptor states is similar in both wet and dry oxide but charging of the wet oxide is one order of magnitude faster.

The largest difference between wet and dry oxide is found in the behaviour of the reverse current under UV illumination. The reverse current is more than 10 times larger in the wet oxide. It also increases with time while the reverse current in the dry oxide decreases and stabilises rapidly at a low level. The generation and annihilation of fast interface states at the SiC/SiO₂ interface involving charge trapping and hydrogen species are believed to be responsible for the observed difference in reverse current behaviour.

Acknowledgement

Chris Harris and Susan Savage of Silicon Carbide Electronics Group at IMC are acknowledged for designing the oxidation experiments and providing the samples. Andrey O. Konstantinov is acknowledged for

his assistance with UV experiments. This work was funded by the Swedish Board of Technical and Industrial Development, NUTEK.

References

- [1] S.M. Savage, L.P. Ramberg, B. Kronlund, K. Bergman, Proceedings of the ESSDERC94, 1994, pp. 753–756.
- [2] E.H. Nicollian, A. Goetzberger, C.N. Berglund, *Appl. Phys. Lett.* 15 (1969) 174–177.
- [3] M. Jargelius, U. Gustafsson, M. Bakowski, Proceedings of the ESSDERC96, 1996, pp. 579–582.
- [4] L.A. Lipkin, J.W. Palmour, *J. Elect. Mater.* 25 (1996) 909–915.
- [5] K. Rottner et al., Proceedings of the International Conference on Silicon Carbide and Related Materials 1995, Institute of Physics Conference Series No. 142, 1995, pp. 721–724.
- [6] K. Rottner, A. Schöner, M. Frischholz, R. Helbig, Proceedings of the MRS Spring Meeting 1996, Symposium E, 423, (accepted).
- [7] C.M. Svensson, in: S.T. Pantelides (Ed.), *The Physics of SiO₂ and Its Interfaces*, Yorktown Heights, New York, 1978, pp. 328–332.

Overview of SiC power electronics

V.E. Chelnokov^{a,*}, A.L. Syrkin^b, V.A. Dmitriev^{a,c}

^a *A.F. Ioffe Institute, Russian Academy of Science, St. Petersburg, 194021, Russia*

^b *University Montpellier II, Montpellier, Cedex 5, 34095, France*

^c *MSRCE, School of Engineering, Howard University, Washington, DC 20059, USA*

Abstract

This paper reviews the status of silicon carbide power electronics. Results on SiC high voltage rectifiers and thyristors are summarized. Current issues in silicon carbide power devices are discussed, including the small device area and high base region resistance of the devices. It is shown that micropipes are not the defects that limit SiC device area. It is some other defects which cause a premature breakdown. To overcome these problems, liquid phase epitaxial growth for high power SiC devices is proposed.

© 1997 Elsevier Science S.A.

Keywords: Silicon carbide; Power semiconductor devices; Liquid phase epitaxy

1. Introduction

Silicon carbide (SiC) has been considered as the premier material for high power semiconductor electronics for a long time [1]. It was predicted [2,3] that, due to fundamental material parameters, SiC devices would have a higher breakdown voltage (at the same doping level) and would operate at a higher forward current density than Si devices. Recently, because of significant progress in SiC technology, these predictions have become reality. SiC rectifiers with blocking voltages of a few kilovolts, and devices operating at a forward current density of up to 1 kA cm^{-2} , have been fabricated. However, the switching power (the product of blocking voltage and forward current) of SiC devices is still much smaller than that of Si devices. In this paper, we analyze the factors which currently limit the power performance of SiC devices.

2. Recent results on SiC power electronics

Recently, significant progress has been achieved on high voltage silicon carbide devices [4]. 4H-SiC Schottky diodes with reverse voltages of over 1 kV have been reported [5]. Barriers were formed on a 4H-SiC homoepitaxial layer grown by chemical vapor deposition (CVD).

The donor concentration and thickness of the layer were $(3\text{--}20) \times 10^{15} \text{ cm}^{-3}$ and $\sim 10 \mu\text{m}$, respectively. The edge termination was made by B^+ ion implantation. The barriers were formed by vacuum evaporation of metals (Au, Ni, and Ti). The Ti/4H-SiC barrier showed a 1750 V blocking voltage and a forward current density, j_f , of 400 A cm^{-2} at 2 V voltage drop. “Specific on-resistance” for this device was $5 \times 10^{-3} \Omega \text{ cm}^2$.

6H-SiC high voltage p-n diodes have been fabricated using CVD techniques [6]. In these devices a 6H-SiC 45 μm thick low-doped layer was grown on an n⁺-SiC substrate followed by a 1.5 μm thick p⁺-layer. Mesa diodes of 160 μm diameter (device area, $A = 2 \times 10^{-4} \text{ cm}^2$) were formed. The maximum reverse voltage for the device exceeded 4.5 kV. The forward current density for these diodes was about 100 A cm^{-2} (forward current, $I_f = 0.02 \text{ A}$) at a voltage drop, V_f , of 6 V, and the corresponding switching power was 90 W.

A 6H-SiC p-n diode with a 2.2 kV breakdown has been reported [7]. The structure, grown by CVD, consisted of n⁻-layer ($N_d \sim 2\text{--}5 \times 10^{15} \text{ cm}^{-3}$, $\sim 24 \mu\text{m}$) and p⁺-layer ($N_a > 10^{18} \text{ cm}^{-3}$, 1 μm). For the device with a mesa area of $4 \times 10^{-4} \text{ cm}^2$, the forward current density was $\sim 1 \text{ A cm}^2$ ($I_f \sim 4 \times 10^{-4} \text{ A}$) at a 3.5 V voltage drop, and the corresponding switching power was $\sim 0.9 \text{ W}$. “Specific on-resistance” for this device was around $0.3 \Omega \text{ cm}^2$.

A 4H-SiC p-n diode ($A = 1.46 \times 10^{-3} \text{ cm}^2$) with a blocking voltage of 1130 V has been realized [8].

* Corresponding author.

The electric breakdown field, E_m , for the diode was $\sim 2 \text{ MV cm}^{-1}$. A forward current of 100 mA ($j_f = 68 \text{ A cm}^{-2}$) was obtained at a V_f of 3.6 V. The corresponding switching power was 113 W. This device had a “specific on-resistance” of $\sim 1 \times 10^{-2} \Omega \text{ cm}^2$.

A 6H-SiC p-n diode was made by sublimation epitaxy on Lely substrate [9]. The blocking voltage was up to 500 V ($E_m \sim 4.5 \text{ MV cm}^{-1}$), and the forward current $\sim 1 \text{ A}$ ($j_f = 1000 \text{ A cm}^{-2}$, $V_f \sim 4.5 \text{ V}$). The switching power was $\sim 500 \text{ W}$. The “specific on-resistance” increased from 1.5×10^{-3} to $1 \times 10^{-2} \Omega \text{ cm}^2$ when the device area increased from 7×10^{-4} to $2 \times 10^{-2} \text{ cm}^2$. Sublimation epitaxy and subsequent ion implantation was employed to fabricate a p-n junction. This diode exhibited a blocking voltage of 220 V ($E_m \sim 3 \text{ MV cm}^{-1}$) and a forward current of $\sim 1 \text{ A}$ (the device area ranged from 0.7×10^{-3} to $1.3 \times 10^{-3} \text{ cm}^2$). The forward current density was approximately 800 A cm^{-2} ($V_f \sim 3.5 \text{ V}$) [10]. Assuming that the device area was $1 \times 10^{-3} \text{ cm}^2$, the “specific on-resistance” and the switching power may be estimated as $1.3 \times 10^{-3} \Omega \text{ cm}^2$ and 180 W, respectively.

6H-SiC grown by liquid phase epitaxy (LPE) on Lely substrate has been used to fabricate a high current p-n junction diode with a 5 mm^2 device area (V.A. Dmitriev, unpublished). The blocking voltage for the diode was 120 V ($E_m \sim 4.5 \text{ MV cm}^{-1}$), and the forward current was 5 A ($j_f = 100 \text{ A cm}^{-2}$, $V_f \sim 4 \text{ V}$). This device had a “specific on-resistance” of about $1 \times 10^{-2} \Omega \text{ cm}^2$ and a switching power of 600 W.

4H-SiC npnp thyristors [11] have been fabricated with areas ranging from 3.2×10^{-3} to $16 \times 10^{-3} \text{ cm}^2$. A blocking voltage of 600 V has been achieved for the smallest device. The forward current was 1.8 A ($j_f = 563 \text{ A cm}^{-2}$) at a voltage drop of 3.7 V. This device had a “specific on-resistance” of $1.5 \times 10^{-3} \Omega \text{ cm}^2$. The switching power was $\sim 1.1 \text{ kW}$. For the larger device ($A = 1.61 \text{ mm}^2$), the blocking voltage dropped to 200 V. However, a forward current of 10 A ($j_f = 621 \text{ A cm}^{-2}$, $V_f = 3.6 \text{ V}$) was achieved. The corresponding switching power was 2 kW and the “specific on-resistance” was $1.2 \times 10^{-3} \Omega \text{ cm}^2$. Recently, however, the characteristics of SiC thyristors have been improved [12]. As a result, a thyristor with a blocking voltage of 700 V and a current of 6 A ($j_f = 1 \text{ kA cm}^{-2}$, $V_f = 3.67 \text{ V}$, $A = 6 \times 10^{-3} \text{ cm}^2$) was obtained. The corresponding switching power for the thyristor was 4.2 kW. This is the highest switching power for SiC devices reported to date. This thyristor had a “specific on-resistance” of $0.82 \times 10^{-3} \Omega \text{ cm}^2$.

The characteristics of the SiC power devices are summarized in Table 1. We may conclude that silicon carbide high voltage devices which operate at a high electric breakdown field and high forward current density have been fabricated. However, the switching power

of these devices is still much smaller than that for Si devices, which routinely exceeds 1 MW.

We note that the “specific on-resistance” of SiC devices has usually been determined as the product of the total resistance of the device structure and the mesa area. This is correct only if the device is cut from the wafer and measurements are done on a single die. If the device is not separated from the wafer, the resistance of the device depends on current spreading in the substrate (i.e. substrate resistivity and thickness) and “specific on-resistance”, determined in this way, will be a function of the device area. In other words, we cannot estimate the resistance of a device with a different area using this “specific on-resistance” value. For this reason we place the term specific on-resistance in quotation marks. In addition in order to compare the switching power of the above devices it is necessary to normalize the forward current value to the same V_f value.

3. Material issues in SiC power electronics

The main problem for high power SiC devices is the low forward current value. The maximum I_f reported so far is about 10 A (see Table 1). As a result, the maximum switching power for SiC devices does not exceed 5 kW. In order to increase the forward current in SiC devices, several material issues need to be solved. We will discuss two of them, namely small device area and small minority carrier diffusion length.

At present the area of SiC devices is usually less than 10^{-2} cm^2 resulting in an I_f value of less than 10 A, even at a current density of 10^3 A cm^{-2} . All attempts to increase the device area have failed because of premature electric breakdown. Fig. 1 summarizes the data (see Table 1) on breakdown voltage versus device area for SiC rectifying devices (including p-n diodes and thyristors). Note that a high breakdown voltage has been achieved only for devices that have a small area. The larger the area, the smaller the reverse voltage obtained for the device. Premature breakdown usually occurs if the device area exceeds 10^{-3} cm^2 . This means that the density of the defects causing the breakdown is about 10^3 cm^{-2} . This is much higher than the current micro-pipe density in SiC substrates. Moreover, the same limit for the device area of 10^{-3} cm^2 was observed for SiC p-n structures grown on Lely crystals having zero micropipes. Thus, we conclude some defects, other than micropipes, are responsible for premature breakdown in SiC devices. To increase the power of SiC devices, the nature of these unknown defects should be established and their density reduced. When the density of these defects is reduced to the value of the current micro-pipe density (micro-pipe density of a few micropipes per cm^2 has been reported [13]), the micro-pipe problem will again arise. Eventually, for high power SiC devices,

Table 1

Characteristics of SiC diodes and thyristors

Device	Polype	Device area (cm ²)	Reverse voltage (V)	Forward current (A)	Forward current density (A cm ⁻²)	Forward voltage (V)	“Specific on- resistance” (mΩ cm ²)	Switching power (kW)	Reference
Schottky diode	4H		1750		400	2	5		[5]
p-n diode	6H	2×10^{-4}	4500	0.02	100	6		0.09	[6]
p-n diode	6H	4×10^{-4}	2200	0.0004	1	3.5	300	0.0009	[7]
p-n diode	4H	1.5×10^{-3}	1130	0.1	68	3.6	12	0.113	[8]
p-n diode	6H	$(0.7-20) \times 10^{-3}$	500	1	1000	4.5	1.5–10	-0.5	[9]
p-n diode	6H	$(0.7-1.3) \times 10^{-3}$	220	1	800	3.5	~ 1.3	-0.18	[10]
p-n diode	6H	5×10^{-2}	120	5	100	4	12	0.6	V.A. Dmitriev, unpublished
thyristor	4H	6×10^{-3}	700	6	1000	3.7	0.82	4.2	[12]
thyristor	4H	3.2×10^{-3}	600	1.8	563	3.7	1.5	1.1	[11]
thyristor	4H	1.61×10^{-2}	200	10	621	3.6	1.2	2	[11]

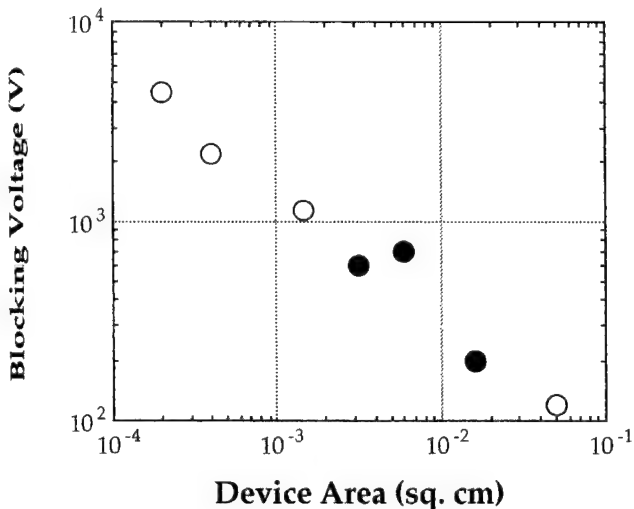


Fig. 1. Breakdown voltage versus device area for SiC devices: open circles: p-n diodes, closed circles: thyristors.

both micropipes and the other defects that cause premature breakdown should be completely eliminated in device structures.

The second problem for silicon carbide power bipolar devices is the small minority carrier diffusion length in SiC p-n structures. High voltage SiC devices require a reasonably thick base region. For a 10 000 V SiC p⁺-n⁻ diode, the thickness of the n-base region, H , should be around 100 μm, and the $N_d - N_a$ concentration in this region should be less than 10^{15} cm^{-3} . The resistivity of this material will be around 5 Ω cm which results in a 50 V drop at a forward current density of 1 kA cm⁻². To modulate the electric conductivity of this base region, the diffusion length of holes, L_p , in the n-base should be larger than 20 μm. So far the maximum value reported for L_p in SiC structures is ~1.5 μm. This value has been measured in 6H-SiC LPE grown diodes [14,15]. For SiC bipolar junction transistors the maximum reported electron diffusion length, L_n , is about

0.8 μm [16]. It is important to note that these values were measured in fabricated p-n structures, not in virgin epitaxial layers.

Obviously, there are many other issues in SiC power electronics, including mesa passivation, high contact and substrate resistance, and high-temperature packaging. But at the current stage of SiC technology these factors contribute specific resistance on the $10^{-4} \Omega \text{ cm}^2$ level, and we believe that the small device area and small carrier diffusion length are of the most critical.

4. Possible solution — LPE growth

One way around the above problems is to use liquid phase epitaxy to grow p-n structures for high power SiC devices. In the early stage of SiC development, LPE was widely used for device fabrication. SiC structures for efficient blue and violet light emitting diodes, high temperature epitaxial field effect transistors, and thyristor pnpn structures, were grown by LPE [17] for the first time. The advantages of silicon carbide LPE are wide doping ranges [18] ($10^{14} \text{ cm}^{-3} < |N_d - N_a| < 10^{20} \text{ cm}^{-3}$), including very high doping levels in p-type material [19] (up to $5 \times 10^{20} \text{ cm}^{-3}$), high growth rate (up to $3 \mu\text{m min}^{-1}$ at 1600°C), and low deep level concentration [20]. A unique feature of SiC LPE is a combination of a high growth rate and low deep center concentration. Recently, it was shown that micropipes do not penetrate into the SiC epitaxial layer grown by LPE from Si-Sc melt [21]. The closing of micropipes during silicon carbide LPE growth from the Si melt has also been observed [19]. Additionally it was found that the dislocation density in the epitaxial layer may be reduced in LPE grown film compared with the substrate.

We propose the use of LPE to grow p-n structures for high power SiC bipolar devices. An example of the structure of a SiC p-n diode is shown in Fig. 2. The

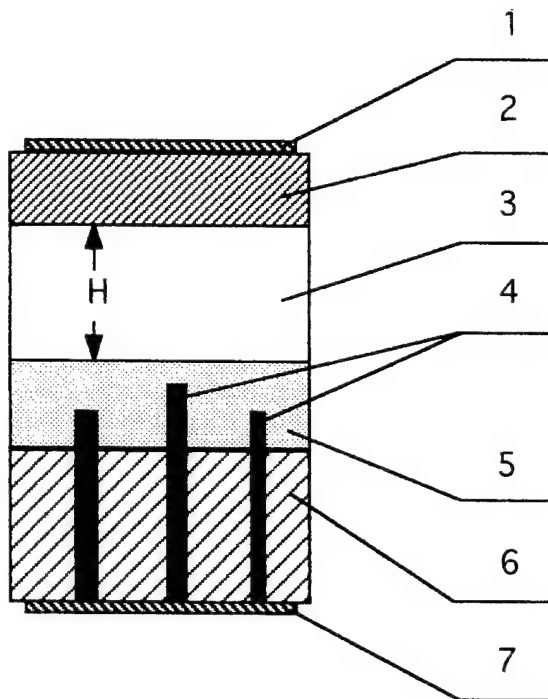


Fig. 2. Schematic drawing of proposed LPE grown SiC high power diode: (1) Ohmic contact to p^+ -SiC, (2) p^+ -layer, (3) n^- -base region, (4) micropipes, (5) n^+ -layer, (6) n^- -4H-SiC substrate, (7) Ohmic contact to n^+ -SiC.

diode consists of a n^+ -4H-SiC substrate and a multilayer structure grown by LPE. The first n^+ -layer serves to cover micropipes and reduce the overall defect density. The following n^- -layer is a base region of the diode. The thickness and doping concentration of the base are determined by required reverse voltage of the device. As mentioned above, for 10 000 V devices the required $N_d - N_a$ concentration is about $1 \times 10^{15} \text{ cm}^{-3}$ and the thickness H is $\sim 100 \mu\text{m}$. This layer may be grown by LPE within a few hours, compared with a few days required by conventional CVD. The top p^+ -layer will be grown with a hole concentration higher than 10^{20} cm^{-3} which will ensure a low contact resistance. We believe that the low defect density and low deep level concentration in LPE grown material will allow us to increase the device area and improve minority carrier diffusion length.

5. Summary

Recently, significant progress in SiC technology has been achieved. SiC devices with blocking voltages of a few kilovolts and forward current densities of 1 kA cm^{-2} have been fabricated. The next step toward high power SiC electronics is to increase the forward current of the devices. This step requires reduction of the on-resistance of the devices. Two main factors that

currently limit the resistance are: (1) device area, and (2) resistivity of the base region of the devices. In order to solve these problems, defect density in the p-n structures should be reduced. We propose to fabricate high power SiC devices, such as diodes and thyristors using liquid phase epitaxy for p-n structure formation. This method has been shown to reduce micropipe and dislocation density in SiC p-n structures and to produce material with the large diffusion length required to modulate electrical conductivity of base region.

Acknowledgement

This work was supported in part by Arizona State University.

References

- [1] J.R. O'Connor, J. Simlants (Eds.) *Silicon Carbide, A High Temperature Semiconductor*, Pergamon Press, Oxford, 1960; H.K. Henisch, R. Roy (Eds.), *Silicon carbide — 1968, Proceedings of the International Conference on Silicon Carbide*, Pergamon Press, New York, 1969.
- [2] A.E. Oblešek, V.E. Chelnokov, in: *Problems of Physics and Technology of Wide Band Gap Semiconductors*, LETI, Leningrad, 1980 pp. 197–211 (in Russian).
- [3] V.E. Chelnokov, *Materials Science and Engineering B* II (1992) 103.
- [4] S. Nakashima, H. Matsunami, S. Yoshida, H. Harima (Eds.), *Silicon Carbide and Related Materials 1995*, Institute of Physics Conference Series No. 142, IOP Publishing, Bristol, 1996.
- [5] A. Itoh, T. Kimoto, H. Matsunami, in: S. Nakashima, H. Matsunami, S. Yoshida, H. Harima (Eds.), *Silicon Carbide and Related Materials 1995*, Institute of Physics Conference Series No. 142, IOP Publishing, Bristol, pp. 689–692.
- [6] O. Kordina, J.P. Bergman, A. Henry, E. Janzen, S. Savage, J. Andre, L.P. Ramberg, U. Lindefelt, W. Hermansson, K. Bergman, *Appl. Phys. Lett.* 67 (11) (1995) 1561.
- [7] P.G. Neudeck, D.J. Larkin, J.A. Powell, L.G. Matus, C.S. Salupo, *Appl. Phys. Lett.* 64 (11) (1994) 1386.
- [8] J.W. Palmour, J.A. Edmond, H.S. Kong, C.H. Carter, Jr, in: M.G. Spencer, R.P. Devaty, J.A. Edmond, M. Asif Khan, R. Kaplan, M. Rahman (Eds.), *Institute of Physics Conference Series No. 137*, IOP Publishing, Bristol, 1994, pp. 499–502.
- [9] M.M. Anikin, P.A. Ivanov, A.A. Lebedev, S.N. Pytko, A.M. Strel'chuk, A.L. Syrkin, in: *Semiciconductor Interfaces and Microstructures*, World Scientific Publishing, Singapore, 1992, pp. 280–311.
- [10] M.M. Anikin, A.A. Lebedev, I.V. Popov, V.E. Sevastyanov, A.L. Syrkin, A.L. Suvorov, V.E. Chelnokov, G.P. Shpiniev, *Pisma v ZhTF* 10 (17) (1984) 1053.
- [11] J.W. Palmour, S.T. Allen, R. Singh, L.A. Lipkin, D.G. Waltz, in: S. Nakashima, H. Matsunami, S. Yoshida, H. Harima (Eds.), *Silicon Carbide and Related Materials 1995*, Institute of Physics Conference Series No. 142, IOP Publishing, Bristol, 1996, pp. 813–816.
- [12] J.W. Palmour, R. Singh, L.A. Lipkin, D.G. Waltz, in: *Transactions of the Third International High Temperature Electronics Conference*, Albuquerque, New Mexico, June 9–14, 1996, vol. 2, p. XVI-9.
- [13] V.F. Tsvetkov, S.T. Allen, H.S. Kong, C.H. Carter, Jr, in: S. Nakashima, H. Matsunami, S. Yoshida, H. Harima (Eds.), *Sili-*

con Carbide and Related Materials 1995, Institute of Physics Conference Series No. 142, IOP Publishing, Bristol, 1996, pp. 17–22.

[14] A.M. Strelchuk, A.L. Syrkin, V.E. Chelnokov, A.E. Cherenkov, V.A. Dmitriev, in: M.G. Spencer, R.P. Devaty, J.A. Edmond, M. Asif Khan, R. Kaplan, M. Rahman (Eds.), Institute of Physics Conference Series No. 137, IOP Publishing, Bristol, 1994, pp. 549–552.

[15] A.M. Strel'chuk, Semiconductors 29 (1995) 614.

[16] Y. Wang, W. Xie, J.A. Cooper, Jr, M.R. Melloch, J.W. Palmour, in: S. Nakashima, H. Matsunami, S. Yoshida, H. Harima (Eds.), Silicon Carbide and Related Materials 1995, Institute of Physics Conference Series No. 142, IOP Publishing, Bristol, 1996, pp. 809–812.

[17] For review see V.A. Dmirriev, in: G.L. Harries (Ed.), Properties of Silicon Carbide, IEE, 1994, pp. 214–227; and V.A. Dmitriev, Physica B 185 (1993) 440.

[18] W. Munch, W. Kurzinger, Solid State Electronics 21 (1978) 1129.

[19] S.N. Rendakova, to be published.

[20] M.M. Anikin, A.S. Zubrilov, A.A. Lebedev, A.P. Strel'chuk, V.E. Chelnokov, Sov. Phys. Semicond. 25 (1991) 289.

[21] R. Yakimova, M. Tuominen, A.S. Bakin, J.-O. Fornell, A. Vehanen, E. Jansen, in: S. Nakashima, H. Matsunami, S. Yoshida, H. Harima (Eds.), Silicon Carbide and Related Materials 1995, Institute of Physics Conference Series No. 142, IOP Publishing, Bristol, 1996, pp. 101–104.

2.5 kV ion-implanted p^+n diodes in 6H-SiC

K.H. Rottner ^{a,*}, A. Schöner ^a, S.M. Savage ^a, M. Frischholz ^a, C. Hallin ^b, O. Kordina ^b,
E. Janzén ^b

^a IMC, PO Box 1084, S-16421 Stockholm-Kista, Sweden

^b Department of Physics and Measurement Technology, Linköping University, S-58183 Linköping, Sweden

Abstract

High-voltage diodes which can block up to 2.5 kV have been fabricated by ion implantation of *p*-type dopants. Junctions with a low forward voltage drop and a leakage current level sufficiently low to allow stable device operation have been demonstrated. This was achieved using a combination of boron and aluminum as implanted acceptor for the *p*-type emitter. The junction termination to control the surface electric field was achieved by the unintentionally induced negative surface charge. For reference, devices with a junction termination extension were also fabricated. Both device types are shown to block the same voltage limited by external flash-over. Using optical beam induced current (OBIC) measurements, we visualized the depletion region of the implanted *pn* junctions and found that all devices have a considerably enlarged lateral depletion width, which is indicative of the expected high surface charge acting on the “self”-terminated devices as surface field reduction. © 1997 Elsevier Science S.A.

Keywords: OBIC; Diodes; Ion implantation; Termination

1. Introduction

Ion implantation to incorporate dopant atoms into SiC has recently become a more-available technology for devices [1–5]. We have fabricated planar high-voltage diodes using ion implantation of boron and co-implantation of boron and aluminum into low doped *n*-type CVD layers. Junction termination was achieved by boron implantation around the periphery of the emitter in order to form a junction termination extension (JTE) structure.

For high-voltage devices, junction termination is a very important issue in order to keep the surface electrical field low enough to prevent premature breakdown. The presence of surface charge effects lowering the surface field and thus providing unintentional termination has been published earlier [6,7]. To visualize this effect, we used optical beam induced current (OBIC) measurements. The objective of this work was to make use of the unintentional termination due to surface charge and evaluate its effectiveness with respect to diodes with a JTE structure.

2. Experiments

2.1. Device structures

Three types of device were processed: devices with a boron implanted emitter (denoted as B devices), devices with aluminum and boron implanted emitters (Al-B devices) and devices with JTE and boron implanted emitters (JTE devices). For the *p*-anodes of the diodes, two different implantation profiles were implemented: for the B-devices boron was used to form the anode, while for the Al-B devices, boron and aluminum were implanted. Boron is known to diffuse rather quickly during the implantation annealing [1]. In particular, close to the surface, an out diffusion of *p*-type dopants might result in a poor contact formation on the implanted region [12]. Owing to the diffusion of boron, the metallurgical *pn* junction is located deeper in the bulk, in a region not damaged by the implantation process. This is expected to increase the blocking capability and decrease the leakage current of the *pn* junction. The differences in diffusion were established by SIMS measurements [1].

The implantation of the dopants was carried out at 600 °C to remove the implantation damage and to electrically activate the implanted species, the samples

* Corresponding author.

were annealed at 1700 °C for 30 min in Argon. The schematic device structures are shown in Fig. 1. The emitter diameter was 200 µm, and the outer diameter of the JTE was 1000 µm. The devices were fabricated on CVD-grown *n*-type layers with a nitrogen doping concentration of $3 \times 10^{15} \text{ cm}^{-3}$ and an epi layer thickness of 30 µm. These layers were grown on 3.5° off oriented 6H-SiC substrates purchased from Cree Inc., Durham NC, USA.

2.2. OBIC method

The OBIC method has been used previously to visualize the electric field distribution in Schottky and bipolar diode structures [6–10]. For photo excitation of the devices, 3.7 eV photons (penetration depth approximately 5 µm) from a mercury arc lamp were used. Wavelength separation was achieved by interference filters selecting a single mercury spectral line. A detailed description of the setup is given in Ref. [11]. By scanning the illuminated spot (approximately 15 µm diameter) across the device surface, a two-dimensional lateral mapping of the depletion region of the devices can be obtained.

3. Results

3.1. *I*–*V* characteristics of the diodes

The current–voltage characteristics of the diodes were measured under DC conditions at room temperature in SF₆ (1 bar). The anode of the diodes was contacted with a probe tip, the backside was glued with conductive epoxy on a copper plate.

The results of the forward voltage drop measurements on the diode types (Al–B and B devices) are shown in Fig. 2(a). It can be seen that the B devices cause a higher forward voltage drop, which leads to increased conduction losses. This can be understood in terms of a high contact resistance on the low doped surface region due to out-diffusion of boron near the surface. The Al–B combination overcomes this problem due to

the high aluminum concentration at the surface, and the device characteristics show increased forward current densities by several orders of magnitude. The blocking characteristics of diodes with and without JTE are shown in Fig. 2(b). The reverse characteristics were found to be independent of the process of anode formation (Al–B or only B) and in all cases, external flash-over between the probe tip and the device periphery limited the maximum blocking voltage.

3.2. OBIC results

OBIC measurements were carried out on the B devices and JTE devices. As expected, the emitter formation process does not have any influence on the surface charge and field distribution outside the emitter area. OBIC images taken at two different blocking voltages (10 and 300 V) applied to an unintentionally terminated diode are shown in Fig. 3(a and b). From Fig. 3, it is obvious that the electrical field distribution is already considerably enlarged at bias voltages around 10 V. The expected depletion width at this voltage would be 2 µm without any surface charges present while the actual measured width of the field distribution is about 60 µm. At 300 V, the bias depletion region is about 80 µm (instead of 10 µm without surface charge). Additionally, the shape of the depletion region starts to become asymmetric, indicating a nonhomogeneity in the electric field distribution which might be due to variations in the surface charge concentration or defects.

OBIC measurements carried out at diodes with JTE gave a different result. Two OBIC images taken at 10 and 300 V are shown in Fig. 3(c and d). It is obvious from the images that the JTE is already partially depleted at 10 V. This does not change at higher bias voltages. In contrast to the results on the unintentionally terminated diodes, the shape of the field distribution remains perfectly circular.

4. Discussion

The experimental breakdown voltage of the implanted diodes was found to be 2.5 kV. Theoretically, junction

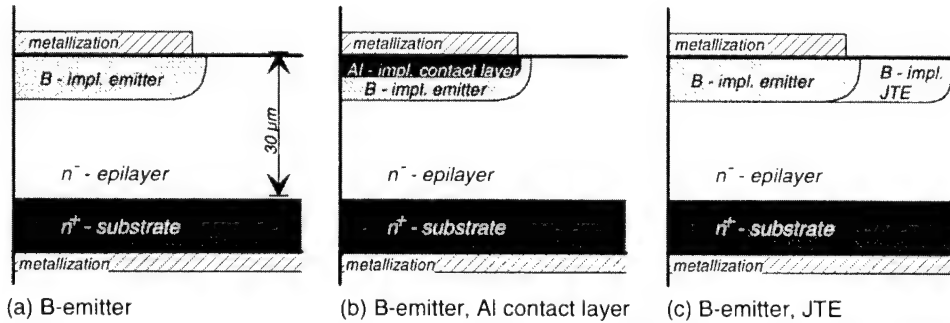


Fig. 1. Schematic structure of the fabricated devices. The diodes shown in (a) and (b) had no intentional termination. The doping concentration of the *n*-layer was, in all cases, $3 \times 10^{15} \text{ cm}^{-3}$.

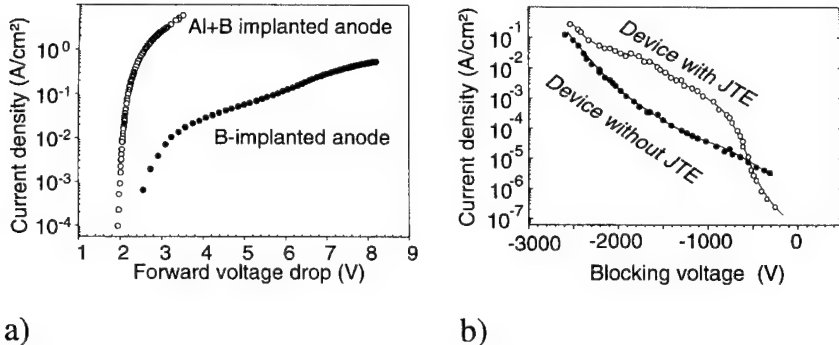


Fig. 2. (a) I - V characteristics of diodes with boron implanted anodes in comparison with anodes formed by a combination of Al and B implantations. (b) Blocking curves of a diode with JTE and one without termination. Although the leakage current levels were different, the maximum blocking voltage was the same for both types.

termination structures would be necessary in order to keep the surface electric fields low enough to avoid premature breakdown. However, the experimental finding that SiC diodes block higher voltages than two-dimensional simulation (neglecting surface charge) predicts was already established in previous studies [6,7] where clear indication was found that on n -SiC, the negative surface charge, acting as junction termination, is responsible for this effect. In agreement with these previous results, our devices did not suffer from having no intentional junction termination. Both device types

– with and without JTE – blocked the same voltage. The OBIC results show significant lateral extension of the depletion region already at very low blocking voltages at the diodes both with and without JTE.

The results of the I - V measurements show that the combination of Al and B for the anode formation by ion implantation is a viable way to achieve decent p n junctions. The reverse leakage current levels at low voltages were found to be around 10^{-5} A cm⁻² at 500 V. With higher voltages, an increase of the leakage current was observed, together with soft breakdown characteris-

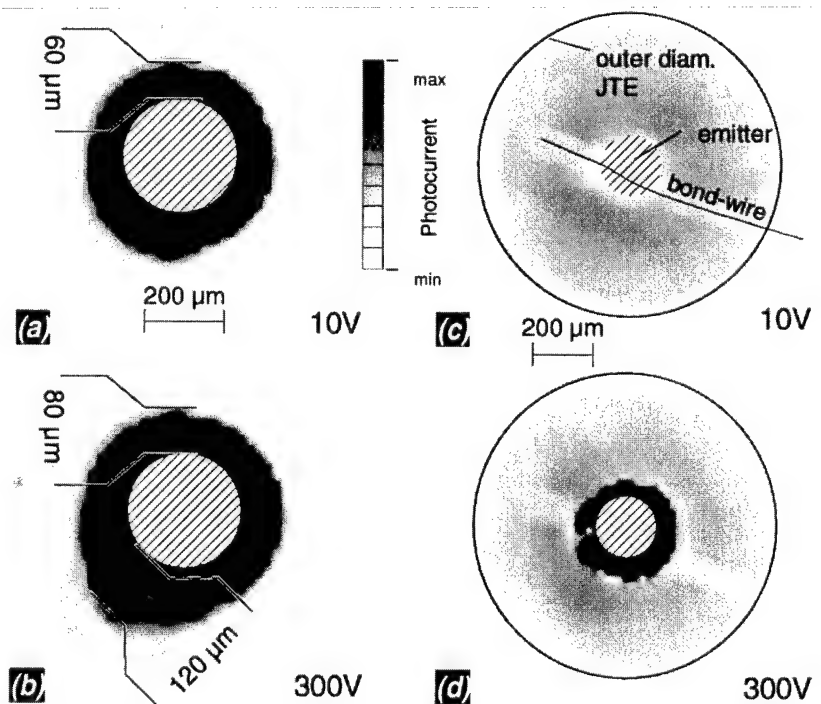


Fig. 3. (a and b) Greyscale encoded OBIC images taken at 10 V (a) and 300 V (b) blocking voltage of diodes without intentional termination. The circular area in the center corresponds to the emitter with the metallization. (c and d) Greyscale encoded OBIC image of a device with JTE at 10 V (c) and 300 V (d) blocking voltage. In (a) the outer diameter of the JTE and the position of the emitter are shown. A further feature is caused by shading effects due to the bonding wire contacting the emitter.

tics. The breakdown itself occurred by external flash-over. This might be due to the lack of any surface passivation and insulation, making devices very sensitive to “environmental” effects – e.g. humidity. The surface electric field distribution is very critical for surface leakage, and since it was not possible to determine exactly where this leakage current is actually flowing, it is premature to speculate about the underlying physical mechanism. However, the current level was low enough to maintain stable device operation without thermal runaway due to power dissipation (approximately 500 W cm⁻² at 2.5 kV)

The forward current voltage curves of these diodes showed an exponential behavior in a large current range with an ideality factor of 1.05. In the high current density region, limitations by serial resistivities were observed, which can be assigned partly to the external circuitry of the *I*–*V* measurement setup.

5. Conclusion

The feasibility of ion implanted diodes for high-voltage applications has been demonstrated. The termination concept of JTE structures was implemented successfully. The OBIC method has proven to be a powerful tool in investigating and visualizing surface charge induced effects on the electric field distribution of devices. We could visualize the effects of the JTE and the surface charges on the lateral depletion width.

Acknowledgement

The work was financed by Asea Brown Boveri and the Swedish National Board for Industrial and Technical Development (NUTEK).

References

- [1] G. Pensl, Proc. in SiC and Related Materials, IoP Publishing no. 142, Bristol and Philadelphia, 1996, p. 275.
- [2] M. Ghezzo, D.M. Brown, E. Downey, J. Kretchmer, J.J. Kopanski, *Appl. Phys. Letters* 63 (1993) 1206.
- [3] N. Ramangul, V. Khemka, R. Tyagi, T.P. Chow, M. Ghezzo, P.G. Neudeck, J. Kretchmer, W. Hennessy, D.M. Brown, in: SiC and Related Materials, IoP Publishing no. 142, Bristol and Philadelphia, 1996, p. 713.
- [4] P.M. Shenoy, B.J. Baliga, *IEEE Electron. Device Lett.* 16 (10) (1995) 454.
- [5] D. Planson, M. Locatelli, S. Ortolland, J.P. Chante, H. Mitlehner, D. Stephani, Proceedings of the 1st International Power Electronics and Motion Control Conference '94, Beijing (accepted for publication).
- [6] K. Rottner, S. Savage, J. André, L. Ramberg, M. Frischholz, R. Helbig, in: SiC and Related Materials, Institute of Physics Publishing, Bristol, Conference Series No. 142, 1996, p. 721.
- [7] K. Rottner, A. Schöner, M. Frischholz, R. Helbig, Proceedings of the Material Research Society, Symposium E, Spring Meeting 96, San Francisco, Proc. vol. 423.
- [8] R. Stengl, *IEEE Trans. Electron. Devices* 34 (4) (1987) 911.
- [9] J. Sandoe, J. Hughes, *Acta Electron.* 25 (3) (1983) 201.
- [10] S. Lindsay, *Phys. Stat. Sol. (a)* 53 (1979) 311.
- [11] M. Frischholz, R. Helbig, *Appl. Surf. Sci.* 65 (1993) 784.
- [12] N. Nordell, S. Savage, A. Schöner, in: SiC and Related Materials, IoP Publishing no. 142, Bristol, 1996, p. 573.



ELSEVIER

High field and high temperature stress of n-SiC MOS capacitors

E. Bano ^{a,*}, T. Ouisse ^a, C. Leonhard ^b, A. Gölz ^b, E.G. Stein Von Kamienski ^b

^a Laboratoire de Physique des Composants à Semiconducteurs (LPCS), UMR-CNRS 5531, ENSERG, 23 rue des Martyrs, 38016 Grenoble, France

^b Institut für Halbleitertechnik, Lehrstuhl II, RWTH Aachen, Sommerfeldstr. 24, D-52074 Aachen, Germany

Abstract

The development of reliable oxides built on SiC has become a very important issue with respect to either passivation processes or metal-oxide–semiconductor (MOS) applications. The aim of this paper is to present a detailed investigation of Fowler–Nordheim electron injections in n-type silicon carbide (SiC) MOS capacitors. A systematic variation in the temperature and in the average oxide field E_{ox} applied during the stress allowed us to evidence both a positive charge and electron trapping. The positive charge build-up is shown to emerge above a threshold field close to 7 MV cm^{-1} . It decreases with temperature, and can be dissociated into two different exponential time processes. The overall results agree with mechanisms based on impact ionization in the oxide, leading to pair creation and subsequent hole trapping. © 1997 Elsevier Science S.A.

Keywords: Silicon carbide; Metal-oxide–semiconductor; Impact-ionization; Fowler–Nordheim injection

1. Introduction

Silicon carbide (SiC) is a promising candidate for high temperature and high power applications [1,2]. The development of reliable oxides built on SiC has become an important issue with respect to metal-oxide–semiconductor (MOS) applications. Several authors have already reported a detailed investigation of the SiC/SiO₂ interface properties [3–9]. In the case of p-type layers, a high interface disorder has been evidenced, which strongly affects the transport properties in the inversion layer of SiC MOS transistors [2,10,11]. Although it has been demonstrated that most of the fixed charge was localised close to the interface [12], only a few reports deal with the properties of bulk traps into the oxide [13–15]. Systematic data, including influence of fabrication conditions, were presented elsewhere for lower oxide fields [13], and here we focus on the build-up of an anomalous positive charge at higher fields. It will be shown that this positive charge build-up most probably results from impact ionization in the oxide, followed by hole trapping. Such phenomena have already been clearly identified in the case of silicon MOS technology. From a comparison between our results and similar data already published in the MOS silicon litera-

ture, we wish to demonstrate that, in the case of SiC, these mechanisms remain essentially unchanged.

2. Devices and experimental details

Fowler–Nordheim electron injections have been carried out on 6H SiC MOS capacitors fabricated at RWTH, using n-type nitrogen-doped epitaxial layers grown on n-type substrates bought from Cree Research Inc. The net doping level of the epitaxial layer was $N_D - N_A = 7 \times 10^{15} \text{ cm}^{-3}$. After a wet chemical cleaning process, an oxide layer of 44 nm was grown at 1150 °C in dry oxygen followed by a 60 nm anneal in Ar at the same temperature. A poly-Si layer of 200 nm was deposited by a standard LPCVD process which was implanted with As and annealed at 1150 °C for 20 s. The poly-Si was metallized with Ti and Au and patterned to dots of 200 and 400 μm diameter. Both the electric field and stress temperature dependence have been investigated, from $T = 291$ to 473 K with a constant injection current I_{inj} of $3 \times 10^{-5} \text{ A cm}^{-2}$, and with I_{inj} varying from 10^{-6} to $7 \times 10^{-5} \text{ A cm}^{-2}$ at $T = 373$ K with total injection doses up to $10^{19} \text{ charges cm}^{-2}$. We studied both the variation in the flat-band voltage V_{FB} and the Fowler–Nordheim voltage V_{FN} , defined here as the voltage required for imposing I_{inj} . However, after each

* Corresponding author. Fax: 33 76 85 60 70; e-mail: bano@enserg.fr

extraction of V_{FB} from the $C(V)$ curve, even on a small gate voltage interval, a discontinuous jump was always observed in the V_{FN} shift curve (Fig. 1). In fact, a partial recovery of the trapped charges occurred due to the time and bias needed for $C(V)$ measurement. To avoid these transients and have a real account of the trapped charges, we only monitored V_{FN} , except in a restricted number of cases, to assess the evolution of the small signal capacitance and conductance characteristics with the injected dose. In such a case, an increase of the conductance peak with the injected charge, especially for the lower doses, reflected an increase in the interface state density (Fig. 2). Besides, no broadening of the peak was observed, which seems to show that the potential fluctuations were not substantially increased, and therefore that the injection was spatially homogeneous.

3. Results and discussion

Typical ΔV_{FN} shifts are shown in Figs. 3(a) and (b). The two kinds of charge build-up suggest to analyse the data in terms of a multiple trapping model. A plot $\ln |d\Delta V_{FN}/dt|$ versus time shows a number of transitions equal to that of the processes involved. Then, the analytical fit of the data gives the trap density N_{ti} and the capture cross section σ_i for the i^{th} trap centre. First, an anomalous positive charge is always prevailing, decreasing with temperature and increasing with current density. This positive charge build-up can be dissociated

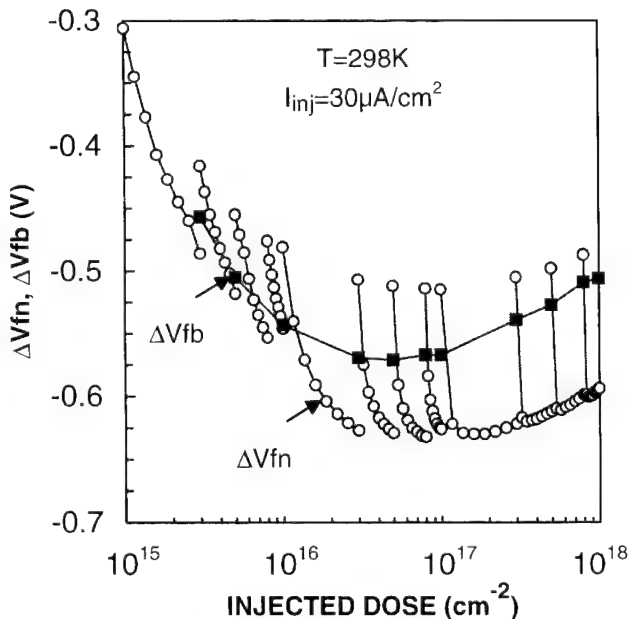


Fig. 1. Fowler–Nordheim and flatband voltage shift as a function of electron dose injected from the substrate, for different steps of injection and $I_{inj}=30 \mu\text{A cm}^{-2}$, at $T=298 \text{ K}$.

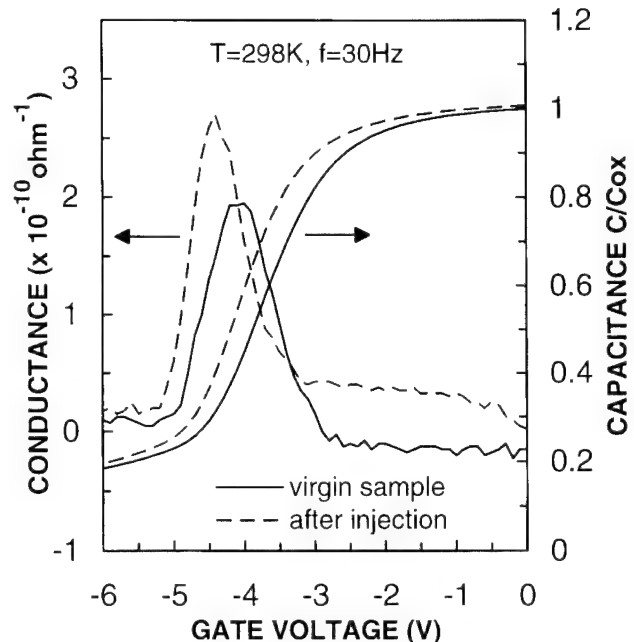


Fig. 2. Conductance and capacitance vs gate voltage for a small signal frequency ($f=30 \text{ Hz}$), at room temperature, after and before an injected dose of 3×10^{17} electrons per cm^2 .

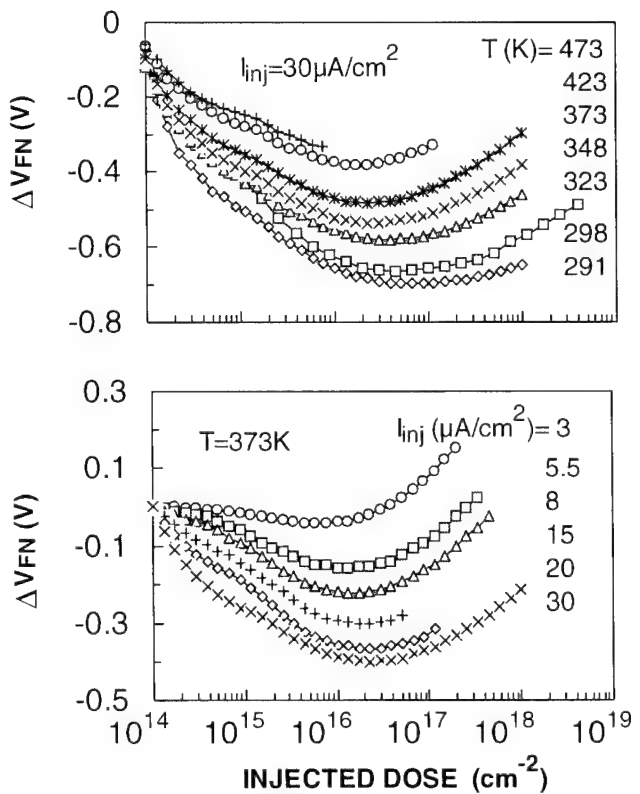


Fig. 3. Variation of the Fowler–Nordheim voltage as a function of electron injected dose: (a) $T=291$ to 473 K at $I_{inj}=30 \mu\text{A cm}^{-2}$, and (b) $I_{inj}=3$ to $30 \mu\text{A cm}^{-2}$ at $T=373\text{K}$.

into two different time processes ($i=1$ and 2) which prevail respectively before and after doses around 10^{15} cm^{-2} . Then, at higher doses, a turn around effect clearly shows that a negative trapping ($i=3$) emerges. The time law used for fitting the three different first-order exponential time processes was

$$\Delta V_{FN}(t) = \frac{t_{ox} 1q}{\epsilon_{ox}} \sum_{i=1}^3 \delta_i N_{ti} [1 - \exp(-I_{inj} \sigma_i t/q)],$$

where $\delta_i = -1$ for $i=1$ and 2 (positive charge trapping) and $+1$ for $i=3$ (electron trapping). q is the elementary charge, t_{ox} is the oxide thickness and ϵ_{ox} the dielectric constant of the oxide. In the case of a positive charge build-up, this modelling might a priori be questionable. For instance, the creation of water and hydrogen-related traps [13,15] should not necessarily obey such a time process. Nevertheless, this procedure will be justified by analysing the electric field and temperature dependence of the trapping parameters.

From Fig. 4, no charge is trapped before a threshold field of around 6.75 MV cm^{-1} , from which the positive charge build-up depends almost linearly on the average electric field E_{ox} . Such a behaviour has already been observed in Si MOS technology [16,17]. Although the cause of an anomalous positive charge formation has been controversial during several years, DiMaria, Arnold and Cartier demonstrated that such a charge build-up was due to impact ionization inside the oxide,

followed by a subsequent hole trapping [16], provided that the oxide film was sufficiently thick ($>20 \text{ nm}$). In SiO_2 on Si films and for $E_{ox} > 7 \text{ MV cm}^{-1}$, they showed that a hot electron energy distribution tail exceeding 9 eV was resulting from high field electron transport in the oxide layer, and such an energy was large enough so as to enable impact ionization [16,17]. The subsequent trapping mechanism can still be modelled by a first-order rate equation, taking into account both hole trapping and free electron-trapped hole annihilation processes, characterised by their capture and annihilation cross section, σ_p and σ_e respectively

$$p(t) = \frac{\alpha \sigma_p N_t}{\alpha \sigma_p + \sigma_e} [1 - \exp(-I_{inj}(\alpha \sigma_p + \sigma_e)t/q)],$$

where α is the band gap ionisation probability, i.e. the appropriate factor which must be multiplied by the electron current to obtain the hole current passing through the oxide. Dimaria *et al.* demonstrated that α dramatically increases with E_{ox} and with the oxide thickness, since this allows enough space for the electron distribution to develop a high energy tail [16]. When σ_e is large against $\alpha \sigma_p$, one expects to find an apparent hole trap density equal to $(\alpha \sigma_p / \sigma_e) N_t$, whereas the apparent capture cross section is now almost given by σ_e . Roughly interpolating and extrapolating the data presented in Fig. 2 of Ref. [16], we would expect α values in the range of 10^{-4} around 300 K , with a total variation of about a factor of 10 for oxide fields between 7 and 8 MV cm^{-1} . Considering capture cross sections in the same range as that found in Ref. [16], i.e. σ_e around 10^{-16} cm^2 and σ_p around 10^{-14} cm^2 , one would have σ_e much larger than $\alpha \sigma_p$. Hence the apparent capture cross section should be almost equal to σ_e , whereas the apparent hole trap density should be given by $(\alpha \sigma_p / \sigma_e) N_t$. This hypothesis seems to be confirmed by Fig. 4: the apparent hole trap density depends linearly on E_{ox} , and roughly increases by a factor of 10 between 6.9 and 7.8 MV cm^{-1} . Besides, the fact that the experimental values of the apparent cross sections (in the 10^{-16} – 10^{-15} cm^2 range) always remain much larger than the value of $\alpha \sigma_p$ estimated above reinforces the compatibility of the model with experiment. Taking from Ref. [16] an α value in the range of 10^{-4} and a real trap density in the range of 1 – $5 \times 10^{12} \text{ cm}^{-2}$, one would expect apparent trap densities of the order of 10^{11} cm^{-2} which is in agreement with the values extracted from the data fit (Fig. 4).

To further confirm that hole trapping is induced by impact ionisation in the oxide, Fowler–Nordheim injections have also been investigated as a function of stress temperature (Fig. 3(a)). The turn around effect shifts to lower doses and Fig. 5 show opposite trends of the positive and negative trapping mechanisms, whereas the

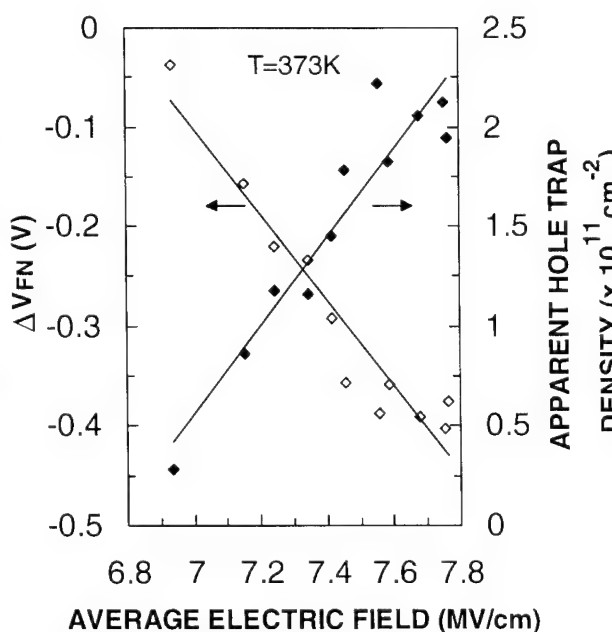


Fig. 4. Dependence of the Fowler–Nordheim shift on the average oxide electric field, for an injected dose of 10^{16} cm^{-2} at $T=373 \text{ K}$, and variation of the total apparent hole trap density vs electric field, as deduced from numerical fits (this density corresponds to the sum of the two positive trapping processes).

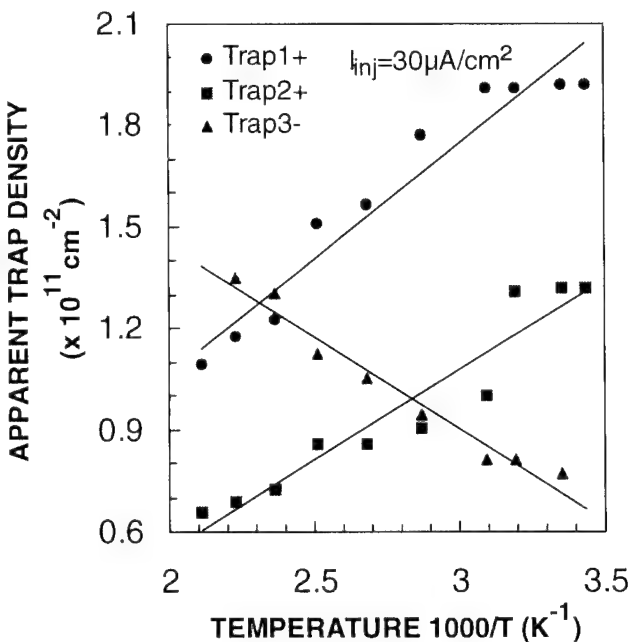


Fig. 5. Extracted values of the apparent trap density corresponding to the three trapping processes, as a function of reciprocal temperature; $I_{\text{inj}} = 30 \mu\text{A cm}^{-2}$.

capture cross sections were found to remain almost constant (Fig. 6). The decrease of the apparent hole trap density can be due either to thermal reemission from traps, or a lowered rate of impact ionization. In the case of a dominant thermal detrapping [13], it should appear in a correlated way on the apparent

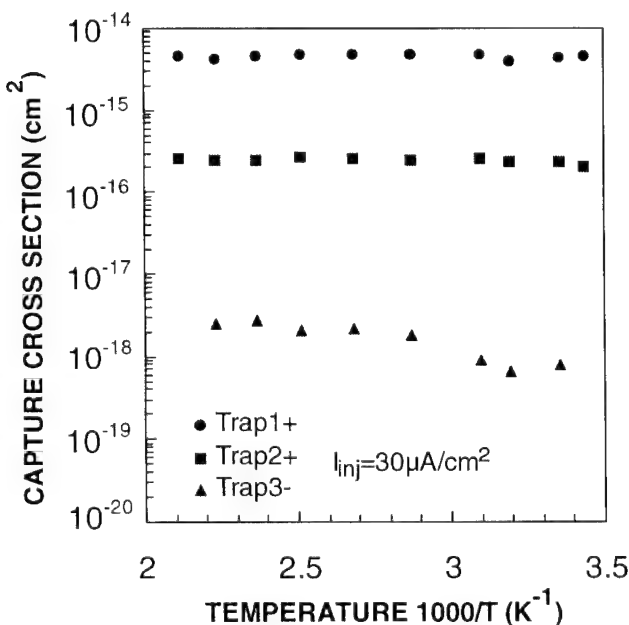


Fig. 6. Extracted values of the capture cross sections corresponding to the three trapping processes, as a function of reciprocal temperature; $I_{\text{inj}} = 30 \mu\text{A cm}^{-2}$.

capture cross section and on the trap density. This is not consistent with the temperature behaviour. We therefore concluded that this decrease is essentially due to that of α . This is an additional indication that hole trapping is due to impact ionization. The increase of T involves a gradual change from a prevailing hole trapping process to electron trapping.

4. Conclusion

Fowler–Nordheim injections have been carried out in n-type SiC MOS capacitors. The high electric field and high temperature dependence allowed us to evidence both a positive charge and electron trapping. The positive charge build-up can be dissociated in two different exponential processes, emerges at a threshold field close to 7 MV cm^{-1} and depends almost linearly on E_{ox} . Besides, it is noticeably reduced by increasing the temperature. The evolution of the apparent trap densities and capture cross sections are given as a function of electric field and temperature. The overall results agree with mechanisms based on impact ionization processes inside the oxide, leading to pair creation and subsequent hole trapping. Such phenomena have already been clearly identified in the case of silicon MOS technology, with moderately thin oxides [16,17]. We can conclude that these processes remain essentially unchanged in the case of n-type SiC. Furthermore, the trap densities are also quite comparable.

Acknowledgement

This work was financially supported by PROCOPE funding.

References

- [1] M. Bhatnagar, B.J. Baliga, IEEE Trans. Electron Dev. 40 (3) (1993) 645.
- [2] J.W. Palmour, J.A. Edmond, H.S. Kong, C.H. Carter Jr, Physica B 185 (1993) 461.
- [3] T. Ouisse, N. Bécourt, C. Jaussaud, F. Templier, J. Appl. Phys. 75 (1) (1994) 604.
- [4] E. Stein von amienski, A. Götz, H. Kurz, Mat. Sci. Eng. B 29 (1995) 131.
- [5] D. Alok, P.K. McLarty, B.J. Baliga, Appl. Phys. Lett. 65 (1994) 2177.
- [6] S.T. Sheppard, J.A. Cooper Jr, M.R. Melloch, J. Appl. Phys. 75 (1994) 3205.
- [7] J.N. Shenoy, M.K. Das, G.L. Chindalore, J.A. Cooper Jr, M.R. Melloch, J.W. Palmour, K.G. Irvine, Inst. Phys. Conf. Ser. 142 (1996) 745.
- [8] E. Bano, T. Ouisse, L. Di Cioccio, S. Karmann, Appl. Phys. Lett. 65 (1994) 2723.
- [9] N. Singh, A. Rys, J. Appl. Phys. 73 (1993) 1279.
- [10] T. Ouisse, T. Billon, Philos. Mag. B 71 (1995) 413.

- [11] T. Ouisse, Philos. Mag. B 73 (1996) 325.
- [12] E. Bano, T. Ouisse, P. Lassagne, T. Billon, C. Jaussaud, Inst. Phys. Conf. Ser. 142 (1996) 729.
- [13] E. Stein von Kamienski, F. Portheine, J. Stein, A. Gölz, H. Kurz, J. Appl. Phys. 79 (1996) 2529.
- [14] V.V. Afanas'ev, M. Bassler, G. Pensl, M.J. Schulz, Microelectron. Engineering 28 (1995) 197.
- [15] E. Stein von Kamienski, C. Leonhard, F. Portheine, A. Gölz, H. Kurz, Mat. Sci. Eng. B 46 (1997) 263–266.
- [16] D.J. DiMaria, D. Arnold, E. Cartier, Appl. Phys. Lett. 60 (1992) 2118.
- [17] D.J. DiMaria, E. Cartier, D. Arnold, J. Appl. Phys. 73 (1993) 3367.

Low frequency noise in silicon carbide Schottky diodes

L. Anghel ^a, T. Ouisse ^{a,*}, T. Billon ^b, P. Lassagne ^b, C. Jaussaud ^b

^a Laboratoire de Physique des Composants à Semiconducteurs (LPCS) UMR-CNRS 5531, ENSERG, 23 rue des Martyrs,
38016 Grenoble, France

^b LETI (CEA-Technologies Avancées), DMITEC-CEN/G, 85X F38041 Grenoble, France

Abstract

The excess low frequency noise of silicon carbide Schottky diodes has been systematically measured on *n*-type SiC devices with Ti gates. The noise results have been related to general properties such as barrier height and doping level. The 1/f noise closely follows a model proposed in Ref. [3] [T.G.M. Kleinpenning, Solid State Electron. 22 (1979) 121–128] and is thus most probably due to mobility fluctuations in the depletion region of the Schottky barrier. © 1997 Elsevier Science S.A.

Keywords: Electrical noise; Schottky diode; Silicon carbide

1. Introduction

The fabrication of high-quality Schottky barriers is a key aspect for developing various SiC components [1]. Devices such as power Schottky diodes and SiC MESFETs would represent serious competitors with respect to silicon and gallium arsenide in the field of fast power switches and high frequency/high power transistors, respectively. Owing to relatively recent improvement in material quality, a detailed investigation of their properties and performance is therefore required. Noise analysis can be useful not only for improving device performance, but also for gaining substantial information on the physical properties of the SiC material. The aim of this paper is to present a systematic evaluation of the low frequency excess noise in 6H-SiC Ti Schottky diodes fabricated at LETI and then to give a quantitative interpretation of the data. We also wish to demonstrate that from the point of view of noise, these devices are, in fact, very conventional and do not exhibit any excess noise that could be due to large defect densities or anomalous properties.

2. Devices

The Schottky diodes have been fabricated at LETI by depositing Ti on 5° off, Si-face, *n*-type 6H-SiC

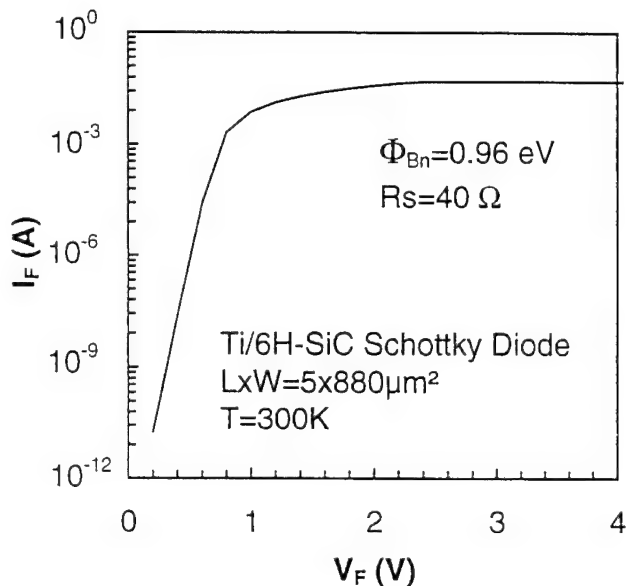


Fig. 1. Typical current voltage characteristic in the forward regime.

epitaxial layers grown on 6H-SiC substrates (Cree Research, Inc., Raleigh, NC). The device area ranged from $100 \times 1 \mu\text{m}$ to $800 \times 100 \mu\text{m}$. The doping level was $N_D - N_A \approx 10^{17} \text{ cm}^{-3}$. $I(V)$ and $C(V)$ characteristics were monitored from 25 °C up to 300 °C. The low frequency (LF) noise measurements (100–100 kHz) were performed at room temperature. Only the forward regime has been investigated by noise measurements in the part where the series resistance was negligible.

* Corresponding author.

3. Current–voltage characteristics

Typical $I(V)$ curves are given in Fig. 1. For all devices, the ideality factor always remained close to one, as can be seen in Fig. 2. This indicates that the thermo-ionic model can safely be used as a first-order approximation for modelling the data in the forward conduction regime. To extract the barrier height, we used plots of I_F/T^2 vs. $1/T$ (Fig. 3), extrapolations of $\ln(I_F)$ at $V_F=0$ or $C(V)$ characteristics. All methods gave similar values, i.e. from 0.93 to 0.96 eV, in agreement with previous results published by other groups [2].

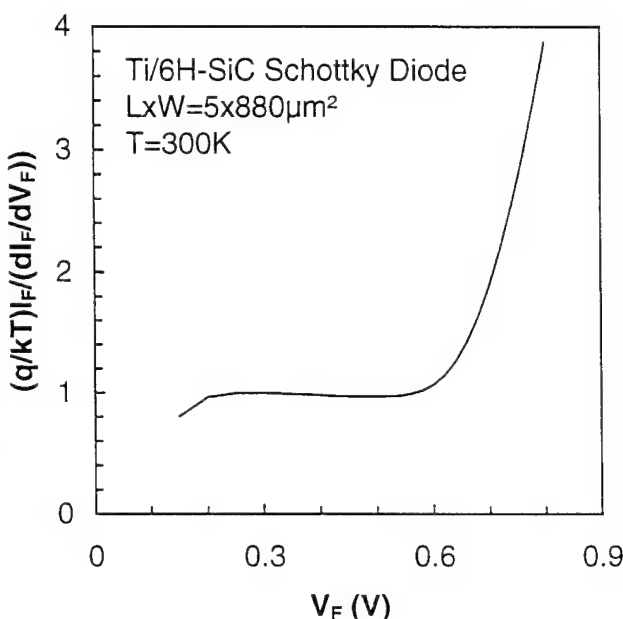


Fig. 2. Assessment of the ideality factor.

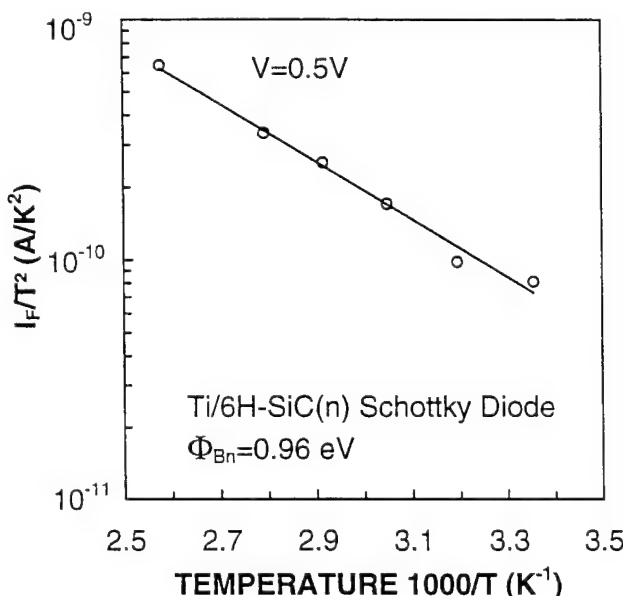


Fig. 3. Extraction of the barrier height by a Richardson's plot.

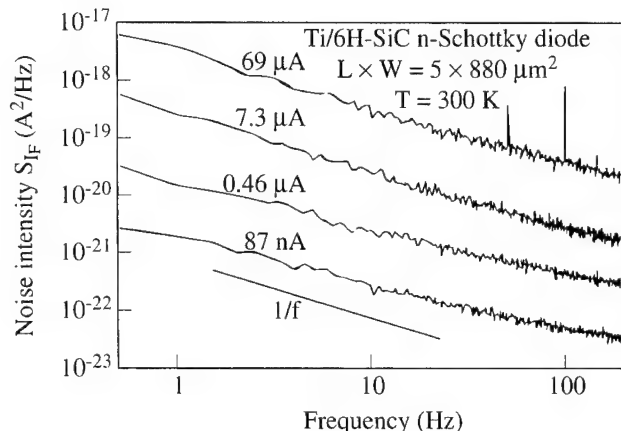


Fig. 4. Typical noise spectra in the forward current regime.

In contrast to the forward bias regime, the activation energy corresponding to the reverse current does not correspond to the barrier height and largely varies depending on the V_R value. Besides, the field dependence of this variation is not compatible with a conventional effect such as Schottky lowering of the effective barrier height. It is worth noting that there was no linear dependence of the reverse current on the sample area. This probably means that part of the reverse current is induced by leakage through the sample edges.

4. Noise results and interpretation

Typical noise spectra in the forward current regime are given in Fig. 4. At low frequency, the diodes exhibit $1/f$ noise and the power spectral density of the current fluctuations is described by the empirical relation $S_{IF} \approx I_F^\beta / f^\gamma$, where I_F is the forward current, f is the frequency, $1 < \beta < 1.4$, and γ remains very close to one, in agreement with experimental results obtained with Schottky diodes fabricated with other semiconductors [3]. It is worth noting that if the limiting conduction mechanism was pure thermo-ionic emission, there would be no reason to observe mobility $1/f$ noise because the carrier mobility does not appear anywhere in such a model. The possible sources of $1/f$ noise can therefore originate either from barrier height fluctuations or mobility noise arising from correction factors to the thermo-ionic model.

Several theories have been proposed to account for the $1/f$ noise appearing in Schottky barriers, most of them invoking carriers number fluctuations: Hsu [4] has interpreted this noise in terms of trapping and multistep tunnelling processes in the depletion region. These processes induce a random fluctuation in the occupancy of the trap centres, which finally leads to local fluctuations of the barrier height and eventually to current noise; besides, other experiments showed that $1/f$ noise could also be generated at the periphery of the diode through

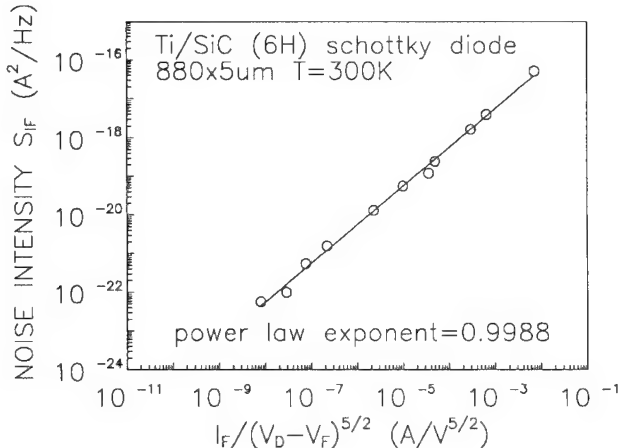


Fig. 5. Noise intensity at 1 Hz versus $I_F/(V_D - V_F)^{5/2}$.

the device edges. Still another model invokes a modulation of the barrier height [3], through trapping or generation-recombination (GR) noise in the depletion region, the charge density fluctuations in the space charge region also inducing local changes in the barrier height. Then, if the GR centers are located at the mid-gap, it was shown that the current noise should be of the form $S_{IF} \approx I_F^3/f^2$ [3]. Alternatively, if the GR centers are located above the mid-gap and only transitions between the conduction band and GR centers are taken into account (trap states uniformly distributed in space as well as in energy and with a constant capture cross-section), the total current noise may exhibit a $1/f$ behaviour and then must vary as $I_F^2/(V_D - V_F)^{3/2}$, where V_D is the diffusion voltage at zero bias [3]. In our case, we never obtained $S_{IF}(I_F)$ dependencies compatible either with that of GR noise in the depletion region or with trapping and multi-step tunnelling. Besides, mobility noise in the neutral part of the semiconductor should follow a law of the form $S_{IF} \approx I_F^2/f$, which is also not supported by the experimental data.

Kleinpenning has proposed an additional mechanism [3]. Normally, an ideal diode, with an $I-V$ characteristic independent of the mobility of free carriers, does not generate mobility $1/f$ noise. However, it is now well established that the simplest form of Richardson's equation, or the thermo-ionic current model, must be corrected to take into account carrier drift and diffusion in the depletion region of the diode (see, for example, Ref. [5]). As a consequence, mobility fluctuations manifesting themselves in the depletion region could also be a source of $1/f$ noise. In that case, mobility noise can be locally described by the celebrated Hooge formula, which states that the relative $1/f$ noise intensity is simply inversely proportional to the number of carriers in the sample. Kleinpenning then gives the total noise density as [5]:

$$S_{IF} = \frac{\alpha I_F}{16\pi f} \left(\frac{kT}{q(V_D - V_F)} \right)^{5/2} \left(\frac{q}{\mu m^*} \right)^2 \left(\frac{m^* \epsilon}{\pi N_D} \right)^{1/2}, \quad (1)$$

where α is the Hooge factor and other symbols have their usual meaning. The difference $V_D - V_F$ can be calculated from Richardson's equation:

$$V_D - V_F = \frac{kT}{q} \ln \left(SA^* T^2 \frac{N_D}{N_C I_F} \right). \quad (2)$$

In our case, $S = 44 \times 10^{-6} \text{ cm}^2$, $A^* = 154 \text{ A}^2 \text{ cm}^2 \text{ K}^2$, $N_D = 10^{17} \text{ cm}^{-3}$ and $\mu = 200 \text{ cm}^2 \text{ V}^{-1} \text{ s}^{-1}$. As can be seen in Fig. 5, a log-log plot of S_{IF} as a function of $I_F/(V_D - V_F)^{5/2}$ gives straight lines, and this was verified for all the devices investigated (about 10 samples). Although a plot of S_{IF} vs. I_F gives a power law exponent which depends on the device area (between 1 and 1.4), in the somewhat more complicated plot of Fig. 5, we found an exponent very close to unity for all samples. Hence, our results are in good agreement with Kleinpenning's model.

We found a Hooge factor $\alpha = 10^{-3}$. Owing to the doping level, this is quite comparable with the values found for usual covalent semiconductors, when lattice scattering prevails [6]. Lower values appearing in the literature are, in general, not due to a better material quality, but to a degradation of the overall mobility by impurity scattering [6]. Our results are thus a good indication that in our devices, the defect or GR centre density remains low at and close to the interface. This is in contrast with other interfaces which can be built on SiC, such as thermal or deposited oxides.

5. Conclusion

The low frequency $1/f$ noise appearing in 6H-SiC Schottky diodes has been investigated for devices with an ideality factor close to unity. None of the existing models based on carriers' number fluctuations agreed with the experiment. In contrast, our data nicely fit the model proposed by Kleinpenning a few years ago, which attributed the current fluctuations to a consequence of mobility fluctuations in the depletion region of the diode. The overall results therefore indicate that the density of traps close to the metal-semiconductor interface must remain within a reasonable range and that at room temperature, generation-recombination processes do not affect the diode behaviour.

References

- [1] R.F. Davis, G. Kelner, M. Shur, J.W. Palmour, J.A. Edmond, Proc. IEEE 79 (1991) 677.
- [2] A. Itoh, O. Takemura, T. Kimoto, H. Matsunami, Inst. Phys. Conf. Ser. 142 (1996) 689–692.
- [3] T.G.M. Kleinpenning, Solid State Electron. 22 (1979) 121–128.
- [4] S.T. Hsu, IEEE Trans. 7 (17) (1972) 496–506.
- [5] S.M. Sze, Physics of Semiconductor Devices, Wiley, New York, 1981.
- [6] F.N. Hooge, IEEE Trans. Electron. Dev. 11 (41) (1994) 1926–1935.

Passivation of interface traps in MOS-Devices on *n*- and *p*-type 6H-SiC

E.G. Stein von Kamienski, C. Leonhard, S. Scharnholz *, A. Götz, H. Kurz

Inst. f. Halbleitertechnik II, RWTH Aachen, Sommerfeldstr. 24, D-52074 Aachen, Germany

Abstract

Interface traps in the SiO_2 –6H-SiC system can be passivated by a high temperature anneal in hydrogen or moistrous atmosphere. The passivation is very effective for deep donor like traps which are reduced towards the $10^{11} \text{ cm}^{-2} \text{ eV}^{-1}$ range. The electrical properties of *n*-channel MOSFETs show that the gate oxides contain only a low density of fixed oxide charges in the low 10^{11} cm^{-2} range for the passivated and the unpassivated state. It is further demonstrated that deep donor-like interface states hardly affect the electrical properties of *n*-channel MOSFETs on 6H-SiC. © 1997 Elsevier Science S.A.

Keywords: Gate oxide; MOSFET; Passivation; SiC

1. Introduction

MOSFETs (metal oxide semiconductor field effect transistor) on SiC are promising devices for low-loss power applications [1]. Their calculated superior device properties depend crucially on the qualities of the gate oxide and the oxide–SiC interfaces. Oxide charges as well as interface states affect the threshold voltage and the conducting behavior of the device. In the SiO_2 –Si system, these defects can effectively be passivated by hydrogen achieving densities below 10^{10} cm^{-2} [2]. The work of several research groups revealed lower oxide charge densities for wet oxidized SiC-wafers compared with dry oxidized ones, especially for *p*-type SiC [3–5]. The influence of hydrogen was already assumed to be the reason for this effect [3]. In this report, a defect passivation for the SiO_2 –SiC system will be presented. It will be demonstrated that the passivation is very effective for deep donor-like traps. This offers the possibility to investigate the influence of these deep donor like traps on the electrical properties of *n*-channel MOSFETs on SiC.

2. Experiment

MOS-capacitors are fabricated using *n*- and *p*-type 6H-SiC epitaxial layers on substrates from Cree Research, Inc., Durham, NC, USA. After a wet chemical cleaning sequence, the oxidation is performed in wet

oxygen at 1150°C resulting in an oxide thickness of 40 nm. The samples are cooled down in the oxidizing atmosphere and heated again to 1150°C in Ar or Ar/H₂ (90:10) for POA (post-oxidation anneal). This process results in water saturated samples for the unannealed case. A detailed process sequence is described elsewhere [6].

N-channel MOSFETs with different gate lengths of 3, 10 and 50 μm and a gate width of 500 μm on *p*-type 6H-SiC are fabricated using a non-self-aligned process. The source and drain diodes are implanted with N at energies ranging from 30 to 200 keV up to a total dose of $2 \times 10^{15} \text{ cm}^{-2}$, followed by an Ar anneal at 1300°C . A field oxide of 300 nm thickness is deposited by a PECVD (plasma enhanced chemical vapour deposition) process. MOSFETs with two different gate oxidation processes are fabricated (M1 and M2): the first gate oxidation is performed in dry oxygen followed by a POA in Ar for 60 min (M1). The second oxide is fabricated in wet oxygen and annealed in Ar/H₂ (90:10) (M2). Both processes are performed at 1150°C and result in an oxide thickness of 50 nm. For metallization of the source and drain diodes as well as the gate contacts, a Ti/Au double-layer is used. No PMA (post-metallization anneal) is performed.

The MOS capacitors as well as the gate oxides of the MOSFETs are characterized by *CV* (capacitance–voltage) measurements after illumination in deep depletion/inversion. Similar to the Jenq technique [7], the accumulated density of interface traps can be derived from the position of the interface state ledges in the *CV*

* Corresponding author.

curves. This method allows to detect interface states on *n*-type SiC, which are located deep below the conduction band edge, as described in more detail elsewhere [8]. The MOSFET-parameters threshold voltage V_T , channel mobility μ_c , interface state density D_{it} and serial resistance R_s are measured at room temperature as described in Refs [9,10].

3. Results and discussion

CV curves from Ar-annealed oxides on *n*-type 6H-SiC reveal a moderate V_{fb} (flatband voltage) shift, but an interface state ledge at -30 V. Equally fabricated oxides on *p*-type 6H-SiC show a large V_{fb} shift of -30 V, but an interface state ledge at moderate bias. These results on the two substrate types correspond to a low density of interface states in the upper half of the band gap in the $10^{11} \text{ cm}^{-2} \text{ eV}^{-1}$ range, but a high density in the $>10^{12} \text{ cm}^{-2} \text{ eV}^{-1}$ range of deep donor-like traps in the lower half of the band gap. Deep donor-like interface traps do not affect the V_{fb} value of MOS capacitors on *n*-type SiC because these defects are filled, and thus neutral at flatband condition. These results demonstrate that the defect densities on the *n*- and *p*-type samples are comparable.

The unannealed (wet) and Ar/H₂-annealed samples show moderate V_{fb} values for both *p*- and *n*-type substrates (Fig. 1). The interface state ledges for the two oxides on *n*-type SiC again correspond well with the V_{fb} values of the *p*-type samples. These results indicate drastically reduced densities of deep donor-like interface traps towards the range of $10^{11} \text{ cm}^{-2} \text{ eV}^{-1}$ for these oxides, as compared with the dry oxidized samples. Additionally, the Ar/H₂-annealed samples reveal reduced hysteresis in

the *CV* characteristics. For the *n*-type sample, this indicates a reduced density of flat interface states near the conduction band edge. For the *p*-type sample this effect corresponds well to the reduction of deep donor-like interface states near the valence band edge.

The low defect densities for the unannealed (wet) and in Ar/H₂-annealed samples give strong evidence for a defect passivation by OH-groups and/or hydrogen. Thus, a passivated and an unpassivated state of the SiO₂-SiC system can be defined. Obviously, the passivation is very effective for the donor-type defects.

Additional high-temperature treatments of the passivated samples above 300 °C increase the negative V_{fb} and interface state ledge-shifts for the *p*- and *n*-type samples, respectively (data not shown here). At the end, these treatments result in identical *C-V* curves, compared with the dry processed samples. From this, it can be concluded that the passivation is lost at temperatures above 300 °C, which can be explained by an outdiffusion of hydrogen. Furthermore, the passivation causes increased oxide trap densities, which are worse for the wet samples [8]. The results from the MOS capacitors can be explained by the passivation of interface states. From the *CV* data, a low density in the $<10^{11} \text{ cm}^{-2}$ range of fixed oxide charges might be expected for all of the presented samples. However, the polarity and density of fixed oxide charges cannot be derived from room temperature *CV* measurements because the influences of interface states and fixed oxide charges cannot be distinguished. To investigate this item, the electrical properties of MOSFETs containing gate-oxides with and without passivation are discussed in the following paragraphs (Figs. 2–4).

The fixed oxide charges directly affect the threshold voltage of MOSFETs. A high density of positive oxide charges would result in a negative V_T value. Instead of

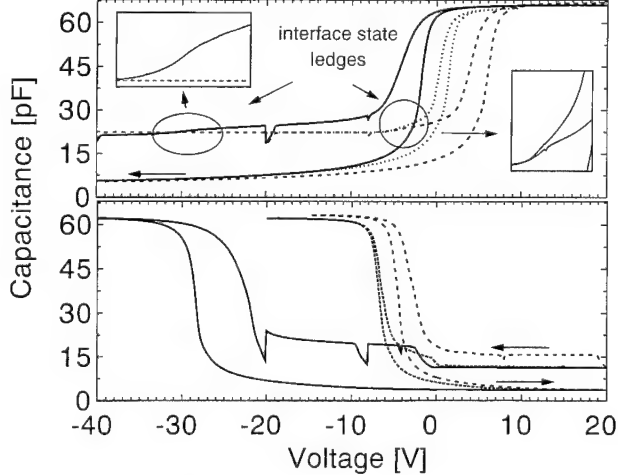


Fig. 1. *CV* data of MOS capacitors on *p*- (bottom) and *n*-type (top) 6H-SiC; wet oxidation (dashed) and POA at 1150 °C in Ar (solid) or Ar/H₂ atmosphere (dotted). The capacitance drop at -20 , -8 and -4 V is an artifact caused by the measurement setup.

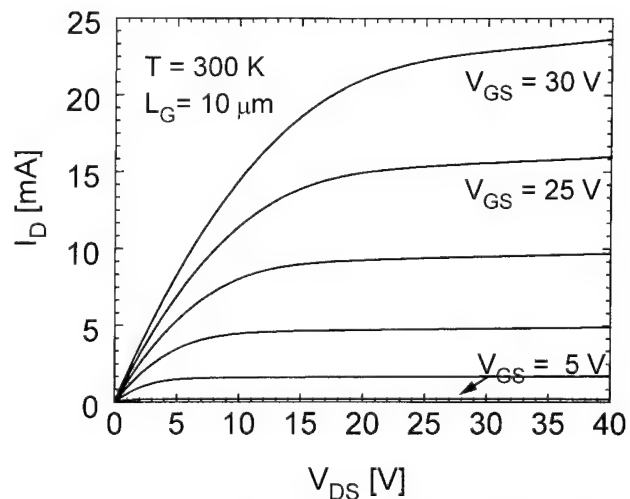


Fig. 2. I_D versus V_{DS} characteristic of 6H-SiC MOSFET, $W/L = 500/10 \mu\text{m}$, unpassivated gate oxide: dry oxidation and 60 min POA in Ar.

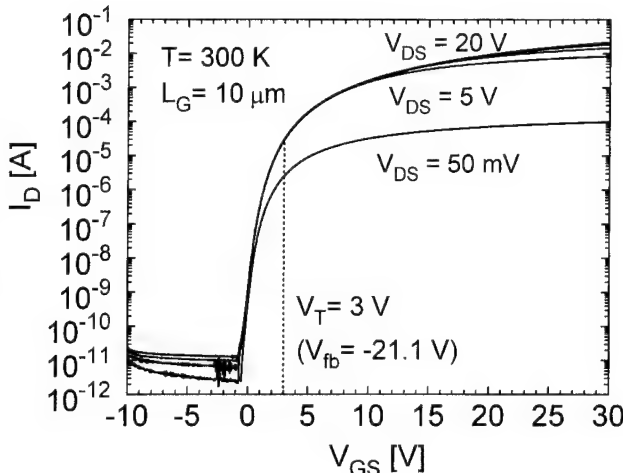


Fig. 3. I_D versus V_G characteristic of 6H-SiC MOSFET, $W/L = 500/10 \mu\text{m}$, unpassivated gate oxide: dry oxidation and 60 min POA in Ar.

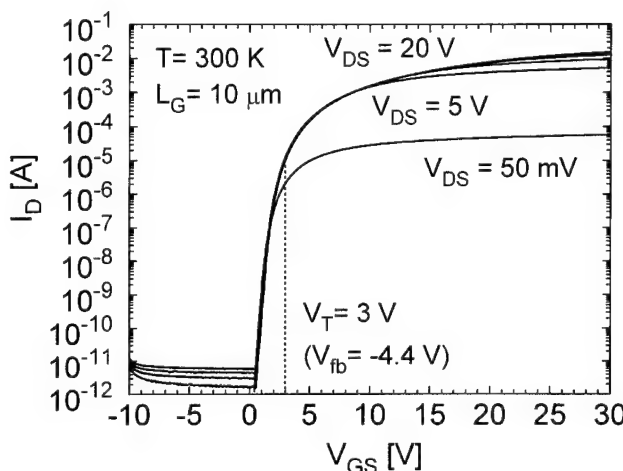


Fig. 4. I_D versus V_G characteristic of 6H-SiC MOSFET, $W/L = 500/10 \mu\text{m}$, passivated gate oxide: wet oxidation and 30 min POA in Ar/H₂.

this, the V_T value of 3 V for the n -channel MOSFET containing the unpassivated gate oxide (M1) indicates that the fixed oxide charge density in this oxide is indeed in the low 10^{11} cm^{-2} range. Additionally, a negative polarity of the charges can be assumed. This impressively demonstrates that the large V_{fb} shift (-21 V) of the unpassivated oxide is due to deep donor-like interface states only.

The MOSFET with the passivated gate oxide (M2) shows the same V_T value of 3 V. Compared with M1, the calculated D_{it} value in M2 is reduced by a factor of two, indicating the passivation of interface states. The channel mobility of $29 \text{ cm}^2 \text{ V}^{-1} \text{ s}^{-1}$ is slightly increased for M2, which can be put down to the reduced interface state density. However, the increase is rather low. Obviously, the high density of deep donor-like interface states ($> 10^{12} \text{ cm}^{-2} \text{ eV}^{-1}$) in M1 hardly affects the electrical properties of n -channel MOSFETs on 6H-SiC. This is the case because in inversion condition these

defects are neutral and thus ineffective to the charge carriers in the channel.

4. Conclusions

A passivation of interface states by hydrogen or OH groups can be achieved for the SiO₂–SiC system. No differences are found for oxides on n - and p -type SiC. In consequence, a passivated and an unpassivated state of the SiO₂–SiC system can be defined. This passivation is highly effective for deep donor-like interface states resulting in low D_{it} values of $10^{11} \text{ cm}^{-2} \text{ eV}^{-1}$. From this, it can be concluded that these defects are due to dangling bonds at the SiO₂–SiC interface. The passivation is unstable at temperatures above 300 °C; thus, it is not usable for high temperature applications exceeding this temperature.

The positive V_T value of 3 V of the unpassivated MOSFET M1 demonstrates that: (1) the high V_{fb} shift of -21 V is due to deep donor-like interface states; and thus (2) the gate oxide contains only a low density ($< 10^{11} \text{ cm}^{-2}$) of fixed oxide charges. The high density of deep donor-like interface states ($> 10^{12} \text{ cm}^{-2} \text{ eV}^{-1}$) hardly affects the electrical properties of this device because they are electrically neutral in the inversion case. Further studies will focus on the passivation of interface states near the conduction band edge, which are electrically active in the inversion channel and thus reduce the channel mobility.

Acknowledgement

We gratefully acknowledge the support of this work by the Bundesministerium f. Bildung, Wissenschaft, Forschung und Technologie (BMBF). Under contract No. 01BM302.

References

- [1] M. Bhatnagar, B.J. Baliga, IEEE Trans. Electron. Dev. 40 (1993) 645.
- [2] P. Balk, The Si–SiO₂ System, Elsevier, Amsterdam, 1988.
- [3] S. Zaima, K. Onoda, Y. Koide, Y. Yasuda, J. Appl. Phys. 68 (1990) 6304.
- [4] M. Yoshikawa, H. Itoh, Y. Morita, I. Nishiyama, S. Misawa, H. Okumura, S. Yoshida, J. Appl. Phys. 70 (1991) 1309.
- [5] J.N. Shenoy, G.L. Chidalore, M.R. Melloch, CooperJ.A., Jr., J.W. Palmour, K.G. Irvine, J. Electron. Mater. 23 (1995) 303.
- [6] E.G. Stein von Kamienski, F. Porteine, J. Stein, A. Götz, H. Kurz, J. Appl. Phys. 79 (1996) 2529.
- [7] C.S. Jenq, PhD thesis, Princeton University, 1978.
- [8] E.G. Stein von Kamienski, C. Leonhard, F. Porteine, A. Götz, H. Kurz, Mat. Sci. Eng. B. 46 (1997) 263–266.
- [9] R. Paul, MOS-Feldeffekttransistoren, Springer-Verlag, Berlin, 1994.
- [10] G. Ghibaudo, Electron. Letters 24 (1988) 543.

Numerical study of avalanche breakdown of 6H-SiC planar *p*–*n* junctions

E. Stefanov ^{a,*}, L. Bailon ^b, J. Barbolla ^b

^a LAAS – CNRS, 7, Avenue Colonel Roche, 31077 Toulouse, Cedex, France

^b Department of Electricity and Electronics - Faculty of Sciences, University of Valladolid, 47071 Valladolid, Spain

Abstract

The effect of the junction curvature, oxide charge density and *n*-epitaxial layer doping on 6H-SiC planar *p*–*n* junction breakdown capabilities is reported. The calculated breakdown voltage of a cylindrical unprotected junction is compared with that of field-plate- (FP-) and multiple field-limiting-ring- (FLR-) guarded junctions with optimized geometries. © 1997 Elsevier Science S.A.

Keywords: Breakdown voltage; GH-SiC, *p*–*n* junction; Junction termination extensions; Floating ring; 2-D numerical analysis

1. Introduction

The design of power devices relies considerably on the design of junctions that have the necessary high voltage handling capabilities. Recent technology developments to fabricate planar devices based on 6H-SiC are encouraging [1], and the opportunity to use some junction termination extension (JTE) techniques directly from Si technology becomes realistic. Various JTEs for planar junctions [2–4] have been reported for SiC devices, but only 50% of the ideal plane breakdown voltage was observed.

We report a numerical study of the effect of the junction curvature on breakdown voltage V_{BR} for planar *p*–*n* junctions in 6H-SiC. The effect of the junction radius r_j , background doping N_B and fixed charge density N_f on V_{BR} is analyzed for a cylindrical *p*–*n* junction with a gaussian profile. Two concepts for planar JTE ($r_j = 1 \mu\text{m}$ and $N_B = 1.5 \times 10^{16} \text{ cm}^{-3}$) are studied: (1) FP-; and (2) multiple-FLR-structures. Ninety percent of the ideal plane parallel junction breakdown voltage was obtained for an optimized FLR system with five rings. The two-dimensional off-state program POWER was used to simulate the breakdown.

2. The program

The two-dimensional off-state simulator POWER [5] is a user-oriented program for power devices. The simu-

lation is based on the solution of Poisson's equation for an arbitrary two-dimensional structure:

$$\nabla \epsilon \nabla \psi = -q(N_D^+ - N_A^- + p - n) - \rho_f, \quad (1)$$

where ψ is the electrostatic potential; ρ_f is the fixed charge density; ϵ is the permittivity, q is the elementary charge, n and p are the electron and hole densities, respectively, and N_D^+ and N_A^- are the ionized donor and acceptor densities. The ionization integrals for the carriers from the resulted electric field are calculated. The criterion for achieving breakdown is when these integrals tend to unity. A special algorithm included in the program ensures fast and automatic search of breakdown voltage. The generation rates were calculated by using the *average set* of the ionization parameters for 6H-SiC given by Ruff et al. [6]. The program has been extended by an efficient algorithm to reduce the number of iterations when adjusting the quasi-Fermi potential of floating guard rings.

3. Device structure and simulation results

Plane parallel *p*–*n* junctions with depths X_j , and planar cylindrical junctions with curvature radius r_j of 0.1, 0.3, 1, 3 and 10 μm are studied. The doping profile in all *p*–*n* junctions is approximated by a gaussian in both the vertical and lateral directions. The profile has a surface concentration $N_s = 1 \times 10^{20} \text{ cm}^{-3}$. The ratio of lateral to vertical diffusion for the planar junction is assumed to be unity. The background doping N_B is in

* Corresponding author.

the range 1×10^{15} – $1 \times 10^{18} \text{ cm}^{-3}$ and the diodes are considered non reach-through. The fixed charge density N_f is taken into account.

Two JTE techniques have been studied for breakdown voltage capabilities. Fig. 1 shows the device structure of multiple FLR protected planar p^+ n diode with substrate doping $N_D = 1.5 \times 10^{16} \text{ cm}^{-3}$ and junction radius $r_j = 1 \mu\text{m}$. The ring spacing $d_r(i)$ is the width of the n -substrate at the surface between two adjacent p -rings. The ring width $W_r(i)$ is the width of the i th ring at the surface. The main junction is reverse biased with applied bias V_R . The second JTE is an FP-guarded planar diode with the same junction radius and substrate doping as for FLR, and is optimized for both the field plate length and oxide thickness.

Fig. 2 shows the calculated breakdown voltage V_{BR} dependence on the background doping for plane parallel p - n junctions with gaussian profile. A comparison is given with the ideal V_{BR} of an abrupt junction. Fig. 3 shows the maximum electric field and depletion width at breakdown. When decreasing the junction depth X_j from 10 to 0.1 μm , the abrupt junction behavior is approached. In this case, the doping gradient in the depletion layer increases due to decrease of the gaussian standard deviation (the surface concentration is kept

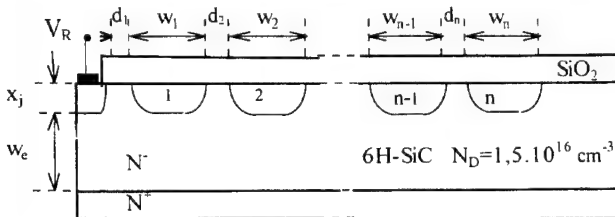


Fig. 1. Device structure of multiple FLR-protected p - n junction.

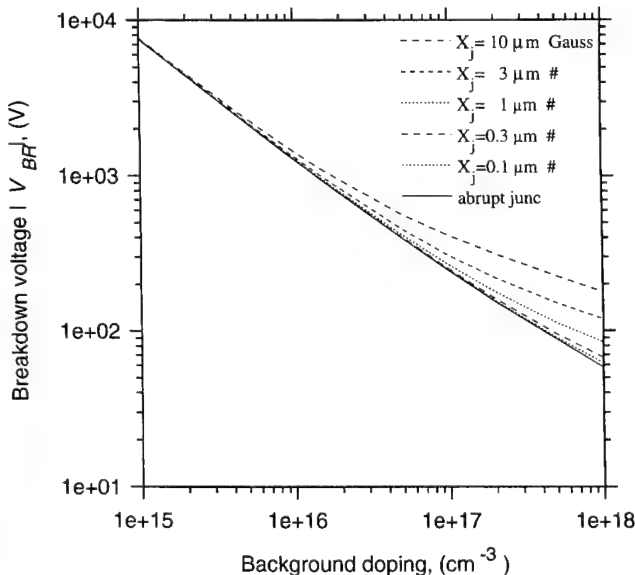


Fig. 2. V_{BR} versus doping for a plane parallel junction.

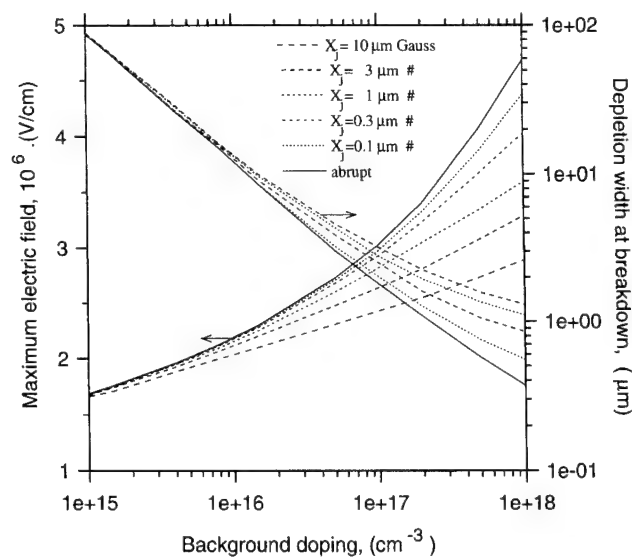


Fig. 3. Maximum electric field and depletion width at breakdown versus doping for plane parallel junctions.

constant). As a result, one side of the junction becomes considerably more doped than the other, and the maximum electric field at the junction becomes higher when increasing the substrate doping.

Fig. 4 shows the maximum electric field dependence on N_B in the case of planar cylindrical junction with gaussian profile. The parameter is the curvature radius r_j and the solid line is for plane abrupt junction. The critical field behavior differs from the one shown in Fig. 3, owing to the additional effect of the junction curvature. In all cases, E_m varies by less than a factor of three in going from $r_j = 0.1 \mu\text{m}$ to $10 \mu\text{m}$. V_{BR} of the planar junction is normalized in respect of the

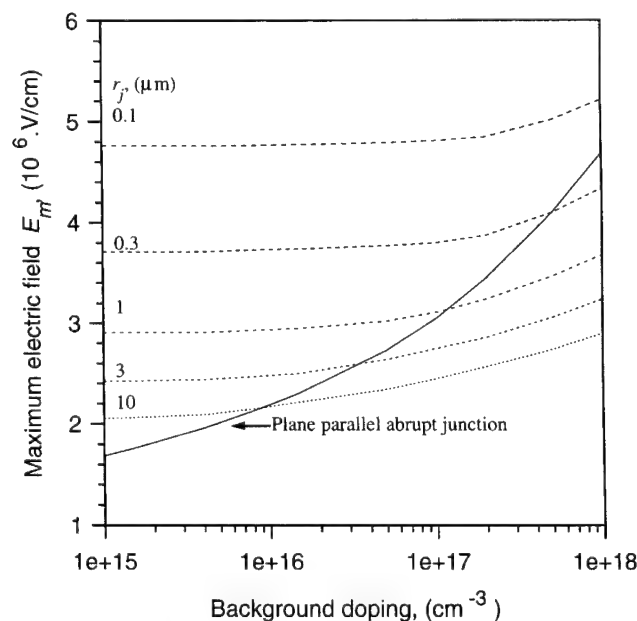


Fig. 4. Maximum electric field versus doping for a planar junction.

breakdown voltage in plane parallel gaussian doped junction with the same junction depth $r_j = X_j$. Both V_{BR} and normalized breakdown voltage versus the substrate doping is given in Fig. 5 for radius $r_j = 0.1, 0.3, 1, 3$ and $10 \mu\text{m}$.

The relatively high fixed charge density present at the $\text{SiO}_2\text{--SiC}$ interface was numerically investigated on unprotected cylindrical $p\text{--}n$ junctions for N_f in the range $0\text{--}5 \times 10^{12} \text{ cm}^{-2}$. Fig. 6 shows both V_{BR} and the normalized breakdown voltage versus background doping for $r_j = 1 \mu\text{m}$. The effect of N_f is much more pronounced for lower doped substrates due to the reduced screening effect of the substrate.

In the FP technique the effect of oxide thickness d_{ox} , FP length L_{FP} and oxide charge are analyzed in order to obtain the maximum V_{BR} . For a non-reach-through junction with $X_j = 1 \mu\text{m}$, background doping

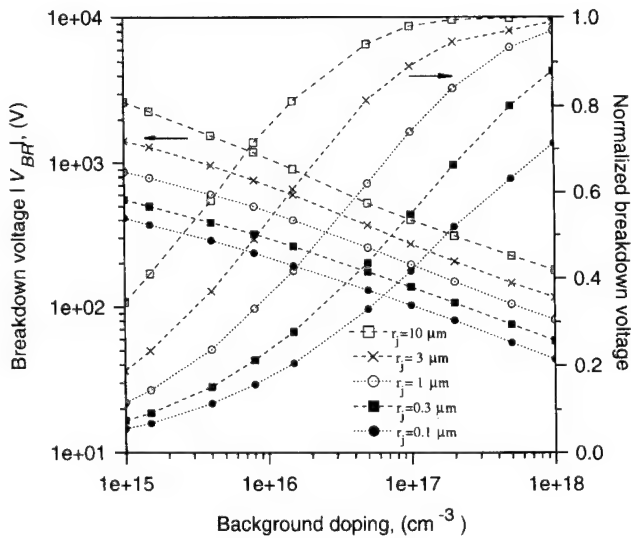


Fig. 5. V_{BR} versus doping; $N_f = 5 \times 10^{10} \text{ cm}^{-2}$.

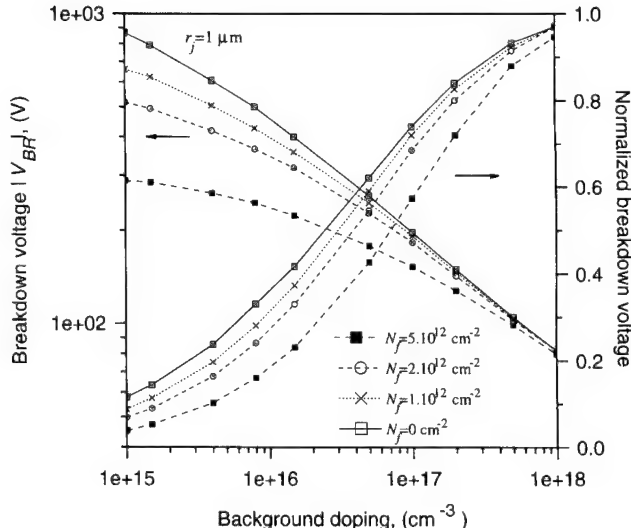


Fig. 6. V_{BR} versus doping; N_f is parameter.

$1.5 \times 10^{16} \text{ cm}^{-3}$, the optimal $V_{BR} = 640 \text{ V}$ is obtained by using $d_{ox} = 0.4 \mu\text{m}$, and $L_{FP} = 10 \mu\text{m}$. An increase of some 60% for the breakdown compared with that for an unprotected cylindrical junction is shown. The normalized breakdown voltage is 0.65 V. The multiple FLR concept was studied by using a new effective method [7] to optimize the basic parameters, exerting influence on the breakdown capabilities: ring-to-ring spacing d_r , ring width W_r , and number of rings. This method consists of modeling the breakdown capabilities of a main junction protected by one ring. The breakdown voltage of such a structure is examined as a function of d_r and W_r . These results are extended to a multiple ring system. As a result, a structure with five floating rings was optimized to give a breakdown at $V_{BR} = 863 \text{ V}$, showing an increase of 110% of the breakdown compared with that for a cylindrical unprotected junction. The normalized breakdown voltage is 0.9 V. The optimized widths of the rings are 8, 4, 2, 2 and 2 μm and the spacings are 0.5, 0.6, 0.7, 1.1 and 1.9 μm . The lateral spread of the structure extends some 30 μm in respect of the main junction. Fig. 8 shows the two-dimensional equipotential lines for the optimized five-FLR system at breakdown.

The V_{BR} sensitivity of both techniques was studied in respect of the oxide charge and compared with that for a cylindrical unprotected junction. The V_{BR} dependence on N_f for the optimized FLR structure is plotted on Fig. 7 (solid line). Fig. 7 gives also a comparison of the normalized breakdown versus N_f for an unprotected junction (dashed line), an FP- (long dashed line) and an FLR-protected (dotted line) junction. The decrease in V_{BR} with the increase in N_f is smaller for an FP junction in the whole calculated range of charge densi-

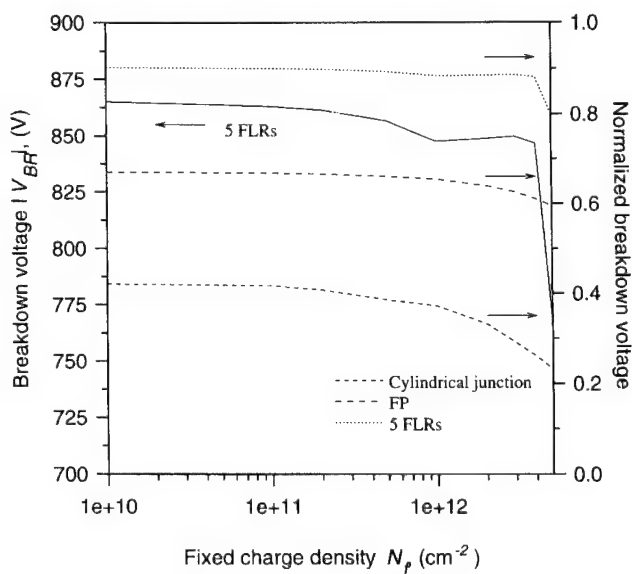


Fig. 7. V_{BR} versus N_f for the optimal FLR system. Comparison of the normalized V_{BR} between the FP- and five-FLR systems, and unprotected cylindrical junction.

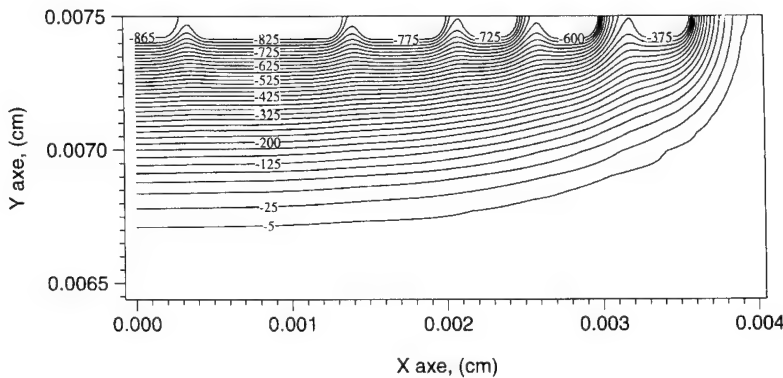


Fig. 8. Two-dimensional equipotential lines for a five-floating-rings protected junction at breakdown, $V_{BR} = 863$ V.

ties. The plate, by means of the field effect, spreads the maximum electric field away from the junction curvature and increases the depletion width. As a result, the electric field reduces and V_{BR} increases. In the FLR structure, two adjacent ring junctions act on the maximum field locus by pushing it deeply in the bulk around the junction curvature. Our optimized five-ring structure was optimized for $N_f = 1 \times 10^{11} \text{ cm}^{-2}$ and saves its excellent breakdown capabilities in the range $0.4 \times 10^{12} \text{ cm}^{-2}$ by showing a negligible decrease. In order to expand the validity for larger N_f , additional optimization of FLR geometry has to be made by increasing the rings number and decreasing the spacings.

4. Conclusion

We analyzed the effect of planar junction radius, n -epitaxy doping and SiO_2 -6H-SiC interface properties on $p-n$ junction breakdown capabilities by two-dimensional device simulation. The efficacy of device termination design has been examined for both field-plate- and five-floating-rings systems' protected junctions. The results presented in the report clearly demonstrate the superiority of the FLR concept, and also the possibility to achieve near ideal efficiency of breakdown capabilities

for shallow junctions. These results could serve as design constraints when designing power devices based on 6H-SiC.

Acknowledgement

This work is supported by EUROFORM-TRTI Human Capital and Mobility Program under Contract No. ERBCHBG CT940696, and by Spanish C.I.C. y T. and Junta de Castilla y Leon.

References

- [1] S. Sheppard, M. Melloch, J. Cooper, IEEE Trans. Electron. Devices 41 (1994) 1257.
- [2] T. Wang, T. Chow, D. Brown, M. Ghezzo, Proceedings of the 4th International Symposium ISPSD and ICS, Tokyo, 1992, p. 303.
- [3] M. Bhatnagar, H. Nakanishi, S. Bothra, P. McMarthy, B. Baliga, Proceedings of the 5th ISPSD, vol. 5, 1993, p. 89.
- [4] Dev Alok, B. Baliga, Proceedings of the 7th ISPSD, vol. 7, 1995, pp. 96–100.
- [5] E. Stefanov, G. Charitat, POWER.2D – User's Guide, Rapport LAAS no. 93306, Toulouse, France, 1993.
- [6] M. Ruff, H. Mitlehner, R. Helbig, IEEE Trans. Electron. Devices 41 (1994) 1040.
- [7] E. Stefanov, L. Bailon, J. Barbolla, Solid State Electron. (submitted).



ELSEVIER

Diamond and Related Materials 6 (1997) 1504–1507

DIAMOND
AND
RELATED
MATERIALS

Temperature dependence of electrical properties of 6H-SiC buried gate JFET

C. Raynaud *, C. Richier, G. Guillot

Laboratoire de Physique de la Matière (UMR CNRS 5511), Institut National des Sciences Appliquées de Lyon,
20 avenue Albert Einstein, 69621 Villeurbanne, cedex, France

Abstract

Drain-to-source current–voltage characteristics were measured on n-channel buried gate junction field effect transistors (JFET) in order to determine the electron mobility as a function of temperature. We suggest a method to extract this mobility by taking into account the incomplete ionization of donors in the channel, due to their relatively high activation energies. The mobility is found to vary as $T^{-2.4}$. We also deal briefly with admittance and DLTS results. The shallow level of aluminum is found at 0.24 eV above the valence band, and a deep level, situated at 0.95 eV below the conduction band and localized close to the surface, is also detected. © 1997 Elsevier Science S.A.

Keywords: 6H-SiC; Mobility; JFET; Temperature dependance

1. Introduction

Due to its wide bandgap (2.9 eV), 6H-silicon carbide has been used to produce various field effect transistors (FETs) for high temperature applications [1]. Among them, junction field effect transistors (JFET) are well suited to current SiC growth technology whereas metal-semiconductor field effect transistors suffer from a lack of high-resistivity substrates. Normally-on transistors are more interesting because of the very low minority carrier lifetime (about 10–80 ns [2]) and n-channels are more interesting from the point of view of carrier mobility, hole mobility being lower than electron mobility [3,4]. It is well known that the carrier mobility can be calculated from drain-to-source current characteristics in the case of a dopant level close to the conduction or valence band (E_c or E_v). In silicon carbide, however, the dopant levels are not so close to the band edge [3] as we will see in Section 4. Therefore, at thermodynamic equilibrium, only part of the donor atoms are ionized, which could lead to an underestimated value of the carrier mobility. We calculated the temperature mobility dependence from drain-to-source current–voltage measurements on a buried gate n-channel JFET, taking into account this incomplete ionization of donors at room temperature.

2. Technical details

The devices used in this study were n-channel buried gate JFETs commercially available and fabricated by Cree Research Inc. and described in detail in Ref. [5]. The channel length, width and thickness are $L=5\text{ }\mu\text{m}$, $Z=1\text{ mm}$ and $a\sim 0.2\text{ }\mu\text{m}$, respectively. A thermal oxidation passivates the surface of the wafer to about 20 nm. The equations used in this work are given by Sze [6]. In the ohmic region, the drain-to-source conductance g_d is given by:

$$\frac{1}{g_d} = R_s + R_d + \frac{1}{g_o} \left(1 - \sqrt{\frac{V_{bi} + |V_g|}{V_{po}}} \right)^{-1} \quad (1)$$

with

$$g_o = qn\mu_n \frac{Za}{L} \quad (2)$$

where R_s and R_d are the source and drain series resistances, μ_n the electron mobility, n the electron concentration in the channel, q the electronic charge, V_{bi} and V_g the built-in potential and the gate bias. The pinch-off voltage V_{po} is defined by

$$V_{po} = V_{bi} + V_t \quad (3)$$

* Corresponding author.

where V_t is the threshold voltage, and is related to the effective thickness of the channel by

$$V_{po} = \frac{qN_d}{2\epsilon_s} a^2 \quad (4)$$

N_d is the doping density in the channel, ϵ_s the dielectric constant of 6H-SiC.

In the saturation region, the drain-to-source saturation current is given by

$$I_{dsat} = \beta(V_g - V_t)^2 \quad (5)$$

where β is a coefficient depending on the geometrical parameters of the transistors, on V_p , μ_n and the electron saturation drift velocity.

The built-in potential is given by

$$V_{bi} = \frac{kT}{q} \ln \left(\frac{n_n p_p}{n_i^2} \right) \quad (6)$$

where n_n and p_p are the free electron and hole concentrations in the n-type and p-type material respectively, k the Boltzmann constant, n_i the intrinsic carrier concentration.

It is important to notice that Eq. (2) is given by Sze with N_d instead of n . In fact the conductance g_o is proportional to the concentration of free carriers in the channel. When the donor levels are very close to E_c (as in silicon), all uncompensated donors are ionized and $N_d = n$ at usual temperatures. In silicon carbide, shallow levels are not so close to E_c and therefore, $n < N_d$ at thermodynamic equilibrium (as it is the case in the channel). But in a space charge region, where the electric field sweeps out the electrons emitted by the dopants, n is equal to N_d , so that CV measurements give the doping level, and more precisely $N_d - N_a$.

3. Electrical characterization

CV measurements performed at 100 kHz to avoid the effects of series resistance give a doping level in the channel of $2.7 \times 10^{17} \text{ cm}^{-3}$ and a built-in potential $V_{bi}(300 \text{ K})$ of 2.55 V. Drain-to-source IV measurements as a function of gate bias and temperature have been performed. Fig. 1 shows results obtained at 323 K. From $I_{ds}^{1/2}$ versus V_g curve, we deduce the threshold voltage $V_t(300 \text{ K})$ and from Eqs. (3) and (4), $V_{po}(300 \text{ K}) = -4.5 \text{ V}$ and the effective channel thickness $a = 0.17 \text{ mm}$. Now we suppose that $\mu_n(300 \text{ K}) = 280 \text{ cm}^2 \text{ V}^{-1} \text{ s}^{-1}$, according to Schaffer et al. [4], the value determined by Hall effect measurements for a n-type material with a similar doping level. The slope of the straight line shown in Fig. 2 therefore gives $n(300 \text{ K}) = 1.1 \times 10^{17} \text{ cm}^{-3}$ and $R_s + R_d = 25 \Omega$.

We developed theoretical calculations based on two ionization energy levels both for N and Al. Taking

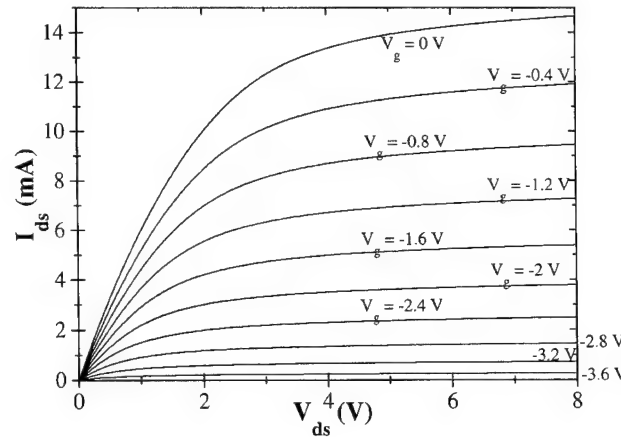


Fig. 1. Drain-to-source current–voltage measurements as a function of gate bias at 323 K.

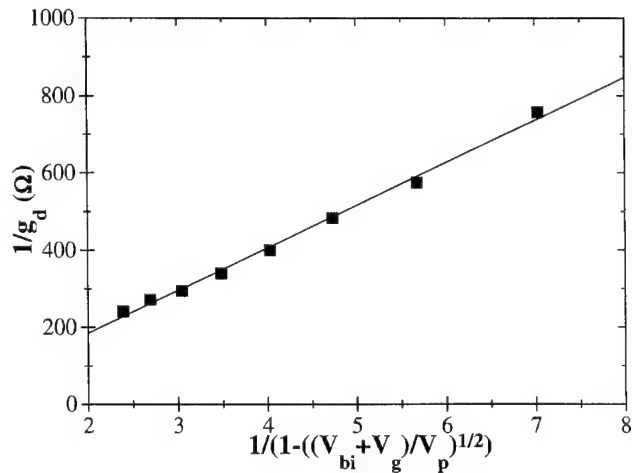


Fig. 2. Reciprocal drain-to-source conductance as a function of reciprocal $V_g^{1/2}$. The slope is proportional to the product $n\mu_n$.

$N_d - N_a = 2.7 \times 10^{17} \text{ cm}^{-3}$ and assuming there are twice as many cubic sites (with an activation energy of $E_{d2} = 0.14 \text{ eV}$) as hexagonal sites ($E_{d1} = 0.082 \text{ eV}$), it is possible to fit the concentration of each impurity level so that $n(300 \text{ K}) = 1.1 \times 10^{17} \text{ cm}^{-3}$ (Fig. 3). Table 1 summarizes all the values used in our calculations. The compensation ratio is found to be less than 1%.

The next step is to calculate $V_{bi}(T)$. $p_p(T)$ is calculated by assuming that the p-type layer is doped at $2 \times 10^{18} \text{ cm}^{-3}$ [5] and using two activation energies of $E_{a1} = 0.22 \text{ eV}$ and $E_{a2} = 0.25 \text{ eV}$, with $N_{a2} = 2N_{a1}$ [7]. It is worth noting that using a single energy level of 0.24 eV with a total concentration $N_a = N_{a2} + N_{a1}$ gives about the same result. Moreover, an error in p-value leads to a small error in the built-in potential, and a smaller one in $g_o(T)$, as shown in Eq. (1).

Knowing $n_n(T)$ and $p_p(T)$, and calculating $n_i(T)$, (Eq. (6)) leads to $V_{bi}(T)$. It is now easy to obtain $g_o(T)$ in the same manner as at room temperature and

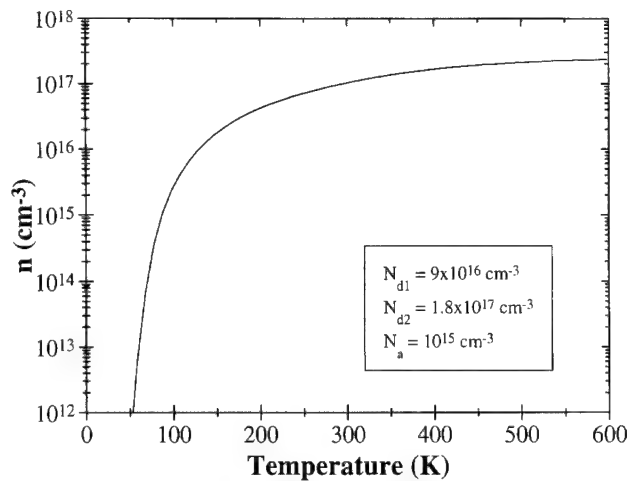


Fig. 3. Theoretical free electron concentration versus temperature.

Table 1
Parameters used for theoretical calculations of free carrier concentrations as a function of temperature

	n-type	p-type
Activation energies of dopants	82 and 137 meV (h and k sites)	220 and 225 meV (h and k sites)
Spin degeneracy factor g	2	4
Mc*	3	
Density-of-states effective mass	0.3 for electrons	1 for holes

*Mc: number of equivalent conduction band minima.

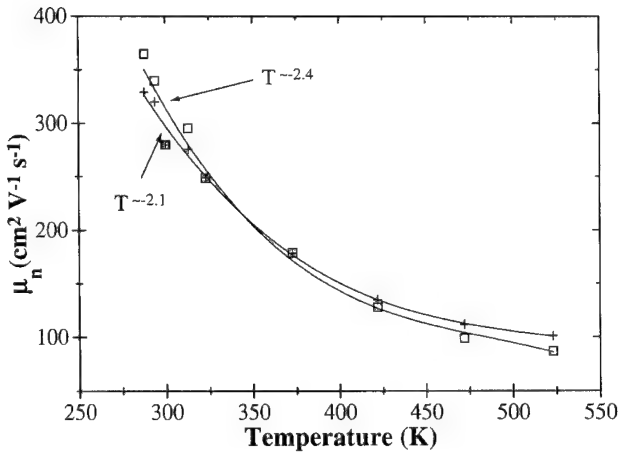


Fig. 4. Electron mobility versus temperature with $E_g = 2.9$ eV (\square), with E_g dependant on temperature ($+$).

finally to obtain $\mu_n(T)$. Fig. 4 shows the electron mobility calculated by taking $E_g = 2.9$ eV and by taking into account the temperature dependence of the bandgap E_g as reported by Dalven [8]. The mobility varies as T^n with $n = -2.4 \pm 0.1$ if $E_g = 2.9$ eV, which is in

agreement with previous Hall effect studies on p-type substrates [9].

4. Admittance spectroscopy and DLTS measurements

Admittance spectroscopy was performed, as described in Ref. [10], as a function of frequency (from 1 kHz to 1 MHz). A defect with an activation energy of $E_a = (0.24 \pm 0.01)$ eV. This value agrees with other values of aluminum activation energies reported in the literature [3,4,7] and justifies the need to take into account the incomplete ionization of dopants to calculate the free carrier mobility, as done below.

DLTS measurements are suitable for detecting deeper levels. Study of the drain-to-source current transients can be used in FETs with a better sensibility than conventional capacitance DLTS [11]. In our experiments, the drain-to-source voltage is set to 50 mV, so that the transistor works in the ohmic regime. The reverse gate bias V_r must be close to the pinch-off voltage, for example $V_r = -5$ V. The pulse is 5 V high during $t_p = 1$ μ s. Fig. 5 shows typical DLTS spectra recorded during such filling pulse conditions. The presence of a peak P1 indicates a deep level with an apparent activation energy of $E_a = 0.95$ eV and a capture cross-section of $\sigma_n = 7 \times 10^{-16}$ cm^2 . The presence of a "smooth peak" P2, which disappears at lower filling times, could be attributed to interface states with a low capture coefficient. The variation of amplitude from one window rate to another may indicate incomplete filling of the traps during the pulse.

Capacitance DLTS measurements carried out at various pulse heights indicate that this defect is located very close to the etched trench. Flatresse and Ouisse [12], who performed noise measurements on similar devices, conclude that the surface generates noise. The presence

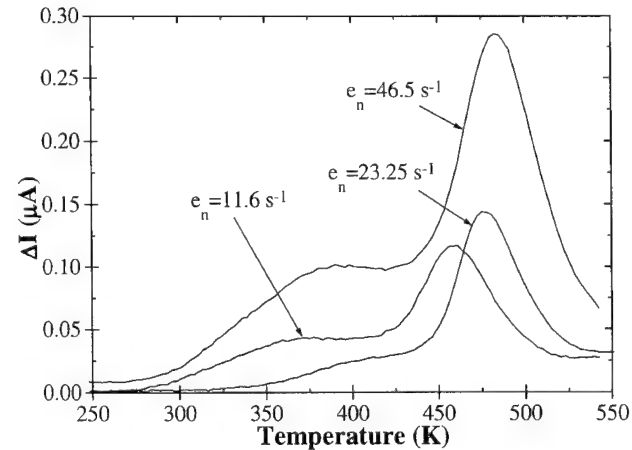


Fig. 5. Drain-to-source current DLTS spectra obtained with $V_r = -5$ V, $V_p = 0$ V, $t_p = 1$ ms, $V_{ds} = 50$ mV, for three emission times.

of a deep level close to the surface could be at the origin of this noise. Therefore, it could be reduced by an improvement of the surface quality.

5. Conclusion

We proposed a procedure to calculate electron mobility from drain-to-source current voltage measurements on JFETs, taking into account the incomplete ionization of impurities as a function of temperature, which is necessary when dopant impurity levels are relatively deep. We found that electron mobility increases with decreasing temperature as $T^{-2.4}$. Finally, DLTS measurements reveal the presence of a deep level at $E_c = -0.95$ eV, located very close to the surface, and probably due to etching or surface treatment.

References

- [1] J.W. Palmour, et al., Proceedings of the 1st High Temperature Electronics Conference, Albuquerque, NM, June 1991, pp. 511–518.
- [2] A.V. Naumov, V.I. Sankin, Sov. Phys. Semicond. 23 (1989) 630–633.
- [3] G. Pensl, W.J. Choyke, Physica B 185 (1993) 264–283.
- [4] W.J. Schaffer et al., Institute of Physics Conference Series No. 137, pp. 155–159.
- [5] J.M. McGarrity et al. IEEE Transactions, Nuclear Sciences 39 (1992) 1974.
- [6] S.M. Sze, Physics of Semiconductor Devices, 2nd edition, Wiley, New York, 1981.
- [7] C. Raynaud et al., Materials Science and Engineering 29 (1995) 122–125.
- [8] R. Dalven, J. Phys. Chem. Solids 46 (1965) 439–441.
- [9] S. Karmann et al., Physica B 185 (1993) 75–78.
- [10] C. Raynaud et al., J. Appl. Phys. 76 (1994) 1956–1958.
- [11] I.D. Hawkins, A.R. Peaker, Appl. Phys. Lett. 48 (1986) 227–229.
- [12] P. Flatresse, T. Ouisse, Solid State Electronics (submitted).

Microwave Power MESFET on 4H-SiC

O. Noblanc *, E. Chartier, C. Arnodo, C. Brylinski

THOMSON CSF, Laboratoire Central de Recherches Domaine de Corbeville, 91404 Orsay, CEDEX, France

Abstract

We present static and microwave characterization of MESFETs processed on n^+ 4H-SiC wafers supplied by Cree Research. An eight-level technology including airbridge interconnections has been performed. Transistors with total gate width up to 6 mm and 1.2 μm gate length optically designed are obtained. High breakdown voltage (up to 140 V) and high drain current (up to 0.7 A) show the high power capability of the transistors. RF characterization was performed. Because of the use of a conductive substrate, parasitic capacitances account for the relatively low values of f_T and f_{max} (4 and 9 GHz, respectively). Power measurements were carried out at 1 and 2 GHz in cw. Output powers up to 1.7 W mm^{-1} were measured with a power added efficiency of 37% at 2 GHz. © 1997 Elsevier Science S.A.

Keywords: MESFET; Power and microwave characteristics; Silicon carbide

1. Introduction

Silicon carbide belongs to the wide band gap semiconductor family. Depending on the polytype (more than 100 are identified), the band gap varies between 2.2 and 3.3 eV. This property makes SiC suitable for high-temperaturure applications. Other physical properties are also very interesting in the same field. The most important are the high breakdown electric field (an order of magnitude higher than in silicon or gallium arsenide), the high thermal conductivity (3 times higher than in silicon) and the high saturation velocity. Besides, SiC wafers and homoepitaxial layers are now commercialy available. This explains why SiC is now extensively studied for possible use in most areas of power electronics. However, a major drawback of SiC is the poor quality of the material. Wafers are still small (1.375" in diameter in 1996), very expensive and contain high defect densities (dislocations and micropipes). Epitaxial layer quality has to improve in order to obtain high current densities. Nevertheless, SiC devices are being developed and very encouraging results have been published, mainly in the fields of Schottky diodes [1,2], microwave power FETs [3,4] and power thyristors [5]. SiC microwave power devices have been identified as possible future candidates for high impedance applications [6]. Presently, at frequencies over 1 GHz,

MESFET transistors are the main SiC devices for which microwave results have been published [3,4]. The best power measurement results presently published are $P_{out}=3.5 \text{ W}$; PAE=45.5% at 6 GHz at $V_{ds}=40 \text{ V}$ on a 2 mm periphery MESFET processed on a 6H-SiC semi-insulating wafer [3].

In this paper, we report static and microwave characterization, including power measurements, of MESFETs fabricated on conductive substrates. Because of the non-uniformity of the active layer doping thickness, the following results concern transistors belonging to the best part of the wafers. The characterizations are performed on MESFETs of various peripheries. In particular, power measurements on 1, 3.6 and 4 mm periphery transistors are presented.

2. MESFET technology

4H-SiC epitaxial structures were supplied by Cree Research, Durham, North Carolina. Conductive substrates were used since semi-insulating substrates were not available at that time. A p^- buffer layer ($Na \approx 3 \times 10^{16} \text{ cm}^{-3}$, 10 μm thick) has been incorporated in the epi structure between the n^+ substrate and the n active layer (0.25 μm thick; $Nd \approx 1.5 \times 10^{17} \text{ cm}^{-3}$). An n^+ cap layer ($Nd \approx 1 \times 10^{19} \text{ cm}^{-3}$, 0.2 μm thick) ends the epitaxial structure.

The first steps in the MESFET process consist of

* Corresponding author.

reactive ion etching for mesa isolation and channel recess. Then thermal oxidation is performed in a wet oxidation furnace at 1150 °C. Evaporated nickel metallization is applied for the source and drain ohmic contacts using the lift-off technique. Rapid thermal annealing is used for the alloying of the contacts. Specific contact resistance in the field of $1 \times 10^{-6} \Omega \text{ cm}^2$ and sheet resistance around 1.4 Ω are measured after alloying. Ti/Pt/Au multilayer metal is evaporated to make the gate contact. The ideality factor and the barrier height of the Schottky contact are in the range of 1.1 and 1 eV, respectively. The leakage current is in the range of 1 μA and the breakdown voltage between 150 and 200 V depending on the wafers. An offset of the gate towards the source side in order to increase the breakdown voltage and reduce source series resistance is performed. The drain-gate and source-gate spacings are 2.5 and 0.5 μm, respectively. Devices with gate lengths of 1.2 μm processed by optical lithography have been reproducibly obtained with 2, 4, 8, 16 and 24 × 250 μm fingers, giving maximum gate widths up to 6 mm (Fig. 1). PECVD-deposited SiO₂ and Si₃N₄ are used for passivation. Source fingers are interconnected by airbridges.

3. DC characterization

DC characterization is performed using a 370 Tektronix curve tracer. Fig. 2(a–c) shows the DC characteristics $I_d(V_{ds}, V_{gs})$, the transfer characteristics $g_m(V_{gs})$ and $I_d(V_{gs})$ and the transconductance over the output conductance $g_m:g_d$ ratio of a 100 μm-wide MESFET. Fig. 3(a and b) shows the DC characteristics

$I_d(V_{ds}, V_{gs})$ of a 4 mm wide MESFET ($16 \times 250 \mu\text{m}$ fingers). In order to limit the dissipated power, the load has been altered to show both the saturated drain current I_{dss} [Fig. 3(a)] at low source-drain voltage and the source-drain breakdown voltage BV_{ds} [Fig. 3(b)]. An I_{dss} value of 700 mA at $V_{gs}=0$ V and a BV_{ds} of 140 V are observed. The maximum output power for a class A amplifier should be at first order greater than 11 W according to the DC characteristics. The observed breakdown cause is not fully understood. The correlation between gate-drain spacing and BV_{ds} is not clear. There is presently evidence of breakdown occurring below the ohmic contacts due to the presence of conductive substrate and p-type buffer layer. This was evidenced by a breakdown voltage BV_{ds} independent on the gate voltage V_{gs} (not shown). A smooth breakdown phenomenon due to the reverse leakage current of the Schottky metallization is more often observed.

4. RF characterization

The dies were cut and packaged in order to use a standard Wiltron test fixture. Small-signal (S) parameters were measured using a HP8510 network analyser. Various source-drain bias voltages were used up to 40 V. MESFETs with periphery up to 6 mm were measured. At $V_{ds}=40$ V, a maximum frequency of oscillation f_{max} of 9 GHz is measured, mainly limited by the parasitic pads capacitances in relation with the use of conductive substrates. The current gain cut-off frequency f_T is 4 GHz. At 2 GHz, the highest small signal maximum

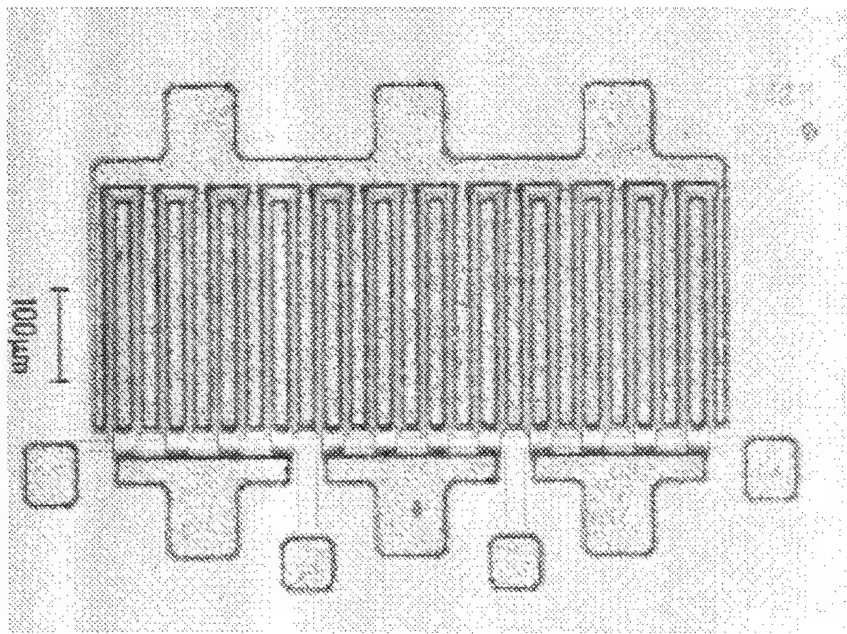


Fig. 1. 6 mm periphery MESFET fabricated on an n^+ 4H-SiC wafer.

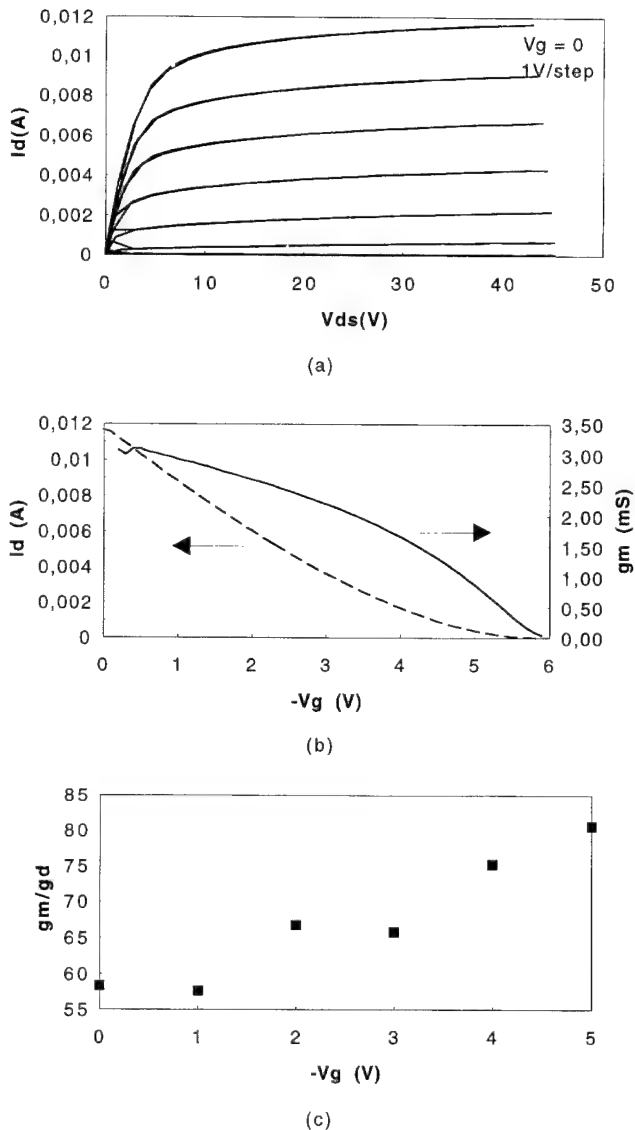


Fig. 2. DC characteristics $I_d(V_{ds}, V_{gs})$ (a), transfer characteristics $g_m(V_{gs})$ and $I_d(V_{gs})$ (b) and g_m/g_d ratio versus V_{gs} (c) of a $100\text{ }\mu\text{m}$ wide MESFET.

available gain (MAG) measured is 13 dB on a 1 mm periphery transistor (Fig. 4).

Fig. 5 shows the measured power performance of a 1 mm periphery 4H-SiC MESFET at 2 GHz. The best matched conditions have been searched. The bias conditions are $V_{ds}=39\text{ V}$; $V_{gs}=-4\text{ V}$; $I_{ds}=91\text{ mA}$. The device delivers 1.7 W with 33% power-added efficiency and 53% drain efficiency with 6.2 dB associated gain. Transistors with larger peripheries were also measured at 1 and 2 GHz. For a 4 mm periphery MESFET at $f=1\text{ GHz}$, the results are $P_{out}=2\text{ W}$, $PAE=32\%$ with 17 dB of associated gain with the following bias conditions: $V_{ds}=40\text{ V}$; $V_{gs}=-3\text{ V}$; $I_{ds}=150\text{ mA}$. At $f=2\text{ GHz}$ and for a 3.6 mm periphery MESFET, the results are: $P_{out}=1.4\text{ W}$, $PAE=17\%$ with 5 dB of associated gain at $V_{ds}=35\text{ V}$; $V_{gs}=-3\text{ V}$; $I_{ds}=160\text{ mA}$. The output

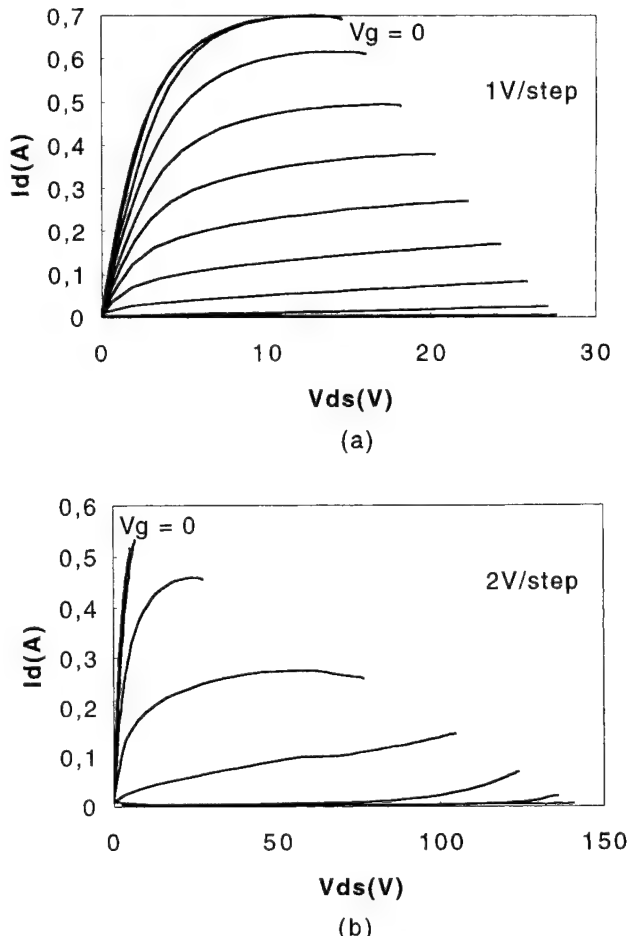


Fig. 3. DC characteristics of a 4 mm periphery MESFET. The gate length is $1.2\text{ }\mu\text{m}$. Both sets of characteristics refer to the same transistor and are displayed separately because of a limited power delivery in the curve tracer.

power density is smaller for the high periphery transistors (3.6 and 4 mm) than for the low ones (1 mm). This can be explained by the influence of conductive substrates that make parasitic capacitances larger for large periphery transistors than for smaller ones, making the impedance tuning difficult for large devices. The future MESFET process on semi-insulating substrates will reduce this drawback.

5. Conclusion

A MESFET process developed on 4H-SiC wafers is presented. Transistors with peripheries up to 6 mm have been realized. DC and RF performance measurements have been carried out. The current densities are still quite low (up to 170 mA mm^{-2}) and we expect higher values in the future in connection with progress in the epitaxial process. In addition, cut-off frequencies are still low compared to what has been already published on MESFETs processed on high resistive or semi-

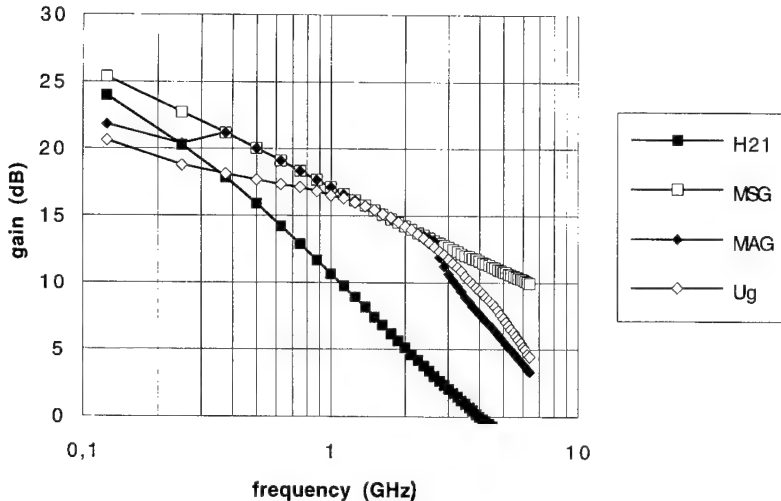


Fig. 4. Small-signal RF characteristics for a 1.2 μm gate length 4H-SiC MESFET of 1 mm periphery made on an n^+ substrate. The bias conditions are $V_{ds}=40$ V and $V_{gs}=-4$ V.

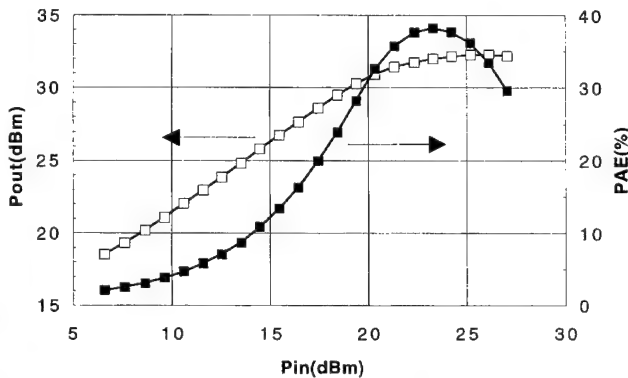


Fig. 5. Power performance for a 1.2 μm gate length 4H-SiC MESFET of 1 mm periphery at 2 GHz. The bias conditions are $V_{ds}=40$ V and $V_{gs}=-4$ V.

insulating substrate [3,4]. Nevertheless power characteristics of those transistors at 1 and 2 GHz are promising. The future use of semi-insulating substrates is expected to increase the performance of the transistors and make the matching easier for large periphery MESFETs.

Acknowledgement

We would like to thank J.M. Coupas for RF power measurements at 1GHz and D. Floriot for his precious advice. This work has been partly supported by the French Ministry of Defense (DRET).

References

- [1] A. Itoh, T. Kimoto and H. Matsunami, IEEE Electron Device Letters 16 (6) (1995) 280.
- [2] A. Itoh, T. Kimoto and H. Matsunami, IEEE Electron Device Letters 17 (3) (1996) 139.
- [3] C.D. Brandt et al., Proceedings of the ICSCRM 95 Conference (Kyoto), September 1995, p. 659.
- [4] S.T. Allen, J.W. Palmour, V.F. Tsvetkov, S.J. Macko, C.H. Carter Jr, K.E. Moore, C.E. Weitzel, K.J. Nordquist, L.L. Pond III, Proceedings of the ICSCRM 95 Conference (Kyoto), September 1995, p. 761.
- [5] J.W. Palmour, S.T. Allen, R. Singh, L.A. Lipkin, D.G. Waltz, Proceedings of the ICSCRM 95 Conference (Kyoto), September 1995, p. 813.
- [6] C.E. Weitzel, IEEE Electron Device Letters 16 (10) (1995) 451.

The potential of SiC and GaN for application in high speed devices

F. Schwierz *, M. Kittler, H. Förster, D. Schipanski

Technische Universität Ilmenau, Fachgebiet Festkörperelektronik, Postfach 100565, 98694 Ilmenau, Germany

Abstract

The potential for high frequency applications of MESFETs made from the wide band gap semiconductors cubic GaN, hexagonal GaN, and 3C-SiC has been investigated by means of device modeling. For comparison, also Si and GaAs MESFETs have been modeled. The influence of nonstationary carrier transport on FET behavior has been estimated using the relaxation time approximation, and taken into account. The three wide band gap semiconductors show considerable potential for application in high frequency MESFETs. Cut-off frequencies exceeding 100 GHz have been predicted for sub-quarter micron gate cubic GaN MESFETs. © 1997 Elsevier Science S.A.

Keywords: Device modeling; High speed devices; MESFET; Wide band gap semiconductors

1. Introduction

In recent years, there has been an increasing interest in using the wide band gap semiconductors SiC and GaN for microwave power amplification. Recently, an experimental 0.5 μm gate SiC MESFET with a maximum frequency of oscillation (f_{\max}) of 42 GHz and a cut-off frequency (f_T) of 13.2 GHz has been reported [1]. Furthermore, AlGaN/GaN heterostructure FETs with f_{\max} above 70 GHz and f_T above 20 GHz have been demonstrated [2, 3].

These encouraging results raise the question about the frequency limits of SiC and GaN based FETs. Several figures of merit have been defined to assess the high frequency potential of semiconductor materials (e.g. Keyes' and Baligas figure of merit [4]), but none of these seems to be useful in estimating the properties of real SiC or GaN based devices.

The aim of this work is to assess the potential of SiC and GaN for high frequency devices. This will be done by modeling 3C-SiC and GaN microwave MESFETs, rather than establishing some figure of merit based on material properties.

2. Transistor model

For our calculations, we used the two region MESFET model proposed by Statz et al. [5]. The main features

of the model are depicted in Fig. 1. The transistor is divided into two regions:

- (1) the ohmic region (region I), where the carrier velocity follows $v = \mu_0 E$, and
- (2) the saturation region (region II), where the carriers have attained their constant saturation velocity v_s .

At the boundary between the two regions, the electric field reaches its critical value E_c . A key point of the transistor model are the two-piece linear velocity-field ($v-E$) characteristics. The $v-E$ characteristics include the main transport properties of the semiconductor material (i.e. the low field and high field transport properties in

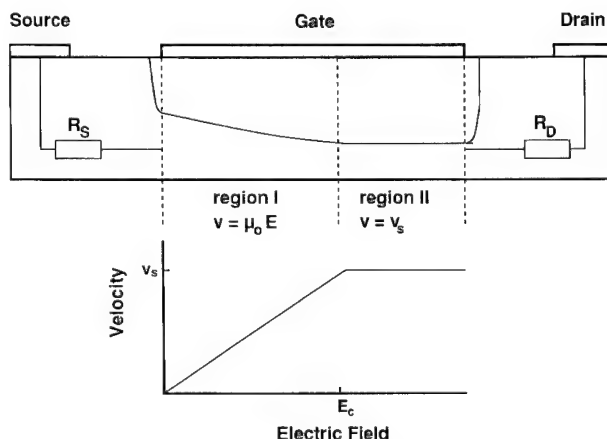


Fig. 1. Two region MESFET model used in this work.

* Corresponding author.

terms of the low field mobility μ_0 and the saturation velocity v_s , and the influence of nonstationary carrier transport (NCT).

State of the art high frequency MESFETs have a gate length in the submicron range. For such short gate MESFETs, NCT becomes an important mechanism. In the case of GaAs FETs for example, the influence of NCT is significant for gate lengths below 1 μm .

We calculated NCT by the relaxation time approximation [6], solving the energy and momentum balance equations

$$\frac{dw}{dt} = qEv - \frac{w - w_0}{\tau_w}, \quad (1)$$

and

$$\frac{d(m_c^* v)}{dt} = qE - \frac{m_c^* v}{\tau_m}, \quad (2)$$

where w is the carrier energy, w_0 the energy in thermal equilibrium, m_c^* the effective carrier mass, v the carrier velocity, t the time, q the electronic charge and E the electric field. τ_m and τ_w are the momentum and energy relaxation times, respectively.

The input parameters necessary for these calculations have been collected from the literature [7–10]. The results (examples are shown in Fig. 2) indicate a velocity overshoot for all of the materials investigated, but the peak velocity and the duration of overshoot vary considerably. It can be shown that NCT in SiC MESFET has no noticeable effect on device behavior. This agrees with the results of Zhou et al. [9]. NCT does, however, influence the device behavior considerably in GaAs, Si and both GaN polytypes (at least for gate lengths in the sub-quarter micron range in the case of Si and GaN).

The results of the relaxation time approximation and the method proposed in Ref. [11] have been used to construct the gate length dependent apparent $v-E$ characteristics for each semiconductor. Using these $v-E$

characteristics and the two region MESFET model mentioned above, the drain current (I_D) and the charge stored at the gate electrode of the device (Q_{Gate}) have been calculated. The transconductance (g_m) and the gate source capacitance (C_{GS}) are obtained by taking the derivative of I_D and Q_{Gate} with respect to the gate source voltage V_{GS} . The fringing capacitance occurring at the gate edges has been taken into account. Finally, the cut-off frequency is determined by $f_T \approx g_m/(2\pi C_{GS})$.

The device structure investigated is a MESFET with a threshold voltage of 0 V, a donor concentration of $5 \times 10^{17} \text{ cm}^{-3}$ in the active layer, and a gate length varying from 0.1 to 5 μm . The parasitic resistances R_S and R_D were taken into account. A gate source voltage of 0.3 V below the built-in voltage of the Schottky gate V_{bi} and a source drain voltage of 2 or 15 V were chosen as bias conditions. The values used for V_{bi} are 0.7 V for Si, 0.8 V for GaAs, and 1.2 V for both SiC and GaN. We compared MESFETs made from cubic and hexagonal GaN, and 3C-SiC, as well as the more conventional semiconductors GaAs and Si.

3. Results and discussion

Using the models described in the preceding section, we calculated the cut-off frequency of MESFETs made from the various semiconductor materials.

To check the validity of our approach, the calculated f_T of GaAs MESFETs was compared to experimental data (Fig. 3). Calculated and experimental cut-off frequencies are in good agreement and show the same gate length dependency. A comparison between calculated and experimental transconductances of GaAs MESFETs also showed good agreement.

Subsequently, we compared MESFETs made from the five different semiconductors. The calculated cut-off frequencies at a low drain source voltage ($V_{DS}=2 \text{ V}$) are

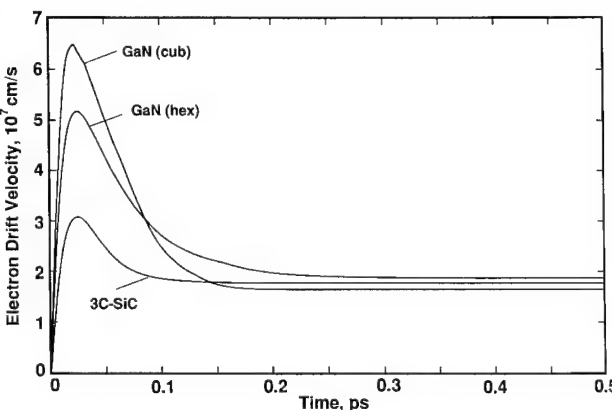


Fig. 2. Transient electron drift velocity in GaN and 3C-SiC (at $t=0$ the electric field is increased from $E=0$ to 500 kV cm^{-1}).

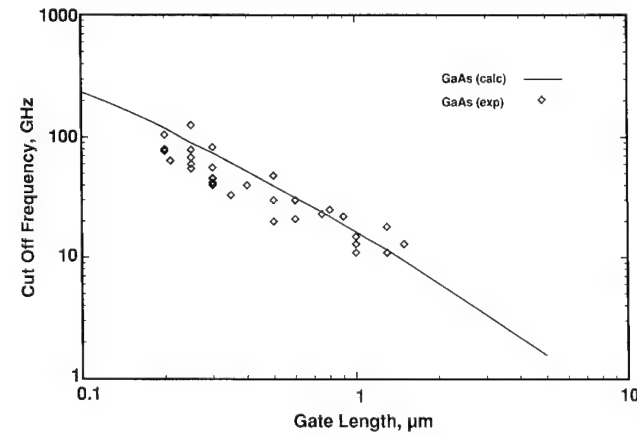


Fig. 3. Comparison of calculated and experimental cut-off frequencies of GaAs MESFETs.

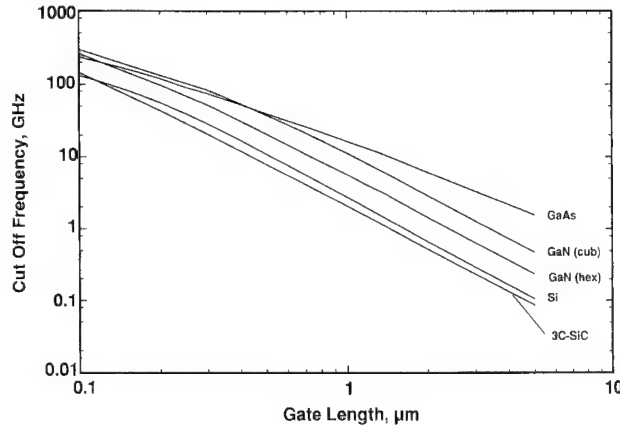


Fig. 4. Calculated cut-off frequency vs gate length ($V_{DS}=2$ V).

shown in Fig. 4. Over the entire range of gate lengths, the cut-off frequency of 3C-SiC MESFETs is lower than that of Si MESFETs (with the same gate length), which in turn is lower than that of GaAs MESFETs. The relatively low f_T for 3C-SiC MESFETs is a result of the low low-field mobility of SiC which overshadows the influence of the high saturation velocity. Note that even for low V_{DS} , cubic GaN MESFETs exhibit higher cut-off frequencies than GaAs MESFETs, for gate lengths below 0.4 μm. This is caused by the relatively high low-field mobility and the high saturation velocity of cubic GaN. The saturation velocity of cubic GaN is about the same as that of hexagonal GaN, but its low-field mobility is about two times higher compared to hexagonal GaN.

When V_{DS} is increased to 15 V (Fig. 5), the behavior

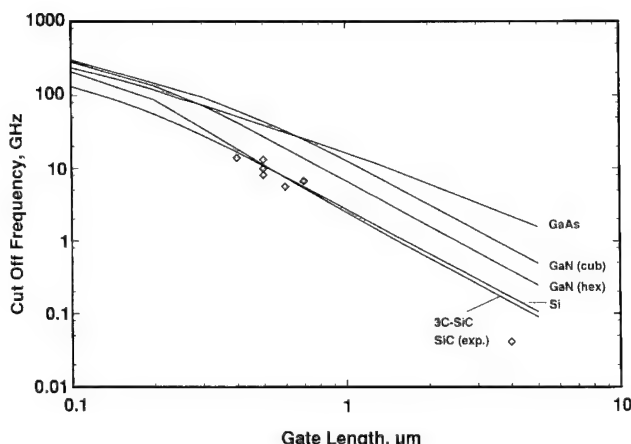


Fig. 5. Calculated cut-off frequency vs gate length ($V_{DS}=15$ V for 3C-SiC and GaN, $V_{DS}=2$ V for Si and GaAs).

of the GaN and 3C-SiC FETs improves considerably. Fig. 5 also shows the experimental data for 4H-SiC and 6H-SiC MESFETs, which are close to the calculated 3C-SiC curve. Zhou et al. [9] analyzed 3C-SiC MESFETs by means of 2D hydrodynamic simulations, and predicted cut-off frequencies over 1 THz for transistors with gate lengths between 12 and 90 nm. These high cut-off frequencies appear too optimistic. For a 100 nm gate 3C-SiC MESFET we obtained an f_T of 210 GHz. Because of the low breakdown fields of Si and GaAs, we made no calculations for Si and GaAs MESFETs at $V_{DS}=15$ V. For GaN MESFETs with gate lengths below 0.3 μm, the predicted cut-off frequency exceeds 75 and 100 GHz in the case of hexagonal and cubic material, respectively. These values demonstrate the potential of both GaN polytypes for application in high frequency devices.

4. Conclusion

The results obtained by device modeling show that the wide band gap semiconductors SiC and GaN have considerable potential for high frequency operation. Especially cubic GaN seems to be a superior material for microwave devices, because it combines the potential for high speed with a high breakdown field. Unfortunately, among all the materials considered, its technology is least developed.

References

- [1] S. Sriram, G. Augustine, A.A. Burk, R.C. Glass, H.M. Hobgood, P.A. Orphanos, L.B. Rowland, T.J. Smith, C.D. Brandt, M.C. Driver, R.H. Hopkins, IEEE Electron Device Lett. 15 (1996) 369.
- [2] M.A. Khan, M.S. Shur, J.N. Kuznia, Q. Chen, J. Burm, W. Schaff, Appl. Phys. Lett. 66 (1995) 1083.
- [3] J. Burm, W.J. Schaff, L.F. Eastman, H. Amano, I. Akasaki, Appl. Phys. Lett. 68 (1996) 2849.
- [4] T.P. Chow, R. Tyagi, Proc. 5th Int. Symp. on Power Semiconductor Devices and ICs (1993) 84.
- [5] H. Statz, H.A. Haus, R.A. Puccel, IEEE Trans. Electron Dev. 21 (1974) 549.
- [6] M. Shur, Electron. Lett. 12 (1976) 615.
- [7] P. Honisch, Ph.D. thesis, TU Ilmenau, 1990.
- [8] P. Graf, F.M. Bufler, B. Meinerzhagen, W.L. Engl, Proc. 40th Int. Sci. Coll. TU Ilmenau (1995) part 3, p. 411.
- [9] J.-R. Zhou, D. Vasileska, D.K. Ferry, Solid-State Electron. 36 (1993) 1289.
- [10] J. Kolnik, I.H. Oguzman, K.F. Brennan, R. Wang, P.P. Ruden, Y. Wang, J. Appl. Phys. 78 (1995) 1033.
- [11] F. Schwierz, M. Roßberg, D. Nuernbergk, H. Förster, D. Schipanski, J.J. Liou, Solid-State Electron. 39 (1996) 1522.

Thermodynamics and high-Pressure growth of (Al, Ga, In)N single crystals

S. Krukowski

High Pressure Research Center, Polish Academy of Sciences, ul. Sokolowska 29/37, 01-142 Warsaw, Poland

Abstract

Thermodynamical properties of AlN, GaN and InN are reviewed. It is shown that significant differences in melting conditions, thermal stability and solubilities in liquid III group metals lead to different possibilities of growing crystals from high-temperature solutions at N₂ pressures up to 20 kbar. It is shown that the best conditions for crystal growth at available pressure and temperature conditions can be achieved for GaN. High-quality 6–10 mm GaN single crystals have been grown at high N₂ pressures in 60–150 hour-long processes. The mechanisms of nucleation and growth of GaN crystals are discussed on the basis of the experimental results. The crystallization of AlN is less efficient owing to the relatively low solubility of AlN in liquid Al. The possibility for the growth of InN crystals is strongly limited since this compound loses its stability at $T > 600^\circ\text{C}$, even at 2 GPa N₂ pressure. The crystals of GaN grown at high pressure are the first to be used for homoepitaxial layer deposition. Both MOCVD and MBE methods have been successfully applied. Structural, electrical and optical properties of both GaN single crystals and homoepitaxial layers are reviewed. © 1997 Elsevier Science S.A.

Keywords: Optoelectronics; III–V nitrides; Thermodynamics; Crystal growth

1. Introduction

In recent years, considerable progress has been achieved in the technology of optoelectronic devices based on nitride semiconductors [1]. The landmark of this development was the fabrication of a highly efficient blue LED by Nakamura [2]. Recently, a new type of blue LED has been manufactured with higher efficiency and better spectral properties [3]. These devices are fabricated by the Metaloorganic Chemical Vapour Deposition (MOCVD) method using sapphire as a substrate.

In parallel, Cree Research Inc., Durham, NC, USA, has been fabricating nitride based blue LEDs using SiC single crystals as substrates [4]. Despite a smaller lattice misfit which is 3.4% for GaN/SiC as compared with 16% for GaN/Al₂O₃, these devices have smaller efficiencies than those fabricated on sapphire. However, it seems that GaN/SiC-based devices have the potential to match the results obtained by Nakamura on sapphire substrates.

Progress in the technology of nitride-based laser devices is much slower. This has been caused by the higher requirements demanded by laser technology, i.e. vertical cavity and cleaved mirror lasers, which have

been announced only recently [5]. The efficiency of these devices is fairly low so that they can operate only for very short times.

Further progress can be achieved in laser technology by the use of lattice matched substrates; gallium nitride single crystals are the best candidates for such purposes. The prospects for their use are good since considerable progress has been achieved in the growth of single crystals of GaN [6]. GaN single crystals are grown from nitrogen solution in liquid gallium under a high nitrogen pressure. The size of these crystals has been increased from 2 mm to 1 cm recently.

Parallel attempts to obtain single crystals of the other nitrides have been less successful. In fact, high-quality AlN crystals of not more than 0.1 mm in size have been grown by the high-pressure method [7]. Even less satisfying results have been achieved in growth of InN crystals with sizes no larger than several μm [8]. The difference in these results is caused by the thermodynamic properties of these three nitrides [7].

In this paper, the thermodynamic properties of the nitrides will be reviewed with an emphasis on their consequences on crystal growth processes. GaN crystals obtained in high-pressure growth experiments will be characterized. A summary of the other nitride crystal

growth experiments will also be given. A short discussion of growth of homoepitaxial layers on GaN substrates will be presented. The properties of the homoepitaxial layers, obtained by MOCVD and Molecular Beam Epitaxy (MBE) methods, will be also described.

2. Thermodynamics

Group III metal nitrides are characterized by high-bonding energies which are 2.88, 2.24 and 1.88 eV bond⁻¹ for AlN, GaN and InN, respectively [9]. These values are considerably lower than the 3.17 and 3.68 eV bond⁻¹ for SiC and diamond, respectively, but much higher than for GaAs, i.e. 1.63 eV bond⁻¹. Therefore, the thermodynamical properties of the nitrides should locate them in between these two groups of semiconductors. However, in some aspects, nitrides are different from group IV and other III-V compound semiconductors. The difference originates from strong bonding of the nitrogen molecule — the bonding energy is 226 kcal mole⁻¹. Therefore, the Gibbs free energy of the constituents G(T), i.e. metal and nitrogen N, is low. Hence, the stability of the system is shifted towards Me and N₂. Accordingly, high nitrogen pressure is necessary in order to attain the stability condition for nitride semiconductors, particularly at higher temperatures.

The nitrogen properties are significantly affected by high pressure [10]; high-pressure isobars are presented in Fig. 1(a). For pressures above 1 kbar, the deviation from ideal gas behavior due to strong repulsion of atomic cores plays a significant role in the increase of the nitrogen chemical potential. The pressure contribution to the nitrogen chemical potential can be expressed by the use of nitrogen activity defined as:

$$\Delta\mu_{N_2} = kT \ln a(p_{N_2}, T) \quad (1)$$

The nitrogen activity plays the role of high-pressure contributer to the ideal gas pressure (for ideal gas, the activity is essentially equal to pressure and is expressed in dimensionless units). The change in the nitrogen activity for high pressure is presented in Fig. 1(b). It is shown that high-pressure activity can be one to two orders of magnitude higher than the pressure. The steep increase of the nitrogen activity plays crucial role in stabilizing of the nitride semiconductors.

The free energies of Me (Me=Al, Ga, In)+N₂ systems are presented in Fig. 2. The curves present the results of low-pressure (1 bar) and high-pressure (11 kbar) calculations. It is shown that the pressure of the order of 11 kbar allows an increase in the equilibrium temperature of GaN by several hundreds of degrees Celsius.

Owing to high bonding energies, melting temperatures are very high. The corresponding pressures are very

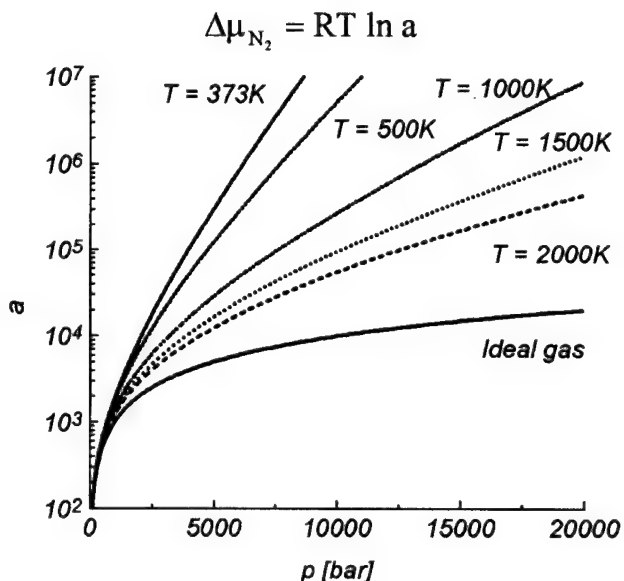
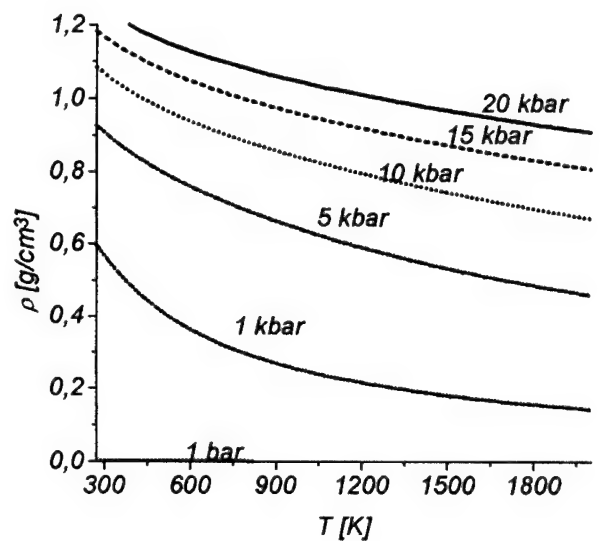


Fig. 1. The nitrogen properties under high pressures: (a) density; and (b) activity.

different, starting from extremely high for InN to relatively low for AlN. The estimated values of melting temperatures and pressures are presented in Table 1. These conditions are unavailable in present-day high-pressure gas equipment; therefore, single nitride crystals can be grown only from the solution. The solubility of nitrogen in liquid metals also suffers from high bonding energies of N₂. The maximum nitrogen solubility, corresponding to the equilibrium between MeN (Me=Al, Ga, In) and nitrogen solution in molten metal, is presented in Fig. 3.

These data indicate the main technical obstacles in the crystallization of high-quality, large single crystals of AlN, GaN and InN. The extremely high nitrogen

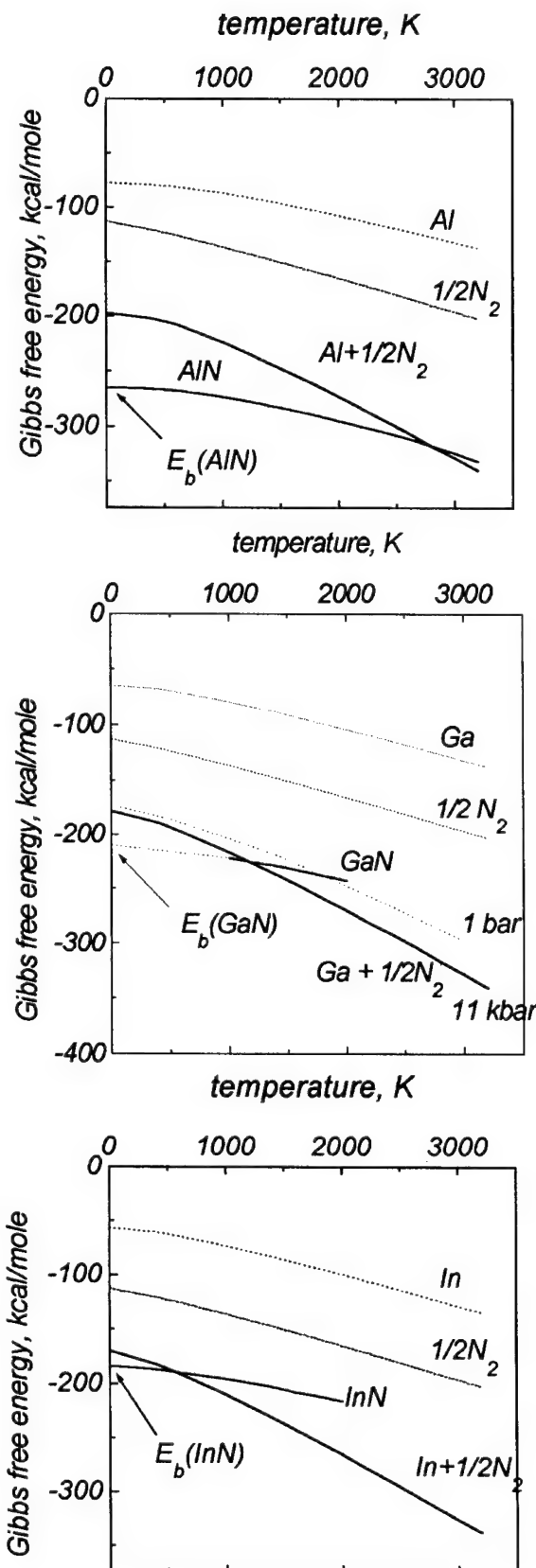


Fig. 2. Gibbs free energies of MeN semiconductors and their constituents: (a) AlN; (b) GaN; and (c) InN.

pressures required for InN stability prevents the use of higher temperatures. For low temperatures, solubility of nitrogen in indium is low; thus, the growth of microcrystals of InN has been achieved [8]. For AlN, the solubility of N in liquid Al is low up to temperatures of 2000 °C, which requires an extremely long growth process [14]. For higher temperatures, the precise control of the thermal conditions, necessary to obtain good quality crystals, is impossible. The optimum choice is therefore to obtain GaN single crystals which can be achieved using temperatures close to 1500 °C and pressures close to 15 kbar. The results of the growth experiments of GaN crystals and their main physical properties are presented below.

3. Growth of group III nitrides single crystals

The experimental system used for GaN growth has been designed for crystal growth processes of a duration longer than 100 h under nitrogen pressures close to 15 kbar and in temperatures higher than 1500 °C. The system has to fulfil all the requirements concerning the purity necessary to avoid growth disturbances and to comply with the standards posed by optoelectronic applications [6].

The system used in high-pressure growth consists of a chamber with both a compressor and temperature control apparatus. The temperature is controlled by a set of four thermocouples arranged along the crucible. The internal diameters of the chamber were: 40, 46 and 60 mm. The diameter of the crucible depends on the diameter of the chamber: it varies from 10 to 22 mm. In order to obtain desired temperature distribution in the growth zone, one- and multi-zone furnaces were used. The scheme of the typical one-zone growth apparatus is presented in Fig. 4. In addition, the results of finite element calculations of the temperature distribution, corresponding to the typical growth conditions, are presented in Fig. 4 [15].

3.1. Gallium nitride

During a typical growth process, the entire crucible is maintained at a temperature lower than the GaN stability temperature for the pressure of the experiment. The growth process then consists of several stages [16]. To begin with, the surface reaction between nitrogen and liquid Ga takes place. We believe that liquid Ga exerts a strong catalytic effect on the decomposition of N_2 molecules. Nitrogen dissolution in liquid Ga creates a thin surface layer of highly supersaturated solution, which leads to the growth of a thin polycrystalline layer of GaN on the entire surface of liquid Ga. The creation of the layer terminates the direct dissolution reaction of nitrogen in liquid Ga. The example of the polycrystalline

Table 1

Melting temperatures and decomposition N_2 pressures for AlN, GaN and InN

Nitride	T^M (K)	Reference	$P_{N_2}^a$ (kbar)	$P_{N_2}^b$ experimental (kbar)	Reference
AlN	3487	[11]	0.2	>0.1	[13]
GaN	2791	[11]	45	>30	[14]
InN	2146	[11,12]	60	>35	[7]

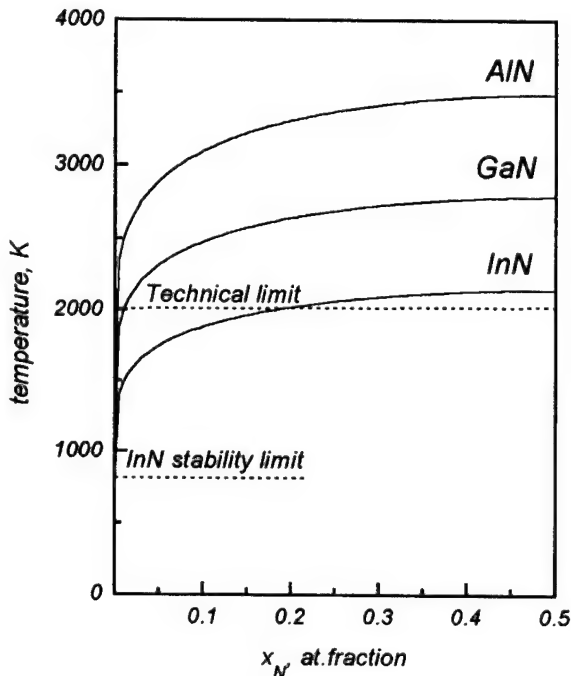
^aExtrapolation of experimental data^bThe highest pressure at which the decomposition was observed.

Fig. 3. Nitrogen solubility on molten III group metals — three phase equilibrium line.

crust obtained during growth of GaN crystals under a high nitrogen pressure is presented in Fig. 5.

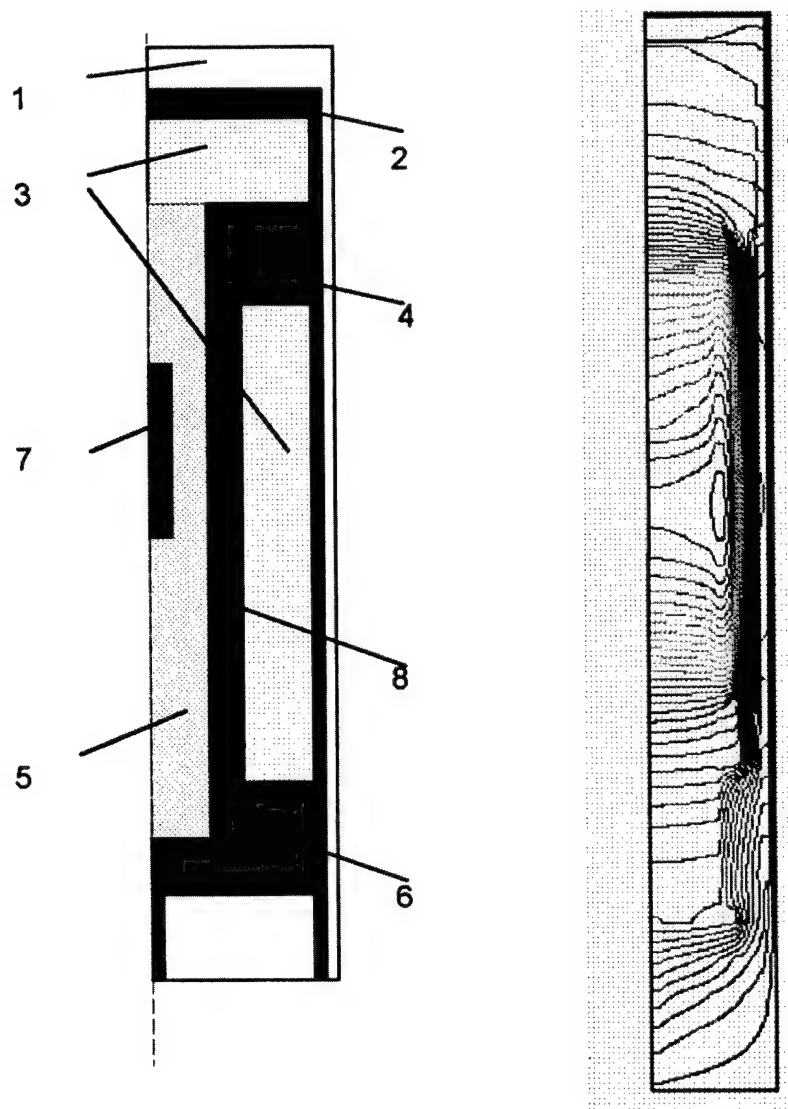
Following this, the course of the growth process depends on the temperature distribution in the crucible and the crucible sizes. Generally, GaN is dissolved in the hot part of the crucible and transported via diffusion and convection into the cold zone. The supersaturation in the cold zone is determined by the temperature difference between the hot and cold zones. In the cold zone, the growth process occurs via elimination of less-favored growth centers. Since the diffusion length, obtained from the estimated growth velocity and the nitrogen diffusivity, is larger than the size of the crucible, the growth centers act as a collective single concentration sink, without creating strong concentration gradients in liquid Ga. The depleted zone is uniform with the highest concentration close to the crucible axis and the smallest at the polycrystalline layer. The nitrogen transport and the growth of the crystals on the internal side of the crust is presented on Fig. 6.

GaN is a strongly anisotropic crystal. Therefore, the

growth velocity strongly depends on the crystallographic orientation of the surface. In our experiments, we observed two basic habits: plate-like and needle-like, depending on the temperature, pressure and temperature gradients of the process. Both plate-like and needle-like crystals have a fast growth direction perpendicular to the polycrystalline surface layer. The fast growth direction of the needle-like crystals is {0001} and for the plate-like crystals is {1010}. The intermediate forms have much reduced sizes, which suggest that the habit selection mechanism is based on the presence or absence of one growth mode.

The needle-like crystals usually have unstable morphology: most frequently they have the skeletal form and are not suitable for application in epitaxial technology. The plate-like crystals are usually of better quality. Examples of such crystals are presented in Fig. 7. The crystalline quality of the obtained crystals depends on the size of the crystals. For the small platelets of 2 mm size, the full width at half maximum (FWHM) of the X-ray rocking curve of (0004)CuK α reflection is equal to 20 arc sec; for larger sizes, it is wider, i.e. up to 40 arc sec for 4 mm crystals. For larger platelets, the rocking curves are split into several 30–40 arc sec peaks indicating the presence of low-angle (1–3 arc min) grain boundaries. Misorientation of the grains increases monotonically from one to the other side of the platelet. Detailed studies of the GaN platelets revealed that they usually consist of two layers which have slightly different lattice constants [17]. The X-ray intensity of both sides of the platelets and the homoepitaxial layer is presented in Fig. 8. The difference in the lattice constants induces strain in the crystal, which leads to its “bending” and contributes to the generation of dislocations during the growth process. The model of the creation of low-angle grain boundaries is presented in Fig. 9. The estimated density of the dislocation is of order of 10^4 cm^{-2} .

The polarity of GaN crystals has been determined by the convergent beam electron diffraction (CBED) method [18]. It has been shown that one side which has better morphological properties is gallium terminated, and the rough one is nitrogen terminated. Detailed microscopic studies of the crystals have been made using transmission electron microscopy (TEM), atomic force microscopy (AFM) and scanning electron microscopy



- 1 - N₂,
- 2 - steel
- 3 - thermal isolation
- 4 - pyrophillite
- 5 - boron nitride
- 6 - graphite
- 7 - Ga (liquid)
- 8 - Al₂O₃ (ceramic)

Fig. 4. One zone high-pressure crystal growth apparatus: (a) scheme of the apparatus; and (b) temperature distribution, calculated using finite element code FIDAP.

(SEM) techniques. These revealed that the gallium terminated surface is atomically flat with occasional monoatomic steps [19,20]. The nitrogen-terminated surface structure strongly depends on the location and the temperature variation during the process. For some

locations, pyramidal structure has been observed, whereas in others, a number of multiaionic steps have been observed. The steps can coalesce creating ridges several microns high. For higher supersaturation the growth instabilities lead to formation of inclusions.

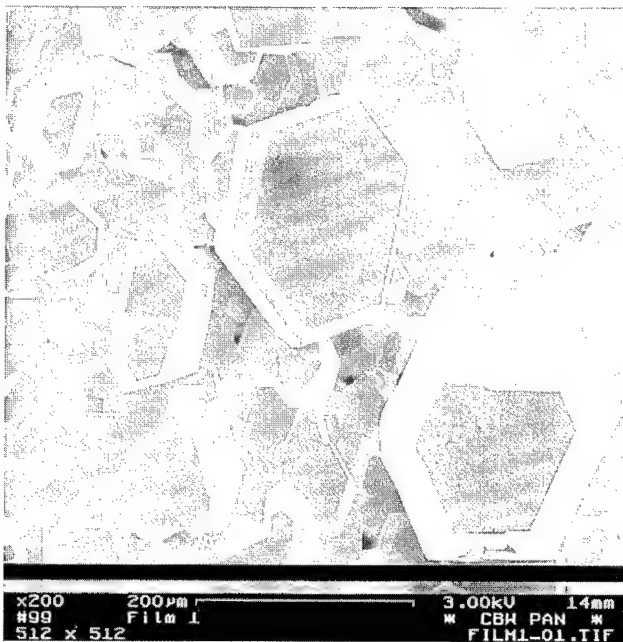


Fig. 5. GaN surface polycrystalline layer obtained under high N₂ pressure.

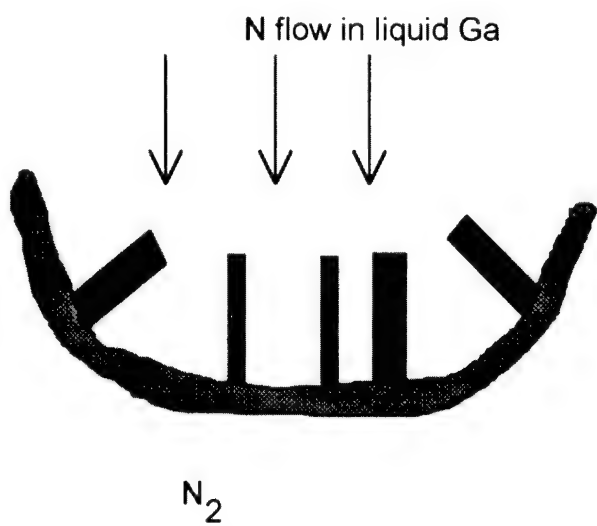


Fig. 6. The growth on the internal side of the crust the geometric arrangement.

The presence of such morphological instabilities is correlated with the different structural properties observed by TEM [19]. The layer close to the surface has a number of dislocations and stacking faults, enhanced by gallium inclusions. The layer having these properties does not exceed 10% of the thickness of the plate. The dominant part of the plate has virtually no stacking faults and much lower dislocation density. The gallium inclusions were not observed. It seems that the defect-free part of the plate results from the growth on the {1010} face and the dislocation heavy part from the growth on the {0001} face. The difference in these

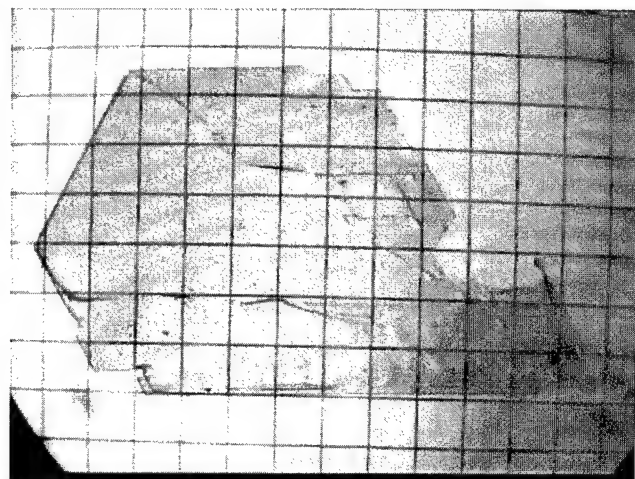


Fig. 7. Plate-like GaN single crystal. The grid spacing corresponds to 1 mm.

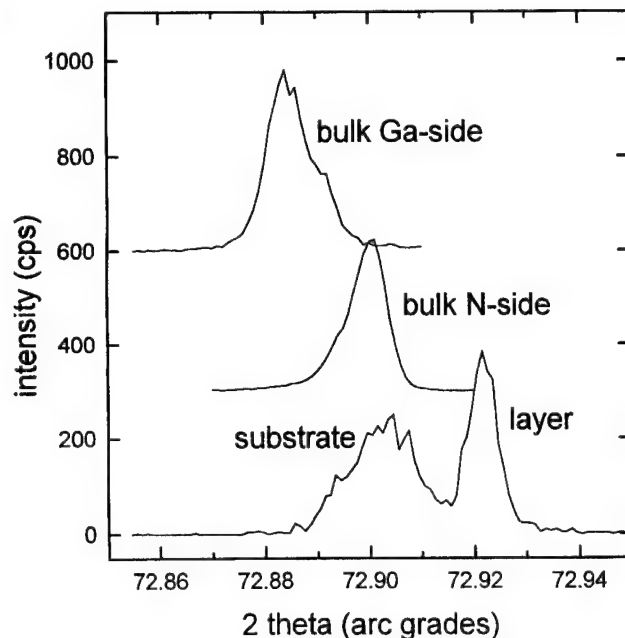


Fig. 8. The intensity X-ray rocking curve of (0004) CuK α reflection of single GaN crystal and homoepitaxial layer.

properties is related to kinetic mechanisms of the growth from the solution.

The electronic and optical properties of these crystals were also investigated [21]. The photoluminescence spectra of the plate-like crystals obtained on Ga-terminated and N-terminated side are presented in Fig. 10. Due to the Burnstein–Moss effect, the optical absorption edge is shifted towards higher energies, and GaN crystals are transparent to near edge luminescence. The luminescence spectrum has a characteristic yellow broad band centered around 2.2 eV and a near band-edge emission at approximately 3.5 eV. A rather small difference between these two crystal sides reflects the

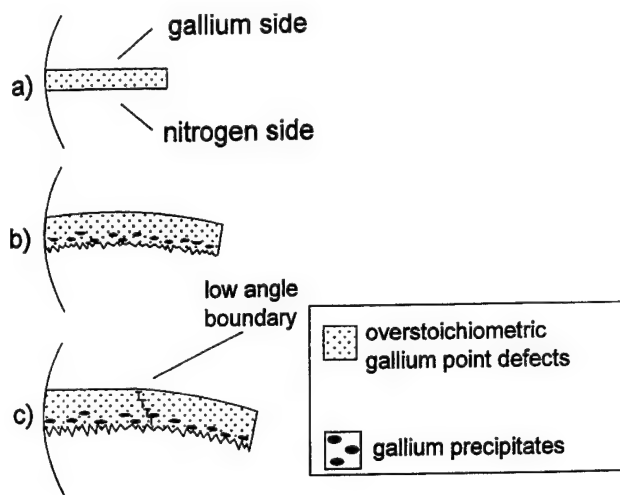


Fig. 9. The model of creation of low-angle boundaries due to the lattice constants difference.

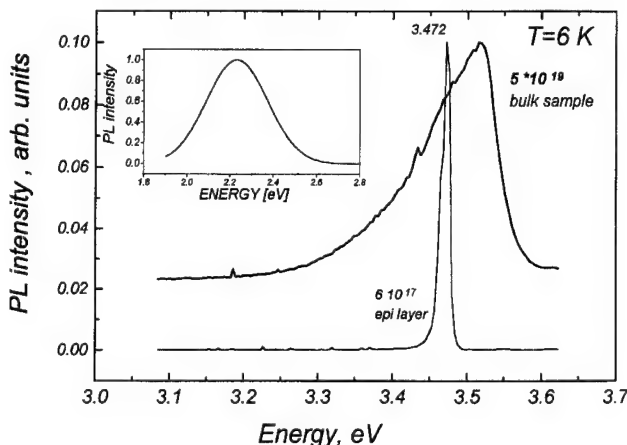


Fig. 10. Photoluminescence spectra of single GaN crystals obtained from the solution.

different structural properties of both sides of the crystals.

GaN single crystals show metallic behavior in the range 4.2–300 K. The GaN electronic properties measured include the Hall effect free carrier density and electron mobility. All GaN crystals are strongly *n*-type with the typical concentrations close to $5 \times 10^{19} \text{ cm}^{-3}$. No significant density variation was observed due to the change of the growth conditions. The free electron density is usually attributed to nitrogen vacancy [22]. The electron mobility is $30\text{--}90 \text{ cm}^2 \text{ V}^{-1}$ due to the high density of native defects in these crystals. Ab initio calculations [23,24] and experimental results [25] confirm that the source of free electrons in GaN are N-vacancies.

3.2. Aluminium nitride

Aluminium nitride crystals have been obtained under partial nitrogen pressures higher than 7 kbars. At lower

pressures, the combustion process starts at temperatures close to 1000 °C [7]. The combustion results depend on the chemical compositions of the gas mixture. For a nitrogen dominant gas mixture, the combustion results in AlN ceramics. When neutral gas dominates, the obtained sample is almost perfectly converted to AlN powder. This result opens up a potential application of Al combustion in high nitrogen pressures for the fabrication of high-quality AlN ceramics for electronic applications. Single AlN crystals obtained from nitrogen solutions under high nitrogen pressures were 0.1 mm in size and were needle-like. The crystalline quality of these crystals is comparable with that of the needle-like GaN single crystals.

3.3. Indium nitride

The largest single crystals of InN, grown from the solution under high pressure of nitrogen, were several μm in size. They had irregular shapes and they were skeletal in forms [8,9]. The attempts to grow larger crystals from the solution under high pressure were not successful.

4. Epitaxial layers

The homoepitaxial layers were grown on GaN single crystals using both MOCVD and MBE techniques. The layers have been grown on plate-like crystals only.

4.1. MOCVD

The homoepitaxial layers were grown by the MOCVD method in a horizontal atmospheric pressure reactors. Usually as-grown crystals were etched, rinsed in deionized water and annealed at a temperature of 800 °C in the MOCVD reactor in an atmosphere of NH₃ and H₂ mixture. The growth was conducted using trimethylgallium (TMG) and ammonia in the temperature range 900–1100 °C. The best results were obtained in the temperature range 1020–1050 °C.

The growth of the layer depends crucially on the substrate polarity. On the gallium-terminated side, the growth is irregular with the tendency to form isolated islands and even the transition to three-dimensional growth is observed. For higher supersaturations, columnar growth has been observed. On the nitrogen-terminated side, the growth mode is two-dimensional. Depending on the TMG:ammonia ratio, the growth morphology changes from the strictly two-dimensional to island type. The two-dimensional growth is controlled by new layer creation. Both two-dimensional nucleation and screw dislocation edge sources have been observed [26].

Both *p*-type and *n*-type layers have been obtained.

The *p*-doping was performed using the metalo-organic MCp₂Mg and subsequent annealing in 700 °C in the presence of N₂. The *n*-doping was obtained by the use of silicon as a controlled donor defect. The homoepitaxial layers were characterized by X-ray and optical methods. The X-ray studies confirmed good crystallographic quality of the layers; the optical measurements include photoluminescence and electroluminescence studies [27]. A typical photoluminescence spectrum is presented in Fig. 11.

4.2. MBE

Homoepitaxial layers were grown by the MBE method using the on surface cracking (OSC) technique of M. Kamp et al. [28]. The MBE system used ammonia as a nitrogen source. The substrate preparation was similar to that adopted for MOCVD grown layers and the substrate temperature during the growth was equal to 680 °C.

The obtained layers were characterized by X-ray, microscopic and optical methods. The maximum of CuK α 1 reflection was slightly shifted owing to a difference in lattice constants caused by different free carrier densities in the layer and the substrate. Optical measurements include photoluminescence studies; an example of a photoluminescence spectrum is given in Fig. 12. The figure includes two lines attributed to donor bound excitons, one line attributed to acceptor bound exciton and, additionally, three narrow lines due to free excitons. They are due to three sub-bands of the valence band. The low-energy lines (i.e. ABE and DBEs) have a half width of the order of 0.4 meV, which is presently the narrowest line reported. The higher energy lines have a half-width of the order of 5 meV.

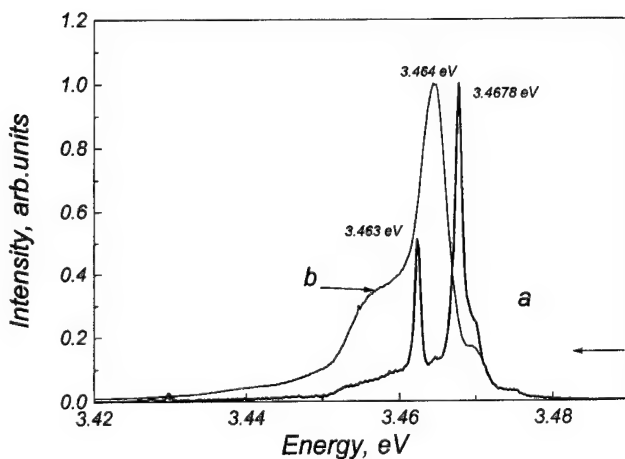


Fig. 11. Photoluminescence spectra of MOCVD grown layers: (a) undoped; and (b) Mg doped, $T=4.2$ K.

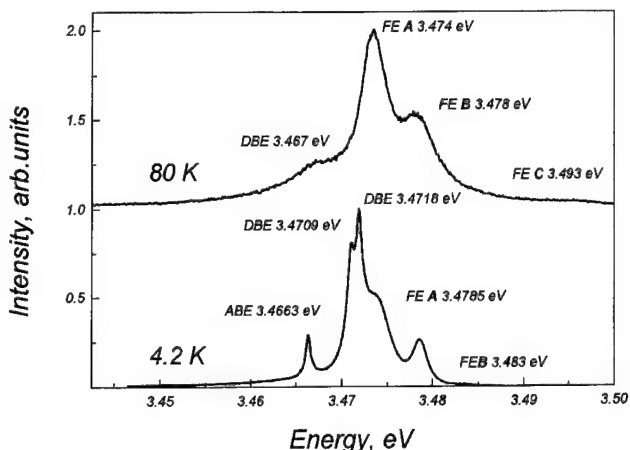


Fig. 12. Photoluminescence spectra of MBE grown layers: (a) $T=4.2$ K; and (b) $T=80$ K.

5. Conclusions

The main results reported in this paper can be summarized as follows:

- (1) the best outlook for the growth of large-substrate quality single crystals currently exists for GaN; InN and AlN suffer from severe thermodynamic obstacles, which makes the stable growth of single crystals extremely difficult;
- (2) the development of high-pressure crystal growth technology allowed us to obtain the GaN single crystals of 10 mm in size;
- (3) the best crystalline quality layers were obtained by the MOCVD method, using GaN as a substrate;
- (4) the optical properties of the MBE grown layers indicates the high quality of the homoepitaxial layers;
- (5) the development of homoepitaxial technology can lead to fabrication of highly efficient lasers, active in the blue and ultraviolet range of the spectrum.

Acknowledgement

The research reported in this work has been supported by the Polish Committee for Scientific Research grant nos. 2P 30B 00809 and 7783495 C/2399.

References

- [1] H. Morkoc, S. Strite, G.B. Gac, M.E. Lin, B. Sverdlov, M. Burns, J. Appl. Phys. 76 (1994) 1363.
- [2] S. Nakamura, T. Mukai, M. Senoh, Jap. J. Appl. Phys. 30 (1991) L1998.
- [3] S. Nakamura, M. Senoh, N. Iwasa, S. Nagahama, Jap. J. Appl. Phys. 30 (1991) L979.
- [4] D.V. Tsvetkov, A.S. Zubrilov, V.I. Nikolaev, V. Soloviev, V.A. Dmitriev, MRS Internet Journal of Nitride Semiconductor Research 1 (1996) no. 35.

[5] S. Nakamura, M. Senoh, S. Nagahama, N. Iwasa, T. Yamada, T. Matsushita, H. Kiyoku, Y. Sugimoto, Jap. J. Appl. Phys. 35 (1996) L217.

[6] I. Grzegory, M. Bockowski, S. Kruckowski, B. Lucznik, M. Wroblewski, S. Porowski, MRS Internet Journal of Nitride Semiconductor Research 1 (1996) no. 20.

[7] I. Grzegory, J. Jun, M. Bockowski, S. Kruckowski, M. Wroblewski, B. Lucznik, S. Porowski, J. Phys. Chem. Solids 56 (1995) 639.

[8] I. Grzegory, S. Kruckowski, J. Jun, M. Bockowski, M. Wroblewski, S. Porowski, AIP Conference Proceedings 309 (1994) 565.

[9] W. Harrison, Electronic Structure and Properties of Solids, Freeman, San Francisco, 1980.

[10] R.T. Jacobsen, R.T. Stewart, M. Jahangiri, J. Phys. Chem. Ref. Data 15 (1986) 735.

[11] J.A. Van Vechten, Phys. Rev. B7 (1973) 1479.

[12] W. Class, Contract Report, NASA-Cr-1171, 1968.

[13] J. Karpinski, J. Jun, S. Porowski, J. Cryst. Growth 66 (1984) 1.

[14] G.A. Slack, T.F. MacNelly, J. Cryst. Growth 34 (1976) 276.

[15] S. Kruckowski, MRS Internet Journal of Nitride Semiconductor Research 1 (1996) no. 27.

[16] I. Grzegory, S. Kruckowski, Phys. Scr. T39 (1991) 242.

[17] M. Leszczynski, I. Grzegory, H. Teisseire, T. Suski, M. Bockowski, J. Jun, J.M. Baranowski, S. Porowski, J. Domagala, J. Cryst. Growth 169 (1996) 235.

[18] F.A. Ponce, P. Bour, W.T. Young, M. Saunders, J.W. Steeds, Appl. Phys. Lett. 69 (1996) 337.

[19] Z. Lilliental-Weber, C. Kisielowski, S. Ruvimov, Y. Chen, J. Washburn, I. Grzegory, M. Bockowski, J. Jun, S. Porowski, J. Electron. Mater. 25 (1996) 1545.

[20] Z. Lilliental-Weber, S. Ruvimov, C. Kisielowski, Y. Chen, W. Swider, J. Washburn, N. Newman, A. Gassmann, X. Liu, L. Schloss, E.R. Weber, I. Grzegory, M. Bockowski, J. Jun, T. Suski, K. Pakula, J.M. Baranowski, S. Porowski, H. Amano, I. Akasaki, Mater. Res. Soc. Proc. 395 (1996) 351.

[21] H. Teisseire, P. Perlin, M. Leszczynski, T. Suski, I. Grzegory, J. Jun, S. Porowski, T.D. Moustakas, J. Appl. Phys. 76 (1994) 4909.

[22] H.P. Maruska, J.J. Tjetjen, Appl. Phys. Lett. 15 (1969) 327.

[23] J. Neugebauer, C.G. Van de Walle, Phys. Rev. B50 (1994) 8067.

[24] P. Boguslawski, E. Briggs, J. Bernholz, Phys. Rev. B51 (1995) 17255.

[25] P. Perlin, T. Suski, H. Teisseire, M. Leszczynski, I. Grzegory, J. Jun, S. Porowski, P. Boguslawski, J. Bernholz, J.C. Chervin, A. Polian, T.D. Moustakas, Phys. Rev. Lett. 75 (1995) 296.

[26] G. Nowak, S. Kruckowski, I. Grzegory, S. Porowski, J. Baranowski, K. Pakula, J. Zak, MRS Internet Journal of Nitride Semiconductor Research 1 (1996) no. 5.

[27] A. Wysmolek, J.M. Baranowski, K. Pakula, K.P. Korona, I. Grzegory, M. Wroblewski, S. Porowski, Proceedings of the International Symposium on Blue Laser and Light Emitting Diodes, Chiba, Published by Ohmsha Ltd, Tokyo, Japan, 1996, p. 492.

[28] H. Teisseire, G. Nowak, M. Leszczynski, I. Grzegory, M. Bockowski, S. Kruckowski, S. Porowski, M. Mayer, A. Pelzman, M. Kamp, K.J. Ebeling, G. Karczewski, MRS Internet Journal of Nitride Semiconductor Research 1 (1996) no. 13.

Residual strains in GaN grown on 6H-SiC

I.P. Nikitina ^{a,*}, M.P. Sheglov ^a, Yu.V. Melnik ^a, K.G. Irvine ^b, V.A. Dmitriev ^{a,b}

^a A.F. Ioffe Institute, 26 Politehnicheskaya str., St. Petersburg, 194021, Russia

^b Cree Research, Inc., 2810 Meridian Parkway, Durham, NC 27713, USA

Abstract

The triple crystal modification of Bond method was used for lattice constant measurements and for the study of residual strains in GaN layers grown on 6H-SiC (0001) substrates. GaN layers grown by MOCVD employing AlN and AlGaN buffer layers and GaN layers grown by HVPE without buffer layer were investigated. It was found that the residual strains in GaN were considerably reduced by use of the AlGaN buffer layer. The dependence of residual strains on thickness and composition of buffer layer could be explained by the different degree of relaxation mismatch stresses and change of thermal stresses in GaN layers, grown on SiC with different buffer layers. © 1997 Elsevier Science S.A.

Keywords: Gallium nitride; Lattice constant; Buffer layer; Stress; Residual strains

1. Introduction

Epitaxial growth of GaN is a subject of great interest for fabrication of light emitting devices. Recently, high-quality GaN epitaxial layers have been grown on SiC and sapphire using different methods, such as MOCVD, HVPE, MBE [1–4]. It was shown that the lattice constant of thin GaN layers grown on SiC and sapphire is different from that for bulk GaN. The c-lattice constant for GaN grown on SiC substrate is usually smaller than that for bulk GaN. On the contrary, the c-lattice constant for GaN grown on sapphire is larger than that for bulk GaN (Table 1). These results indicate that considerable residual strain is always present in thin GaN heteroepitaxial layers. When the thickness of GaN layer exceeds a certain critical value, the formation of cracks is observed. Critical thickness depends on the substrate used, the buffer layer and the growth technique [5,10,11]. Two main factors may cause stresses and strains in epitaxial layers: (1) the lattice mismatch and (2) the difference in thermal expansion coefficients (TEC) between the layer and the substrate. The values of lattice constants and TEC for GaN, SiC, sapphire and AlN are shown in Table 2. The relaxation of stresses in GaN grown on sapphire was studied in several reports

[10–12]. It was suggested that the observed residual strain is thermal in nature.

In this paper, we report on the effect of buffer layer on residual strains in GaN epitaxial layers grown on SiC substrates.

2. Experimental procedure and results

GaN layers were grown on SiC-6H (0001) by HVPE without buffer layer and by MOCVD using AlN and AlGaN buffer layers. The thickness of GaN layers ranged from 1 to 2.3 μm. The thickness of AlN buffer was 500 Å, and the thickness of the AlGaN buffer for different samples was 500, 1500 and 3000 Å. The content of AlN in AlGaN buffer was 20, 30 and 50%. The thickness of the substrates was 300 μm. All layers were free from cracks.

We examined crystal quality of GaN layers using a double crystal X-ray spectrometer. Rocking curves were measured at (ω) and ($\omega, 2\theta$) modes with the SiC-6H (0006) monochromator. Typical RC(ω) for three groups of samples are demonstrated in Fig. 1 [(a) for the GaN layer grown directly on SiC, (b) for GaN grown on SiC with AlN buffer layer and (c) for GaN grown with AlGaN buffer layer]. The FWHM of RC(ω) ranged from 80 to 340 arcsec. Measurements of GaN lattice constants were performed using a triple crystal modification of the Bond method [13,14] on symmetric

* Corresponding author. Fax: +7 (812) 247-6425;
e-mail: ini@shuttle.ioffe.rssi.ru

Table 1
C-lattice constant in GaN layers grown on SiC and sapphire

Substrate	Buffer layer	Thickness of GaN (μm)	Lattice constant C (\AA)	References
Sapphire	AlN	1.0	5.191	[5]
Sapphire	AlN	0.75	5.1930	[6]
Sapphire	AlN	1.0	5.1900	[7]
SiC-6H	AlN	1.0	5.1816	[7]
SiC-6H	AlN	0.5	5.178	[8]
GaN bulk	—	—	5.18561	[9]

Table 2
Lattice constants and TEC for GaN, SiC-6H, AlN and sapphire

	c (\AA)	a (\AA)	$\alpha_c \times 10^6$	$\alpha_a \times 10^6$
GaN	5.18561	3.188	3.17	5.59
SiC-6H	15.1173	3.0806	4.68	4.2
AlN	4.9792	3.1114	5.3	4.2
Sapphire	12.991	4.758	8.5	7.5

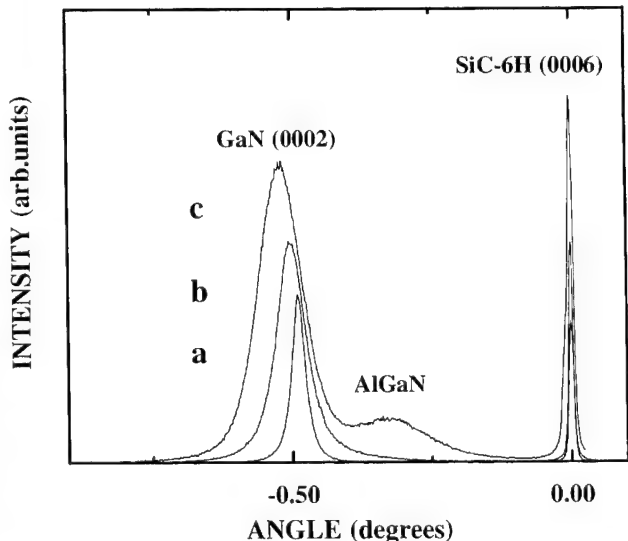


Fig. 1. Typical $\text{RC}(\omega)$ for three groups of samples: (a) for GaN layer grown directly on SiC; (b) for GaN grown on SiC with AlN buffer layer; and (c) for GaN grown with AlGaN buffer layer.

(0004) CuK_α and asymmetric (11̄24) CuK_α reflections. SiC-6H crystals served as monochromator and analyser. This method is more useful in the case of mosaic and bending crystals, especially for asymmetric reflections. This allowed us to determine lattice constants with an accuracy of $5 \times 10^{-5} \text{ \AA}$.

To estimate normal and tangent strains in GaN layers, we compared measured values of the lattice constants with those for the bulk GaN crystal, referred by Leszczinski et al. [9]. These values at $T=294^\circ\text{C}$ are: $c=5.18561 \text{ \AA}$, $a=3.1880 \text{ \AA}$. Residual strains were determined as:

$$\epsilon_\perp = (C_l - C_b)/C_b$$

and $\epsilon_\parallel = (a_l - a_b)/a_b$, where the index 'l' corresponds to the layer, and the index 'b' corresponds to the bulk crystal.

The results obtained for all GaN layers are shown in Table 3. From the table, the following deductions can be made:

- (1) The largest residual strains are observed in the layers grown directly on SiC. Normal strains are negative and tangent ones are positive.
- (2) AlN thick 500 \AA buffer layer reduces the absolute values of the strains.
- (3) AlGaN buffer layers cause further reduction of strains and may change the signs of them depending on the composition and thickness of the buffer layer.

3. Discussion

The analysis of obtained results allows us to assume that, for the GaN/SiC heterostructure, the relaxation of mismatch stresses is not complete, and the GaN layer lattice constants at the growth temperature are not equal

Table 3
Residual strains in GaN layers

NN	Buffer layer	% AlN in buffer	Thickness of buffer (\AA)	$\epsilon_\perp \times 10^3$	$\epsilon_\parallel \times 10^3$
1		0	0	-1.14	+2.51
2		0	0	-1.02	+1.88
3	Non	0	0	-1.37	+2.92
4		0	0	-1.35	+2.79
5		20	1500	-0.35	+0.77
6		20	1500	-0.31	+0.72
7		20	1500	-0.45	+0.75
8		20	1500	-0.28	+0.50
9		20	3000	+0.23	-0.35
10	AlGaN	30	3000	-0.02	0
11		30	3000	+0.17	-0.41
12		30	3000	+0.25	-0.44
13		30	3000	+0.23	-0.44
14		30	3000	+0.45	-0.78
15		50	500	-0.43	+0.78
16		50	500	-0.31	+0.69
17		100	500	-0.77	+1.22
18	AlN	100	500	-0.58	+1.22
19		100	500	-0.54	+0.85

Table 4
FWHM of $\text{RC}(\omega)$ on (0002) and (11̄2̄) reflections

Sample	Buffer layer	FWHM (0002) arcsec	FWHM (11̄2̄) arcsec	$\epsilon_{\perp} \times 10^3$	$\epsilon_{\parallel} \times 10^3$
1	Non	115	270	-1.14	+2.51
4	Non	55	240	-1.35	+2.79
11	AlGaN	270	220	+0.17	-0.41
14	AlGaN	270	240	+0.45	-0.78

to those for bulk crystal. We think that this is true for GaN layers grown directly on SiC substrates and especially for the layers grown with buffer layers. If this is true, at the growth temperature, the tangent strain should be negative, and the normal strain should be positive since the lattice constant a of the substrate is smaller than that of the layer. When the sample is cooled down from the growth temperature to room temperature, thermoelastic stresses appear. Since the TEC of SiC < TEC of GaN, the GaN layer expands in the (0001) plane, and therefore the tangent strain becomes positive. The resulting residual strains are defined by the relative values of mismatch and thermal stresses. The complete compensation of one stress by the other is possible if the lattice mismatch and the difference in TEC have the same signs. When we use AlN or AlGaN as a buffer layer, the lattice mismatch decreases on both interfaces. This leads to a decrease in the degree of relaxation of mismatch stresses. However, the TEC of solid solution is likely to be close to TEC of GaN. This results in a decrease in thermal stresses. Thus, an almost total compensation of stresses and strains is possible in GaN layers grown with AlGaN buffer layer (see sample 10 from Table 3).

As for the degree of relaxation of mismatch stresses, we believe that it is related to the type of threading dislocations (TD) in the GaN layer. We compared the FWHM of $\text{RC}(\omega)$ for (0002) and (11̄2̄) reflections for the layers grown without buffer layer (they have the largest residual strains and $\epsilon_{\perp} < 0, \epsilon_{\parallel} > 0$) with those for the layers grown with the AlGaN buffer layer (they have residual strains with opposite signs). These FWHM values are shown in the Table 4. The half widths of $\text{RC}(\omega)$ for (0002) reflection are smaller than that for (11̄2̄) reflection from the layers grown without buffer layer; in contrast, the half widths of RC for symmetric and asymmetric reflections from the layers, grown with AlGaN buffer layer are comparable. According to the conclusion given by Heying et al. [15], this would be explained by type of TD in the layers: a large difference between the half widths is caused by the formation of pure edge TDs with Burgers vector, parallel to the interface. Comparable half width values are associated with the formation of screw or mixed screw/edge TDs. Therefore, it can be assumed that the almost total relaxation of mismatch stresses is accompanied by the formation of pure edge type TDs. The degree of relax-

ation of mismatch stresses decreases in the case of the formation of screw or mixed screw/edge TDs. Furthermore, we suppose that this relaxation may be almost complete if an initial stage of the growth is accompanied by strong misorientation of GaN grains in the (0001) plane and weak misorientation around the [0001] direction.

4. Conclusion

Residual strains in GaN grown on SiC-6H without a buffer layer and with AlN and AlGaN buffer layers were studied using triple crystal modification of the Bond method. It was found that the AlGaN buffer layer considerably reduces residual strains in GaN layers. The GaN layers free of residual strains may be grown on SiC-6H substrates, varying thickness and composition of AlGaN buffer. It was assumed that:

- (1) residual strains are caused by a lattice mismatch as well as a difference in TEC, acting in opposition;
- (2) AlGaN buffer layer decreases thermal stresses and relaxation degree of mismatch stresses depending on its thickness and composition; and
- (3) the relaxation degree of mismatch stresses is connected with the type of threading dislocations in the GaN layer.

Acknowledgement

The authors would like to thank Dr R. Kutt and K. Vassilevski for useful discussions.

References

- [1] I. Akasaki, H. Amano, Y. Koide, K. Hiramatsu, N. Sawaki, *J. Cryst. Growth* 98 (1989) 209.
- [2] M.E. Lin, B. Swerdlow, G.L. Zhou, H. Morcoc, *Appl. Phys. Lett.* 62 (1993) 3479.
- [3] I. Akasaki, H. Amano, *J. Electrochem. Soc.* 141 (1994) 2266.
- [4] Yu.V. Melnik, I.P. Nikitina, A.S. Zubrilov, A.A. Sitnikova, Yu.G. Musikhin, V.A. Dmitriev, *Inst. Phys. Conf.* 142 (1996) 863.
- [5] K. Hiramatsu, Th. Detchprohm, I. Akasaki, *J. Appl. Phys.* 32 (4) (1993) 1528.
- [6] W. Rieger, T. Metzger, H. Angerer, R. Dimitrov, O. Ambacher, M. Stutzman, *Appl. Phys. Lett.* 68 (7) (1995) 970.

- [7] Wei Li, Wei Xin Ni, *Appl. Phys. Lett.* 68 (19) (1996) 2705.
- [8] F.A. Ponce, B.S. Kruger, Major J.S., Jr, W.E. Plano, D.F. Welch, *Appl. Phys. Lett.* 67 (3) (1995) 410.
- [9] M. Leszczinski, T. Suski, H. Teisseyre, P. Perlin, I. Grzegory, J. Jun, S. Porowski, T.D. Moustakas, *J. Appl. Phys.* 76 (8) (1994) 4909.
- [10] N. Itoh, J.C. Rhee, T. Kawabata, S. Koike, *J. Appl. Phys.* 58 (1985) 1828.
- [11] T. Kozawa, T. Kachi, H. Kano, H. Nagase, N. Koide, K. Manabe, *J. Appl. Phys.* 77 (9) (1995) 4389.
- [12] T. Detchprohm, K. Hiramatsu, K. Itoh, I. Akasaki, *Jpn. J. Appl. Phys.* 31 (1992) L1454.
- [13] E.I. Golovenchin, N.V. Morosov, S.S. Ruvimov, V.A. Sanina, L.M. Sapognikova, L.M. Sorokin, P.P. Sirnikov, M.P. Sheglov, *Superconductivity: Phys., Chem., Techn.* (in Russian) 3 (5) (1990) 773.
- [14] P.F. Fewster, N.L. Andrew, *J. Phys. D: Appl. Phys.* 28 (4A) (1995) A97.
- [15] B. Heying, X.H. Wu, S. Keller, Y. Li, D. Kapolnek, B.P. Keller, S.P. DenBaar, J.S. Speck, *Appl. Phys. Lett.* 68 (5) (1996) 64.

Structural and electrical properties of Schottky barriers on n-GaN

E.V. Kalinina ^{a,*}, N.I. Kuznetsov ^a, A.I. Babanin ^a, V.A. Dmitriev ^a, A.V. Shchukarev ^b

^a A.F. Ioffe Physico-Technical Institute, 26 Politehnicheskaya str., 194021 St. Petersburg, Russia

^b Mekhanobr Analyt Co., 8a 21 Liniya V.I., 199026 St. Petersburg, Russia

Abstract

Cr, Au and Ni Schottky barriers were formed on n-GaN. Fundamental parameters of the barriers (barrier height, electron affinity of GaN, and effective Richardson coefficient) were calculated from results of current–voltage and capacitance–voltage measurements. Interface chemistry of Cr, Au and Ni barriers on n-GaN was studied using Auger electron spectroscopy (AES) and angle-resolved X-ray photoelectron spectroscopy (AR XPS). A correlation between the chemical reactivity of metals and the value of the effective Richardson coefficient was established. © 1997 Elsevier Science S.A.

Keywords: GaN; Schottky barrier; Effective Richardson coefficient; Interface

1. Introduction

Recently extensive and detail study has been done on Schottky barriers formed on n-GaN. Different metals have been employed to form the Schottky barriers: Au [1], Pt, Pd [2], Au, Pd, Cr, Ti, Pt, Ni [3], Pd, Pt [4]. Epitaxial n-GaN layers grown by metal organic chemical vapor deposition (MOCVD) or hydride vapor phase epitaxy (HVPE) on sapphire substrates have been used for these studies. Characteristics of Cr, Au and Ni Schottky barriers formed on n-GaN epitaxial layers grown on SiC substrates have also been reported [5]. The values of the barrier height, built-in potential and the GaN electron affinity determined in those papers are in good agreement. However, the values of the effective Richardson coefficient differ significantly for the metals investigated. In the present work, we investigated the interface chemistry for the barriers described in Ref. [5].

2. Experimental procedure

Epitaxial n-GaN layers were grown by MOCVD on 6H-SiC (0001) substrates [5]. The concentration of uncompensated donors, $N_d - N_a$, in the GaN layers ranged from 10^{16} to 10^{18} cm^{-3} . The thickness of the layers was approx. 1 μm . Schottky barriers were formed

by vacuum thermal evaporation of metals: Cr, Au and Ni. Al was evaporated to form Ohmic contacts to n-GaN. The metals were evaporated in a vacuum of approx. $3 \times 10^{-4} \text{ Pa}$ through shadow masks. The barrier area (S) was $7 \times 10^{-4} \text{ cm}^2$. The thickness of the metals ranged from 0.1 to 0.15 μm for electrical and AES measurements, and from 30 to 50 Å for XPS measurements. A schematic drawing of the structure is shown in Fig. 1.

The current–voltage ($I-V$) characteristics of the barriers were measured in the temperature range from 100 to 450 K. The capacitance–voltage ($C-V$) characteristics were measured at frequencies of 1 and 10 kHz and 1 MHz at 300 K. The distribution of the chemical elements across of the metals/GaN structures was studied by AES depth profiling using Ar^+ ions. Phase formations on metals/GaN interfaces were investigated by AR XPS. Photoelectron take-off angle varied from 15 to 75°.

Al (Cr, Au, Ni) Al

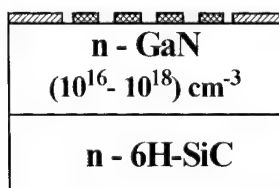


Fig. 1. Schematic drawing of a sample with Schottky barriers and Ohmic contacts.

* Corresponding author. Fax: 00 7 812 247 6425.

3. Results and discussion

3.1. Electrical characteristics of the barriers

For all investigated barriers, C – V characteristics were linear when plotted in (C^{-2}) – (V) coordinates. This dependence indicates an uniform depth profile of the donor impurity concentration in the epitaxial layers. The values of built-in potential (V_i), barrier height (φ_{bn}), and GaN electron affinity (χ_s) were calculated using the well-known equations [6]:

$$V_i = V_o + \frac{kT}{q} \quad (1)$$

$$q\varphi_{bn} = q(V_i + V_n) + kT \quad (2)$$

$$q\chi_s = q\varphi_m - q\varphi_{bn}, \quad (3)$$

where V_o is the cut-off voltage of the C – V characteristics, V_n is the difference in the energies between the bottom of the conduction band and the Fermi level, φ_m is the work function for the metal and q is the charge of electron. Measured and calculated V_o , φ_m , V_i and χ_s values for all barriers investigated are given in Table 1.

The reverse leakage current was about 100 μ A at a reverse voltage of approx. 15 V for Au and Ni Schottky barriers, and approx. 5 V for Cr barriers. At a forward voltage ranging from approx. 3 kT/q to approx. 1.5 V, the forward I – V characteristics may be described by the well-known formula:

$$I = I_o \exp\left(\frac{qV}{nkT}\right) \quad (4)$$

where n is the ideality factor and I_o is the saturation current. Saturation current was determined from I – V characteristics. The values of I_o for all barriers investigated are given in Table 1. In contrast, the saturation current is determined by the equation:

$$I_o = SA^*T^2 \exp\left(-\frac{q\varphi_{bn}}{nkT}\right) \quad (5)$$

Table 1
Parameters of Schottky barriers obtained from I – V and C – V measurements

Cr		Au		Ni	
$q\varphi_m = 4.6$ eV		$q\varphi_m = 5.1$ eV		$q\varphi_m = 5.2$ eV	
I – V	C – V	I – V	C – V	I – V	C – V
N_d (cm^{-3})	–	6×10^{17}	–	6×10^{17}	1×10^{18}
V_o (V)	–	0.58	–	0.97	–
n (300 K)	1.05	–	1.15	–	1.17
$q\varphi_{bn}$ (eV)	0.53	0.58	1.03	1.03	1.15
V_i (V)	0.49	0.55	0.99	1.00	1.14
$q\chi_s$ (eV)	4.07	4.02	4.07	4.07	4.06
I_o (A/cm^2)	7.6×10^{-5}	–	3×10^{-9}	–	3.5×10^{-10}
A^* ($\text{A}/\text{cm}^2\text{K}^2$)	0.12	–	296	–	102

where A^* is the effective Richardson coefficient. The values of A^* were calculated from Eq. (5) using experimental data (Table 1).

The calculated values of A^* differ significantly for all metals investigated. Usually, the value of this coefficient is determined by the properties both at the semiconductor and the metal/semiconductor interface [6]. In our case, all metals were evaporated on the same sample and the chemical treatment of n-GaN surface before evaporation was identical. To understand the nature of the difference in measured effective Richardson coefficient, we investigated the composition of metal/GaN interfaces.

3.2. Interface composition

The distributions of the chemical elements across metal/GaN structures measured by AES are shown in Fig. 2. The sharpest boundary was between n-GaN and Ni, having a very thin interface region. Au/GaN and Cr/GaN structures had wider interface regions. Ni and Cr films and interfaces between these metals and n-GaN had noticeable quantity of carbon. Cr film and Cr/GaN interface had a noticeable quantity of oxygen.

The distributions of the chemical elements across the interface of the barriers was also investigated by AR XPS. Depth profile reconstruction (Fig. 3) was done in accordance with Ref. [7]. It was found that each metal interface has a specific chemical composition. All used films were found to be contaminated with carbon. This fact is probably due to surface contamination occurring during metal deposition. Oxygen was detected in interface regions. The oxygen concentration was lowest for the Au/GaN interface and highest for the Cr/GaN interface. XPS N1s spectra (Fig. 4) indicate that Au/GaN and Cr/GaN interfaces contain oxynitride layers. We propose that the oxynitride layer at the Au/GaN is a native gallium oxynitride which is always present on the GaN surface.

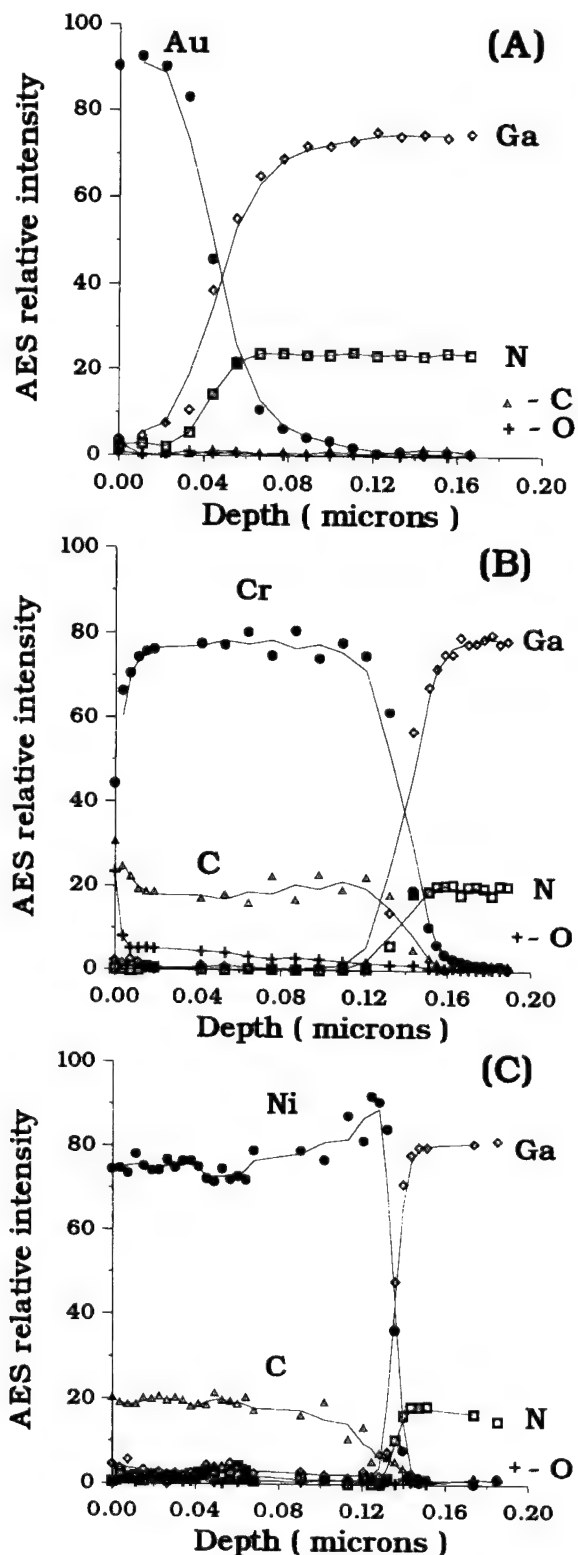


Fig. 2. AES depth profiles for Schottky barriers formed on n-GaN: (A) Au; (B) Cr; (C) Ni.

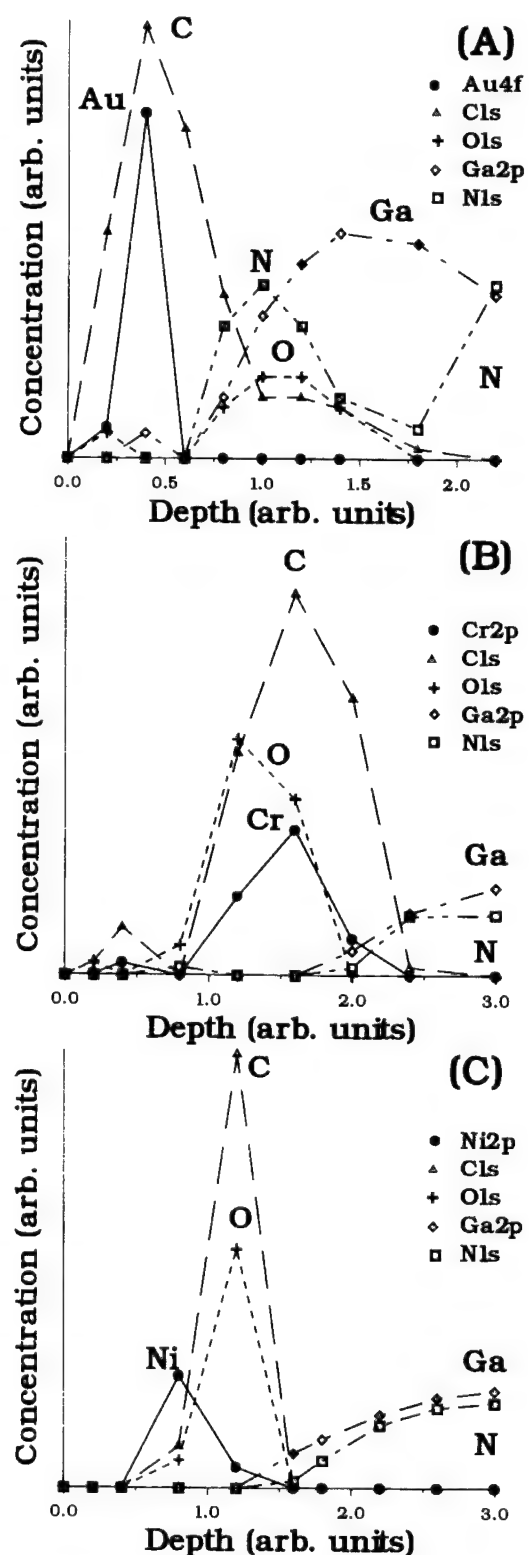


Fig. 3. Element depth profiles for metal/n-GaN interfaces reconstructed from AR XPS data, the metal thickness are: (A) Au (30 Å); (B) Cr (50 Å); (C) Ni (40 Å).

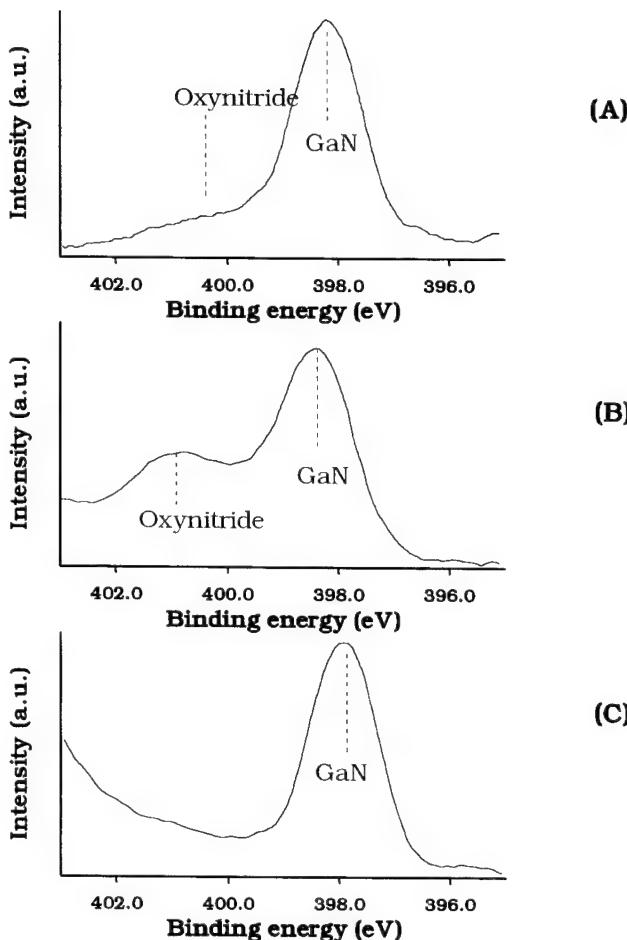


Fig. 4. N1s X-ray photoelectron spectra for metal/n-GaN interfaces:
(A) Au; (B) Cr; (C) Ni.

The most chemically active Cr reacts with native oxynitride (and possibly with n-GaN) forming a thin transition layer which consists of gallium and chromium oxynitrides and probably chromium nitrides. Moreover, the binding energy of $\text{Cr}2\text{p}_{3/2}$ line is measured as $E_b=576.9$ eV, and this energy corresponds to Cr in Cr_2O_3 [8]. Thus, the formation of a small quantity of Cr_2C_3 is also possible.

The binding energy of the $\text{Ni}2\text{p}_{3/2}$ line is $E_b=855.6$ eV. This value corresponds to Ni in NiO [8]. It seems that Ni deposition is followed by the reaction:



The formation of a small quantity of Ni_3C is also possible.

The above results indicate that the composition of metal/GaN interfaces is determined by the chemical reactivity of the metal. We propose that the difference in interface properties explains the difference in effective Richardson coefficient for the reported Schottky barriers. The higher the chemical reactivity of metals, the smaller the value of the effective Richardson coefficient.

4. Conclusions

Cr, Au and Ni Schottky barriers were formed on n-GaN. Barrier characteristics were measured using $C-V$ and $I-V$ methods. Auger electron spectroscopy and angle-resolved X-ray photoelectron spectroscopy were employed to study the interface of the barriers. It was found that the interface composition is determined by the chemical reactivity of the metals deposited. We believe that the significant difference in effective Richardson coefficient of the barriers formed with different metals is due to the observed difference in interface composition.

Acknowledgement

This work was supported in part by the Arizona State University.

References

- [1] M.R.H. Khan, T. Detchprohm, P. Hacke, K. Hiramatsu, N. Sawaki, Transactions of the 2nd International High Temperature Electr. Conference, Charlotte, NC, 1994, p. 231.
- [2] J.D. Guo, M.S. Feng, R.J. Guo, F.M. Pan, C.Y. Chang, Appl. Phys. Lett. 67 (1995) 2657.
- [3] C. Schmitz, A.T. Ping, I. Adesida, M. Asif Khan, Mat. Res. Soc. Symp. Proc. 395 (Pittsburg, PA: Mater. Res. Society, 1996), p. 837.
- [4] L. Wang, T.-H. Lim, M.I. Nathan, P.I. Cohen, P.P. Ruden, M. Asif Khan, EMC-37, Charlotte, USA, M7, 1995, A32.
- [5] E.V. Kalinina, N.I. Kuznetsov, V.A. Dmitriev, K.G. Irvine, CarterC.H., Jr., J. Electr. Mater. 25 (1996) 831.
- [6] E.H. Rhoderick, Metal-Semiconductor Contacts, Clarendon Press, Oxford, 1978.
- [7] S.N. Dubrovensky, A.V. Shchukarev, The 8th International Conference on Quantitative Surface Analysis, Surrey, UK, 1994, p. 70.
- [8] J. Chastain, Handbook of X-ray Photoelectron Spectroscopy, Perkin-Elmer, USA, 1992, p. 261.

Structural properties of GaN grown on SiC substrates by hydride vapor phase epitaxy

Yu.V. Melnik, I.P. Nikitina *, A.E. Nikolaev, V.A. Dmitriev ¹

A.F. Ioffe Institute and Cree Research Eastern European Division, 26 Politehnicheskaya St, St. Petersburg, Russia

Abstract

Hydride vapor phase epitaxy (HVPE) was used for GaN deposition on SiC substrates without a buffer layer. The influence of substrate parameters (structural perfection, surface polarity, misorientation) on the structural properties of GaN layers was investigated. X-ray differential diffractometry (XRDD) and the triple crystal modification of the Bond method were used to study the structural properties. The X-ray mapping was done over a 30 mm diameter 6H-SiC substrate. It was shown, that the full width at half maximum (FWHM) of X-ray ω -scan rocking curves (RC) from GaN layers monotonically increases as the FWHM of the RC from the substrate increases. © 1997 Elsevier Science S.A.

Keywords: Epitaxy; Gallium nitrides; Substrates; Structural properties

1. Introduction

GaN is one of the most promising materials for application in blue and UV light emitting devices. One of the severest problems hindering progress in this field is the lack of a suitable substrate material for the growth of III-nitrides films. GaAs, SiC, ZnO, LiGaO, AlMgO and sapphire have all been used as substrates for the epitaxial growth of group III-nitrides.

The principal advantage of SiC substrates compared to sapphire substrates is the smaller lattice mismatch (3.5 versus 16%). High quality GaN films can be grown on SiC substrates by MOCVD or MBE [1,2], but in most cases the growth requires an AlN buffer, which restricts development of the vertical device configuration.

Recently, we reported a high-quality GaN grown on SiC substrates by hydride vapor phase epitaxy (HVPE) without a buffer layer [3]. In this study, we investigate the effect of substrate parameters on the surface morphology and crystal structure of GaN layers.

2. Experimental procedures

GaN epitaxial layers were grown using the HVPE growth system with a two-zone resistance furnace. In a horizontal open flow reactor, HCl was reacted with liquid Ga to form GaCl gas which was transported to the growth zone and reacted with NH₃ resulting in GaN deposition on the SiC substrate. Argon was used as an ambient gas. 6H-SiC and 4H-SiC 30 mm diameter wafers manufactured by Cree Research Inc. were used as substrates. Both on- and off-axis substrates were used. The GaN films were grown on both the silicon and carbon faces of the substrates. The growth temperature was usually kept at between 950 and 1050 °C and the GaN growth rate was controlled from 0.02 to 0.6 μm min⁻¹. The layer thickness ranged from 0.2 to 2 μm. The layers had a nonuniformity in thickness of less than 5% across the 30 mm-diameter SiC substrates.

3. Structural properties of GaN

The GaN film quality was found to be determined by a number of factors. They are: growth conditions and substrate properties, surface polarity, misorientation and perfection of crystal structure.

In contrast to MBE growth, in our study the quality of the films strongly depended on the SiC surface

* Corresponding author.

¹Current address: Howard University, 2300 Sixth Street, NW, Washington DC 20059, USA.

polarity [4]. The best GaN layers were grown on the on-axis (0001)Si face of SiC substrates. These layers had a smooth, mirror-like surface over the entire wafer and a high crystal quality (Fig. 1(a)). Growth on the C-face resulted in GaN with a poor crystalline quality and rough surface. This agrees with the report on GaN film growth by MOCVD [5].

The films grown on (0001)Si off-axis substrates had

a stepped surface (Fig. 1(b)). No detectable effect of substrate polytype was observed on GaN surface morphology and crystal quality. All GaN layers described below were grown on the (0001)Si face of 6H-SiC on-axis wafers.

The structural quality of GaN films was studied by X-ray diffractometry (XRD) using double- and triple crystal spectrometers. RC in (ω) and $(\omega, 2\theta)$ modes

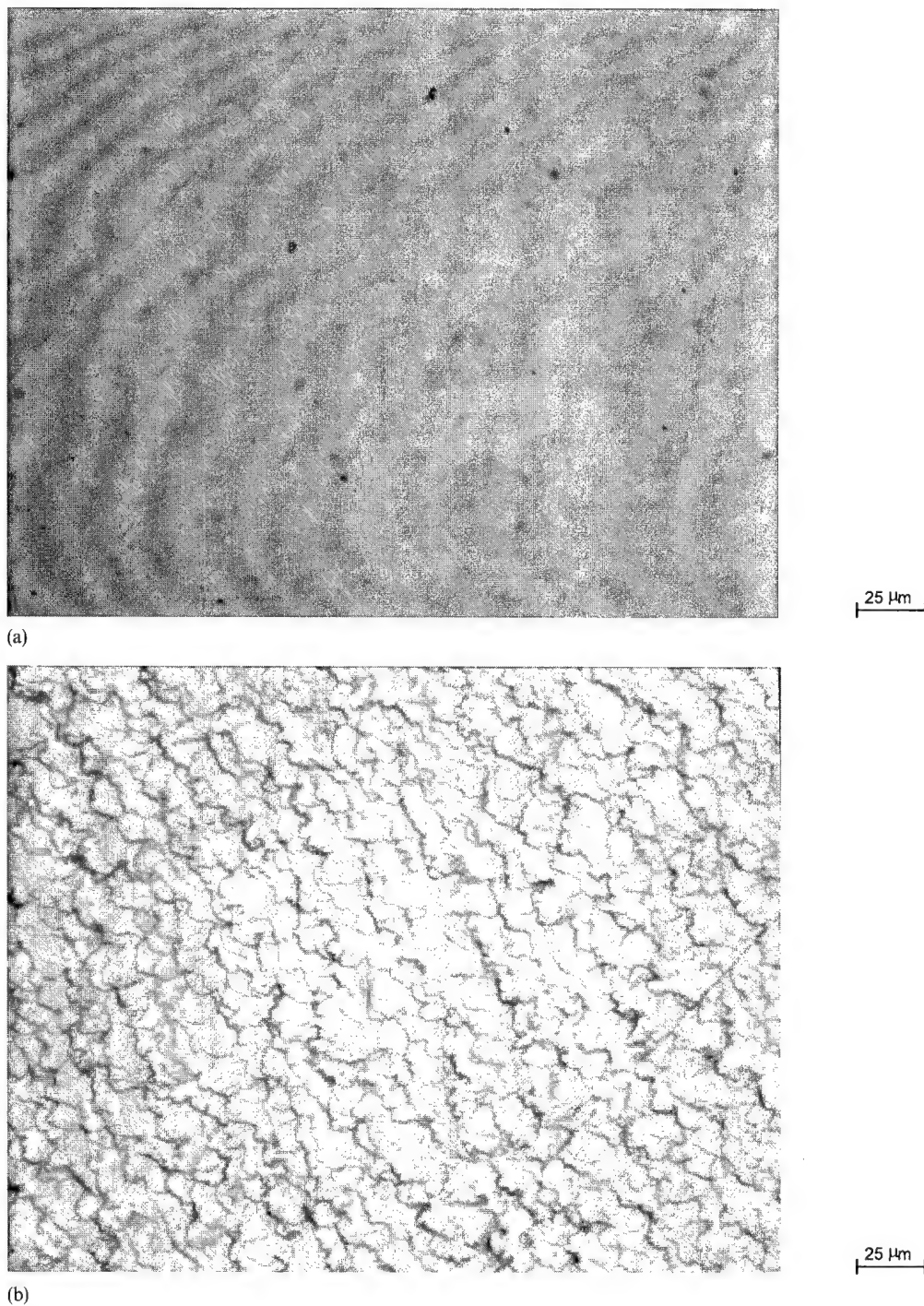


Fig. 1. SEM micrograph of surface morphology of GaN grown on on-axis (a), and 3.5° off-axis (b) SiC substrates.

Table 1
The FWHM values for RC and block sizes of GaN layers

Sample	(0002) CuK α		(0004) CuK α		$W(\omega, 2\theta) (0004) / W(\omega, 2\theta) (0002)$	Block size (\AA)
	$W(\omega)$ (arcsec)	$W(\omega, 2\theta)$ (arcsec)	$W(\omega)$ (arcsec)	$W(\omega, 2\theta)$ (arcsec)		
1	420	120	440	240	2.0	1400
2	220	90	300	180	2.0	1850
3	150	70	150	120	1.7	2400
4	70	34				4900

were measured on (0002), (0004) and asymmetrical (112̄4) CuK α reflections. The FWHM of double crystal RC(ω) for (0002) GaN reflection varied from 65 to 150 arcsec for the layers grown at the same growth conditions. The X-ray differential diffractometry (XRDD) method [1] was applied to evaluate a dislocation distribution in GaN layers. The results obtained are shown in Table 1. Analysis of these data allows us to conclude that the crystal structure of GaN layers may be described as an intermediate between a uniform dislocation distribution and a mosaic structure. Misorientation of mosaic blocks is responsible for RC(ω) broadening. It is accompanied by decreases in block sizes from 4900 to 1400 \AA , resulting in the broadening of RC($\omega, 2\theta$).

The X-ray mapping was done over a 30 mm diameter 6H-SiC substrate at 24 points (Fig. 2). The thickness of epilayer was 0.6 μm . It can be seen from Fig. 2 that the FWHM values at 7 points (shaded square) are considerably larger than those in the other 17. These are precisely the points where crystal quality of the substrate is poor. All these points are on the periphery of the substrate. It was found that the substrate has a domain structure in these 7 points (Fig. 3) and the layer does also. If the

misorientation angle between domains in the substrate is smaller than the FWHM of RC(ω) from every domain, an abnormal broadening of RC(ω) from the layer is observed (Fig. 3(a)). If the misorientation angle is comparable to FWHM or higher, separated peaks

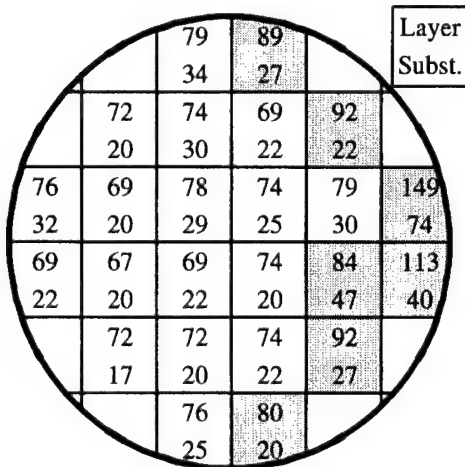


Fig. 2. Wafer map of FWHM RC(ω) from 30 mm diameter GaN/SiC-6H structure. The FWHM value for RC(ω) is shown at the top of every square and the FWHM value for RC(ω) measured from the SiC- substrate is shown at the bottom of every square.

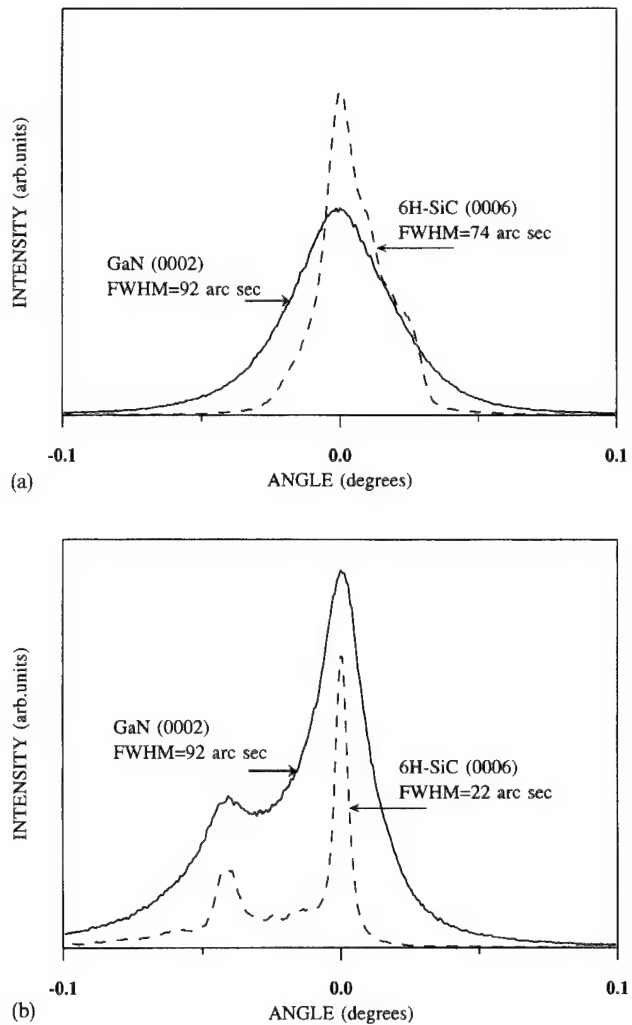


Fig. 3. Rocking curves of an ω -scan from GaN layer in areas, where the substrate has a domain structure: (a) misorientation angle between domains in the substrate is comparable with the FWHM RC(ω) from every domain; (b) misorientation angle is larger than the FWHM RC(ω) from every domain.

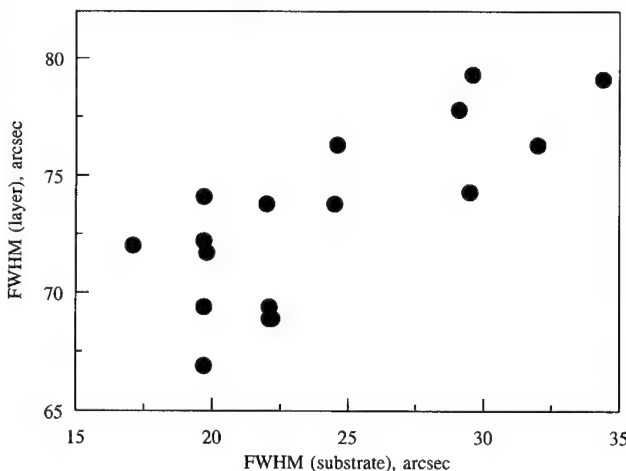


Fig. 4. The FWHM of $\text{RC}(\omega)$ for GaN layer versus the FWHM of $\text{RC}(\omega)$ for the SiC-6H substrate, excepting the shaded points on Fig. 2.

appear from the domains in the layer (Fig. 3(b)). For the 17 substrate points free from domains, the FWHM values measured from the GaN layer (Fig. 4) monotonically increase as the FWHM of RC from the substrate increases. We believe that the spread of experimental data relative to the linear dependence can be explained by different degrees of misorientation in GaN grains in the (0001) plane at the initial stage of the growth. Thus the structural quality of GaN grown on SiC by HVPE is defined dominantly by the structural quality of the substrate.

As shown above, high quality GaN layers on SiC may be grown using HVPE without a buffer layer. Nevertheless there are rather large residual thermal strains in these layers [6]. If the thickness of the layer exceeds $\approx 1.5 \mu\text{m}$ these strains cause cracks to form near GaN/SiC interface. As the thickness of the layer increases these cracks may propagate into the layer. To estimate normal (ϵ_{\perp}) and tangent (ϵ_{\parallel}) strains in the layers the triple crystal modification of the Bond method was used. Residual strains were calculated using the

following lattice constants for the bulk GaN crystal: $a = 3.1880 \text{ \AA}$, $c = 5.18561 \text{ \AA}$ [7]. The ϵ_{\perp} values ranged from -0.9×10^{-3} to -1.4×10^{-3} . The ϵ_{\parallel} values ranged from $+1.0 \times 10^{-3}$ to $+2.9 \times 10^{-3}$. Such high residual strains are primarily thermal in nature and result in the formation of cracks when the thickness of the layer exceeds $\approx 1.5 \mu\text{m}$.

4. Summary

The structural properties of GaN grown on SiC substrates by hydride vapor phase epitaxy without a buffer layer were investigated. It was shown that high quality GaN layers may be grown on the Si-face of a SiC substrate. GaN layers grown on on-axis SiC substrate had a smooth mirror-like surface. The FWHM of double-crystal $\text{RC}(\omega)$ for (0002) GaN reflection varied from 65 to 150 arcsec for the layers grown at the same growth conditions. The FWHM of RC from GaN layers monotonically increases as the FWHM of RC from the substrate increases. Thus the structural quality of GaN is mainly defined by the structural quality of SiC substrate.

References

- [1] I.P. Nikitina, V.A. Dmitriev, Inst. Phys. Conf. Series 141 (1994) 431–436.
- [2] M.E. Lin, B. Sverdlov, G.L. Zhou, H. Morcoc, Appl. Phys. Lett. 62 (1993) 3479–3481.
- [3] Yu.V. Melnik, I.P. Nikitina, A.S. Zubrilov, A.A. Sitnikova, V.A. Dmitriev, Inst. Phys. Conf. Series 142 (1996) 863–866.
- [4] S. Sinharoy, G. Augustine, L.B. Rowland, A.K. Agarwal, R.L. Messham, M.C. Driver, R.H. Hopkins, J. Vac. Sci. Technol. A 14 (3) (1996) 896–899.
- [5] T. Sasaki, T. Matsuoka, J. Appl. Phys. 64 (9) (1988) 4531–4535.
- [6] I.P. Nikitina, M.P. Sheglov, Yu.V. Melnik, K.G. Irvine, V.A. Dmitriev, Diamond Relat. Mater. (this issue)
- [7] M. Leszczynski, T. Suski, H. Teisseire, P. Perlin, I. Grzegory, J. Jun, S. Porowski, T.D. Moustakas, J. Appl. Phys. 76 (8) (1994) 4909–4911.

Contactless characterisation of 2D-electrons in GaN/AlGaN HFETs

H. Alause ^{a,*}, C. Skierbiszewski ^a, M. Dyakonov ^a, W. Knap ^a, M.L. Sadowski ^{b,1}, S. Huant ^b,
J. Young ^c, M. Asif Khan ^c, Q. Chen ^c

^a Groupe d'Etudes des Semiconducteurs, Université Montpellier 2 – C.N.R.S., UMR357, Place E. Bataillon, 34095 Montpellier, France

^b High Magnetic Field Laboratory, MPI-FKF and CNRS, BP 166, 38042 Grenoble, France

^c A.P.A. Optics Inc., Blaine, MN, USA

Abstract

We report on properties of 2D carriers in an GaN/AlGaN heterojunction investigated by an optical method. This method consists of a cyclotron resonance (CR) experiment where optical absorption is measured under fixed magnetic fields up to 13 T. We introduce a theoretical approach that allows to interpret cyclotron resonance due to the thin 2D layer on the sapphire substrate. The presented contactless characterisation method gives access to some very important parameters of the bidimensional gas such as the carrier concentration, their mobility and their effective mass. © 1997 Elsevier Science S.A.

Keywords: GaN/GaAlN heterostructures; Bidimensional electron gas; Cyclotron resonance; Contactless characterisation

1. Introduction

III–V nitride transistor technology is maturing fast [1]. AlGaN/GaN heterostructures based FETs are focusing interest for their potential high temperature applications [2]. Traditional characterisation methods by transport measurements require technological processes of the samples which can be difficult to perform on these kind of samples. Another problem of transport measurements can arise in the presence of a highly doped layer or substrate which can induce parallel conduction.

In this work, we present an optical contactless characterisation: a cyclotron resonance experiment on a two-dimensional electron gas confined at the GaN/AlGaN interface. The high quality of the sample allowed the observation of well resolved cyclotron resonance (CR) absorption peaks. In view of an accurate modellisation of these experimental data, a complete calculation of the ratio of the optical transmissions $T(B)/T(0)$ (under magnetic field and without magnetic field) was carried out including the exact resonant contribution of the

bidimensional electron gas and the effect of the multireflections in the substrate.

2. Experiment

A fast Fourier transform (FFT) spectrometer and a superconducting coil have been used. The magnetic field was kept constant and we recorded the spectra as a function of the far-infrared radiation frequency. All measurements were performed at 2 K, in a magnetic field up to 13 T. Examples of experimental results for different spectral resolutions and magnetic fields are shown in Fig. 1.

The spectra taken with 0.5 cm^{-1} resolution show oscillations mainly due to interferences in the sapphire substrate (Fig. 1, left). High resolution increases the coherence length of the FTIR beam and allows coherent multireflections in the substrate as schematised on Fig. 2. The oscillations are averaged for lower resolution (3 cm^{-1}) and the CR minimum that clearly moves to higher energies with an increasing magnetic field can be observed (Fig. 1, right).

The absorption peaks at different magnetic fields show a non-Lorentzian behaviour that must be fitted by an accurate function. Parameters of the fit are the carrier concentration N_s and mobility m . Effective mass can be

* Corresponding author. Fax: 33 67 14 3760;
e-mail: alause@ges.univ-montp2.fr

¹Institute of Experimental Physics, Warsaw University, Hoza 69, 0-681 Warsaw, Poland.

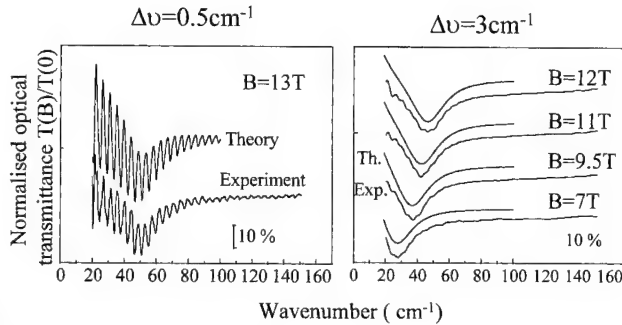


Fig. 1. Experimental cyclotron resonance measurements under different magnetic fields and at 2 different resolutions Δn . Theoretical transmissions are represented for each measurement.

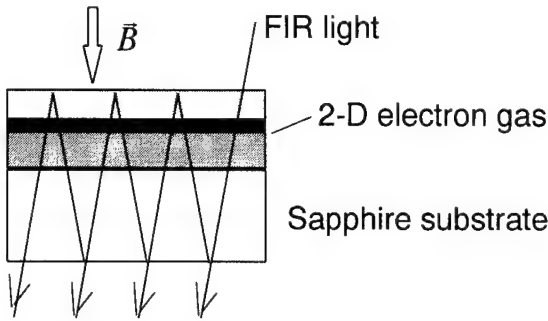


Fig. 2. The structure of the sample leads to optical multireflections in the substrate and generates an interference pattern.

evaluated as well [3]. We found that in the range up to 13 T in studied HFETs, μ and N_s are constant with magnetic field.

3. Interpretation of the results

In order to interpret the CR data, one has normally to deal with a complete calculation of the magneto-optical response of the multilayer system. In our case, this standard approach can be drastically simplified. This is because, in the experimental range 20–200 cm^{-1} , all phonon contributions can be safely neglected and all (complex) values of the refractive index reduce to the same average dielectric constant ($\epsilon \approx 9.5$). The only resonant contribution comes from the 2D layer, whose magneto optical properties are described by the dynamic conductivity

$$\sigma_{\pm} = \frac{1}{\epsilon_0 c} \frac{N_s e^2 \tau_c}{m_c} \frac{1}{1 - i \tau_c (\omega \pm \omega_c)}, \quad (1)$$

where $\omega_c = eB/m_c$ is the cyclotron frequency, m_c the effective mass, N_s the surface carrier density, τ_c the scattering time and \pm corresponds to two light polarisations. As a result, we describe the transmission of our sample by a simple model which considers only a purely two-dimensional electron gas located between the

vacuum and a dispersionless polar medium with average refractive index $n \approx 3.08$. In this case

$$T_{\pm}(B) = \frac{16n^2}{|(n+1)(n+1+\sigma_{\pm}) \exp(-ikd) - (n-1)(n-1-\sigma_{\pm}) \exp(ikd)|^2}, \quad (2)$$

and averaged over oscillations

$$T_{\pm}(B) = \frac{16n^2}{(n+1)^2 |n+1+\sigma_{\pm}|^2 - (n-1)^2 |n-1-\sigma_{\pm}|^2}, \quad (3)$$

where n is the refractive index and k is the wave vector. The transmission of the light, with equal amount of left and right polarisations, is $T = (T_+ + T_-)/2$.

In the case of a bidimensional electron gas in GaN on a sapphire substrate, the measured value of $T(B)/T(0)$ cannot be correctly fitted by a simple Lorentzian line [4]. This is because $\omega_c \tau$ is comparable to 1 and the absorption line is non-Lorentzian (Fig. 3, top). Moreover, the free carrier absorption at $B=0$ in the 2D electron gas is important and leads to a highly asymmetrical lineshape for $T(B)/T(0)$. This clearly appears on the calculated and measured absorption line (Fig. 3, bottom).

4. Discussion

Results of fitting procedure of Eqs. (2) and (3) to experimental data are shown in Fig. 1. At higher resolution, the effect of multireflection in the substrate is very important and is well-reproduced by Eq. (2). The calculations satisfactorily reproduce both the interference and the asymmetry of the CR absorption line. The fitting parameters are ω_c , μ and N_s . We want to stress

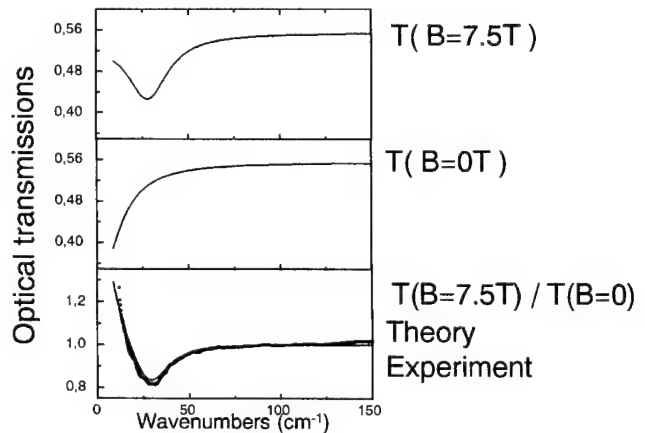


Fig. 3. Calculations steps of $T(B)/T(0)$. On top, optical transmission of the sample under magnetic field; in the middle, transmission at 0 magnetic field; and at the bottom, ratio of the two precedent curves compared to experimental results.

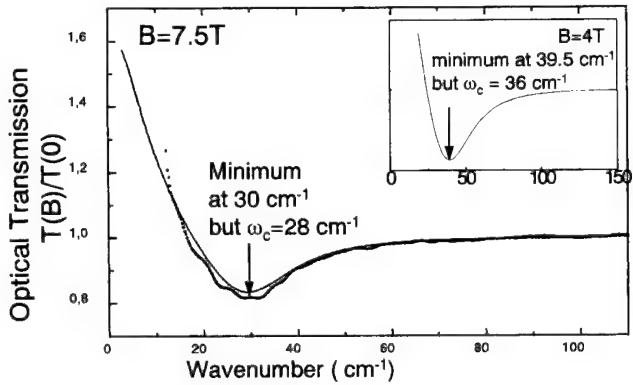


Fig. 4. Experimental optical transmission superimposed with its theoretical fit at $B=7.5$ T and (inset) at $B=4$ T.

that because the line is non-Lorentzian, the values of ω_c , read directly from the CR minima and determined by the fit are slightly different. At $B=7.5$ T, the line minimum is 6% shifted from the value of ω_c obtained by the accurate fitting, at low magnetic fields the effect is even more important and the value of ω_c at 4 T is 10% lower than the minimum in the transmission spectra (see Fig. 4). The exact calculation allows to get accurate determination of carrier density ($N_s=4.0\times 10^{12}\text{ cm}^{-2}$), carrier mobility ($\mu=3900\text{ cm}^2\text{ V}^{-1}\text{ s}^{-1}$) and the cyclotron mass ($m^*=0.24m_0$).

5. Conclusion

We showed that the cyclotron absorption peak can be accurately interpreted even if the absorption line is strongly non-Lorentzian and is perturbed by multireflections in the sapphire substrate.

Carrier concentration, mobility and effective mass, can be determined thanks to an accurate fit of the experimentally observed cyclotron transmission line. This way we presented a valuable contactless characterisation method, especially when transport measurements cannot be performed because of strong parallel conduction due to a short circuiting highly doped GaN buffer for example.

References

- [1] See, for instance, The Proceedings of the First Topical Workshop on Gallium Nitride (TWN'95), Nagoya, Japan.
- [2] M. Asif Khan, J.N. Kuznia, J.M. Van Hove, N. Pan, J. Carter, Appl. Phys. Lett. 60 (1992) 3027; see also, M. Asif Khan, J.N. Kuznia, J.M. Van Hove, D.T. Olson, S. Krishnankutty, R.M. Kolbas, Appl. Phys. Lett. 58 (1991) 526.
- [3] W. Knap, H. Alause, J.M. Bluet, J. Camassel, J. Young, M. Asif Khan, Q. Chen, S. Huant, M. Shur, Solid State Commun. 99 (1996) 195.
- [4] U. Merkt, Festkörperprobleme, Advances in Solid State Physics (1987) 27.



ELSEVIER

Identification of the cubic and hexagonal polytypes of GaN with X-ray absorption measurements

M. Katsikini ^{a,b}, E.C. Paloura ^{a,*}, T.S. Cheng ^c, C.T. Foxon ^c

^a Aristotle University of Thessaloniki, Department of Physics, GR-54006 Thessaloniki, Greece

^b Hahn-Meitner Institute (A.S), Glienicker Str. 100, D-14109 Berlin, Germany

^c University of Nottingham, Department of Physics, Nottingham, NG7 2RD, UK

Abstract

Angle-resolved near-edge X-ray absorption spectroscopy (NEXAFS) at the N-K-edge is used for the study of cubic and hexagonal thin GaN films grown on GaP. It is demonstrated that the NEXAFS spectra depend on the crystal symmetry, and they can be used as a fingerprint of the symmetry of the examined crystal. Deviations from the cubic or hexagonal symmetries towards a mixed-phase crystal are clearly detectable and can be quantified. Finally, from the characteristic angular dependence of the NEXAFS resonance intensities in the hexagonal GaN, the directions of maximum charge density are determined. © 1997 Elsevier Science S.A.

Keywords: GaN; Cubic polytypes; Hexagonal polytypes; X-Ray absorption

1. Introduction

GaN has recently attracted a lot of interest because it finds applications in devices that operate in the blue-UV region [1,2]. GaN crystallises in either the stable wurtzite (α) or the metastable zinc-blende (β) phase. The successful stabilisation of the β -GaN phase depends on a number of factors, including the type and crystal orientation of the substrate and the growth conditions, whereas growth often results in mixed-phase crystals [3,4].

Near-edge X-ray absorption fine structure (NEXAFS) spectroscopy is a non-destructive characterisation technique that gives information about the energies of the antibonding molecular orbitals or the unfilled states in the conduction band of crystalline solids, i.e. a NEXAFS spectrum is directly proportional to the partial DOS in the conduction band [5]. The NEXAFS spectra have a characteristic structure that depends on the crystal group symmetry and the local symmetry around the absorbing atom [6,7]. Here, we propose the application of NEXAFS spectroscopy for the determination of the directions of maximum electron charge density (MECD) and the fractions of α - and β -phases present in mixed-phase GaN.

2. Sample preparation and experimental conditions

The samples were grown on (001) n^+ -GaP by molecular beam epitaxy [4]. The α - and β -GaN polytypes (MG84 and MG108, respectively) were stabilised by the control of an impinging arsenic flux on the growth surface, whereas MG89 is a mixed-phase sample. The angle-dependent NEXAFS spectra were recorded at the N-K-edge, in the energy range 390–450 eV, using light from the SX-700-I plane grating monochromator at the electron storage ring BESSY in Berlin. The spectra reported here were recorded in the fluorescence yield mode using a high-purity Ge detector. Details on the experimental set-up have been reported previously [6]. The measurements were performed for different angles of incidence ϑ ($10^\circ < \vartheta < 90^\circ$ with a step of 10°), where ϑ is defined by the incident beam and the sample surface, as shown in the inset of Fig. 1.

3. Results and discussion

The NEXAFS spectra were fitted using a step function to simulate transitions to the continuum and a number of Gaussians to simulate transitions to bound states. Prior to fitting, the spectra were subjected to linear

* Corresponding author.

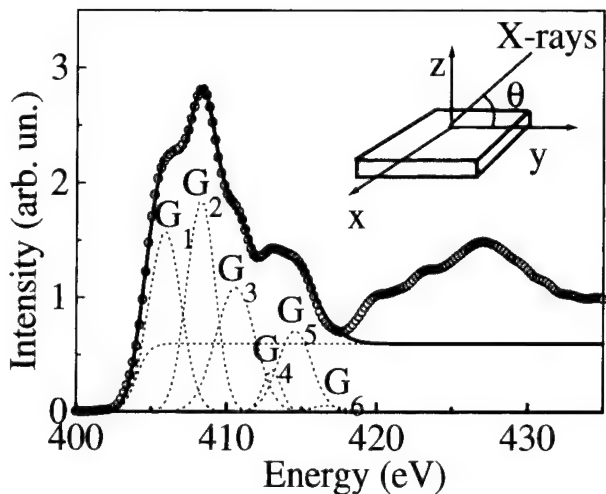


Fig. 1. Fitting of an N-K-edge NEXAFS spectrum recorded from the α -GaN sample at $\theta=70^\circ$. θ is measured with respect to the sample surface, as indicated in the inset.

background subtraction and normalisation to the atomic limit. The energy positions, ΔE_i , of the various resonances are measured relative to the absorption edge, which is defined as the inflection point of the step function. The fitting of a NEXAFS spectrum from the hexagonal sample MG84, recorded at $\theta=70^\circ$, is shown in Fig. 1. The error in the determination of the areas under the peaks can be found using the Thomas-Reihe-Kuhn sum rule [8], according to which, the total oscillator strength remains constant and does not depend on the angle of incidence. In the present case, the error is of the order of 2.5%.

For cubic symmetry and for the case of a 1s initial state, the allowed transitions are $1a_1 \rightarrow t_2^*$, where t_2 belongs to a three-dimensional irreducible representation (T_2) of the group T_d , and are observed with the same intensity at different angles of incidence. In contrast to that, the NEXAFS spectra of a hexagonal sample (C_{6v}) show angular dependence. The allowed dipole transitions that occur in a C_{6v} material are $1a_1 \rightarrow a_1^*$ and $1a_1 \rightarrow e_1^*$, which are strongest for grazing and normal incidence, respectively. In the $1a_1 \rightarrow a_1^*$ transition, the final state results from mixing of s and p_z atomic orbitals, whereas in $1a_1 \rightarrow e_1^*$, the final state can result from p_x and p_y atomic orbitals [9].

From the fitting of the spectra of the cubic sample, it was found that the energy positions ΔE_i , the FWHM and the area under the resonances are, within the experimental error, independent of θ , as theoretically expected. Contrary to the behaviour of the cubic sample, the NEXAFS spectra of the hexagonal α -GaN sample have a strong angular dependence as shown in Fig. 2, and the areas under the peaks have a linear dependence on $\cos^2 \theta$. The reduced intensity of a NEXAFS resonance is defined as the area under the resonance normalised to that corresponding to the magic angle $\theta=54.7^\circ$. The

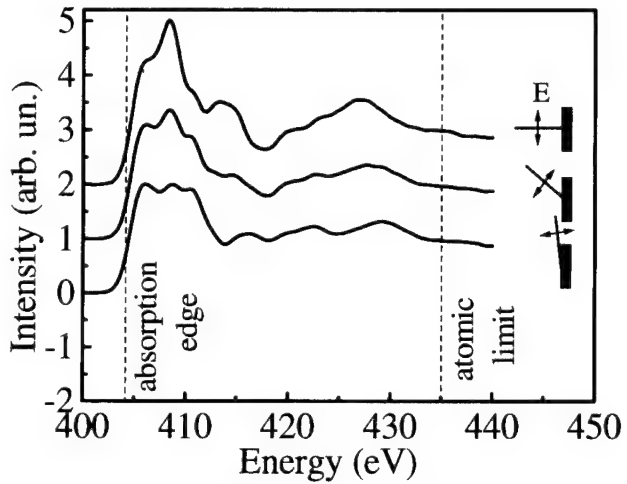


Fig. 2. The angular dependence of the NEXAFS spectra shown for normal incidence ($\theta=90^\circ$, top curve), grazing incidence ($\theta=20^\circ$, bottom curve) and the angle of $\theta=50^\circ$ (middle curve). The positions of the absorption edge and the atomic limit are shown in dashed lines.

magic angle is the characteristic angle for a sample with hexagonal symmetry for which the NEXAFS spectra are independent of the angle between the final state vector or plane molecular orbital and the normal to the sample surface.

From the angular dependence of the reduced intensities of the NEXAFS resonances, the directions of maximum electron charge density (MECD) with respect to the surface normal can be determined. For the $1a_1 \rightarrow e_1^*$ transition, the reduced intensity I of the transition is given by:

$$I = 1.6[1 - 0.5 \sin^2 \gamma - (1 - 1.5 \sin^2 \gamma) \cos^2 \theta], \quad (1)$$

where γ is the angle of the normal to the plane orbital to the surface normal. For the $1a_1 \rightarrow a_1^*$, the reduced intensity I' is given by:

$$I' = 1.33 \sin^2 \alpha + (2.67 - 4 \sin^2 \alpha) \cos^2 \theta, \quad (2)$$

where α is the angle of the vector orbital with the sample surface. Using Eqs. (1) and (2), the directions of MECD can be determined with an error of about $\pm 5^\circ$. The transitions labelled G_4 and G_6 correspond to plane orbitals parallel to the surface ($\gamma=0^\circ$) and vector orbitals normal to the surface ($\alpha=0^\circ$), respectively. G_3 corresponds to vector orbitals, which are at an angle of 53.4° with the c -axis. The transition G_1 is independent of the angle of incidence and therefore corresponds to angle equal to 54.7° , which is the magic angle. Finally, the Gaussians G_2 and G_5 give angles with a mean average of about 37° .

Besides the information resulting from the intensity of the transitions, further information can be extracted about the crystal structure from the values of ΔE_i . Our measurements show that for the pure cubic and hexagonal samples, the energy positions of the resonances as

Table 1

Energy positions of the NEXAFS resonances for the pure cubic and hexagonal GaN films

Sample	ΔE_1 (eV)	ΔE_2 (eV)	ΔE_3 (eV)	ΔE_4 (eV)	ΔE_5 (eV)	ΔE_6 (eV)
β -GaN	1.94	4.79	7.23	8.71	11.39	—
α -GaN	1.91	4.26	6.54	9.00	10.52	12.70

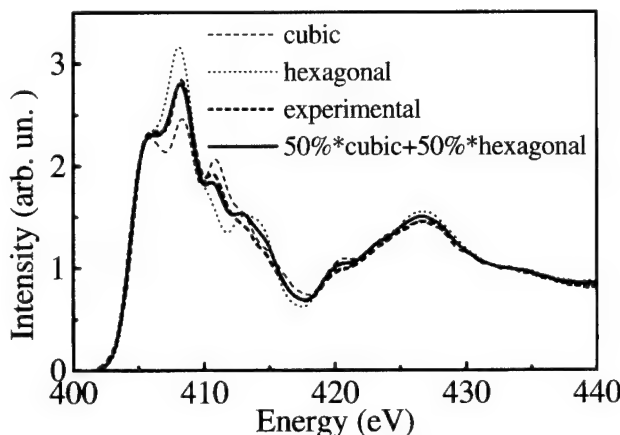


Fig. 3. NEXAFS spectra from the mixed, the cubic and the hexagonal samples and the calculated spectrum assuming 50% cubic and 50% hexagonal fractions, respectively.

well as their FWHM do not change with the angle of incidence. Therefore, the angular resolved NEXAFS spectra can be used as a fingerprint of the structure of an unknown sample. The measured values of the ΔE_i are listed in Table 1. Angular dependence of the FWHM and ΔE_i of the Gaussians is an indication of coexistence of hexagonal and cubic phases. Given the constancy of the ΔE_i for the pure cubic and hexagonal structure, it is proposed that the NEXAFS spectra of a mixed phase sample can be approximated as a weighted average of the spectra from the pure cubic and hexagonal samples recorded at the same angle of incidence. Following this procedure, the NEXAFS spectra from the mixed phase sample MG89 can be reproduced by averaging the NEXAFS spectra from pure cubic and hexagonal samples weighted by 50% and 50%, respectively. The resulting spectrum is shown in Fig. 3 (continuous line) along with the recorded spectra from the mixed (thick dashed line), the cubic (dashed line) and hexagonal (dotted line) samples. As shown in Fig. 3, this simple model for the NEXAFS structure of a mixed crystal predicts quite accurately the experimental spectrum.

4. Conclusions

It is demonstrated that the N-K-edge NEXAFS spectra, which probe the nitrogen p partial density of

unfilled states, can be used as a fingerprint of the cubic or hexagonal symmetry in GaN thin films. Deviations from the α - or β -GaN structures towards a mixed phase crystal are clearly detectable since they lead to angular dependent shifts of the NEXAFS resonances. The NEXAFS spectra from a mixed-phase crystal can be simulated using a weighted average of the spectra from the pure α - and β -GaN samples, and thus the fractions of the coexisting α - and β -phases can be determined. It should be pointed out that NEXAFS is a non-destructive technique and can be applied to the as-received samples. Therefore, the measurements are free of artefacts induced by damage during surface cleaning or sample preparation. Finally, from the θ -dependence of the resonance intensities in the spectra of a hexagonal sample, the directions of MECD are determined, and they are found to deviate from the directions of the bond angles. This result is in agreement with the calculations of Miwa et al., according to which, the directions of MECD are within 30° on either side of the bond axis [10].

Acknowledgement

This work was realised with financial support from the EC-HCM (CHGE-CT93-0027) program.

References

- [1] S. Strite, H. Morkoc, J. Vac. Sci. Technol. B10 (1992) 1237.
- [2] S. Nakamura, T. Mukai, M. Senoh, Appl. Phys. Lett. 64 (1994) 1687.
- [3] T. Lei, M. Fanciulli, R.J. Molnar, T.D. Moustakas, R.J. Graham, J. Scanlon, Appl. Phys. Lett. 59 (1991) 944.
- [4] T.S. Cheng, L.C. Jenkins, S.E. Hooper, C.T. Foxon, J.W. Orton, D.E. Lacklison, Appl. Phys. Lett. 66 (1995) 1509.
- [5] J.C. Fuggle, J.E. Inglesfield, Unoccupied Electrical States: Fundamentals for XANES, EELS, IPS and BLS, Springer, Berlin, 1992.
- [6] M. Katsikini, E.C. Paloura, T.D. Moustakas, Appl. Phys. Lett. 69 (1996) 4206.
- [7] J. Stöhr, NEXAFS Spectroscopy, Springer, Berlin, 1992.
- [8] J. Berkowitz, in: Photoabsorption, Photoionization and Photo-electron Spectroscopy, Academic Press, New York, 1979, p. 56.
- [9] F.A. Cotton, Chemical Applications of Group Theory, Wiley-Interscience, New York, 1971.
- [10] K. Miwa, A. Fukumoto, Phys. Rev. B48 (1993) 7897.

Colour sensing applications of hydrogenated amorphous silicon carbide

Gerhard Müller

Daimler Benz AG, Forschung und Technik, Postfach 80 04 65, D-81663 München, Germany

Abstract

Varying the stoichiometric parameter x in hydrogenated amorphous silicon carbide alloys ($a\text{-Si}_{1-x}\text{C}_x\text{:H}$) allows the optical bandgap to be shifted continuously throughout the entire visible range. Throughout this range, all bandgaps are direct, i.e. efficient optical absorption takes place within thin films with thicknesses of the order of 1 μm . It is shown how the optoelectronic properties of $a\text{-Si}_{1-x}\text{C}_x\text{:H}$ films and devices on glass substrates can be used in combination with crystalline silicon photosensors to construct different kinds of colour sensing devices. Considering the low-temperature-deposition potential of these alloys, our results suggest that $a\text{-Si}_{1-x}\text{C}_x\text{:H}$ films are likely to play an important role within emerging thin-film-on-ASIC (TFA) technologies. © 1997 Elsevier Science S.A.

Keywords: Optoelectronics; Colour sensors; Micro analysis systems; Amorphous semi-conductors

1. Introduction

During the past decade the technology of hydrogenated amorphous silicon ($a\text{-Si:H}$) has evolved to maturity. To date several kinds of large-area optoelectronic devices have become commercially available which derive from this technology [1]. In the early days of the $a\text{-Si:H}$ field, the applied interest into this material was largely driven by the desire to develop cheap and efficient thin-film solar cells on glass substrates [2]. This particular field of large-area optoelectronics also benefitted considerably from the development of the higher-bandgap amorphous silicon carbide ($a\text{-Si}_{1-x}\text{C}_x\text{:H}$) alloy system [3]. These latter films allowed doped and highly transparent entrance windows to single- and multi-junction solar cells to be made and significant improvements in the solar cell conversion efficiency to be obtained [1–3]. In the present paper we review some of our previous work on $a\text{-Si}_{1-x}\text{C}_x\text{:H}$ alloys [4–9] focusing on colour sensing devices. In the following the preparation and properties of such devices are discussed and some potential applications are pointed out.

2. Preparation and material properties of $a\text{-Si}_{1-x}\text{C}_x\text{:H}$ alloys

Like silicon oxide and silicon nitride, amorphous silicon carbide films can be plasma-deposited from

$\text{SiH}_4/\text{CH}_4/\text{H}_2$ mixtures. In addition to CH_4 also a large variety of alternative carbon precursors have been investigated. Substrate temperatures during deposition usually range between 200 and 400 °C which allows $a\text{-Si}_{1-x}\text{C}_x\text{:H}$ films to be deposited either onto glass substrates or pre-processed silicon wafers.

With respect to their crystalline (c-) counterparts the structural properties of amorphous (a-) SiC films differ in three important respects:

- (1) the amorphous SiC films contain significant concentrations of bonded hydrogen ($C_{\text{H}} > 10\%$). The films are therefore commonly denoted by $a\text{-Si}_{1-x}\text{C}_x\text{:H}$;
- (2) the stoichiometric parameter x can be continuously varied in the range $0 < x < 1$;
- (3) the $a\text{-SiC:H}$ matrix consists of a random arrangement of Si and C atoms, i.e. the Si-C double-layer structure characteristic of the c-SiC lattice is not preserved.

These structural properties give rise to a number of material properties which can be exploited to arrive at different kinds of device applications [4–9]:

- (1) the optical bandgap continuously increases from about 1.7 to approximately 3.4 eV as the stoichiometry of the $a\text{-Si}_{1-x}\text{C}_x\text{:H}$ films is varied from hydrogenated amorphous silicon ($a\text{-Si:H}$) via $a\text{-SiC:H}$ towards diamond-like carbon ($a\text{-C:H}$);
- (2) due to the relaxed long-range order all bandgaps

are quasi-direct, i.e. efficient optical absorption takes place within thin films with thicknesses of the order of 1 μm ;

- (3) silicon-rich alloys ($x < 0.2$) exhibit an efficient photoconductivity and can be doped to exhibit p or n-type conduction;
- (4) a-SiC:H films with Si/C ratios close to stoichiometry ($x \approx 0.5$) exhibit an extreme inertness in all kinds of wet chemical silicon etches such as KOH and HF.

In the context of the present paper the optical and optoelectronic properties (1 to 3) are of primary concern. Property (4), on the other hand, makes the wider-bandgap alloys extremely interesting as etch-resistant passivation layers. For this latter reason, a-SiC:H layers are also likely to play an increasing or even enabling role within the developing field of silicon micromachining [10].

3. Colour sensing devices

For colour sensing, a-Si_{1-x}C_x:H films or devices are deposited on glass substrates and placed in front of crystalline silicon photodiodes or photodiode arrays (hybrid approach). Alternatively, they can be directly

deposited on top of a silicon wafer containing integrated photodiodes (TFA-approach; TFA = thin-film-on ASIC). In this manner both actively and passively filtering devices can be made [7,8].

3.1. Actively filtering devices

As an example of an actively filtering device, consider the arrangement shown in Fig. 1(a). In this device a short-wavelength-sensitive a-Si:H ($x=0$) photodiode with a transparent rear contact is mounted on top of a c-Si photodiode. In this device short-wavelength light is almost completely absorbed within the a-Si:H photodiode whereas longer-wavelength light is able to penetrate into the underlying c-Si one. As can be seen from Fig. 1(b), the dividing line for the a-Si:H and c-Si sensitivities is in the range of 700 nm, i.e. in a wavelength range roughly corresponding to the a-Si:H bandgap. Light sources with a relatively broad spectrum, therefore, can be distinguished on the basis of the relative amounts of light absorbed within the a-Si:H and c-Si photodiodes. As a consequence, each light source can be represented by a two-component signal vector, or, as shown in Fig. 1(c), by the ratio of the c-Si and a-Si:H output signals.

A particularly interesting feature of such photodiode

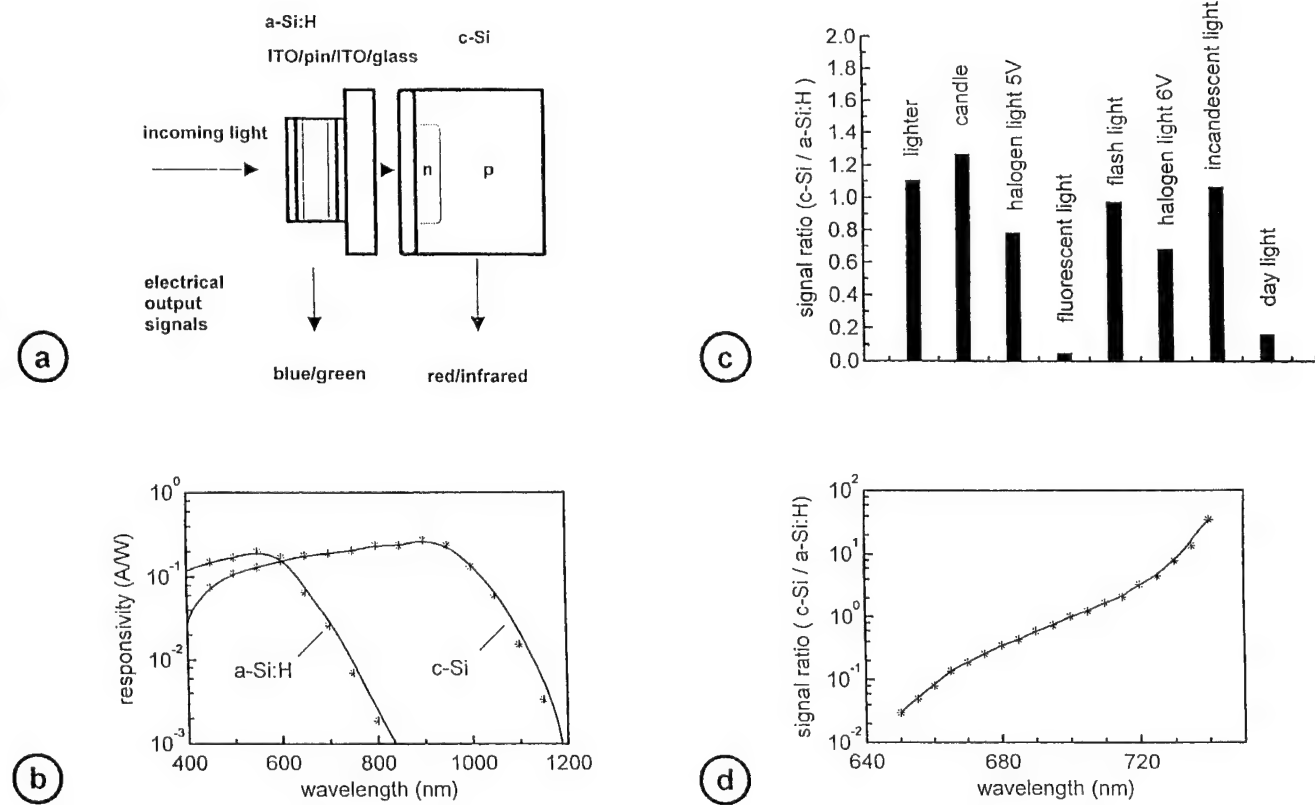


Fig. 1. a-Si:H/c-Si colour sensor stacks: (a) geometric arrangement; (b) spectral response of the a-Si:H and c-Si photodiodes; (c) classification of light sources in the signal plane; (d) monochromatic resolution power of the a-Si:H/c-Si photodiode stack.

stacks is that their monochromatic resolution is limited by the exponential tailing of the a-Si:H valence and conduction bands which is a general property of amorphous semiconductor materials. As shown in Fig. 1(d) this tailing leads to a wavelength interval, about 100 nm wide, in which the ratio of the c-Si and a-Si:H output signals varies exponentially as the wavelength of a monochromatic light source is scanned from short to increasingly longer wavelengths. Quantitatively, we estimate the monochromatic resolution $\Delta\lambda$ in this wavelength interval to be somewhere in the range between 0.1 to 1 nm. Experimentally, we find that our sensor can easily distinguish arterial from venous blood, for instance, or different brands of red wine, i.e. colour differences hardly visible or even invisible to the human eye [7].

Varying the thickness of the a-Si:H photodiodes, the wavelength interval of high monochromatic resolution can be shifted to some extent. Larger changes are possible by shifting the a-Si:H bandgap towards larger or smaller photon energies by means of alloying with carbon or germanium, respectively. In this context it has to be noted that the density of recombination centres in the amorphous semiconductor films is relatively low in the a-Si:H case whereas it increases sharply as the optical gap is shifted towards higher or lower photon energies [3]. Due to this effect highly performing thin-film photodiodes are limited to a bandgap range extending from about 1.5 up to 1.9 eV. Sticking to the principle of active filtering, the thin-film photodiodes can be replaced by thin-film photoconductors which only rely on majority carrier transport. In this latter case, a somewhat larger bandgap range from about 1.2 up to 2.1 eV is accessible to the actively filtering mode.

3.2. Passively filtering devices

In the examples presented above the amorphous semiconductor materials served the double purpose of actively generating an electrical output signal and of passively filtering the light entering the underlying c-Si photodiodes. Considerably more freedom of design is possible in case the amorphous semiconductor films are used as passive optical filters for c-Si photodiodes and photodiode arrays only. A possible arrangement for a passively filtering device is shown in Fig. 2. In this latter case the entire bandgap range accessible within the a-Si_{1-x}C_x:H alloy system can be used to give a pair of c-Si photodiodes with different handicaps with respect to their short-wavelength photoresponse. With E_g varying from 1.7 eV ($x=0$) to 3.4 eV ($x=1$), the region of high monochromatic resolution can be scanned through the entire visible range. With devices of this latter kind, colour sensors with a monochromatic resolution in the blue and ultraviolet region of the visible spectrum have been realised [8].

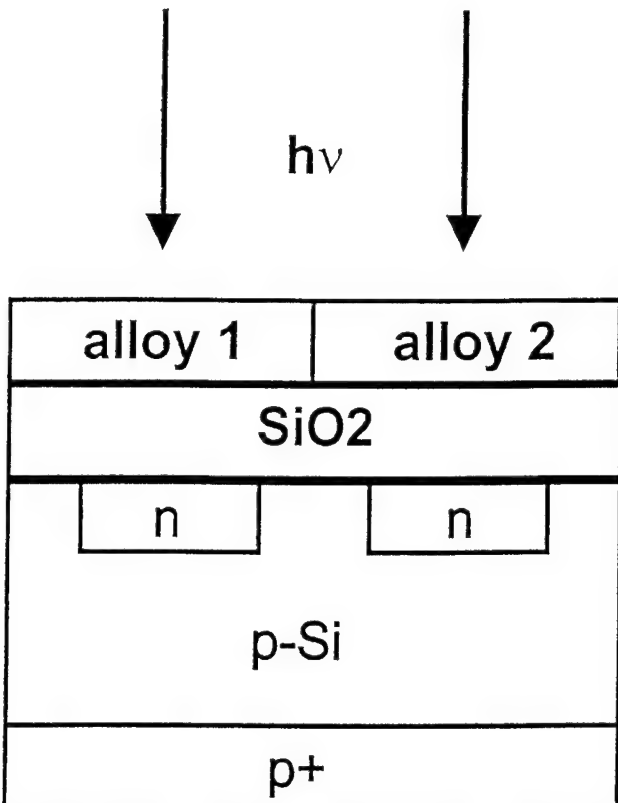


Fig. 2. Cross section through a passively filtering device using two a-Si_{1-x}C_x:H filters with different values of x on both pixel elements.

From the above it is clear that a colour sensitivity can be reached by replacing conventional photodiodes with a scalar grey-scale output by devices with a higher-dimensional vectorial output. The examples described above have shown that surprising results can already be obtained by setting up devices generating simple two-component outputs. A possible approach to obtaining higher-dimensional output signals is depositing laterally graded a-Si_{1-x}C_x:H alloy films. The method of growing such films is illustrated in Fig. 3. As shown there, a narrow slit diaphragm is slowly moved across a glass or a semiconductor substrate during deposition by means of a stepping motor. During this motion the relative abundance of the silicon and carbon bearing precursor gases is varied so that a lateral grading of the optical bandgap is obtained.

A graded bandgap filter deposited in this way is shown in Fig. 4(a). In this case the substrate has been a piece of Corning 7059 glass. For colour discrimination purposes we have mounted such filters in front of a commercial CCD line sensor. Upon illumination with defocused light, different spatial intensity patterns are developed by the CCD line sensor with the form of the patterns being characteristic of the spectral content of the light sources. In order to give an idea of the spectral discrimination power of such devices we have illuminated our sensors with narrow-band quasi-monochro-

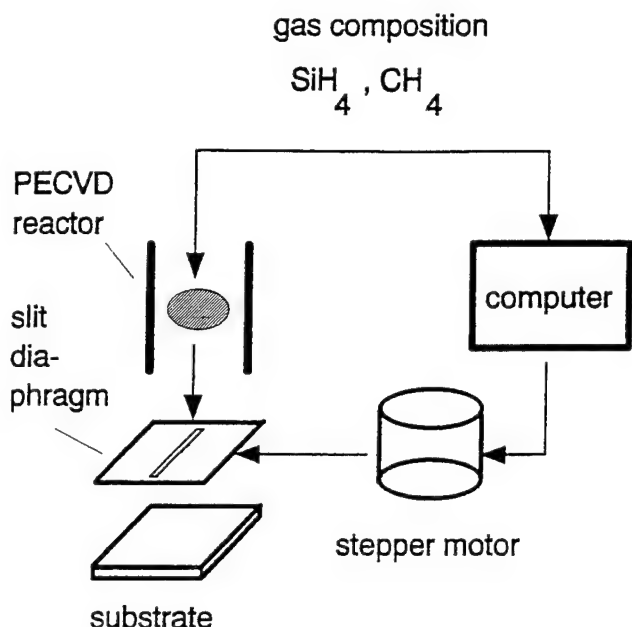


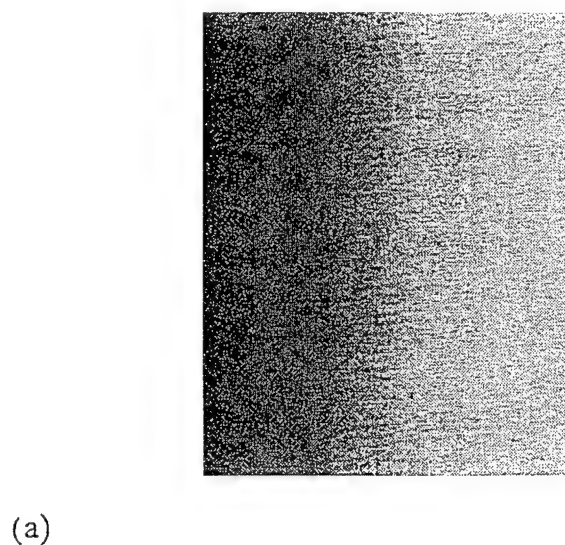
Fig. 3. Method of growing laterally graded bandgap filters.

matic light sources. Fig. 4(b) shows that short-wavelength light is only transmitted through the higher-bandgap parts of the filters. Longer-wavelength light, on the other hand, is seen to penetrate material of increasingly smaller bandgap. From this latter figure it is easily seen that wavelength differences of several nm are easily distinguishable.

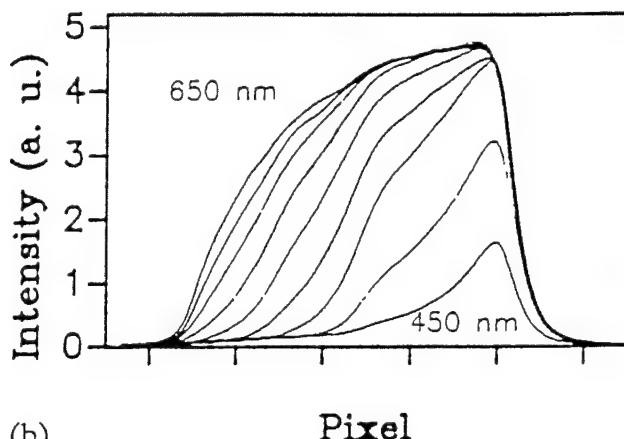
More complex spectra result in spatial intensity patterns different from the ones shown in Fig. 4(b). Fig. 5(a) shows a pattern produced by superimposing two quasi-monochromatic light sources ($\Delta\lambda=25 \text{ nm}$) on the surface of the colour sensing device. The superposition of the light sources is seen to result in some additional structure in the spatial intensity pattern. This additional structure is revealed more clearly from the differentiated pattern shown in Fig. 5(b). There, two lines clearly show up, corresponding to sources centred at $\lambda=500$ and 650 nm . Although such a differentiation technique can give only a rough idea about the optical input spectra [7], this method does not give precise results due to the neglect of interference effects within the graded-bandgap filters and/or effects of non-uniform illumination. Different light sources, however, can be distinguished with considerable resolution by applying pattern recognition techniques to the spatial intensity patterns produced at the output of the CCD line sensor. Such techniques are commonly used to analyse output data arising from gas sensor arrays.

3.3. Colour sensors versus spectrometers

The above results have shown that interesting optoelectronic applications are possible using a- $\text{Si}_{1-x}\text{C}_x:\text{H}$



(a)



(b)

Fig. 4. (a) Graded-bandgap filter produced by varying the stoichiometric parameter x along one of the substrate dimensions. Along this dimension the optical bandgap increases continuously from 1.7 to 3.4 eV; (b) spatial intensity patterns obtained by illuminating the graded-bandgap filter with defocussed monochromatic light. The monochromatic wavelength was increased from 450 to 650 nm in 25 nm steps.

films. Such sensors cannot replace conventional spectrometers with diffraction gratings which directly yield physically interpretable information about the spectral content of light sources. The advantage of our devices, however, is that very small and rugged devices can be built. As a consequence, they are much more easily integrated into complex measurement systems than conventional spectrometers whose size is limited by the lengths of internal light paths which can often amount to several centimetres.

A possible future application of such sensors is in the field of chemical analysis. As is well known, many chemical analysis techniques rely on colour change reactions in which suitable indicator molecules are added to the liquid samples to be analysed. Currently, many

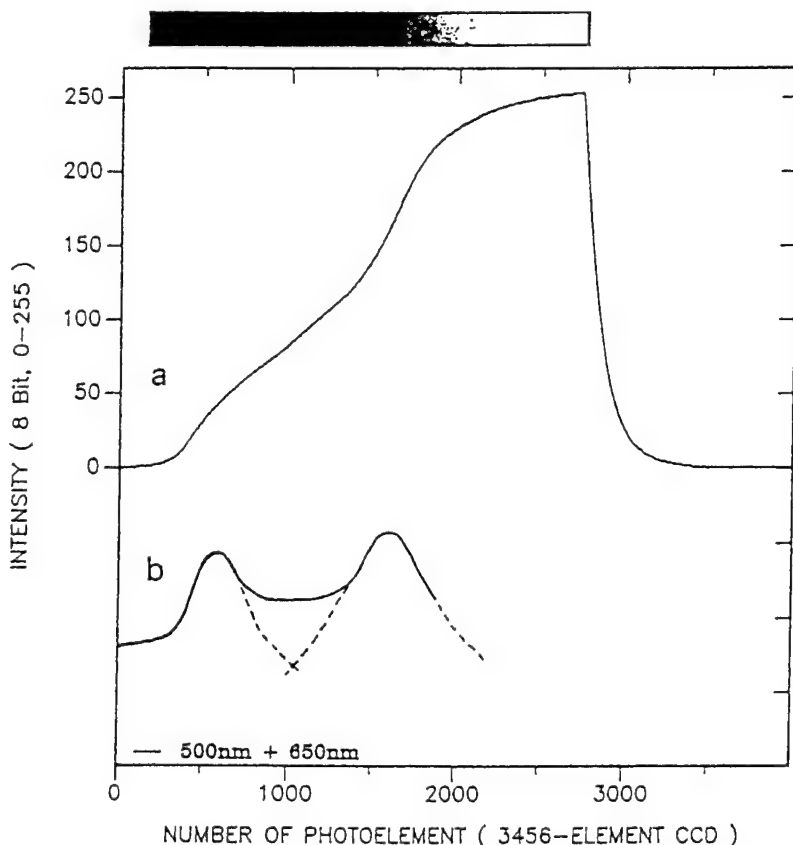


Fig. 5. Response of a graded-bandgap colour sensor to two quasi-monochromatic light sources: (a) spatial intensity pattern produced by the graded-bandgap filter; (b) differentiated spatial intensity pattern. The filter grading is indicated by the shadowing in the top.

micromachining approaches are being taken towards complete microanalysis systems [11]. The ruggedness of our colour sensing devices makes them ideal subsystems within such miniaturised and automated analysis systems. Whether a hybrid approach or a fully monolithic TFA approach is to be taken depends on purely economical boundary conditions such as the market size for such medical and environmental analysis systems and the price a customer is willing to pay for an individual device.

Acknowledgement

The author is indebted to continuous interest and support by Drs. B. Thomas, S. Paasche and M. König.

References

- [1] For a review see: J. Kanicki (Ed.), *Amorphous and Microcrystalline Semiconductor Devices*, Artech House, Boston, 1991.
- [2] A. Catalano, Solar cells made of amorphous and microcrystalline semiconductors, Ref. [2], pp. 9–76.
- [3] For a review see: W. Luft, Y.S. Tsuo, *Hydrogenated Amorphous Silicon Alloy Deposition Processes*, Marcel Dekker, Inc., New York, Basel, Hong Kong, 1993.
- [4] G. Müller, G. Krötz, SiC as a new sensor material, Proc. 7th Int. Conf. on Solid State Sensors and Actuators, Yokohama, Japan, May 1993.
- [5] G. Müller, G. Krötz, E. Niemann, SiC for sensors and high-temperature electronics, *Sensors and Actuators* 43 (1994) 259–268.
- [6] G. Krötz, G. Müller, G. Derst, Ch. Wilbertz, S. Kalbitzer, Thin-film SiC as an optical and optoelectronic material, *Diamond Relat. Mater.* 3 (1994) 917–921.
- [7] J. Wind, G. Krötz, R. Schmiedgen, W. Legner, J. Binder, V. Hechtenberg, G. Müller, Colour detection using amorphous semiconductor thin-films, *Sensors and Actuators A* 36 (1993) 187–192.
- [8] Final report BRITE/Euram Project, *Diamond and Silicon Carbide Sensors (DISCS)*, 1993.
- [9] G. Müller, P.P. Deimel, W. Hellmich, Chr. Wagner, Proc. EMRS Spring Conf. 1996, Straßburg; Symposium B.
- [10] W. Lang, Silicon microstructuring technology, *Materials Science and Engineering*, R17, No 1, 1 September 1996.
- [11] M. Lambrechts, W. Sansen, *Biosensors: Microelectrochemical Devices*, Institute of Physics Publishing, Bristol, Philadelphia, New York, 1992.

Surface and bulk effects in ex-situ hydrogenated α -SiC thin films

J. Kalomirios ^a, E.C. Paloura ^{a,*}, C. Janowitz ^b, B. Theys ^c, A. Anagnostopoulos ^a

^a Aristotle University of Thessaloniki, Department of Physics, GR-54006 Thessaloniki, Greece

^b Humboldt University, Institute of Physics, Invalidenstrasse 110, D-10115 Berlin, Germany

^c CNRS, Laboratoire de Physique des Solides de Bellevue, 1 Place A. Briand, 92195 Meudon, Cedex, France

Abstract

The effect of ex-situ hydrogenation on the bulk and surface properties of amorphous SiC (α -SiC) thin films has been investigated using a number of bulk- and surface-sensitive characterisation techniques. The diffusion coefficient of deuterium in α -SiC is found to be equal to $3\text{--}4 \times 10^{-15} \text{ cm}^2 \text{ s}^{-1}$. It is shown that atomic hydrogen causes drastic changes in the dielectric function, due to preferential Si etching from the film surface, and the formation of a carbon surface layer rich in sp^2 bonds. Furthermore, the atomic hydrogen diffuses in the bulk and causes an increase of the optical band gap and a concurrent decrease in conductivity, due to partial passivation of dangling bonds. © 1997 Elsevier Science S.A.

Keywords: A-SiC; Etching; Hydrogenation; Ellipsometry

1. Introduction

Amorphous Si–C alloys (α -SiC) have been the subject of intensive study due to their potential applications in micro- and optoelectronic devices [1]. The problem of in-situ (during growth) hydrogen incorporation and the resulting changes in bulk and surface properties has been addressed in the past [2]. However, the effect of ex-situ hydrogenation (low-temperature annealing in a hydrogen rf glow discharge) on the surface and bulk properties of α -SiC has not yet been studied in detail. Ex-situ hydrogenation simulates processing environments such as plasma-enhanced chemical vapour deposition and reactive ion etching, where atomic hydrogen coexists with other reactive species. Furthermore, atomic hydrogen is highly reactive and thus finds applications in the surface cleaning and plasma etching of several material systems [3] as well as in the passivation of point and extended defects [4].

In this paper we present a study of the concurrent bulk and surface modifications occurring in thin α -SiC films upon exposure to atomic hydrogen. To date the effect of ex-situ hydrogenation on α -SiC has been limited to the study of surface-property modification [5–7].

2. Sample preparation and experimental details

The amorphous SiC films were deposited at room temperature by rf sputtering on Corning glass 7059

substrates from a SiC target of constant composition [2]. The film thickness of the as-grown films was in the range 0.8–1 μm . The films were annealed for 2 h in a hydrogen or deuterium glow discharge at 13.56 MHz in a capacitively coupled quartz reactor. During the process the sample temperature was 230 °C, the hydrogen pressure ranged from 100 to 150 mTorr, while the rf power took values in the range 100–150 W. In the following, the ratio of the rf power over the hydrogen pressure (W/P) is used to describe the plasma conditions (the reference as-grown sample is labelled S_0). The process was applied repeatedly, and yielded reproducible results which are unique to the plasma hydrogenation process and are not observed in control samples which were annealed at 230 °C either in vacuum or in molecular H₂.

The dark conductivity measurements were conducted in the four-probe configuration geometry in the temperature range 130–450 K using low-resistance ohmic contacts fabricated using indium evaporation. The optical transmission and the visible ultraviolet (VUV) ellipsometry spectra were recorded in the energy ranges 1.5–3.0 eV and 2.5–24 eV, respectively. The ellipsometry measurements were conducted using the linearly polarised radiation at the 2m-Seya Namioka beamline at the electron storage ring BESSY in Berlin [9]. Finally, the deuterium profiles were obtained using a Cameca IMS 4f SIMS (secondary ion mass spectroscopy) analyser using a cesium primary beam.

* Corresponding author. E-mail: paloura@physics.auth.gr

3. Results and discussion

3.1. Bulk properties: absorption, conductivity and SIMS profiling

The bulk-diffused atomic hydrogen passivates dangling bonds, leading to an increase of the optical band gap and a reduction in the DC conductivity. The diffusion of atomic hydrogen in the bulk was verified by SIMS profiling of deuterated samples, which shows that deuterium (and consequently hydrogen) diffuse in the bulk of the film to a depth which depends on the hydrogenation conditions and is of the order of a few hundred nm. In a sample deuterated for 2 h at 150 mTorr and with 150 W of coupled rf power, the deuterium concentration reaches the SIMS detection limit at a depth of 250 nm from the surface. The deuterium profile is correctly fitted with an erfc function, with a diffusion coefficient of $3\text{--}4 \times 10^{-15} \text{ cm}^2 \text{ s}^{-1}$.

The variation of the absorption coefficient α versus the incident photon energy E for the hydrogenated ($S_1\text{--}S_4$) and the reference (S_0) samples are shown in Fig. 1. The dependence of the optical band gap E_g on hydrogenation conditions was determined using the Tauc approximation, i.e. in a plot of $(\alpha E)^{1/2}$ versus photon energy, and the linear part is extrapolated to the $\alpha=0$ value. The values of the E_g are listed in Table 1 along with the corresponding W/P ratios. The E_g of the material is found to increase with hydrogen incorpora-

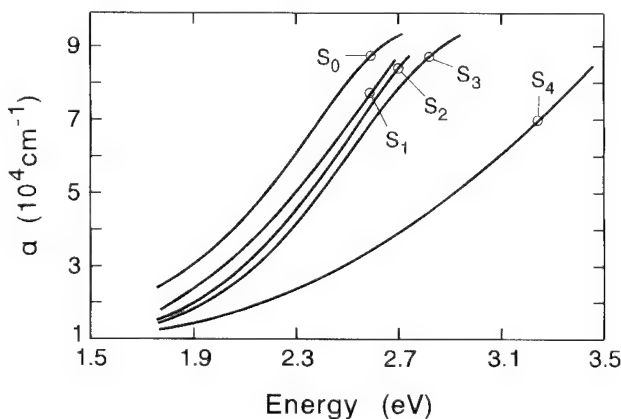


Fig. 1. Absorption coefficient α versus the photon energy E for the reference and a series of hydrogenated films.

Table 1
 E_g as a function of the plasma hydrogenation conditions

Sample	W/P (W/mbar)	E_g (eV)
S_0		1.28
S_1	0.67	1.39
S_2	0.33	1.47
S_3	0.5	1.52
S_4	1.0	1.57

tion, the effect being stronger for higher values of W/P . It should be noted that the effect is clearly seen in films hydrogenated either in the embedded (between the rf and ground electrodes) or downstream configuration. Among the films discussed here, S_1 was hydrogenated in a downstream configuration where the effect of surface bombardment and UV enhancement is reduced. The measured increase of E_g is attributed to saturation of dangling bonds and elimination of states at the band edges [8].

The dark DC conductivity curves of a typical hydrogenated ($\alpha\text{-SiC:H}$) and the reference ($\alpha\text{-SiC}$) samples are shown in Fig. 2. The overall decrease in the values of conductivity after hydrogenation is attributed to the partial passivation of defect states in the gap, resulting in a decrease of the DOS at the Fermi level. The activation energy for conduction for both the as-grown and hydrogenated samples, calculated from the $\sigma-10^3/T$ curves, is found equal to about 0.2 and 0.075 eV in the high- and low-temperature ranges, respectively. This result indicates that conduction is dominated by a hopping transport process, in agreement with previously reported results [9, 10].

3.2. Surface properties: VUV ellipsometry

To study loss features related to plasmon excitation we measured the dielectric function in the photon energy range 2.5–24.0 eV by means of VUV spectroscopic ellipsometry. The data were analysed with an isotropic two-phase model and assuming an ideal interface between the isotropic sample and vacuum. The loss function as calculated from the dielectric function is shown in Fig. 3. The loss function is not shown in the energy range $10 \text{ eV} < h\nu < 15 \text{ eV}$ due to a possible contri-

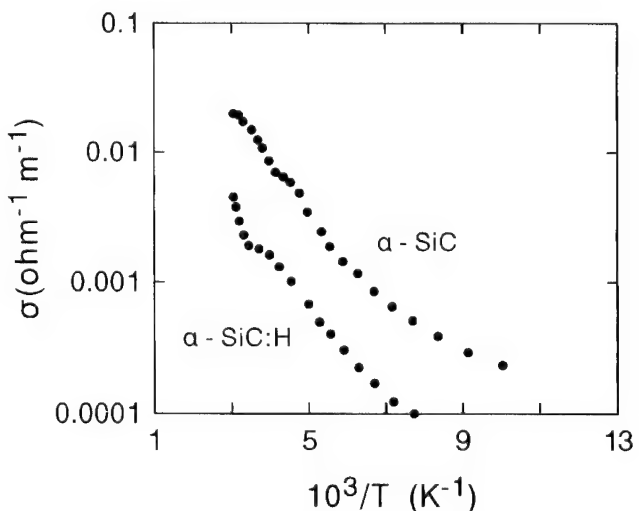


Fig. 2. Dark DC conductivity curves versus $10^3/T$ for the reference and a hydrogenated sample.

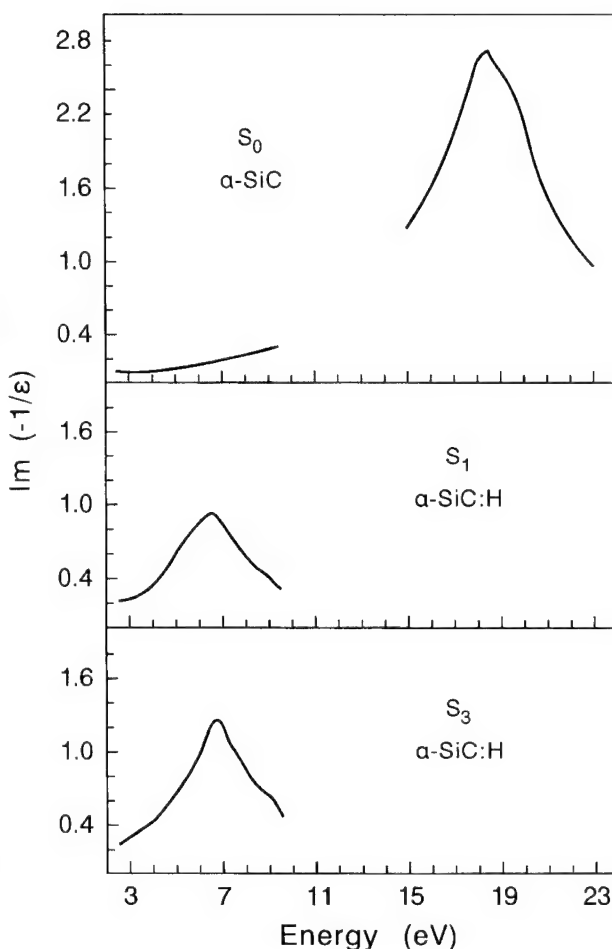


Fig. 3. Loss function ($\text{Im}(-1/\epsilon)$) calculated from the dielectric function spectra.

bution from second-order radiation. Furthermore, measurements at $E > 10$ eV are impeded by the surface roughness induced by the hydrogenation process [5]. As shown in Fig. 3, the as-grown α -SiC films do not have peaks below 19 eV while the hydrogenated samples have strong features around 6.5 eV. The plasmon in the energy range 6–7 eV is characteristic of C compounds with some degree of sp^2 bonding [11]. Among the elements which could be involved in the formation of the surface layer (Si, C, H and to a minor degree O), only carbon can produce loss features in the 6–7 eV range. Therefore, we ascribe the 7 eV loss peak in our spectra to π bonds of carbon atoms. Based on the ellipsometry results we can conclude that the surface of the ex-situ hydrogenated films consists of carbon atoms with some fraction in sp^2 configuration, possibly also bonded to hydrogen and, to a minor degree, oxygen atoms. This view is also corroborated by surface investigation with X-ray diffraction and X-ray photoelectron spectroscopy [7,8].

4. Conclusions

From the results presented above it is evident that ex-situ hydrogenation is a processing step which can drastically change both the bulk and the surface electronic properties of α -SiC films. The bulk changes amount to passivation of dangling bonds and widening of the optical gap, an effect which is also observed in in-situ hydrogenated α -SiC films. The diffusion coefficient of ${}^2\text{H}$ was determined from the SIMS profiles of deuterated samples, and was found to be $3\text{--}4 \times 10^{-15} \text{ cm}^2 \text{ s}^{-1}$. To the best of our knowledge, this is the first time that the diffusion coefficient of ${}^2\text{H}$ in α -SiC has been reported as measured from controlled diffusion experiments. However, the concurrent changes of the surface properties is a phenomenon which has not been observed in rf-sputtered in-situ hydrogenated films, and is characteristic of the ex-situ process. Atomic hydrogen induces preferential Si etching which promotes the formation of a surface carbon layer which is rich in sp^2 bonding, which has to be solely attributed to the properties of atomic hydrogen. The above results can contribute to a better understanding of the mechanisms for residue formation, which occurs during dry etching of SiC.

Acknowledgement

We wish to thank Ms. M. Miloche for the SIMS measurements. This work was realised with financial support from the GSRT (PENED 1432).

References

- [1] T. Matsuoka, Y. Kuwano, IEEE Trans. Electron Dev. 37 (1990) 397.
- [2] J.A. Kalomiros, A. Papadopoulos, S. Logothetidis, L. Magafas, N. Georgoulas, A. Thanailakis, Phys. Rev. B 49 (1994) 8191.
- [3] W. Tsai, M. Delfino, M.E. Day, T. Sheng, B.C. Chung, S. Salimian, J. Vac. Sci. Technol. A 11 (1993) 2525.
- [4] S.J. Pearton (Ed.), Hydrogen in Compound Semiconductors, Trans Tech, Zürich, 1994, and references therein.
- [5] J.A. Kalomiros, E.C. Paloura, A. Ginoudi, S. Kennou, S. Ladas, Ch. Lioutas, N. Vouroutzis, G. Voutsas, D. Girginoudi, N. Georgoulas, A. Thanailakis, Solid State Commun. 96 (1995) 735.
- [6] S. Kennou, S. Ladas, E.C. Paloura, J.A. Kalomiros, Appl. Surf. Sci. 90 (1995) 283.
- [7] C. Janowitz, J. Kalomiros, A. Ginoudi, E.C. Paloura, R.L. Johnson, Solid State Commun. 99 (1996) 29.
- [8] E.A. Fagen, in: J. Stuke (Ed.), Proceedings of the International Conference on Amorphous and Liquid Semiconductors, Taylor and Francis, London, 1973, p. 601.
- [9] R. Dutta, P.K. Banerjee, S.S. Mitra, Solid State Commun. 42 (1982) 219.
- [10] J. Bullot, M.P. Schmidt, Phys. Status Solidi b 143 (1987) 345.
- [11] P. Kovarik, E.B.D. Bourdon, R.H. Prince, Phys. Rev. B 48 (1993) 12123.



ELSEVIER

Diamond and Related Materials 6 (1997) 1550–1554

**DIAMOND
AND
RELATED
MATERIALS**

Optical study of boron nitride thin films prepared by plasma-enhanced chemical vapor deposition

M.C. Polo ^{a,1}, M. Ben el Mekki ^a, J.L. Andújar ^b, N. Mestres ^c, J. Pascual ^a

^a Departament de Física, Universitat Autònoma de Barcelona, E-08193 Bellaterra, Spain

^b Departament de Física Aplicada i Electrònica, Universitat de Barcelona, Av. Diagonal 647, E-08028 Barcelona, Spain

^c Institut de Ciència de Materials de Barcelona, E-08193 Bellaterra, Spain

Abstract

We investigate the effects of finite off-normal incidence on the polarized infrared reflectivity spectra of hexagonal boron nitride films deposited on Si substrates by radio frequency plasma enhanced chemical vapor deposition, using B_2H_6 (1% in H_2) and NH_3 gases. The experimental observation of a sharp structure associated to the coupling of the incident light with the LO component of the twofold stretching mode, and the absence of similar coupling effects with the LO component of the bending mode, indicates that the *c*-axis is parallel to the film surface. We also show that the infrared spectra are not modified when one rotates the sample perpendicularly to the growth direction. Therefore, we conclude that the principal axis of the polycrystalline boron nitride films is randomly oriented within the plane parallel to the film surface. Finally, we show that these optical results are in full agreement with high resolution transmission electron microscopy studies. © 1997 Elsevier Science S.A.

Keywords: BN films; Polarized IR reflection spectroscopy; R.f. Plasma CVD; TEM

1. Introduction

Recently, an important research activity has been focused on the preparation of thin films of boron nitride (BN) owing to the outstanding properties of this III–V compound such as high hardness, optical transparency, chemical inertness, high thermal conductivity, high electrical resistivity and low dielectric losses. Boron nitride shows several structures [1]: cubic, hexagonal (h-BN), turbostratic – which is a disordered modification of h-BN, and amorphous. In particular, h-BN films have been successfully applied as optical and mechanical protective coatings and as dielectric layers in microelectronics devices [2]. However, a better knowledge of the properties of the BN films is necessary to further development of their applications.

Transmission electron microscopy (TEM) has been widely used to study the microstructure of the BN films [3–5]. The major disadvantage of this technique is that it requires a laborious sample preparation which becomes more difficult in the case of hard films. Fourier-transform infrared (FT-IR) spectroscopy is, on the other

hand, a non-destructive technique that has been proved as a powerful characterization tool to identify the several phases of BN. Most studies deal with absorption measurements in transmission mode at normal incidence [6,7] where only the TO vibrational modes can be excited. In contrast, very few studies report reflection measurements [8] and, to our knowledge, only two papers performed polarized infrared reflection (PIRR) spectroscopy [9,10]. Besides the TO modes, the LO modes can be observed in the infrared reflection spectra of thin films, which gives more information about the film properties. In this work we present a PIRR study to determine the structure of h-BN thin films obtained by radio frequency plasma-enhanced chemical vapor deposition (rf-PECVD). As the optical properties of h-BN are anisotropic, different vibration modes can be excited depending on both, the orientation of the sp^2 -bonded basal planes with respect to the surface substrate and the polarization of the light. We have simulated the reflectance spectra for each possible configuration using the classical oscillator model and the Fresnel equations, and, as an application of this theoretical model, we have determined the *c*-axis orientation of h-BN films. Finally, we have used high resolution cross-sectional TEM studies of the films to confirm the PIRR results.

¹ Permanent address: Departament de Física Aplicada i Electrònica, Universitat de Barcelona, Av. Diagonal 647, E-08028 Barcelona, Spain.

2. Crystal structure and IR activity

The hexagonal phase of BN belongs to the space group D_{6h}^4 . At the center of the Brillouin zone, of the 12 normal modes of vibration 3 are infrared active, a non-degenerated mode (A_{2u}) and a twofold degenerated mode (E_{1u}). More specifically, the A_{2u} mode is an out-of-plane bending vibration excited by polarized light parallel to the principal axis. The corresponding ω_{TO} and ω_{LO} frequencies are 783 and 828 cm^{-1} respectively, measured in bulk BN. The E_{1u} mode corresponds to an in-plane stretching vibration and can be excited with polarized light perpendicular to the threefold axis. The corresponding ω_{TO} and ω_{LO} frequencies are 1367 and 1610 cm^{-1} respectively, again measured in the bulk [11].

For very thin layers, with thicknesses below the micrometric scale, the reflectivity spectra show a sharp feature at the TO frequency of the corresponding IR active mode [12]. For the standard analysis of the infrared reflectivity one always assumes normal incidence conditions. However, most experimental apparatus support finite values of the angle of incidence. In most cases this is sufficient to allow the observation of fine structures in the IRR spectra associated to the longitudinal polar modes. These features can be greatly enhanced when performing experiments under wide incident angle conditions [9,13].

In the case of h-BN with two IR active modes, one polarized parallel and the other perpendicular to the principal axis, off-normal incidence PIRR experiments can be used to determine the orientation of the grown films. Fig. 1 shows the reflectivity spectra one expects for the incident electric field polarized perpendicular (s) or parallel (p) to the plane of incidence. The three configurations correspond to cases where the principal axis: (i) is parallel to the film surface and perpendicular to the plane of incidence (Fig. 1(a)); (ii) is parallel to both, the film surface and the plane of incidence (Fig. 1(b)); and (iii) is perpendicular to the film surface (Fig. 1(c)). In the three cases, the interface reflection matrices are always diagonal and the reflectivity is easily calculated from the three-phases (ambient–film–substrate) system [14]. We use the standard Lorenz approach to give the complex dielectric dispersion of ϵ_{\parallel} and ϵ_{\perp} in terms of oscillators with parameters obtained from optimum fits to IRR spectra of bulk BN [11]. The angle of incidence considered here is 30° . Notice that the LO component of E_{1u} is only allowed when the principal axis is lying in the film (Figs. 1(a) and (b)). On the contrary, the LO mode of A_{2u} is only allowed when the c -axis is perpendicular to the sample surface. Cases (i) and (ii) can be distinguished from each other if one observes that both TO modes, E_{1u} and A_{2u} , cannot be simultaneously detected for a given polarization.

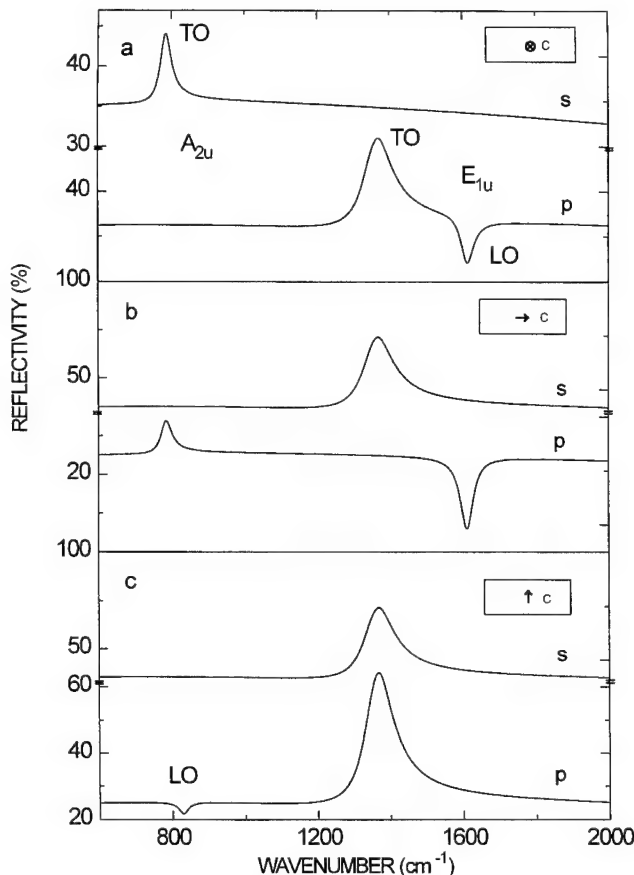


Fig. 1. Calculated polarized IR reflectivity spectra of a 200 nm h-BN film and for an angle of incidence of 30° when: (a) the c -axis is perpendicular to the plane of incidence and parallel to the film surface; (b) the c -axis is parallel to both, the plane of incidence and the film surface; and (c) the c -axis is parallel to the plane of incidence and perpendicular to the film surface.

3. Experimental procedure

The BN films were grown on silicon(100) in a RF (13.56 MHz) capacitively coupled by glow discharge decomposition of B_2H_6 (1% in H_2) and NH_3 gases. In the discharges, the gas flow rate of NH_3 was 5 sccm and the flow rate of the $\text{B}_2\text{H}_6\text{--H}_2$ gas mixture was varied from 50 to 100 sccm. Other deposition conditions were: total gas pressure, 30 Pa; substrate temperature, 300°C ; and RF power density, 0.5 W cm^{-2} . Different film thicknesses were obtained in the range 100–600 nm by changing the deposition time. The atomic ratio was close to the stoichiometric value ($\text{B:N}=1:1$) as calculated by X-ray photoelectron spectroscopy (XPS). The films were highly transparent in the visible–near UV region (250–800 nm). Atomic force microscopy revealed a surface roughness of the films below 2 nm, calculated as the standard deviation of all heights in a selected area of $10\text{ }\mu\text{m} \times 10\text{ }\mu\text{m}$.

Infrared transmission and PIRR spectra were obtained under vacuum with a DA3 Bomem FT-IR

spectrometer in the wave number range 500–4000 cm⁻¹ with a resolution of 4 cm⁻¹. Cross-sectional high resolution TEM and dark field (DF) images as well as selected area diffraction (SAD) patterns were recorded using a Philips CM30 electron microscope operating at 300 kV.

4. Results and discussion

Fig. 2 shows the PIRR spectra of a 200 nm film which was grown at 100 sccm of the B₂H₆–H₂ mixture. In order to see off-normal incidence effects, three experimental configurations with 15, 35 and 50° angles of incidence are displayed in Fig. 2. The first we find, is that there is not a direct correspondence between the experimental spectra and any of the cases discussed before (see Fig. 1). In particular, for s polarization, both TO phonon modes are simultaneously observed. On the contrary, for p-polarization only the LO component of E_{1u} is present. For this polarization the LO coupling with the incident electric field is strongly enhanced when one opens the angle of incidence from 15° (Fig. 2(a)) to 35° (Fig. 2(b)). In this last case, one would expect to find a pronounced dip at the LO frequency of the A_{2u} mode if the c-axis had a component perpendicular to the film surface (see Fig. 1(c)). Since this is not the case, one can conclude that the c-axis lies parallel to the film

surface. Notice that the sensitivity of the experiment to identify LO modes decreases when one uses wider angles of incidence (Fig. 2(c)). This is because experimental conditions are approaching the Brewster angle where the phase of the reflectivity amplitude changes at the ambient-film interface.

The experimental data can be regarded as an admixture of cases (a) and (b) displayed in Fig. 1. In order to see if there is a preferential orientation of the c-axis in the plane of the film, we have performed complementary experiments where the samples have been rotated along the axis perpendicular to the surface. The collected spectra are exactly the same as the ones reported in Fig. 2. Therefore, we can conclude that the polycrystalline h-BN films have the c-axis parallel to the film surface and that the grains do not have a preferential orientation in it.

To give more quantitative information, we have performed a fit analysis using two independent oscillators. In Fig. 3 the dotted line shows the theoretical fit to the p-polarized spectrum measured taking an angle of incidence of 15° (this corresponds to the experimental results displayed in Fig. 2(a)). Similar quality fits are obtained for different configurations of polarization and angles of incidence. The parameters used in the fitting are: $\omega_{TO} = 790 \text{ cm}^{-1}$, $\omega_{LO} = 828 \text{ cm}^{-1}$ and $\Gamma = 30 \text{ cm}^{-1}$ for the A_{2u} vibration; and $\omega_{TO} = 1386 \text{ cm}^{-1}$, $\omega_{LO} = 1599 \text{ cm}^{-1}$ and $\Gamma = 50 \text{ cm}^{-1}$ for the E_{1u} modes. The model accounts fairly well for the low energy mode. On the contrary, it fails to fit the shoulder which appears at the high energy side of the stretching mode. This broad band has been traditionally associated to local mode lattice vibrations induced by the presence of impurities, like the stretching C-C vibrations, stretching B-O

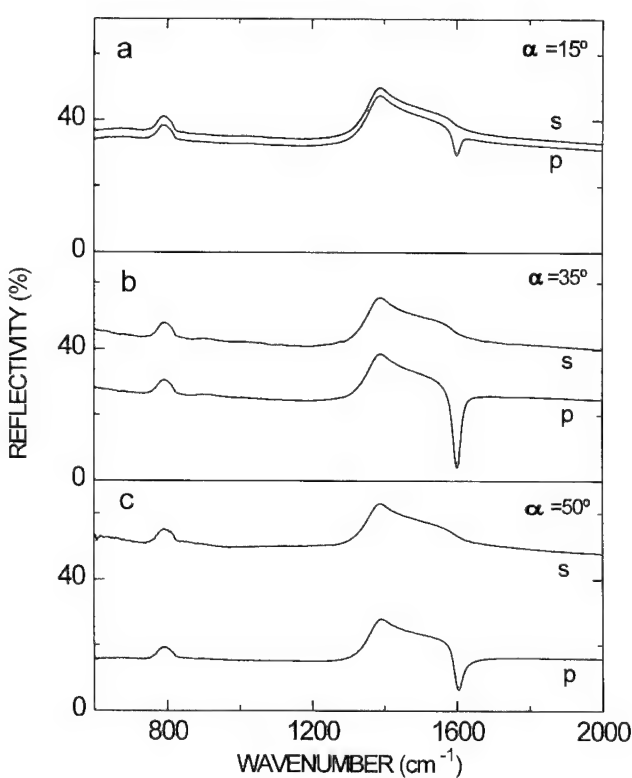


Fig. 2. Experimental polarized IR reflectivity spectra of a 190-nm thick h-BN film for different angles of incidence.

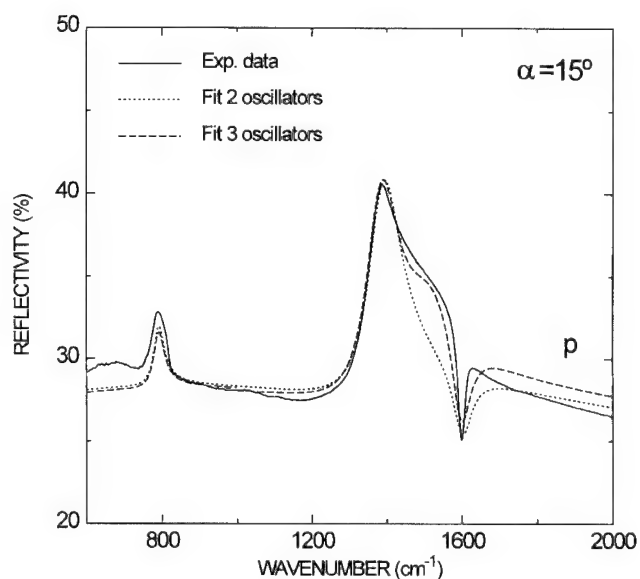


Fig. 3. Experimental and calculated p-polarized IR reflectivity spectra of a h-BN sample 190-nm thick for an angle of incidence of 15°.

vibrations, and also bending N–H₂ vibrations [15]. Nevertheless, we believe that all these possibilities have to be ruled out for our samples. XPS analysis shows that the contamination with carbon is negligible and only affects the uppermost atomic layers near the surface. The same argument is valid for oxygen. Besides, the 1s peak of B has a maximum at 190.6 eV, in agreement with B–N bond surrounding, and the lineshape of the peak does not show any asymmetry near 193.0 eV, the energy associated to the presence of B–O bonds. Finally, from IRR and transmission measurements in our samples, a band is found at 3430 cm⁻¹ which correspond to the N–H stretching vibration. Since the band is very weak, one would expect a much weaker IR activity for the corresponding N–H₂ bending vibration at 1540 cm⁻¹. Thus, it would not justify the intense shoulder found in this energy region. Gieck et al. [11] have suggested that the broad shoulder is probably due to the contribution of two-phonons processes. We simulate all two-phonon contributions with an oscillator of frequencies $\omega_{TO}=1510\text{ cm}^{-1}$ and $\omega_{LO}=1640\text{ cm}^{-1}$, and a broad damping $\Gamma=150\text{ cm}^{-1}$. The addition of this average mode to the fitting model gives a calculated spectrum (dashed line in Fig. 3) in good agreement with the experimental data in the whole energy range.

The results of these optical studies are ascertained by TEM measurements. Fig. 4 shows a cross-sectional high resolution TEM image and SAD pattern of the investigated BN film. Interestingly, a textured microstructure is observed throughout the film, showing h-BN lattice fringes aligned nearly perpendicular to the substrate with an interplanar distance of about 0.35 nm. The SAD pattern shows two bright arcs, corresponding to h-BN(002) reflection along with continuous rings ascribed to (100) and (110) h-BN reflections. This orientation is corroborated in DF images [16] obtained by tilting the incident beam so that the beams diffracted towards the arcs passed through the objective aperture. In such conditions, bright areas denote h-BN crystallites contributing to (002) reflection and having their *c*-axis parallel to the substrate surface. However, such a contrast is not observed in the DF image made using the dark part of the (002) h-BN ring.

5. Conclusions

We have shown that a careful analysis of the stretching and bending vibrational modes observed in the PIRR spectra of h-BN thin films can be used to determine the orientation of the principal axis in a non-destructive and very easy way. We find that polycrystalline h-BN thin films deposited on (001) Si substrates by RF plasma enhanced CVD, have the *c*-axis contained in the plane parallel to the film surface and randomly oriented. The optical studies coincide with high resolution TEM

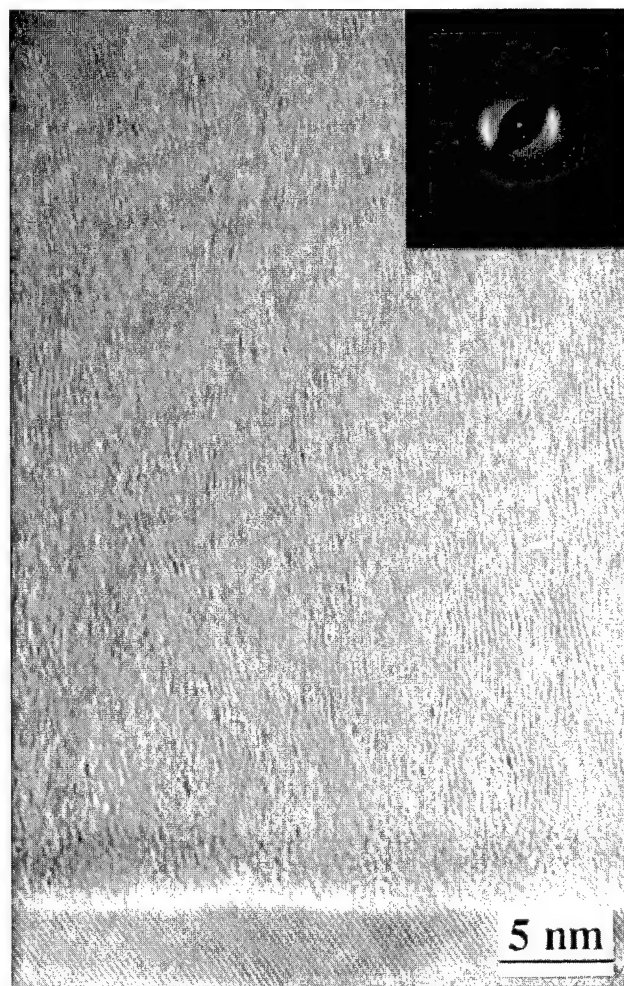


Fig. 4. Cross-sectional high resolution TEM image and selected area diffraction pattern of a 190-nm thick BN film showing a h-BN oriented structure.

results. Therefore, PIRR spectroscopy appears as a very powerful tool to investigate structural properties of anisotropic thin films.

Acknowledgement

This work was partially supported by the Comisión Interministerial de Ciencia y Tecnología of the Spanish Government under contract MAT93-0298. Technical assistance of the Serveis Científico-Tècnics of UB is gratefully acknowledged. One of us (M.B.M.) acknowledges financial support from the Agencia Española de Cooperación Internacional.

References

- [1] J.J. Pouch, S.A. Alterovitz (Eds.), *Synthesis and Properties of Boron Nitride*, Trans Tech, Zürich, 1990.

- [2] D.R. Cote, S.V. Nguyen, W.J. Cote, S.L. Pennington, A.K. Stamper, D.V. Podlesnik, IBM J. Res. Dev. 39 (1995) 437.
- [3] D.J. Kester, K.S. Ailey, R.F. Davis, K.L. More, J. Mater. Res. 8 (1993) 1213.
- [4] D.L. Medlin, T.A. Friedmann, P.B. Mirkarimi, M.J. Mills, K.F. McCarty, J. Appl. Phys. 76 (1994) 295.
- [5] S. Watanabe, S. Miyake, W. Zhou, Y. Ikuhara, T. Suzuki, M. Murakawa, Appl. Phys. Lett. 66 (1995) 1478.
- [6] A.S. Rozenberg, Y.A. Sinenko, N.V. Chukanov, J. Mater. Sci. 28 (1993) 5675.
- [7] S. Jäger, K. Bewilogua, C.P. Klages, Thin Solid Films 245 (1994) 50.
- [8] T.A. Friedmann, P.B. Mirkarimi, D.L. Medlin, K.F. McCarty, E.J. Klaus, D.R. Boehme, H.A. Johnsen, M.J. Mills, D.K. Ottesen, J. Appl. Phys. 76 (1994) 308.
- [9] M. Okamoato, Y. Utsumi, Y. Osaka, Jpn. J. Appl. Phys. 31 (1992) 3455.
- [10] M.F. Plass, W. Fukarek, S. Mändl, W. Mäller, Appl. Phys. Lett. 69 (1996) 46.
- [11] R. Geick, C.H. Perry, G. Rupprecht, Phys. Rev. 146 (1966) 543.
- [12] R.T. Holm, P.H. Klein, P.E.R. Nordquist, J. Appl. Phys. 60 (1996) 1479.
- [13] A. Goulet, J. Camassel, L. Martin, J. Pascual, E. Philippot, Phys. Rev. B 40 (1989) 5750.
- [14] R.M.A. Azzam, N.M. Bashara, Ellipsometry and Polarized Light, North-Holland, Amsterdam, 1977.
- [15] C. Gómez-Aleixandre, A. Essafti, M. Fernández, J.L.G. Fierro, J.M. Albella, J. Phys. Chem. and references therein 100 (1996) 2148.
- [16] J.L. Andújar, E. Bertrán, Y. Maniette, J. Appl. Phys. 80 (1996) 6553.



ELSEVIER

DIAMOND
AND
RELATED
MATERIALS

Diamond and Related Materials 6 (1997) 1555–1558

Electrical properties of PECVD amorphous silicon–carbon alloys from amorphous–crystalline heterojunctions

L.F. Marsal ^{a,*}, J. Pallarès ^a, X. Correig ^a, M. Domínguez ^b, D. Bardés ^b,
J. Calderer ^b, R. Alcubilla ^b

^a Departament d'Enginyeria Electrònica, Universitat Rovira i Virgili, Autovia de Salou s/n, 43006 Tarragona, Spain

^b Departament d'Enginyeria Electrònica, Universitat Politècnica de Catalunya, C/Gran Capità s/n, Campus Nord C-4, 08071 Barcelona, Spain

Abstract

Heterojunction diodes fabricated by plasma enhanced chemical vapour deposition of *n*-type amorphous silicon carbide on *p*-type crystalline silicon are analysed by measuring their current–voltage characteristics. Two carrier transport mechanisms are believed to be at the origin of the forward current. At low bias voltage, the current is due to recombination in the amorphous side of the space charge region, while at higher voltages, the current becomes space charge limited. At reverse bias, the current can be explained by tunnelling models. The space charge limited currents in these heterojunctions have been used to determine the density of states in the *n*-type a-Si_{1-x}C_x:H gap. The results show the increase in localized states when approaching the conduction band edge. © 1997 Elsevier Science S.A.

Keywords: Amorphous silicon–carbon alloys; Density of states; Heterojunction; Space-charge limited current; Transport mechanisms

1. Introduction

Hydrogenated amorphous silicon carbon alloys (a-Si_{1-x}C_x:H) are of great interest because of their wide optical band gap (1.7–3 eV), which can be controlled by varying the carbon composition and also because they can be deposited at low temperature. a-Si_{1-x}C_x:H films are used in many different electronic and optoelectronic applications such as thin film light emitting diodes [1], heterojunction bipolar transistors [2], etc. Despite all the research into the physics and technology of this material, many problems still remain unsolved. Of these, one of the most important is the determination of defect states in the gap. It is of paramount importance to know the density of states in the gap if the optoelectronic properties of the resulting devices are to be predicted.

A variety of optical and electrical measurement techniques have been developed to determine the density of states in the gap (DOS): field effect [3], DLTS [4], etc. The results seem to be dependent on the deposition process (sputtering, glow discharge, etc.), deposition

parameters (substrate temperature, doping, etc.), type of test structure (Schottky, *p-i-n*, MIS, etc.) and measurement technique (optical, electrical). Hence, the results obtained by different groups are often difficult to compare.

In this context, and in order to assess the utility of a-Si_{1-x}C_x:H in device applications, hydrogenated amorphous (a) silicon carbon–crystalline (c) silicon heterojunction diodes (a-Si_{1-x}C_x–c-Si) were fabricated and their electrical properties investigated by measuring their current–voltage characteristics. Finally, from the existence of space charge limited currents [5] the energy distribution of localized states in the gap in the a-Si_{1-x}C_x layer was determined.

2. Experimental details

(*n*) a-Si_{1-x}C_x:H–(*p*) c-Si heterojunctions were studied using a diode structure. The starting material is *p*-type Czochralski silicon, with <100> orientation and an average resistivity value of 1 Ω cm. A back boron diffusion was carried out to improve the back contact. A

* Corresponding author: Tel: +34 77 559625; Fax: +34 77559710; E-mail: lmarsal@etse.urv.es

0.4 µm-thick a-Si_{1-x}C_x:H layer was deposited by plasma enhanced chemical vapour deposition (PECVD) from a mixture of methane (CH₄) and silane (SiH₄) and with a substrate temperature of 350 °C. N-type doping was achieved by adding phosphine (PH₃) to silane. In order to reach dopant saturation, a PH₃:SiH₄ ratio of 1:20 was used. Before film deposition, the reactor bell jar was cleaned using CF₄/O₂ plasma and evacuated down to 1 × 10⁻³ torr. A parallel-plate radio frequency (RF) reactor has been used with a power density of 31 mW cm⁻² supplied at 13.56 MHz. The semiconductor surface was HF etched prior to deposition. A 1:10 HF etching was carried out before the metal deposition. Finally, ohmic contacts were obtained by evaporating pure aluminium with an area of 625 µm². The gas flow ratio $r=0.6$ ($r=[\text{CH}_4]/[\text{CH}_4]+[\text{SiH}_4]$) was used and the carbon content $x=0.2$ was determined by X-ray photoelectron spectroscopy (XPS). A mobility gap $E_g \approx 1.95$ eV has been reported as a reference value. The dark current–voltage was measured between -5 and 5 V with an HP4145A semiconductor parameter analyser at room temperature.

3. Results and discussion

3.1. Diode current–voltage characteristics

Fig. 1 shows the current versus voltage characteristics of a representative (n) a-Si_{1-x}C_x:H–(p) c-Si heterojunction diode measured at room temperature. As shown in Fig. 1, the forward current measured has two distinct

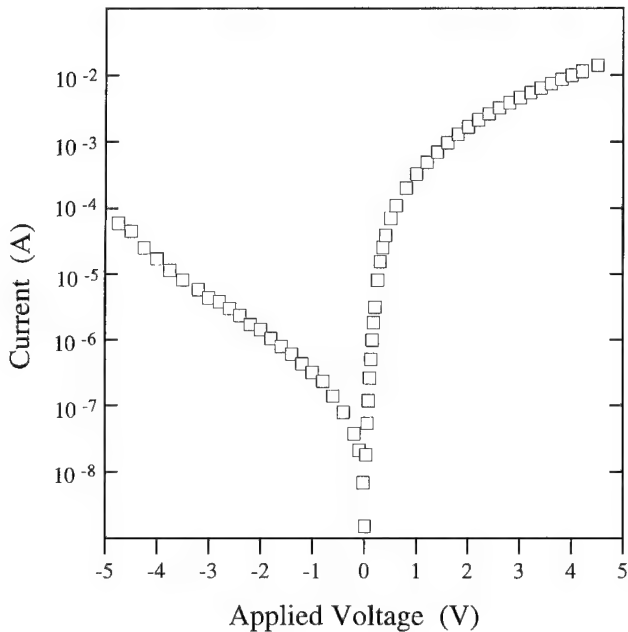


Fig. 1. Current–voltage characteristics of a (n) a-Si_{1-x}C_x:H–(p) c-Si heterojunction diode measured at room temperature.

regions. In the low forward voltage region, the behaviour can be described by an exponential function. However, at higher forward biases, a non-negligible part of the applied voltage falls in the quasi-neutral bulk region of the a-Si_{1-x}C_x layer and the characteristic deviates from exponential behaviour.

Hence, at forward bias and low current (<0.4 V) the relationship between the current and the applied voltage can be written as:

$$I = I_o \left[\exp\left(\frac{qV}{\eta kT}\right) - 1 \right], \quad (1)$$

where I_o is the saturation current, k is Boltzmann's constant, T is the absolute temperature, q is the electron charge and η is the ideality factor. The values of the ideality factor and the saturation current obtained in this low-voltage region are $\eta=1.3$ and $I_o=6.3 \times 10^{-9}$ A. This value of η may correspond to a recombination mechanism in the amorphous side of the space charge region if there is a trap distribution with a high density of tail states [6]. Comparable results have been reported by other authors in similar structures: Magafas et al. [7] proposed that recombination is the dominant transport mechanism in a-SiC–c-Si (*p*) heterojunctions and Rahman et al. [8] explained the low bias range *I*–*V* characteristic in a-SiC (*p*⁺)–c-Si (*n*) heterostructures at low temperature through recombination and tunnelling mechanisms.

Fig. 2 shows the forward current characteristic on a log–log scale. As can be seen, at high voltages ($V>0.4$), the current increases superlinearly, which suggests that the current was not limited by the resistance of the a-Si_{1-x}C_x:H layer. This superlinear or power-law depen-

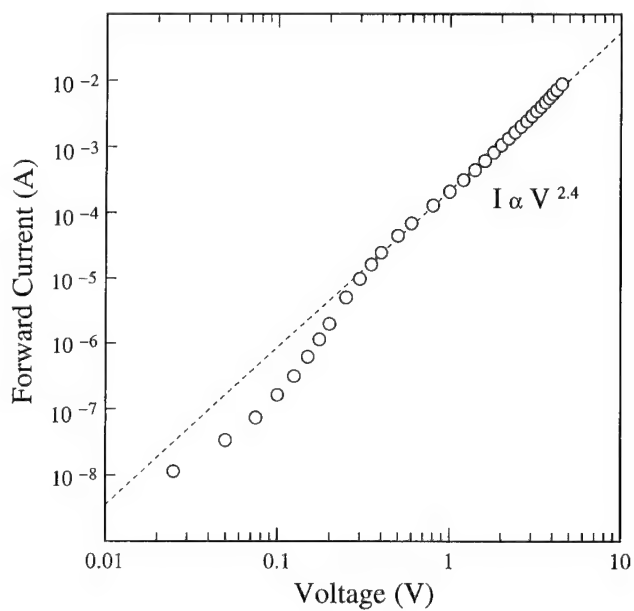


Fig. 2. Forward current characteristic on a log–log scale of an (n) a-Si_{1-x}C_x:H–(p) c-Si heterojunction diode.

dence between current and voltage is characteristic of space-charge limited currents (SCLC) [5]. When the carriers injected into the $a\text{-Si}_{1-x}\text{C}_x\text{:H}$ layer are enough to significantly displace the Fermi level from its equilibrium position ($>kT$), the current increases superlinearly. In these conditions the current–voltage relationship is given by:

$$I = KV^m \quad (2)$$

where m depends on the density of states in the $a\text{-Si}_{1-x}\text{C}_x\text{:H}$ bandgap and K depends on film thickness, trap distribution and conductivity. The values obtained by fitting in this region are: $m=2.4$ and $K=1.9 \times 10^{-4} \text{ A V}^{-2.4}$.

As can be seen in Fig. 1, the reverse characteristics show higher currents than those expected for a mechanism of generation in the depletion region. Given the structural disorder in the amorphous- $\text{Si}_{1-x}\text{C}_x$, two possible current transport mechanisms are considered: a multi-step tunnelling of holes from the silicon valence band into the $a\text{-SiC}$ conduction band via the bandgap states [9] and a Zener-type tunnelling of holes from the Si valence band into the $a\text{-Si}_{1-x}\text{C}_x$ conduction band [10].

So, assuming the band gap states exist, the reverse current can be expressed as [9]:

$$I_r = -ABN_t V_r \exp[-DWE_r^{3/2}(V_d - V_r)^{-1/2}], \quad (3)$$

where A is the area, N_t is the density of available states in the depletion region, E_r is the tunnelling barrier for each step, W is the number of steps required to traverse the entire energy barrier, V_d is the diffusion voltage, and B and D are constants. However, the reverse characteristic behaves quite differently. Fig. 3(a and b) shows the reverse characteristic at low and high voltages, respectively. This experimental current–voltage characteristic can be fitted better by the following empirical relationship:

$$I_r \propto -V_r \exp(-CV_r), \quad (4)$$

where C is a constant. Eq. (4) is an agreement with Eq. (3) if the average barrier E_r is a function of the electric field. This seems physically reasonable; however, the functional variation required is complex.

3.2. Space charge limited current: density of states

The existence of applied voltages over 0.4 V of space charge limited currents in these heterojunctions enables this device to be used as a test structure for a first-order measurement of the density of states. The density of states distribution for n -type $a\text{-Si}_{1-x}\text{C}_x\text{:H}$ has been obtained by the differential method of Nespurek and Sworoski [11]. This method, although it is approximate and leads only to a qualitative estimation of $g(E)$ above the Fermi level, requires only the current–voltage

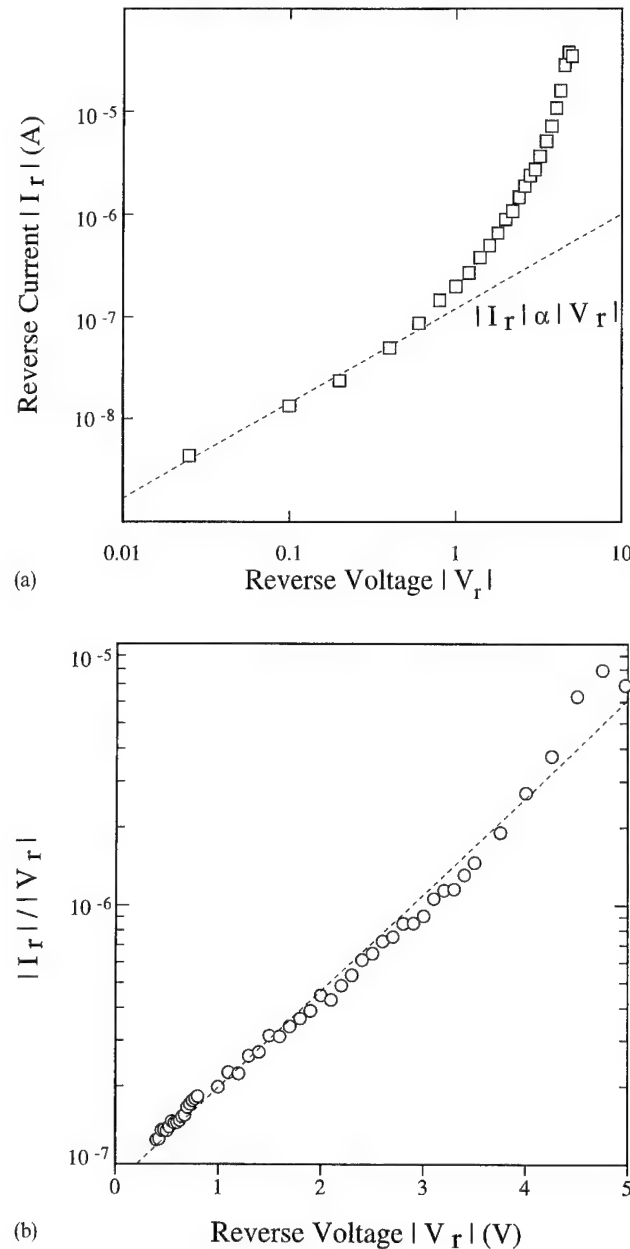


Fig. 3. (a) Logarithmic plot of the reverse current–voltage curve; (b) semi-logarithmic plot of the reverse $|I_r/V_r|$ versus voltage curve.

characteristic to be known, a measurement that is routinely carried out in device characterization.

The Fermi level shift relative to the conduction band, due to the applied voltage, is given by [11]:

$$E_c - E_{fn} = kT \ln \left(\frac{qAN_c\mu_c\chi_1 V}{IL} \right), \quad (5)$$

where E_c is the conduction band edge, N_c is the effective density of states at the conduction band, L is the sample thickness, μ_c is the mobility and χ_1 is a constant which lies between 1 and 2 and that takes into account the non-uniformities of the carrier density within the film.

The density of localized states is given by [11]:

$$g(E_{\text{fm}}) = \chi_2 \frac{\epsilon\epsilon_0}{qL^2 kT} \frac{V}{m-1}, \quad (6)$$

where $\epsilon\epsilon_0$ is the dielectric constant of the a-Si_{1-x}C_x:H, χ_2 is a constant which lies between 0.5 and 1 and takes into account the non-uniformities of the internal field, and m is the voltage dependent slope of the $I-V$ curve. The experimental dark forward log(I)-log(V) data were fitted to a polynomial function and m was obtained by direct differentiation of this function, $m=d(\ln I)/d(\ln V)$. The states distribution $g(E)$ versus $E-E_c$ for n -type a-Si_{1-x}C_x:H obtained from SCLC measurements is shown in Fig. 4. In the same Fig. 4, the results are compared with the density of states for a-Si:H-c-Si heterojunction determined by SCLC [12]. The results confirm the increase in localized states when approaching the conduction band edge. The shallow states, constituting the conduction band tail, increase in density upon carbon alloying. However, the slopes of the distribution (kT_c) do not significantly change over the range of the scanned energies. The results are in agreement with recent published results: Bayley et al. [13], who found $kT_c \approx 22-67$ meV for the same range of the scanned energies in a-Si_{1-x}C_x:H glow-discharge films through transient photocurrent decay measurements.

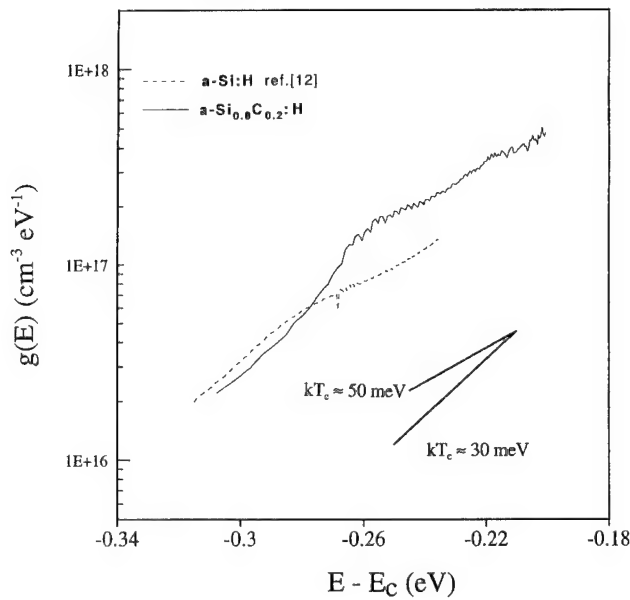


Fig. 4. Comparison between bulk density of states profile versus $E-E_c$ for (n) a-Si_{1-x}C_x:H-(p) c-Si and (n) a-Si:H(p) c-Si.

4. Conclusions

This paper discusses the manufacture of n -type a-Si_{1-x}C_x:H- p -type Si heterojunction diodes using PECVD deposition process. The electrical properties were investigated by measuring their current-voltage characteristics. The forward current was characterized in two different bias range: at low bias voltage, the current is probably dominated by recombination in the space charge region; at high bias voltage the current becomes space charge limited. The reverse characteristics show a leakage current and it can be described by multi-step tunnelling-recombination mechanisms. The results show that there is an increase in localized states when approaching the conduction band edge.

Acknowledgement

This work was partially supported by the Comisión Interministerial de Ciencia y Tecnología (CICYT) program No. TIC96-1058.

References

- [1] S.P. Lau, J.M. Marshall, T.E. Dyer, A.R. Hepburn, J.F. Davies, J. Non-Cryst. Solids 164-166 (1993) 813.
- [2] K. Sasaki, M.M. Rahman, S. Furukawa, IEEE Electron. Devices Lett. 6 (1985) 311.
- [3] A. Madan, P.G. LeComber, W.E. Spear, J. Non-Cryst. Solids 20 (1976) 239.
- [4] D.V. Lang, J.D. Cohen, J.P. Harbison, Phys. Rev. B 25 (1982) 5285.
- [5] Murray A. Lampert and Peter Mark, Current Injection In Solids, Academic Press, New York, 1970.
- [6] J. Pallarès, L.F. Marsal, X. Correig, J. Calderer, R. Alcubilla, Solid State Electron. 41 (1997) 17.
- [7] L. Magafas, N. Georgoulas, A. Thanailakis, Semiconductor Sci. Technol. 7 (1992) 1363.
- [8] M.M. Rahman, C.Y. Yang, D. Sugarto, A.S. Byrne, M. Ju, K. Tran, K.H. Lui, T. Asano, W.F. Stickle, J. Appl. Phys. 67 (1990) 7065.
- [9] A.R. Riben, D.L. Feucht, Int. J. Electron. 20 (1966) 583.
- [10] A.R. Riben, D.L. Feucht, Solid State Electron. 9 (1966) 1055.
- [11] S. Nespurek, J. Swaroski, J. Appl. Phys. 51 (1980) 2098.
- [12] L.F. Marsal, J. Pallarès, X. Correig, J. Calderer, R. Alcubilla, Proceedings of the 18th IEEE International Semiconductor Conference, CAS'95, Sinaia, Romania, 1995, p. 111.
- [13] P.A. Bayley, J.M. Marshall, C. Main, D.P. Webb, R.A.C.M.M. Van Swaaij, J. Bezemer, J. Non-Cryst. Solids 198-200 (1996) 161.

Effects of thermal and laser annealing on silicon carbide nanopowder produced in radio frequency glow discharge

G. Viera *, S.N. Sharma, J. Costa, R.Q. Zhang, J.L. Andújar, E. Bertran

LFCF, Departament de Física Aplicada i Electrònica, Universitat de Barcelona. Av. Diagonal 647, E08028 Barcelona, Spain

Abstract

Hydrogenated SiC nanoparticles of high purity have been produced in radio frequency (RF) glow discharges from silane and methane gas mixtures. These nanoparticles show high surface reactivity and can undergo spontaneous oxidation when exposed to the atmosphere. In order to analyze the chemical stability of SiC particles, we present a study of the structural, chemical and compositional modifications induced by thermal annealing at different temperatures (400, 600 and 800 °C). The post-treated powder was analyzed by RAMAN, FTIR and XPS spectroscopy. The effects of the thermal annealing of SiC powder include: change of colour from yellow to dark brown; hydrogen desorption; and an increase in C–C and Si–C bonds in detriment to Si–Si bonds. In addition, annealing with a KrF excimer laser induced the presence of Si and SiC nanocrystallites. © 1997 Elsevier Science S.A.

Keywords: Glow discharge; Nanoparticles; Thermal annealing; Silicon carbide; Laser annealing; Powder

1. Introduction

Nanometric SiC powder is a promising raw material for advanced ceramic engineering due to its high melting point [1]. The materials sintered from SiC powder exhibit new mechanical properties such as superplasticity [2] and high strength at high temperatures [3]. Moreover, nanoscale filters or the support for a catalytic surface might be interesting applications of the SiC nanopowder.

Low pressure (<1 torr) and low temperature RF plasmas (or plasma-enhanced chemical vapour deposition, PECVD) of methane and silane gas mixtures are claimed to be a suitable source of silicon carbide nanoparticles [4,5]. This technique has already been used in our laboratory to produce ultrafine silicon particles [6–8]. A review of other preparation methods can be found in Ref. [1]. The PECVD technique allows an easy control of the size distribution, composition and structure through the variation of process parameters (pressure, gas flow, RF power density and RF power modulation).

The nanometric size (20–80 nm) and the high hydrogen content of SiC particles produced in RF glow discharge has been previously reported [4,5].

Furthermore, spectroscopic studies showed that: (1) the hydrogen atoms are bonded to carbon atoms rather than to silicon [4]; and (2) the optical gap decreases as the silicon content increases [4]. One problem related to PECVD nanometric powders is their chemical stability [5]. In this paper, an intensive study of the effects of thermal and laser annealing on the structural properties of the SiC nanometric powder and on their chemical activity is presented. The powder was prepared rich in silicon in order to monitor better the evolution of Si–O and Si–Si bonds. We evaluated the induced changes by diverse structural and vibrational characterization techniques (TEM, FTIR, XPS and Raman). The properties of our nanometric powders were compared with those of standard β -SiC micrometric powder.

2. Experimental

The nanoparticles were produced in a capacitively-coupled RF PECVD reactor [8] by glow discharge decomposition of methane and silane mixtures at room temperature. The RF power source operated at 13.56 MHz and was modulated externally by a square-wave generator at 200 mHz with a duty cycle of 50%. The averaged power absorbed in the discharge,

* Corresponding author.

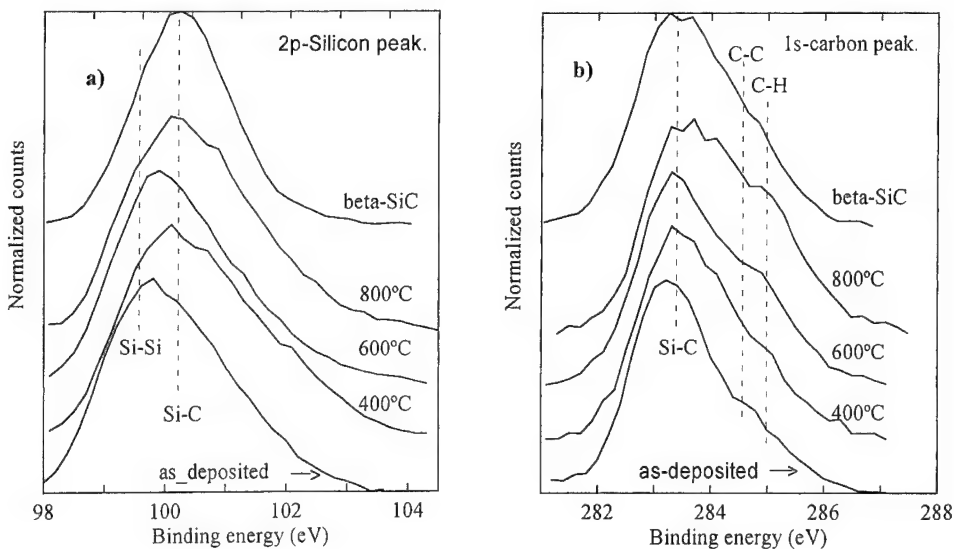


Fig. 1. XPS spectra of C(1s) (a) and Si(2p) (b) core-levels of $\text{Si}_{0.63}\text{C}_{0.37}$ powder at different annealing temperatures and β -SiC powder.

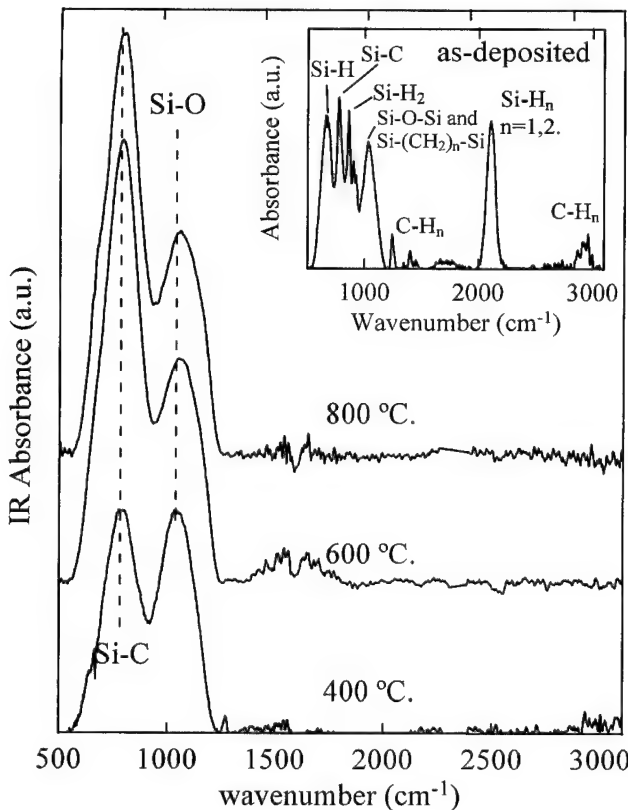


Fig. 2. Infrared vibrational spectra of $\text{Si}_{0.63}\text{C}_{0.37}$ powder at different annealing temperatures. The spectra have been normalized to the Si-O peak area, which is considered constant since the thermal annealing was performed in vacuum conditions (10^{-4} Pa). The inset in the figure corresponds to IR spectra of as-deposited $\text{Si}_{0.63}\text{C}_{0.37}$ powder.

calculated via the subtractive method [9], was around 58 W (145 mW cm^{-2}). In order to produce silicon-rich powder, the relative gas flow fraction of silane,

$R = [\text{SiH}_4]/([\text{SiH}_4] + [\text{CH}_4])$, was fixed at 0.4 and the pressure was kept constant at 40 Pa [4,5].

The as-deposited samples were annealed rapidly ($\sim 250 \text{ }^{\circ}\text{C min}^{-1}$) to 400, 600 and 800 °C in a vacuum chamber at 10^{-4} Pa, where the temperature was then held for a further 30 min. In addition, they were treated with a pulsed KrF excimer laser.

Electron microscopy images and electron diffraction patterns were obtained with a Philips CM30 microscope operating at 300 kV. The vibrational analysis was carried out on an FTIR Nicolet 5ZDX in the spectral wavenumber range $400\text{--}4000 \text{ cm}^{-1}$. Micro-RAMAN back-scattering measurements were performed with the 488 nm line of an Ar laser. XPS analysis was performed using a Perkin-Elmer PHI 5500 ESCA system, with the K- α line of Al (1486.6 eV) as the monochromatic X-ray source.

3. Results and discussion

The Si(2p) (a) and C(1s) (b) XPS curves for silicon rich $\text{Si}_{0.63}\text{C}_{0.37}$ nanometric (composition estimated by this technique) and β -SiC micrometric powders are shown in Fig. 1. For our as-deposited powder, the spectrum is an envelope of XPS peaks arising from silicon bonded to silicon at 99.4 eV and to carbon at 100.2 eV [10]. With the increase in annealing temperature from 400 to 800 °C, the Si(2p) XPS curves show a slight increase in the binding energy as compared with unannealed powders. This can be attributed to the increment in Si-C/Si-Si bonds owing to a change in the chemical environment of the Si atoms from a carbon-free environment to a carbon-containing environment. In the C(1s) XPS spectra, there are contributions from

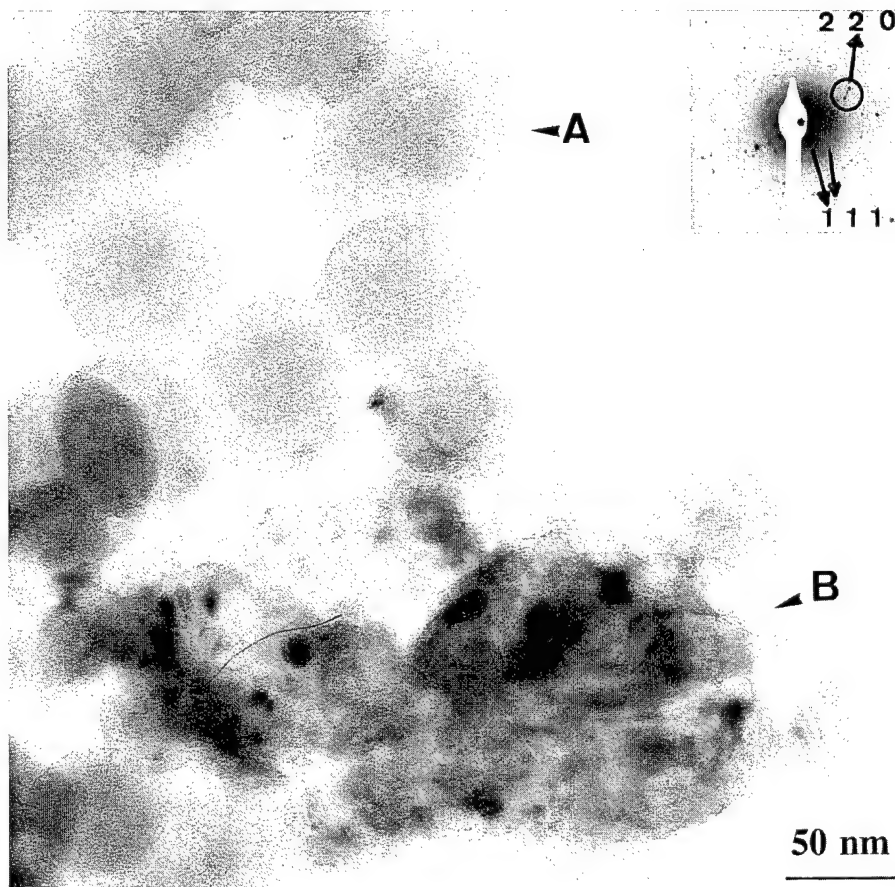


Fig. 3. TEM image of as-deposited SiC powder (A) and powder crystallized with a pulsed KrF excimer laser (B). The inset shows the electron diffraction pattern corresponding to the crystallized powder.

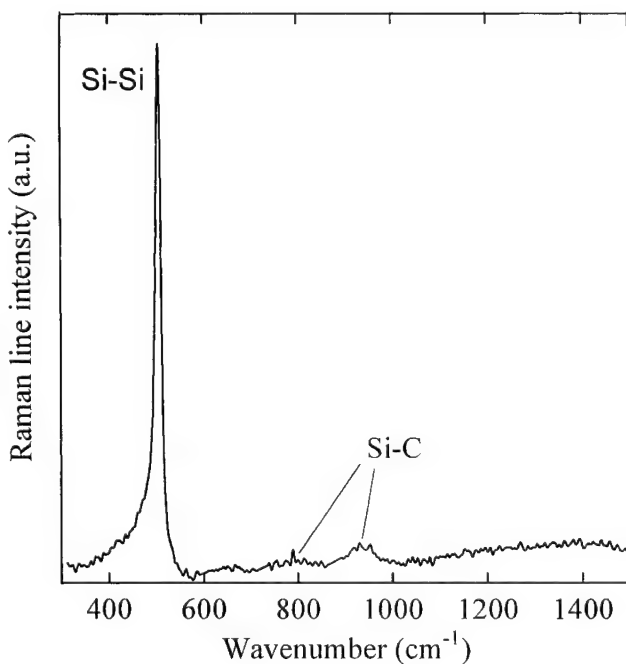


Fig. 4. Raman spectrum of KrF excimer laser annealed $\text{Si}_{0.63} \text{C}_{0.37}$ powder. The laser power density on the sample was $2.4 \text{ mW } \mu\text{m}^{-2}$.

Si–C, C–C and C–H species corresponding to binding energies of 283.2, 284.6 and 285 eV, respectively [11]. As the annealing temperature is raised from 400 to 800 °C, the shift of the C(1s) XPS curves towards higher binding energy points to the predominant formation of C–C bonds. The increment in both C–C and Si–C bonds with the increase in annealing temperature could be a result of hydrogen evolution due to the breaking of Si–H and C–H related bonds. The reduction in Si–Si bonds and the increase in C–C bonds with increase in annealing temperature is in agreement with earlier reports, where carbon clusters have been found to replace Si–Si bonds since the C–C–C nearest neighbour distance is 4.12 Å in diamond and 4.26 Å in graphite, which matches with the Si–Si bond length of 3.8 Å in crystalline Si [12]. Thus, in order to increase the number density of SiC bonds over C–C bonds, higher annealing temperatures (>1000 °C) are required [11].

From both Si(2p) and C(1s) XPS curves, the structure of our annealed powders was found to resemble standard β -SiC powders, as evident from their similar peak positions, thus indicating similar chemical environments.

The infrared (IR) vibrational spectra corresponding to $\text{Si}_{0.63} \text{C}_{0.37}$ powders at different annealing temper-

atures are shown in Fig. 2. The spectra have been normalized to the Si–O peak area, which is supposed to be constant since the powder was annealed in a vacuum chamber at a low pressure at 10^{-4} Pa. This supposition was supported by O(1s) XPS measurements. The inset in the figure represents the IR spectra of as-deposited $\text{Si}_{0.63}\text{C}_{0.37}$ powders, which show the usual IR features of hydrogenated silicon–carbon alloy thin films [13]. The stretching band of silicon–hydrogen modes appeared at 2100 cm^{-1} , their SiH_2 bending vibrations at $\sim 900\text{ cm}^{-1}$, and their SiH wagging modes at $\sim 650\text{ cm}^{-1}$. A band around 775 cm^{-1} suggested the presence of Si–C modes [14] or SiCH_3 [13] wagging modes. The peak at 1040 cm^{-1} could be due to an envelope of Si–CH_n [10], Si–O–Si [16] and Si–O–C [15] vibrations. The peaks at 870 and at 930 cm^{-1} can be identified as $\text{O}_3\text{–SiH}$ and $\text{O}_2\text{–SiH}_2$ bending vibrations, respectively [16]. For the C–H absorption bands, the peaks at $\sim 1400\text{ cm}^{-1}$ and between 2800 and 3000 cm^{-1} correspond to CH_n bending vibrations and stretching vibrations, respectively.

In the IR spectrum of Fig. 2, corresponding to an annealing temperature of $400\text{ }^\circ\text{C}$, SiH stretching vibrations were found to be absent and only weak signals of C–H vibrations can be observed, which vanish at higher temperatures ($>400\text{ }^\circ\text{C}$); this is related to the fact that the C–H bond has a higher heat of formation than the Si–H bond [4]. The absorption at 1038 cm^{-1} at $400\text{ }^\circ\text{C}$ could be due to an enhancement of the $\text{Si}(\text{CH}_2)_n\text{Si}$ groups as a consequence of the breaking of Si–H bonds or it could also be associated with Si–O related modes owing to the oxidation from residual gas in the reactor (H_2O). Between 400 and $600\text{ }^\circ\text{C}$, a different structural change was observed due to the complete breaking of C–H bonds, leading to an enhancement of the number of Si–C bonds. Moreover, beyond $600\text{ }^\circ\text{C}$, no appreciable change in the number density of SiC/SiO bonds could be observed.

As shown in Fig. 2, with increase in annealing temperature, the positions of the silicon–carbon and silicon–oxygen related modes are found to shift to higher wavenumbers, i.e. from 775 and 1022 cm^{-1} at room temperature, to 781 and 1038 cm^{-1} at $400\text{ }^\circ\text{C}$, to 788 and 1047 cm^{-1} at $600\text{ }^\circ\text{C}$, and to 797 and 1051 cm^{-1} at $800\text{ }^\circ\text{C}$, respectively. This is due to the different interactions of the Si–C oscillator with its surroundings [17] and due to the change in the oxidation state of silicon [11], respectively, with the increase in annealing temperature.

TEM studies revealed that thermal treatments up to $800\text{ }^\circ\text{C}$ do not apparently produce changes in size and shape of the powder. In order to crystallize the powder, a pulsed KrF excimer laser was used. Fig. 3 shows a TEM image of amorphous and spherical as-deposited powder and sinterized crystallized powder. The inset shows the electron diffraction pattern of the crystallized

portion, which contains individual diffraction spots from Si and SiC crystals. HRTEM images revealed the presence of Si and SiC crystalline domains around of 20 nm . In addition, the Raman spectrum of crystallized $\text{Si}_{0.63}\text{C}_{0.37}$ powder (Fig. 4), shows the Si–Si crystalline mode at 508 cm^{-1} with contributions from Si–C at 790 and 970 cm^{-1} [17]. The difference between the Si and SiC peak intensities can be related to the higher silicon content of this powder and to the higher Raman efficiency of the Si bonds over the SiC bonds.

4. Conclusions

Silicon-rich SiC nanometric powder was produced at room temperature from methane and silane gas mixtures in a capacitively-coupled RF plasma reactor. The IR studies at higher annealing temperatures indicated the enhancement in the number of Si–C bonds with concurrent development of higher oxidation states of silicon. XPS studies at higher annealing temperatures showed the dominance of mainly C–C and Si–C bonds and a decrease in Si–Si bonds. TEM micrographs and electron diffraction pattern of Si-rich powder upon laser annealing showed the presence of Si and SiC nanocrystals.

Acknowledgement

The authors thank the Serveis Científico-Tècnics of the Universitat de Barcelona for the TEM, XPS and Raman measurements, and the group of our laboratory, Capas Finas y Dispositivos Superconductores, for the use of the pulsed KrF excimer laser. This work was partially supported by the BRITE-EURAM programme of the European Community and by the CICYT of the Ministerio de Educación y Ciencia of Spain.

References

- [1] R.A. Andrievski, J. Mater. Sci. 29 (1994) 614.
- [2] P. Greil, G. Petzow, H. Tanaka, Ceramics Int. 13 (1987) 19.
- [3] J.W. Chen, L.A. Xue, J. Am. Ceramic Soc. 73 (1994) 421.
- [4] E. Bertran, J. Costa, G. Viera, R.Q. Zhang, J. Vacuum Sci. Technol. A 14 (1996) 567.
- [5] J. Costa, G. Viera, R.Q. Zhang, J.L. Andújar, E. Pascual, E. Bertran, Mater. Res. Soc. Symp. Proc. 410 (1996) 173.
- [6] E. Bertran, J. Costa, G. Sardin, J. Campmany, J.L. Andújar, A. Canillas, Plasma Sources Sci. Technol. 3 (1994) 348.
- [7] P. Roura, J. Costa, G. Sardin, J.R. Morante, E. Bertran, Phys. Rev. B 50 (1994) 18124.
- [8] J. Costa, G. Sardin, J. Campmany, E. Bertran, Vacuum 45 (1994) 1117.
- [9] C.M. Horwitz, J. Vacuum Sci. Technol. A 1 (1983) 1795.
- [10] E. Gat, M.A. El Klakani, M. Charker, A. Jean, S. Boily, H. Pépin, J.C. Kieffer, J. Durand, B. Cros, F. Rousseau, S. Gujrathi, J. Mater. Res. 7 (1992) 2478.

- [11] E. Bouillon, F. Langlais, R. Pailler, R. Naslain, F. Cruge, J.C. Sarthou, A. Delpuech, C. Laffon, P. Lagarde, M. Monthoux, A. Oberlin, *J. Mater. Sci.* 26 (1991) 1333.
- [12] Y. Katayama, K. Usami, T. Shimada, *Phil. Mag.* 43 (1981) 283.
- [13] H. Wieder, M. Cardona, R.C. Guarniv, *Phys. Stat. Sol.* 92 (1979) 99.
- [14] Y. Catherine, G. Turban, *Thin Solid Films* 70 (1980) 101.
- [15] D.S. Kim, Y.H. Lee, *Thin Sol. Films* 26 (1995) 192.
- [16] D.V. Tsu, G. Lucovsky, B.N. Davidson, *Phys. Rev. B* 40 (1989) 1795.
- [17] B. Pivac, K. Furio, M. Milun, T. Valla, A. Borghesi, A. Sassella, *J. Appl. Phys.* 75 (1994) 3586.

Emission and excitation spectra of silicon-related luminescent centers in CVD-grown diamond films

M.C. Rossi ^{a,*}, S. Salvatori ^a, F. Galluzzi ^a, R.M. Montereali ^b, F. Somma ^c

^a Third University of Rome, Department of Electronic Engineering, Via Vasca Navale 84, 00146 Rome, Italy

^b ENEA, Dipartimento Innovazione, CR Frascati, PO Box 65, 00044 Frascati, (RM), Italy

^c Third University of Rome, Department of Physics, Via Vasca Navale 84, 00146 Rome, Italy

Abstract

Luminescence properties of silicon-related centers in CVD-grown diamond films and their spatial distribution along the growth direction have been investigated. It is found that the lineshape and peak position of the emission band depend both on excitation energy and light focalization depth, suggesting the coexistence of two optical centers related to isolated vacancies and to silicon-vacancy complexes. A simple model of the electronic structure of this defect is proposed. © 1997 Elsevier Science S.A.

Keywords: CVD diamond; Photoluminescence; Defect centers

1. Introduction

The understanding of nucleation processes in CVD diamond films grown on silicon is a key factor for controlling material quality and its applications. Actually, the carbon–silicon interface region is strongly defected owing to both silicon surface pretreatments and interdiffusion processes [1,2]. In order to understand the interactions between Si and C during the diamond growth, a detailed investigation on Si-related defects is here reported based on photoluminescence (PL) and Raman spectroscopies. Both techniques represent powerful tools for polycrystalline diamond characterization, the former giving information on the structure and the distribution of defects [3], the latter giving insight into crystalline quality and residual stress [4].

2. Experimental

Polycrystalline diamond films have been grown by hot filament chemical vapor deposition (HFCVD) on *p*-type ⟨100⟩ oriented Si substrates. Details on the growth conditions can be found elsewhere [5]. Emission spectra were measured at room temperature and at 77 K using excitation by different lines from He–Ne, Ar⁺ and

dye lasers. Spectra were analyzed by a 1681 SPEX monochromator using 1200 lines mm⁻¹ gratings in first order and detected by a cooled RCA 7102 photomultiplier. Raman spectra, excited at 633 nm, were recorded at room temperature by a DIOR system with microfocusing optics.

3. Results and discussion

A typical PL spectrum excited at 457 nm is reported in Fig. 1. The main feature is a strong zero phonon band at about 1.68 eV and its vibronic structure, in particular one- and two-phonon replicas, located at 1.62 and 1.56 eV, respectively. From a standard fitting procedure, a Huang–Rhys factor of about 0.1 was deduced, indicating a weak electron–phonon coupling, in agreement with previous works [6]. In addition to the 1.68 eV band, PL spectra also show a featureless broad emission (see Fig. 1), which can be related to amorphous carbon phases. Lineshape and peak position of the 1.68 eV emission band depend on the excitation wavelength, as it is shown in Fig. 2(a and b). At variance with previous results [7], from the deconvolution of the emission band, two distinct components were found, a Lorentzian line peaked at 1.673 with a linewidth $W = 8$ meV, and a gaussian line peaked at 1.681 eV with

* Corresponding author.

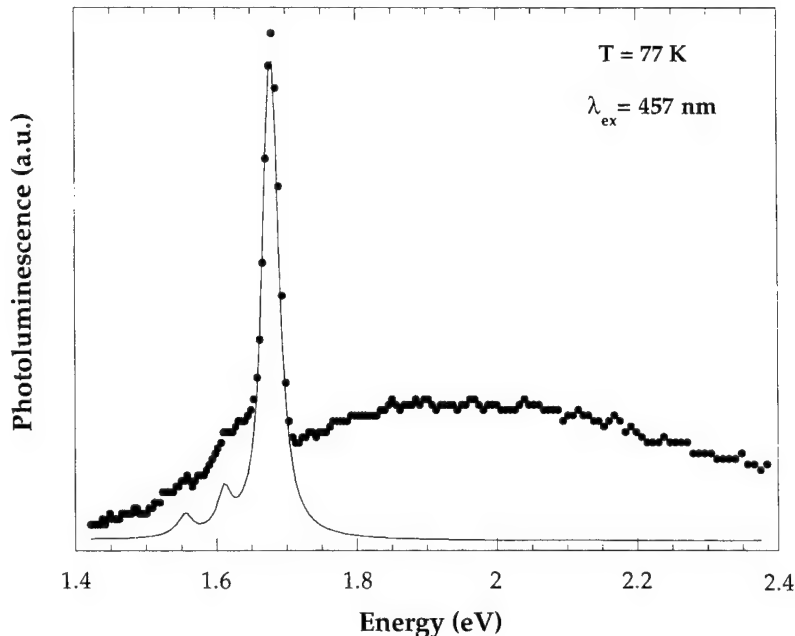


Fig. 1. Photoluminescence spectrum for CVD-grown diamond film (dots). Continuous line represents a best fit for PL data subtracted off background (see text for details).

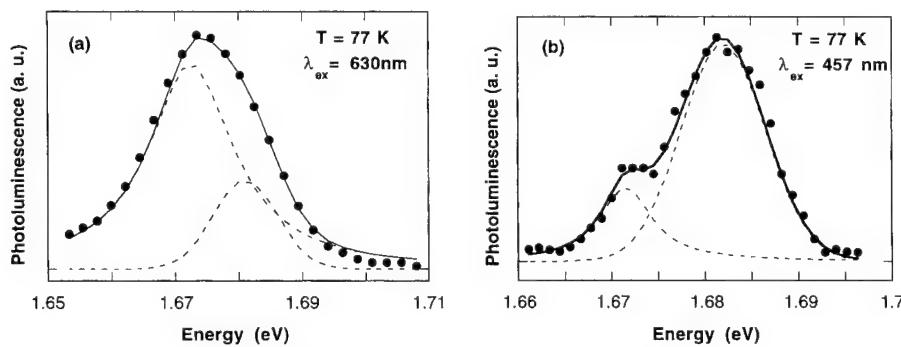


Fig. 2. Lineshapes of the emission band at different excitation wavelengths: (a) 630 nm; (b) 457 nm. The dotted lines represent deconvolution of spectral data with a lorentzian component peaked at 1.672 eV and with a gaussian component peaked at 1.681 eV.

$W=5$ meV. Peak energies of the two components are very close to the position of two phonon lines frequently reported in the literature and attributed to isolated carbon vacancies (GR1 center at 1.673 eV) [8], and to silicon-vacancy complexes (center at 1.681 eV) [9].

Excitation profiles of these components, measured in the 1.9–2.0 eV (dye laser excitation) and 2.5–2.7 eV (Ar^+ laser excitation) ranges, are shown in Fig. 3. Their behavior is very similar in both excitation ranges, exhibiting a sharp resonant enhancement in the red region and a monotonic decrease in the blue region. This fact suggests a very similar electronic configuration for the two centers.

The observed sharp resonance in the excitation spectra can be attributed to the presence of a second excited state, about 0.3 eV higher than the first excited state at 1.68 eV. These transition energies appear to be in fair

agreement with energies calculated for a simple hydrogenic center, having an ionization energy of about 2.2–2.3 eV, as sketched in Fig. 4. According to this figure, irradiation with 1.7–2.2 eV photon energies induces radiative transitions to bound excited states, which are followed by nonradiative transitions to the lowest-lying excited state, responsible for luminescence. On the other hand, under excitation with photon energies higher than the ionization energy, free carriers are generated, which can be trapped back by the centers, relax to the first excited state and eventually make a radiative transition to the ground state.

The spatial distribution of 1.673 and 1.681 components and their relationship with the film microstructure have been investigated by photoluminescence and Raman measurements at different light focalization depths. Indeed Raman data obtained by focusing the

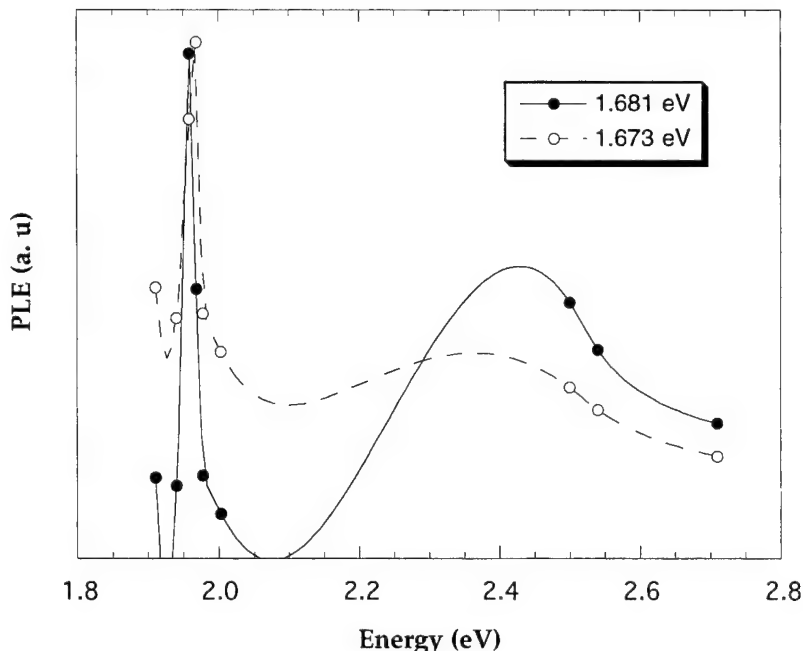


Fig. 3. Photoluminescence excitation spectra for the 1.681 (full dots) and 1.673 eV (open dots) components. Lines are guides for the eyes.

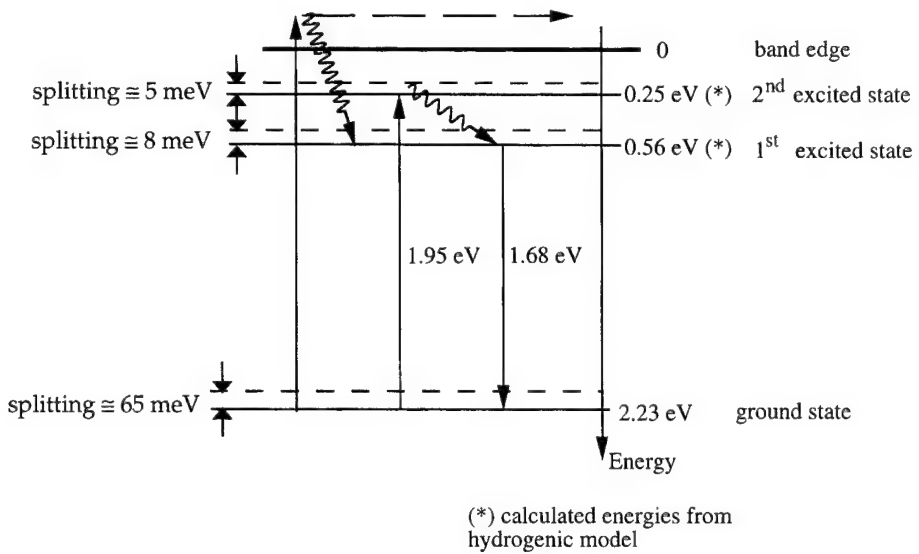


Fig. 4. Schematic representation of electronic energy levels for the 1.681 eV (continuous lines) and for the 1.673 eV (dashed lines) optical centers. For the sake of clarity, electronic transitions are only indicated for the 1.681 eV center.

exciting light on the diamond surface and at the diamond–silicon interface (Fig. 5) show that the diamond peak is sharp at the diamond surface ($\text{FWHM} = 7 \text{ cm}^{-1}$) and becomes broader close to the silicon substrate ($\text{FWHM} = 10 \text{ cm}^{-1}$). This result indicates a poorer microcrystalline quality close to the diamond–silicon interface usually observed during the initial stage of the growth [2]. In addition the Raman peak position exhibits a shift $\Delta\nu = 2 \text{ cm}^{-1}$ towards higher energy, suggesting the existence of internal stress [10].

A similar spatial distribution analysis has been performed for the luminescence emission band located at 1.68 eV. Lineshapes of the 1.68 eV photoluminescence band also depend on light focalization depth, as it is reported in Fig. 6. Light focused on the diamond surface causes an enhancement of the 1.673 eV component related to carbon vacancies while close to the silicon–diamond interface, a major contribution arises from the 1.681 eV component related to silicon-vacancy complexes occurs. These results confirm that silicon im-

Normalized Intensity

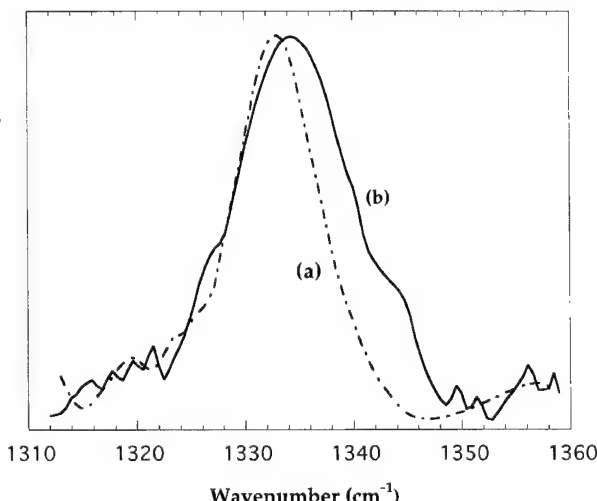


Fig. 5. Diamond Raman peak for different light focalization depths (corresponding to different depths within the film thickness): (a) growth side and (b) silicon–diamond interface.

Normalized Intensity

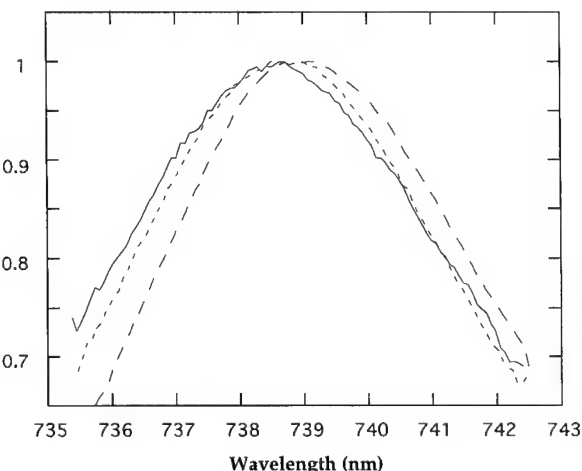


Fig. 6. Lineshapes of the 1.68 eV PL band excited at $\lambda=633$ nm for light focused on the diamond growth side (dashed line), in the middle of the film (dotted line) and close to the silicon–diamond interface.

impurities are preferentially distributed close to the diamond–silicon interface, where small size diamond

grains and large distributions of grain boundaries are expected.

4. Conclusion

Photoluminescence and Raman spectroscopies have been used to study electronic properties and spatial distribution of Si-related defects in polycrystalline diamond films. PL spectra are mainly characterized by a strongly asymmetric emission band, which has been deconvoluted into two lines, whose contribution to the main band depends both on excitation energy and light penetration depth within the film thickness. Quite similar PL excitation spectra have been detected for these two components, suggesting that both emission lines are related to carbon vacancies, either isolated or close to silicon atom impurities. The spatial dependence of PL peak energies and lineshapes reflects the spatial profile of silicon impurities incorporated during the diamond growth.

References

- [1] W.J.P. Van Enckevort, in: H.E. Spear, J.P. Dismukes (Eds.), *Synthetic Diamond: Emerging CVD Science and Technology*, Wiley, New York, 1994.
- [2] W. Zhu in: L.S. Pan, D.R. Kania (eds), *Diamond: Electronic Properties and Applications*, Kluwer, Dordrecht, 1995.
- [3] A.T. Collins, *Diamond Relat. Mater.* 1 (1992) 457.
- [4] P. Ascarelli, E. Cappelli, G. Mattei, F. Pinzari, S. Martelli, *Diamond Relat. Mater.* 4 (1995) 464.
- [5] G. De Cesare, S. Salvatori, R. Vincenzoni, P. Ascarelli, E. Cappelli, F. Pinzari, F. Galluzzi, *Diamond Relat. Mater.* 4 (1995) 628.
- [6] A.T. Collins, L. Allers, C.J.H. Wort, G.A. Scarsbrook, *Diamond Relat. Mater.* 3 (1994) 932.
- [7] L. Bergman, R.J. Nemanich, *J. Appl. Phys.* 78 (1995) 6709.
- [8] A.T. Collins, M. Kamo, Y. Sato, *J. Mater. Res.* 5 (1990) 2507.
- [9] J.A. Freitas, U. Strom, A.T. Collins, *Diamond Relat. Mater.* 2 (1993) 87.
- [10] E. Gheeraert, A. Deneuville, M. Bonnot, L. Abello, *Diamond Relat. Mater.* 1 (1992) 525.

Amorphous $\text{GaAs}_{1-x}\text{N}_x$ thin films on crystalline Si substrates: growth and characterizations

Dave Lollman *, Khalifa Aguir, Benoît Roumiguières, Hervé Carchano

Laboratoire EPCM, Service A62, Faculté des Sciences de Saint Jérôme, Université d'Aix-Marseille III, 13397 Marseille cedex 20, France

Abstract

This work deals with the growth and study of a new nitride in thin films: $\text{GaAs}_{1-x}\text{N}_x$. The material is deposited in its amorphous form on crystalline Si substrates by means of RF sputtering of a GaAs target in an atmosphere of argon and ammonia. Raman spectroscopy used to study the physico-chemical properties of the film structure pointed out that $\text{GaAs}_{1-x}\text{N}_x$ is a wide gap material which is formed by the substitution of arsenic by nitrogen in the GaAs network (J. Bandet, K. Aguir, D. Lollman, A. Fennouh, H. Carchano, *Jpn. J. Appl. Phys.*, 36 (1997) 11).

In order to investigate the electrical properties of $\text{GaAs}_{1-x}\text{N}_x$ in view of potential applications in optoelectronic systems, $J-V$ and $C-V$ characteristics have been performed. $J-V$ results show that the heterostructures exhibit a drastic increase in resistivity with nitrogen incorporation. The conduction passes from a diode-type one for $x=0$ to an approximately symmetrical one with nitridation, i.e. for $x>0$. The films present convenient high resistivity values for insulating character consideration. Furthermore, $C-V$ results obtained present a manifest MIS-like behaviour with however the existence of a flat-band voltage (V_{FB}). © 1997 Elsevier Science S.A.

Keywords: Amorphous III–V semiconductors; $\text{GaAs}_{1-x}\text{N}_x$ thin films; High resistivity; MIS structures

1. Introduction

With the advent of reduced dimensions of very large scale integrated (VLSI) devices, there has been increasing interests in recent years to control the composition of alternate thin film depositions with specific built-in properties. As far as silicon-based devices are concerned, much of the success of this basic semiconductor used is due to the exceptionally opportune properties of the SiO_2/Si interface. The fabrication of thermal SiO_2/Si interfaces has been drastically optimized to give electronically active interface state densities of less than one defect per $10^4\text{--}10^6$ interfacial Si atoms [1]. This small interfacial state density is critical for metal–insulator–semiconductor (MIS) device operation enabling the Fermi level to move throughout the forbidden band gap in order to achieve inversion.

The techniques that have received considerable attention include anodic, thermal or plasma-oxidation and dielectric deposition. Even though some of these techniques have achieved a certain degree of feasibility on

GaAs-based MOSFETs and MISFETs [2], the MOS and MIS properties of these structures are relatively poor. The prime reason for that is due to the mediocre surface electronic properties detained by GaAs. These undesirable properties include high state density, high surface recombination density and pinning of its Fermi level. All of these limit considerably the use of GaAs in VLSI device applications. Aiming at overcoming this barrier, considerable efforts have been undertaken to develop a MOS or MIS technology for GaAs (and other III–IV semiconductors) similar to that of Si. As work progressed, it became apparent that, unlike the SiO_2/Si interface, the chemistry between the III–IV semiconductors and their native oxides do not lead to a chemically stable and defect-free interface.

For these reasons, and in view of investigating the fabrication of a successful integrated MIS structure device, we retained the approach of depositing a high-quality dielectric layer onto the semiconductor surface to act as the gate insulator. As we focused our study, in a first stage, on the insulating layer itself, we have grown amorphous $\text{GaAs}_{1-x}\text{N}_x$ thin films on Si substrates for easy preliminary investigations. The long

* Corresponding author. Tel: 04 91 28 81 53; Fax: 04 91 28 94 03.

term objective would be, of course, a study of MIS structures using GaAs as a substrate.

2. Device fabrication and experimental set-up

The substrates used were Si wafers (p-type) because of their relatively low cost and the high purity of their surface obtained by means of classical chemical processing. The surface oxides and impurities were etched by Shiraki technique [3] prior to film deposition. The cleaning processes, after degreasing in trichloroethylene, acetone and ethanol successively, consisted of a first surface chemical etching in a solution of H_2SO_4/H_2O_2 (1:1), then boiling in pure HNO_3 , and the oxide etched off in a dilute (10%) HF solution.

Thin films of amorphous $GaAs_{1-x}N_x$ (thickness $\approx 5000 \text{ \AA}$) were then grown using a conventional capacitive coupled RF (13.56 MHz) sputtering of a water-cooled polycrystalline GaAs target by means of a plasma mixture of argon and a nitrogen carrier gas (NH_3). The deposition chamber (Fig. 1) is pumped down to high vacuum conditions (approx. $7 \times 10^{-7} \text{ mbar}$) and the partial pressure of NH_3 (P_{NH_3}) is adjusted to the desired value (from 0 to $10 \times 10^{-3} \text{ mbar}$) by means of an MKS capacitive gauge. Argon is then introduced into the chamber through a mass flow controller, bringing the total working pressure to $50 \times 10^{-3} \text{ mbar}$. The gases (supplied by Air Liquide Co.) rated purities of 99.9997%. The RF input power was 25 W corresponding

to a self bias voltage V_{DC} of 600 V. During deposition, the substrate temperature was maintained at 150°C .

In order to fabricate a simple heterojunction diode, an ohmic contact was formed on the back side of the c-Si wafer by evaporating aluminium. Gate contacts were formed by depositing gold discs of $5 \times 10^{-3} \text{ cm}^2$ area, 1000 \AA thick, on the as-deposited a- $GaAs_{1-x}N_x$ films. The Au contacts act as excellent ohmic contacts with a-GaAs [4], and this property has been verified for our a- $GaAs_{1-x}N_x$ films as well in our laboratory.

The $J-V$ characteristics were carried out at room temperature by means of an HP 4140B pico-ampere-meter/d.c.-voltage source and $C-V$ characteristics performed by an HP 4275A.

3. Electrical characterizations

3.1. Current–voltage characteristics

$J-V$ characteristics of the a- $GaAs_{1-x}N_x/c\text{-Si(p)}$ heterojunctions have been performed at room temperature as a function of applied bias voltage in order to study the influence of nitrogen incorporation in the deposited films.

Fig. 2 shows the P_{NH_3} and the voltage dependence of the current density J from which it can be seen that the a- $GaAs_{1-x}N_x/c\text{-Si(p)}$ junctions exhibit a drastic falling off of forward and reverse currents with nitrogen incorporation. The conduction passes from a diode-type

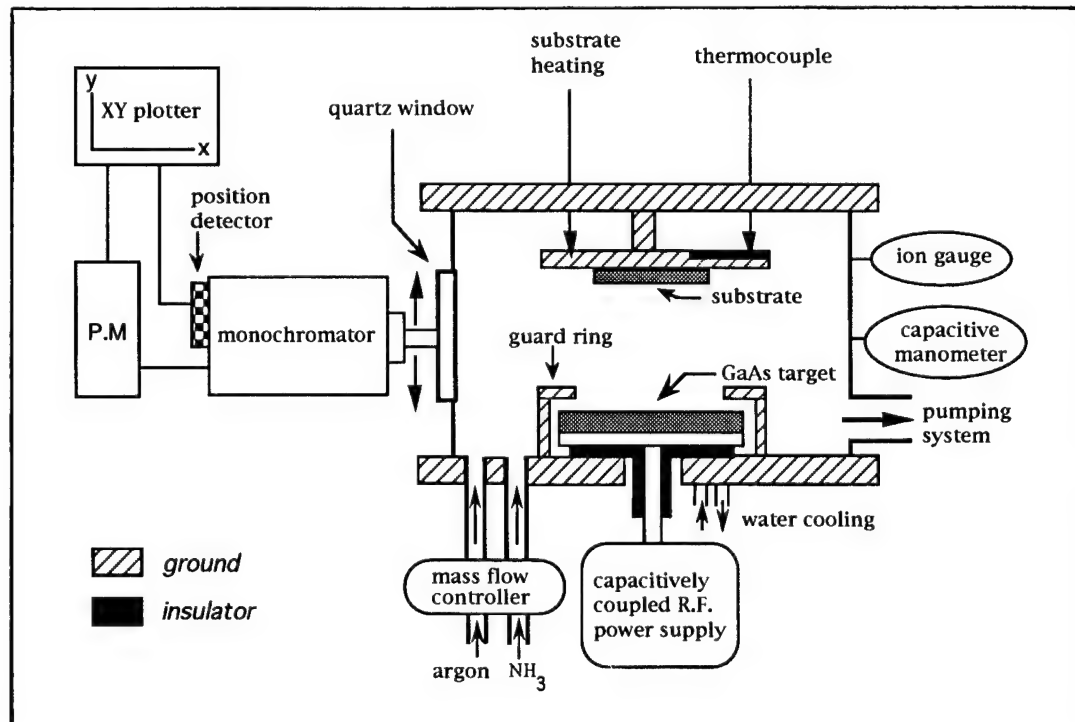


Fig. 1. Experimental set-up for RF sputtering.

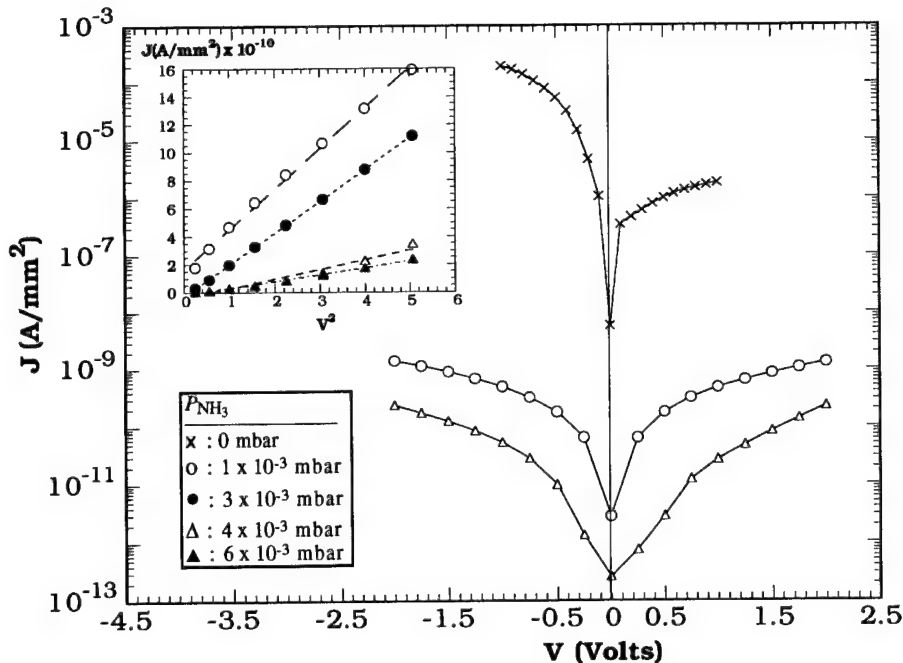


Fig. 2. J - V characteristics as a function of P_{NH_3} for different a-GaAs_{1-x}N_x/c-Si(p) heterostructures. The inset shows the linear relationship between direct current J and V^2 . (Note that current values for zero bias voltage are not significative).

behaviour for $x=0$ (i.e. $P_{\text{NH}_3}=0$ mbar) to an approximately symmetrical one with nitridation. A first analysis [5] of the first curve of Fig. 2 ($P_{\text{NH}_3}=0$ mbar) enabled us to conclude that the transport mechanisms for a-GaAs_{1-x}N_x/c-Si(p) with $x=0$ involve tunneling for forward current while the reverse current may be reasonably ascribed to a generation current.

For the other samples (i.e. for $P_{\text{NH}_3}>0$ mbar), we have taken as evidence the manifest evolution of the J - V characteristics to study the effect of nitrogen incorporation in our films. When P_{NH_3} is increased in the reactor, a rapid decrease in the current densities is observed, and the J - V curves become quasi-symmetrical with respect to the current axis. The symmetry between reverse and forward currents however suggests other conduction phenomena. Various conduction models exist in the literature. The space charge limited current model seems to be the most in agreement with our results. Hence, in the inset of Fig. 2, we have plotted variations of forward current densities as a function of the square of applied bias voltage (V^2). The procedure adopted here is to define a general tendency of all curves towards a single model which would confirm our hypothesis instead of fitting an individual model to each curve. Consider the curves of the inset which illustrate the evolution $J(V^2)$. The symbol dots represent experimental data while the connecting lines, linear "fits".

According to this model, the voltage dependence of the junction current can be expressed as [6]

$$J = \frac{\epsilon_i \mu V^2}{d^3}$$

where ϵ_i is the insulator dielectric permittivity, μ the carrier mobility and d the insulator thickness.

Owing to the symmetrical behaviour exhibited by the samples, the same phenomenon has been found for the reverse current evolution: it seems to be governed by the space charge limited current model as well.

3.2. Capacitance–voltage characteristics

In the absence of nitrogen (i.e. for a-GaAs_{1-x}N_x/c-Si(p) with $x=0$), we have already shown that the capacitance–voltage characteristics indicate that the abrupt heterojunction model is applicable to a-GaAs/c-Si(p) [5]. For samples containing nitrogen (obtained with $P_{\text{NH}_3}>0$ mbar), we present on Fig. 3 the C - V characteristics of four typical samples elaborated with different N concentrations. All measurements have been carried out at the same frequency of 1 MHz.

The comparison of these results to those obtained on a-GaAs/c-Si(p) structure [5] undoubtedly enables us to conclude on the improvement of the dielectric properties due to the presence of nitrogen in the films. Note that it is clearly evidenced that the sample obtained for $P_{\text{NH}_3}=6 \times 10^{-3}$ mbar present a MIS-like characteristic with remarkably marked zones of accumulation, depletion and inversion. Moreover, the rapid slope of the depletion zone of samples in this range of P_{NH_3} predicts a relatively low interface density of states [6].

We can therefore envisage a MIS-type characteristic for samples fabricated with a P_{NH_3} around 6×10^{-3} mbar, where the amorphous compound

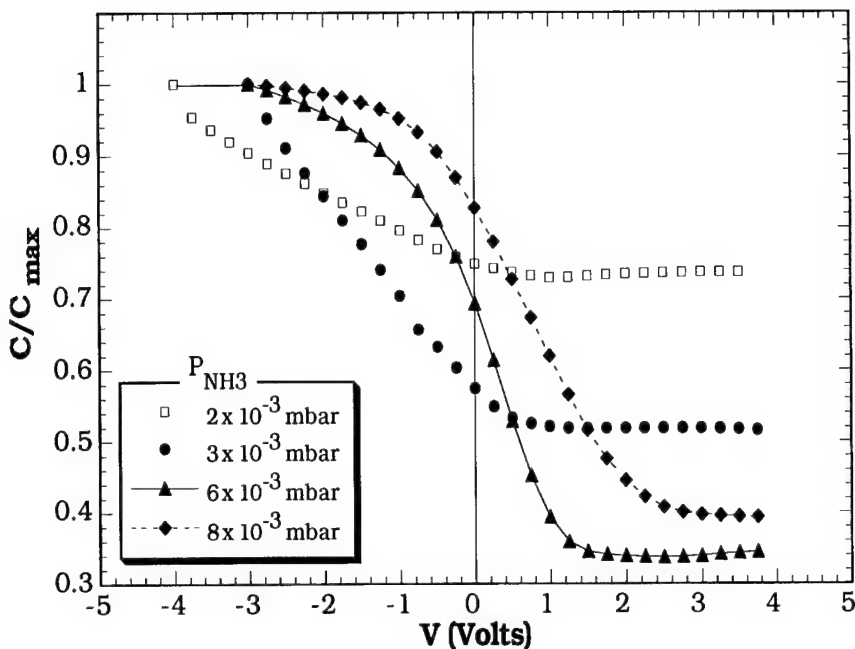


Fig. 3. $C-V$ characteristics of a-GaAs_{1-x}N_x/c-Si(p) heterostructures as a function of P_{NH_3} measured at 1 MHz.

(a-GaAs_{1-x}N_x) would behave like a dielectric layer with high resistivity [7].

4. Conclusion

In conclusion, a-GaAs_{1-x}N_x/c-Si(p) heterojunctions have been successfully fabricated by RF reactive sputtering, and studied electrically by current-voltage and capacitance-voltage measurements.

The current-voltage measurements suggest that the forward current in these junctions when $P_{\text{NH}_3} = 0$ mbar involves multi-tunneling capture-emission for forward current and a generation mechanism for reverse current. For $P_{\text{NH}_3} > 0$ mbar samples (i.e. $x > 0$), the system rapidly tends to a MIS-type behaviour. The hypothesis of a conduction by space charge limited current is proposed.

$C-V$ measurements show a remarkable MIS characteristic for samples fabricated with a P_{NH_3} of around 6×10^{-3} mbar.

References

- [1] J.J. Simonne, J. Buxo, *Insulating Films on Semiconductors*, Elsevier Science, Amsterdam, 1986.
- [2] A. Colquhoun, E. Kohn, H.L. Hartnagel, *IEEE Trans. Electron. Devices* 25 (1978) 375.
- [3] A. Ishizaka, Y. Shiraki, *J. Electrochem. Soc.* 133 (1986) 666.
- [4] K. Aguir, PhD Thesis, Toulouse, France, 1987.
- [5] K. Aguir, A. Fennouh, H. Carchano, J.L. Seguin, B. El Hadadi, F. Lalande, *Thin Solid Films* 257 (1995) 98.
- [6] S.M. Sze, *Physics of Semiconductors Devices*, 2nd Edn., Wiley, New York, 1981.
- [7] K. Aguir, A. Fennouh, H. Carchano, D. Lollman, *J. Phys. III* 5 (1995) 1573.



ELSEVIER

Diamond and Related Materials 6 (1997) 1573-1574

**DIAMOND
AND
RELATED
MATERIALS**

Conference Calendar

Title	Place	Date	Further Information from:
Diamond Films '97	Edinburgh, UK	August 3-8 1997	Ms. Glenda Bland Conference Secretariat 22 Plas Taliessin Portway Village Marina Penarth CF64 1TN Wales United Kingdom Tel: 44 (0) 1222 700053 Fax: 44 (0) 1222 700665 E-mail: enquiries@global.meeting.co.uk
13th International Symposium on Plasma Chemistry	Beijing China	August 14-23 1997	Dr. Lin He The Chinese Society of Theoretical & Applied Mechanics 15 Zhong Guan Cun Road Beijing 100080 China Fax: (86-10) 62559588 E-mail: cstam@sun.ihep.ac.cn
International Conference on Ion Sources (ICIS 97)	Taormina Italy	September 7-13 1997	Dr. Giovanni Ciavola INFN-LNS, Via S. Sofia 44 95123 Catania Italy Tel/fax: 39 95 542300 E-mail: ICIS97@LNS.infn.it
10th International Conference on Surface Modification of Metals by Ion Beams	Gatlinburg, Tennessee, USA	September 21-26 1997	Vicki Barnes Oak Ridge National Laboratory Building 3137, MS-6057 Oak Ridge TN 37831-6057 E-mail: smmib@ornl.gov
Lasers in Synthesis, Characterization and Processing of Diamond	Tashkent Uzbekistan	October 6-9 1997	Dr. Victor Ralchenko General Physics Institute ul. Vavilova 38 117942 Moscow Russia Tel: 7 (095) 132-8229 Fax: 7 (095) 135-3002 E-mail: ralchen@kapella.gpi.ru
24th International thermal Conductivity Conference and 12th International thermal Expansion Symposium	Pittsburgh, PA USA	October 26-29 1997	Peter S. Gaal Conference Chairman Anter Corporation 1700 Universal Road Pittsburgh, PA 15235 Tel: 412 795 6410 Fax: 412 795 8225 E-mail: psg@anter.com Conference home page: http://www.anter.com/conferences

Title	Place	Date	Further Information from:
Gordon Conference on Diamond Synthesis	Queen's College Oxford England	August 23-28 1998	Karen K. Gleason Department of Chemical Engineering Room 66-468 Massachusetts Institute of Technology Cambridge, MA 02139 Tel: 617 253 5066 Fax: 617 258 5042 E-mail: kkgleasn@mit.edu



ELSEVIER

Author Index for Volume 6

Aboelfotoh, M.O., 1388
Achete, C.A., 551
Achtziger, N., 1436
Aebi, P., 282
Afanas'ev, V., 1472
Aguir, K., 1568
Agulló-Rueda, F., 1210
Ahn, J., 48
Akashi, M., 356
Akkerman, Z., 153
Ako, F., 847
Alause, H., 1536
Albrecht, M., 747, 1467
Alcubilla, R., 1555
Aldinger, F., 608
Alexenko, A.E., 89
Allers, L., 353
Allon-Alaluf, M., 555
Alnot, P., 107, 505
Amaratunga, G.A.J., 207, 700
Anagnostopoulos, A., 1226, 1494, 1547
Anderle, M., 559
Ando, T., 1036
Andreyev, A.V., 28
Andújar, J.L., 579, 589, 604, 1550, 1559
Anghel, L., 1226, 1494, 1547
Anikin, M., 1249
Anthony, T.R., 120
Apakina, V.N., 564
Arnault, J.C., 235
Arnodo, C., 1428, 1508
Ashfold, M.N.R., 247, 569, 817, 898
Asif Khan, M., 1536
Aslam, D.M., 394
Asmussen, J., 1097
Aspnes, D.E., 196
Auer, N., 944
Avigal, Y., 381, 526

Babaev, V.G., 89, 640
Babanyan, A.I., 1528
Babina, V.M., 640
Bacon, D., 687
Badzian, A., 130
Bailon, L., 1500
Bakowski, M., 1476
Baldwin, S.K. Jr., 202
Balster, T., 1353
Bano, E., 1489
Baral, B., 374, 869
Baránková, H., 224
Baranov, A.M., 902, 1106
Barbolla, J., 1500
Bardés, D., 1555
Bárdos, L., 224

Barrat, S., 41
Barrett, D.L., 1262
Baruchel, J., 1249
Bassler, M., 1472
Batori, V., 645
Battaile, C.C., 1198
Bauer-Grosse, E., 41
Baumann, P.K., 398, 403
Beardmore, G., 450
Beccard, R., 1301
Bechstedt, F., 1346
Beera, R.A., 430
Behr, D., 654, 1111
Belyavina, N.N., 927
Ben el Mekki, M., 1550
Benko, E., 931, 1192
Bendorf, C., 533, 964
Berberich, S., 1306
Bergman, J.P., 1324
Berg, S., 224
Bernard, C., 1249
Bernhardt, J., 1349
Bertran, E., 589, 1559
Bewick, A., 1135
Bezhenar, N.P., 927
Bielanska, E., 931
Bill, J., 608
Billon, T., 1226, 1494, 1547
Blanquet, E., 1249
Bluet, J.M., 1385, 1463
Bobrov, K., 736
Bodganovic, I., 320
Boettger, E., 298
Boiko, Y., 860
Boman, M., 1143
Bonnot, R., 1463
Borges, C.F.M., 440
Borges, C.P., 551
Borst, T., 329
Bougdira, J., 107, 505
Bozeman, S.P., 398, 403
Bozhko, S.A., 927
Bozzolo, N., 41
Bregadze, A.Y., 89
Bremser, M.D., 191, 196
Brenn, R., 149, 654
Breskin, A., 687
Brierley, C.J., 386
Brookes, C.A., 348
Brown, W.D., 430, 952
Bruch, C., 107, 505
Brumitt, K., 390
Brunet, F., 774, 778, 843
Brylinski, C., 1405, 1428, 1508
Buchkremer-Hermanns, H., 411
Buckley-Golder, I.M., 344

Burdina, K.P., 987
Butler, J.E., 1135, 1198

Cabioch, T., 261
Calderer, J., 1555
Calliari, L., 559
Camassel, J., 1385, 1463
Cappuccio, G., 807
Carchano, H., 1568
Carlsson, J.-O., 1143
Carlsson, J.O., 85
Carter, C.H., 1400
Cassette, S., 1428
Chakk, Y., 681
Chakrabarti, K., 991
Chakrabarti, R., 991
Chalker, P.R., 333, 344, 839
Chan, S.S.M., 333, 374
Chartier, E., 1508
Chatei, H., 107, 505
Chaudhuri, S., 991
Chechik, R., 687
Chelnokov, V.E., 1480
Chen, D., 983
Cheng, T.S., 1539
Chen, Q., 1536
Chen, W.M., 1378, 1381
Chhowalla, M., 207
Chin, K.K., 940
Chourou, K., 1249
Choyke, W.J., 1243, 1333
Christiansen, K., 1467
Christiansen, S., 1467
Cimalla, V., 1311
Clavaguera-Mora, M.T., 1306
Clavaguera, N., 1306
Clement, R.E., 169
Clough, F.J., 879
Colineau, E., 778
Collaborationb, ISOLD., 1436
Collins, A.T., 516
Collins, R.W., 55
Constantinidis, G., 1459
Constant, L., 664
Contreras, S., 1329
Cooper, M.A., 1226, 1494, 1547
Corat, E.J., 472, 490, 1172
Cordery, A., 537
Correig, X., 1555
Costa, J., 1559
Couto, M.S., 975
Cremades, A., 95
Croitoru, N., 555, 1152
Cunningham, A.J., 1000

D'Evelyn, M.P., 511, 791, 812
 Dalibor, T., 1333, 1396
 Davidson, J.L., 398, 403
 Davis, R.F., 196, 1282
 Davis, T.J., 1062, 1135
 Da, Y., 673
 Day, A.R., 325
 Dedulle, J.M., 1249
 Deguchi, M., 367
 Delafond, J., 261
 Delclos, S., 758
 De Martino, C., 559
 Dementjev, A.P., 486
 Demo, P., 1092
 Demuynck, L., 235
 Deneuville, A., 516, 774, 778, 843
 Dennig, P.A., 1036
 Der Sahagian, S., 721
 Devaty, R.P., 1243, 1333
 Dezauzier, C., 1329
 Dieguez, I., 41
 Dimitrakopoulos, G.P., 1362
 Dluzniewski, M., 721
 Dmitriev, V.A., 1480, 1524, 1528, 1532
 Dominguez, M., 1555
 Donnelly, C.M., 787
 Donnelly, K., 390
 Dontas, I., 1424
 Dorignac, D., 758
 Dorsch, W., 1269
 Dowling, D.P., 390
 Doyle, J.P., 1388
 Drawl, W., 55
 Dreher, E., 830, 1129
 Dub, S.N., 574
 Dumkum, C., 802
 Dyakonov, M., 1536

Ebert, W., 329, 940
 Ecke, G., 1311
 Eckstein, R., 1269
 Edwards, N.V., 196
 Eggell, R.G., 874
 Egilsson, T., 1289
 Egret, S., 879
 Ehrhardt, H., 255, 621, 645
 Eichhorn, G., 1311
 El Felk, Z., 1306
 Ellison, A., 1272, 1289, 1369
 Eloy, R., 390
 Erler, F., 1414
 Esteve, J., 579
 Etsion, I., 381
 Everitt a, N.M., 826, 826, 826

Fabis, P.M., 191
 Falkovsky, L.A., 1385
 Fanciulli, M., 725
 Fan, Q.H., 422
 Fecht, H.J., 308, 344, 839
 Fedorin, I.A., 640
 Feldermann, H., 1129
 Fernandes, A., 769
 Ferreira, N.G., 472, 490, 1172
 Filippov, V.B., 1005

Fisgeer, B., 526, 736
 Fisher, D., 146
 Fissel, A., 1316
 Fizzotti, F., 320, 1051
 Flodström, A., 81
 Flöter, A., 298
 Flynn, D., 230
 Folman, M., 681, 736
 Fookes, A., 893
 Foord, J.S., 219, 658, 676, 869, 874
 Forkel-Wirth, D., 1436
 Förster, H., 1512
 Fourches-Coulon, N., 542
 Fox, N.A., 450, 569, 1135
 Foxon, C.T., 1539
 Franceschini, D.F., 551, 631
 Francois, N., 959
 Franke, M., 1349
 Frauenheim, T., 207
 Freire, F.L., 551
 Freire, F.L. Jr., 551
 Freitag, K., 1436
 Freudenstein, R., 584
 Friedbacher, G., 1031
 Friedrich, M., 33, 612
 Frischholz, M., 1396, 1485
 Fuchs, N., 752, 1010
 Fujimori, N., 1057
 Fukarek, W., 594
 Fukui, M., 1
 Furthmüller, J., 1346
 Fusco, G., 559, 725, 783

Galluzzi, F., 361, 712, 1564
 García, I., 1210
 Gärtner, H., 149
 Gat, R., 791
 Geddes, J., 787
 George, M.A., 398, 403
 Germi, P., 774
 Gheeraert, E., 516, 774, 778, 843
 Gilmore, A., 1062
 Gimeno, S., 604
 Girshick, S.L., 481
 Giudice, A.L., 1051
 Glotzman, O., 381, 796
 Gluche, P., 329
 Golding, B., 325
 Götz, A., 1374, 1420, 1489, 1497
 Gonon, P., 314, 860
 González, M., 856
 González Sirgo, M., 1445
 Gösele, U., 1365
 Gouzman, I., 526
 Gracio, J., 422
 Gradinaru, G., 1392
 Gradinaru, S.A., 1392
 Grant, D.M., 802
 Grasserbauer, M., 1031
 Graupner, R., 1358
 Gray, K.J., 191
 Griffith, P.W., 822
 Grillenberger, J., 1436
 Grönig, P., 282
 Groß, S., 1420
 Gross, M., 1129

Grossman, E., 687
 Gu, C., 673
 Guillot, G., 1504
 Güllich, H., 654
 Guo, W.H., 12
 Guseva, M.B., 89, 640
 Gutheit, T., 649
 Gütter, H., 649

Hahn, I.T., 959
 Hahn, J., 612, 1005
 Hakovirta, M., 694
 Hallin, C., 1289, 1297, 1369, 1378, 1381, 1485
 Halperin, G., 381
 Hammerschmidt, A., 944
 Hartmann, P., 456, 763
 Hase, N., 367
 Hashimoto, M., 1047
 Hassard, J.F., 353
 Hatanaka, Y., 1081
 Hatta, A., 717, 743, 1015, 1041
 Hattori, R., 884, 889
 Haubner, R., 240, 286, 406, 456, 494, 763
 Hayashi, K., 303
 Hayashi, Y., 1117, 1117
 Heera, V., 1432
 Heindl, J., 1269
 Heinz, K., 1349
 Heissenstein, H., 1440
 Helbig, R., 1293, 1321, 1440, 1467
 Hemer, R., 752
 Henry, A., 1289, 1369
 Herres, N., 654
 Heszler, P., 85
 Heydemann, V.D., 1262
 Hinneberg, H.-J., 1019
 Hiraki, A., 717, 743, 1015, 1041
 Hirakuri, K.K., 1031
 Hoffman, A., 381, 526, 681, 687, 736, 796
 Hofmann, D., 1269
 Hofssäss, H., 830, 1129
 Hokazono, A., 339, 865
 Hollering, M., 1358, 1451
 Holmes, D.S., 308
 Hong, B., 55
 Howard, A.S., 353
 Huang, J.T., 12
 Huant, S., 1536
 Hudson, J.B., 511, 791
 Hudson, M.D., 386
 Hug, G., 261
 Hurtós, E., 1306
 Hwang, J., 12
 Hylén, A.-L., 1456
 Hyun, S., 325

Ibach, H., 1353
 Ibarra, A., 856
 Iha, K., 490, 1172
 Imai, T., 1057
 Inushima, T., 835, 852
 Irvine, K.G., 1524
 Ishikura, T., 339
 Isoya, J., 99, 356
 Ito, T., 717, 743, 1015, 1041

Ivanov, I.G., 1289
 Iwasaki, Y., 889

Jackman, R.B., 219, 333, 374, 658, 676, 869,
 874
 Jaeger, M.D., 325
 Jäger, W., 649
 Jakšic, M., 320
 Jamieson, D., 314
 Jamieson, D.N., 860
 Janowitz, C., 1226, 1494, 1547
 Janssen, R., 1420
 Janzén, E., 1266, 1272, 1289, 1297, 1369,
 1378, 1381, 1456, 1485
 Jaouen, M., 261
 Järrendahl, K., 1282
 Jaussaud, C., 1226, 1494, 1547
 Jeon, M.H., 743
 Jian-xia, L., 673
 Jiang, N., 743, 1041
 Jin, Z., 673
 Ji, R., 48
 Johnson, J.N., 1000
 Johnson, S.E., 569
 Johnston, C., 333, 344, 839
 Jr, 551, 1400
 Jürgensen, H., 1301

Käckell, P., 1346
 Kaiser, U., 1316
 Kajimura, K., 303
 Kalaugher, E., 826, 826, 826
 Kalinina, E.V., 1528
 Kalisha, R., 516, 526, 687
 Kalomiros, J., 1226, 1494, 1547
 Kallss, W., 240
 Kaitenhäuser, M., 1436
 Kanda, H., 28, 99, 146, 356, 708
 Kang, W.P., 398, 403
 Karakostas, T., 1362
 Karasawa, S., 835
 Karuzskii, A.L., 564
 Katsikini, M., 1539
 Kawarada, H., 277, 339, 865
 Kawasaki, S., 889
 Kelly, T.C., 390
 Ke, N., 983
 Kennou, S., 1424
 Kern, R.S., 1282
 Kerns, D.V., 398, 403
 Khanolkar, A.A., 430
 Kharlashina, N.N., 172
 Khin, Y.Y., 1015
 Khomich, A.V., 417
 Khrichtchev, L.Yu., 694, 1026
 Khvostov, V.V., 89, 640
 Kiflawi, I., 146
 Kimoto, T., 1276, 1333
 Kim, S.H., 959
 Kimura, T., 1047
 Kitabatake, M., 367
 Kitagawa, M., 367
 Kittler, M., 1512
 Klages, C.-P., 293
 Klibanov, L., 1152

Klose, S., 308, 344, 839
 Klotzbücher, T., 599
 Knapper, M.P., 569
 Knap, W., 1536
 Knuyt, G., 435, 1092
 Kobashi, K., 266, 272
 Kogan, M.S., 564
 Kohly, W., 308
 Kohn, E., 329, 940
 Koide, Y., 847
 Koidl, P., 149, 654, 1111
 Kola, P.V., 390
 Kolitsch, A., 594
 Komarov, S.F., 511, 791
 Kominou, P., 1362
 Komori, M., 501
 Kondrashov, P.E., 902
 Kono, S., 463
 Konov, V.I., 417
 Konstantinov, A.O., 1297
 Konwerska-Hrabowska, J., 617
 Konyashin, I., 608
 Konyashin, I.Y., 89
 Kordina, O., 1289, 1297, 1369, 1378, 1381,
 1485
 Korony, G., 1392
 Kotera, H., 367
 Kožíšek, Z., 1092
 Krannich, G., 1005
 Kreissig, U., 626
 Kreutz, E.W., 599
 Krötz, G., 1338
 Kruger, C.H., 202, 476
 Krüger, J.K., 107, 505
 Krukowski, S., 1515
 Kuang, Y., 55
 Kühn, M., 626
 Kulisch, W., 584, 906
 Kumazawa, Y., 1057
 Kuo, K.-P., 1097
 Kupfer, H., 33
 Kurz, H., 1374, 1420, 1497
 Kusakabe, K., 668
 Küttel, O.M., 282
 Kuzmik, J., 1459
 Kuznetsov, N.I., 1528
 Kvít, A.V., 564

Labeau, M., 1249
 Lacerda, M.M., 631
 Lacher, F., 1111
 Ladas, S., 1424
 Lade, R.J., 569
 Lagrange, J.P., 516, 778
 Laimer, J., 406
 Lam, Y.W., 521, 635
 Lancin, M., 542
 Lang, A.R., 1226, 1494, 1547
 Lappalainen, R., 694, 1026, 1207
 Larson, J.M., 481
 Lash, A.A., 640
 Lassagne, P., 1226, 1494, 1547
 Laufer, S., 1019
 Lawson, S.C., 99
 Lebedev, Y.A., 224
 Leckey, R.C.G., 1358

Lee, C.S., 521, 635
 Lee, J., 55
 Lee, J.-J., 511
 Lee, J.-W., 959
 Lee, N., 130
 Lee, S.T., 635
 Leidich, D., 1365
 Leite, N.F., 472, 490, 1172
 Lempert, G.D., 687
 Le Normand, F., 235, 664
 Leonhard, C., 1489, 1497
 Leoni, M., 807
 Lévêque, G., 1463
 Leycuras, A., 1385
 Ley, L., 730, 747, 1358, 1451
 Liao, X.Z., 521
 Licht, T., 1436
 Lifshitz, Y., 687
 Lindefelt, U., 1289
 Lindner, J., 1414
 Lindsay, J.W., 481
 Lindström, J.L., 1378
 Linnarsson, M., 1293
 Lipkin, L.A., 1400
 Lippold, G., 906
 Lisicki, M., 617
 Li, X., 1117, 1117
 Lloyd, L., 390
 Loader, C.B., 822
 Locher, R., 149, 308, 654
 Loeffler, J., 608
 Loginova, O.B., 931
 Loh, K.P., 219, 874
 Lollman, D., 1568
 Lorenz, H.P., 6
 Lossy, R., 1445
 Lousa, A., 604
 Lucazeau, E., 843
 Ludena, G.M.L., 89
 Luithardt, W., 533
 Lupich, I.N., 574
 Lüpke, G., 1374
 Lu, X., 673
 Lux, B., 240, 286, 406, 456, 494, 763

Machet, J., 970
 Madar, R., 1249, 1369
 Maeda, H., 668
 Maillard-Schaller, E., 282
 Mainwood, A., 353
 Mainz, B., 1019
 Maity, A.B., 991
 Makepeace, A.P.W., 1226, 1494, 1547
 Malave, A., 906
 Malogolovets, V.G., 574
 Malov, Y., 1097
 Malshe, A.P., 430, 952
 Mambo, J., 774, 778
 Manfredotti, C., 320, 1051
 Mankelevich, Y.A., 1051
 Marek, T., 1269
 Marhic, C., 542
 Marinelli, M., 717
 Mariotto, G., 631
 Markiv, V.Ya., 927
 Marsal, L.F., 1555

Marshall, R.D., 374, 676
 Martineau, P.M., 1226, 1494, 1547
 Martinu, L., 440
 Mary, S., 1135
 Maslyuk, B.A., 574
 Matsunami, H., 1276, 1333
 Mattern, B., 1358
 Matthée, T., 293
 Matz, W., 1432
 Ma, Y., 476
 May, P.W., 247, 348, 450, 1135
 McCarty, K.F., 1219
 McColl, I.R., 802
 McCullough, R.W., 787
 McGrath, J.J., 394
 McKeag, R.D., 374
 McKenzie, D.R., 207
 Meaden, G., 893, 898
 Meaden, G.M., 822
 Medlin, D.L., 1219
 Meilunas, R.J., 1157
 Melnik, N.N., 564
 Melnik, Y., 1524, 1532
 Mendes de Barros, R.C., 472, 490, 1172
 Meng, Q., 673
 Meng, Y., 120
 Mergens, M., 599
 Messier, R., 55
 Mestres, N., 1550
 Meunier, F., 970
 Meyer, C., 1374
 Meykens, K., 435, 1092
 Michelakis, K., 1459
 Migulin, V.V., 417
 Mihalcea, C., 906
 Mikhailut, E.Y., 1106
 Milita, S., 1249, 1369
 Miller, A.J., 386
 Milne, W.I., 48, 783, 879
 Milosavljevic, I., 398, 403
 Mina, G., 559
 Mirri, K., 320
 Mitchel, W., 1392
 Mitsuda, Y., 468
 Mitsuhashi, M., 852
 Mitura, E., 721
 Mitura, S., 721
 Mityagin, Y.A., 564
 Miyata, K., 266
 Mizuochi, Y., 277
 Moelle, C., 344, 839
 Moisan, M., 440
 Mollá, J., 856
 Möller, W., 594
 Moll, J.A., 721
 Moll, J.J., 721
 Monemar, B., 1378, 1381
 Montereali, R.M., 1564
 Morita, Y., 356
 Mori, Y., 743, 1015
 Morooka, S., 668
 Morris, W.G., 791
 Mounier, E., 1182
 Mucera, G., 1051
 Müller, G., 1542
 Müller, S., 1269
 Murakami, M., 847
 Murzin, V.N., 564
 Mutsukura, N., 547
 Nagano, M., 501
 Nagasawa, H., 277
 Nakai, H., 1047
 Nakama, T., 852
 Nakamura, K., 339
 Nakamura, N., 1047
 Nakanishi, Y., 1081
 Nam, O.H., 196
 Naseem, H.A., 430, 952
 Nazaré, M.H., 769
 Nemanich, R.J., 398, 403
 Nennowitz, O., 1414
 Nesládek, M., 435, 704, 1092
 Nesteruk, I.G., 1067
 Neves, A., 769
 Nicholson b, E.D., 826, 826, 826
 Nicholson, E., 898
 Nicholson, E.D., 817, 893
 Nicholson, J., 898
 Nickel, K.G., 935
 Niedzielski, P., 721
 Niemann, E., 1365
 Nikitina, I.P., 1524, 1532
 Nikolaev, A.E., 1532
 Nishimori, T., 463
 Nishino, S., 1117, 1117
 Nishino, T., 717
 Nishitani-Gamo, M., 1036
 Nistor, L.C., 159
 Noblanc, O., 1428, 1508
 Noda, H., 865
 Nordell, N., 1293, 1388
 Nöth, H., 286
 Novikov, N.V., 574
 Novoselova, E.G., 902
 Nugent, K., 314
 Nyberg, T., 85, 224
 Obermeier, E., 1445, 1448
 Obraztsova, E.D., 159
 Obraztsov, A.N., 1124
 Oelhafen, P., 830
 Oesterschulze, E., 906
 Ogashawara, A., 835
 Ogawa, T., 1015
 Ohshima, T., 356
 Ohya, S., 835
 Okamoto, M., 1015
 Oksman, M., 1152
 Okushi, H., 303, 1124
 Oku, T., 847
 Olejniczak, W., 1081
 Olszyna, A., 617
 Opalev, O.A., 426
 Oprchal, H., 940
 Orlikovsky, A.A., 564
 Otsuki, A., 847
 Ouisse, T., 1226, 1489, 1494, 1547
 Ovuka, Z., 1476
 Owano, T.G., 202, 476
 Pace, E., 361
 Paderno, Y., 1005
 Pal, A.K., 991
 Pallarès, J., 1555
 Palmour, J.W., 1400
 Paloura, E.C., 1226, 1494, 1539, 1547
 Pang, L.Y.S., 333
 Paoletti, A., 717
 Papaioannou, V., 1362
 Parikh, N., 196
 Park, Y.S., 959
 Partridge, P.G., 893, 898
 Pascual, J., 1550
 Pauleau, Y., 1182
 Pauser, H., 406
 Pavlovsky, I.Y., 1124
 Pawłowski, S., 1081
 Pearce, T., 893
 Pécz, B., 1297, 1362, 1428
 Pekko, P., 1207
 Peng, S., 983
 Pensl, G., 1262, 1333, 1396, 1472
 Peppermüller, C., 1293, 1321, 1440
 Pereira, E., 422
 Perestorin, A.V., 564
 Pereverteilo, V.M., 931
 Pernet, M., 774
 Perry, W.G., 196
 Petukhov, M.N., 486
 Pezoldt, J., 1311, 1414
 Pfennighaus, K., 1316
 Philipp, F., 758
 Philosoph, B., 516
 Pickard, C.D.O., 1062
 Pintaske, R., 1005
 Piqueras, J., 95
 Plass, M.F., 594
 Plitzko, J., 935
 Pobol, I.L., 1067
 Pochet, T., 320
 Podzyarey, G.A., 574
 Polesello, P., 320, 1051
 Polini, R., 235
 Polo, M.C., 579, 1550
 Polushin, N.I., 987
 Polyakov, V.B., 172
 Pongratz, P., 752, 763, 1010
 Pons, M., 1249
 Prawer, S., 314, 860
 Prieur, E., 1272
 Przymusiala, P., 721
 Quaeyhaegens, C., 435, 1092
 Rackaitis, M., 1
 Radamson, H., 1369
 Radnóczki, G., 1428
 Ralchenko, V.G., 159, 417
 Ramesham, R., 17
 Räsänen, M., 694, 1026
 Rats, D., 758
 Ravindra, N.M., 1157
 Rawles, R.E., 791
 Raynaud, C., 1504
 Reece, D.M., 386

Rego, C.A., 247
 Reichert, W., 1445, 1448
 Reiß, H., 298
 Reinke, S., 584
 Reislöhner, U., 1436
 Rémy, M., 107, 505
 Ren, H., 411
 Richier, C., 1504
 Richter, F., 612, 626, 1005
 Richter, V., 516
 Richter, W., 1316
 Riley, J.D., 1358
 Ristein, J., 730
 Rittmayer, G., 944
 Rivière, J.P., 261
 Robert, J.L., 1329
 Robertson, J., 212, 255, 700, 783, 879
 Rochotzki, R., 33
 Rodríguez-Viejo, J., 1306
 Rodway, D., 658
 Romanus, H., 1414
 Ronning, C., 830, 1129
 Rosa, J., 704, 1092
 Rose, M.F., 17
 Rösler, M., 935
 Rosser, K.N., 247, 450, 569
 Rossi, M., 444
 Rossi, M.C., 361, 712, 1564
 Rössler, U., 1342
 Rottner, K., 1293, 1321, 1396
 Rottner, K.H., 1485
 Roumiguères, B., 1568
 Rüb, M., 1436
 Rusli, 700

Sachdev, H., 286, 494
 Sadowski, M.L., 1536
 Saito, T., 668
 Sakai, S., 468
 Sakamoto, H., 463
 Salvatori, S., 361, 712, 1564
 Samlenski, R., 149, 654
 Samokhvalov, N.V., 426
 Sánchez, G., 579
 Sánchez Olías, J., 1210
 Sasaki, T., 743, 1015, 1041
 Sato, Y., 99, 1036
 Sattel, S., 255
 Savage, J.A., 386, 658
 Savage, S.M., 1485
 Scardi, P., 807
 Schaarschmidt, G., 1019
 Schaefer, J.A., 1353
 Schäfer, J., 730
 Schäfer, L., 293
 Schardt, J., 1349
 Scharmann, F., 1311
 Scharnholz, S., 1497
 Scheibe, H.J., 687
 Scheib, M., 255, 645
 Schelz, S., 440
 Schilling, W., 6
 Schipanski, D., 1311, 1512
 Schlaphbach, L., 282
 Schmidt, A., 293
 Schmidt, I., 964

Schmitz, D., 1301
 Scholz, R., 1365
 Scholz, W., 906
 Schöner, A., 1293, 1321, 1388, 1396, 1485
 Schreck, M., 95, 752, 1010
 Schröter, B., 1316
 Schultrich, B., 687
 Schulze, N., 1262
 Schulz, G., 649
 Schwan, J., 645
 Schwierz, F., 1512
 Seal, M., 975
 Sebastian, M., 1129
 Seidman, A., 1152
 Sekiguchi, T., 303
 Sekita, M., 1036
 Semoto, K., 1047
 Sergeichev, K.F., 417
 Serin, V., 758
 Sessa, V., 444, 807
 Sharma, S.N., 1559
 Shatwell, R.A., 822
 Shchukarev, A.V., 1528
 Shechter, H., 736
 Shefer, E., 687
 Sheglov, M.P., 1524
 Shima, S., 367
 Shimizu, R., 272
 Shintani, Y., 266, 272
 Shiomi, H., 835
 Shipko, A.A., 1067
 Shirafuji, J., 884, 889
 Shiraishi, T., 835, 852
 Shiryaev, A.A., 172
 Shi, X., 230
 Sieber, N., 1451
 Silva, R.F., 769
 Šimůnek, A., 944
 Singh, M., 1378
 Singh, R., 1400
 Siokou, A., 1424
 Sirineni, G.M.R., 952
 Sittas, G., 146
 Skierbiszewski, C., 1536
 Skorupa, W., 1414, 1432, 1445
 Slater, D.B., 1400
 Smirnov, I.S., 902
 Smith, F.W., 153
 Smolin, A.A., 159, 417
 Snitka, V., 1
 Sokolowska, A., 721
 Somma, F., 1564
 Son, N.T., 1378, 1381
 Sörman, E., 1378, 1381
 Souw, E.-K., 1157
 Spaeth, C., 626
 Speisser, C., 235
 Spie, L., 1414
 Sridhara, S., 1333
 Srolowitz, D.J., 1198
 Stals, L.M., 435, 704, 1092
 Stammier, M., 747
 Stampfli, A.P.J., 1358
 Stanishevsky, A., 721
 Stanishevsky, A.V., 1026
 Starke, U., 1349
 Starýga, E., 721

Stauden, T., 1311
 Steeds, J.W., 1062, 1135
 Stefanov, E., 1500
 Stein von Kamienski, E., 1374, 1420
 Stein Von Kamienski, E.G., 1489, 1497
 Stenberg, G., 1143
 Stöckel, R., 747
 Stoemenos, J., 1306, 1362, 1448
 Stokes, E.B., 511
 Störi, H., 406
 Strauch, G., 1301
 Strauss, Y.E., 55
 Strelnitskij, V.E., 426
 Stritzker, B., 752, 1010
 Strunk, H.P., 747, 1269, 1467
 Sudarshan, T.S., 1392
 Suetin, N.V., 1051
 Sugino, T., 884, 889
 Sun, Y., 230
 Sun, Z., 230
 Suvorov, A.V., 1400
 Svensson, B.G., 1388
 Sychov, I.A., 417
 Syrkin, A.L., 1463, 1480
 Syväjärvi, M., 1266, 1456
 Szeles, C., 1157
 Szmidt, J., 721
 Szűcs, F., 344, 839

Tachibana, T., 266, 272
 Tadic, T., 320
 Tagliaferro, A., 559, 725, 783
 Takai, Y., 272
 Takakuwa, Y., 463
 Tanabe, K., 1057
 Tanaka, S., 1282
 Tarutani, M., 272
 Tass, Z., 255
 Tautz, F.S., 1353
 Tay, B.K., 230
 Tereshin, A.A., 1097
 Terranova, M.L., 444, 807
 Theel, T., 645
 Therin, M., 390
 Theys, B., 1226, 1494, 1547
 Thiele, J.-U., 830
 Thomas, P., 1329
 Thompson, D.J., 676
 Thorpe, M.F., 325
 Thürer, K.-H., 1010
 Tkachenko, S.D., 564
 Tong, F.-M., 1157
 Tong Lee, S., 521
 Tracey, S., 676
 Trava-Airoldi, V.J., 472, 490, 1172
 Tsang, R.S., 247
 Tsong, T.T., 55
 Tsuno, T., 1057
 Tsuruga, S., 668
 Tucciarone, A., 717
 Tuominen, M., 1272, 1369, 1456
 Tuomi, T., 1272, 1369
 Turban, G., 542

Ubhi, H.S., 822
 Uhlig, H., 608

Uhrmacher, M., 1436
 Ulcinas, A., 1
 Ulrich, S., 621, 645
 Urasaki, T., 501
 Urban, K., 649
 Utsch, J., 411
 Uzan-Saguy, C., 516

Vackář, J., 944
 Vandenbulcke, L., 758
 Vandevelde, T., 435
 Vaněček, M., 704, 1092
 van Enckevort, W.J.P., 975
 Van Landuyt, J., 159
 Vanzetti, L., 559
 Vasquez, S., 551
 Vázquez, A.J., 1210
 Vehanen, A., 1272
 Verhoeven, H., 298
 Vescan, A., 329
 Viera, G., 1559
 Vila, R., 856
 Vittone, E., 320, 1051
 Vlasov, I.I., 417
 Voellmar, S., 687
 Volchkov, N.A., 564
 Volkov, Y.Y., 426
 Vorliček, V., 704
 Voronina, S.V., 417
 Voronkin, M.A., 574

Wächter, R., 537
 Wagner, C., 1338
 Wahl, E.H., 476
 Wakiyama, K., 501
 Wang, L.C., 743
 Wang, W.L., 579
 Wang, W.N., 569, 1062, 1135
 Wang, X., 230
 Ward, B.L., 398, 403

Watanabe, H., 303, 1124
 Watanabe, K., 99, 708, 1036
 Watanabe, T., 852
 Weeks, J.R., 817
 Wei, A., 983
 Weill, N., 390
 Weishart, H., 1414, 1432
 Weiss, H., 411
 Wellenhofer, G., 1342
 Welzel, T., 33
 Werner, M., 308, 344, 839
 Werninghaus, T., 612, 1019
 Wesner, D.A., 599
 White, M., 394
 Whitfield, M.D., 658, 676
 Wickramanayaka, S., 1081
 Widmayer, P., 621
 Wiech, G., 944
 Wiescher, D., 255
 Wild, C., 1111
 Winnacker, A., 1269
 Wisbey, A., 822, 898
 Wischmeyer, F., 1365
 Witthuhn, W., 1436
 Wittig, J., 398, 403
 Wittorf, D., 649
 Woelk, E.G., 1301
 Wong, K.W., 635
 Wong, S.P., 983
 Won, J., 1041
 Won, J.H., 743
 Woo, H.K., 635
 Wróbel, A.M., 1081
 Wurzinger, P., 752, 763

Xiu-di, S., 673

Yagi, H., 1041
 Yakimova, R., 1266, 1272, 1369, 1456
 Yamamoto, K., 1036

Yamamoto, Y., 1057
 Yamanaka, S., 303
 Yamashita, S., 339
 Yang, B.X., 153
 Yang, G.S., 394
 Yin, Y., 207
 Yin, Z., 153
 Yokoba, M., 847
 Yokota, Y., 266
 Yoon, S.F., 48
 Yoshida, K.-i., 547
 Yoshii, M., 1031
 Younes, C.M., 450
 Young, J., 1536
 Yugo, S., 1047
 Yun, W.S., 959
 Yu, Z., 81

Zachai, R., 298, 649
 Zahn, D.R.T., 33, 612, 1019
 Zak, J., 721
 Zalicki, P., 476
 Zanghellini, E., 551
 Zare, R.N., 476
 Zarabian, M., 542
 Zekentes, K., 1362
 Zgongc, K., 812
 Zhang, L.Y., 348
 Zhang, R.J., 521
 Zhang, R.Q., 589, 1559
 Zhang, Y., 635
 Zhao, M., 202
 Zheleva, T., 196
 Zheng, Z., 230
 Zhong-de, X., 673
 Zhou, G., 272
 Zhuk, A.Z., 640
 Ziegler, A., 1358
 Ziemann, P., 621
 Zou, G., 673
 Zukauskas, D., 1



ELSEVIER

Subject Index

2-D numerical analysis
Numerical study of avalanche breakdown of 6H-SiC planar *p-n* junctions, 1500

3C-SiC heteroepitaxy
Optical investigation of thick 3C-SiC layers deposited on bulk silicon by CVD, 1385

4H-SiC
Growth-related structural defects in seeded sublimation-grown SiC, 1272
High quality 4H-SiC grown on various substrate orientations, 1289

4H silicon carbide
Radiation-induced defect centers in 4H silicon carbide, 1333

6H-, 4H-SiC
Hydrogen incorporation in epitaxial layers of 4H- and 6H-silicon carbide grown by vapor phase epitaxy, 1293

6H-SiC
Growth-related structural defects in seeded sublimation-grown SiC, 1272
Angle resolved photoemission and the band structure of 6H-SiC, 1358
OBIC studies on 6H-SiC Schottky rectifiers with different surface pretreatments, 1396
Temperature dependence of electrical properties of 6H-SiC buried gate JFET, 1504

a-Axis
High quality 4H-SiC grown on various substrate orientations, 1289

A-SiC
Low frequency noise in silicon carbide Schottky diodes, 1494
Surface and bulk effects in ex-situ hydrogenated α -SiC thin films, 1547

Al-, B-doping
Hydrogen incorporation in epitaxial layers of 4H- and 6H-silicon carbide grown by vapor phase epitaxy, 1293

Aluminum nitride
Growth and doping via gas-source molecular beam epitaxy of SiC and SiC/AlN heterostructures and their microstructural and electrical characterization, 1282

Amorphous III-V semiconductors
Amorphous GaAs_{1-x}N_x thin films on crystalline Si substrates: growth and characterizations, 1568

Amorphous semi-conductors
Colour sensing applications of hydrogenated amorphous silicon carbide, 1542

Amorphous silicon-carbon alloys
Electrical properties of PECVD amorphous silicon-carbon alloys from amorphous-crystalline heterojunctions, 1555

Atomic force microscopy
Aluminium implantation of *p*-SiC for ohmic contacts, 1414

Atomic structure
Investigation of modified 3C SiC(100) surfaces by surface-sensitive techniques, 1353

Band structure
Progress in the study of optical and related properties of SiC since 1992, 1243

Bending
Wafer warpage, crystal bending and interface properties of 4H-SiC epi-wafers, 1369

Bidimensional electron gas
Contactless characterisation of 2D-electrons in GaN/AlGaN HFETs, 1536

BN films
Optical study of boron nitride thin films prepared by plasma-enhanced chemical vapor deposition, 1550

Bonded SOI
 β -SiC films on SOI substrates for high temperature applications, 1448

Boron
Hydrogen-, boron-, and hydrogen-boron-related low temperature photoluminescence of 6H-SiC, 1321

Breakdown voltage
Numerical study of avalanche breakdown of 6H-SiC planar *p-n* junctions, 1500

Buffer layer
Residual strains in GaN grown on 6H-SiC, 1524

c-Axis
High quality 4H-SiC grown on various substrate orientations, 1289

C/Si ratio dependance
Surface polarity dependence in step-controlled epitaxy: progress in SiC epitaxy, 1276

Carbon cluster model
“Carbon cluster model” for electronic states at SiC/SiO₂ interfaces, 1472

Carbonization
Micropipe defects and voids at β -SiC/Si(100) interfaces, 1365

Carrier density of *p* SiC
Valence band dispersion of hexagonal SiC, 1342

Chemical
Preferential etching of SiC crystals, 1456

Chemical bonding
Investigation of modified 3C SiC(100) surfaces by surface-sensitive techniques, 1353

CMOS
SiC device technology: remaining issues, 1400

Colour sensors
Colour sensing applications of hydrogenated amorphous silicon carbide, 1542

Contactless characterisation
Contactless characterisation of 2D-electrons in GaN/AlGaN HFETs, 1536

Crystal growth
Thermodynamics and high-pressure growth of (Al, Ga, In)N single crystals, 1515

Cubic polytypes
Identification of the cubic and hexagonal polytypes of GaN with X-ray absorption measurements, 1539

CVD diamond
Emission and excitation spectra of silicon-related luminescent centers in CVD-grown diamond films, 1564

Cyclotron resonance
 Contactless characterisation of 2D-electrons in GaN/AlGaN HFETs, 1536

Deep levels
 Deep luminescent centres in electron-irradiated 6H SiC, 1378
 Characterization of electrically active deep level defects in 4H and 6H SiC, 1388

Deep level transient spectroscopy
 Radiation-induced defect centers in 4H silicon carbide, 1333

Defect centers
 Emission and excitation spectra of silicon-related luminescent centers in CVD-grown diamond films, 1564

Defects
 Defects formation in sublimation grown 6H-SiC single crystal boules, 1249
 Deep luminescent centres in electron-irradiated 6H SiC, 1378
 Optically detected magnetic resonance studies of defects in 3C SiC epitaxial layers, 1381
 Characterization of electrically active deep level defects in 4H and 6H SiC, 1388
 Preferential etching of SiC crystals, 1456

Density of interface states
 "Carbon cluster model" for electronic states at SiC/SiO₂ interfaces, 1472

Density of states
 Electrical properties of PECVD amorphous silicon–carbon alloys from amorphous–crystalline heterojunctions, 1555

Device modeling
 The potential of SiC and GaN for application in high speed devices, 1512

Diodes
 2.5 kV ion-implanted p^+n diodes in 6H-SiC, 1485

Dissolution
 Growth of SiC from the liquid phase: wetting and dissolution of SiC, 1266

DLTS
 Characterization of electrically active deep level defects in 4H and 6H SiC, 1388

Drift
 Investigation of walk-out phenomena in SiC mesa diodes with SiO₂/Si₃N₄ passivation, 1476

Effective masses
 Progress in the study of optical and related properties of SiC since 1992, 1243

Effective Richardson coefficient
 Structural and electrical properties of Schottky barriers on n-GaN, 1528

Electrical activation
 Investigation of the effects of high temperature implantation and post implantation annealing on the electrical behavior of nitrogen implanted β -SiC films, 1445

Electrical noise
 Low frequency noise in silicon carbide Schottky diodes, 1494
 Surface and bulk effects in ex-situ hydrogenated α -SiC thin films, 1547

Electronic band structure
 Valence band dispersion of hexagonal SiC, 1342

Electronic field
 High field/high temperature performance of semi-insulating silicon carbide, 1392

Electronic states
 Angle resolved photoemission and the band structure of 6H-SiC, 1358

Electron irradiation
 Deep luminescent centres in electron-irradiated 6H SiC, 1378

Electron microscopy
 Micropipe defects and voids at β -SiC/Si(100) interfaces, 1365
 TEM study of Ni and Ni₂Si ohmic contacts to SiC, 1428

Ellipsometry
 Low frequency noise in silicon carbide Schottky diodes, 1494
 Surface and bulk effects in ex-situ hydrogenated α -SiC thin films, 1547

Epitaxial β -SiC
 Topology of twin junctions in epitaxial β -SiC, 1362

Epitaxial layer uniformity
 Optical investigation of thick 3C-SiC layers deposited on bulk silicon by CVD, 1385

Epitaxy
 The origin of 3C polytype inclusions in epitaxial layers of silicon carbide grown by chemical vapour deposition, 1297
 Structural properties of GaN grown on SiC substrates by hydride vapor phase epitaxy, 1532

Etching
 Preferential etching of SiC crystals, 1456
 Low frequency noise in silicon carbide Schottky diodes, 1494
 Surface and bulk effects in ex-situ hydrogenated α -SiC thin films, 1547

Experiments
 Progress in the study of optical and related properties of SiC since 1992, 1243

Extended crystalline defects
 Sublimation growth of 4H- and 6H-SiC boule crystals, 1262

First principles calculation
 Polyytypism and surface structure of SiC, 1346

Floating ring
 Numerical study of avalanche breakdown of 6H-SiC planar $p-n$ junctions, 1500

Fowler–Nordheim injection
 High field and high temperature stress of n-SiC MOS capacitors, 1489

GaAs_{1-x}N_x thin films
 Amorphous GaAs_{1-x}N_x thin films on crystalline Si substrates: growth and characterizations, 1568

Gallium nitride
 Residual strains in GaN grown on 6H-SiC, 1524

Gallium nitrides
 Structural properties of GaN grown on SiC substrates by hydride vapor phase epitaxy, 1532

GaN
 Structural and electrical properties of Schottky barriers on n-GaN, 1528
 Identification of the cubic and hexagonal polytypes of GaN with X-ray absorption measurements, 1539

GaN/GaAlN heterostructures
 Contactless characterisation of 2D-electrons in GaN/AlGaN HFETs, 1536

Gate oxide
 Passivation of interface traps in MOS-Devices on n - and p -type 6H-SiC, 1497

β -SiC
 Investigation of the effects of high temperature implantation and post implantation annealing on the electrical behavior of nitrogen implanted β -SiC films, 1445

β -SiC; Hall effect; High temperature
 Analysis of transport properties of β -SiC films: determination of donor density and compensation ratio, 1329

β -SiC on SOI
 β -SiC films on SOI substrates for high temperature applications, 1448

GH-SiC, p–n junction
 Numerical study of avalanche breakdown of 6H-SiC planar $p-n$ junctions, 1500

Glow discharge
Effects of thermal and laser annealing on silicon carbide nanopowder produced in radio frequency glow discharge, 1559

Growth
Growth of SiC from the liquid phase: wetting and dissolution of SiC, 1266

Growth model
The kinetic growth model applied to micropipes in 6H-SiC, 1269

Hafnium
Hafnium, cadmium and indium impurities in 4H-SiC observed by perturbed angular correlation spectroscopy, 1436

Heat diffusion
Thermal properties of β -SiC epitaxial layers between 150 °C and 500 °C measured by using microstructures, 1338

Heterojunction
Electrical properties of PECVD amorphous silicon–carbon alloys from amorphous–crystalline heterojunctions, 1555

Hexagonal polytypes
Identification of the cubic and hexagonal polytypes of GaN with X-ray absorption measurements, 1539

High resistivity
Amorphous $\text{GaAs}_{1-x}\text{N}_x$ thin films on crystalline Si substrates: growth and characterizations, 1568

High speed devices
The potential of SiC and GaN for application in high speed devices, 1512

High temperature
Thermal properties of β -SiC epitaxial layers between 150 °C and 500 °C measured by using microstructures, 1338
 β -SiC films on SOI substrates for high temperature applications, 1448

High temperature nitrogen implantation
Investigation of the effects of high temperature implantation and post implantation annealing on the electrical behavior of nitrogen implanted β -SiC films, 1445

Hydrogen
Hydrogen-, boron-, and hydrogen-boron-related low temperature photoluminescence of 6H-SiC, 1321

Hydrogenation
Low frequency noise in silicon carbide Schottky diodes, 1494
Surface and bulk effects in ex-situ hydrogenated α -SiC thin films, 1547

Hydrogen incorporation
Hydrogen incorporation in epitaxial layers of 4H- and 6H-silicon carbide grown by vapor phase epitaxy, 1293

III–V nitrides
Thermodynamics and high-pressure growth of (Al, Ga, In)N single crystals, 1515

Impact-ionization
High field and high temperature stress of n-SiC MOS capacitors, 1489

Implantation
Ion beam assisted deposition of a tungsten compound layer on 6H-silicon carbide, 1432
Hafnium, cadmium and indium impurities in 4H-SiC observed by perturbed angular correlation spectroscopy, 1436

Interface
Wafer warpage, crystal bending and interface properties of 4H-SiC epi-wafers, 1369
Structural and electrical properties of Schottky barriers on n-GaN, 1528

Interfacial connectivity
Topology of twin junctions in epitaxial β -SiC, 1362

Ion implantation
SiC device technology: remaining issues, 1400
2.5 kV ion-implanted p^+n diodes in 6H-SiC, 1485

JFET
Temperature dependence of electrical properties of 6H-SiC buried gate JFET, 1504

Junction termination extensions
Numerical study of avalanche breakdown of 6H-SiC planar $p-n$ junctions, 1500

Kinetics
Growth and doping via gas-source molecular beam epitaxy of SiC and SiC/AlN heterostructures and their microstructural and electrical characterization, 1282

Laser annealing
Effects of thermal and laser annealing on silicon carbide nanopowder produced in radio frequency glow discharge, 1559

Lattice constant
Residual strains in GaN grown on 6H-SiC, 1524

Liquid phase
Growth of SiC from the liquid phase: wetting and dissolution of SiC, 1266

Liquid phase epitaxy
Overview of SiC power electronics, 1480

Low-energy electron diffraction
Structure and morphology of SiC surfaces studied by LEED, AES, HREELS and STM, 1349

Low temperature photoluminescence
Radiation-induced defect centers in 4H silicon carbide, 1333

LPCVD
Growth of SiC films obtained by LPCVD, 1306

Mesa diodes
Investigation of walk-out phenomena in SiC mesa diodes with $\text{SiO}_2/\text{Si}_3\text{N}_4$ passivation, 1476

MESFET
Microwave Power MESFET on 4H-SiC, 1508
The potential of SiC and GaN for application in high speed devices, 1512

Metal–organic precursors
Growth of SiC films obtained by LPCVD, 1306

Metal-oxide–semiconductor
High field and high temperature stress of n-SiC MOS capacitors, 1489

Metallization
Aluminium implantation of p -SiC for ohmic contacts, 1414

Micro analysis systems
Colour sensing applications of hydrogenated amorphous silicon carbide, 1542

Micropipes
The kinetic growth model applied to micropipes in 6H-SiC, 1269
Micropipe defects and voids at β -SiC/Si(100) interfaces, 1365
SiC device technology: remaining issues, 1400

Microtwins development
Growth of SiC films obtained by LPCVD, 1306

Microwave power
Silicon carbide for microwave power applications, 1405

MIS structures
Amorphous $\text{GaAs}_{1-x}\text{N}_x$ thin films on crystalline Si substrates: growth and characterizations, 1568

Mobility
Temperature dependence of electrical properties of 6H-SiC buried gate JFET, 1504

MOCVD
SiC and group III nitride growth in MOVPE production reactors, 1301

Modelling
SiC and group III nitride growth in MOVPE production reactors, 1301

Molecular beam epitaxy
Growth and doping via gas-source molecular beam epitaxy of SiC

and SiC/AlN heterostructures and their microstructural and electrical characterization, 1282

Chemical conversion of Si to SiC by solid source MBE and RTCVD, 1311

Hexagonal and cubic SiC thin films on SiC deposited by solid source MBE, 1316

Morphology
Growth of SiC from the liquid phase: wetting and dissolution of SiC, 1266

Structure and morphology of SiC surfaces studied by LEED, AES, HREELS and STM, 1349

MOS-structure
“Carbon cluster model” for electronic states at SiC/SiO₂ interfaces, 1472

MOSFET
Passivation of interface traps in MOS-Devices on *n*- and *p*-type 6H-SiC, 1497

Nanoparticles
Effects of thermal and laser annealing on silicon carbide nanopowder produced in radio frequency glow discharge, 1559

Nitride
SiC and group III nitride growth in MOVPE production reactors, 1301

Nitrogen donors
Sublimation growth of 4H- and 6H-SiC boule crystals, 1262

Nondestructive testing
Nonlinear optical mapping of 3C-inclusions in 6H-SiC-epilayers, 1374

OBIC
OBIC studies on 6H-SiC Schottky rectifiers with different surface pretreatments, 1396

2.5 kV ion-implanted *p*⁺*n* diodes in 6H-SiC, 1485

ODMR
Optically detected magnetic resonance studies of defects in 3C SiC epitaxial layers, 1381

Ohmic contact
Aluminium implantation of *p*-SiC for ohmic contacts, 1414

Ohmic contacts
TEM study of Ni and Ni₂Si ohmic contacts to SiC, 1428

Optoelectronics
Thermodynamics and high-pressure growth of (Al, Ga, In)N single crystals, 1515

Colour sensing applications of hydrogenated amorphous silicon carbide, 1542

Oxide interface
SiC device technology: remaining issues, 1400

Oxide passivation
Investigation of walk-out phenomena in SiC mesa diodes with SiO₂/Si₃N₄ passivation, 1476

PAC
Hafnium, cadmium and indium impurities in 4H-SiC observed by perturbed angular correlation spectroscopy, 1436

Passivation
Passivation of interface traps in MOS-Devices on *n*- and *p*-type 6H-SiC, 1497

Phosphorous
Nuclear transmutation doping of 6H-silicon carbide with phosphorous, 1440

Photoelectron spectroscopy
Angle resolved photoemission and the band structure of 6H-SiC, 1358

Surface chemistry of 6H-SiC(0001̄) after reactive ion etching, 1451

Photoluminescence
High quality 4H-SiC grown on various substrate orientations, 1289

Hydrogen-, boron-, and hydrogen-boron-related low temperature photoluminescence of 6H-SiC, 1321

Deep luminescent centres in electron-irradiated 6H SiC, 1378

Optically detected magnetic resonance studies of defects in 3C SiC epitaxial layers, 1381

Nuclear transmutation doping of 6H-silicon carbide with phosphorous, 1440

Emission and excitation spectra of silicon-related luminescent centers in CVD-grown diamond films, 1564

Planar defects
Topology of twin junctions in epitaxial β-SiC, 1362

pn-junction
Nuclear transmutation doping of 6H-silicon carbide with phosphorous, 1440

Polarized IR reflection spectroscopy
Optical study of boron nitride thin films prepared by plasma-enhanced chemical vapor deposition, 1550

Poly-SiC
Growth of SiC films obtained by LPCVD, 1306

Polytypism
Chemical conversion of Si to SiC by solid source MBE and RTCVD, 1311

Post implantation annealing
Investigation of the effects of high temperature implantation and post implantation annealing on the electrical behavior of nitrogen implanted β-SiC films, 1445

Powder
Effects of thermal and laser annealing on silicon carbide nanopowder produced in radio frequency glow discharge, 1559

Power and microwave characteristics
Microwave Power MESFET on 4H-SiC, 1508

Power semiconductor devices
Overview of SiC power electronics, 1480

Pre-deposition processing
Fabrication of high-quality oxides on SiC by remote PECVD, 1420

Preferential
Preferential etching of SiC crystals, 1456

Radiation-induced deep defect centers
Radiation-induced defect centers in 4H silicon carbide, 1333

Reactive ion etching
Surface chemistry of 6H-SiC(0001̄) after reactive ion etching, 1451

Schottky contact investigation on reactive ion etched 6H α-SiC, 1459

Reflection high energy electron diffraction
Chemical conversion of Si to SiC by solid source MBE and RTCVD, 1311

Remote PECVD
Fabrication of high-quality oxides on SiC by remote PECVD, 1420

Residual strains
Residual strains in GaN grown on 6H-SiC, 1524

Resistivity
High field/high temperature performance of semi-insulating silicon carbide, 1392

Review
Progress in the study of optical and related properties of SiC since 1992, 1243

R.f. Plasma CVD
Optical study of boron nitride thin films prepared by plasma-enhanced chemical vapor deposition, 1550

Rhenium
An interface study of vapor-deposited rhenium with the two (0001) polar faces of single crystal 6H-SiC, 1424

RIE
 Comparative investigation of ECR-RIE patterns on Si and C faces of 6H-SiC using a CF₄/O₂ gas mixture, 1463

Roughness
 Optical investigation of thick 3C-SiC layers deposited on bulk silicon by CVD, 1385

Rutherford backscattering spectrometry
 Anisotropic oxidation of silicon carbide, 1467

Scanning force microscopy
 The kinetic growth model applied to micropipes in 6H-SiC, 1269

Schottky barrier
 Structural and electrical properties of Schottky barriers on n-GaN, 1528

Schottky contacts
 OBIC studies on 6H-SiC Schottky rectifiers with different surface pretreatments, 1396
 Schottky contact investigation on reactive ion etched 6H α -SiC, 1459

Schottky diode
 Low frequency noise in silicon carbide Schottky diodes, 1494
 Surface and bulk effects in ex-situ hydrogenated α -SiC thin films, 1547

Schottky diodes
 SiC device technology: remaining issues, 1400

Second harmonic generation
 Nonlinear optical mapping of 3C-inclusions in 6H-SiC-epilayers, 1374

SiC
 The origin of 3C polytype inclusions in epitaxial layers of silicon carbide grown by chemical vapour deposition, 1297
 SiC and group III nitride growth in MOVPE production reactors, 1301
 Hydrogen-, boron-, and hydrogen-boron-related low temperature photoluminescence of 6H-SiC, 1321
 Thermal properties of β -SiC epitaxial layers between 150 C and 500 C measured by using microstructures, 1338
 Deep luminescent centres in electron-irradiated 6H SiC, 1378
 SiC device technology: remaining issues, 1400
 Nuclear transmutation doping of 6H-silicon carbide with phosphorous, 1440
 Preferential etching of SiC crystals, 1456
 Comparative investigation of ECR-RIE patterns on Si and C faces of 6H-SiC using a CF₄/O₂ gas mixture, 1463
 Passivation of interface traps in MOS-Devices on *n*- and *p*-type 6H-SiC, 1497

SiC; Bound excitation; Time resolved; Minority carrier lifetimes
 SiC, studied by time resolved photoluminescence spectroscopy, 1324

SiC/SiO₂-interface
 "Carbon cluster model" for electronic states at SiC/SiO₂ interfaces, 1472

SiCOI
 β -SiC films on SOI substrates for high temperature applications, 1448

SiC polytypes
 Sublimation growth of 4H- and 6H-SiC boule crystals, 1262

SiC thin films
 Optically detected magnetic resonance studies of defects in 3C SiC epitaxial layers, 1381

SiC vapor phase epitaxy
 Hydrogen incorporation in epitaxial layers of 4H- and 6H-silicon carbide grown by vapor phase epitaxy, 1293

Silicon carbide
 Progress in the study of optical and related properties of SiC since 1992, 1243
 Defects formation in sublimation grown 6H-SiC single crystal boules, 1249

Growth of SiC from the liquid phase: wetting and dissolution of SiC, 1266
 Growth and doping via gas-source molecular beam epitaxy of SiC and SiC/AlN heterostructures and their microstructural and electrical characterization, 1282
 Chemical conversion of Si to SiC by solid source MBE and RTCVD, 1311
 Hexagonal and cubic SiC thin films on SiC deposited by solid source MBE, 1316
 Polytypism and surface structure of SiC, 1346
 Structure and morphology of SiC surfaces studied by LEED, AES, HREELS and STM, 1349
 Micropipe defects and voids at β -SiC/Si(100) interfaces, 1365
 High field/high temperature performance of semi-insulating silicon carbide, 1392
 Silicon carbide for microwave power applications, 1405
 Fabrication of high-quality oxides on SiC by remote PECVD, 1420
 An interface study of vapor-deposited rhenium with the two (0001) polar faces of single crystal 6H-SiC, 1424
 TEM study of Ni and Ni₂Si ohmic contacts to SiC, 1428
 Ion beam assisted deposition of a tungsten compound layer on 6H-silicon carbide, 1432
 Hafnium, cadmium and indium impurities in 4H-SiC observed by perturbed angular correlation spectroscopy, 1436
 Surface chemistry of 6H-SiC(0001) after reactive ion etching, 1451
 Schottky contact investigation on reactive ion etched 6H α -SiC, 1459
 Anisotropic oxidation of silicon carbide, 1467
 Overview of SiC power electronics, 1480
 High field and high temperature stress of n-SiC MOS capacitors, 1489
 Low frequency noise in silicon carbide Schottky diodes, 1494
 Microwave Power MESFET on 4H-SiC, 1508
 Surface and bulk effects in ex-situ hydrogenated α -SiC thin films, 1547
 Effects of thermal and laser annealing on silicon carbide nanopowder produced in radio frequency glow discharge, 1559

SIMS
 Characterization of electrically active deep level defects in 4H and 6H SiC, 1388

Space-charge limited current
 Electrical properties of PECVD amorphous silicon–carbon alloys from amorphous–crystalline heterojunctions, 1555

Spin orbit interaction
 Valence band dispersion of hexagonal SiC, 1342

Stacking fault
 The origin of 3C polytype inclusions in epitaxial layers of silicon carbide grown by chemical vapour deposition, 1297

Step-controlled epitaxy
 Surface polarity dependence in step-controlled epitaxy: progress in SiC epitaxy, 1276

Step bunching
 Surface polarity dependence in step-controlled epitaxy: progress in SiC epitaxy, 1276

Strain relaxation
 Optical investigation of thick 3C–SiC layers deposited on bulk silicon by CVD, 1385

Stress
 Residual strains in GaN grown on 6H-SiC, 1524

Structural properties
 Structural properties of GaN grown on SiC substrates by hydride vapor phase epitaxy, 1532

Sublimation
 Growth-related structural defects in seeded sublimation-grown SiC, 1272

Sublimation growth
 Sublimation growth of 4H- and 6H-SiC boule crystals, 1262

Substrates
 Structural properties of GaN grown on SiC substrates by hydride vapor phase epitaxy, 1532

Surface characterization
 Investigation of modified 3C SiC(100) surfaces by surface-sensitive techniques, 1353

Surface energy
 Growth of SiC from the liquid phase: wetting and dissolution of SiC, 1266

Surface morphology
 Comparative investigation of ECR-RIE patterns on Si and C faces of 6H-SiC using a CF₄/O₂ gas mixture, 1463

Surface polarity dependence
 Surface polarity dependence in step-controlled epitaxy: progress in SiC epitaxy, 1276

Surface pretreatment
 OBIC studies on 6H-SiC Schottky rectifiers with different surface pretreatments, 1396

Surface structure
 Polyytypism and surface structure of SiC, 1346
 Structure and morphology of SiC surfaces studied by LEED, AES, HREELS and STM, 1349

Synchrotron radiation
 Defects formation in sublimation grown 6H-SiC single crystal boules, 1249

Synchrotron X-ray photography
 Growth-related structural defects in seeded sublimation-grown SiC, 1272

TEM
 Optical study of boron nitride thin films prepared by plasma-enhanced chemical vapor deposition, 1550

Temperature
 High field/high temperature performance of semi-insulating silicon carbide, 1392

Temperature dependence
 Temperature dependence of electrical properties of 6H-SiC buried gate JFET, 1504

Termination
 2.5 kV ion-implanted p^+n diodes in 6H-SiC, 1485

Theory
 Polyytypism and surface structure of SiC, 1346

Thermal annealing
 Effects of thermal and laser annealing on silicon carbide nanopowder produced in radio frequency glow discharge, 1559

Thermal conductivity
 Thermal properties of β -SiC epitaxial layers between 150 C and 500 C measured by using microstructures, 1338

Thermal oxidation
 Fabrication of high-quality oxides on SiC by remote PECVD, 1420
 Anisotropic oxidation of silicon carbide, 1467

Thermal stability
 Radiation-induced defect centers in 4H silicon carbide, 1333

Thermodynamics
 Thermodynamics and high-pressure growth of (Al, Ga, In)N single crystals, 1515

Thin films
 Nonlinear optical mapping of 3C-inclusions in 6H-SiC-epilayers, 1374

Thyristors
 SiC device technology: remaining issues, 1400

Topography
 Wafer warpage, crystal bending and interface properties of 4H-SiC epi-wafers, 1369

Transmission electron microscopy
 Aluminium implantation of p -SiC for ohmic contacts, 1414
 Anisotropic oxidation of silicon carbide, 1467

Transmission electron microscopy (TEM)
 The origin of 3C polytype inclusions in epitaxial layers of silicon carbide grown by chemical vapour deposition, 1297

Transport mechanisms
 Electrical properties of PECVD amorphous silicon-carbon alloys from amorphous-crystalline heterojunctions, 1555

Tungsten Carbide
 Ion beam assisted deposition of a tungsten compound layer on 6H-silicon carbide, 1432

Vacancy complexes
 Deep luminescent centres in electron-irradiated 6H SiC, 1378

Vibrational spectroscopy
 Investigation of modified 3C SiC(100) surfaces by surface-sensitive techniques, 1353

Walk-out
 Investigation of walk-out phenomena in SiC mesa diodes with SiO₂/Si₃N₄ passivation, 1476

Wetting
 Growth of SiC from the liquid phase: wetting and dissolution of SiC, 1266

Wide band gap semiconductors
 The potential of SiC and GaN for application in high speed devices, 1512

Work function
 An interface study of vapor-deposited rhenium with the two (0001) polar faces of single crystal 6H-SiC, 1424

X-Ray absorption
 Identification of the cubic and hexagonal polytypes of GaN with X-ray absorption measurements, 1539

X-ray diffraction
 Wafer warpage, crystal bending and interface properties of 4H-SiC epi-wafers, 1369

X-ray photoelectron spectroscopy
 An interface study of vapor-deposited rhenium with the two (0001) polar faces of single crystal 6H-SiC, 1424